ISSN 0288-4534
CODEN: KONAE7

KONA Powder and Particle Journal

No.29 (2011)

Published by Hosokawa Powder Technology Foundation

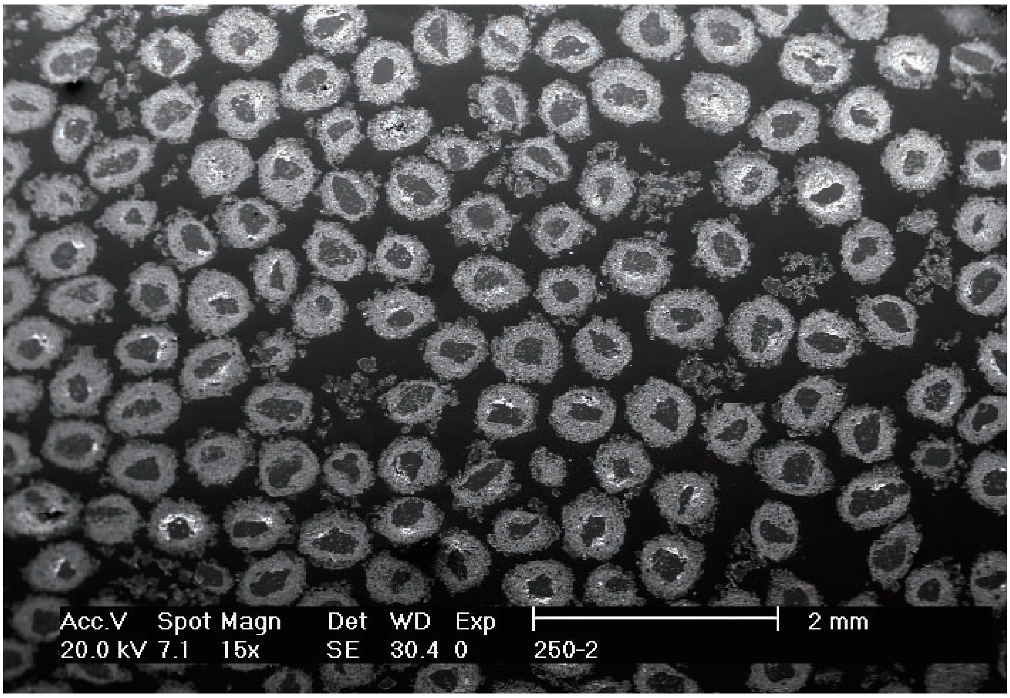

available online – www.kona.or.jp

KONA Powder and Particle Journal

http://www.kona.or.jp

KONA is a refereed scientific journal that publishes articles on powder and particle sciences and technology. KONA has been published annually since 1983 in Japan. KONA is distributed to researchers, members of the scientific community, universities and research libraries throughout the world.

About the Cover of Journal "KONA"

The Chinese character "粉" is pronounced "KONA" in Japanese, and means "Powder". The hand written "粉" is after the late Mr. Eiichi Hosokawa, founder of the Hosokawa Micron Corporation.

Headquarters of Hosokawa Micron Corporation

Editorial Board

Y. Tsuji	Editor-in-Chief (Professor Emeritus of Osaka Univ., JAPAN)

Asia / Oceania Editorial Board

H. Emi	(Professor Emeritus of Kanazawa Univ., JAPAN)
Y. Fukumori	(Kobe Gakuin Univ., JAPAN)
J. Hidaka	(Doshisha Univ., JAPAN)
K. Higashitani	(Kyoto Univ., JAPAN)
Y. Kang	(Chungnam National Univ., KOREA)
Y. Kousaka	(Professor Emeritus of Osaka Prefecture Univ., JAPAN)
J. Li	(Chinese Academy of Science)
H. Masuda	(Professor Emeritus of Kyoto Univ., JAPAN)
M. Naito	(Osaka Univ., JAPAN)
K. Nogi	(Osaka Univ., JAPAN)
Pradip	(Tata Research Development and Design Centre)
M. Rhodes	(Monash Univ., AUSTRALIA)
M. Takahashi	(Nagoya Institute of Technology, JAPAN)
W. Tanthapanichakoon	(National Science and Technology Development Agency, THAILAND)
Secretariat	
T. Yokoyama	(Hosokawa Powder Technology Foundation, JAPAN)

Europe / Africa Editorial Board

M. Ghadiri	Chairman (Univ. of Leeds, UNITED KINGDOM)
B. Biscans	(Univ. de Toulouse, FRANCE)
N.Z. Lyakhov	(Institute of Solid State Chemistry, RUSSIA)
J. Marijnissen	(Univ. of Delft, NETHERLANDS)
W. Peukert	(Univ. Erlangen, GERMANY)
S.E. Pratsinis	(ETH Züich, SWITZERLAND)
Secretariat	
P. Krubeck	(Hosokawa Alpine AG, GERMANY)
J. Stein	(Hosokawa Alpine AG, GERMANY)

American Editorial Board

B.M. Moudgil	Chairman (Univ. of Florida., U.S.A.)
D.W. Fuerstenau	Vice Chairman (Univ. of California, U.S.A.)
F. Concha	(Univ. of Concepció, CHILE)
R. Flagan	(California Institute of Technology, U.S.A.)
A.I. Hickey	(Univ. of North Carolina, U.S.A.)
R. Hogg	(Pennsylvania State Univ., U.S.A.)
V.A. Marple	(Univ. of Minnesota, USA)
S.B. Savage	(McGill Univ., CANADA)
Secretariat	
C.C. Huang	(Hosokawa Micron International INC, U.S.A.)

■Publication Office

Hosokawa Powder Technology Foundation
Shodai- Tajika 1-9, Hirakata, Osaka, 573-1132 Japan
e-mail : info@kona.or.jp

KONA Powder and Particie Journal No. 29 (2011)

CONTENTS

＜Review Papers＞

＜Original Research Papers＞

< Information Articles >

The Letter from the Editor

Brij M. Moudgil
American Editorial Board Chairman

As theChair for the Editorial Board of the Americas, I am honored to share my thoughts with you on powder and particle technology opportunities and challenges.

First of all, I would like to express our profound sadness and sincere condolences to the families of the people across the globe that lost their lives in the recent disasters, particularly the people of Japan who are enduring extremely difficult times as a result of the recent Tsunami and earthquakes. Coping with natural disasters is never easy, however, technological innovation in several areas, including powder and particle technology, are playing a critical role in helping future generations deal with such disasters more efficiently. Predictive methodologies and sensor technologies are advancing, and eventually it will be possible to minimize the loss of human life with early warning of impending natural disasters. Furthermore, discoveries, innovations and technology advancements are taking place to enhance the resilience of materials which promises to minimize the loss of life and damage to infrastructure upon exposure to sudden changes in the environment. Rapid response technologies to provide immediate assistance to victims are being developed that do not require conventional sources of energy. Minimizing the healthcare risks through deployment of appropriate mitigation technologies remains a high and immediate priority for surviving communities.

Powder and particle technology are currently utilized, and are inherent, for innovation and design of sensors, nano-composites, solar-cells, water-filtration and resilient materials, which are critical for early warning of disasters, minimizing damage during disaster and providing immediate assistance after the disaster. However, the knowledge of powder and particle technology is diffused in several fields with a drastic decrease in core competency in powder and particle technology. The academic and industrial leaders in powder and particle technology should make an effort to develop educational resources and attract the scientists working in several advanced materials areas to specifically address the necessary technological advances.

Globally, powder and particle technology remains strong, largely due to the economic growth in Asia. New wealth creation is leading the improvements in the quality of life in China, India, Brazil and other developing countries. Similar growth is noted in other parts of the world, with increasing demand for powder and particle mediated products. So it is no surprise that the powder and particle industry continues to gain importance in the developing economies. Overall, despite the challenges faced by western economies, powder technology is recognized as an essential business with great global opportunity.

New equipment developments constitute major technological advances in the powder and particle industry. However, transformational changes are needed to go beyond the advances in equipment design and the integration of mechanization and automation.

Producing the next generation of scientists and engineers to support the powder and particle industry is among our most significant challenges.

Unfortunately, with a few notable exceptions, powder and particle engineering education is in a weaker condition nationally and internationally mostly due to availability of financially more rewarding and seemingly more glamorous professional options to younger people. With shrinking science and engineering enrollments and faculty sizes viability of a number of powder and particle technology courses is at risk around the world.

Lack of awareness of the importance of particle technology, beyond the academics and industry practitioners who are directly involved, makes it harder to recruit talented students to the field. Shortage of research funding further compounds this problem. Companies should help by offering scholarships and internships to students who are interested in powder technology research. They should also emphasize to university administration about the strategic importance of powder and particle technology as the society moves forward. Furthermore, industry and professional society leadership can meet with national funding agencies and convey the importance of public-private partnership in maintaining a viable education and research infrastructure in this important field.

Globalization and outsourcing are inspiring curricular changes that emphasize individual as well as interdisciplinary learning and promote an understanding of the ethical, social and business aspects of the profession along with a geopolitical understanding of the industry. Innovations in education can be motivating in attracting students. With information technology advances, it may be attractive to develop joint powder technology-related education programs involving a consortium of universities.

Overall, I believe it is a time of unique opportunity for revitalizing, if not reinventing powder and particle technology education. Diverse international partnership opportunities in research and education can provide the platform for not only sustaining education but also to capitalize the teaching excellence and practice experience across countries. Powder and particle technology professional societies can provide a vital link for establishing and implementing global education and training partnerships.

Public education and awareness is a challenge and opportunity and particle and powders technology community should increase their participation in public forums. They may also consider making charitable contributions to educational institutions. No gift is more significant than the gift of education. A strong powder and particle technology community would be a fitting legacy to the founder of KONA -Mr. Masuo Hosokawa' s visionary contributions to the field.

Comment of the Cover Photograph

Seeded Granulation

Nejat Rahmanian[1] and Mojtaba Ghadiri

Institute of Particle Science and Engineering
University of Leeds, Leeds, UK

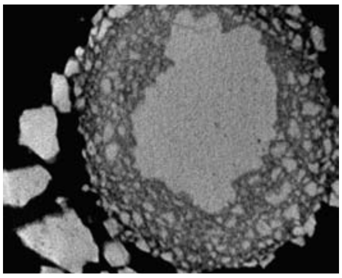

Fig. 1a X-ray micro-tomographic image of the central cross section of a granule.

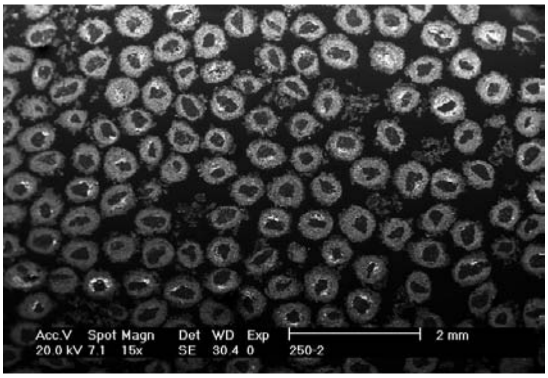

Fig. 1b For front cover:
SEM image of internal structure of over 100 granules.

We have serendipitously found that we can make 'seeded granules' by Cyclomix under certain operating conditions and feed powder particle size distribution. The Scanning Electron Micrograph on the front cover shows a number of seeded granules, embedded in a resin on a plane and cut and polished to show the internal structure. Every granule has consistently a seed, which is a large particle from the top end of the size distribution of the feed powder.

Cyclomix is manufactured by Hosokawa Micron (B.V.), the Netherlands, and falls in the category of high shear mixers and granulators. It is a very fast mixer, as shown by our mixing studies1), using the Positron Emission Particle Tracking facilities of the University of Birmingham. It has also been developed into a high shear granulator2), the context in which we have been using it. In a research programme supported by the Granulation Consortium, consisting of Borax Europe, Hosokawa Micron (B.V.), Pfizer, Procter and Gamble and the Engineering and Physical Research Council of UK, we have been investigating the effect of scaling up of granulators on the internal structure and physical and mechanical properties of the granules3,4). Different commercial grades of calcium carbonate were used as model materials and aqueous polyethylene glycol (PEG) as the binder. Using the X-ray micro-tomography facility of our Institute, we observed that under certain conditions we got a feature at the core of the granules, as shown in the figure below5). Detailed examinations revealed this to be a large particle from the feed powder, due to the fact that we had been using a wide size distribution. We could also produce the same structure by adding some course powder to the feed. The particular noteworthy feature is that each coarse particle can produce a granule, but only under certain conditions. A regime map has been identified for production of consistent seeded granule structure5), based on the size distribution of the feed powder and the concept of critical Stokes numbers for coalescence, deformation and breakage of wet granules6).

References

1) Ng, B.H., Kwan, C.C., ding, Y.L., Ghadiri, M. and Fan, X.F. (2007). Solids motion of calcium carbonate particles in a high shear mixer granulator: A comparison between dry and wet conditions. *Powder Technology*, 171, 1-11.
2) van der Wel, P.G.J. (1998). High intensity mixer. *European Patent Application EP 0885 652 A1*.
3) Rahmanian, N., Ng, B. H., Hassanpour, A., Ghadiri, M., Ding, Y., Jia, X. and Antony, J. (2008). Scale-up of high shear mixer granulators. KONA, No. 26, 190-204.
4) Hassanpour, A., Kwan, C.C., Ng, B.H., Rahmanian, N., Ding, Y.L., Antony, S.J., Jia, X., Ghadiri, M. (2009). Effect of granulation scale-up on the strength of granules. *Powder Technology*, 189(2) 304-312.
5) Rahmanian, N., Ghadiri, M., and Jia, X. (2011). Seeded granulation. *Powder Technology*, 206, 53-62.
6) Tardos, G.I., Hapgood, K.P., Ipadeola, O.O, Michaels, J.N. (2004). Stress measurements in high-shear granulators using calibrated "test" particles: application to scale-up. *Powder Technology*, 140, 217-227.

---

[1] Department of Chemical Engineering, Universiti Teknologi PETRONAS, Tronoh 31750, Malaysia

Froth Flotation in Saline Water[†]

S. Castro*
Department of Metallurgical Engineering, University of Concepcion[1]
J. S. Laskowski
Department on Mining Engineering, University of British Columbia[2]

Abstract

The use of seawater in mining/metallurgical operations seems to be the only sustainable solution in many zones with limited resources of fresh water. This requires new flotation technologies for processes which are to be carried out in highly concentrated electrolyte solutions. This paper reviews fundamental aspects of flotation in aqueous solutions with high concentration of inorganic electrolytes. Salt flotation, the process of flotation of inherently hydrophobic solids in concentrated electrolyte solutions, is especially suitable for theoretical analysis since no other organic agents are used in it. Starting from this example, the case of flotation of sulfide ores (chalcocite, chalcopyrite, pyrite and molybdenite) is discussed. The flotation of Cu-Mo sulfide ores requires the use of flotation agents, which are different for the inherently hydrophobic molybdenite and hydrophilic copper sulfides. The process is commonly carried out in alkaline pH adjusted with lime to depress pyrite, but in seawater depressing effect of Ca ions on molybdenite flotation is augmented, and different pyrite depressants are needed.

Keywords: Froth flotation, Salt flotation, Cu sulfides flotation; saline water; seawater flotation

1. Introduction

Water is a medium in which flotation takes place and flotation efficiency is highly dependent on water quality. In general, water is becoming a scarce resource for mineral processing plants, and in arid regions the need of saving freshwater for communities is imperative. Rivers and groundwater are being increasingly depleted at an alarming rate in many dry places. Hence, the use of water with a high concentration of inorganic electrolytes in flotation plants is being increasingly important. The use of seawater could be a sustainable solution for many dry zones located close to sea. The oceans represent the earth's major water reservoir. About 96.5-97% of the earth's water is seawater, while another 1.7%-2% is locked in icecaps and glaciers. Fresh water accounts for only around 0.5%-0.8% of the earth's total water supply[1)].

Closed water circuits in flotation plants result in a high electrolyte concentration in the process water. Hence, the question arises how the ionic strength of the process water affects flotation. Many different chemical additives (e.g. collectors which may be weak or strong electrolytes, either low molecular weight polymers used as dispersants or high molecular weight polymers used as flocculants, etc.) are utilized in flotation processes. The properties of aqueous solutions of some of these compounds are strongly affected by ionic strength. At the same time ionic strength affects directly particle-particle (coagulation/flocculation) and particle-bubble (flotation) interactions. The simplest flotation system in which only inorganic compounds, for instance NaCl, are utilized as flotation agent is so-called *salt flotation*.

The aim of this paper is to review fundamental aspects of flotation in aqueous solutions with substantial concentration of inorganic salts, and to discuss available information on the use of seawater in commercial flotation operations. We limit the scope of this paper to the range of electrolyte concentrations comparable with concentration of seawater that is to the range up to 1 M NaCl. This eliminates from

---

[†] Accepted: July 8th, 2011
[1] Concepción, Chile
[2] Vancouver, B.C., Canada
* Corresponding author
E-mail: scastro@udec.cl
TEL: (+56) 41-2204956 FAX: (+56) 41-2243418

ⓒ 2011 Hosokawa Powder Technology Foundation

our discussion the case of potash ore flotation, the flotation process which is carried out in saturated NaCl-KCl brine (at 20 ℃, 1,450 kg of the NaCl-KCl saturated aqueous solution contains about 0.300 kg of NaCl, 0.150 kg of KCl and 1 kg of water[2]; thus, the saturated brine is about 6-7 mole/L solution of NaCl and KCl).

2. Salt Flotation Process

2.1 Flotation of inherently hydrophobic minerals in salty water

Klassen and Mokrousov[3] in their monograph on fundamentals of flotation dedicated one chapter to the phenomenon of "salt flotation"; the term coined to describe the flotation of inherently hydrophobic minerals in concentrated electrolyte solutions without any organic agents. As demonstrated by Klassen[4], this process may be quite efficient if the floated mineral is highly hydrophobic; very hydrophobic bituminous coals were shown to float in 0.3-0.5 M NaCl solutions quite well, while less hydrophobic low rank coals did not. **Fig. 1** taken from the publication that appeared in 1983[5] confirms such a relationship quite clearly.

Fig. 1 shows the flotation rate constants obtained from batch flotation tests in which coals varying in rank were floated in 0.5 MNaCl. Moisture content in coal is a function of its rank; it is very low for very hydrophobic bituminous coals, and is much higher for lower-rank coals which are much more hydrophilic. Since all these experiments were carried out at the same electrolyte concentration (0.5 MNaCl) these results cannot be ascribed to a changing coalescence of bubbles and is clearly a function of hydrophobicity of the floated particles. But since small inorganic ions cannot change solid wettability these results show what could be expected, namely that only very hydrophobic particles can float under such conditions.

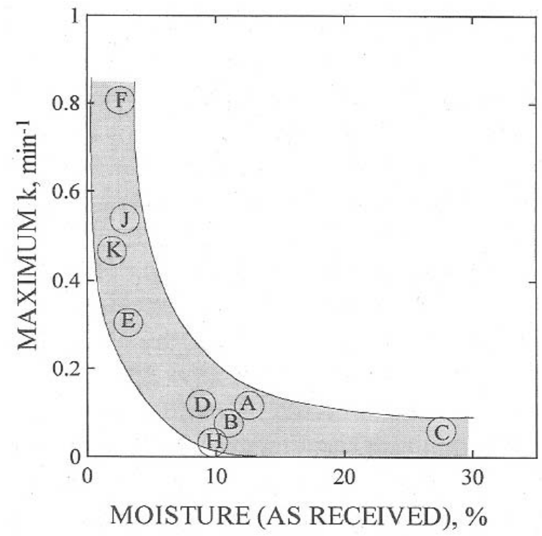

Fig. 1 Maximum flotation rate constants (salt flotation in 0.5M NaCl) versus moisture content for U.S. western coals (after Fuertenau et al., 1983)[5].

In order to study these effects further, a model was needed for which electrical charge and hydrophobicity could be independently maintained, and methylated silica was used as a model of hydrophobic surface[6,7]. Surface properties of this model system are characterized in **Fig. 2**[6]. The surface of silica is completely hydrophilic but it can be made hydrophobic by reaction with trimethyl chlorosilane. The hydrophobicity depends on the number of surface hydroxyls that actually reacts with silane. Since quite a large number of the surface hydroxyls do not react with silane, the zeta potential values for both methylated hydrophobic silica and hydrophilic silica – as demonstrated by the bottom (b) part of **Fig. 2** - are the same.

Fig. 3 shows the results of the flotation tests in which methylated quartz particles were floated in aqueous solutions of KCl at a constant pH of 6.1-6.5[8]. Flotation rate does not only depend on hydrophobicity of the particles but also - since these particles

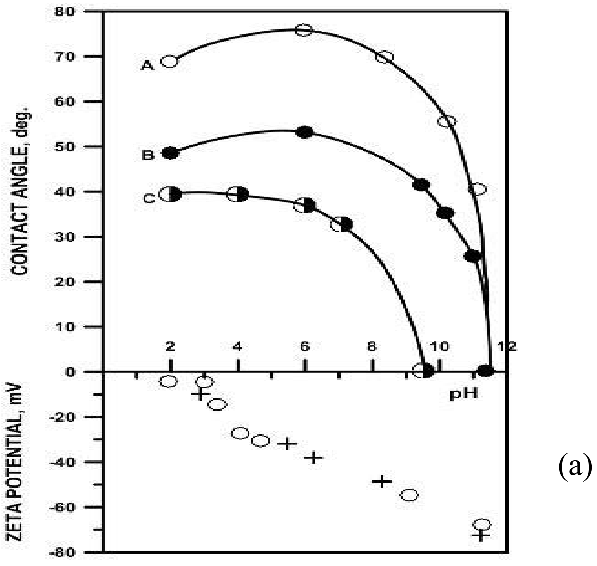

Fig. 2 Effect of pH and pre-treatment on contact angle of methylated silica. (A) Silica coated in 0.04 M trimethyl chlorosilane solution; (B) Silica coated in 0.001 M solution; (C) Silica heated at 450℃ for 20 hrs before coating in 0.001 M solution. Bottom part: (o) Methylated hydrophobic silica; (+) Pure hydrophilic silica [after Laskowski and Kitchener (1969)[6]]. (b)

carry electrical charge - the particle-to-bubble attachment which depends on the energy barrier opposing the attachment (equivalent of activation energy in chemical reactions)[8,9]. The particles used in these experiments were hydrophobic (θ = 53 deg.), however the tests were carried out over the pH range (6.1-6.5) where the zeta potential of the methylated quartz particles is in the range of -35 – -40 mV. As seen from **Fig. 3**, the rate of the flotation process carried out under such conditions clearly depends on electrolyte concentration and the correlation of the flotation rate and the energy barrier is quite good (**Fig. 4**)[8]. These findings explain very well the salt flotation phenomenon.

2.2 Effect of electrolytes on bubble coalescence

Flotation requires small bubbles and the flotation rate constant is proportional to the bubble surface area flux, Sb; (Sb depends not only on the amount of air pumped into a cell, it increases with decreasing the size of bubbles). Dispersion of gas into bubbles is the heart of the flotation process. In conventional flotation process the size of bubbles is determined by bubble coalescence which can be entirely prevented by a frother[10,11].

Frothers are best characterized by their critical co-

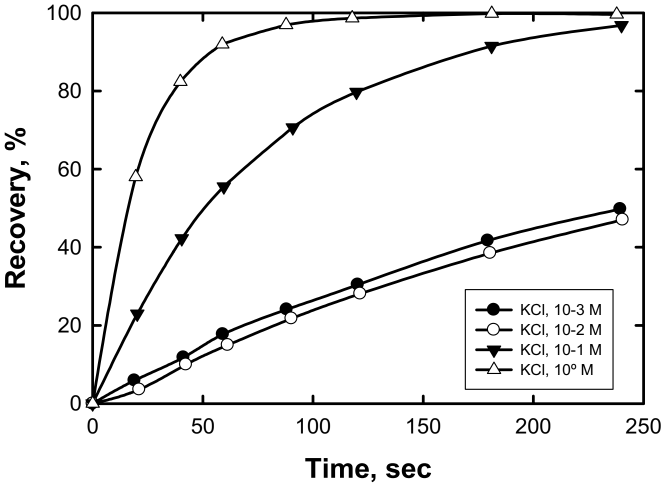

Fig. 3 The effect of KCl concentration on flotation of the methylated quartz particles (θ =53°) at pH 6.1 to 6.5 (after Laskowski et al., 1991)[8].

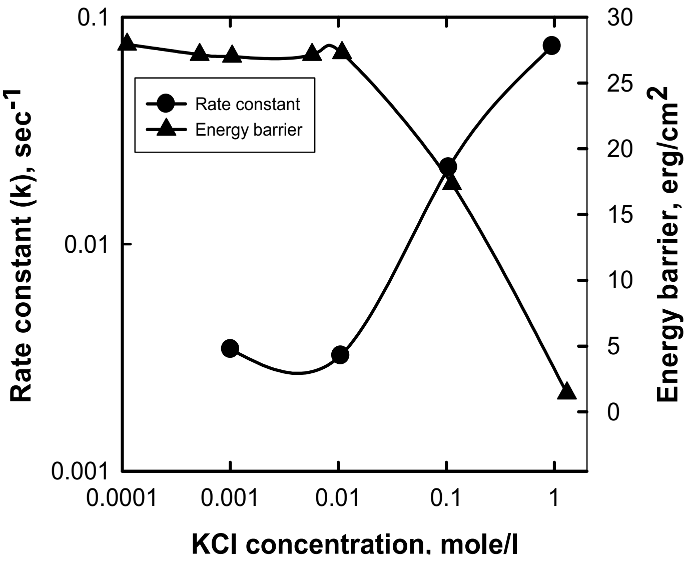

Fig. 4 The effect of KCl concentration on the flotation rate constant and the energy barrier; θ =53° at pH 6.1 to 6.5 (after Laskowski et al., 1991)[8].

alescence concentration (Cho and Laskowski[10,11]. As **Fig. 5** shows, the critical coalescence concentration of MIBC in water is about 10 p.p.m. At the concentrations higher then that the bubbles generated in MIBC solutions are stable and do not coalesce. Bubble coalescence can also be prevented by increasing electrolyte concentration. As **Fig. 5** shows, in concentrated electrolyte systems the bubbles are stable and do not coalesce even in the absence of a frother.

This is further illustrated in **Fig. 6**[13] which shows the results obtained while working with seawater. It is quite obvious that bubbles do not coalesce in seawater and thus fine bubbles can be produced in seawater without addition of a frother.

The salt flotation then meets all the flotation process requirements:

(i) In the environment of high ionic strength, the energy barrier opposing attachment of the hydrophobic particles to bubbles is reduced making attachment possible;
(ii) At the same time, fine bubbles are generated under such conditions.

The quoted results explain satisfactorily the salt flotation phenomenon, the process in which inherently hydrophobic particles are floated without the use of any organic agents (we will return to the problem of flotation of anisotropic hydrophobic minerals in salt solutions at the end of this publication).

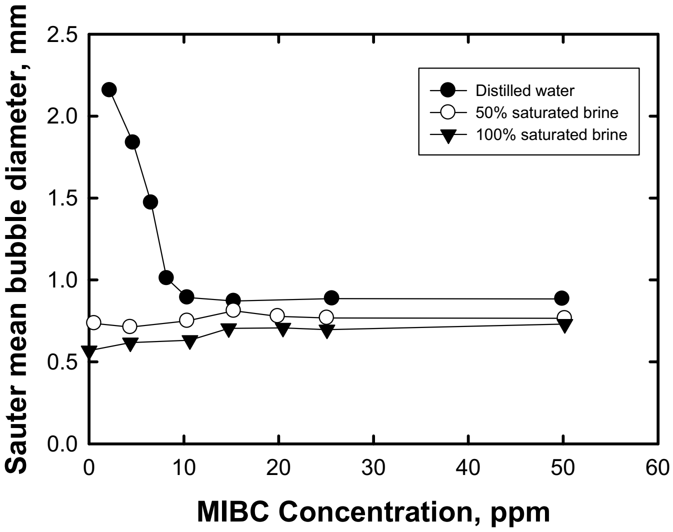

Fig. 5 Sauter mean bubble diameter as a function of MIBC concentration and electrolyte concentration (after Laskowski et al., 2003)[12].[the term "brine" used here stands for saturated solution of KCl +NaCl (about 6 mole/L)].

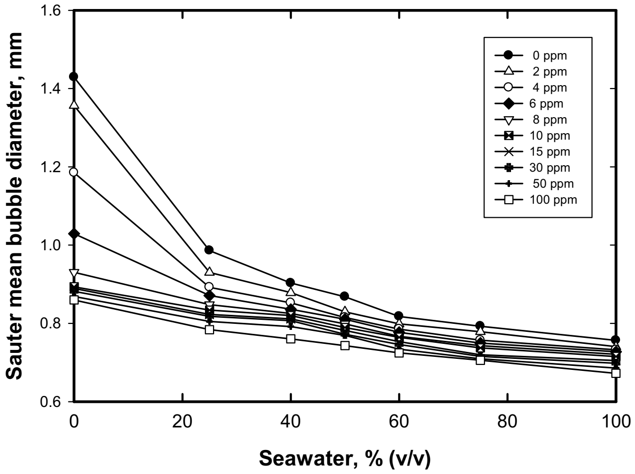

Fig. 6 Effect of MIBC frother on bubble size in seawater (Castro et al., 2010)[13]

3. Flotation with non-thio collectors

In this section we are going to use the results published by Onoda and Fuerstenau14) and Yousef et al.15). The first paper is on the effect of inorganic ions on flotation of quartz with cationic collector (dodecylammonium acetate), and the second one is on flotation of phosphate ore with anionic collector (sodium oleate) in seawater. Both papers show that the flotation is possible in electrolyte solutions.

Onoda and Fuerstenau14) demonstrated that the influence of electrolyte concentration depends upon collector concentration. At low collector concentrations the depressing effect of inorganic ions was clear, however at high collector concentrations where the collector is strongly adsorbed through hydrocarbon chain interactions (hemi-micellisation), inorganic ions were shown to have little effect on quartz flotation.

Yousef at al15) studied flotation in seawater of a calcareous phosphate ore, composed of francolite, calcite and dolomite. It could be expected that in the environment of seawater, the environment that contains both Ca^{2+} and Mg^{2+} ions, the use of anionic surfactant will require prior removal of these ions. It was demonstrated that the use of sodium carbonate (soda ash) in combination with sodium silicate could overcome the harmful effect of such bivalent cations in the flotation of the phosphate ore with fatty acids in seawater.

4. Flotation of sulfides with thio-collectors

Quite a few papers have been published on the flotation of copper sulfides. In this area both the results of small scale flotation tests with pure minerals, as well as batch flotation tests with copper ores are available.

Lekki and Laskowski in 197216) published a paper on the effect of saline mine water (14-17g/L NaCl) on flotation of chalcocite, and on the flotation of copper ores from the mines in Poland containing chalcocite and different gangue. They showed that NaCl depresses flotation of chalcocite in a Hallimond tube if the process is carried out without any frother. As **Fig. 7** demonstrates, in the presence of α-terpineol (frother) the trend is reversed and the flotation in salty water is better than in distilled water.

Alvarez and Castro17) studied in 1976 the flotation of chalcocite, chalcopyrite, and pyrite in NaCl solutions (0.5M), and in seawater. A pure sample of chalcocite was floated with isopropyl xanthate and a significantly lower floatability was observed in NaCl solutions in neutral and acid pH range (**Fig. 8**). A narrow peak of recovery was observed in seawater with a maximum around pH 9, showing a poorer floatability compared with sodium chloride in the entire range of pH. Chalcopyrite was more resistant to the effect of salinity. On the other hand pyrite was strongly depressed in NaCl solutions and seawater by pH regulated with HCl/NaOH, as is shown in **Fig. 9**.

The tests shown in **Fig. 7** were conducted at pH of 9.7. As **Fig. 8** implies, this is the best pH for flotation of chalcocite under such conditions. **Fig. 7** indicates that the effect of NaCl strongly depends on α-terpineol concentration (a very strong frother); at α-terpineol concentrations lower than about 10 mg/L the flotation in the presence of NaCl was worse than in

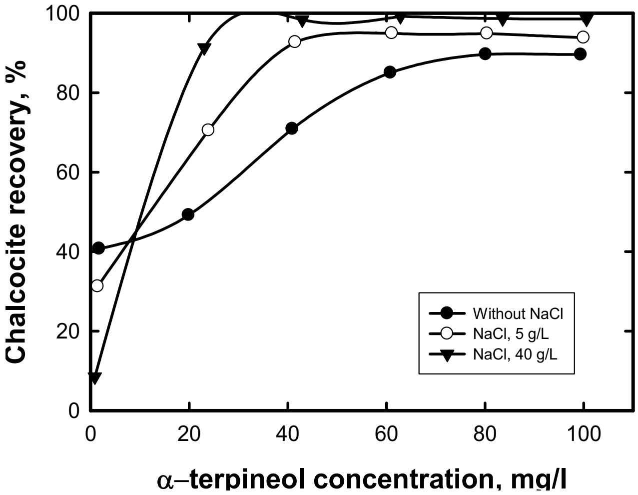

Fig. 7 Flotation of chalcocite as a function of α-terpineol in NaCl solutions (EtX=3mg/g; pH=9.7). (Lekki and Laskowski, 1972)16).

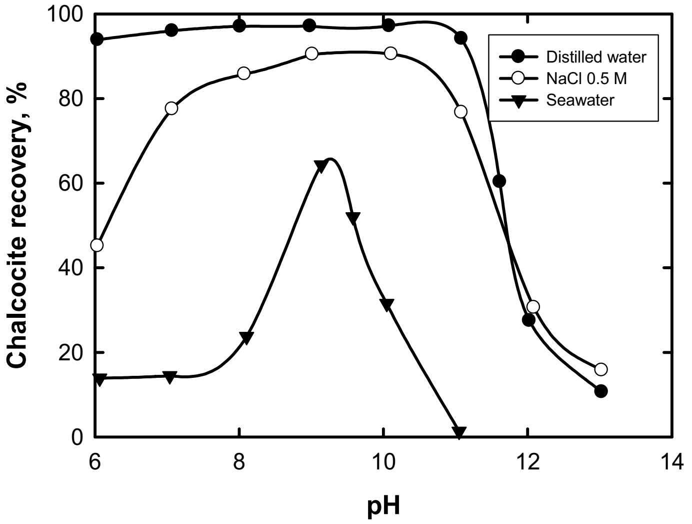

Fig. 8 Effect of pH (adjusted by NaOH/HCl) on the flotation of chalcocite in a Hallimond tube (15 mg/L IsopX and 10 mg/L amyl alcohol) (Alvarez and Castro, 1976)[17].

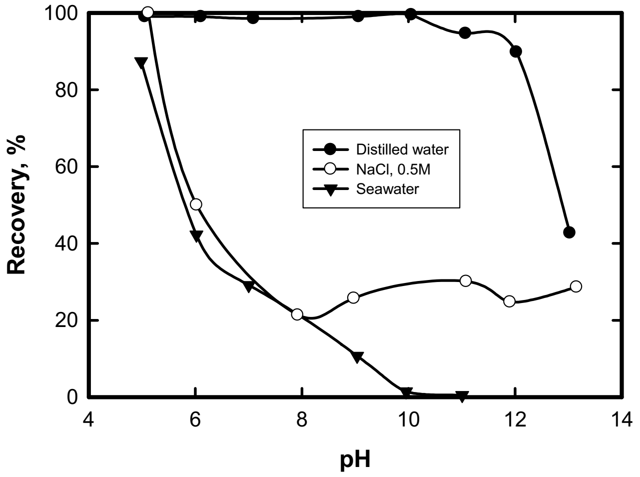

Fig. 9 Effect of pH (adjusted by NaOH/HCl) on the flotation of pyrite in a Hallimond tube (15 mg/L IsopX and 10 mg/L amyl alcohol). (Alvarez and Castro, 1976)[17].

distilled water, but it was better than in distilled water at the higher α-terpineol concentrations. Different (weaker) frother was used in the other tests (**Fig. 8** and **9**) and the concentration utilized in these tests was 10 mg/L. These concentrations are too close to the border line and so these results do not lend themselves to ready analysis. Interesting are the results of the flotation tests with pyrite in **Fig. 9**. They show much poorer flotation of pyrite in seawater when compared with the flotation results in distilled water. It must be borne in mind, however, that the electrochemical conditions (galvanic effects) play a very important role in the flotation of real sulfide ores, and that the single-mineral tests in such cases may be very different from those carried out with an ore.

The presence of ions dissolved from Cu and Fe sulfides during conditioning with seawater and NaCl solutions was significant. The flotation of chalcocite was decreased when it was floated in NaCl solutions previously conditioned with pyrite, suggesting the effect of dissolved ions. The tests carried out with different ions revealed that Cu^{2+} ions were able to depress pyrite and chalcocite in 0.5 M NaCl , but the flotation of chalcopyrite was not affected. See **Fig. 10**.

5. Flotation plant practice with the use of saline water and seawater

In the 1930', small mills in Chile (e.g. *Tocopilla*) floated a chalcopyrite ore in seawater[18]. In 1975, pilot

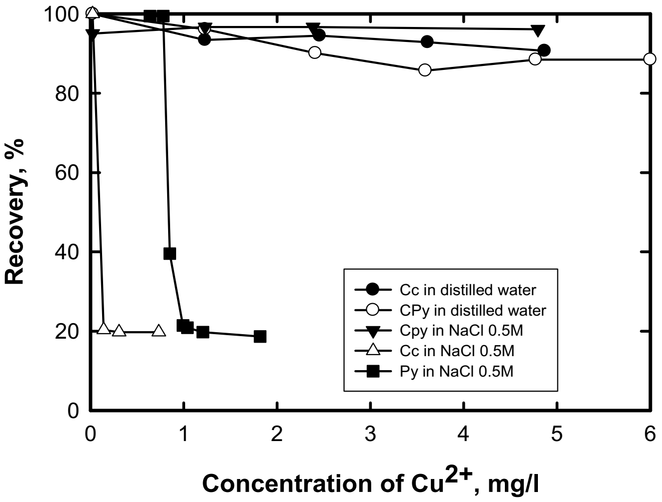

Fig. 10 Effect of Cu^{2+} ions on the flotation of chalcocite, chalcopyrite and pyrite in distilled water and NaCl 0.5M solutions with IsopX and MIBC (for chalcopyrite α-terpineol was used as frother).

plant tests were reported for the flotation of a copper sulfide ore in seawater from the *Andacollo* deposit. It was found that due to the frothing properties of seawater at pH 9.5, the rougher circuit operated well even without a frother[19].

At present, in a small mill (*Planta Las Luces-Minera Las Cenizas S.A.-Taltal, Chile*) a copper sulfide ore (mainly chalcocite) is successfully floated with seawater by using around 36% of fresh seawater and 64% of recycled seawater from the tailings dam[20].

Recently, a new large flotation plant (95,000 tpd) is operating with seawater in Chile. It is the *Esperanza* plant (Antofagasta Minerals S.A.), which is producing a bulk Cu-Au concentrate[21]. It is planned to use 70% of recycled seawater, as the pilot plant tests showed that this is better for Mo and Au recovery.

Other base metal sulfide ores (Cu-Pb-Zn; Pb-Zn) can also be successfully floated by xanthates[22] in seawater and in water with increased electrolyte concentrations. In seawater and in salty water, a lower consumption of reagents in bulk flotation – particularly frother- was noted. However, experiments carried out with synthetic seawater, showed that certain frothers increased the volume of the froth (Dowfroth type), and others decreased it (Flotol). At the same time, the froth produced in seawater and polymetallic ores, easily carries gangue slimes, and much attention must be paid to cleaning stages. Lime is often necessary for froth control. However, with excess of lime the froth could be too heavily loaded and of insufficient volume. Fresh water is often used as wash water in the concentrate filters to remove excess of chloride ions from the concentrates.

A very stable flotation was reported with the use of seawater at a natural pH of 8 at Texada Mill (iron operation with Cu, Au, Ag by-products) and also a reduced consumption of reagents was reported by Haig-Smillie (1974)[23]. At the Raglan concentrator (Quebec, Canada), which processes a copper-nickel ore in salty water (30,000 p.p.m.), a frother is not employed at all[24]. In Australia, at the Mt Keith operation, a low grade nickel ore is floated in hyper-saline process water, at 60,000–80,000 ppm of salts[25, 24, 26]). Similarly, at Batu Hijau, a copper-gold ore concentrator in Indonesia, the seawater usage was also accompanied by a reduction in reagent consumption when floating at pH 8.5-9.0[15].

6. Flotation of inherently hydrophobic anisotropic minerals in salt solutions

In case of isotropic minerals, all sides of the crystal are created by breaking the same type of bonds with resulting mineral surfaces being homogeneous and having identical electrical charge. For instance, in the case of quartz, new surfaces formed when larger pieces of quartz are crushed are created by breaking identical Si-O bonds. As a result all the new quartz surfaces have the same composition.

The sides of anisotropic mineral crystals are created by breaking different bonds – one, which is formed by the rupture of van der Waals bonds and the other, which is formed by rupture of strong either ionic or covalent bonds. The minerals like molybdenite and graphite belong to this group. **Fig. 11** shows their crystallo-chemical structure. These minerals have a sheet-structure (which is also referred to as laminar crystal structure). The van der Waals bonds between subsequent layers are weak, and they are easily broken during crushing/grinding with the newly exposed surfaces being hydrophobic. The edges of such minerals are, however, hydrophilic. So, the properties of such particles are different at the basal planes (faces) and at the edges, also electrical charge at these surfaces differs. Since the ratio of planes-to-edges changes with the particle size (it decreases with decreasing particle size) these particles, depending on particles size, exhibit different properties[27,28]; finer particles are more hydrophilic than coarse particles. Therefore, the surface properties measured on large polished specimens may be very different from the properties of fine particles.

As it is has been shown in the first part of this paper, hydrophobic particles of bituminous coal float quite well in concentrated electrolyte solutions (salt flotation). This flotation, however, depends on wettability of the floated particles, and low rank coals which are not that hydrophobic float poorly under such conditions. Because inherently hydrophobic minerals are anisotropic the salt flotation of these minerals is not a clear cut case.

It has been reported that the ores of native sulfur, and also talc, can be floated in salt solutions[29]. The salt flotation of molybdenite has not been extensively studied but this topic is extremely important if seawater is to be used in processing of Cu-Mo ores. Molybdenite response to increasing salt concentration will be here discussed using Castro et al's[30] unpublished results.

Flotation tests were carried out in a Partridge-Smith micro-flotation cell with a sample of cleaned molybdenite concentrate, in the presence of 10 mg/L isopropyl xanthate and 10 mg/L MIBC, and pH adjusted either by NaOH or CaO. These results reveal that while low concentrations of NaCl (below 0.1 M) do not affect floatability of molybdenite, over the 0.1 – 1 M concentration range depression is appreciable. The loss of molybdenite floatability in alkaline solutions is strongly increased by NaCl addition. The depressant effect of CaO is greatly increased by NaCl.

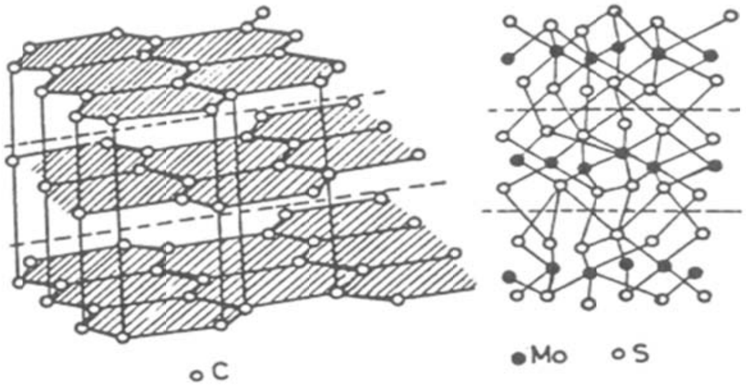

Fig. 11 Crystallo-chemical structure of graphite and molybdenite.

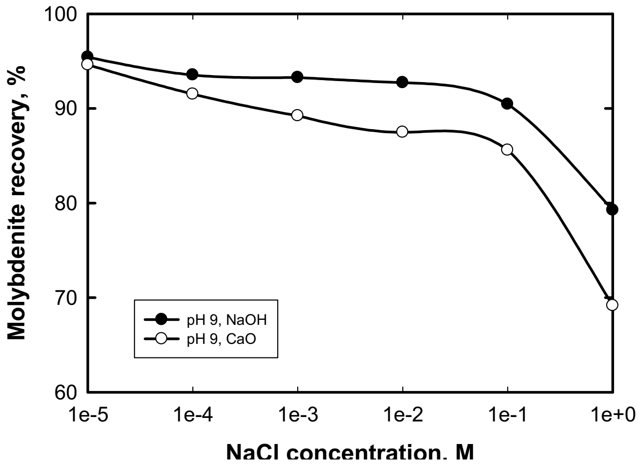

Fig. 12 Effect of NaCl concentration on the flotation of molybdenite at pH 9 adjusted either by NaOH or CaO[30].

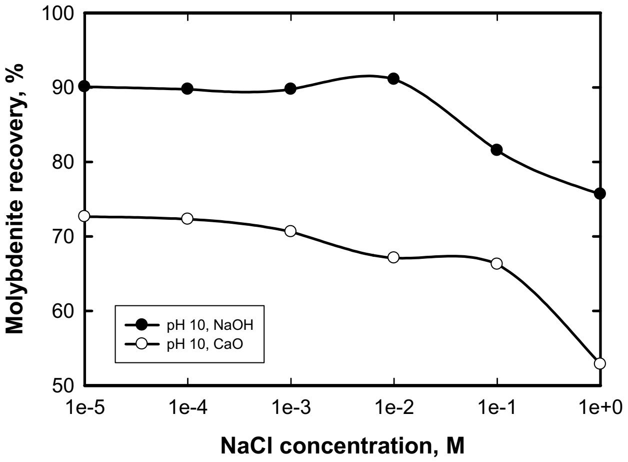

Fig. 13 Effect of NaCl concentration on the flotation of molybdenite at a pH of 10 adjusted either by NaOH or CaO[30].

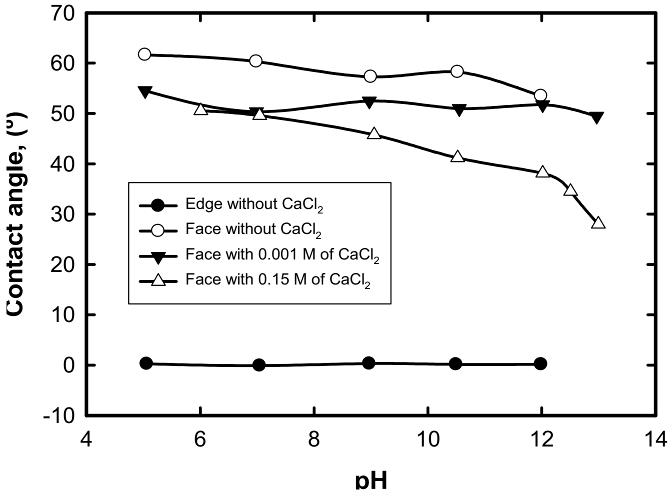

Fig. 14 Effect of pH on contact angle measured on faces and edges of MoS_2 crystal (López-Valdivieso et al., 2006)[31].

These experiments were carried out in the absence of a non-polar collector (diesel oil or kerosene), and it is reasonable to expect an improvement of floatability when such a collector is used.

As more recent tests on the surface properties of molybdenite carried out with the use of Atomic Force Microscopy revealed[31], the common interpretations may be too simplified in the case of this mineral. We are used to depict the basal planes of anisotropic minerals as hydrophobic and homogenous. The AFM picture of molybdenite surface obtained by cleaving confirmed Komiyama et al's findings[32] that molybdenite faces are not fully hydrophobic and have terraces and rims of nanometric size. Therefore, the basal planes are not really planes, because these are highly heterogeneous surfaces with a lot of nano-size topographic structures (e.g., crater structures). And such a surface is not very hydrophobic (**Fig. 14**). This later picture may well explain why the salt flotation of molybdenite is so different from the salt flotation of bituminous coal.

Fig. 14 shows that the hydrophobicity of basal planes further decreases in alkaline solutions, and especially in the presence of Ca^{2+} ions. Based on the AFM picture which indicates that the molybdenite basal surfaces are very heterogeneous it is possible to explain these phenomena. If thiomolybdate species are responsible for the electrical charge at the edges, these edges also exist on the "planes" and the effect of Ca^{2+} ions can be explained by formation of calcium thiomolybdate[33].

7. Conclusions

1. Because hydrophobic surfaces usually carry electrical charge, the attachment of the hydrophobic

particles to bubbles is opposed by an energy barrier. With increasing ionic strength such a barrier is reduced and flotation of hydrophobic solids (e.g. bituminous coal) is very good in 0.3 – 0.5 M NaCl solutions. Bubble coalescence, which determines bubble size in flotation systems, is prevented at such salt concentrations, reducing the bubble size (similarly to a frother). These are the principles on which the so-called salt flotation process is based.

2. In salt solutions, flotation of molybdenite is not as good as flotation of bituminous coal. This may be explained by anisotropic properties of molybdenite and heterogeneous nature of the plane surfaces, as revealed by recent AFM studies.
3. Flotation of quartz with cationic collector (dodecylamine) in not affected in concentrated electrolyte solutions at high collector dosages that is over the concentration range over which this collector adsorbs in the form of hemi-micelles.
4. Flotation of phosphate ores with fatty acids (anionic collector) requires removal of Ca^{2+} and Mg^{2+} ions, if seawater is used in the flotation.
5. The detrimental effect of lime (calcium ions) on floatability of molybdenite is higher in sodium chloride solutions and seawater than in fresh water.
6. Copper sulfide minerals, such as, chalcocite and chalcopyrite float well, both in salty water and seawater in the pH range of 8.0-9.5; however, the flotation recovery abruptly decreases at pH higher than 10, particularly in the case of chalcocite.
7. The flotation of pyrite in sodium chloride solutions and seawater decreases with increasing pH more than in fresh water. However, when molybdenite is present in a sufide ore, it is recommended that lime be replaced by other pyrite depressant, able to operate at lower pH, in order to prevent Mo losses.

References

1) Greenlee, L. F., Lawlerb, D.F., Freeman, B.D., Marrotc, B. and Moulinc (2009): Reverse osmosis desalination: water sources, technology, and today's challenges. Water Research, Vol. 43, pp. 2317–2348.
2) Gaska, R.A., Goodenough, R.D. and Stuart, G.A. (1965): Ammonia as a solvent, Chem. Eng. Progress, Vol. 61, pp. 139-144.
3) Klassen, V.I. and Mokrousov, V.A. (1963): "An Introduction to the theory of flotation", Butterworths, London.
4) Klassen, V.I. (1963): "Coal flotation. Gosgortiekhizdat", Moscow, (Russian text).
5) Fuerstenau, D.W., Rosenbaum, J.M. and Laskowski, J.S. (1983): Effect of surface functional groups on the flotation of coal. Coll. & Surf., Vol. 8, pp. 153-164.
6) Laskowski, J.S. and Kitchener, J.A. (1969): The hydrophilic-hydrophobic transition on silica, J. Coll. Interf. Sci., Vol. 29, pp. 670-679.
7) Lamb, R.N. and Furlong, D.N. (1982): Controlled wettability of quartz surfaces, J. Chem. Soc., Faraday Transactions I, Vol. 78, pp. 61-73.
8) Laskowski, J.S., Xu, Z. and Yoon, R.H. (1991): Energy barrier in particle to bubble attachment and its effect on flotation kinetics, Proc. 17th Int. Mineral Processing Congress, Dresden, pp. 237-249.
9) Laskowski, J.S. (1986): The relationship between floatability and hydrophobicity, "Advances in Mineral Processing" (P. Somasundaran, ed.), SME, Littleton, pp. 189-208.
10) Cho, Y.S. and Laskowski, J.S. (2002): Effect of flotation frothers on bubbles size and foam stability, Int. J. Mineral Processing, Vol. 64, pp. 69-80.
11) Cho, Y.S. and Laskowski, J.S. (2002): Bubble coalescence and its effect on dynamic foam stability, Can. J. Chemical Engineering, Vol. 80, pp. 299-305.
12) Laskowski, J.S., Cho, Y.S. and Ding, K. (2003): Effect of frothers on bubble size and foam stability in potash ore flotation systems. Can. J. Chemical Engineering, Vol. 81, pp. 63-69.
13) Castro, S., Venegas, I., Landero, A. and Laskowski, J.S. (2010): Frothing in seawater flotation systems, Proc. XXV Int. Mineral Processing Congress, Brisbane, pp. 4039-4047.
14) Onoda, G.Y. and Fuerstenau, D.W. (1964): Amine flotation of quartz in the presence of inorganic electrolytes. Proc. 7th Int. Mineral Processing Congress (N. Arbiter, ed.), Gordon and Breach, pp. 301-306.
15) Yousaf, A.A., Arafa, M.A., Ibrahim, S.S. and Abdel Khadek, M.A. (2003): Seawater usage in flotation for minerals beneficiation in arid regions, Proc.22nd Int. Mineral Processing Congress (Lorenzen and Bradshaw, eds.), Cape Town, Vol. 2, pp. 1023-1033.
16) Lekki, J. and Laskowski, J.S. (1972): Influencia del NaCl sobre la flotación de minerales sulfurados de cobre, Minerales, Vol. 27, No. 118, pp. 3-7 (Spanish text).
17) Alvarez, J. and Castro, S. (1976): Flotation of chalcocite and chalcopyrite in seawater and salty water, Proc. IV EncontroNacional de Tratamento de Minerios, São José Dos Campos, Brazil, Anais Vol. 1, pp. 39-44 (Spanish text).
18) Burn, A.K. (1930): The flotation of chalcopyrite in seawater, Bulletin Institution of Mining and Metallurgy, N° 314.
19) Morales, J.E. (1975): Flotation of the Andacollo's ore in pilot plant by using seawater. Minerales, n° 130, Vol.30, pp. 16-22.
20) Monardes, A. (2009): Use of seawater in grinding-flotation and tailing dam operations at Las Luces plant (Minera Las Cenizas-Taltal), Proc. XI Simposium on

Mineral processing (MOLY-COP 2009), Puyehue, Chile, (Spanish text).

21) Parraguez, L., Bernal, L. and Cartagena, G. (2009): Chemical study for selectivity and recovery of metal sulfides by flotation using seawater. Proc. VI International Mineral Processing Seminar (PROCEMIN 2009), Santiago, pp. 323-333.

22) Rey, M. and Raffinot, P. (1966): Flotation of ores in sea water: High frothing; soluble xanthate collecting, World Mining, June, pp. 18-21.

23) Haig-Smillie, L.D. (1974): Sea water flotation, Proc. 6th Annual Meeting of Canadian Mineral Processors, pp. 263-281.

24) Quinn, J.J., Kracht, W., Gomez, C.O., Gagnon, C. and Finch, J.A. (2007): Comparing the effect of salts and frother (MIBC) on gas dispersion and froth properties, Minerals Engineering, 20, pp. 1296-1302.

25) Senior, G.D., and Thomas S.A. (2005): Development and implementation of a new flowsheet for the flotation of a low grade nickel ore, International Journal of Mineral Processing, 78, pp. 49-61.

26) George, C.W. (1996): The Mt. Keith operation, Proc. Nickel ´96 Mineral to Market (E.J. Grimsey and I. Neuss, eds.), Austral. Institution of Mining and Metallurgy, Melbourne, pp. 19-23.

27) Chander, S., Wie, J.M. and Fuerstenau, D.W. (1975): On the native floatability and surface properties of naturally hydrophobic solids, Advances in Interfacial Phenomena of Particulate/Solution/Gas Systems; Applications to Flotation Research (P. Somasundaran and R.B. Grieves, eds.), AIChE Symposium Series, 150, Vol. 71, pp. 183-188.

28) Castro, S.H. and Correa, A. (1995): The effect of particle size on the surface energy and wettability of molybdenite, Proc. 1st UBC-McGill Int. Symposium on Processing of Hydrophobic Minerals and Fine Coal (J.S. Laskowski and G.W. Poling, eds.), Met. Soc. of CIM, pp. 43-57.

29) Laskowski, J.S. (1966): Flotation of inherently hydrophobic minerals in concentrated solutions of inorganic salts, Trans. of Silesian University of Technology, Mining, Issue no. 16, (Polish text).

30) Castro, S., Jara, C., Muñoz, M. and Laskowski, J.S., Floatability of molybdenite in aqueous sodium chloride solutions (Unpublished).

31) López-Valdivieso, A., Madrid-Ortega, I., Reyes-Bahena, J.L., Sánchez-López, A.A. and Song, S. (2006): Propiedades de la interface molibdenita/solución acuosa y su relación con la flotabilidad del mineral. Proc. 16thCongreso Int. de MetalurgiaExtractiva, Saltillo, Mexico, pp. 299-310.

32) Komiyama, M., Koyohara, K., Fujikawa, T., Ebihara, T., Kubota, T. and Okamoto, Y. (2004): Crater structure on a molybdenite basal plane observed by ultrahigh vacuum tuneling microscopy and its implication to hydrotreating, J. Molecular Catalysis A:Chemical, Vol. 215, pp. 143-147.

33) Fuerstenau, D.W. and Chander, S. (1972): On the natural floatability of molybdenite. Trans. SME, Vol. 255, pp. 62-69.

Author’s short biography

Sergio Castro

Sergio Castro is a Professor of mineral processing (flotation and surface chemistry) in the Department of Metallurgical Engineering at the University of Concepción-Chile. He received a B. Sc. degree in Chemistry from the University of Chile in 1972, with subsequent graduate studies on colloid and surface chemistry in mineral processing. He joined the Engineering Faculty of the University of Concepcion in 1974. Visiting scientist in the Department of Mining and Mineral Process Engineering, at the University of British Columbia-Canada, in 1985. His research interests are in fundamentals and applied research on copper and molybdenum flotation. His research has lead to over 100 technical papers and, as editor, 8 technical books. In 2008 he was elected as a member of the Council of the International Mineral Processing Congress (IMPC).

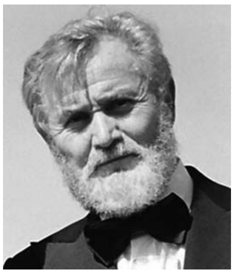

Janusz S. Laskowski

Professor Janusz Laskowski obtained all his degrees, including Ph. D. in 1963, from the Silesian University of Technology, Gliwice, Poland. His education also included one year stay as a postgraduate student with Department of Colloid Chemistry, Lomonosov University, Moscow, and one year stay as a post-doctoral fellow with Dr. J.A. Kitchener at Imperial College, London.

He was associate professor of mineral processing at Silesian University of Technology until 1972, and then was appointed professor at Wroclaw Technical University. In 1979, he chaired the 13th Int. Mineral Processing Congress in Warsaw. Since 1982 until 2001 (when he retired) he was professor of mineral processing at the Department of Mining Engineering, University of British Columbia, Vancouver, Canada.

He spent sabbatical leaves with Departamento de Minas, Universidad de Chile, Santiago (1971/72); Department of Materials Science and Mineral Engineering, University of California, Berkeley (1981); Surface Chemistry Group at Ecole Nationale Superiéure de Géologie, Nancy, France (1988/89) and Department of Chemical Engineering, University of Cape Town, South Africa (1996).

After retiring in 2001, Janusz Laskowski remains active in academic research and teaching. He currently pursues collaborative research with the Universidad de Concepcion in Chile, Universidad Autónoma de San Luis Potosi, Mexico, CSIRO Institute in Melbourne, and University of Cape Town in South Africa. He has authored 260 papers in journals and conference proceedings, two books, “Coal Flotation and Fine Coal Utilization” (Elsevier 2001) and “Physical Chemistry in Mineral Processing” (Slask, Poland, 1969) which updated was translated into Spanish in 1974 “Fundamentos Fisicoquimicos de la Mineralurgia” (Universidad de Concepcion, 1974). Edited and co-edited several volumes including the Proceedings of the 13th Int. Mineral Processing Congress, Warsaw, 1979. Over the period from 1984 to 2005 was Editor-in-Chief of Coal Preparation international journal.

Dr. Laskowski was elected a Fellow of Canadian Institute of Mining in 1995. He has been the recipient of many professional awards: the Arthur F. Taggart Award from the Society of Mining Engineers in 2000; the Alcan Award of the Metallurgical Society of CIM in 2004; the Lifetime Achievement Award in 2008 at the 24th International Mineral Processing Congress, Beijing; and the Antoine Gaudin Award of SME/AIME in 2010. On December 4, 2009, he received the Medalla Rectoral and was decorated as a Distinguished University Visitor by Chile’s Universidad de Concepción.

Use of Virtual Impactor (VI) Technology in Biological Aerosol Detection[†]

Jim Ho
Biological Detection Section, Defence Research and Development Canada Suffield[1]

Abstract

Detecting biological threat aerosol is difficult in that a small cloud lasting only a few seconds at a point location may contain sufficient material to infect large numbers of exposed individuals. Clinical analytical methods require relative large amounts of the sample in liquid form to facilitate positive measurements. Biological agents may be fragile because of their lipid membranes that can be susceptible to harsh sample collection treatment. Damaged organisms may render subsequent analyses to be invalid. Virtual impaction (VI) sample collectors have been theorized to provide usable concentration rates yet are sufficiently gentle with the aerosol particles to preserve cellular viability. This review will discuss different implementations of VI technology and examine their merits. Outstanding issues will be outlined to aid future experimentation.

Keywords: virtual impactor, biological aerosol, anthrax, aerosol samplers, threat agents

Introduction

That humans get infected by microorganisms, mostly from infectious agents transported in the air, is not surprising as people get sick all the time (Verreault et al. 2008). Daily biological threats are such common occurrences that we have become accepting of the fact. Occasionally, concern may be elevated when travellers get infected in enclosed environments like aircraft. Sometimes fatalities do take place, for example, infections caused during hospitalization. Yet, the concern for these episodes has not heightened public awareness to the point where drastic solutions are called for.

However, recent events (Riedel, 2004) have changed that complacency somewhat. What happened in the Middle East in the early 1990's and subsequent World Trade Center events prompted military and public health organisations to seek solutions that can be used to measure the occurrence of nuclear biological and chemical (NBC) threats. For example, Ho and Duncan (2005) described the anthrax scenario that resulted in two fatalities at the Brentwood postal station in Washington DC. Using knowledge of the aerosol source and location of the targets, they were able to estimate the lethal dosage that caused the fatalities, the first time that this could be done. Blatny et al. (2010) led a team to investigate the spread of airborne Legionella bacteria from a pulp waste treatment plant in Norway that had previously caused a number of fatalities in a nearby town. They discovered that the source of live organisms came from large bubbling tanks that continuously emit aerosol particles into the air. To be clear, prior to this time period, there had always been a low level requirement for ways to detect military threats. But since then, the demand for detection technologies jumped by orders of magnitude and significant funding became available. However, biological detection for threats in militarily or civilians settings have always been a difficult problem to solve. Indeed, for the past thirty years, scientists and engineers from around the world have been engaged in solving the problem. But the issues are so recalcitrant that after billions of dollars spent, the illusive hand held biological detector is still nowhere in sight.

Briefly, the problem can be summarized thus. There is a need to detect, within seconds, a small cloud of particulate biological aerosol being transported by wind over a long distance. The particles

---

[†] Accepted: July 8th, 2011

[1] Station Main Box 4000, Ralston, Alberta, T0J 2N0, Canada
E-mail: Jim.ho@drdc-rddc.gc.ca
TEL: (+1) 403-5444804 FAX: (+1) 403-5443388

© 2011 Hosokawa Powder Technology Foundation

are superimposed over a background of environmental contaminants. The detection technology has to sort these materials in real time without incurring more than one false alarm per week. Given these requirements, it can be seen how the first requirement for a detector system is to concentrate the particles, preferably while they are still in the air, before submitting them for analysis. For the concentration step, the virtual impactor (VI) appears to be the ideal solution. This review will attempt to focus on the role played by VI technologies in solving problems associated with biological detection. It is assumed that the reader will have familiarity with VI as previously reviewed by Marple (2004). Having an understanding of naturally occurring bioaerosols and their transport characteristics in nature as reviewed by Jones and Harrison (2004) is helpful. Some authors like Eubanks et al. (2007) discussed both chemical and biological threats but this review will be restricted to addressing bacterial and viral threats.

The dichotomous sampler

Although Marple (1970) provided a detailed description of the VI in his PhD thesis, it was Loo and Cork (1988) who designed the dichotomous sampler (DS) using VI technology. The sampler was subsequently marketed by a company called Sierra-Andersen for particle measurements in the environment (Environmental Monitoring Systems, Laboratory, 1985). The usefulness of the DS in characterizing biological aerosol was first demonstrated in out door field trials. Ho et al. (1990) used a DS to characterize artificially generated biological aerosol whilst detecting light scatter signals from a standoff laser based system. Further chamber work with the DS (Ho, 1991) led to the discovery that over 80-90% of the live individuals from artificially generated biological aerosol particles were to be found in the >2.5 μm fraction as aggregates. This and a series of related laser standoff biological detection studies were summarized by Evans et al. (1994).

The DS, using one single nozzle coupling, serves as an ideal device to provide a simplified illustration for how VI works (**Fig. 1**). The Sierra Andersen instrument was designed with an inlet flow rate of 1 m^3/hr or 16.7 l/min, shown at the top of the right hand illustration. Particles are focused into a narrow accelerating stream exiting at the “virtual impactor nozzle”. On exit, the bulk of the total flow is split into the “fine” stream (<2.5 μm, 15 l/min) while 1.67 l/m is captured by the “virtual impactor receiver

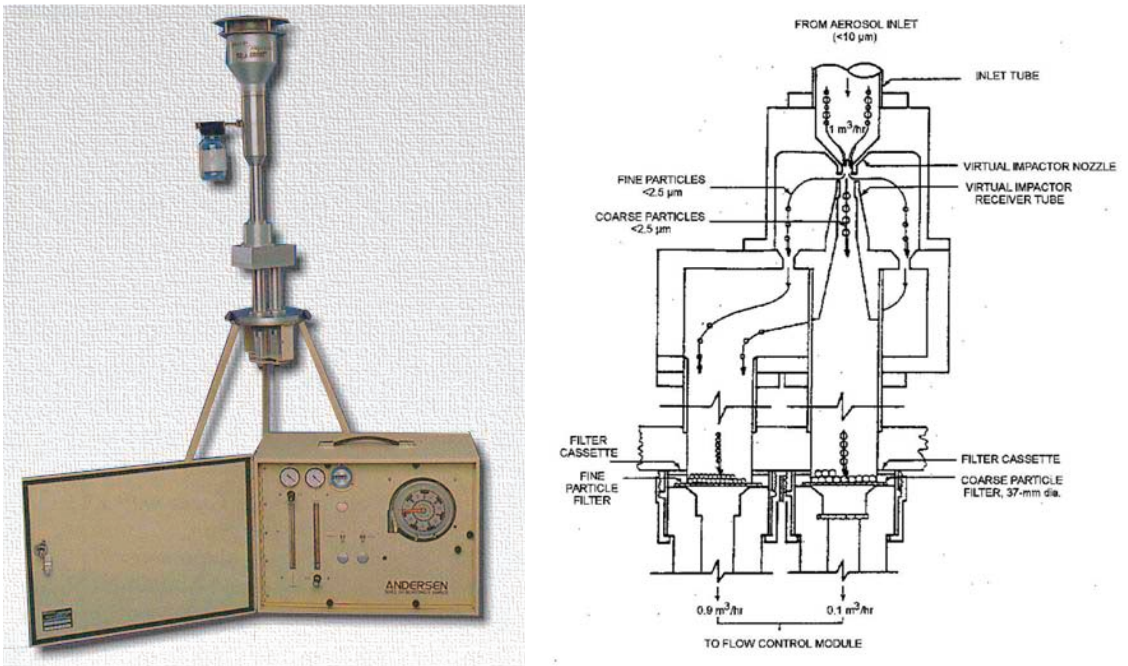

Fig. 1 The Andersen model 244 dichotomous sampler (left) and the virtual impactor (right) as implemented in the model 244 and marketed by Sierra Andersen company. The instrument was designed with an inlet flow rate of 1 m^3/hr or 16.76 l/min ; 15 l/min ; 1.67 l/min. Of this total flow, 15 l/min was diverted into the “fine” (<2.5 μm) stream while 1.67 l/min went straight down the “coarse” (>2.5 μm) stream. Particles were collected on glass fiber filters for later analysis (Lai and Chen, 2000). Information on the instrument can be found in the Sierra Andersen instruction manual (Environmental Monitoring Systems, Laboratory, 1985). Mathematical treatment for the VI can be found in Marple and Chien (1980).

tube" that goes straight down the "coarse" (>2.5 μm) stream. The two divergent size segregated particle trains are subsequently collected on separate glass fiber filters for later analysis (Lai and Chen, 2000).

In this simplified illustrated version of VI, it can be seen that the bulk of the particles >2.5 μm are segregated and thus concentrated, a beneficial outcome if the agents of interest are mostly in this size group. In actual implementation of the multi-jet VI technology (Marple and Chien, 1980), the fine particle stream is "dumped" as exhaust. Some workers may be interested in capturing fine particles (<2.5 μm) of a smaller size cutoff. Sioutas et al. (1994) developed a slit version of VI that has a lower particle size 50% cutoff at 0.1- 0.25 μm. Conceptually, a lower cutoff size may be of relevance for individual viruses that may appear under electron microscopic view to fit into nanometer size range. However, a low size cutoff is not a significant concern for capturing human transmitted viral aerosol as Tellier (2006) pointed out that influenza virus exist as aggregates of about 5-10 μm in diameter. Recently, Lindsley et al. (2010), measuring particles from human cough, confirmed that 35% of the influenza RNA was contained in particles >4 μm in aerodynamic diameter, while 23% was in particles 1 to 4 μm and 42% in particles <1 μm. The evidence suggests that VI technology may be suitable for collecting bacterial and viral aerosols that exist in the environment.

Early attempts at integrating VI sampling to liquid chemistry

In the 1970s the US Army contracted Bendix Corp. to build the XM19 biological detector (**Fig. 2 and 3**). It was accompanied by the XM2 liquid collector for saving material for post analysis. Each unit consisted of a virtual impactor that ran at a flow rate of 1200 to 1400 l/min. In the XM19, the large particle fraction was impacted on a moving plastic tape dispensed from a cassette (Barrett and Miller, 1975). Particulate material on the tape was treated with Luminol reagents and if the sampled area contained bound iron in captured bacterial agents (Neufeld et al., 1965), the resultant chemiluminescent signal would be detected via analogue electronics that led to the sounding of an alarm. Simultaneously, the XM2 would be triggered to collect a liquid sample of impinged particles. The liquid sample was to be sent to a microbiological facility for confirmatory studies. Theoretically, the detection approach was based on good microbiological principles (Sotnikov, 1970; Miller and Vogelhut, 1978 and Andre et al., 2003). However, it was not realized at the time, environmental aerosol contained an abundance of non-specific particles rich in iron which caused interference that led to many false alarms (Vong et al. 2007).

Fig. 2 XM19 biological detector showing the virtual impactor stack.

Fig. 3 The XM19 showing the particle impingement tape cassette and liquid chemistry plumbing.

Although the XM19 was rejected by the US Army in early 1983 (Smart, 2005), the XM2 was later given a new coat of desert colour paint for deployment during the first Gulf war. In a declassified report (Rostker, 2000), it was mentioned that the collector was used to obtain liquid samples for anthrax testing by handheld test strip technology. It was also mentioned that the test kit was not very effective due to too many false positives.

The mass spectrometry phase

During the mid to late 1990's, there was a heightened awareness of potential bioterrorism occurrence world wide. Great efforts were put towards chemical and biological (CB) detection using the most sophisticated technologies regardless of cost. Bruker was a prominent instrument maker associated with mass spectrometry and they were contracted to produce an instrument that could detect CB agents in real time (Griest et al. 2001). To accomplish the required sensitivity and speed, VI technology was implemented (**Fig. 4**). The desired performance characteristics were ambitious, as seen in this quote:

"The air sampler concentrates size-classified airborne particles that may host toxins, viruses, and other dangerous biological warfare agents such as anthrax spores. These particles are heated in a pyrolyzer in the presence of a methylating reagent. As a result, the membrane lipid fatty acids in the microorganisms break off of the phospholipid and form volatile methyl esters that are ionized in the presence of a chemical ionization reagent gas that converts them into intact charged molecules, or ions. The ions are separated in an ion trap mass spectrometer. A computer examines the resulting mass spectrum and determines whether a biological warfare agent is present in the air; if so, it identifies the agent from its spectrum. For example, bacteria are identified from the presence or absence and ratios of several key fatty acids". (www.ornl.gov/info/ornlreview/measure/analy/direct/chem-bio.htm [accessed on 9 March 2011]). Fox (2005) provided a detailed account of the development of the US military CBMS system and commented on its susceptibility to false alarms. History has shown that mass spectrometry did not become commonly adopted for general applications in biological detection. However, Bruker took all the lessons learnt from this work and in 2010, marketed an instrument specifically for laboratory identification of clinically relevant microorganisms (Prod'hom et al. 2010). Success in applying such instrument technique required very precise sample preparation as described by Freiwald and Sauer (2009), a regime unlikely to be met by field portable instruments.

An attempt to develop a liquid reagent based biological chemical detector (BCD)

Only a relatively few cells are known to constitute an infectious dose (10^1-10^4 cells). Borthwick et al. (2005) explained the difficulty in using antibody based immunological methods for measuring infectious dose of a variety of bacterial pathogens. The solution they selected was to sonicate the bacterial spore samples in order to detect 10^6 spores/ml. Without such treatment, the concentrations required were 10-100 times higher. In the early 1990's there was a concerted effort to develop a liquid reagent based biological chemical detector (BCD) by automating antibody based detection methods. However, obtaining sufficient biological aerosol material within a short time was a significant hurdle. To develop the BCD, it was thought that VI technology would provide the necessary concentrating effect to gather enough aerosol particles in liquid fractions. **Fig. 5a** shows a VI designed to concentrate 100 l air and render the particles into a liquid stream at a continuous flow rate of 100 μl/min.

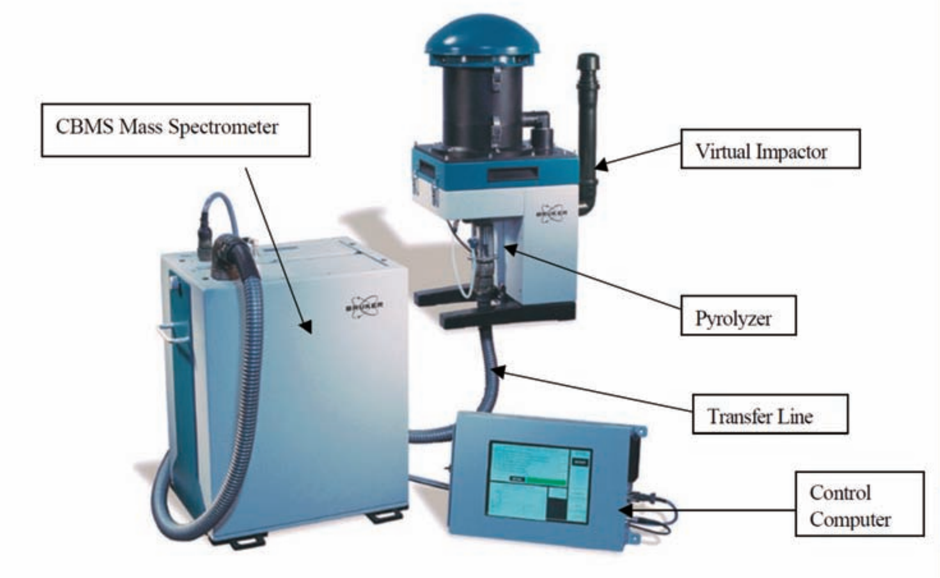

Fig. 4 A portable mass spectrometer coupled to a virtual impactor for concentrating biological aerosols particles (www.armedforces-int.com/article/bruker-daltonics-inc-nbc-instruments.html accessed 9 March 2011).

Several defense laboratories were tasked to characterize the inlet concentrator using a non virulent stimulant for anthrax. Chamber trials using *Bacillus subtilis* (BG) spore aerosol, a method pioneered by Ferry et al. (1949), revealed that on each test occasion, the concentrator had a collection efficiently of 0.01 to 1% (unpublished). When the internal wall of the VI was examined, it was discovered that much of the aerosol particles adhered to the walls at the two orifice stages (**Fig. 5c and d**). In hindsight, it is now well understood that biological cells naturally adhere to surfaces. Abu-Lail and Camesano (2003) studied the role of polysaccharides in bacterial adhesion using atomic force microscopy (AFM). Using data from a variety of sources, table 1 summarizes the typical adhesion forces measured by AFM. Bakker et al. (2004) observed that different organisms taken from a variety of habitats exhibited different adhesion forces, suggesting that more than just simple physical forces exert an influence. The lesson from this illustration is that in designing VI devices of high throughput efficiency, knowledge of the nature of biological stickiness is essential. Overcoming the problem can be a difficult task. Ironically, the lack of success in making the BCD perform to expectations was not due to low VI concentration efficiency. It was discovered that antibody fractions raised for a strain of anthrax were non specific; there was cross reactivity with other organisms (Phillips and Martin, 1988; Quinlan and Foegeding, 1997; Longchamp and Leighton, 1999). The project was abandoned due to this lack of reaction specificity.

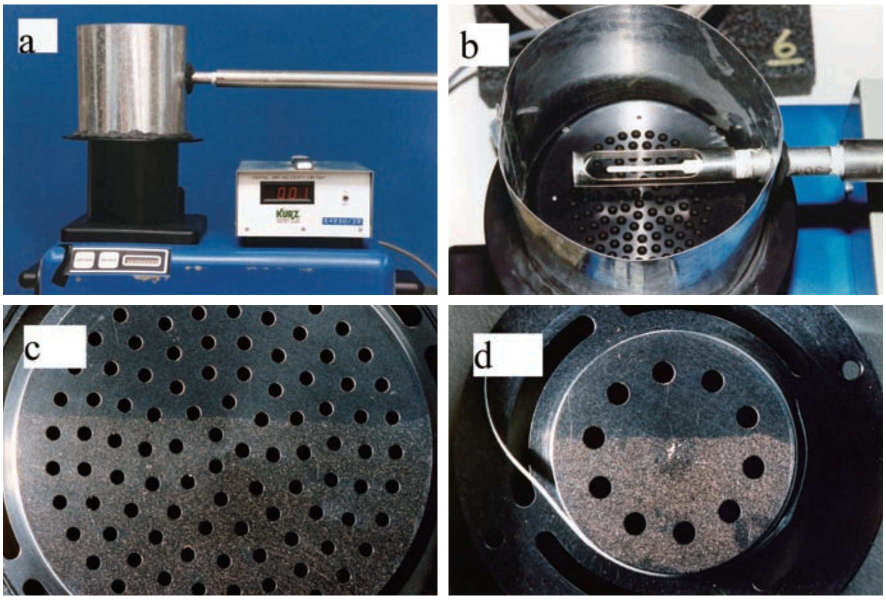

Fig. 5 Virtual impactor designed for a biological detector based on immunological measurements using specific antibody preparations. a. external view showing an attachment to facilitate flow rate measurements, b anemometer probe above the first concentrator stage, c view of first concentrator surface after processing a biological aerosol and d similar view of the second concentrator stage. Part of the surfaces in c & d were wiped clean to provide refractive contrast. Note significant built up of particulate dust on the internal surfaces.

Table 1 Typical adhesion forces measured by atomic force microscopy, values taken from a number of open literature sources

Organism	Substrate	Force (nN)	Level
Antibody to E. coli	Glass	0.6	Low
Azospirillum brasilense extracellular polymers	Polystyrene substrata	0.8 ± 0.2	Low
Pseudomonas sp.	Aluminum	5.6 ± 0.8	Medium
Desulfovibrio desulfuricans	Aluminum	5.4 ± 0.6	Medium
Bacterial cell	Bacterial cell	6.5-6.8	Medium
Bacillus mycoides spores	Glass	7.4 ± 3.7	Medium
Aspergillus niger spores 33% RH	Mica	30-40	High
Caulobacter cresentus	Glass	590	V. high

Development of optical based detectors for particle in air analysis

By the early 1990s it became clear that there was an urgent need for biological detectors capable of continuous operation (24 × 7), requiring no liquid reagents and had few false alarms. The Fluorescence Aerodynamic Particle Sizer (FLAPS) was developed by the Defence Research and Development Canada Suffield in collaboration with TSI Inc. (Hairston et al. 1997). The detection principle was based on the theory that live bacterial spore particles fluoresce when excited by UV light, demonstrated later using flow cytometry methods (Laflamme et al. 2005),

Using the FLAPS instrument for studying background air, it was noted that fluorescent particles were not in great abundance, at least at some locations like semi desert environments. To correctly implement statistical techniques in alarm algorithms, there was a need to increase the fluorescent counts obtained over a short time span (in seconds). The best way to accomplish this was to use a virtual impactor (Ho et al. 1999).

As a way to enrich the population of background fluorescent particles for better statistical counting, a prototype aerosol concentrator constructed by Carl Peterson (model XMX, SCP Engineering, St. Paul, MN) was used as a front end to the FLAPS intake. This was a modified version of the original XM2 used for concentrating biological aerosol, as reported previously (Brenner et al. 1988). Ho et al. (1999) employed a smaller version, designed for optimal size, weight and power consumption. It operated at 400-600 l/min, concentrating to 1 l/min delivered to the FLAPS optical intake. Improved particle throughput provided by this setup facilitated a rapid sampling time of 3 seconds. In practice, due to the slow computers available at the time (mid 1990's), an additional 1 second penalty was incurred for computational and data handling overhead. By this protocol, aerosol data expressed as aerodynamic size distribution and fluorescence intensity could be collected continuously every 4 seconds over long periods unattended by the operator. **Fig. 6** shows a modern implementation of a DC motor driven VI with coupling to an optical system.

Ho et al. (2004) characterized ambient aerosol in a forested environment in Umea, Sweden using a FLAPS coupled to a virtual impactor as shown in **Fig. 6** With a reference collector system, live bacterial aerosol particles were measured by impaction on growth medium with a slit sampler (Ho et al. 2005). During the week of sampling, there were three major episodes of thunderstorm accompanied by rain. Coincidentally, during the same periods, a significant number of live particles were seen to increase above background levels. At about the same time as the appearance of live particles, the FLAPS also measured concomitant increase in fluorescent particles. Interestingly, these same fluorescent particles exhibited a shift in median size distribution during the same time (**Fig. 7**). The phenomenon of median size shift to-

Fig. 6 Prototype FLAPS3 showing a virtual impactor on the left and the particle detection electronics on the right. The coupling of the two systems was accomplished via a spring loaded aerosol transfer tube shown as a golden extension on the right unit. Combining the two units with four clasps resulted in a single one person portable instrument that was designed to be weather proof. In practice, it performed well during a tropical storm. Consequently, it was possible to sample biological aerosol content during rainy periods. This capability opened up a hitherto unprecedented opportunity to explore the presence of biological aerosol content associated with rain episodes.

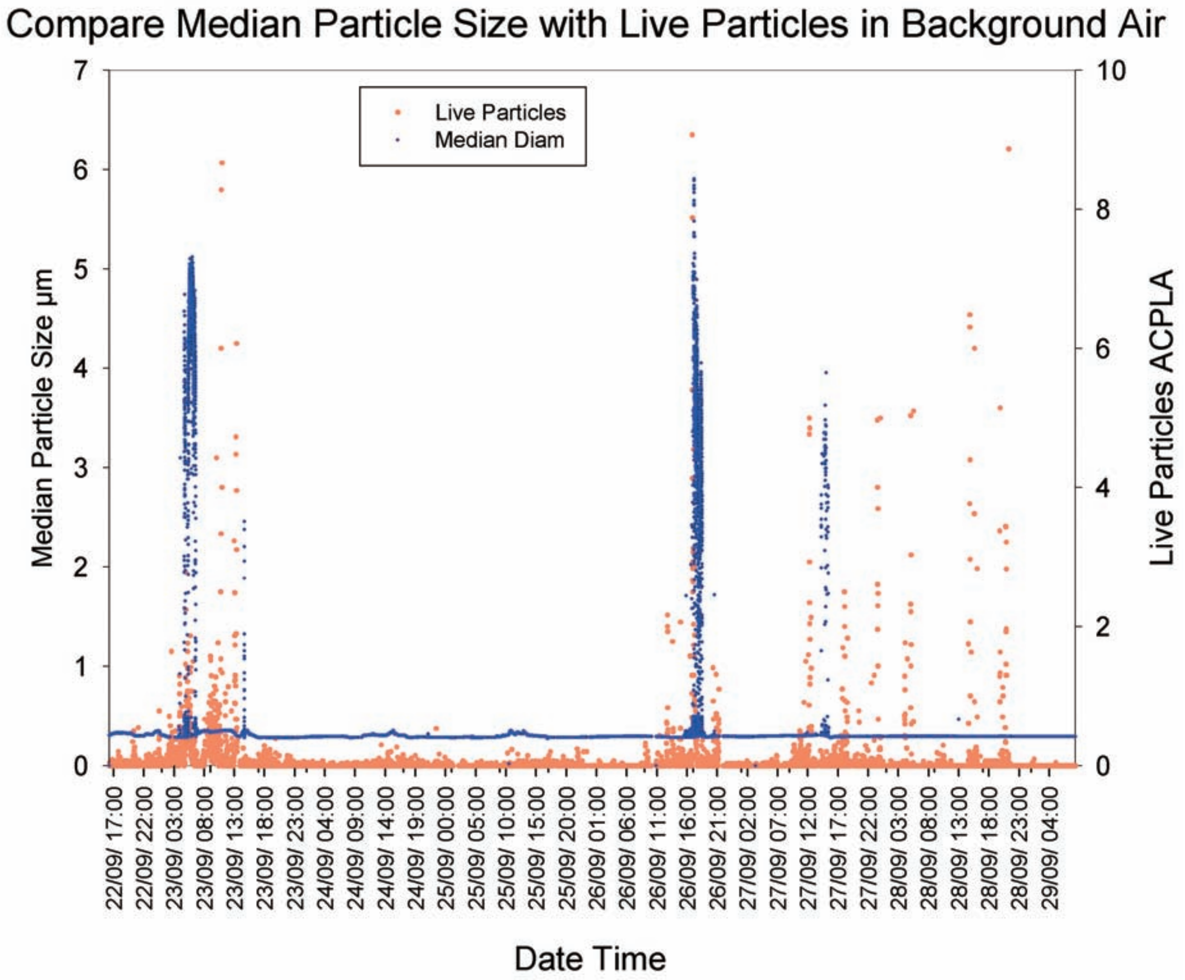

Fig. 7 Sampling background air over a one week period in Umea, Sweden. Live particles were measured using conventional slit impaction on growth agar while fluorescent particles were obtained with a FLAPS instrument. There were three major periods of thunderstorm accompanied by rain, depicted by the fluorescent signals (blue dots). The data show that when there were live bacterial particles present, the median particle size distribution also increased at about the same time.

wards the 5-6 µm during thunderstorm related activity has been observed previously by the same author in other locations like Northern Australia and Singapore (unpublished). Recently, Huffman et al (2010) who measured background biological aerosol in Europe using a naturally aspirated FLAPS instrument noted that the appearance of 3 µm particles could be associated with biological content.

In the late 1990s the US Army contracted a newer version of the XM2 to be built, calling it the SCP 1021 (SCP Dynamics, Inc., Minneapolis, MN). It was characterized by solid and liquid aerosols in a chamber using polycarbonate membrane filters as reference sampling method (Kesavan and Doherty, 2001). Working at a flow rate of 1350 l/min, the SCP 1021 registered 25-30% efficiency for particles between 4-5 µm. In contrast, Bergman et al. (2005) performed similar characterization of the (SCP 1026) but used an AGI-30 as reference. For a variety of test aerosol materials they consistently measured close to 80-90% efficiency for particles >2 µm. The discrepancy may be explained by the difference in the reference sampling method.

Complex VI systems

A VI device consisting of complex multi slit inlet was described by Mainelis et al. (2005) and was employed as the aerosol concentrator for a stand alone biological detector. Operating at 1760-3300 l/min, these workers claimed a concentration ratio of 7.5×10^5 when tested with 3 μm standard latex calibration beads. In contrast, Han and Mainelis (2010) achieved concentration a ratio of 1×10^6 when employing an electrostatic precipitator method. From these observations, it would appear VI technology has evolved to become fairly competitive with other technologies.

Sampling viral aerosol

Apart from the work of Brenner et al. (1988) who used the original XM2 to measure viral aerosol particles in the environment, there has been a recent report on the use of VI technology to concentrate and sample virus aerosol (Cooper, 2010). A virtual impactor (XMX/2L-MIL, Dycor Technologies Ltd, Edmonton, Alberta, Canada) operating at a flow rate of 600 l/min was challenged in a 12 m^3 chamber with MS2 viral aerosol (**Fig. 8**). It was reported that sampling efficiency was about 25% when compared to glass impingers at low to medium aerosol concentrations. However, at high challenge concentrations, the VI performance was very close to the reference samplers. In a live avian flu virus sampling campaign, Schofield et al. (2005) using a similar device, captured culturable viruses from an infected chicken barn. This may be a good illustration of the gentle processing characteristics of the VI sampler as viruses have been known to be fragile (Verreault et al. 2008).

Fig. 8 A commercially available virtual impactor that can be configured to collect aerosol particles in sequential 1-2 ml liquid fractions. Conventional 96 well plates may be used to archive the time stamped samples. The instrument can also be configured for single liquid tube or a dry filter collector (Dycor Technologies Ltd, Edmonton, Alberta, Canada).

Miniaturization of the VI technology

The future in the application of VI technology may be in miniaturization of the components. The Hwang group at Yonsei University in Korea designed and built a micro electro mechanical system (MEMS) based VI with a cut off size at 1 μm (Park et al. 2009). Using *Staphylococcus epidermidis* as the biological simulant, they reported an impressive collection efficiency of 74-76% based on culturable particles. As discussed earlier, bacteria adhere to surfaces due to inherent stickiness related to polysaccharides. Hwang's group noted that this was a problem in their narrow liquid channels. Their solution to solving bacterial wall losses was to introduce a 1 kV 1 kHz ac current to the liquid channels. An observed improvement of 12% was obtained (Kim et al. 2010). In another paper, while sampling indoor biological aerosol content, they measured the presence of bacteria, fungi, and actinomycetes (Yoon et al. 2010). It was also demonstrated that cutlurable cell concentrations were linearly correlated with ATP content.

Conclusions

It can be seen that a variety of machines have successfully integrated VI technologies to liquid chemistries like antibody based reactions or PCR methods. However, this review has revealed major weaknesses in the way detectors are being tested and the use of non standard reference samplers has been mentioned. First, the challenge aerosol used to test the instruments is always presented as a continuous stream. To properly mimic a threat aerosol, the cloud should be presented as short duration puffs. Ho at al. (2010) introduced a method to generate precise puffs of biological challenge aerosol designed to resemble brief emissions encountered in clean room environments. Adopting this method will provide a more meaningful way to determine if a VI equipped device is more effective than the naturally aspirated version. The naturally aspirated mode will serve as the experimental control. Secondly, the instrument must be tested in outdoor environments where background contaminants can properly stress alarming algorithms. There is at present no standard method to test detectors to determine the effectiveness of alarming technologies. As mentioned earlier, microbial particles are naturally sticky, so thirdly, the size of the aerosol particles should resemble threat material consisting of aggregates of individuals as reported by Duncan and Ho (2008). It is generally accepted that challenge particles should be within the range of 2-5 µm in diameter although some workers may even go beyond 10 µm (Druett and May, 1952; Thomas et al., 2008). But large particles are difficult to generate with any consistency so aiming for the 2-5 µn range is recommended.

References

Abu-Lail, N. I. and T. A. Camesano (2003): Polysaccharide properties probed with atomic force microscopy. Journal of Microscopy, **212**(3), pp. 217-238.

Andre, P., S. Bilger, P. Remy, S. Bettinger and D. J. M. Vidon (2003): Effects of iron and oxygen species scavengers on Listeria spp. chemiluminescence. Biochemical and Biophysical Research Communications, **304**(4), pp. 807-811.

Bakker, D. P., B. R. Postmus, H. J. Busscher and H. C. Van Der Mei (2004): Bacterial strains isolated from different niches can exhibit different patterns of adhesion to substrata. Applied and Environmental Microbiology, **70**(6), pp. 3758-3760.

Barrett, W.J., Miller, H. C. (1975): Investigation of Luminol and Collection Tape Components and the Effects of Airborne Interferents on the XM19 Detector. Quarterly progress rept. no. 2, SOUTHERN RESEARCH INST BIRMINGHAM AL, ADA007274.

Bergman, W., J. Shinn R., Lochner, S. Sawyer, F. Milanovich and R. Mariella Jr. (2005): High air flow, low pressure drop, bio-aerosol collector using a multi-slit virtual impactor. Journal of Aerosol Science, **36**, pp. 619-638.

Blatny, J., J. Ho, G. Skogan, E. Fykse, T. Aarskaug and V. Waagen (2010): Airborne Legionella bacteria from pulp waste treatment plant: aerosol particles characterized as aggregates and their potential hazard. Aerobiologia, **27**(2), pp.147-162.

Borthwick, K. A. J., T. E. Love, M. B. McDonnell and W. T. Coakley (2005): Improvement of immunodetection of bacterial spore antigen by ultrasonic cavitation. Analytical Chemistry, **77**(22), pp. 7242-7245.

Brenner, K. P., P. V. Scarpino and C. S. Clark (1988): Animal viruses, coliphages, and bacteria in aerosols and wastewater at a spray irrigation site. Appl Environ Microbiol., **54**(2), pp. 409-15.

Cooper, C. W. (2010): High volume air sampling for viral aerosols: a comparative approach. AFIT/GES/ENV/10-M01, US Air Force Institute of Technology, Wright-Patterson Air Force Base, Ohio.

Druett, H. A. and K. R. May (1952): A wind tunnel for the study of airborne infections. J Hyg (Lond), **50**(1), pp. 69-81.

Duncan, S., and Ho, J. (2008): Estimation of viable spores in Bacillus atrophaeus (BG) particles of 1 to 9 μm size range. Clean—Soil Air Water, **36**, pp.584–592.

Environmental Monitoring Systems, Laboratory, (1985): “Operating Procedure for the Sierra Series 244E Dichotomous sampler Equipped with the Andersen Model 246B PM10 Inle”, EMSL, Research Triangle Park, N.C.

Eubanks, L. M., T. J. Dickerson and K. D. Janda (2007): Technological advancements for the detection of and protection against biological and chemical warfare agents. Chem. Soc. Rev., **36**(3), pp. 458-470.

Evans, B.T.N., Yee, E., Roy, G. and Ho, J. (1994): Remote Detection and Mapping of Bioaerosols. J. Aerosol Sci., **25**, pp.1549-1566.

Ferry, R. M., L. E. Farr and M. G. Hartman (1949): The Preparation and Measurement of the Concentration of Dilute Bacterial Aerosols. Chemical Reviews, **44**(2), pp. 389-417.

Fox, A. (2005): Mass spectrometry identification and biodetection, lessons learned and future developments in Identification of microorganisms by mass spectrometry, pp. 64-89. Ed C. L. Wilkens and J. O. Lay, John Wiley & Sons, Inc., Hoboken, N.J.

Freiwald, A. and S. Sauer (2009): Phylogenetic classification and identification of bacteria by mass spectrometry. Nature Protocols, **4**(5), pp. 732-742.

Griest, W. H., M. B. Wise, K. J. Hart, S. A. Lammert, C. V. Thompson and A. A. Vass (2001): Biological agent detection and identification by the block II chemical biological mass spectrometer, Field Analytical Chemistry and Technology, **5**(4), pp. 177-184.

Hairston, P., J. Ho, F.R. Quant (1997): Design of an instrument for Real-time Detection of Bioaerosols Using Simultaneous Measurement of Particle Aerodynamic Size and Intrinsic Fluorescence, J. Aerosol Sc., **28**, pp. 471-482.

Han, T., H. R. An and G. Mainelis (2010): Performance of an Electrostatic Precipitator with Superhydrophobic Surface when Collecting Airborne Bacteria. Aerosol Science and Technology, **44**(5), pp. 339 - 348.

Ho, J., Evans, B.T.N. and Roy, G. (1990): “Laser Detection and Mapping of Biological Simulants. III. Dichotomous Sampler Measurements of Aerosol Concentrations as Related to LIDAR Signals (U)”. Suffield Report No. 532, (Unclassified).

Ho, J. (1991): “Characteristics of Simulant Aerosols for Study of the BCD Inlet Nozzle”. DRES Suffield Report No. 543, (Unclassified).

Ho, J., M. Spence and P. Hairston (1999): Measurement of Biological Aerosol with a Fluorescent Aerodynamic Particle Sizer (FLAPS): Correlation of Optical data with Biological Data,. Aerobiologia, **15**, pp. 281-291.

Ho, J., T. Tjarnhage, J. Burke and L. Stadnyk (2004): Background aerosol sampling: optical characterisitcs of live particles associated with thundershowers in Umea, Sweden in September 2003. Proceedings, the 8th International Symposium on Protection against Chemical and Biological Warfare Agents (including bioterrorism), Gothenburg, Sweden.

Ho, J. and S. Duncan (2005): Estimating aerosol hazards from an anthrax letter, J. Aerosol Sci., **36**, pp. 701-709.

Ho, J., M. Spence and S. Duncan (2005): An approach towards characterizing a reference sampler for culturable biological particle measurement, J. Aerosol Sci., **36**, pp. 557-573.

Ho, J., N. Stanley and T. Kuehn (2010): Feasibility of using real-time optical methods for detecting the presence of viable bacteria aerosols at low concentrations in clean room environments. Aerobiologia, **27**(2), pp.163-172.

Huffman, J. A., B. Treutlein and U. Poschl (2010): Fluorescent biological aerosol particle concentrations and size distributions measured with an Ultraviolet Aerodynamic Particle Sizer (UV-APS) in Central Europe. Atmospheric Chemistry and Physics, **10**(7), pp. 3215-3233.

Jones, A. M. and R. M. Harrison (2004): The effects of meteorological factors on atmospheric bioaerosol concentrations-a review, The Science of the Total Environment, **326**(1-3), pp. 151-80.

Kesavan, J., & Doherty, R. W. (2001): Characterization of the SCP 1021 Aerosol Sampler. Edgewood Chemical Biological Center Report ECBC-TR-211, Aberdeen Proving Ground, MD. National Technical Information Service, 5285, Port Royal Road, Springfield, VA 22161, report ADA397460, www.ntis.gov.

Kim, M. G., Y. H. Kim, H. L. Kim, C. W. Park, Y. H. Joe, J. Hwang and Y. J. Kim (2010): Wall loss reduction technique using an electrodynamic disturbance for airborne particle processing chip applications, Journal of Micromechanics and Microengineering, **20**(3), pp. 1-12.

Laflamme, C., Verreault, D., Lavigne, S., Trudel, L., Ho, J., Duchaine, C. (2005): Autofluorescence as a viability marker for detection of bacterial spores, Frontiers in Bioscience, **10**, pp. 1647-1653.

Lai, C. Y. and C. C. Chen (2000): Performance characteristics of PM10 samplers under calm air conditions. J Air Waste Manag Assoc., **50**(4), pp.578-87.

Lindsley, W. G., F. M. Blachere, R. E. Thewlis, A. Vishnu, K. A. Davis, G. Cao, J. E. Palmer, K. E. Clark, M. A. Fisher, R. Khakoo and D. H. Beezhold (2010): Measurements of Airborne Influenza Virus in Aerosol Particles from Human Coughs. Plos One 5(11), e15100.

Longchamp, P. and T. Leighton (1999): Molecular recognition specificity of Bacillus anthracis spore antibodies, Journal of Applied Microbiology, **87**, pp. 246-249.

Loo, B. W. and C. P. Cork (1988): Development of High-Efficiency Virtual Impactors. Aerosol Science and Technology, **9**(3), pp. 167-176.

Mainelis, G., D. Masquelier, A. Makarewicz and J. Dzenitis (2005) : Performance characteristics of the aerosol collectors of the autonomous pathogen detection system (APDS), Aerosol Science and Technology, **39**(5), pp. 461-471.

Marple, V. A. (1970): "A Fundamental Study of Inertial Impactors," PhD Thesis, Mechanical Engineering Department, University of Minnesota, Particle Technology Laboratory Publ. No. 144.

Marple, V. A. and C. M. Chien (1980): Virtual impactors: A theoretical study, Environmental Science and Technology, **14**(8), pp. 976-985.

Marple, V. A. (2004): History of Impactors - The first 110 years, Aerosol Science and Technology, **38**(3), pp. 247-292.

Miller, C. A. and P. O. Vogelhut (1978): Chemiluminescent detection of bacteria: experimental and theoretical limits, Appl Environ Microbiol., **35**(4), pp. 813-6.

Neufeld, H. A., C. J. Conklin and R. D. Towner (1965): Chemiluminescence of Luminol in Presence of Hematin Compounds, Analytical Biochemistry, **12**(2), pp. 303-309.

Park, D., Y. H. Kim, C. W. Park, J. Hwang and Y. J. Kim (2009): New bio-aerosol collector using a micromachined virtual impactor, Journal of Aerosol Science **40**(5), pp. 415-422.

Phillips, A.P. and K.L. Martin (1988): Investigation of spore surface antigens in the genus Bacillus by the use of polyclonal antibodies in immunofluorescence tests, Journal of Applied Bacteriology, **64**(1), pp. 47-55.

Prod'hom, G., A. Bizzini, C. Durussel, J. Bille and G. Greub (2010): Matrix-Assisted Laser Desorption Ionization-Time of Flight Mass Spectrometry for Direct Bacterial Identification from Positive Blood Culture Pellets. Journal of Clinical Microbiology, **48**(4), pp. 1481-1483.

Quinlan, J.J. and P.M. Foegeding (1997): Monoclonal antibodies for use in detection of Bacillus and Clostridium spores, Applied and Environmental Microbiology, **63**, pp. 482-487.

Riedel, S. (2004): Biological warfare and bioterrorism: a historical review, Proc (Bayl Univ Med Cent), **17**(4), pp. 400-6.

Rostker, B. (2000): Close-out report biological warfare investigation, Special Assistant for Gulf War Illnesses, Department of Defense declassified by CBDCOM Security Class Review Board 20 Jan 1998. http://www.gulflink.osd.mil/bw/index.html.

Schofield, L. Ho, J., Kournikakis, B. and Booth T. (2005): Avian influenza aerosol sampling campaign in the British Columbia Fraser valley April 9-19 2004, Sampling of rare biological events, DRDC Suffield TM 2005-032.

Sioutas, C., P. Koutrakis and R. M. Burton (1994): Development of a Low Cutpoint Slit Virtual Impactor for Sampling Ambient Fine Particles, Journal of Aerosol Science, **25**(7), pp. 1321-1330.

Smart, J.K. (2005): History of Chemical and Biological Detectors, Alarms, and Warning Systems" Chemical and Biological Defense Information Analysis Center, Vol. 6, No. 4. Aberdeen Proving Ground, MD 21010-5424. http://www.wood.army.mil/ccmuseum/ccmuseum/Library/Detectors_History.pdf.

Sotnikov, G.G. (1970): Detection of iron-porphyrin proteins with a biochemiluminescent method in search of extraterrestrial life, Life Sci Space Res. **8**, pp. 90-8.

Tellier, R. (2006): Review of aerosol transmission of influenza A virus, Emerging Infectious Diseases, **12**(11), pp. 1657-1662.

Thomas, R. J., D. Webber, W. Sellors, A. Collinge, A. Frost, A. J. Stagg, S. C. Bailey, P. N. Jayasekera, R. R. Taylor, S. Eley and R. W. Titball (2008): Characterization and deposition of respirable large- and small-particle bioaerosols, Applied and Environmental Microbiology, **74**(20), pp. 6437-6443.

Verreault, D., S. Moineau and C. Duchaine (2008) : Methods for sampling of airborne viruses, Microbiol Mol Biol Rev., **72**(3), pp. 413-44.

Vong, L., A. Laes and S. Blain (2007): Determination of iron-porphyrin-like complexes at nanomolar levels in seawater, Analytica Chimica Acta, **588**(2), pp. 237-244.

Yoon, K. Y., C. W. Park, J. H. Byeon and J. Hwang (2010): Design and Application of an Inertial Impactor in Combination with an ATP Bioluminescence Detector for In Situ Rapid Estimation of the Efficacies of Air Controlling Devices on Removal of Bioaerosols, Environmental Science & Technology, **44**(5), pp. 1742-1746.

Author's short biography

Jim Ho

Jim Ho is defence scientist with the Defence Research and Development Canada at Suffield. He received BSc. and MSc. degrees from McGill University in microbiology and a PhD. from the University of Kentucky in microbial biochemistry. He has been working on the development of biological detection systems since the early 1980's. In the beginning, he demonstrated the possibility of using LIDAR systems for biological detection. Then he invented an aerosol point biological detector that could reveal if a particle had "live" characteristics. This instrument is currently commercialized by TSI Inc. as models 3313, 3314 and 3317. His current research is focused on characterizing naturally occurring live biological aerosols in different locations around the world. The information gathered has become useful in a variety of areas especially in developing alarm algorithms. He has discovered that minimizing false alarms for detection system is the next most critical phase in biological detection.

Control of Particle Tribocharging[†]

Shuji Matsusaka
Department of Chemical Engineering, Kyoto University[1]

Abstract

When two different materials are brought into contact and separated, an electrical charge is transferred from one to the other. This phenomenon is called contact electrification, contact charging, or tribocharging. Charged particles cause various secondary phenomena during powder processing, such as deposition, adhesion, and electrostatic discharge. Additionally, charged particles are used in many industrial applications such as electrophotography, electrostatic powder coating, and separation; thus, particle charge control is very important for improving particle performance. However, there are still many unknown effects, and in some cases, inconsistent results have been reported. In this review, the basic concepts and theories of charge transfer between solid surfaces are summarized and a description of particle charging caused by repeated impacts on a wall is formulated. On the basis of these concepts and formulations, novel methods of controlling particle tribocharging are presented. In particular, a method using an applied electric field is expected to be applicable in industrial fields.

Keywords: Electrostatics, Tribocharging, Particle electrification, Charge control, Electric field

1. Introduction

Powders and particulate solids are widely used in industry. When handled in air, their surfaces become triboelectrically charged and several other phenomena occur. For instance, in pneumatic transport lines and fluidized beds, particles become charged and adhere to the walls[1-5]. If the particles are excessively charged, an electrostatic discharge will occur, which can cause fire and explosion hazards[6-8]. Additionally, electrostatic forces can control the motion of charged particles; thus, many applications have been developed[9], e.g., electrophotography[10, 11], electrostatic powder coating[12-14], electrostatic precipitation[15], particle separation[16, 17], and the construction of electromechanical valves for solids[18, 19]. Moreover, the charge on particles can provide useful information regarding the state of various processes, e.g., powder flow rate[20-23], concentration distribution[24], and several others[25].

The contact charging and electromechanics of particles have been studied for many years[26-30]; however, there are still many unknown effects, and in some cases, inconsistent results have been reported. This lack of reliable information is due to the many relevant factors, such as chemical, physical, and electrical properties and environmental conditions, all of which affect the process. To analyze and control particle charging, the measurement of electrostatic charge[10, 31-38] and the evaluation of electrostatic characteristics[39-48] are important. To improve existing processes and to develop new applications, it is necessary to obtain an in-depth understanding of these qualities based on theoretical analyses.

In the present review, the basic concepts and theories of charge transfer between solid surfaces are summarized and a model of particle charging caused by repeated impacts on a wall is formulated. On the basis of these concepts and the results of the formulation, new methods for the control of particle tribocharging are presented.

[†] Accepted: August 1st, 2011

[1] Katsura, Nishikyo-ku, Kyoto, 615-8510 Japan
E-mail: matsu@cheme.kyoto-u.ac.jp
TEL: (+81) 75 383 3054 FAX: (+81) 75 383 3054

ⓒ 2011 Hosokawa Powder Technology Foundation

2. Basic concepts of Contact Electrification

When two different materials are brought into contact and separated, an electric charge is usually transferred from one to the other. This phenomenon is called “contact electrification” or “contact charging.” When they are rubbed, the phenomenon of “tribocharging” or “frictional electrification” occurs. Similarly, short-term contact results in “impact charging.” Contact electrification can also be classified into three categories according to the contacting materials: metal–metal contact, metal–insulator contact, and insulator–insulator contact.

The contact electrification of metals usually goes unnoticed because the transferred charge moves away from the contact point because of the conductivity of the materials. However, when the metals are isolated (electrically) after the contact, the transferred charge can be measured. This transfer of charge is explained in terms of electron transfer arising from the difference in the work functions of the two surfaces. Assuming that electron transfer takes place by tunneling (so that the thermodynamic equilibrium is maintained), the contact potential difference V_c is given by[27)]

$$V_c = V_{1/2} = -\frac{(\phi_1 - \phi_2)}{e} \tag{1}$$

where $V_{1/2}$ is the contact potential difference between metal 1 and metal 2[31)], ϕ_1 and ϕ_2 are the work functions of the surfaces, and e is the elementary charge. The amount of charge transferred is equal to the product of the contact potential difference V_c and the capacitance C_0 between the two bodies. The capacitance depends on the state of the contacting surfaces. Although the position of the electrons may vary after the metals are separated, the net charge transferred Δq_c can be approximated by the following equation:

$$\Delta q_c = C_0 V_c \tag{2}$$

The charge transfer in insulator-metal contact can be explained using a model of metal-to-metal electron transfer. This method assumes that an apparent or effective work function can be assigned to the insulator. The amount of charge transferred is determined so as to equalize the energy levels of the two materials. This concept was substantiated experimentally by Davies[49)]. Murata and Kittaka[50)], also produced evidence of electron transfer by comparing contact charging experiments to photoelectric emission experiments. The main criticism of the effective work function model is that there are no available free electrons in an insulator. To resolve this situation and to explain the charge transfer for insulator-insulator contacts, several modified models have been developed[29, 51, 52)]. Some of these methods are similar to those developed for insulator-metal contact; however, the movement of electrons in the body is more restricted. In one of these models, it is assumed that the energy levels available to the electron are only on the surface, not in the bulk; the available level is called the ‘surface state’ [53-55)]. When insulators come into contact, electrons move from the filled surface states of one insulator to the empty surface states of the other insulator. The driving force for the charge transfer between the surfaces is the difference in the effective work functions of the two surfaces. The charge transfer will cease when the Fermi levels of the two materials are equal.

The physicochemical structure of the surface states is difficult to strictly define. Fabish and Duke[56, 57)] proposed a molecular-ion-state model, which assumes that polymers have donor and acceptor states and that charge is carried by electrons. Thus, despite the inclusion of ‘ion’ in the name of the model, it is actually an electron transfer model. In their model, the distribution of the molecular-ion-state is assumed to be a Gaussian distribution. Yanagida et al.[58)] calculated the level of the highest occupied molecular orbital (HOMO) of an oligomer using a semi-empirical molecular orbital method. The values calculated using this model were nearly proportional to the measured values of the threshold energy of photoemission, which corresponds to the effective work function of the polymers. This result shows that quantum chemical calculations are applicable to the evaluation of the tribocharging of polymers. Yoshida et al.[59)] and Shirakawa et al.[60)] studied charge transfer in a polymer–metal contact system using another molecular orbital method and paying particular attention to surface defects. When an atom is missing a neighbor to which it would be able to bind, a dangling bond occurs. This kind of defect can be made during frictional contact. Although the number of quantitative analyses remains limited, it is expected that quantum chemical calculations can be used to understand charge transfer between surfaces.

3. Mechanism of Particle Charging

3.1 Condenser model

The contact region between two bodies can be treated as though it were a capacitor. When a particle impacts and rebounds on a wall, the contact time is short; however, this time is sufficient to allow charge transfer. Therefore, the transferred charge Δq caused by the impact can be represented using a condenser model, i.e.,[61]

$$\Delta q = k_c C V \tag{3}$$

where k_c is the charging efficiency, C is the capacitance, and V is the total potential difference. The capacitance C is given by

$$C = \frac{\varepsilon_0 S}{z_0} \tag{4}$$

where ε_0 is the absolute permittivity of the gas, S is the contact area, and z_0 is the critical gap (which includes the geometrical factors between the contact bodies). The total potential difference V at the contact gap is given by

$$V = V_c - V_e - V_b + V_{ex} \tag{5}$$

where V_c is the potential difference based on the surface work functions and V_e is the potential difference arising from the image charge, which is given by

$$V_e = k_e q \tag{6}$$

where q is the particle charge held on the particle before contact. V_b is the potential difference arising from the space charge caused by the surrounding charged particles, and which is given by

$$V_b = k_b q \tag{7}$$

V_{ex} is the potential difference arising from other electric fields. For instance, an external electric field may be applied to the system. In addition, when the wall is an insulator, the wall surface can retain charge and form an electric field, thus affecting the total potential difference. If the charge accumulates via contact charging, the total potential difference will decrease with increasing surface charge[62].

3.2 Charge relaxation model

Matsuyama and Yamamoto[63, 64] proposed another charging model, called the 'charge relaxation model'. When the two bodies are brought into contact with each other, charge is transferred across the contact gap; however, if the charge transferred to the particle is high enough, relaxation of the transferred charge occurs because of the action of gas discharge during the separation process. To determine the breakdown voltage in the gap, the Paschen curve is applied. This method is widely used in air insulating technology to provide the gas breakdown limit voltage between two parallel electrodes as a function of pressure and gap distance[65]. The remaining charge depends on the dielectric constant, the particle diameter, and the breakdown voltage of the gas.

3.3 Impact on a wall

In powder handling operations, individual particles acquire charge during collisions with the surrounding walls. An understanding of the charging process of a single particle is a basic requirement for the development of a theory of tribocharging of particles[66]. Several studies have been reported in which a single particle of a few millimeters in diameter was made to collide with a metal target and the transferred charge was measured[63, 64, 67-73]. Single-particle experiments with a larger sphere (31 mm in diameter)[61] or with a particle as small as 100–300 μm[74] were also performed. Watanabe et al.[75-77] also constructed a new test rig for small particles with which the initial charge and charge transfer due to a single impact on a target plate could be measured. These methods have several advantages, i.e., the contact state during the particle collision can be reproduced by controlling the impact velocity and angle. The impact charge for a zero initial charge is the characteristic charge; it increases with increasing impact velocity. The effect of impact angle on tribocharging was investigated using an inclined target and a rotating target[78]. The charge of a particle increases with the impact angle up to 60° and thereafter decreases. This charging tendency can be explained using a rolling–slipping model. For $\theta \leq 60°$, the effective contact area increases with the angle, because of the increase in the rotation of the particle on the target. For $\theta > 60°$, the effect of the slip on the target increases with the angle; thus, the effective contact area decreases. The effects of contact conditions such as contact time and contact area on particle charging were investigated by Ireland[79,80].

3.4 Repeated impacts of a single particle

When a particle repeatedly collides with a wall, the charge on the particle varies according to the electrostatic properties and the state of the collisions. To begin the analysis of successive impact charging, single-particle experiments were carried out using two metal targets, showing that the charge generated by the first impact affects subsequent instances of impact charging[72].

Repeated impact tests to study the charge accumulation were carried out by Matsusaka et al.[61]. To control the contact area easily, a large sphere (made of synthetic rubber) was used. The transferred charge caused by an impact decreased with the number of impacts. The accumulated charge approached a limiting value, which tended to decrease as the time interval between impacts increased. This was because the leakage of the electrostatic charge increased with increasing elapsed time.

It is possible to determine the particle charge generated by repeated impacts. First, the condenser model is applied to this formulation. To obtain the charge q_c as a function of the number of collisions n, a continuous quantity $\mathrm{d}q_c/\mathrm{d}n$ is used, i.e.,

$$\frac{\mathrm{d}q_c}{\mathrm{d}n} = k_c CV \tag{8}$$

The leakage of electrostatic charge $\mathrm{d}q_r/\mathrm{d}t$ is approximated by[43)]

$$\frac{\mathrm{d}q_r}{\mathrm{d}t} = -k_r q \tag{9}$$

where k_r is a constant. If the frequency of particle collisions is defined as f, Eq. (9) can be rewritten as

$$\frac{\mathrm{d}q_r}{\mathrm{d}n} = -\frac{k_r}{f}q \tag{10}$$

From the above equations, the net charge transfer is given by

$$\frac{\mathrm{d}q}{\mathrm{d}n} = \frac{\mathrm{d}q_c}{\mathrm{d}n} + \frac{\mathrm{d}q_r}{\mathrm{d}n} \tag{11}$$

Solving Eq. (11) with initial conditions $n = 0$ and $q = q_0$, one arrives at the following exponential equation:

$$q = q_0 \exp\left(-\frac{n}{n_0}\right) + q_\infty \left\{1 - \exp\left(-\frac{n}{n_0}\right)\right\} \tag{12}$$

where n_0 is the relaxation number and q_∞ is the equilibrium charge.

It should be noted that an equation of the same form as Eq. (12) can also be derived from the charge relaxation model from the phenomenological level. The charge relaxation model and the condenser model have certain differences. In the condenser model, q_∞ is proportional to the contact potential difference V_c; whereas, in the charge relaxation model, q_∞ is independent of V_c.

3.5 Particle charging in gas–solids pipe flow

In gas–solids pipe flow, particles repeatedly collide with the inner wall causing charge transfer[81)]. When a metal pipe is grounded, the charge transferred from the particles to the wall flows to ground, and can be detected as an electric current[21, 82-88)].

When the effect of particle–particle interactions on particle charging is negligible in dilute-phase gas–solids pipe flows, each particle can freely collide with the inner wall. Under these conditions, the electric current is proportional to the mass flow rate of particles. For dense-phase gas–solids pipe flows, the surrounding particles prevent free particle–wall contact, and consequently, the efficiency of the charge transfer is reduced. For smaller particles, the efficiency decreases because of agglomeration. In addition, the initial charge on particles affects the electric current. In powder handling operations, particles collide with different walls before arriving at the current detection pipe, e.g., hopper, feeder, chute, disperser, etc., and thus, the polarity and amount of charge on particles varies according to experimental conditions. To estimate the charge transferred from the particles to the wall, the initial charge must be known beforehand.

Particle charging in gas-solids pipe flow can be formulated as follows. When a particle moves from x to $x + \Delta x$ along the pipe axis, the variation of the charge can be derived from Eq. (12) as follows:

$$\begin{aligned}\Delta q &= q(x + \Delta x) - q(x)\\ &= (q_\infty - q_0)\left\{\exp\left(-\frac{n(x)}{n_0}\right)\right\}\left\{1 - \exp\left(-\frac{n(\Delta x)}{n_0}\right)\right\}\end{aligned} \tag{13}$$

The charges transferred from the particles to the pipe wall can be analyzed in terms of electric currents. When some length Δx is isolated electrically and grounded, the electric current I flowing to ground is expressed as[21)]

$$\begin{aligned}\frac{I}{W_p} &= -\frac{\Delta q}{m_p}\\ &= (q_{m0} - q_{m\infty})\left\{\exp\left(-\frac{n(x)}{n_0}\right)\right\}\left\{1 - \exp\left(-\frac{n(\Delta x)}{n_0}\right)\right\}\end{aligned} \tag{14}$$

where W_p is the mass flow rate of particles, m_p is the mass of the particle, q_{m0} and $q_{m\infty}$ are the specific charge at $x = 0$ and $x = \infty$, respectively. When the point x at the inlet of the detection pipe is redefined as zero, Eq. (14) becomes

$$\frac{I}{W_p} = (q_{m0} - q_{m\infty})\left\{1 - \exp\left(-\frac{n(\Delta x)}{n_0}\right)\right\} \tag{15}$$

Furthermore, Eq. (15) is rewritten as

$$\frac{I}{W_p} = a q_{m0} + b \tag{16}$$

where, a and b are constants. Using Eq. (16), one finds that the transferred charge is proportional to the initial charge on the particles.

The above theoretical approach can be used to analyze the charge distribution. Although the particle charge distribution depends on manifold factors, the primary factors are considered to be the number of particle collisions, the initial charge on the particles, and the state of the impact. Introducing the probability density functions for these factors, one can obtain the equation of particle charge distribution[89].

The maximum (or the equilibrium) charge of particles in gas–solids pipe flow was studied by Matsuyama and Yamamoto[90]. They conducted a theoretical calculation based on the charge relaxation model, taking into account the space charge effect and made comparisons with the experimental data in the literature.

3.6 Control of tribocharging

In general, the reproducibility of the tribocharging of particles is poor; however, the control of the charge on particles can be made possible by employing the tribocharging principles. In this section, typical triboelectric characteristics in dilute phase gas–solids flow is described and useful methods for controlling tribocharging are explained.

Matsusaka et al.[91] conducted experiments on the tribocharging of micrometer-sized alumina particles in gas–solids pipe flow using different kinds of pipes. The particles were charged positively by being placed in contact with the stainless steel walls. As for the aluminum, copper, and brass pipes, the particles were charged negatively. Although the absolute value of the specific charge increased with increasing pipe length, the rate of increase gradually decreased and the specific charge approached an equilibrium value that depended on the wall material. To apply the theoretical model to the experimental results, one can assume that the frequency of the particle-wall impacts per unit pipe length is constant, i.e., the number of impacts n is proportional to the pipe length L; therefore, Eq. (12) can be rewritten as

$$q_m(L) = q_{m0}\exp\left(-\frac{L}{L_0}\right) + q_{m\infty}\left\{1-\exp\left(-\frac{L}{L_0}\right)\right\} \tag{17}$$

where L_0 is the characteristic length of the particle charging. This equation can also be used to evaluate the particle charging efficiency γ_q, i.e.,

$$\gamma_q = \frac{q_m - q_{m0}}{q_{m\infty} - q_{m0}} = 1 - \exp\left(-\frac{L}{L_0}\right) \tag{18}$$

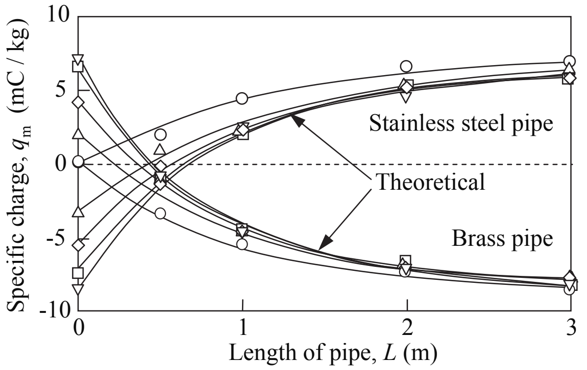

Fig. 1 Effect of initial charge and pipe material on particle charging (alumina particles, count median diameter: 3.3 µm, pipe diameter: 6 mm, air velocity: 40 m/s, mass flow ratio: 5×10^{-4} kg-particle/kg-air).

The effect of the initial charge on particles and pipe material on particle charging is shown in **Fig. 1** [91]. As the experimental results are in good agreement with the results calculated using Eq. (17), the tribocharging of particles can accurately be estimated; moreover, a particle charging control system made of two different materials A and B can be realized. **Fig. 2** illustrates a model of the control system in which two different pipes (of length ΔL_A and ΔL_B) are arranged in series. The specific charges of the particles q_{mAk} and q_{mBk} after making contact with A and B, respectively, in the k-th component are represented by the following recurrence relations:

$$q_{mAk} = q_{mBk-1}\exp\left(-\frac{\Delta L_A}{L_{A0}}\right) + q_{mA\infty}\left\{1-\exp\left(-\frac{\Delta L_A}{L_{A0}}\right)\right\} \tag{19}$$

and

$$q_{mBk} = q_{mAk}\exp\left(-\frac{\Delta L_B}{L_{B0}}\right) + q_{mB\infty}\left\{1-\exp\left(-\frac{\Delta L_B}{L_{B0}}\right)\right\} \tag{20}$$

where $q_{mA\infty}$ and $q_{mB\infty}$ are the equilibrium specific charges, and L_{A0} and L_{B0} are the characteristic lengths for contact with pipe material A and B, respectively.

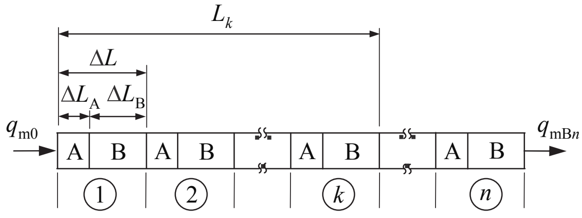

Fig. 2 A model of a particle charging control system made of two different materials, A and B.

The result for the specific charge obtained by connecting 1-m brass pipe and 1-m stainless steel pipe alternately is shown in **Fig. 3** [91]. The particles are charged, negatively in the brass pipes, and positively in the stainless steel pipes. As a result, the values of the specific charge are within a certain range. The experimental results can be represented by Eqs. (19) and (20)

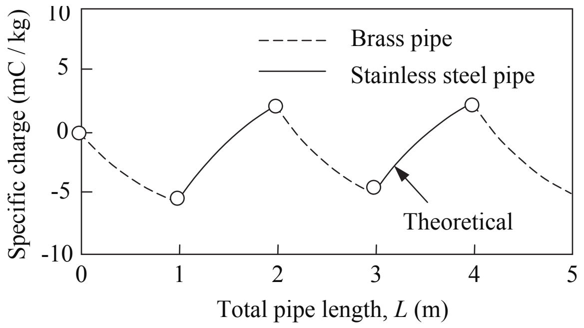

Fig. 3 Control of particle charging by a system combining two different pipe materials (alumina particles, count median diameter: 3.3 μm, pipe diameter: 6 mm, air velocity: 40 m/s, mass flow ratio: 5×10^{-4} kg-particle/kg-air).

Examples of the general calculation to control tribocharging in gas-solids pipe flow using two different pipe materials A and B are shown in **Fig. 4**. Although the charge fluctuates positively and negatively, the fluctuation level decreases with the decrease in the individual pipe lengths. The polarity and amount of charge is controlled by changing the pipe length ratio, i.e., $r_{\mathrm{A}} = \Delta L_{\mathrm{A}} / (\Delta L_{\mathrm{A}} + \Delta L_{\mathrm{B}})$ or $r_{\mathrm{B}} = \Delta L_{\mathrm{B}} / (\Delta L_{\mathrm{A}} + \Delta L_{\mathrm{B}}) = 1 - r_{\mathrm{A}}$. Therefore, the charge on particles can be changed positively, negatively, or neutrally using two different materials.

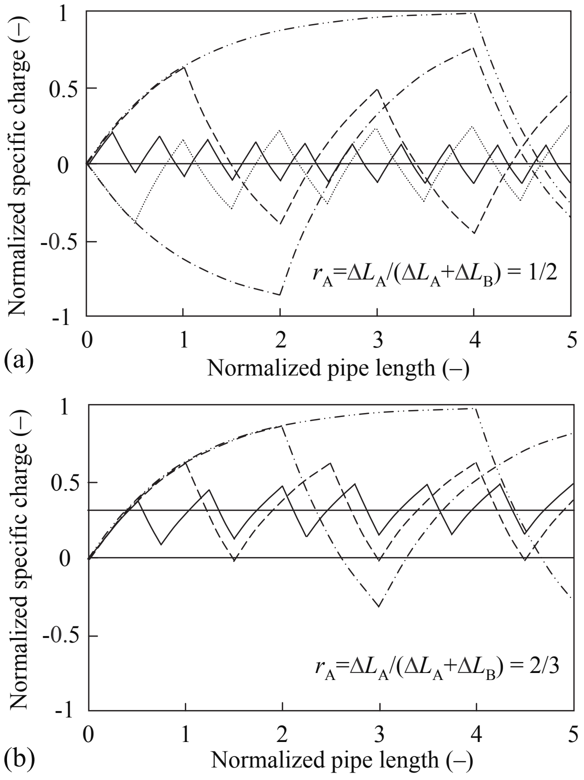

Fig. 4 Normalized calculations of tribocharging in gas–solids pipe flow using two different pipe materials ($q_{\mathrm{mA}\infty} = 1$, $q_{\mathrm{mB}\infty} = -1$, $L_{\mathrm{A0}} = 1$, $L_{\mathrm{B0}} = 1$).

The recurrence relation mentioned above can be solved as follows

$$q_{\mathrm{mB}k} = q_{\mathrm{m0}} \exp\left(-\frac{L_k}{L_{\mathrm{AB0}}}\right) + q^*_{\mathrm{mB}} \left\{1 - \exp\left(-\frac{L_k}{L_{\mathrm{AB0}}}\right)\right\} \tag{21}$$

where

$$q^*_{\mathrm{mB}} = q_{\mathrm{mA}\infty} \left\{1 - \frac{1 - \exp\left(-\frac{r_{\mathrm{B}}\Delta L}{L_{\mathrm{B0}}}\right)}{1 - \exp\left(-\frac{\Delta L}{L_{\mathrm{AB0}}}\right)}\right\} + q_{\mathrm{mB}\infty} \frac{1 - \exp\left(-\frac{r_{\mathrm{B}}\Delta L}{L_{\mathrm{B0}}}\right)}{1 - \exp\left(-\frac{\Delta L}{L_{\mathrm{AB0}}}\right)} \tag{22}$$

and

$$L_{\mathrm{AB0}} = \frac{L_{\mathrm{A0}} L_{\mathrm{B0}}}{r_{\mathrm{B}} L_{\mathrm{A0}} + r_{\mathrm{A}} L_{\mathrm{B0}}} \tag{23}$$

When the pipe length $\Delta L_{\mathrm{A}} \rightarrow 0$, the specific charge is expressed as a continuous function, i.e.,

$$q_{\mathrm{m}} = q_{\mathrm{m0}} \exp\left(-\frac{L}{L_{\mathrm{AB0}}}\right) + q^*_{\mathrm{m}\infty} \left\{1 - \exp\left(-\frac{L}{L_{\mathrm{AB0}}}\right)\right\} \tag{24}$$

where

$$q^*_{\mathrm{m}\infty} = q_{\mathrm{mA}\infty} \left(1 - \frac{r_{\mathrm{B}} L_{\mathrm{AB0}}}{L_{\mathrm{B0}}}\right) + q_{\mathrm{mB}\infty} \frac{r_{\mathrm{B}} L_{\mathrm{AB0}}}{L_{\mathrm{B0}}} = \frac{q_{\mathrm{mA}\infty} r_{\mathrm{A}} L_{\mathrm{B0}} + q_{\mathrm{mB}\infty} r_{\mathrm{B}} L_{\mathrm{A0}}}{r_{\mathrm{B}} L_{\mathrm{A0}} + r_{\mathrm{A}} L_{\mathrm{B0}}} \tag{25}$$

This system can be arranged in different shapes and structures. **Fig. 5** shows a high-efficiency particle charger with an inverted, truncated cone[92]. Micrometer-sized dielectric particles that are introduced into the charger from the tangential direction at the top are carried spirally downward and discharged in the tangential direction at the bottom. The particles are triboelectrically charged by contact with the inside wall of the charger via centrifugal force. When two different metals, A and B, are affixed to the inside wall, particles will make contact with these materials alternately. **Fig. 6** shows an example of

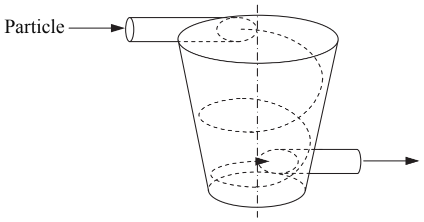

(a) Bird's-eye view

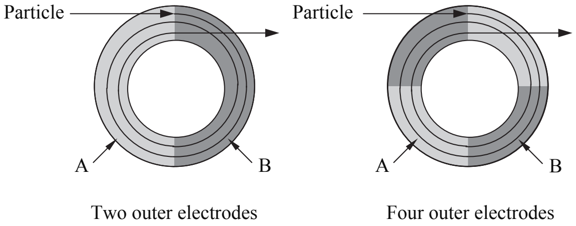

(b) Top view

Fig. 5 Particle charger using centrifugal contact.

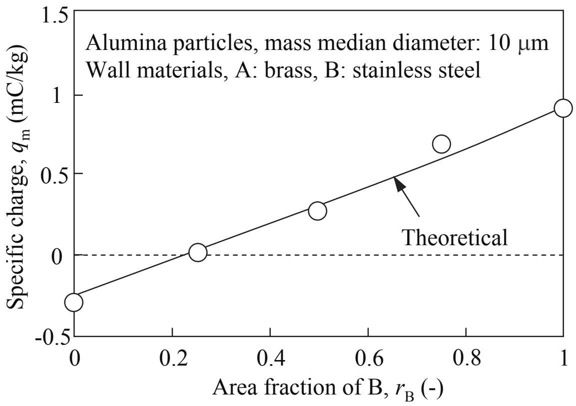

Fig. 6 Effect of area fraction of wall materials on particle charging (spherical alumina particles, mass median diameter: 10 µm).

the experimental results obtained using the particle charger[92]. The charge on particles is estimated theoretically and can be controlled by changing the area fraction of the wall materials. The charge control range is determined by the two contact potential differences between the particles and the two walls, A and B

Furthermore, when applying an external electric field to the system, the contact potential difference can easily be changed; as a result, the charge control range becomes wider. **Fig. 7** shows the concept of particle charge control based on contact potential difference. The contact potential difference V consists of the four factors, as expressed in Eq. (5), i.e., V_c based on the surface work functions, V_e arising from the image charge, V_b arising from the space charge, and V_{ex} arising from an applied electric field. Therefore, in the case of $V < 0$ the particles are negatively charged, and for $V > 0$ they are positively charged. In addition, the amount of charge on the particles can be controlled by varying the contact potential V. A particle charger using an applied electric field system is shown in **Fig. 8**. This charger is also based on the centrifugal contact method. When two different voltages are applied, particle charging is similar to that using two different materials, as shown in **Fig. 6**.
Particle charging control based on contact potential difference in an applied electric field is easier and safer than corona discharge methods. In addition, the device can be customized to meet the needs of each application. Therefore, this control method is expected to be applicable in many industrial fields.

4. Conclusion

As described in this review, much research on particle tribocharging has been carried out over the last several decades. Although there are still unknown effects in the mechanism of tribocharging, the charge accumulation on particles can be formulated in terms of electron transfer. Tribocharging depends on the contact potential difference, which can be controlled via an applied electric field or by controlling the materials of the apparatus; therefore, particle charging can be estimated theoretically using these factors. In addition, as the particle charging is a surface phenomenon related to the contact between two bodies, the contact efficiency is also important when analyzing the particle charging process.

In this review, to control the charge on particles, novel methods based on applied electric fields (to control the contact potential difference) and centrifugal force (to enhance the contact efficiency) have been presented. These methods, which are both easy and safe, can be designed so as to meet the needs of different situations, and thus, are expected to be applicable in many industrial fields.

Acknowledgements

This work was supported by Grant-in-Aid for Scientific Research (B) (No. 23360341) from the Japan Society for the Promotion of Science and Grant no. S0901039 from MEXT, Japan.

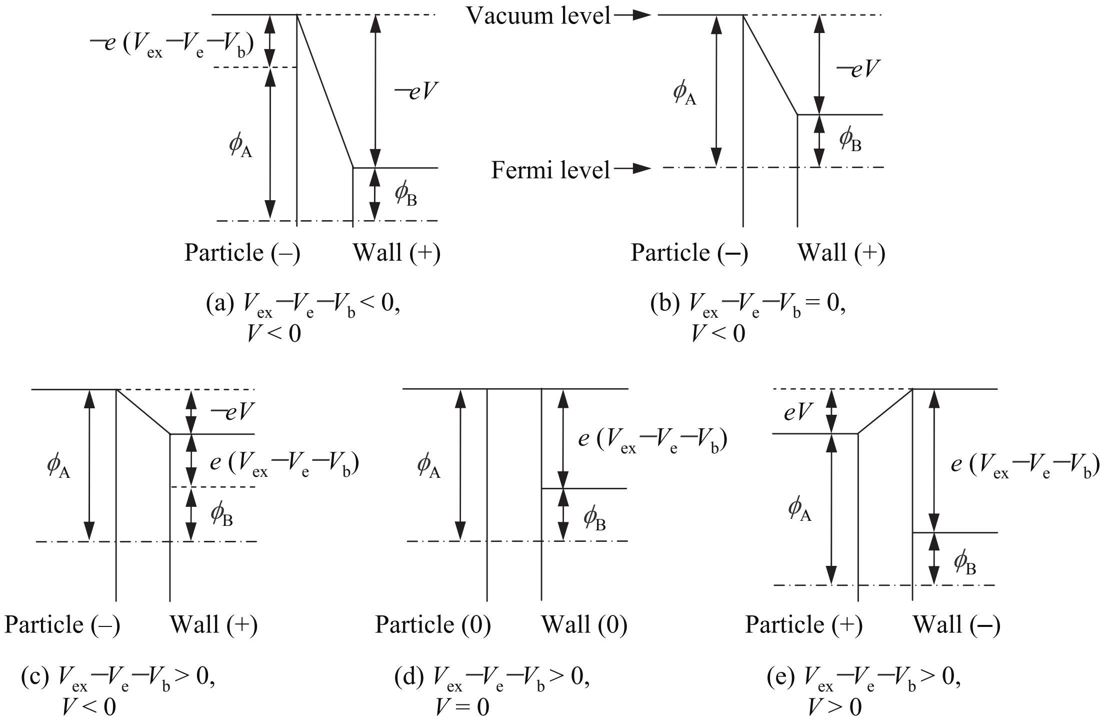

(a) $V_{ex}-V_e-V_b<0$, $V<0$

(b) $V_{ex}-V_e-V_b=0$, $V<0$

(c) $V_{ex}-V_e-V_b>0$, $V<0$

(d) $V_{ex}-V_e-V_b>0$, $V=0$

(e) $V_{ex}-V_e-V_b>0$, $V>0$

Fig. 7 Conceptual model of particle charge control based on contact potential difference ($V = V_c - V_e - V_b + V_{ex}$, $V_c < 0$, see Eq. (5)).

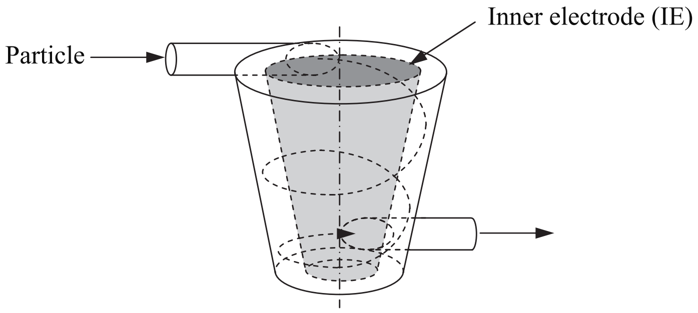

(a) Bird's-eye view

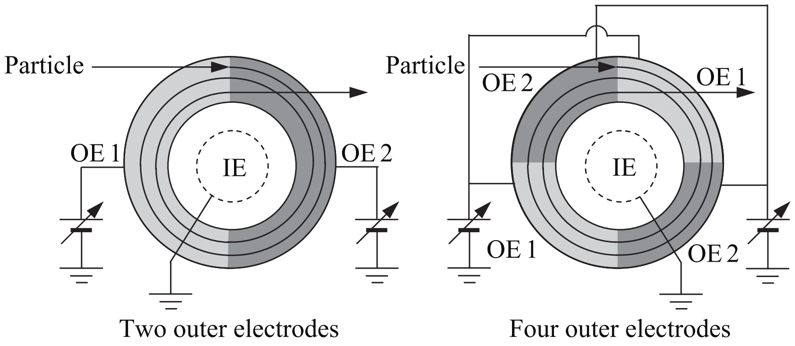

(b) Top view

Fig. 8 Particle charger using centrifugal contact in an electric field system.

References

1) Joseph, S. and Klinzing, G.E. (1983): Vertical gas–solid transition flow with electrostatics, Powder Technology, vol. 36, pp. 79-87.
2) Nifuku, M., Ishikawa, T. and Sasaki, T. (1989): Static electrification phenomena in pneumatic transportation of coal, Journal of Electrostatics, vol. 23, pp. 45-54.
3) Guardiola, J., Rojo, V. and Ramos, G. (1996): Influence of particle size, fluidization velocity and relative humidity on fluidized bed electrostatics, Journal of Electrostatics, vol. 37, pp. 1-20.
4) Adhiwidjaja, I., Matsusaka, S., Yabe, S. and Masuda, H. (2000): Simultaneous phenomenon of particle deposition and reentrainment in charged aerosol flow—effects of particle charge and external electric field on the deposition layer, Advanced Powder Technology, vol. 11, pp. 221-233.
5) Yao, J., Zhang, Y., Wang, C.-H., Matsusaka, S. and Masuda, H. (2004): Electrostatics of the granular flow in a pneumatic conveying system, Industrial & Engineering Chemistry Research, vol. 43, pp. 7181-7199.
6) Jones, T.B. and King, J.L. (1991): “Powder Handling and Electrostatics: Understanding and Preventing Hazards”, Lewis, Chelsea.
7) Ohsawa, A. (2003): Computer simulation for assessment of electrostatic hazards in filling operations with powder, Powder Technology, vol. 135/136, pp. 216-222.
8) Nifuku, M. and Katoh, H. (2003): A study on the static electrification of powders during pneumatic transportation and the ignition of dust cloud, Powder Technology, vol. 135/136, pp. 234-242.
9) Mazumder, M.K. (1999): Electrostatic processes. In: Webster, J. (Ed.), “Wiley Encyclopedia of Electrical and Electronics Engineering”, John Wiley & Sons, Inc., vol. 7, pp. 15- 39.
10) Schein, L.B. (1992/1996): “Electrophotography and Development Physics”, 2nd ed., Springer-Verlag, Berlin/Laplacian Press.
11) Schein, L.B. (1999): Recent advances in our understanding of toner charging, Journal of Electrostatics, vol. 46, pp. 29-36.
12) Hughes, J. F. (1984): Electrostatic Powder Coating, Research Studies Press, Wiley, New York.
13) Bailey, A.G. (1998): The science and technology of electrostatic powder spraying, transport and coating, Journal of Electrostatics, vol. 45, pp.85-120.
14) Kleber, W. and Makin, B. (1998): Triboelectric powder coating: a practical approach for industrial use, Particulate Science and Technology, vol. 16, pp. 43-53.
15) Lawless, P.A. (1999): Electrostatic precipitators, In: Webster, J. (Ed.), “Wiley Encyclopedia of Electrical and Electronics Engineering”, John Wiley & Sons, Inc., vol. 7, pp. 1- 15.
16) Gupta, R., Gidaspow, D. and Wasan, D.T. (1993): Electrostatic separation of powder mixtures based on the work functions of its constituents, Powder Technology, vol. 75, pp. 79-87.
17) Yanar, D.K. and Kwetkus, B.A. (1995): Electrostatic separation of polymer powders, Journal of Electrostatics, vol. 35, pp. 257-266.
18) Ghadiri, M., Martin, C.M., Morgan, J.E.P. and Clift, R. (1992): An electromechanical valve for solids, Powder Technology, vol. 73, pp. 21-35.
19) Balachandran, W., Hu, D., Ghadiri, M., Law, S.E. and Thompson, S.A. (1997): The study of the performance of an electrostatic valve used for bulk transport of particulate materials, IEEE Transactions on Industry Applications, vol. 33, pp. 871-878.
20) O’Neill, B.C. and Willis, C.A. (1987): An electrostatic method for the measurement of powder flow rates in pipes, Electrostatics ’87, IOP Publishing, Oxford, pp. 303-306.
21) Matsusaka, S. and Masuda, H. (2006): Simultaneous measurement of mass flow rate and charge-to-mass ratio of particles in gas–solids pipe flow, Chemical Engineering Science, vol. 61, pp. 2254-2261.
22) Gajewski, J.B. (2006): Non-contact electrostatic flow probes for measuring the flow rate and charge in the two-phase gas–solids flows, Chemical Engineering Science, vol. 61, pp. 2262-2270.
23) Gajewski, J.B. (2008): Electrostatic nonintrusive method for measuring the electric charge, mass flow rate, and velocity of particulates in the two-phase gas–solid pipe flows—its only or as many as 50 years of historical evolution, IEEE Transactions on Industry Applications, vol. 44, pp. 1418-1430.
24) Machida, M. and Scarlett, B. (2005): Process tomography system by electrostatic charge carried by particles, IEEE Sensors Journal, vol. 5, 251-259.
25) Matsusaka, S., Fukuda, H., Sakura, Y., Masuda, H. and Ghadiri, M. (2008): Analysis of pulsating electric signals generated in gas–solids pipe flow, Chemical Engineering Science, vol. 63, pp. 1353-1360.
26) Schnurmann, R. (1941): Contact electrification of solid particles, Proceedings of the Physical Society, vol. 53, pp. 547-553.
27) Harper, W.R. (1951): The Volta effect as a cause of static electrification, Proceedings of the Royal Society of London Series A, vol. 205, 83-103.
28) Harper, W.R. (1967): “Contact and Frictional Electrification”, Clarendon Press, Oxford.
29) Lowell, J. and Rose-Innes, A.C. (1980): Contact electrification, Advances in Physics, vol. 29, pp. 947-1023.
30) Jones, T.B. (1995): “Electromechanics of Particles”, Cambridge University Press, Cambridge.
31) Matsusaka, S. and Masuda, H. (2003): Electrostatics of particles, Advanced Powder Technology, vol. 14, pp. 143-166.
32) Matsusaka, S., Maruyama, H., Matsuyama, T. and Ghadiri, M. (2010): Triboelectric Charging of Powders: A review, Chemical Engineering Science, vol. 65, pp. 5781-5807.
33) Mazumder, M.K., Ware, R.E., Yokoyama, T., Rubin, B. J. and Kamp, D. (1991): Measurement of particle size

and electrostatic charge distributions on toners using E-SPART analyzer, IEEE Transactions on Industry Applications, vol. 27, pp. 611-619.

34) Masuda, H., Gotoh, K. and Orita, N. (1993): Charge distribution measurement of aerosol particles, Journal of Aerosol Research, Japan, vol. 8, pp. 325-332.
35) Matsusaka, S., Oki, M. and Masuda, H. (2003): Bipolar charge distribution of a mixture of particles with different electrostatic characteristics in gas–solids pipe flow, Powder Technology, vol. 135/136, pp. 150-155.
36) Epping, R.H. and Kuettner, A. (2002): Free air beam in an electric field for determination of the electrostatic charge of powders between 1 and 200 µm, Journal of Electrostatics, vol. 55, pp. 279-288.
37) Ahn, Y.C., Kim, D.H., Kim, S.C., Hwang, E.G., Lee, C.G., Kim, G.T., Shin, H.S., Lee, J.K. and Lee, S.H. (2004): Measurement and control of triboelectrically charged silica and glassy carbon particles, Particulate Science and Technology, vol. 22, pp. 305-320.
38) Matsusaka, S., Yoshitani, K., Tago, H., Nii, T., Masuda, H. and Iwamatsu, T. (2008): Sampling of charged fine particles by motion control under ac field, Journal of the Society of Powder Technology, Japan, vol. 45, pp. 387-394.
39) Kittaka, S. and Murata, Y. (1976): A new system for measuring the charging tendency of solid particles, Journal of Electrostatics, vol. 2, pp. 111-119.
40) Murata, Y. (1979): Photoelectric emission and contact charging of some synthetic high polymers, Japanese Journal of Applied Physics, vol. 18, pp. 1-8.
41) Yoshida, H., Fukuzono, T. and Masuda, H. (1991): Measurement of contact potential difference between a powder bed and a metal, Journal of the Society of Powder Technology, Japan, vol. 28, pp. 226-231.
42) Yoshida, H., Fukuzono, T., Ami, H., Iguchi, Y. and Masuda, H. (1992): The effect of the surface modification of particles on the contact potential difference between a powder bed and metal, Journal of the Society of Powder Technology, Japan, vol. 29, pp. 504-510.
43) Itakura, T., Masuda, H., Ohtsuka, C. and Matsusaka, S. (1996): The contact potential difference of powder and the tribo-charge, Journal of Electrostatics, vol. 38, pp. 213-226.
44) Higashiyama, Y., Ujiie, Y. and Asano, K. (1997): Triboelectrification of plastic particles on a vibrating feeder laminated with a plastic film, Journal of Electrostatics, vol. 42, pp. 63-68.
45) Tanoue, K., Morita, K., Maruyama, H. and Masuda, H. (2001): Influence of functional group on the electrification of organic pigments, AIChE Journal, vol. 47, pp. 2419-2424.
46) Rowley, G. (2001): Quantifying electrostatic interactions in pharmaceutical solid systems, International Journal of Pharmaceutics, vol. 227, pp. 47-55.
47) Zhao, H., Castle, G.S.P. and Inculet, I.I. (2002): The measurement of bipolar charge in polydisperse powders using a vertical array of Faraday pail sensors, Journal of Electrostatics, vol. 55, pp. 261-278.
48) Iuga, A., Calin, L., Neamtu, V., Mihalcioiu, A. and Dascalescu, L. (2005): Tribocharging of plastics granulates in a fluidized bed device, Journal of Electrostatics, vol. 63, pp. 937-942.
49) Davies, D.K. (1969): Charge generation on dielectric surfaces, British Journal of Applied Physics: Journal of Physics. D, vol. 2, pp. 1533-1537.
50) Murata, Y. and Kittaka, S. (1979): Evidence of electron transfer as the mechanism of static charge generation by contact of polymers with metals, Japanese Journal of Applied Physics, vol. 18, p. 421.
51) Lee, L.-H. (1994): Dual mechanism for metal–polymer contact electrification, Journal of Electrostatics, vol. 32, pp. 1-29.
52) Bailey, A.G. (2001): The charging of insulator surfaces, Journal of Electrostatics, vol. 51/52, pp. 82-90.
53) Gutman, E. J. and Hartmann, G. C. (1992): Triboelectric properties of two-component developers for xerography, Journal of Imaging Science and Technology, vol. 36, pp. 335-349.
54) Anderson, J.H. (1994): A comparison of experimental data and model predictions for tribocharging of two-component electrophotographic developers, Journal of Imaging Science and Technology, vol. 38, pp. 378-382.
55) Cotler P., Castle, G.S.P. and Schein, L.B. (1995): General model of sphere–sphere insulator contact electrification, Journal of Electrostatics, vol. 36, pp. 165-173.
56) Fabish, T.J. and Duke, C.B. (1977): Molecular charge states and contact charge exchange in polymers, Journal of Applied Physics, vol. 48, pp. 4256-4266.
57) Duke, C.B. and Fabish, T.J. (1978): Contact electrification of polymers: a quantitative model, Journal of Applied Physics, vol. 49, pp. 315-321.
58) Yanagida, K., Okada, O. and Oka, K. (1993): Low-energy electronic states related to contact electrification of pendant-group polymers: photoemission and contact potential difference measurement, Japanese Journal of Applied Physics, vol. 32, pp. 5603-5610.
59) Yoshida, M., Ii, N. Shimosaka, A., Shirakawa, Y. and Hidaka, J. (2006): Experimental and theoretical approaches to charging behavior of polymer particles, Chemical Engineering Science, vol. 61, pp. 2239-2248.
60) Shirakawa, Y., Ii, N., Yoshida, M., Takashima, R., Shimosaka, A. and Hidaka, J. (2008): Quantum chemical calculation of electron transfer at metal/polymer interfaces, Journal of the Society of Powder Technology, Japan, vol. 45, pp. 366-372.
61) Matsusaka, S., Ghadiri, M. and Masuda, H. (2000): Electrification of an elastic sphere by repeated impacts on a metal plate, Journal of Physics D: Applied Physics, vol. 33, pp. 2311-2319.
62) Matsusaka, S., Nishida, T., Gotoh, Y. and Masuda, H. (2003): Electrification of fine particles by impact on a polymer film target, Advanced Powder Technology, vol. 14, pp. 127-138.
63) Matsuyama, T. and Yamamoto, H. (1995): Charge relaxation process dominates contact charging of a

particle in atmospheric conditions, Journal of Physics D: Applied Physics, vol. 28, pp. 2418-2423.

64) Matsuyama, T. and Yamamoto, H. (1995): Characterizing the electrostatic charging of polymer particles by impact charging experiments, Advanced Powder Technology, vol. 6, pp. 211-220.

65) Paschen, F. (1889): Ueber die zum Funkenübergang in Luft, Wasserstoff und Kohlensäure bei verschiedenen Drucken erforderliche Potentialdifferenz, Annalen der Physik, vol. 273, pp. 69-96.

66) Bailey, A.G. (1993): Charging of solids and powders, Journal of Electrostatics, vol. 30, pp. 167-180.

67) Masui, N. and Murata, Y. (1983): Electrification of polymer particles by impact on a metal plate, Japanese Journal of Applied Physics, vol. 22, pp. 1057-1062.

68) Masui, N. and Murata, Y. (1984): Mechanisms of charge build-up on a polymer particle by repeated impact, Japanese Journal of Applied Physics, vol. 23, pp. 550-555.

69) Yamamoto, H. and Scarlett, B. (1986): Triboelectric charging of polymer particles by impact, Particle Characterization, vol. 3, pp. 117-121.

70) Matsuyama, T. and Yamamoto, H. (1989): Charge transfer between a single polymer particle and a metal plate due to impact, KONA Powder and Particle, vol. 7, pp. 15-21.

71) Matsuyama, T. and Yamamoto, H. (1994): Charge transfer between a polymer particle and a metal plate due to impact, IEEE Transactions on Industry Applications, vol. 30, pp. 602-607.

72) Matsuyama, T. and Yamamoto, H. (1995): Electrification of single polymer particles by successive impacts with metal targets, IEEE Transactions on Industry Applications, vol. 31, pp. 1441-1445.

73) Matsuyama, T. and Yamamoto, H. (1997): Charge-relaxation process dominates contact charging of a particle in atmospheric condition: II. The general model, Journal of Physics D: Applied Physics, vol. 30, pp. 2170-2175.

74) Matsuyama, T., Ogu, M., Yamamoto, H., Marijnissen, J. C. M. and Scarlett, B. (2003): Impact charging experiments with single particles of hundred micrometre size, Powder Technology, vol. 135/136, pp. 14-22.

75) Watanabe, H., Samimi, A., Ding, Y. L., Ghadiri, M., Matsuyama, T. and Pitt, K.G. (2006): Measurement of charge transfer due to single particle impact, Particle & Particle Systems Characterization, vol. 23, pp. 133-137.

76) Watanabe, H., Ghadiri, M., Matsuyama, T., Ding, Y.L., Pitt, K.G., Maruyama, H., Matsusaka, S. and Masuda, H. (2007): Triboelectrification of pharmaceutical powders by particle impact, International Journal of Pharmaceutics, vol. 334, pp. 149-155.

77) Watanabe, H., Ghadiri, M., Matsuyama, T., Ding, Y. L. and Pitt, K.G. (2007): New instrument for tribocharge measurement due to single particle impacts, Review of Scientific Instruments, vol. 78, 024706.

78) Ema, A. Yasuda, D., Tanoue, K. and Masuda, H. (2003): Tribo-charge and rebound characteristics of particles impact on inclined or rotating metal target, Powder Technology, vol. 135/136, pp. 2-13.

79) Ireland, P.M. (2010): Triboelectrification of particulate flows on surfaces: Part I — Experiments, Powder Technology, vol. 198, pp. 189-198.

80) Ireland, P.M. (2010): Triboelectrification of particulate flows on surfaces: Part II — Mechanisms and models, Powder Technology, vol. 198, pp. 199-210.

81) Cole, B.N., Baum, M.R. and Mobbs, F.R. (1969–1970): An investigation of electrostatic charging effects in high-speed gas–solids pipe flows, Proceedings Institution of Mechanical Engineers, vol. 184, pp. 77-83.

82) Masuda, H., Komatsu, T. and Iinoya, K. (1976): The static electrification of particles in gas–solids pipe flow, AIChE Journal, vol. 22, pp. 558-564.

83) Cartwright, P., Singh, S., Bailey, A.G. and Rose, L.J. (1985. Electrostatic charging characteristics of polyethylene powder during pneumatic conveying, IEEE Transactions on Industry Applications, vol. IA-21, pp. 541-546.

84) Nieh, S. and Nguyen, T. (1988): Effects of humidity, conveying velocity, and particle size on electrostatic charges of glass beads in a gaseous suspension flow, Journal of Electrostatics, vol. 21, pp. 99-114.

85) Gajewski, A. (1989): Measuring the charging tendency of polystyrene particles in pneumatic conveyance, Journal of Electrostatics 23, pp. 55-66.

86) Masuda, H., Matsusaka, S. and Nagatani, S. (1994): Measurements of powder flow rate in gas–solids pipe flow based on the static electrification of particles, Advanced Powder Technology, vol. 5, pp. 241-254.

87) Masuda, H., Matsusaka, S., Akiba, S. and Shimomura, H. (1998): Electrification of fine particles in gas–solids pipe flow, KONA Powder and Particle, vol. 16, pp. 216-222.

88) Masuda, H., Matsusaka, S. and Shimomura, H. (1998): Measurement of mass flow rate of polymer powder based on static electrification of particles, Advanced Powder Technology, vol. 9, pp. 169-179.

89) Matsusaka, S., Umemoto, H., Nishitani, M. and Masuda, H. (2002): Electrostatic charge distribution of particles in gas–solids pipe flow, Journal of Electrostatics, vol. 55, pp. 81-96.

90) Matsuyama, T. and Yamamoto, H. (2008): Maximum electrostatic charge of powder in pipe flow, Journal of the Society of Powder Technology, Japan, vol. 45, pp. 373-379.

91) Matsusaka, S., Oki, M. and Masuda, H. (2007): Control of electrostatic charge on particles by impact charging, Advanced Powder Technology, vol. 18, pp. 229-244.

92) Matsusaka, S., Ando, K. and Tanaka, Y. (2008): Development of electrostatic charge controller for particles in gases using centrifugal contact, Journal of the Society of Powder Technology, Japan, vol. 45, pp. 380-386.

Author’s short biography

Shuji Matsusaka

Shuji Matsusaka is a Professor of Chemical Engineering at Kyoto University. He received his B.Sc. and M.Sc. degrees from Hiroshima University and Ph.D. from Kyoto University. Dr Matsusaka’s current research interests are characterizing particle electrification, adhesion, and flowability as well as micro- and nano-particle handling in gases.

In-situ Characterization of Drying Particulate Coatings[†]

Masato Yamamura
Department of Applied Chemistry,
Kyushu Institute of Technology[1]

Abstract

Film thin drying is a process to create functional interfaces in solidifying liquids, rather than to separate volatile components from solutions or suspensions. Indeed, recent developments in coating technologies have shed light on self-organization in evaporating complex thin fluids. In particulate coatings, final properties of dried film depend not only on initial liquid compositions but also the imposed drying conditions, which significantly influence local particle distributions, contact area of rigid and/or deformable particles, anisotropic particle orientation, and amounts of adsorbed molecules on particle surfaces. It is of importance to understand how a directional film shrinkage and spontaneous solidification constrain the particle motions, and how they induce particular film structures in a non-equilibrium state. Recently, there has been a great deal of progress in measurement techniques and numerical approaches for analyzing transient structures in evaporating thin liquid films. This article presents an overview of current research activities on local, in-situ determination of (i) fluid properties at air-liquid and liquid-liquid interfaces, and (ii) distributions of particles or solutes in the thickness direction in shrinking films.

Keywords: coating, drying, suspension, interfaces, modeling

1. Introduction

Drastic changes in local structures and physical properties emerge when thin liquid film suspension or solution coatings dry or solidify. Typical examples include molecular adsorptions at interfaces, reductions in solvent diffusivity due to polymer-chain entanglements, phase separation, crystallization, and bubble nucleation in concentration solutions, the electrostatic ordering and/or disordering of particles, air invasion in pore spaces, stress developments due to capillary forces and/or an anisotropic film shrinkage, buckling, cracking and other deformations of interfaces to release the stress, and even chemical reactions by irradiations of ultraviolet lights or electron beams. The major difficulty stems from the fact that these local phenomena can co-exist in the liquid with different time scales, and significantly influence the bulk fluid properties, which, in turn, alter the local dynamic events in the fluids in a complicated manner. Because of complexity of the system, the physics of drying of thin films is still far from complete understanding, and what determines the characteristics of final film products often remains unresolved.

Despite formidable difficulties inherent in film drying, there has been a great deal of progress in experimental and numerical analyses of evaporating thin films. In this short review, we attempt to provide a brief guide to the recent in-situ monitoring techniques (**Table 1**) and some modeling approaches on micro-structuring of suspension and solution films. In order to access how the drying operation impacts the fluid structures, we restrict ourselves on a simple case of a non-reactive, initially homogeneous, single liquid film coated on an impermeable, smooth solid surface. Drying of multi-layer liquid coating would receive extensive practical interests, but it is beyond the scope of this review. Section 2 emphasizes variations in local fluid properties at air-liquid and liquid-liquid interfaces for evaporating liquid films. Some new, non- contact measurement techniques

---

[†] August 25th, 2011

[1] 1-1 Sensui-cho, Tobata-ku, Kitakyushu-city,
804-8550 JAPAN
E-mail: yamamura@che.kyutech.ac.jp
TEL: (+81)93-884-3344 FAX: (+81)93-884-3300

© 2011 Hosokawa Powder Technology Foundation

Table 1 In-situ measurement techniques for drying films

Properties	Methods	Ref.
Surface viscosity & interfacial tension	Ripplon surface wave	1-3
	Laser-induced surface deformation	4-7
Concentration profiles	Confocal Raman spectroscopy	17-20
	Infrared microscopy	27
	Magnetic resonance	21
	Cryogenic scanning electron microscopy	22-26
Tensile Stress	Cantilever beam deflection	35-55
	Distortion of flexible reflective membrane	56
Drying rate	Confocal Raman spectroscopy	17-20
	Infrared spectroscopy	27,57
	Mass loss	58
	Temperature variation	59
	Heat flux variation	60
	Gas Chromatography	61
Reaction rate	Infrared spectroscopy	54-55
Domain size	Light scattering	62-63

are introduced for determining local surface viscosities and surface tensions. Section 3 assesses how the unidirectional film shrinkage competes against motions of particles or solutes to give particular concentration profiles in the film. Some advanced optical techniques for determining the local distributions are introduced and compared with other methods. The applications of the techniques to mono-dispersed particles, bimodal particles, surfactant solutions, polymer solutions, and combinations of these systems are discussed, and comparisons with numerical models are also addressed. Brief summaries and concluding remarks are shown in Section 4.

2. Local fluid Properties at air-liquid Interface

Monitoring of local viscosities and interfacial tensions at air-liquid and liquid-liquid interfaces is the key to understand how the solvent dries from a liquid surface. Indeed, a driving force for the solvent diffusion is provided by a partial pressure difference between the liquid-gas interface and the gas far from the interface. Furthermore, a significant drop in evaporation rate arises when a decrease in the solvent concentration causes diffusion coefficients of solvents to be decreased by orders of magnitude due to complex molecular interactions. However, conventional techniques based on mechanical contacts are hopeless to capture the time-dependent variations in interfacial properties without disturbing concentration and/or temperature profiles in the fluid. Recently, some attempts have been reported to use (i) thermally excited capillary waves called “ripplons” on a fluid surface, and (ii) fluid surface deformations imposed by a sudden laser irradiation, for non-contact measurement of surface viscosities and interfacial tensions.

2.1 Surface Wave (SW) methods [1)-3)]

The liquid surface is, even macroscopically uniform, covered by capillary waves with amplitudes of the order of nanometers and the wavelengths of ~ 100 mm. When a laser light is irradiated on a fluid surface with propagating surface waves, the waves act as a diffraction grating and induce Doppler-shifted scattered components in response to the propagation speed. The scattered light signals include information on frequencies ω and attenuation rates Γ of the surface waves. For Newtonian fluids of constant density ρ, these two quantities are the function of fluid viscosity m and surface tension σ for a given wavenumber k as:

$$\omega^2 = \left(\frac{\sigma}{\rho}\right)k^3 ,$$

$$\Gamma = 2\left(\frac{\sigma}{\rho}\right)k^2 .$$

Thus we can determine these two fluid properties by analyzing the scattered light signals. An example of the schematic experimental setup is shown in **Fig. 1**. The linearly S-polarized laser light was first divided into P-waves (incident beam) and S-waves (reference beam) by using a beam splitter, and then the frequencies of the split lights were shifted using acousto-optic modulators (AOM) to eliminate the influence of undesired external oscillations of the system. The scattered light, showing a heterodyne interference with the reference light, was received by a photomultiplier tube and processed by a high-speed fast Fourier transform (FFT) analyzer. This method has advantages over conventional methods as

(1) Non-contact technique applicable on fluids with micro/nano structures or even at high temperatures

(2) Suitable for real-time observation

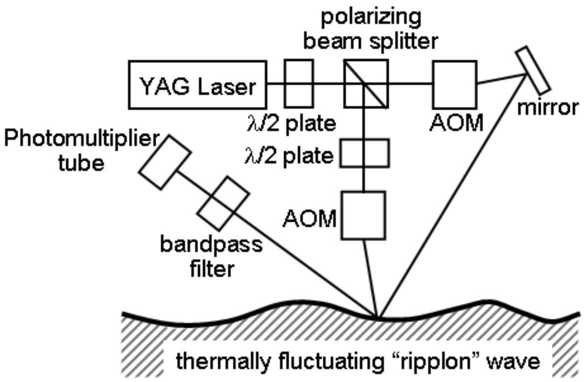

Fig. 1 Schematic setup of SW method[3)].

(3) Local properties can be determined within orders of nanometers in thickness

2.1.1 Pure liquids

Oki and Nagasaka[2] applied the SW method to measure viscosities and surface tensions of pure Newtonian liquids (water, tetrahydrofuran, methyl ethyl ketone, methyl alcohol). They used 20 mW Nd:YAG laser with a wavelength of 532 nm as a light source in order to monitor the traveling surface waves, and the diffraction grating was chosen to be approximately 100 μm within a beam diameter of 750 μm. The determined kinematic viscosities ranged between 0.5 and 2 mm^2/s, and showed a good agreement with those determined by the conventional falling ball methods. In addition, the static surface tension using Ripplon method well reproduced the data measured by the Wilhelmy method, showing the validity of the SW method in a quantitative sense.

2.1.2 Polymeric liquid

The SW method was also applied to polymeric solutions of cellulose acetate butyrate (CAB) dissolved in methyl ethyl ketone (MEK)[2]. The polymer can adsorb onto the liquid surface to reduce the surface tension. When the adsorption and desorption of polymers are too slow compared with the surface wave modulation, the adsorption layer behaves like an insoluble molecular film, and thus shows different interfacial kinetics from pure liquids. The surface tension measurements revealed that, the measured surface tensions using the SW method monotonically decreased with increasing CAB concentrations, while no variations was observed by the Wilhelmy plate method, indicating that the former method can capture the variations in interfacial properties due to the existence of adsorption film in a molecular scale.

2.1.3 Photo-responsive liquid

The SW technique was successfully extended to monitor anisotropic variations in surface tensions of solutions containing photo-responsive azobenzene derivatives[3]. When an ultraviolet light is irradiated onto the solution, an intra-molecular rotation around the double bond N=N gives rise to a transition from its trans to its cis form. The molecules then tend to align perpendicular to the polarized direction of light when the cis form re-converts to trans form. Interestingly, the measured static surface tension revealed a particular anisotropic feature under a UV light irradiation: the surface tension along X-direction was kept constant, but that along the perpendicular direction increased with time. This is, to the best of the author's knowledge, the first experimental evidence that the light-induced molecular orientations at the air-liquid interface can be directly monitored during drying. Furthermore, the alternate exposure to UV light (365 nm) and visible light (435 nm) showed a particular increase and decrease in surface tension, indicating that the photo-induced transition between trans and cis forms allows us to switch the interfacial property in a sequential manner.

However, the application of the SW technique is currently limited to pure fluids or solutions, and no data is currently available for particle dispersion systems. Furthermore, the validity of the measured surface properties has not yet been verified when the characteristic size of particles or solutes exceeds the amplitude of surface waves. Nevertheless, this technique suggests some directions for understanding the drying kinetics in a molecular scale on the evaporating thin films.

2.2 Laser-induced surface deformation (LISD) method[4)-7)]

The alternative non-contact approach to determine fluid viscosity at air-liquid interface has been proposed by imposing a surface deformation by light. When a laser light is irradiated into a planar surface of a liquid, the difference in refractive index induces a force to deform the air-liquid interface against the surface tension. A simple estimation[4] showed that an irradiation of 300 mW laser with a Gaussian profile of 100 μm in width gives the absolute surface displacement of 2 nm for water. When the irradiation stops, the capillary pressure in the liquid promotes a viscous flow to level the surface. The surface liquid viscosity can be determined by using a relaxation behavior of the surface deformation with a characteristic delay time. This non-contact measurement technique is often called laser interface manipulation (LIM) or laser induced surface deformation (LISD) method.

2.2.1 Pure liquid

Yoshitake et al.[5] successfully determine the kinematic viscosities of pure liquids using the LISD method. They used 0.6 W Nd–yttritium–aluminum–garnet laser light as a source to excite the surface deformation and another probe laser to monitor its relaxation. They demonstrated that the LISD method is applicable to measure viscosities of homogenous Newtonian liquids for the wide range from 1 to 10^6 cSt, which is much higher than those determined by the surface wave method. The artificial excitation of light-induced surface deformation allows us to promote the surface flow even in high viscosity fluids, and thus provides a great advantage of the LISD technique over the other methods. This technique also seems to be promising to determine the fluid properties of gelling, evaporating, and cross-linking fluids, which can exhibit time-dependent drastic changes in interfacial properties.

2.2.2 Stratified two immiscible liquids

Mitani and Sakai[7] have successfully extended this technique to measure ultralow interfacial tension of liquid-liquid interfaces with a surfactant and an electrolyte. They demonstrated that static interfacial tensions for heptane-water-sodium di(2-ethylhexyl) sulfosuccinate system drastically decreased as increasing the electrolyte concentration and showed the lowest tension below 1μN/m at a certain electrolyte content. The significant reduction in interfacial tension by orders of magnitude can be attributed to the suppressed ionization of surfactant molecules by the electrolyte counter-ions.

It is worth noting that their analysis is essentially based on the motion of bulk Newtonian fluids by simply assuming that the adsorption and desorption of surfactant molecules are so fast that they play a negligible role in the leveling of the surface deformation. As described in 2-1-2, this assumption may break when the adsorbed molecules at the air-liquid interface act as a distinct insoluble layer, usually referred to as "elastic layer", and impact the local fluid motions. More detailed studies would be needed to understand how the surface relaxation behavior observed by the LISD method is influenced by the local events at liquid-liquid interfaces.

2.3 Numerical modeling of periodic variations in surface properties[8)-9)]

In continuous coating processes, a liquid film on a moving substrate is often subject to air blowing from slit and/or round nozzles. The resulting periodic variations in heat and mass transfers across the gas-liquid interface strongly impact the viscosity and surface tension through its coupling with the local temperature and concentration. However, no direct experimental evidence is currently available for describing the periodic variations in fluid surface properties in industrial dryers, because of difficulties in measurements under high speed, high temperature, and fast airflow conditions. Indeed, most previous drying studies have simply assumed constant mass/heat transfer coefficients, and hence uniform interfacial properties[10)-16)].

One of the successful computational approaches for predicting the drying behavior on a moving substrate is to numerically move the profiles in heat/mass transfer coefficients at the same speed as, but in the opposite direction to, the substrate motion[8)]. Such a conceptually simple procedure enables us to determine the periodic variations in surface properties. **Fig. 2** presents one of the extreme cases when a polymeric liquid film is introduced at a constant speed into an impingement dryer, in which 10 m/s hot air is vertically impinged from regularly-spaced slit nozzles onto the coating surface[9)]. The spatial concentration variation results in sequential spikes in the surface tension and the fluid viscosity (**Fig. 2**). The former tends to induce interfacial Marangoni stress to drive surface flows, whereas the latter resists the liquid motion. The previous drying models using spatially-uniform mass/heat transfer coefficients hardly predict such a periodic growth and relaxation in interfacial fluid properties.

However, no physical models are currently available for describing the dynamics of evaporating nanoparticle suspensions under periodic air blowing conditions. Though the aforementioned SW and LISD methods would be suitable for the local in-situ monitoring at a given spot of laser irradiation, a precise, in-plane scanning of the measuring point is required to obtain the two-dimensional profiles of interfacial fluid properties. The development of non-contact, two-dimensional imaging techniques would provide us a new direction for understanding how the fluid on moving coatings responds to the spatial variations in evaporative conditions.

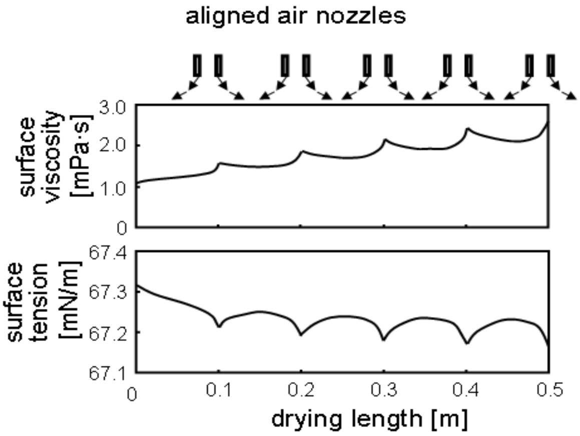

Fig. 2 Periodic variations in viscosity and surface tension in air drier[9)].

3. Local Concentration Profiles in Shrinking Films

Fluid properties in drying films in a thickness direction are equal to that at the air-liquid interface only in the case when the shrinking rate is sufficiently slow compared to diffusion rates of solutes or particles. The ratio between the shrinkage and diffusion rates is usually referred to as Peclet number $Pe=E_0H_0/D_0$ where E_0 is the characteristic shrinkage rate of the film, H_0 the film height, and D_0 the diffusion coefficient of solute or particles in the fluid. In suspension systems in which the density of dispersing particles are larger than that of the solvent, the sedimentation number can be similarly defined as the ratio between the sedimentation rate and the diffusion rate as $Ns=U_0/E_0$ where U_0 is the rate of gravity-driven particle sedimentation. The composition profiles become uniform across the film when $Pe<<1$ and $Ns<<1$. The solutes or particles are accumulates at the evaporating surface for $Pe>>1$, and dense particles can settle down by gravity for $Ns>>1$. In the intermediate cases, the solutes or particles are enriched at the top or bottom surface, or even at both interfaces, depending on the fluid properties and the drying conditions. Indeed, the enriched polymer distribution at the film-substrate interface is required in some industrial coating applications to improve adhesion of films to the substrate. Because the shrinkage, diffusion and sedimentation rates can change during drying, the initial values of these rates are often taken as the characteristic rates for the simplicity.

Well-designed, in-situ experimental techniques to determine the depth profiles of particle or solute concentrations have been reported in the literatures, which include (1) confocal micro Raman spectroscopy (RMS), (2) Infrared microscopy (IRM), (3) Magnetic resonance (MR), and (4) Cryogenic scanning electron microscopy (Cryo-SEM). Here some experimental examples as well as numerical modeling results are introduced in particular fluid systems to access how they can capture dynamic drying behavior in polymeric and/or suspension films.

3.1 Confocal Micro Raman spectroscopy (RMS)17)-20)

A confocal microscope combined with Raman spectroscopy has been developed to measure concentration profiles in thin polymeric solvent coatings with a spatial resolution of 1-2 μm. A typical experimental setup proposed by Schabel et al.17) is show in **Fig. 3**. A laser beam with a wavelength of 514 nm or 633 nm enters from below and is focused at a spot in a liquid sample drying in an airflow channel. The laser spot moves in the sample by means of a piezo nanopositioning system. The backscattered light is directed through a pinhole in order to obtain light from a certain spatial region in the film. After a calibration by taking Raman spectra of fluids with given concentrations, the local concentration can be determined by calculating the ratio of the light intensities of the characteristic Raman peaks.

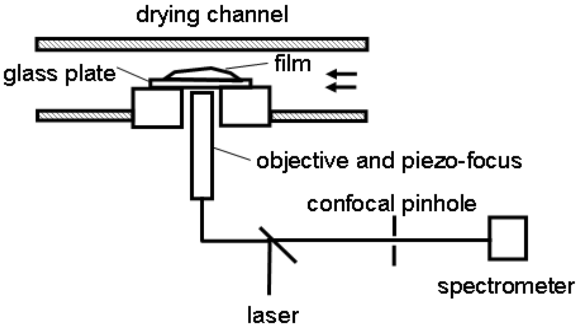

Fig. 3 schematic setup of RMS method17).

3.1.1 Polymer-solvent system

The concentration profiles in 75 μm thick polyvynil acetate (PVAc)-toluene films have been successfully measured by choosing the characteristic Raman wavelength of 2941 cm^{-1} for PVAc and 3062 nm^{-1} for toluene17). The measured concentration profile of toluene after 30 s drying revealed a particular concentration gradient in the vicinity of the evaporating surface, showing non-uniform solvent distributions in the coating. Note that the final polymer concentration profile becomes uniform when all solvent completely evaporates. The non-uniform solute distribution can remain in the coating in a particular case when a thin surface layer with low solvent concentrations, and hence low solvent diffusivities, can trap the solvent inside the film, usually referred to as skinning. Because of the limited spatial resolution of the local measurements, no experimental data are currently available to directly determine local concentrations inside a skin layer.

3.1.2 Polymer-solvent-solvent system

One of the major advantages of the RMS is a straightforward extension to multi-component systems. Krenn et al.18) used the RMS method to measure the residual solvents in polyvynil acetate (PVAc)-toluene films evaporating in methanol vapor. The methanol can penetrate into the liquid film during the evaporation of toluene to give a ternary solution. In the airflow without the preloaded methanol, the toluene content in the liquid film decreased in the early evaporation stage but soon reaches a constant value, showing that a surface skinning due to a drop in the diffusion coefficient traps toluene inside the film. When the methanol vapor is loaded in the airflow, on the contrary, the RMS measurements revealed that the evaporation of toluene was significantly enhanced by the introduction of methanol vapor. Both the toluene and methanol contents finally decrease with time after the gas loading ends, resulting in dried films with less residual solvents. Such a gas loading of a secondary solvent provides a useful route to promote a preferential solvent diffusion from multi-component thin liquid films.

3.1.3 Particle-solvent system

The RMS method has also been successfully applied to measure local particle distributions in drying water films. Ludwig et al.[19] carefully considered a decrease in Raman signals due to a light scattering from particle surfaces, and provided the first experimental evidence that the particle concentration profile at Pe = 0.04 is uniform across the film when acrylic latex particles with 100 nm in diameter were dispersed in water. This is consistent with the aforementioned discussion that the particles neither accumulate at the air-liquid interface nor settle down at the substrate-liquid interface when the Brownian motion of particles are sufficiently fast compared to the film shrinkage and the particle sedimentation. Their optical configurations allowed to scan the 75 μm thick film in 30 s with a spatial resolution of 2~3 μm.

3.1.4 Particle-solvent-surfactant system

In electrostatic repulsive particle systems, the local particle ordering significantly influences the surfactant distribution. Arnold et al.[20] have successfully applied the RMS method to measure surfactant distributions in aqueous dispersions of charged, deformable latex particles. They prepared suspensions of acrylic latex particles with 110 nm or 30 nm in diameter, and determined the concentration profiles of sodium dodecyl sulfate (SDS) added as an anionic surfactant. Surprisingly, the surfactant concentration profiles under low pH conditions are heterogeneous and vary in the thickness direction to show a particular "zigzag" profiles, whereas those at high pH are homogeneous throughout the film. The arising questions are (i) why does the transition from a homogeneous to a heterogeneous surfactant distribution happen, and (ii) how does the non-uniform surfactant distribution relax during drying. A possible explanation for the former is that, a homogeneous compaction of particles in repulsive systems at high pH tends to trap free surfactant molecules in narrow inter-particle spaces, resulting in a drastic decrease in surfactant mobility to give the uniform distributions. In less stable systems at low pH, on the contrary, possible particle flocculation gives a more open structure, in which surfactants diffuse to form micrometer-sized aggregates in inter-particle spaces[20]. However, such aggregates were not visible in their optical configuration because of a spatial resolution limit. In addition, the effect of drying conditions on time-dependent surfactant distributions across the film has not yet well explored.

3.2 Magnetic resonance

Alternatively, Gorce et al.[21] obtained water concentration profiles in 255-420 μm thick aqueous dispersion systems of spherical alkyd particles by Magnetic Resonance (MR) method with a pixel resolution better than 10 μm. ^{1}H NMR signals averaged over 256 scans revealed a uniform water concentration distribution for Pe = 0.2, showing qualitative agreement with the RMS results[19]. At higher Peclet number of Pe = 16, on the other hand, a linear gradient in the water profile was observed after 7 min drying, indicating that the particles are accumulated near the air-liquid interface because of the fast film shrinkage. Interestingly, the measured local volume fraction of water near the evaporating surface was below the value corresponding to a face-centered cubic (FCC) particle packing, indicating that particles at the top surface reached a closed-packing structure and started to deform from their spherical shape.

3.3 Cryogenic scanning electron microscopy[22)-26)]

In a visualization of particle distributions using cryoSEM, samples dried for various amounts of time are plunged into liquid ethane to vitrify. Then the samples are fractured under liquid nitrogen to expose the coating cross-section, sublimed for a few minutes to reveal the particles, and imaged in a SEM at low temperatures.

3.3.1 Hard particle-solvent system

Recently, Cardinal et al.[22] successfully visualized the particle distributions in early evaporation stages for different Peclet (Pe) and sedimentation numbers (Ns). They prepared aqueous suspensions of monodisperse, non-deformable silica particles with diameters ranging from 200 nm to 1 μm, and observed the cross section at different drying times. CryoSEM images revealed a layer of highly concentrated particles at the top for Pe = 250 and Ns = 0.08, whereas the sediment at the bottom and a particle-free layer on the top for Pe = 1.8 and Ns = 200. In the intermediate case of Pe=4.2 and Ns=0.08, the diffusion plays a role in determining the particle distribution and the particle profile remains uniform across the film.

3.3.2 Soft particle-solvent system

The drying of deformable latex particle suspensions generally involves three stages of (i) consolidation, (ii) compaction, and (iii) coalescence[23]. In the consolidation stage, the solvent evaporation concentrates the suspension as would in hard-particle systems, and gives rise to the particle accumulation on the top surface for high Peclet numbers. In the second stage after particles reach a critical volume fraction for closed packing, capillary forces tends to compact the neighboring particles as the air begins to invade the pore space to form pendular rings hanging between the particles. In the last stage, polymer chains can diffuse through partially-flattened particle surfaces, leading to a homogeneous polymer film after the polymer migration completes. Ma et al.[24] used mono- disperse polystyrene and polymethylmethacrylate-co-n-butyl acrylate latexes suspended in water to observe these three stages of latex film formation by cryoSEM. Furthermore, they demonstrated a well-refined imaging technique by carefully considering the artifacts in freezing, fracturing, and sublimination procedures. However, the effect of drying condition on particle distributions has not been fully described.

3.3.3 Bimodal hard particle-solvent system

As mentioned in 3-1-1, a final distribution of solids in binary systems is uniform through a film after the complete evaporation of volatile components. However, this is not the case in ternary systems containing the third component in suspensions, because a preferential segregation of particles during drying significantly influences the distribution of other components. Typical example includes bimodal particle dispersions, in which one particulate component can be accumulated at the air-liquid interface for high Pe but not so is the other. Recently, CryoSEM technique has been applied to observe the particle distributions in a bimodal silica dispersion containing particles of 1 μm in diameter and 200 nm in diameter[22]. The microscope observation revealed a top layer composed of smaller particles and a bottom layer of small particles dispersed between large particles, indicating that the small particles were accumulated at the evaporating surface, whereas the larger particles settled down toward the substrate-liquid interface. A simple extension of drying regime map (shown below in 3-5-1) to the bimodal system showed that the small particles are in a evaporation-dominated regime, whereas the larger particles are in sedimentation regime, suggesting that their cryoSEM observations well reproduce the predicted drying map.

3.3.4 Bimodal soft particle-solvent system

On the contrary, no preferential segregation of smaller particles has been observed for a bimodal aqueous suspension containing hollow polystyrene latex of 0.5 μm in diameter and polyvynil acetate latex of 0.1 μm in diameter[25]. CryoSEM observations revealed that hollow PS particles showed a homogeneous distribution across the film, and surrounded by smaller particles coalescing each other. As the film dried further, the voids filled with water was replaced by air, and the particles eventually collapsed due to strong capillary forces. Because of the complexity of the system, the dynamics of the particle segregation in such deformable, bimodal particular systems is still an ongoing debate.

3.3.5 Particle-polymer-solvent system

An addition of soluble polymeric binder in a particle suspension is common in many industrial coating applications such as paper coatings, optical films, paints, conductive films, fuel cells, capacitors etc. Binders provide adhesion to a substrate to improve a mechanical strength of film, reduce pore spaces between particles, adsorb on particle surfaces to alter interfacial forces, and sometimes acts as a surfactant. As expected from 3-1-1 and 3-1-3, both the particle and the binder can segregate in shrinking coatings, depending on Pe and Ns of each component. The local distribution of binder significantly impacts that of particles though the coupling with an increase in bulk liquid viscosity, and thus a decrease in particle diffusivity, as well as a drop in film shrinkage rate due to polymer chain entanglements in the vicinity of the evaporating interfaces. The former tends to reduce Pe and Ns, whereas the latter promotes lower Pe but higher Ns, giving rise to a complex variation in concentration distributions due to the existence of binders.

In order to verify the suppressed particle sedimentation at higher binder concentrations, cryoSEM observations were performed in silica-polyvinylalcohol-water systems[26]. The specimens were deposited on 5×7 mm silicon wafers, dried for five minutes, and then plunged into liquid ethane to freeze the sample. In the absence of binder, the exposed cross-section of the sample showed a particle-free zone, indicating that the coating was in the sedimentation regime. In contrast, the thickness of the particle-free zone significantly reduced in coatings prepared with 1 vol % PVA, providing evidence that the particle distribution became more homogeneous in the presence of binder.

3.4 Infrared microscopy (IRM)

Guigner et al.[27] measured the water distribution in drying O/W emulsion films by means of infrared microscopy (IRM). The polydimethylsiloxane/water emulsion was prepared by adding a surfactant with a linear alkyl group with 13 carbon atoms as a hydrophobic part and with eight ethoxy groups as a hydrophilic part. The IR analysis was performed in transmission mode by irradiating the beam though the cross section of the liquid sandwiched between two CaF_2 crystal plates. The 50 μm beam spot moved along the vertical direction of samples in 10 mm thick, and time- dependent concentration profiles of the surfactant was obtained for 16 days drying. The validity of the IR measurement was confirmed by comparing the water fraction cumulated over the whole sample height with the total mass loss of the film. The local distribution measurements showed that a strong concentration gradient of water first developed at the air-liquid interface but it became more heterogeneous after 20 h drying. The simultaneous attenuated total reflection (ATR) spectroscopy revealed that the water content in the vicinity of emulsion-substrate interface first decreased, and then increased in a certain drying time, and eventually decreased again as the water further dried. This peculiar increase in the local water concentration was attributed to the possible coalescence events of neighboring emulsions in the concentrating fluids. However, the spatial resolution of the concentration measurements was orders of magnitude larger than the characteristic emulsion size of 0.3 μm. No direct experimental evidence for the emulsion coalescence was currently provided, and the detailed drying mechanism is still an ongoing debate. A novel in-situ monitoring with a finer resolution would allow us to capture local dynamic events on each emulsion surfaces, and give a new physical insight in the drying systems involving liquid-liquid interfaces.

3.5 Numerical modeling[28)-31)]

3.5.1 Particle-solvent system - continuous model -

The Pe-dependent variations in the particle distribution have been predicted by the one-dimensional continuous model under no bulk flow. Routh and Zimmerman[28] first proposed a physical model for spherical particles by considering the competition between the film shrinkage and the particle diffusion. They solved the time-dependent conservation equation for the volume fraction of particles under a constant film shrinkage rate but at different Peclet numbers. In their computations, the compressibility of the dispersion was given to diverge at the maximum particle volume fraction in close packing limit. The computational results for Pe=10 showed a sharp discontinuity in volume fraction between a close packed region and the region still at the initial condition, showing the same trends observed in experiments[21),22]. However, their computations have been limited to the Peclet numbers below 10. For Pe>10, the volume fraction in the packed region tends to exceed the close packing limit, resulting in an unphysical situation due to numerical instabilities.

The model has been recently extended to higher Pe, including the particle sedimentation by gravity[22]. The examples of numerically predicted particle distributions are shown in **Fig. 4**. At low Ns, the evaporation and diffusion compete, and the sedimentation plays a minor role. The particle distribution becomes uniform for low Pe (a), while the fast evaporation for high Pe accumulates particles at the air-liquid interface to give a skinning (c). At high Ns and low Pe, on the other hand, the evaporation is unimportant and the sedimentation and diffusion compete (b). The effects of sedimentation and evaporation coexist for higher Ns and Pe, and the particle can be accumulated both at the top and the bottom surfaces (d).

The characteristic particle distributions are summarized in a universal drying region map for a given initial particle volume fraction of 0.1 (**Fig. 5**). The curves in the figure represent the conditions where the coating reaches 90 % of the maximum packing fraction in less than half the time needed for the entire coating to reach the fraction limit. Cardinal et al.[22] demonstrated that the predicted three drying regimes agree well with cross-sectional observations of particle distributions by cryoSEM. It is worth noting that the drying regime map strongly depends on the initial particle concentration in the liquid. Indeed, the numerical results revealed that the diffusion regime shrinks, but the evaporation regime expands, at higher particle contents because the resulting increase

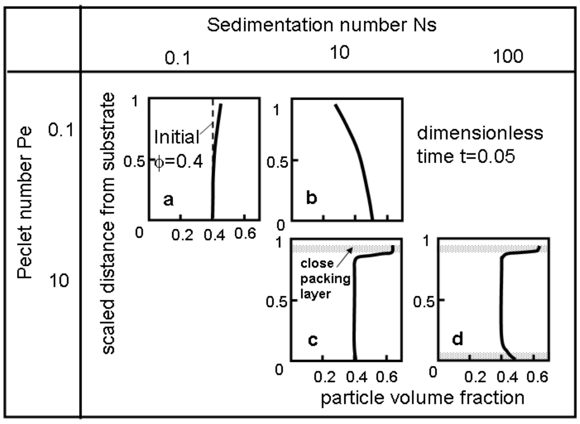

Fig. 4 Variations in particle distribution as a function of Peclet number (Pe) and sedimentation number (Ns)[22].

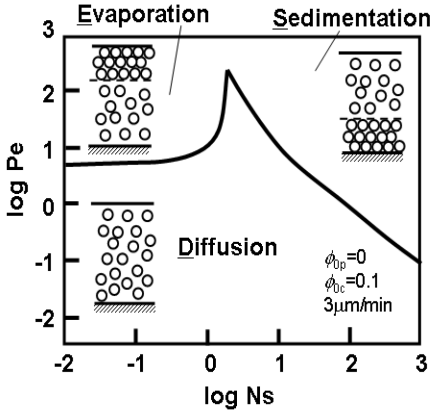

Fig. 5 Drying regime map[22].

in bulk fluid viscosity resists the particle motion, and hence, more particles can be trapped at the receding air-liquid interface.

Although these drying models are useful to predict the drying behavior in suspension, the continuous models simply neglected interfacial contributions of each particle. Supposing particles floating on an air-liquid interface, concave menisci between the particles create a low pressure in the liquid, which promotes a driving force for liquid motion toward the evaporating interface, depending on the meniscus curvature, and thus liquid contact angles on the particle surface. In *non-spherical* particles, the capillary forces would strongly influence the orientation of particles, which, in turn, give rise to a complex deformation of the free surface.

3.5.2 Particle-solvent system - discrete model-

In order to access how the local alignment of particles impacts the drying behavior, some numerical attempts have been proposed to solve motions of each particle in shrinking films[29)-30)]. Ohta et al.[30] recently showed drying-induced structural transitions in suspensions of rod-like nanoparticles by using a connected-sphere model. The rod-like particle was simply represented by the serial connection of spherical segments, and the Langevin equation for each segment was numerically solved under a constant film shrinkage rate of 0.01 m/s. Ordered and disordered particle domains coexisted in dried films when the computation started with a random particle configuration, whereas a well-ordered particular film was obtained with a aligned initial particle configuration under a high zeta potential condition. However, the effects of Pe and Ns on the particle orientation have not yet well explored. Further systematic studies would be required to compare such a "discrete" suspension model with the previous bulk models as well as the experimental observations by RMS, MR, and cryoSEM described above.

3.5.3 Particle-solvent-surfactant system

The particle segregation can impact a surfactant distribution, especially in the case when they adsorb on particle surfaces. Gundabala et al.[31] numerically solved the 1D conservation equation for surfactant in the limit of high particle Peclet number. For simplicity, they assumed that surfactant molecules partly adsorbed onto the particles and partly remained in the bulk solution. The particle distribution was assumed to show a sharp profile given by a Heaviside step function at high Pe. Furthermore, they assumed that the particle layer involved the close packed particle volume fraction and linearly grew with time. The computed surfactant concentration showed a particular discontinuous profile: surfactant distributions showed local peaks both at the bottom surface of the particle layer and the evaporating surface (**Fig. 6**). The discontinuity arises because the low void fraction in the particle layer gives slower surfactant diffusion toward the air-liquid interface. The sharp concentration profiles then relax as the drying proceeds, and eventually the surfactant was enriched at the top and bottom surfaces of the film, indicating a drying-induced segregation of surfactants in particulate coatings. The enriched surfactant concentration at the bottom surface showed a good agreement with experimental observations by attenuated total reflection (ATR). Their computations also demonstrated

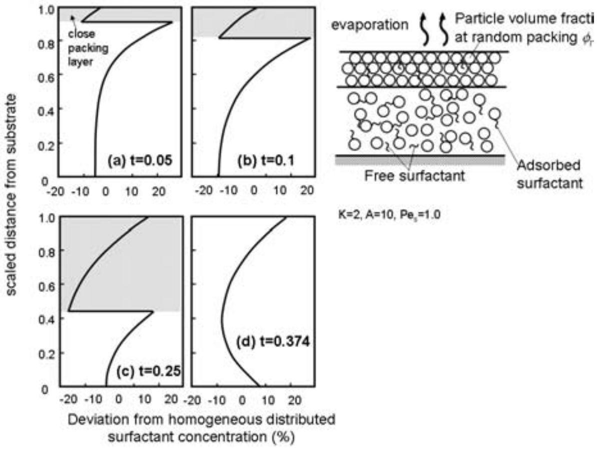

Fig. 6 Variations in surfactant distribution in shrinking suspension film[31)].

that the surfactant concentration at the evaporating surface increased, whereas that at the bottom surface decreased, as increasing the maximum surface adsorption onto the particle. This fact suggests that the surfactant distribution in the shrinking suspension film is tunable by properly choosing adsorption isotherms of the surfactant as well as the evaporation conditions. However, no experimental data is currently available to validate the predicted discontinuous surfactant distribution inside the film. The RMS or IRM may be useful tool to verify the computations in detail.

3.5.4 Particle-polymer-solvent system

Recently, Buss et al.[26)] developed a 1D isothermal model that combines two conservation equations for particle and polymeric binder. For simplicity, they neglect (i) polymer adsorption onto the particles, (ii) capillary forces between particles at the free surface, (iii) drying in lateral direction, (iv) temperature variations due to solvent evaporation, and (v) the cross[32)-34)] and non-Fickian[15)] terms for the multi-component diffusion. Their model is a straightforward extension of previous models[22)] for particle-solvent systems aforementioned in 3-5-1. The variations in fluid viscosity and solvent evaporation rate were taken into account by using empirical poly-nominal function of viscosity with respect to polymer volume fraction, and the concentration-dependent solvent activity given by Flory-Huggins theory. The numerical computations show that the evaporation regime, in which particles tend to be accumulated at the top surface, expands as increasing polymer content since both the diffusion and sedimentation of particles are slowed down in the presence of the soluble binders, showing a qualitative agreement with cryoSEM observations.

Here we should note that their computations were limited to the dimensionless drying time of 0.35, above which the particle concentration reaches the maximum packing fraction. The resultant binder concentration remained so low that the computed partial pressure of solvent, and thus the film shrinkage rate, was almost independent on the polymer contents. Thus the raise in liquid viscosity, rather than a reduced evaporation rate, plays a major role in the predicted particle distributions during time. A rigorous model that can overcome the computational limit at high particle packing fractions would be required to obtain final concentration distributions of binders in dried coatings. Furthermore, the effect of binder adsorption at the particle-liquid and air-liquid interfaces should be taken into account because it would significantly alter the local distributions as described in 3-5-3. Nevertheless, to the best of the author's knowledge, their work is the first to predict the particle segregation behavior in ternary coating systems of practical interest.

4. Concluding Remarks

This paper reviews the recent progress in in-situ measurement techniques and numerical approaches for determining local distributions of particles or solutes in evaporating thin liquid films. The ripplon surface wave (SW) and laser-induced surface deformation (LISD) methods are suitable to measure local surface properties at the air-liquid and liquid-liquid interfaces by detecting a motion of interfacial waves with the amplitude of orders of nanometers. However, two-dimensional imaging along the interface is usually required in practical coating applications to determine heterogeneous in-plane distributions of physical properties. A high-speed 2D scanning or a direct 2D imaging may be required in the future applications of these techniques.

The concentration distributions in the thickness direction have been successfully measured by confocal micro Raman spectroscopy (RMS), Infrared microscopy (IRM), and Magnetic resonance (MR), and summarized by using non-dimensional numbers of Pe and Ns. Despite the formidable consistency with the computational results for hard particle-solvent and polymer-solvent systems, the spatial resolutions of these techniques are currently not sufficient to elucidate the detailed drying kinetics in suspensions of deformable particles[23)-25)], those containing surfactants[20), 31)], suspensions on a moving substrate under practical high speed operating conditions, and even phase-separating fluid systems involving three-dimensional, interconnected domain structures. Furthermore, these spectroscopes require an optical transparency of the sample at the wavelength of interest, and thus might not be suitable for measurements of thick, opaque samples with amounts of absorption and/or scattering of irradiated light. Cryogenic scanning electron microscopy (Cryo-SEM) involves the higher spatial resolution compared with those methods, yet the sampling rate of the images is limited to relatively low speeds because of careful procedures required for the sample freezing.

These local property measurements provide complementary information for *averaged* physical quantities obtained by other techniques. The UV-VIS or infrared spectroscopy[54)-55)] and the laser scattering (LS)[62)-63)] respectively give information on reaction rates and characteristic domain sizes in the evaporating coatings, but these properties are averaged in the thickness direction as a laser beam passes through the film to give integrated signals. In the drying rate measurements by the mass loss[58)], the heat-flux variation[60)], and the gas chromatography[61)], the measurable evaporation rates of solvent are in principal averaged in-plane along the evaporating surface, whereas the tensile stress measurement by the cantilever beam deflection (CBD)[35)-51)] method detects forces averaged both in the thickness and span-wise directions. **Fig. 7** schematically depicts possible combinations of these techniques with the aforementioned local property measurements. Indeed, some previous studies[54)-55)] have successfully demonstrated the simultaneous measurements of averaged stresses and reaction rates during the solvent evaporation. Other proper combinations for local and averaged measurement techniques will results in a better understanding of microstructure formation in evaporating thin liquid films.

Acknowledgements

The author acknowledges the financial support of Japan Society for the Promotion of Science (JSPS) KAKENHI (23560912) Grant-in-Aid for Scientific Research C.

References

1) Nishio T., and Nagasaka Y. ((1995)): Simultaneous Measurement of surface tension and kinematic viscosity using thermal fluctuations, International Journal of Thermophysics, 16, pp.1087-1097.

2) Oki, K., and Nagasaka, Y. (2008): Dynamic Observation of the Behavior of the Surface of Liquid Films of Polymer–Organic Solvent System by Ripplon Surface Laser-Light Scattering Method, Kagaku Kogaku Ronbunshu, 34, pp.587-593.

3) Oki, K. and Nagasaka, Y. ((2009)): Measurements of

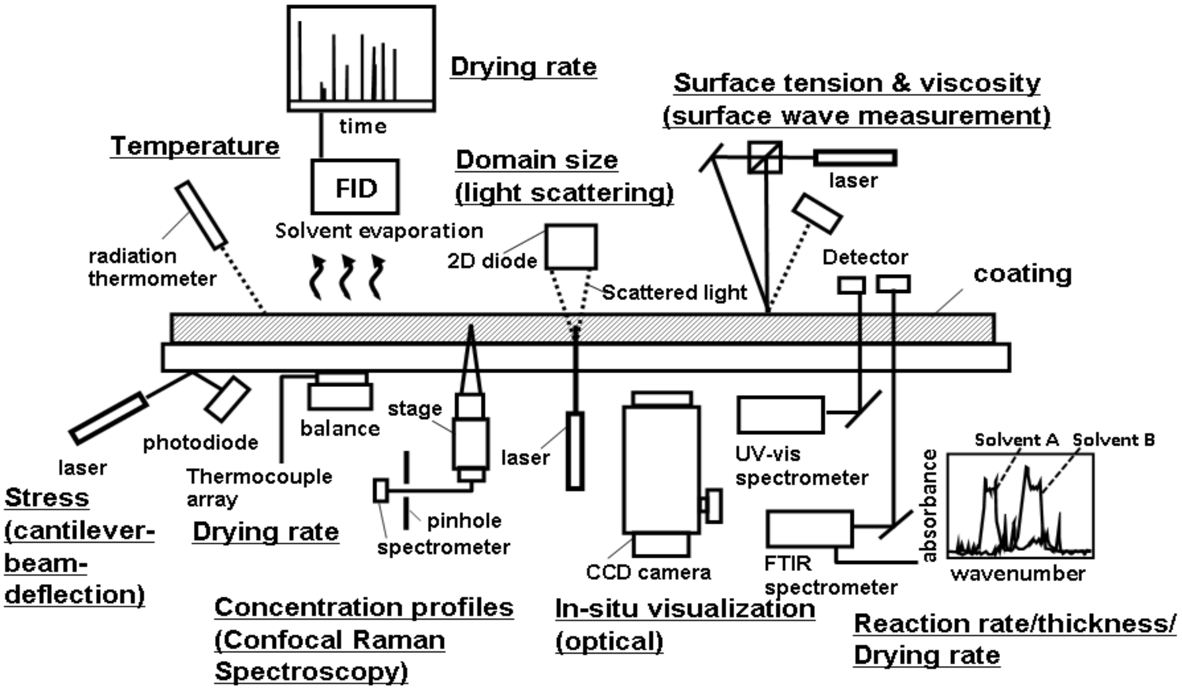

Fig. 7 Integrated in-situ measurement devices for evaporating thin complex fluids.

anisotropic surface properties of liquid films of azobenzene derivatives, Colloids and Surfaces A: Physicochem. Eng. Aspects, 333, pp.182-186.

4) Sakai K., Mizuno D., and Takagi K. (2001): Measurement of liquid surface properties by laser-induced surface deformation spectroscopy, Physical Review E, 63, 046302.

5) Yoshitake, Y., Mitani, S., Sakai, K., and Takagi, K. (2005): Measurement of high viscosity with laser induced surface deformation technique, Journal of Applied Physics, 97, 024901-1-024901-6.

6) Sakai K., Tachibana, K., Mitani. S., Takagi K. (2003): Laser excitation of high-frequency capillary waves, Journal of Colloid and Interface Science, 264 pp.446-451.

7) Mitani S., and Sakai K. (2002): Measurement of ultralow interfacial tension with a laser interface manipulation technique, Physical Review E, 66, 031604.

8) Yamamura M., Uchinomiya, T., Mawatari, Y., and Kage, H. (2007): Asymmetric surface roughness formation on moving non-isothermal liquid coatings, International Polymer Processing, 22, pp.22-26.

9) Yamamura M. Uchinomiya, T., Mawatari Y., and Kage H. (2009): Drying-induced Surface Roughening of Polymeric Coating under Periodic Air Blowing, AIChE Journal, 55, pp.1648-1658.

10) Cairncross R.A, Jeyadev S, Dunham R.F, Evans K, Francis L.F. and Scriven L.E. (1995): Modeling and design of an industrial dryer with convective and radiant heating. Journal of Applied Polymer Science, 58, pp.1279-1290.

11) Price PE Jr, and Cairncross, R.A. (1999): Optimization of single-zone drying of polymer solution coatings to avoid blister defects, Drying Technology, 17, pp.1303-1311.

12) Wong, S.S, Altinkaya, SA. and Mallapragada, S.K, (2004): Drying of semicrystalline polymers: mathematical modeling and experimental characterization of poly(vinyl alcohol films, Polymer, 45, pp.5151-5161.

13) Cairncross, R.A, Francis, L.F. and Scriven, L.E. (1996): Predicting drying in coatings that react and gel:drying regime maps, AIChE Journal, 42, pp.55-67.

14) Alsoy, S. and Duda, J.L. (2002): Influence of swelling and diffusion-induced convection on polymer sorption processes, AIChE Journal, 48, pp.1849-1855.

15) Vinjamur, M. and Cairncross, R.A. (2002): Non-Fickian nonisothermal model for drying of polymer coatings, AIChE Journal, 48, pp.2444-2458.

16) Okuzono, T. Ozawa, K. and Doi, M. (2006): Simple model of skin formation caused by solvent evaporation in polymer solutions, Physical Review Letters, 97, 136103-1-136103-4.

17) Schabel, W., Ludwig, I. and Kind, M. (2004): Measurements of concentration profiles in polymeric solvent coatings by means of an inverse confocal micro Raman spectrometer-initial results, Drying Technology, 22, pp.285-294.

18) Krenn, J., Scharfer, P., Kind, M., and Schabel, W. (2009): Drying of solvent-borne coatings with preloaded drying gas, Eur. Phys. J., 166, pp.45-48.

19) Ludwig, I., Schabel, W., Kind, M., Castaing, J.C., and Ferlin, P. (2007): Drying and Film Formation of Industrial Waterborne Latices, AIChE Journal, 53, pp.549-560.

20) Arnold, C., Thalmann, F., Marques, C., Marie, P. and Holl, Y. (2010): Surfactant distribution in waterborne acrylic films. 1. Bulk Investigation, Journal of Physical Chemistry B, 114, pp.9135-9147.

21) Gorce, J.P., Bovey, D., McDonald, P. J., Palasz, P., Taylor, D. and Keddie, J.L. (2002): Vertical water distribution during the drying of polymer films cast from aqueous emulsions, European Physical Journal E, 8, pp.421-429.

22) Cardinal, C.M., Jung, Y.D., Ahn, K.H. and Francis, L. F. (2010): Drying regime maps for particulate coatings, AIChE Journal, 56, pp.2769-2780.

23) Sutanto, E., Ma, Y., Davis, H.T. and Scriven, L.E. (2001): Cryogenic Scanning Electron Microscopy of early stages of film formation in drying latex coatings, ACS Symposium Series, 790, pp.174-192.

24) Ma, Y., Davis, H.T. and Scriven, L.E. (2005): Microstructure development in drying latex coatings, Progress in Organic Coatings, 52, pp.46-62.

25) Cardinal, C.M., Francis, L.E., Scriven, L.E. (2009): Drying and collapse of hollow latex, Journal of Coatings Technology and Research, 6, pp.457-469.

26) Buss, F., Roberts, C.C., Crawford, K.S., Peters, K. and Francis, L. (2011): Effect of soluble polymer binder on particle distribution in a drying particulate coating, Journal of Colloid and Interface Science, 359 pp.112-120.

27) Guigner, D., Fischer, C. and Holl, Y. (2001): Film formation from concentrated reactive silicone emulsions. 1. Drying mechanism, Langmuir, 17, pp.3598-3606.

28) Routh, A.F., Zimmerman, W.B. (2004): Distribution of Particles during Solvent Evaporation from Films, Chemical Engineering Science, 59, pp.2961-2968.

29) Fujita, M. and Yamaguchi, Y. (2007): Simulation of 3D Crystallization of Colloidal Nanoparticles on a Substrate during Drying, International Polymer Processing, 22, pp.16-21.

30) Ohta, S., Inasawa, S., Koike, O., Fujita, M. and Yamaguchi, Y. (2009): Formation of well-aligned thin films of rod-like nanoparticles via solvent evaporation: a simulation study, Applied Physics Express, 2, 065002-1- 065002-3.

31) Gundabala, V., W.B., Zimmerman, A.F. and Routh, (2004): A model for surfactant distribution in latex coatings, Langmuir, 20, 8721.

32) Zielinski, J.M. and Hanley, R.F. (1999): Practical friction-based approach to modeling multicomponent diffusion, AIChE Journal, 45, pp.1-12.

33) Price, Jr. P.E. and Romdhane, I.H. (2003): Multicomponent diffusion theory and its application to polymer-solvent systems, AIChE Journal, 49, pp.309-322.

34) Yamamura, M., Kajiwara, T. and Kage, H. (2003): Mul-

ticomponent diffusion in phase separating polymer blends with different frictional interactions : a mean-friction model, Chemical Engineering Science, 58, pp.3891-3899.
35) Corcoran, E.M. (1969): Determining Stresses in Organic Coatings using Plate Beam Deflection, Journal of Paint Technology, 41, pp.635-640.
36) Perera, D.Y. and Eynde, D.V. (1981): Considerations on a Cantilever (Beam) Method for Measuring the Internal Stress in Organic Coatings, Journal of Coating Technology, 53, pp.39-44.
37) Chiu, R.C. and Cima, M. J. (1993): Drying of Granular Ceramic Films; II, Drying Stress and Saturation Uniformity, Journal of American Ceramic Society, 76, pp.2769-2777.
38) Lewis, J.A., Blackman, K.A., Ogden, A. L., Payne, J.A. and Francis, L.F. (1996): Rheological Property and Stress Development during Drying of Tape-Cast Ceramic Layers, Journal of American Ceramic Society, 79, pp.3225-3234.
39) Payne, J.A., McCormick, A.V. and Francis, L.F. (1997): In situ stress measurement apparatus for liquid applied coatings, Rev. Sci. Instrum., 68, pp.4564-4568.
40) Payne, J.A., Francis, L.F. and McCormick, A.V. (1997): The effects of Processing Variables on Stress Development in Ultraviolet-Cured Coatings, Journal of Applied Polymer Science, 66, pp.1267-1277.
41) Petersen, C., Heldmann, C. and Johannsmann, D. (1999): Internal Stresses during Film Formation of Polymer Latices, Langmuir, 15, pp.7745-7751.
42) Lei, H., Payne, J.A., McCormick, A.V., Francis, L.F., Gerberich, W.W. and Scriven, L.E. (2001): Stress development in drying coatings, Journal of Applied Polymer Science, 81, pp.1000-1013.
43) Lei, H., Francis, L.F., Gerberich, W.W. and Scriven, L.E. (2002): Stress development in drying coatings after solidification, AIChE Journal, 48(3), pp.437-451.
44) Francis, L.F., McCormick, A.V. and Vaessen, D.M. (2002): Development and Measurement of Stress in Polymer Coatings, Journal of Materials Science, 37, pp.4717-4731.
45) Martinez, C.J. and Lewis, J.A. (2002): Shape Evolution and Stress Development during Latex-Silica Film Formation, Langmuir, 18, pp.4689-4698.
46) Tirumkudulu, M.S. and Russel, W.B. (2004): Role of Capillary Stresses in Film Formation, Langmuir, 20, pp.2947-2961.
47) Wedin, P., Martinez, C.J., Lewis, J.A., Daicic, J. and Bergstrom, L. (2004): Stress Development during Drying of Calcium Carbonate Suspensions Containing Carboxymethylcellulose and Latex Particles, Journal of Colloid and Interface Science, 272, pp.1-9.
48) Wedin, P., Lewis, J.A. and Bergstrom, L. (2005): Soluble Organic Additive Effects on Stress Development during Drying of Calcium Carbonate Suspensions, Journal of Colloid and Interface Science, 290, pp.134-144.
49) Kiennemann, J., Chartier, T., Pagnoux, C., Baumard, J.F., Huger, M., and Lamerant, J.M. (2005): Drying Mechanisms and Stress Development in Aqueous Alumina Tape Casting, Journal of European Ceramic Society, 25, pp.1551-1564.
50) Lan, W. and Xiao, P. (2007): Drying Stress of Yttria-Stabilized-Zirconia Slurry on a Metal Substrate, Journal of the European Ceramic Society, 27, pp.3117-3125.
51) Kim, S., Sung, J.H., Ahn, K.H. and Lee, S.J. (2009): Drying of the silica/PVA suspension: effect of suspension microstructure, Langmuir, 25, pp.6155-6161.
52) Shiga, T., Narita, T., Tachi, K., Okada, A., Takahashi, H. and Kurauchi, T. (1997): Measurement of Internal Stresses in Coatings Using Time Resolved Fluorescence, Polymer Engineering and Science, 37, pp.24-30.
53) Shiga, T., Narita, T., Ikawa, T. and Okada, A. (1998): Stress Monitoring in Thin Polymer Coatings Using Time Resolved Fluorescence, Polymer Engineering and Science, 38, pp.693-698.
54) Stolov, A.A., Xie, T., Penelle, J. and Hsu, S.L. (2001): An Analysis of Photopolymerization Kinetics and Stress Development in Multifunctional Acrylate Coatings, Polymer Engineering and Science, 41, pp.314-328.
55) Stolov, A.A., Xie, T., Penelle, J. and Hsu, S.L. (2000): Simultaneous Measurement of Polymerization Kinetics and Stress Development in Radiation-Cured Coatings: A New Experimental Approach and Relationship between the Degree of Conversion and Stress, Macromolecules, 33, pp.6970-6976.
56) Koenig, A.M., Bourgeat-Lami, E., Mellon V., von der Ehe, K., Routh, A.F. and Jahannsmann, D. (2010): Dilational lateral stress in drying latex films, Langmuir, 26, pp.3815-3820.
57) Suzuki, I., Yasui, Y., Udagawa, A. and Kawate, K. (2004): Drying process monitoring by rapid scanning FT-IR spectrometer, Industrial Coating Research, 5, pp.107-123.
58) Yamamura, M., Horiuchi, K., Kajiwara, T., and Adachi, K. (2002): Decrease in solvent evaporation rate due to phase separation in polymer films, AIChE Journal, 48, pp.2711-2714.
59) Imakoma, H., Nagaoka, S., and Takigawa, T. (2007): Measurement of drying rate of water-based coat by temperature change method, Kagaku Kogaku Ronbunshu, 33, pp.586-592.
60) Yamamura, M. Ohara, K., Mawatari, Y., and Kage, H. (2009): Measuring the drying rate of liquid film coatings using heat-flux method, Drying Technology, 27, pp.817-820.
61) Vinjamur, M., and Cairncross, R. (2001): A high airflow drying experimental set-up to study drying behavior of polymer solvent coatings, Drying Technology, 19, pp.1591-1612.
62) Miyake, Y., Sekiguchi, Y., and Kohjiya, S. (1993): Formation of percolated structure during solvent casting of polymer blend-solvent systems, Kagaku Kogaku Ronbunshu, 26, pp.543-550.
63) Ermi, B.D., Nisato, G., Douglas, J.F., Rogers, J.A. and

Karim., A. (1998): Coupling between phase separation and surface deformation modes in self-organizing polymer blend films, Physical Review Letters, 81, pp.3900-3903.

Author's short biography

Dr. Masato Yamamura

Dr. Masato Yamamura is an Associate Professor at Kyushu Institute of Technology. He received his B.Eng and M.Eng degrees (Chemical Engineering) from Kyoto University in 1991 and 1993, and in 1998 he earned his Ph.D. in Chemical Engineering from Kyoto University under the supervision of Prof. Fumimaru Ogino. Since 1996, he has been a faculty member in the Department of Applied Chemistry at the institute. He was a visiting scholar at University of Minnesota in 1999 and 2000. Currently he is a board member of International Society of Coating Science and Technology (ISCST), a scientific committee member of European Coating Symposium (ECS), and one of the vice chairs of Division of Materials & Interfaces in the Society of Chemical Engineers of Japan.

On the Adhesion Between Individual Particles[†]

Hans-Jürgen Butt[1]*, Marcin Makowski[1,2], Michael Kappl[1] and Arkadiusz Ptak[2]
Max Planck Institute for Polymer Research[1]
Poznan University of Technology, Institute of Physics[2]

Abstract

A dream in powder technology is to predict the structure and flow of a powder from precise knowledge of the interactions between the particles. The most important interaction is adhesion. In this paper several aspects of adhesion are discussed. First, the influence of humidity and capillary forces is analyzed. To calculate capillary forces the structure of the microcontact needs to be known with an accuracy much better than 1 nm. Determining the structure of a microcontact with such resolution is demanding, if possible at all. Considering that wear can lead to a change of the atomic structure such knowledge is practically impossible. Second, the work to break an adhesive contact depends on the effective spring constant by which the force is applied. Third, adhesion forces depend on the separation speed and not only the surface chemistry and the structure of the particles in the contact region. Fourth, we suggest to distinguish between contact and bridging adhesion.

Keywords: granular matter, powder particles, capillary force, surface energy, work of adhesion, dynamic force spectroscopy, polymer, bridging adhesion

1. Introduction

Adhesion between particles determines the flow and structure of a powder[1-3]. It is of great importance in many applications, ranging from the properties of soil in agriculture to the energy efficient transport of granular materials. In this paper we address several aspects which are relevant when attempting to quantitatively predict the adhesion between powder particles. In a scientific context "quantitative prediction" means understanding. Therefore the aspects discussed here are central in the understanding of adhesion in a powder.

Precise knowledge of adhesion is a prerequisite for predicting the flow behavior of a cohesive powder from first principles[4-9]. A quantitative prediction is not in sight within the next decade. At first sight the task does not seem to be too difficult. If we for example consider the flow of a powder consisting of spherical particles, e. g. glass ballotinis, knowledge of the velocities and torques of all particles at a given moment and knowledge of the interaction forces should suffice to calculate the dynamics of the system in the future from Newtons equation of motion, if the boundary conditions are given. Since computer power increases and programs become more efficient one should expect that a deterministic prediction is in sight. Here, we argue that this is most likely not the case and that a deterministic prediction including the individual adhesion forces will hardly be possible.

In this paper we would like to address several fundamental problems, which complicate a prediction of adhesion and the flow of a powder. First, we address one specific, although often dominating interaction, the capillary interaction. Capillary forces depend on the precise structure of the particle surfaces. We argue that it will be difficult or even impossible to generate the information on the structure at the required precision. Furthermore, the structure of the microcontact might change due to wear, leading to changing adhesion. Then we focus on the relation between adhesion force and work of adhesion. For contact adhesion we argue that the work of adhesion depends on the way two particles are separated.

[†] Accepted: September 12th, 2011
[1] Ackermannweg 10, 55128 Mainz, Germany
[2] Nieszawska 13A, 60-965 Poznan, Poland
[*] Corresponding author
E-mail: butt@mpip-mainz.mpg.de
TEL: (+49) 6131 379 111, FAX: (+49) 6131 379 310

© 2011 Hosokawa Powder Technology Foundation

Third, we address the fact that the adhesion force is not a constant, which only depends on the materials, the shape and size of the contacting particles, and on external parameters such as temperature or pressure. The adhesion force also depends on how fast two particles are separated. Finally, we discriminate between contact and bridging adhesion. Bridging adhesion is often observed between surfaces in a polymer solution or melt. In contact adhesion the adhesion force is the appropriate parameter describing the separation process. In bridging adhesion the work of separation is more relevant.

Naively one would expect that adhesion forces between similarly prepared particles of equal size are always the same. This is, however, not the case. Rather than a single value, distributions of adhesion forces are observed and adhesion forces vary by typically a factor of two to ten even within relatively monodisperse powders[10-15)]. As a cause of this variation surface roughness and surface heterogeneity have been suggested[16-20)]. Roughness can cause a significant change in the contact area of two particles, depending on where precisely they are in contact. Heterogeneity in chemical composition or molecular structure at different length scales can cause a different energy of adhesion. It may cause a variation in the effective adhesion force depending on the precise location of contact.

Recent experiments on adhesion forces showed that for a nanoscopic tip of an atomic force microscope (AFM) on a silicon wafer or on mica the adhesion force can be measured repeatedly with a variation of only 2-5%[21)]. These experiments, however, also pointed out an additional problem: That the atomic structure of the contact changes due to the stresses in the contact region. In the adhesion experiments a random noise and slower fluctuations of adhesion forces were measured. The slower variations are most likely caused by structural rearrangements of the tip on the atomic level. In this paper we address this problem with respect to capillary forces.

2. Capillary forces between particles

When two hydrophilic particles get into contact and the surrounding atmosphere contains some humidity, water will condense into the gap between the particles and form a meniscus. Meniscus formation might also occur due to addition of a certain amount of liquid to the powder. Here we will focus on the case of capillary condensation. The meniscus causes an attractive force, which is typically stronger than the van der Waals attraction. Two factors contribute to the force[22, 23)]: First, the direct action of the surface tension along the three-phase contact line. Second, the reduced capillary pressure in the meniscus acting over the whole cross-section.

Two equations are of fundamental importance for an understanding of capillary forces: The Young-Laplace equation and the Kelvin equation. The Young-Laplace equation relates the curvature of a liquid interface to the pressure difference ΔP between the two fluid phases. In the absence of gravitation or if the objects are so small that gravitation is negligible the Young-Laplace equation reads:

$$\Delta P = \gamma\left(\frac{1}{r_1} + \frac{1}{r_2}\right) \tag{1}$$

Here, γ is the surface tension of the liquid-vapor interface and r_1 and r_2 are the so-called principal radii of curvature that describe the curvature $1/r_1 + 1/r_2$ of the interface.

The vapor pressure of a liquid depends on the curvature of its surface. Both are connected which is described by the Kelvin equation. The Kelvin equation relates the vapor pressure P to the curvature of the surface of the condensed liquid:

$$k_B T \ln\frac{P}{P_0} = \gamma V_m\left(\frac{1}{r_1} + \frac{1}{r_2}\right) \tag{2}$$

Here, $k_B = 1.381 \times 10^{-23}$ J K^{-1} is Boltzmann's constant, T is the temperature, P is the saturation vapor pressure of a vapor in equilibrium with the curved surface, P_0 is the saturation vapor pressure over a planar liquid surface, and V_m is the molecular volume of one liquid molecule. For spherical drops of radius r_d the Kelvin equation can be written as

$$P = P_0 \exp\left(-\frac{2\gamma V_m}{k_B T r_d}\right) \tag{3}$$

The constant $2\gamma V_m/k_B T$ characterizes the curvature for which the vapor pressure changes by a factor e. It is convenient to define a constant called Kelvin length:

$$\lambda_K = \frac{\gamma V_m}{k_B T} \tag{4}$$

The Kelvin length characterizes the range of capillary forces. It is 0.52 nm for water and ethanol, 0.95 nm for n-hexane, and 0.88 nm for chloroform, all at 25℃[24)].

As one example we calculate the capillary force for a cone with an opening angle of close to 90° in contact with a plane (**Fig. 1**). For simplicity we assume that both surfaces are perfectly wetted (contact angle is zero). Water will condense into the gap until the curvature has reached the value given by the Kelvin equation:

$$\frac{1}{l}-\frac{1}{r}=\frac{1}{\lambda_K}\ln\frac{P}{P_0} \qquad (5)$$

The curvature corresponding to r is counted negative because it is concave with respect to the vapor phase. With $2r = l\tan\vartheta$ we get

$$\frac{\tan\vartheta}{2r}-\frac{1}{r}=\frac{1}{\lambda_K}\ln\frac{P}{P_0}\Rightarrow r=\frac{\lambda_K}{2}\,\frac{\tan\vartheta-2}{\ln(P/P_0)} \qquad (6)$$

When ϑ is the angle between the surface of the cone and the horizontal. Please note that $P < P_0$. Unless the vapor is oversaturated $(P\ /\ P_0)$ is negative. The total capillary force is

$$F=2\pi l\gamma-\pi l^2\gamma\left(\frac{1}{l}-\frac{1}{r}\right) \qquad (7)$$

Here, the first term is due to the surface tension around the periphery of the meniscus while the second term is caused by the capillary pressure. Inserting

$$F=\frac{\pi\gamma\lambda_K}{\ln(P/P_0)}\left(1-\frac{4}{\tan^2\vartheta}\right) \qquad (8)$$

The capillary adhesion force increases with increasing humidity and decreasing angle ϑ. The shape of the adhesion force-versus-humidity curve depends sensitively on the structure of the two interacting surface. For example, for a perfectly smooth macroscopic sphere it is constant except for high humidity, where it decreases[21, 25, 26].

To demonstrate this sensitive influence of the structure we calculated the capillary force between a cone and a plate when a small asperity, e.g. some contamination, prevents the cone from approaching closer than 0.4 nm (dashed line in **Fig. 1**). The capillary adhesive force is zero below a relative humidity of 27%. Then it increases, but it is much lower than the capillary adhesion of a cone without asperity.

To calculate the capillary adhesion we used a simple continuum theory and we neglected other interfacial forces such as van der Waals forces. It is certainly questionable if continuum theory leads to realistic results on molecular length scales. Computer simulations have to be applied to get more accurate results[27-30]. Computer simulations will lead to different results than continuum theory. The main message, however, will still be valid: Capillary forces are dominated by the structure of the surfaces on molecular length scales. In order to predict capillary forces between two particles one needs to know the structure much better than the length scale given by the Kelvin length. This is practically difficult, if possible at all.

In the above argument we assumed that the molecular structure of the surfaces in the contact region does not change. Unfortunately, this assumption is often not fulfilled, in particular not for oxides at high humidity[21]. Long range surface forces such as the capillary force or van der Waals forces are compensated by short range forces of the atoms in the direct contact. This causes strong stresses in the contact region[31-34], which might well lead to a rearrangement of atoms.

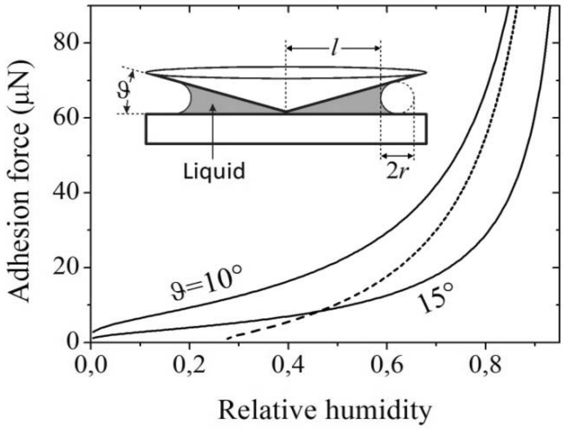

Fig. 1 Adhesion force caused by a capillary meniscus between a hydrophilic cone and a hydrophilic plate versus relative humidity. Results for two different conical angles are shown (continuous lines). The dashed line is the capillary adhesion force for a cone with ϑ =10° but an asperity of 0.4 nm size at the very end.

3. Adhesion force and work of adhesion

From a thermodynamic point of view, the work required to separate two contacting surfaces should be given by the differences in surface and interfacial energies in the system before and after separation. It can be related to the surface energies according to $w_{adh}=\gamma_1+\gamma_2-\gamma_{12}$, there γ_1 and γ_2 are the surface energies of the two bare particle surfaces and γ_{12} is the interfacial energy of the interface between the particles. The quantity w_{adh} is called the Dupre work of adhesion per unit area. In principle, the actual work w_{adh} required to separate two contacting particles should be given by $W_{adh}=w_{adh}A-E_{el}$, where A is the contact area and E_{el} is the elastic energy stored in the contact deformation. In practice however, the actual work required to separate the particles will not only depend on their chemical composition and structure or on the physical conditions such as temperature, humidity, etc. It will also depend on the specific process of separation. For the cleavage of two bodies or for the separation of complex objects this has long been recognized. It is, however, also true for the separation of two simple objects such as elastic spheres.

To illustrate this we consider the most fundamental adhesion experiment possible: Two elastic spheres in contact (**Fig. 2**). The first sphere is assumed to be fixed. It might have infinite radius so that it becomes a plane. We start to pull on the second sphere with an elastic spring of spring constant k. When the force applied is gradually increased at some threshold force F_{adh} the bond between the two spheres will break and the second sphere will be released. At this point the deflection of the spring is $\Delta x = F_{adh}/k$. This threshold force is called adhesion force. The work of separation W_{adh}, that is the work required to separate the first sphere from the second, is carried out by loading the spring:

$$W_{adh} = \frac{k}{2}\Delta x^2 = \frac{F_{adh}^2}{2k} \tag{9}$$

For a given adhesion force the work of separation increases with decreasing spring constant. This reflects simply the fact that during the separation process, the spring is loaded and stores elastic energy. This energy is suddenly released upon rupture of the adhesive bond between the particles and dissipated e. g. by viscous damping of the spring oscillation. Thus, the value of W_{adh} depends on the way how the two particles are separated.

Eq. (9) would lead to the paradoxical conclusion that for an infinitely stiff spring the work of adhesion should go to zero. This will never happen since the particles themselves react elastically and act as a spring. If the external spring becomes very stiff the effective spring constant will be given by the elastic deformation of the particles. To predict the effective spring constant of the contact one has to chose an appropriate contact mechanics model. Elastic deformation of adhesive particles is commonly described using the theory of Johnson, Kendall, and Roberts (JKR)[35]. In the following we apply the JKR theory to calculate the minimum work required to separate two particles. For two spherical particles of radii R_1 and R_2, Young's moduli E_1 and E_2, and Poisson ratios ν_1 and ν_2 we define the reduced radius R^* and reduced Young's modulus E^*:

$$\frac{1}{R^*} = \frac{1}{R_1} + \frac{1}{R_2} \quad \text{and} \quad \frac{1}{E^*} = \frac{1-\nu_1^2}{E_1} + \frac{1-\nu_2^2}{E_2} \tag{10}$$

In JKR theory the adhesion force between the two particles is given by

$$F_{adh} = \frac{3}{2}\pi w_{adh} R^* \tag{11}$$

The actual work to separate the two particles can be obtained by integrating the force versus the distance:

$$W_{adh} = \int_{\delta_0}^{\delta_r} F d\delta = \int_{a_0}^{a_r} F \frac{d\delta}{da} da \tag{12}$$

Here, δ is the overlap (indentation) of the particles and a is the contact radius. At a contact radius a_0 no force is acting on the particles. When starting to pull, the contact radius decreases until at a force given by Eq. (11) it reaches a critical value a_r. Then the particles are separated. In the framework of JKR theory the force is related to the contact radius by[36, 37]

$$F = \frac{4E^* a^3}{3R^*} - 2\sqrt{2\pi E^* w_{adh} a^3} \tag{13}$$

Also the indentation can be expressed as a function of the contact radius leading to

$$\delta = \frac{a^2}{R^*} - \sqrt{\frac{2\pi w_{adh} a}{E*}} \Rightarrow \frac{d\delta}{da} = \frac{2a}{R^*} - \sqrt{\frac{\pi w_{adh}}{2aE*}} \tag{14}$$

From Eq. (13) the two contact radii can be calculated with $F = 0$ and $F = 3\pi w_{adh} R^*/2$ to be

$$a_0 = \left(\frac{9\pi w_{adh} R^{*2}}{2E^*}\right)^{1/3} \quad \text{and} \quad a_r = \left(\frac{9\pi w_{adh} R^{*2}}{8E^*}\right)^{1/3} \tag{15}$$

Integrating Eq. (12) with the limits given by Eq. (15) leads to a work of separation between two particles of

$$W_{adh} = 1.2027 \cdot \left(\frac{\pi^5 w_{adh}^5 R^{*4}}{E^{*2}}\right)^{1/3} \tag{16}$$

This minimal work of separation cannot be further reduced by using a stiffer spring. It is the sum of the work we have to do against surface forces and the elastic energy stored in the neck formed between the particles at the point of separation.

The work of adhesion is different for the case of the contact mechanics model of Derjaguin, Muller and Toporov (DMT theory). There, the elastic contact between two particles is described by a Hertzian contact with a constant additional load $F_L = 2\pi w_{adh}{}^*$ due to the surface forces acting outside the contact zone. Separation between the particles occurs at zero contact radius and without deformation of the particles. Thus, the DMT model assumes that all elastic energy stored in the contact deformation is recovered during separation. The minimal work of separation for the DMT model can be calculated from[37,38)]

$$W_{adh} = F_L \delta_0 - E_{el} \tag{17}$$

Here, δ_0 is the indentation due to F_L and E_{el} is the elastic energy. For a Hertzian contact with external load F_L these quantities are given by

$$E_{el} = \frac{2}{5} F_L \delta_0 \tag{18}$$

and

$$\delta_0 = \left(\frac{9F_L^2}{16E^{*2}R^*} \right)^{\frac{1}{3}} \tag{19}$$

Inserting Eqs. (18) and (19) into Eq. (17) results in a work of separation for the DMT model of

$$W_{adh} = 1.572 \cdot \left(\frac{\pi^5 w_{adh}^5 R^{*4}}{E^{*2}} \right)^{1/3} \tag{20}$$

This minimal work of separation is larger than that for the JKR model (Eq. 16) despite the fact that it does not contain any losses due to contact deformations at the point of separation. This is counterintuitive, but originates from the fact that due to the different assumptions in the DMT model, this model also predicts a higher value of the adhesion force than the JKR model.

One might argue that the separation of two spheres via a spring is not the most fundamental way to measure adhesion forces. For example, in the centrifuge technique[39-41)] one does not need a spring to separate one sphere from the other. Or one might take a magnetic particle and apply a magnetic field to separate the sphere from a surface. Replacing the spring force by a centri\fugal force or a magnetic force does, however, not fundamentally change the situation. For example in the case of a centrifuge work has to be done to bring the particle to a velocity v so that the centrifugal force mv^2/r just exceeds F_{adh} . Here, r_c is the radius of the centrifuge and m is the mass of the particle. The minimal work required is equal to the kinetic energy of the particle just before release, which is

$$W_{adh} = \frac{mv^2}{2} = \frac{r_c F_{adh}}{2} \tag{21}$$

It increases with the radius of the centrifuge and depends thus on the specific way of centrifugation.

To relate the fundamental considerations to particles in a powder, we consider a chain of spheres within a cohesive powder. The individual particles are supposed to stick together by physical forces such as van der Waals and capillary forces. An example of a chain of particles is shown in **Fig. 3**. It was created by first making a highly porous material as described in ref.[42)]. Then the material was placed into the chamber of a scanning electron microscope and the cantilever of an AFM was moved into the powder. Finally the cantilever was slowly retracted again. Due to adhesive forces the particles formed chain-like aggregates.

To describe the rupture of a chain of particles we take the simplest assumptions. All particles are assumed to be spherical and identical in size, the surfaces are perfectly homogeneous and smooth and similar in surface energy, the particles are assumed to react purely elastic, the first particle is assumed to be fixed at the bottom to the substrate, the last particle is attached to an infinitely stiff spring. Thus, we neglect the work required to load the spring. When one starts to pull on such a chain (**Fig. 4a**), first the particles will roll and slide over each other until they form a straight chain (**Fig. 4b**). Then the particles will be stretch elastically (**Fig. 4c**). For real particles the stretching will be small, but it is never zero. Eventually the chain will rupture (**Fig. 4d**). Just before rupture the work done to elastically deform the chain of spheres is according to Eq. (16)

$$W_{adh} = 1.2027 \cdot N \cdot \left(\frac{\pi^5 w_{adh}^5 R^{*4}}{E^{*2}} \right)^{1/3} \tag{22}$$

Here, N is the number of particles in the chain considered. With increasing Young's modulus the work of separation decreases.

In summary, the work of separation between two particles is not a constant, but depends on how precisely separation is achieved. It will for example depend on the spring constant with which one draws the two particles apart and on the elastic response of the contact itself. On the other hand, the Dupré work of adhesion per unit area w_{adh} is a thermodynamical well defined quantity that only depends on the materials involved and the environmental conditions. While w_{adh} could in principle be determined from adhesion force measurements using relations like Eq. (11), it is practically a demanding task due to the presence of surface inhomogeneities and surface roughness that

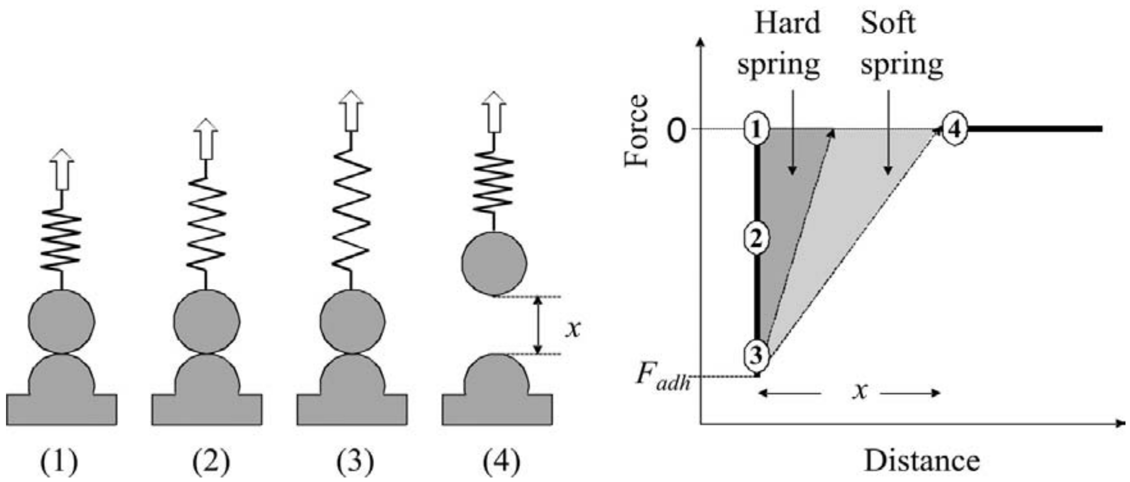

Fig. 2 Schematic of two particles adhering to each other. One is rigidly fixed to a substrate. With a spring the second particle is moved away from the first one. The corresponding force-versus-distance plot is schematically shown on the right.

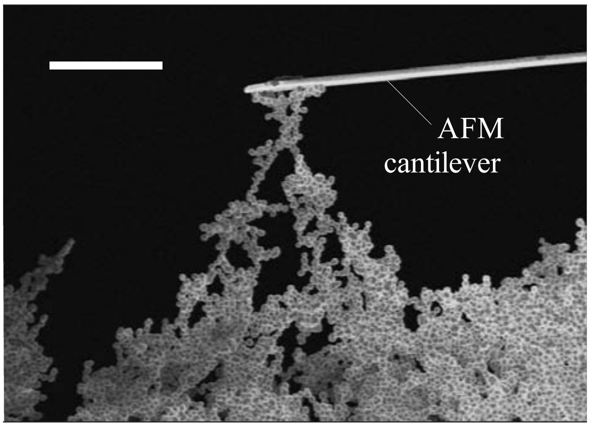

Fig. 3 Scanning electron micrograph of a highly porous powder made of silicon oxide spheres of 1.5 µm diameter. The cantilever of an atomic force microscope had been moved into the powder and then been retracted. See ref.[92] for details.

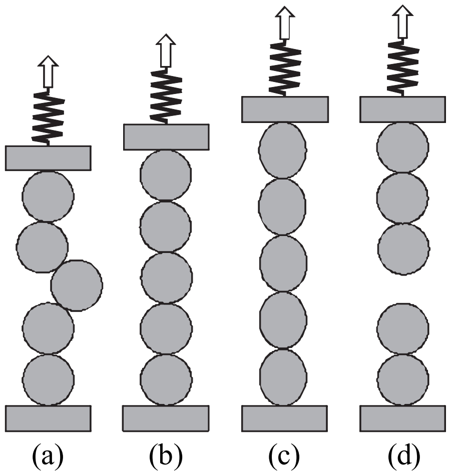

Fig. 4 Schematic of a chain of particles hold together by attractive forces. The bottom particle is rigidly fixed to a substrate. With a stiff spring the top particle is moved upwards.

often dominate adhesion forces.

4. Adhesion force and separation speed

In this section we demonstrate that also the adhesion force is not a constant, which only depends on the materials, but that it depends on the separation speed. It is well known that the rupture force of single chemical bonds depends on the loading rate[43-49]. The loading rate is the speed, with which the force applied to the bond increases. Assuming that an activation barrier has to be overcome to break a bond Bell[50] and Evans & Ritchie[51] proposed a model, which was later modified and improved[52,53]. The model treats the unbinding process as an escape from a potential well under the influence of the external loading force. This external force tilts the interaction potential and facilitates thermally activated escape from the bound state (**Fig. 5**). The rate constant of bond rupture $k_{off}(F)$ scales with the exponent of the applied force F according to[50]:

$$k_{off}(F) = k^0_{off}\ \exp\left(\frac{F x_\beta}{k_B T}\right) \tag{23}$$

Here, k^0_{off} is the intrinsic (force-free) off-rate constant and x_β is the distance between the bound state and the transition state along the direction of the external pulling force. In experiments, the loading force is usually ramped linearly in time:

$$F(t) = r_F\, t \tag{24}$$

The force loading rate r_F is the product of the spring constant of the external spring and the pulling speed. The solution of eq. 1 for a constant loading rate leads to a mean rupture force

$$F_{adh} = F_\beta \ln\left(\frac{r_F}{F_\beta k^0_{off}}\right) \tag{25}$$

Here, $F_\beta = k_B T/x_\beta$ is the so-called thermal fluctuation force[54]. Thus, F_{adh} is predicted to grow linearly with $\ln(r_F)$. Eq. 25 provides a simple way to extract the values x_β and k^0_{off} from the slope and intercept of the F_{adh}-versus-$\ln(r_F)$ curve fitted to experimental data. This behavior was observed experimentally. Linear dependencies were found for protein-ligand interactions[46-49], the rupture of molecularly thin films[55,56], and the adhesion between an AFM tip and a thiol monolayer on gold[57-59].

The Bell-Evans model has, however, a serious limitation. It assumes that x_β is constant during the application of an external pulling force. In reality, x_β significantly decreases under pulling force in the case of the potentials describing real interatomic and/or intermolecular interactions, e.g. the Morse or van der Waals potentials.

Dudko et al.[53] developed a new model and showed that the Bell-Evans model as well as the microscopic model by Hummer and Szabo[52] are particular cases of their more general approach (the DHS model). In the DHS model the rate constant of bond rupture depends on the shape of the potential well and the activation barrier. Dudko et al. specified the free-energy surface and finally obtained an expression for the mean rupture force:

$$\langle F\rangle = \frac{\Delta G_\beta}{\nu x_\beta}\left\{1 - \left[\frac{k_B T}{\Delta G_\beta}\ln\frac{k^0_{off} k_B T \exp\left(\frac{\Delta G_\beta}{k_B T} + 0.577\right)}{x_\beta r_F}\right]^\nu\right\} \tag{26}$$

ΔG_β is the free energy of activation in the absence of external forces and 0.577 is the so-called Euler-Mascheroni constant. The parameter ν varies typically between 0.5 and 0.7. It depends on the shape of the free-energy surface.

Although the DHS model is more sophisticated than the Bell-Evans model, it is still analytically tractable. We have used it for a quantitative characterization of the adhesion between a silicon nitride AFM tip and a hydrophobic thiol monolayer[57-60]. As examples the adhesion force-versus-logarithm of the loading rate is plotted in **Fig. 6** for two different alkyl thiols: 1-dodecanethiol ($HS(CH_2)_{11}CH_3$) and 11-mercapto-1-undecanol ($HS(CH_2)_{11}OH$). 11-mercapto-1-undecanol, which has a hydroxy terminal group, exhibits strong hydrophilic properties. Therefore, the strong adhesion force (**Fig. 6a**) is due mostly to hydrogen bridges between the interacting surfaces and also – in some degree – to capillary forces. The later becomes dominant at relative humidity higher than 20%.

The adhesion force-versus-loading rate measured on monolayers of 1-dodecanethiol shows two regimes. At loading rates higher than 7×10^4 nN/s it increases more steeply than at lower loading rates (**Fig. 6b**). For monolayers of 1-dodecanethiol van der Waals forces are the dominating interactions. One possible interpretation is to attribute the two-regimes to a change of the cooperativity. At low loading rates the molecules show a cooperative binding while at high loading rates the bonds behave uncooperatively during separation. Then, the resultant adhesion force of such a multibond can be expressed as[54]:

$$\begin{aligned} F_{ad} &= NF_\beta\left[\ln\left(\frac{r_F}{F_\beta k^0_{off}}\right) - \ln\left(\frac{F_{ad}}{F_\beta}\right)\right] \\ &= NF_S - NF_\beta \ln\left(\frac{F_{ad}}{F_\beta}\right) \end{aligned} \tag{27}$$

Here, N is the number of single independent bonds in parallel and F_s is the rupture force of a single bond. The adhesion force for an uncooperative multibond depends on the loading rate similarly as for a single bond and can be fitted with the DHS model (**Fig. 6b**, solid line). As a result one can obtain the parameters describing the effective interaction potential of the multibond. If N is estimated (e.g. according to the method described earlier[58]) one can calculate the parameters of the interaction potential of an average single bond[57]. The situation looks different at lower loading rates ($< 7 \times 10^4$ nN/s). Rebinding of the single bonds becomes possible and they begin to behave cooperatively during the rupture process. Then, the resultant bond acts rather as a single macroscopic bond than as many individual bonds. In the case of such a macroscopic bond the resultant adhe-

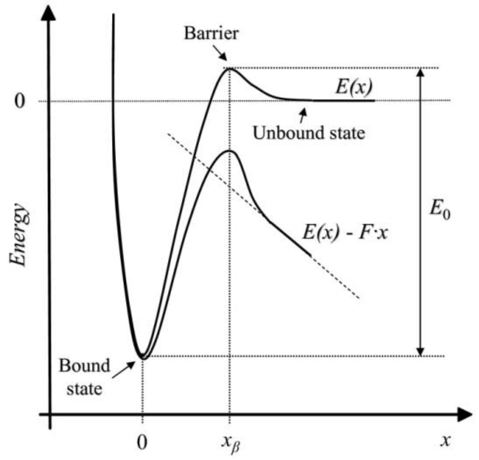

Fig. 5 Schematic of the interaction potential of a bond with an activation barrier. The external force applied by the spring F tilts the potential and lowers the activation barrier E_0.

sion force depends weakly on the loading rate[54].

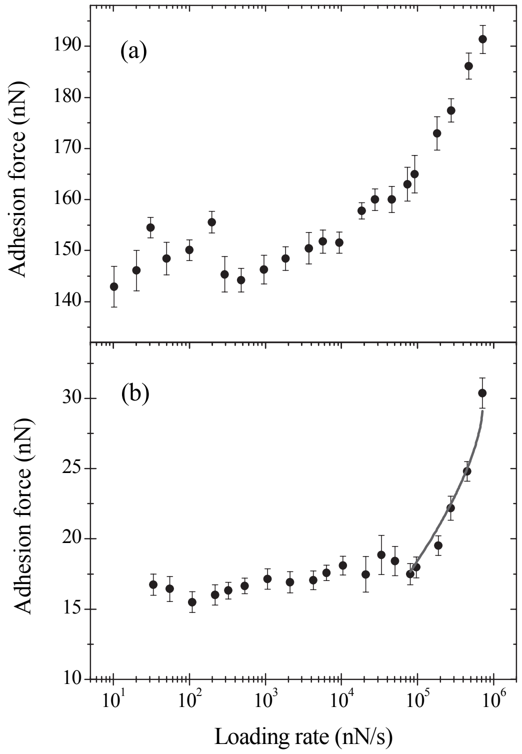

Fig. 6 Adhesion force-versus-loading rate plotted at a logarithmic scale for the interaction between a silicon nitride AFM tip and monolayers of 11-mercapto-1-undecanol (a) and 1-dodecanethiol (b) at a relative humidity of 20%. The solid line (b) represents a fit of the DHS model to experimental data at high loading rates (>7 × 10^4 nN/s). For details see ref.[59].

5. Contact and bridging adhesion

Until now we described adhesion between surfaces mediated by steeply decreasing attractive forces such as van der Waals or capillary forces. Once two particles are separated by only few Angstroms the attraction is so weak that they typically jump completely out of contact. We call it contact adhesion. Once contact is broken, the attraction is overridden by the external pulling force and the two particles are fully separated. In polymer solutions or polymer melts often another type of adhesion is observed[61-63]: bridging adhesion. In such a system, individual polymer chains bind to two particles simultaneously. As the distance between these two particles increases the bridging polymer chains are first stretched and then they detach. In contrast to contact adhesion, bridging adhesion can be long-ranged. The typical distance is given by the contour length of the polymer chains.

We discriminate between two kinds of bridging adhesion. In the first case the[64] polymer chain is attached at one end to one particle and with the other end to the other particle. When the two particles are separated the polymer is stretched. From the entropically favorable random coil configuration it changes to the more ordered stretched state. This requires a force and work to be carried out. Two models are used to describe the stretching force: the wormlike chain (WLC) and the freely-jointed chain (FJC) model. In the WLC model the polymer is described as an elastic cylinder with a constant bending elasticity and of constant length L [65]. The force required to stretch a WLC with persistence length l_P and length L to a distance x is given by[66,67]

$$F(x) = \frac{k_BT}{l_P}\left[\frac{x}{L} + \frac{1}{4\cdot(1-x/L)^2} - \frac{1}{4}\right] \tag{28}$$

In the FJC model the polymer is divided into rigid elements of length l_K, the Kuhn length, linked through perfectly flexible joints without any interactions. Force and distance are related by[68-70]

$$\frac{x}{L} = \coth\left(\frac{Fl_K}{k_BT}\right) - \frac{k_BT}{Fl_K} \tag{29}$$

One technique to measure the force required to stretch an individual polymer chain are magnetic tweezers. In this method one end of the polymer is fixed on a surface of a glass slide. The other is attached to a magnetic bead[71]. The bead is moved by an external magnetic field. The displacement of the bead, which is equal to the stretched length of a polymer, is monitored by optical microscopy. Alternatively, a polymer chain can be stretched by an optical tweezer[72]. Here, similar to the previous technique the distance between particles is measured by an optical microscope giving the extension of a chain. Both methods are highly force sensitive, but the preparation and the methods themselves are technically demanding. Therefore many measurements were carried out with atomic force microscopy. Force-versus-distance measurements on single molecules are often referred to as single molecule force spectroscopy[73-75].

As one example we show the force curve measured between a microfabricated AFM tip and a silicon surface (**Fig. 7**)[76]. The interstitial space was completely filled with the melt of a diblock copolymer consisting of one block of poly(dimethyl siloxane) and one block of poly(ethylmethyl siloxane) (PDMS-*b*-PEMS, M_w=15100). Upon retraction, adhesion peaks were observed which we interpret as bridging of single polymer chains. Typically, in each force curve 5 to 10 adhesion peaks were observed, which we attribute to 5-10 polymer chains bridging tip and silicon wafer. Adhesion peaks could be fitted with the WLC (and FJC) model.

A second type of bridging adhesion was observed with polyelectrolytes. Polyelectrolytes are polymers, which bear multiple charges in aqueous electrolyte due to dissociable groups. Single molecule adhesion experiments showed that the force to desorb a single polyelectrolyte chain is constant until the end of the chain desorbes[77-81]. This implies a desorption process similar to the peeling of a tape. Using continuum theory the force required to desorb a polyelectrolyte from a surface was calculated[78,82-84].

As an example for tape-like bridging we show results obtained with a biomimetic DOPA containing polymer (**Fig. 8**). The antetype for this polymer was derived from mussel adhesion. Mussels are well known for their ability to cling to surfaces 85, 86). Therefore they secrete specialized adhesion proteins with a high content of the catecholic amino acid 3,4-dihydroxyphenylalanine (DOPA)[87,88]. Both natural and synthetic adhesives containing DOPA showed strong adhesion under wet conditions[88-91]. To analyze the adhesion mediated by DOPA the mussel-mimetic polymer poly(dopamine methacrylamide)-co-(butylamine methacrylamide) (p(DMA-co-BMA)) with free catechol groups[64] was synthezised. The ratio of catechol groups was varied. Using an AFM, the adhesion of single p(DMA-co-BMA) chains to titanium in aqueous medium was measured.

To measure the bridging of single DOPA-containing polymer chains first a titanium surface was rinsed with an aqueous polymer solution. Since the DOPA binds strongly to titanium, a partially coated surface was obtained. Then the sample was rinsed to remove excess polymer. Finally the sample was mounted in an AFM and force curves were recorded at random positions in aqueous electrolyte with a titanium-coated tip. After a contact adhesion the constant force plateaus were observed with a characteristic value of 60 pN (**Fig. 8**). In few cases two plateaus, corresponding to two polymer chains bridging tip and sample were observed, as shown in **Fig. 8**.

Both types of bridging lead to a qualitatively different adhesion when considering micron or macroscopic contacts rather than nanoscopic contacts. In nanoscopic contacts single or few chain events are observed. For larger contacts many bridging polymers will lead to force-vs-distance curves, which show a long range attraction. The range of the attraction scales with the contour length of the polymers.

This changes the relation of adhesion force and work of adhesion. For contact adhesion an adhesion force has to be overcome. The work of adhesion can be reduced by using a stiff spring to separate the two particles. In bridging adhesion the adhesive force might be low, but it has to be applied over a long distance (**Fig. 9**). Thus, in bridging adhesion the force of adhesion might be low, but the work of adhesion can be high and it cannot be significantly reduced by choosing an appropriate spring.

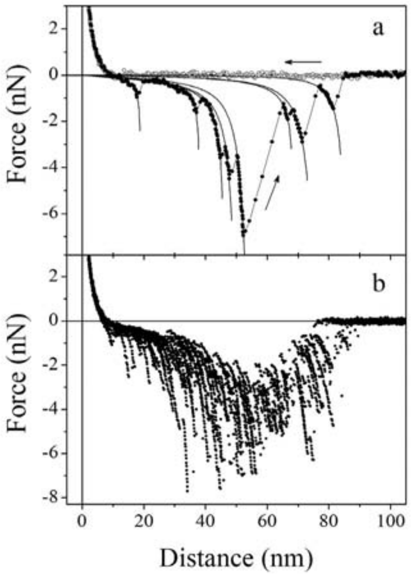

Fig. 7 (a) Typical force curve measured in PDMS-b-PEMS on silicon oxide[76]. Approaching (○) and retracting parts (●) are shown. Each adhesion peak is stepwise fitted with the WLC model (continuous lines). (b) Superposition of 20 individual force curves (retracting parts).

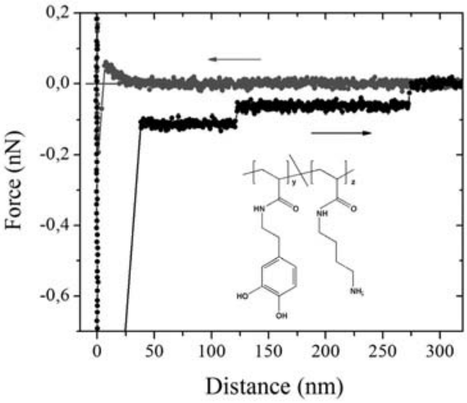

Fig. 8 Representative force-versus-distance curve obtained with p(DMA-co-BMA) (20% DMA, 80% BMA). The sample had been immersed in p(DMA-co-BMA) before the experiment. The force curve was recorded with titanium-coated tips and titanium-coated samples in aqueous 1 mM KNO_3 pH 6.8 solution. Red is the approaching part, black the retracting part of the force curve. For details see ref.[64].

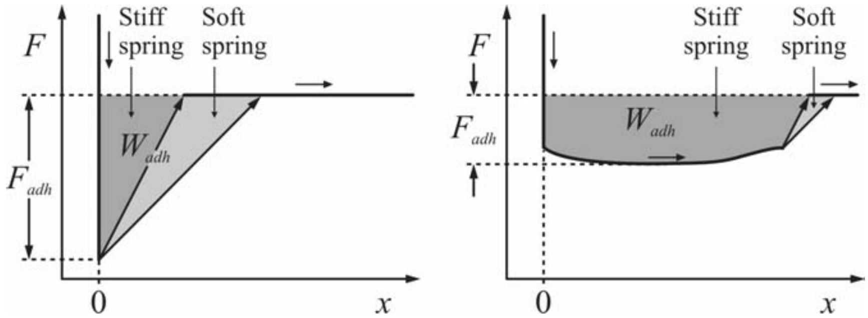

Fig. 9 Schematic of retracting force-versus-distance curves in the case of contact (left) and bridging adhesion (right).

6. Conclusions

For contact adhesion a threshold force has to be overcome to separate two particles. This adhesion force, depends on the materials and the precise structure of the microcontacting regions. For the case of capillary adhesion the length scale for which the structure has to be known for a quantitative calculation is given by the Kelvin length. For water the Kelvin length is 0.5 nm. The actual work required to separate two particles depends on their elastic properties and the effective external spring. In addition, we demonstrated experimentally that the adhesion force depends on the separation speed.

In polymer solutions or melts adhesion is often dominated by bridging polymers. Bridging adhesion is characterized by a long range attractive force. The range is given by the length of the polymer chain. In bridging adhesion the work of adhesion is appropriate to describe adhesion because the adhesion force can be low, but the work of adhesion can be high. In contact adhesion the work of adhesion depends critically on the effective spring constant of the spring used to draw the particles apart. In bridging adhesion the work of adhesion only weakly depends on the external spring.

References

1) Tomas, J. (2000): Particle adhesion fundamentals and bulk powder consolidation, KONA - Powder and Particle, 18, pp.157-169.

2) Herminghaus, S. (2005): Dynamics of wet granular matter, Advances in Physics, 54, pp.221-261.

3) Mitarai, N. and Nori, F. (2006): Wet granular materials, Advances in Physics, 55, pp.1-45.

4) Brilliantov, N.V., Albers, N., Spahn, F., and Poschel, T. (2007): Collision dynamics of granular particles with adhesion, Phys. Rev. E, 76, 051302.

5) Rock, M., Morgeneyer, M., Schwedes, J., Kadau, D., Brendel, L., and Wolf, D.E. (2008): Steady state flow of cohesive and non-cohesive powders, Granular Matter, 10, pp.285-293.

6) Luding, S. (2008): Cohesive, frictional powders: contact models for tension, Granular Matter, 10, pp.235-

246.
7) Godlieb, W., Deen, N.G., and Kuipers, J.A.M. (2008): On the relationship between operating pressure and granular temperature: A discrete particle simulation study, Powder Technol., 182, pp.250-256.
8) Schenker, I., Filser, F.T., Gauckler, L.J., Aste, T., and Herrmann, H.J. (2009): Quantification of the heterogeneity of particle packings, Phys. Rev. E, 80, 021302.
9) Zeng, Q.H., Yu, A.B., and Lu, G.Q. (2010): Evaluation of interaction forces between nanoparticles by molecular dynamics simulation, Ind. Eng. Chem. Res., 49, pp.12793-12797.
10) Krupp, H. (1967): Particle adhesion: Theory and experiment, Adv. Colloid Interface Sci., 1, pp.111-239.
11) Polke, R. (1969): Adhesion of solids at elevated temperatures, Bull. Soc. Special Chim. France, A3241, pp.51-54.
12) Polke, R., Krupp, H., and Rumpf, H. (1973): Einflüsse auf die Adhäsion von Feststoffteilchen, in Chemie, physikalische Chemie und Anwendungstechnik der grenzflächenaktiven Stoffe, V.I.K.f.g. Stoffe, Editor., Carl Hanser Verlag: München.
13) Podczeck, F., Newton, J.M., and James, M.B. (1995): Adhesion and friction between powders and polymer or aluminum surfaces determined by a centrifuge technique, Powder Technol., 83, pp.201-209.
14) Heim, L.O., Blum, J., Preuss, M., and Butt, H.-J. (1999): Adhesion and friction forces between spherical micrometer-sized particles, Phys. Rev. Lett., 83, pp.3328-3331.
15) Heim, L., Ecke, S., Preuss, M., and Butt, H.-J. (2002): Adhesion forces between individual gold and polystyrene particles, J. Adh. Sci. Technol., 16, pp.829-843.
16) Rumpf, H. (1974): Die Wissenschaft des Agglomerierens, Chemie-Ing.-Techn., 46, pp. 1-11.
17) Götzinger, M. and Peukert, W. (2004): Particle adhesion force distributions on rough surfaces, Langmuir, 20, pp.5298-5303.
18) Cooper, K., Gupta, A., and Beaudoin, S. (2001): Simulation of the adhesion of particles to surfaces, J. Colloid Interface Sci., 234, pp.284-292.
19) Rabinovich, Y.I., Adler, J.J., Ata, A., and Moudgil, B.M. (2000): Adhesion between nanoscale rough surfaces. II. Measurement and comparison with theory, J. Colloid Interface Sci., 232, pp.17-24.
20) Peukert, W., Mehler, C., and Gotzinger, M. (2002): Novel concepts for characterization of heterogeneous particulate surfaces, Appl. Surf. Sci., 196, pp.30-40.
21) Farshchi, M., Kappl, M., Cheng, Y., Gutmann, J.S., and Butt, H.-J. (2006): On the adhesion between fine particles and nanocontacts: An atomic force microscope study, Langmuir, 22, pp.2171-2184.
22) Fisher, R.A. (1926): On the capillary forces in an ideal soil, J. Agric. Sci., 16, pp.492-505.
23) Haines, W.B. (1927): Studies in the physical properties of soils. IV. A further contribution to the theory of capillary phenomena in soil, J. Agric. Sci., 17, pp.264-290.
24) Butt, H.J., Golovko, D.M., and Bonaccurso, E. (2007): On the derivation of Young's equation for sessile drops: Nonequlibrium effects due to evaporation, J. Phys. Chem. B, 111, pp.5277-5283.
25) Pakarinen, O.H., Foster, A.S., Paajanen, M., Kalinainen, T., Katainen, J., Makkonen, I., Lahtinen, J., and Nieminen, R.M. (2005): Towards an accurate description of the capillary force in nanoparticle-surface interactions, Modelling Simul. Mater. Sci. Eng., 13, pp.1175-1186.
26) Butt, H.J. and Kappl, M. (2009): Normal capillary forces, Adv. Colloid Interface Sci., 146, pp.48-60.
27) Binder, K. and Landau, D.P. (1992): Capillary condensation in the lattice gas model: A Monte Carlo study, J. Chem. Phys., 96, pp.1444-1454.
28) Wensink, E.J.W., Hoffmann, A.C., Apol, M.E.F., and Berendsen, H.J.C. (2000): Properties of adsorbed water layers and the effect of adsorbed layers on interparticle forces by liquid bridging, Langmuir, 16, pp.7392-7400.
29) Shinto, H., Uranishi, K., Miyahara, M., and Higashitani, K. (2002): Wetting-induced interaction between rigid nanoparticle and plate: A Monte Carlo study, J. Chem. Phys., 116, pp.9500-9509.
30) Jang, J., Yang, M., and Schatz, G. (2007): Microscopic origin of the humidity dependence of the adhesion force in atomic force microscopy, J. Chem. Phys., 126, pp.174705.
31) Gould, S.A.C., Drake, B., Prater, C.B., Weisenhorn, A.L., Manne, S., Kelderman, G.L., Butt, H.J., Hansma, H., Hansma, P.K., Magonov, S., and Cantow, H.J. (1990): The atomic force microscope - a tool for science and industry, Ultramicroscopy, 33, pp. 93-98.
32) Chen, Y., Best, A., Butt, H.-J., Boehler, R., Haschke, T., and Wiechert, W. (2006): Pressure distribution in a mechanical microcontact, Appl. Phys. Lett., 88, pp.234101.
33) Chen, Y., Best, A., Haschke, T., Wiechert, W., and Butt, H.-J. (2007): Stress and failure at mechanical contacts of microspheres under uniaxial loading, J. Appl. Phys., 101, pp. 084908.
34) Chen, Y., Koynov, K., and Butt, H.-J. (2007): Fatigue in a microcontact of a brittle material, J. Mater. Res., 22, pp.3196-3200.
35) Johnson, K.L., Kendall, K., and Roberts, A.D. (1971): Surface energy and contact of elastic solids, Proc. R. Soc. Lond. A, 324, pp.301-313.
36) Johnson, K.L. (1985): "Contact Mechanics", Cambridge: Cambridge University Press.
37) Butt, H.-J. and Kappl, M. (2010): "Surface and Interfacial Forces", Weinheim: Wiley-VCH.
38) Maugis, D. (2000): Contact, Adhesion and Rupture of Elastic Solids. Solid-State Sciences, ed. M. Cardona, et al. Vol. 130. Berlin: Springer.
39) Larsen, R.I. (1958): The adhesion and removal of particles attached to air filter surfaces, Am. Ind. Hyg. Assoc. J., 19, pp.265-270.
40) Böhme, G., Kling, W., Krupp, H., Lange, H., and Sandstede, G. (1964): Haftung kleiner Teilchen an Feststof-

fen, Zeitschr. angewandte Physik, 6, pp.486-490.

41) Podczeck, F. and Newton, J.M. (1995): Developement of an ultracentrifuge technique to determine the adhesion and friction properties between particles and surfaces, J. Pharm. Sci., 84, pp.1067-1071.

42) Blum, J. and Schräpler, R. (2004): Structure and mechanical properties of high-porosity macroscopic agglomerates formed by random ballistic deposition, Phys. Rev. Lett., 93, 115503.

43) Lee, G.U., Chrisey, L.A., and Colton, R.J. (1994): Direct measurem,ent of the forces between complementary strands of DNA, Science, 266, pp.771-773.

44) Lee, G.U., Kidwell, D.A., and Colton, R.J. (1994): Sensing discrete streptavidin biotin interactions with atomic force microscopy, Langmuir, 10, pp.354-357.

45) Florin, E.L., Moy, V.T., and Gaub, H.E. (1994): Adhesion forces between individual ligand-receptor pairs, Science, 264, pp.415-417.

46) Merkel, R., Nassoy, P., Leung, A., Ritchie, K., and Evans, E. (1999): Energy landscapes of receptor-ligand bonds explored with dynamic force spectroscopy, Nature, 397, pp. 50-53.

47) Strunz, T., Oroszlan, K., Schafer, R., and Güntherodt, H.J. (1999): Dynamic force spectroscopy of single DNA molecules, Proc. Natl. Acad. Sci. USA, 96, pp.11277-11282.

48) Neuert, G., Albrecht, C., Pamir, E., and Gaub, H.E. (2006): Dynamic force spectroscopy of the digoxigenin-antibody complex, FEBS Lett., 580, pp.505-509.

49) Maki, T., Kidoaki, S., Usui, K., Suzuki, H., Ito, M., Ito, F., Hayashizaki, Y., and Matsuda, T. (2007): Dynamic force spectroscopy of the specific interaction between the PDZ domain and its recognition peptides, Langmuir, 23, pp.2668-2673.

50) Bell, G.I. (1978): Models for the specific adhesion of cells to cells, Science, 200, pp. 618-627.

51) Evans, E. and Ritchie, K. (1997): Dynamic strength of molecular adhesion bonds, Biophys. J., 72, pp.1541-1555.

52) Hummer, G. and Szabo, A. (2003): Kinetics from nonequilibrium single-molecule pulling experiments, Biophy. J., 85, pp.5-15.

53) Dudko, O.K., Filippov, A.E., Klafter, J., and Urbakh, M. (2003): Beyond the conventional description of dynamic force spectroscopy of adhesion bonds, Proc. Natl. Acad. Sci. USA, 100, pp.11378-11381.

54) Evans, E. (2001): Probing the relation between forcelifetime-and chemistry in single molecular bonds, Annu. Rev. Biophys. Biomol. Struct., 30, pp.105-128.

55) Butt, H.-J. and Franz, V. (2002): Rupture of molecular thin films observed in atomic force microscopy. I. Theory, Phys. Rev. E, 66, p. 031601.

56) Loi, S., Sun, G.X., Franz, V., and Butt, H.-J. (2002): Rupture of molecular thin films observed in atomic force microscopy. II. Experiment, Phys. Rev. E, 66, p. 031602.

57) Ptak, A., Gojzewski, H., Kappl, M., and Butt, H.J. (2010): Quantitative analysis of the interaction between an atomic force microscopy tip and a hydrophobic monolayer, J. Phys. Chem. C, 114, pp.21572-21578.

58) Ptak, A., Kappl, M., Moreno-Flores, S., Gojzewski, H., and Butt, H.J. (2009): Quantitative Characterization of Nanoadhesion by Dynamic Force Spectroscopy, Langmuir, 25, pp.256-261.

59) Gojzewski, H., Kappl, M., Ptak, A., and Butt, H.-J. (2010): The effect of humidity on the nanoscale adhesion of self-assembled thiol monolayers by means of dynamic force spectroscopy, Langmuir, 26, pp.1837-1847.

60) Ptak, A., Gojzewski, H., Kappl, M., and Butt, H.J. (2011): Influence of humidity on the nanoadhesion between a hydrophobic and a hydrophilic surface, Chemical Physics Letters, 503, pp.66-70.

61) Napper, D.H. (1983): “Polymeric Stabilization of Colloidal Dispersions”, London: Academic Press. 428.

62) Likos, C.N. (2001): Effective interactions in soft condensed matter physics, Physics Reports, 348, pp.267-439.

63) Kleshchanok, D., Tuinier, R., and Lang, P.R. (2008): Direct measurements of polymer-induced forces, J. Phys.: Condens. Matter, 20, 073101.

64) Wang, J., Tahir, M.N., Kappl, M., Tremel, W., Metz, N., Barz, M., Theato, P., and Butt, H.-J. (2008): Influence of binding site density in wet bioadhesion, Advanced Materials, 20, pp.3872-3876.

65) Kratky, O. and Porod, G. (1949): Röntgenuntersuchung gelöster Fadenmoleküle, Recl. Trav. Chim. Pays-Bas, 68, pp.1106-1122.

66) Bustamante, C., Marko, J.F., Siggia, E.D., and Smith, S. (1994): Entropic elasticity of λ-phage DNA, Science, 265, pp.1599-1600.

67) Marko, J.F. and Siggia, E.D. (1995): Stretching DNA, Macromolecules, 28, pp.8759-8770.

68) Kuhn, W. and Grün, F. (1942): Beziehungen zwischen elastischen Konstanten und Dehnungsdoppelbrechung hochelastischer Stoffe, Kolloid-Zeitschrift, 101, pp.248-271.

69) Casassa, E.F. (1967): Equilibrium distribution of flexible polymer chains between a macroscopic solution phase and small voids, Polymer Letters, 5, pp.773-778.

70) Fixman, M. and Kovac, J. (1973): Polymer conformational statistics. III. Modified Gaussian models of stiff chains, J. Chem. Phys., 58, pp.1564-1568.

71) Smith, S.B., Finzi, L., and Bustamante, C. (1992): Direct mechanical measurements of the elasticity of single DNA molecules by using magnetic beads, Science, 258, pp. 1122-1126.

72) Smith, S.B., Cui, Y., and Bustamante, C. (1996): Overstretching B-DNA: The elastic response of individual double-strande and single-stranded DNA molecules, Science, 271, pp.795-799.

73) Dammer, U., Popescu, O., Wagner, P., Anselmetti, D., Güntherodt, H.J., and Misevic, G.N. (1995): Binding strength between cell adhesion proteoglycans measured by atomic force microscopy, Science, 267, pp.1173-1175.

74) Rief, M., Oesterhelt, F., Heymann, B., and Gaub, H.E. (1997): Single molecule force spectroscopy on polysaccharides by atomic force microscopy, Science, 275, pp.1295-1297.

75) Janshoff, A., Neitzert, M., Oberdörfer, Y., and Fuchs, H. (2000): Force spectroscopy of molecular systems - single molecule spectroscopy of polymers and biomolecules, Angew. Chem. Int. Ed., 39, pp.3212-3237.

76) Sun, G. and Butt, H.-J. (2004): Adhesion between solid surface in a polymer melt: Bridging of single chains, Macromolecules, 37, pp.6086-6089.

77) Chatellier, X., Senden, T.J., Joanny, J.F., and de Meglio, J.M. (1998): Detachment of a single polyelectrolyte chain adsorbed on a charged surface, Eurphys. Lett., 41, pp.303-308.

78) Hugel, T., Grosholz, M., Clausen-Schaumann, H., Pfau, A., Gaub, H., and Seitz, M. (2001): Elasticity of single polyelectrolyte chains and their desorption from solid supports studied by AFM based single molecule force spectroscopy, Macromolecules, 34, pp.1039-1047.

79) Cui, S.X., Liu, C.J., Wang, Z.Q., Zhang, X., Strandman, S., and Tenhu, H. (2004): Single molecule force spectroscopy on polyelectrolytes: Effect of spacer on adhesion force and linear charge density on rigidity, Macromolecules, 37, pp.946-953.

80) Friedsam, C., Del Campo Bécares, A., Jonas, U., Seitz, M., and Gaub, H.E. (2004): Adsorption of polyacrylic acid on self-assembled monolayers investigated by single-molecule force spectroscopy, New J. Phys., 6, pp.9-16.

81) Long, J., Xu, Z., and Masliyah, J.H. (2006): Adhesion of single polyelectrolyte molecules on silica, mica, and bitumen surfaces, Langmuir, 22, pp.1652-1659.

82) Chatellier, X. and Joanny, J.F. (1998): Pull-off of a polyelectrocltye chain from an oppositely charged surface, Phys. Rev. E, 57, pp.6923-6935.

83) Netz, R.R. and Joanny, J.F. (1999): Adsorption of semiflexible polyelectroltyes on charged planar surfaces: Charge compensation, charge reversal, and multilayer formation, Macromolecules, 32, pp.9013-9025.

84) Hanke, F., Livadaru, L., and Kreuzer, H.J. (2005): Adsorption forces on a single polymer molecule in contact with a solid surface, Europhys. lett., 69, pp.242-248.

85) Waite, J.H. (2002): Adhesion à la moule, Integr. Comp. Biol., 42, pp.1172-1180.

86) Silverman, H.G. and Roberto, F.F. (2007): Understanding marine mussel adhesion, Marine Biotechnology, 9, pp.661-681.

87) Waite, J.H. and Tanzer, M.L. (1981): Polyphenolic substance of Mytilus edulis: Novel adhesive containing L-dopa hydroxyproline, Science, 212, pp.1038-1040.

88) Lee, H., Scherer, N.F., and Messersmith, P.B. (2006): Single-molecule mechanics of muscle adhesion, Proc. Natl. Acad. Sci. USA, 29, pp.12999-13003.

89) Yu, M. and Deming, T.J. (1998): Synthetic polypeptide mimics of marine adhesives, Macromolecules, 31, pp.4739-4745.

90) Yu, M., Hwang, J., and Deming, T.J. (1999): Role of L-3,4-dihydroxyphenylalanine in mussel adhesive proteins, J. Am. Chem. Soc., 121, pp.5825-5826.

91) Lin, Q., Gourdon, D., Sun, C., Holten-Andersen, N., Andersen, T.H., Waite, J.H., and Israelachvili, J.N. (2007): Adhesion mechanism of the mussel foot proteins mfp-1 and mfp-3, Proc. Natl. Acad. Sci. USA, 104, pp.3782-3786.

92) Heim, L., Butt, H.-J., Schräpler, R., and Blum, J. (2005): Analyzing the compaction of high-porosity microscopic agglomerates, Aust. J. Chem., 58, pp.1-3.

Author's short biography

Hans-Jürgen Butt

Hans-Jürgen Butt studied physics at the Universities of Hamburg and Güttingen, he received his Diploma in 1986. Then he moved to Frankfurt to work in Ernst Bamberg's group at the Max Planck Institute for Biophysics on light induced proton transport of bacteriorhodpsin. After his PhD in 1989 as a postdoc in Santa Barbara with Paul Hansma he got into contact with the newly developed atomic force microscope. From 1990-96 back in Frankfurt as a researcher he studied biological objects with the atomic force microscope. In 1996 he went to the Johannes Gutenberg-University in Mainz as associate professor for physical chemistry. There he focussed on the physics and chemistry of interfaces. Three years later he joined the the University of Siegen as full professor. In 2002 he followed a call to the Max Planck Institute for Polymer Research in Mainz, where he is a director. Hans-Jürgen Butt is married and has three children.

Marcin Makowski

Marcin Makowski studied Technical Physics at the Poznan University of Technology (PUT). He got his master and engineering title in 2008 in a field of nanotechnology. His thesis was on probing adhesion interaction at atomic scale between silicon interfaces using scanning probe microscopy. In the same year he started to work on his Ph.D in group of Prof R. Czajka in Solid State spectroscopy Division at The Institute of Physics at PUT. His work there concerned developing system based on PXI-device for Dynamic Force Spectroscopy measurements. Since October 2009 he has worked in the group of Prof. Hans-Jürgen Butt at MPI for Polymer Research. His main focus is to measure single molecule wet bio-adhesion of polymers mimicking strongly adhesive properties of mussels protein.

Michael Kappl

Michael Kappl graduated in Physics at the TU Munich. He received his PhD from the Max Planck Institute of Biophysics in Frankfurt and worked at the Universities of Mainz and Siegen. Since 2002 he is working as a project leader at the Max Planck Institute of Polymer Research in Mainz. His research interests are physical chemistry of interfaces, surface forces and granular matter. Since 2007 he is also head of the focused ion beam service laboratory at the MPI for Polymer Research.

Arkadiusz Ptak

Arkadiusz Ptak is an assistant professor at the Institute of Physics, Poznan University of Technology, Poland. He got his PhD in physics in 1999 from Adam Mickiewicz University in Poznan. In 2000-2002, he was a postdoc (a fellow of the Science and Technology Agency of Japan) at the National Institute of Advanced Industrial Science and Technology in Tsukuba, Japan. Subsequently, he got a research fellowship from the Alexander von Humboldt Foundation and worked at the Max Planck Institute for Polymer Research in Mainz, Germany, in 2004-2006. His research interest focuses on molecular and surface physics, particularly on nanoadhesion and nanomechanical properties of thin films, biomolecules, polymers, etc. Dr. A. Ptak is an editor in the Central European Journal of Physics, section "anophysics"

Electrical Tomography: a review of Configurations and Applications to Particulate Processes[†]

M. G. Rasteiro[1*], R. Silva[1], F. A. P. Garcia1 and P. Faia[2]
Department of Chemical Engineering, Faculty of Sciences and Technology, University of Coimbra[1]
Department of Electric and Computers Engineering, Faculty of Sciences and Technology, University of Coimbra[2]

Abstract

Despite decades of research, the study of suspension flows still continues to be a subject of great scientific interest. In the development of accurate models for suspension-related processes, prior knowledge of several flow characteristics is essential, such as spatial distribution of phases, flow regimen, relative velocity between phases, etc. Several non-invasive techniques of flow characterisation can be found in the literature, however, electrical tomography offers a vast field of possibilities due to its low cost, portability and, above all, safety of handling. In this paper, a review of the use of electrical tomography for industrial/process monitoring purposes will be presented, giving information about the evolution throughout the years and about the limitations and advantages of the different configurations. Moreover, the signal de-convolution strategies, to obtain the images of the process, will also be discussed. The most recent advances in both fields will be presented. Additionally, information about the strategy adopted by the authors to produce a portable EIT system will be described. Finally, the future challenges for electrical tomography will be addressed.

Keywords: Electrical tomography, ECT, EIT, ERT, disperse systems

1. Introduction

Despite decades of research, the study of suspension flows still continues to be a subject of great scientific interest. In the development of accurate models for suspension-related processes, prior knowledge of several flow characteristics is essential, such as spatial distribution of phases, flow regimen, relative velocity between phases, including transient dynamic changes in multiphase processes, among others. Several non-invasive techniques of flow characterisation can be found in the literature1), however, electrical tomography offers a vast field of possibilities due to its low cost, portability and, above all, safety of handling, since there is no need to use radiation which requires special handling and leads to dangerous waste.

Tomography offers a unique opportunity to reveal the complexities of the internal structure of an object without the need to invade it. The concept of tomography was first published by a Norwegian physicist, Abel2), for an object with axi-symmetrical geometry. Nearly 100 years later, an Austrian mathematician, Radon3), extended Abel's idea for objects with arbitrary shapes. The root of the word tomography is derived from the Greek words "tomos" meaning "to slice" and "graph" meaning "image" . Advances on the use of the tomography technique, namely computerised tomography (CT) and computerised axial tomography (CAT), were presented by Godfrey Hounsfield of Great Britain and Allen Cormack of the United States during the 1970s4). Since then it has become widely used as a medical diagnostic technique. In this case, a narrow beam of X-rays sweeps across an area of the body and is recorded with a radiation detector as a pattern of electrical impulses. Data from many sweeps are integrated by a computer, which uses the radiation absorption figures to assess the density of the tissues at thousands of points. The densities are used to produce a detailed cross-sectional image of the internal structure under scrutiny.

Later, the concept of tomography and its non-invasive way of imaging was extended to beyond

---

[†] Accepted: September 12th, 2011
[1] 3030-790 Coimbra, Portugal
[2] 3030-290 Coimbra, Portugal
[*] Corresponding author
E-mail: mgr@eq.uc.pt
TEL: (+351)239798700 FAX: (+351)239798703

ⓒ 2011 Hosokawa Powder Technology Foundation

the medical field. Tomography has been developed over the last decade into a reliable tool for imaging numerous industrial applications[5-7]. Currently, there are a number of tomographic techniques other than the electrical methods discussed in this paper available for studying complex multiphase phenomena. These include, for example, X-ray, γ-ray and positron emission tomography systems[8], magnetic resonance imaging[9], ultrasonic systems[10], optical[11, 12] and infrared[13] tomography. Each of these techniques has its advantages, disadvantages and limitations. The choice of a particular technique is usually dictated by many, very often contradictory factors, depending on the application envisaged, including the characteristics of the medium, the objective of the measurement, the dimensions of the equipment, etc.

Electrical tomography is one of the available methods. It is relatively fast and simple to operate, has a rugged construction and is sufficiently robust to cope with most industrial environments. The apparent drawback of electrical tomography is its relatively low spatial resolution — typically 3-10% of the pipe diameter[14]. This, however, should be viewed in the context of the practical industrial applications. Moreover, more sophisticated inversion algorithms can improve the sensitivity of this technique. Electrical tomography is used to obtain both qualitative and quantitative data needed in modelling multiphase systems. Tomographic data can provide, in a non-invasive way, cross-sectional profiles of the distribution of materials or velocities in a process vessel or pipeline, or supply information about transient phenomena in the process. Results obtained from tomographic measurements can then be applied for process design or process control. Electrical tomography is, in certain cases, the most attractive method for real-time imaging of industrial processes, because of its inherent simplicity and low cost.

Electrical tomography can be further divided into two methodologies: electrical capacitance tomography (ECT) and electrical impedance tomography (EIT). Electrical resistance tomography (ERT) is a particular case of electrical impedance tomography. ECT and EIT produce images based upon variations in permittivity and conductivity, respectively. Recently, Yu et al[15]. have introduced another electrical technique, the electromagnetic tomography (EMT). Of these methodologies, ERT is the most widely and easily implemented, ideally for purely resistive mediums[16].

For heterogeneous systems comprising materials with different electrical properties, ECT and EIT can monitor dynamic processes such as: mixing; cyclones; fluidised beds; pneumatic, hydraulic and belt-conveyed transportation; etc. ECT and EIT are low-cost, but, in general, low-resolution, imaging methods. The rate at which images can be produced varies, depending on the data acquisition system, the measurement protocol, and the method of image reconstruction. Increasing the measurement speed permits faster dynamic processes to be captured, although this can increase the noise level, which in turn reduces the image quality. Tomography can be applied off-line or on-line. For off-line measurements, the capture time can be set fast relative to the dynamic changes in the process and the data processing time can be slow. The spatial resolution is normally high in this case. For on-line measurements, both the data capture time and the processing time have to be fast relative to the control time. This usually leads to poorer spatial resolution. Other factors that affect image quality are the physical nature of the measurements, and the method of image reconstruction used. In process applications, the interest is often in some average quantity, such as void fraction, throughput, mean velocity, etc. For model validation, higher resolution of the images is required.

In this paper, a review of the use of electrical tomography for industrial/process monitoring purposes will be presented, giving information about the evolution along the years and about the limitations and advantages of the different configurations. Moreover, the signal de-convolution strategies and reconstruction techniques used to obtain the images of the process will also be discussed. The most recent advances in both fields will be presented. Additionally, several applications of the different electrical tomography configurations will be addressed. Finally, a brief description of the strategy adopted by the authors to produce a portable EIT system with high resolution will be presented, discussing the approach implemented for signal injection, which allows us to deal with more conductive media, as can usually be found at the industrial level, and also the reconstruction approach, which allows us to obtain sharper images. Results obtained with this new system in a pilot rig conveying solid/liquid suspensions will be presented. To finalise, the future challenges for electrical tomography will be addressed, namely the possibility to use it for control purposes and also to deal with complex suspensions, with a disperse phase with non-isometric objects.

2. Fundamentals of Electrical Tomography

The theoretical model connecting the dielectric permittivity (or electrical conductivity) of a two-phase mixture to the volume fraction of one material dispersed within another was first presented by Maxwell [17]. In his calculations, Maxwell assumed that small spheres of one material are uniformly distributed in the continuous phase of another material and that a homogeneous electrical field is disturbed by their presence. The spheres are assumed to be of equal diameter and small compared to the distance between them. The distribution of electrical properties inside a pipe, corresponding to the particle distribution, is obtained from measurements of electrical quantities, such as capacitance or conductance, between pairs of sensors located around the pipe's wall, and by applying an appropriate reconstruction algorithm which mathematically links the measured values with that distribution.

The concept of describing the composition of a multiphase system based on the above principles has been used for many years to monitor gas-solid, gas-liquid or liquid-solid systems. Small capacitance probes have been used repeatedly to measure the local solids concentration in gas-solid flows[18, 19]. These probes have also been used in the oil and gas industry[20].

Normally, excitation sources (voltage or current) for use with electrical tomography are of low frequency (below 5 MHz). Thus, these systems are mainly described by the equations governing the electrostatic field. When the flux (or current) lines meet an interface of different permittivity or conductivity, they deflect. Typically, the electrodes are installed at equal intervals around the periphery of the process vessel or pipe, in order to extract the maximum information. Capacitance-sensing electrodes are usually installed in a non-invasive way (outside the pipe made of dielectric material). Their area has to be large enough to give a sufficient capacitance change. Resistivity-sensing electrodes can be very small. They are usually placed flush with the inner surface of the pipe, in contact with the media, but they are still considered non-intrusive.

3. Capacitance Tomography

The objective of ECT is to reconstruct the dielectric properties of an object from the measurement of electrical capacitance taken between all possible pairs of electrodes. **Fig. 1** shows a cross-sectional view of an ECT sensor equipped with eight electrodes.

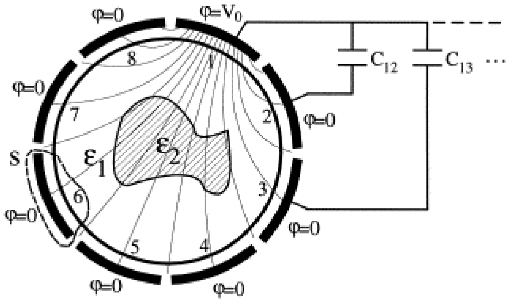

Fig. 1 Schematic representation of the measurement principle of an ECT system (adapted from[21]).

The electrodes can be either external or internal. External electrodes are used if the pipe is made of an insulating material, and internal ones have to be used if the pipe is made of a conducting material. External electrodes are easier to design and to maintain. They remain unaltered for a long time because they are not subjected to extreme temperatures, pressure or turbulence. So, they do not become contaminated by the materials flowing in the pipe. The main inconvenience of these electrodes is the non-linearity in the characteristics. Proper correction factors have to be used in order to make the characteristics linear. Internal electrodes are more complex to design, because they may have to withstand extreme conditions, and may even be subjected to corrosion. However, the change in capacitance can be assumed directly proportional to the change in permittivity inside the vessel.

The electrodes are excited one by one and the capacitance values between the excited electrode and the remaining ones are measured. It can be easily shown that for N electrodes there are $L=N(N-1)/2$ independent measurements. This is because capacitances $C_{i,j}=C_{j,i}$ and $C_{i,i}$, i.e. self-capacitance, is not measured. The measurement protocol, as described, can be imagined as a rotation of the electrical field around the pipe cross-section in discrete steps, by an angle $\alpha=360°/N$. This is analogous to the source-detector movement in computerised tomography used in medical imaging.

The relationship between the spatial distribution of the permittivity and the measured capacitances can be derived from Maxwell's equation. For an ECT system, only one electrode is excited at one time, the others are always at virtual earth potential. Thus, the total electric flux, calculated over all the electrode surfaces, equals zero. The data acquired is used to construct the permittivity distribution images.The magnitude of the inter-electrode capacitance is usually very small. Therefore, the measurements can be easily influenced by exterior earth capacitances, larger than the measured signals. To eliminate these effects the electrodes have to be externally shielded. The choice of the number of electrodes is the result of a balance between the spatial resolution required and the image acquisition rate. Speeds of 100 frames per second are frequently used in ECT.

The frequency of the electrical signal imposed is usually of the order of 1 MHz. Thus, the corresponding wavelength of the electromagnetic radiation is of the order of hundreds of meters, exceeding the sensor size by several orders of magnitude. The electrical potential distribution inside the measuring volume can then be described by the electrostatic field theory.

ECT requires, as has been described, a more complex sensor array than ERT, and difficulties arise when dealing with conductive materials[22, 23]. Thus, it is suitable for processes dealing with insulating mixtures of different permittivities. ECT is a fairly low-resolution imaging technique, but possesses a good overall accuracy for volume fraction estimation in flows of disperse systems[24]. The images can be used in deciding on the adequate control actions to be taken. Moreover, using dual plane sensors, the technique can, additionally, supply information on the particle velocity via cross-correlation of the cross-sectional averaged time series[24].

4. Resistivity Tomography

In true electrical impedance tomography, the complex impedance of a mixture is used. It is based on a phase-sensitive measurement, where the resistive component is detected by the in-phase measurement and the capacitive component by the quadrature phase measurement[14]. In this case the differences in both the real and imaginary parts of the impedance are measured[25-27]. The invention of electrical impedance tomography is attributed to John G. Webster in a publication from 1978[28]: however, the first practical application of EIT occurred in 1984[29] through the work of Barber and Brown. Both EIT and ERT (a particular case of EIT) can be used to investigate processes where the continuous phase is electrically conducting. ERT is used for purely resistive media[16].

In EIT, an electrical current is injected through a set of electrodes placed in the boundary of the domain under study, thereby resulting in an electrical field that is conditioned by the material distribution within the domain[30]. The resulting electrical potentials at the domain perimeter can be measured using the remaining electrodes, and those values are fed to an inverse algorithm to attain the previously unknown conductivity/resistivity distribution. The procedure is only complete when all electrodes are used for injection or projection, so the cycle has as many projections as the number of electrodes (see **Fig. 2**). A characterisation of the distribution of the electrical field is used to deduce the material distribution within the domain. In the case of ERT, which is easier to implement[27, 32, 33], the aim is to reconstruct the distribution of electrical conductivity within a system. Similar to true EIT, in an ERT system the electrical current flow is induced between one pair of neighbouring electrodes, whereas differential potentials between all remaining pairs of adjacent electrodes are measured.

This procedure is repeated for all pairs of neighbouring electrodes until a full rotation of the electrical field is obtained. It can easily be shown that the

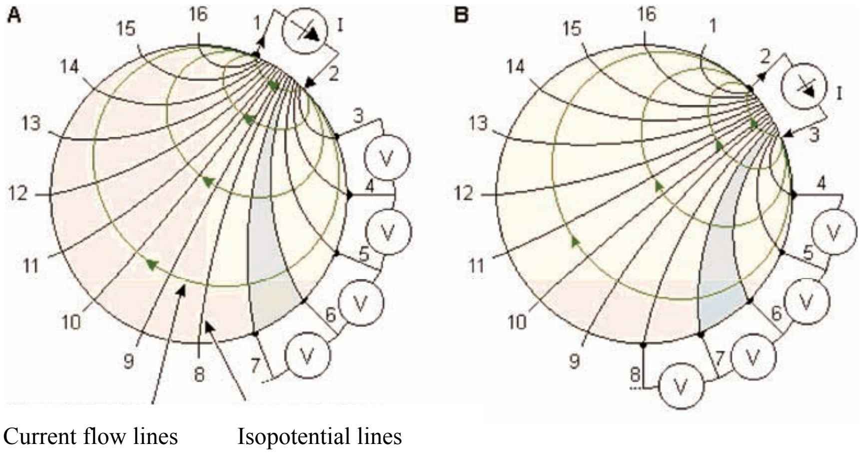

Fig. 2 EIT adjacent injection and measurement protocol for the first (A) and second (B) projections (adapted from[31]).

number of independent differential voltage measurements for an N-electrode system is $L=N(N-3)/2$, for the adjacent injection and measuring protocols, the electrode pair used for exciting the domain is excluded from the measurements. The frequency of alternating current in an ERT system is typically 20-150 kHz, so the quasi-static conditions can be justified. The current varies synchronically in the measurement volume and Ohm's law can be applied.

Recent advances have been directed both to the sensor design and to the acquisition system. The use of discrete electrodes is limited to aqueous-based fluids that present continuous admittance[26]. When large bubbles are present, some electrodes may lose contact with the conductive fluid and the results become inconsistent. In this case, conductive ring electrodes present a good possibility to overcome that problem[26]. Additionally, flush-mounted electrodes, as is required by resistivity tomography, can introduce another problem since the surface of the electrodes can be easily altered with time. Particular attention has to be paid to this aspect when dealing with extreme process conditions. In particular, the effect of temperature can dramatically change the conductivity of the fluid. Thus, temperature compensation has to be applied to the current or voltage measurements, when it changes a lot in the process over time.

Regarding the data acquisition system, new developments allow acquisition speeds of 1000 frames/s[26]. The current injection strategy is also important to guarantee better acquisition times and better sensitivity. Using a voltage-controlled current source together with an equal width pulse synthesizer to produce synthetic wave forms for electric field excitation and demodulation leads to less noisy data[26]. The voltage source must have low output impedance. When using a voltage source, the current supplied to the system increases as the fluid conductivity increases. This is particularly important in the case of a highly conductive medium (conductivities above 2 S/m) which is quite frequent in real industrial processes[27, 34].

Other parameters that have to be carefully considered when using EIT or ERT, besides the shape and size of the electrodes as mentioned above, is the separation distance between electrodes and the frequency of excitation of the electrical current. These parameters condition the current density distribution between electrodes and determine the true effective measuring volume[35]. The effect of the size of the electrodes can be substantially reduced through calibration[36]. As with ECT, EIT can also be used to measure the disperse phase velocity by using dual plane sensors and applying a cross-correlation algorithm[37, 38]. A minimum acquisition speed of 100 frames per second is necessary to obtain accurate estimates of the velocity distribution[37].

5. Image Reconstruction

In electrical tomography techniques, the measurements are sensitive within a 3D region (i.e. a volume); the sensitivity varies across the nominal sensing zone, and the sensitivity for a particular position within this zone also depends on the spatial variation of the physical parameter being imaged within the entire sensing zone. This non-linear behaviour makes image reconstruction difficult. Both capacitance and resistivity tomography are governed by a similar set of partial differential equations, and the reconstruction algorithms have many similarities. Reconstructing an image from the measurements (capacitances in ECT, potential differences in EIT) is called the inverse problem, whilst calculating the measurements from a known image is called the forward problem. In this case, the problem is one of mapping a set of theoretical parameters into a set of experimentally measured values. In the case of ECT, this would mean calculating the capacitance values for a given distribution of dielectric permittivity inside the system. This problem has a unique solution. The inverse problem, however, in addition to the difficulties caused by non-linearity, is also usually ill-posed and ill-conditioned. Mathematically, we are faced with a matrix inversion problem. In the case of ECT, the inverse problem is equivalent to finding the material distribution inside the system based on a set of capacitance values. This is what we usually call a reconstruction problem. The aim is to obtain the reciprocal of operator F which gives the original distribution of dielectric properties $\varepsilon = \varepsilon(\gamma)$ from the measured values of capacitance C^o:

$$\varepsilon(\gamma) = F^{-1}[C^o] \tag{1}$$

There is no analytical solution to this problem, mainly because of its non-linearity. The number of unknowns is much higher than the available data. So, there is an infinite number of solutions which match the capacitance measurements. The only possibility is to construct a permittivity distribution that best fits the measurements.

For EIT, a similar approach has to be followed. The forward problem calculates the electrical potentials in the boundary using an initial estimation of the conductivity/resistivity distribution, while the inverse problem reconstructs the conductivity/resistivity distribution based on the electrical potentials measured in the boundary, through the use of an adequate mathematical procedure. The distribution of the electrical field in the domain can be modelled in the forward problem using Maxwell laws[39]. The problem of finding the solution for the inverse problem is tackled by solving first the forward problem, which is used as an effective calibration. The boundary voltages or capacitances are usually calculated using finite element methods (FEM) for a known distribution of permittivity or conductivity. The sensitivity matrix is obtained from the measured values (voltage or capacitance). This solution is then supplied to the reconstruction technique to obtain the values of permittivity or conductivity in the system nodes from the measured capacitance or voltage/current values. The sensitivity matrix and the measured boundary values are used to interpret the changes (permittivity/conductivity) in the system nodes.

There are several methods for reconstructing EIT and ECT images which can be broadly divided into three classes: linear (single-step and iterative methods); non-linear iterative methods; and heuristic multivariate methods.

Linear methods

Linear methods are fast, as images are generated by simply multiplying the measurements by a single, pre-calculated matrix. Linear back-projection (LBP) is the most widely used linear method. In LBP, the matrix is the transposal of an estimated solution to the forward problem, based upon either field gradients or more commonly, sensitivity maps (the area in the measuring volume is divided into sensitivity areas)[40]. In the first case, we speak about non-iterative linear methods. An iterative back-projection algorithm was proposed by Yang[41] which is much more accurate. LBP tends to produce, in general, poor, heavily smoothed images because the transposed solution from the forward problem is, in fact, a poor estimate of the solution to the inverse problem that is actually required. It is assumed that the electrical field is not distorted by changes in permittivity/conductivity, similar to what happens in X-ray or γ-ray tomography. Mathematically, this approach is correct when the dielectric properties of the phase components are close to one another. However, LBP methods can provide a fast on-line qualitative view of the process. The linear methods have been improved by including approaches based upon ridge-regression or eigenanalysis[42]. In practice, LBP has been used successfully for gas-solids or gas-oil systems[21].

Non-linear methods

Non-linear methods use numerical forward solvers to predict measurements and use sensitivity maps associated with an estimate of the image to calculate measurement residuals. The estimated image is then updated via a non-linear iterative scheme such as the modified Newton Raphson (NR)[43] or adaptive mesh regenerating techniques[44]. NR can introduce significant artificial errors in the solution. Regularisation methods such as the Marquard and the Tikhonov methods have to be applied to obtain a better approximation at each step[26]. The regularisation can, nevertheless, introduce further noise in the final image[26]. In direct inverse solution algorithms such as the sensitivity conjugate gradients method (SCG), the algorithm searches for the minimised residual vector, and leads to images with improved accuracy[26]. These methods are generally called multi step inverse solution algorithms (STM) and normally provide a better description of the dynamic nature of the process[38]. Adopting non-linear iterative methods offers more flexibility in the measurement protocol that can be used. However, the considerable computational load makes them much slower than linear or heuristic methods. Non-linear iterative methods are currently too slow for real-time image reconstruction, although this may change through a combination of efficient algorithms[45] and the continued fall in computing costs. Cho et al.[46] applied an adaptive mesh grouping method based on fuzzy genetic algorithm to decrease image reconstruction time. Mesh optimisation is also an important step towards higher resolution images[34]. So far, this type of method is most suited for off-line image reconstruction.

Heuristic methods

Heuristic methods can be linear or non-linear. The relationship between training (or calibration) sets of images and measurements is modelled empirically. The training set can be calculated (numerically or analytically), or obtained experimentally. Linear heuristic models include multiple linear regression[47]. Non-linear methods include self-organised maps and artificial neural networks[48]. For process applications, image reconstruction is often an intermediate step towards calculating other variables so heuristic models can, in principle, relate the measurements directly to the variable of interest[49].

6. Applications

ECT and EIT have been used to study a wide range of different systems. The bulk of the work has used ECT and EIT as research tools, in which model systems are studied on small-scale rigs or in pilot plants. The transferral from the research environment to real-life process monitoring has been slow, although some examples have been reported.

Some up-to-date electrical tomography applications

In a work by Larachi et al., the hydrodynamics of gas-liquid packed beds was studied experimentally using twin-plane electrical capacitance tomography(50). The distribution of solids concentration in different processes plays a key role in the process industry, thus several examples of the use of electrical tomography are in the field of solids distribution visualisation. Experimental studies were carried out to measure the solids concentration in a cyclone separator using ECT(51). ECT and EIT were also used to monitor the flow regimes during hydraulic (solid-liquid) and pneumatic (solid-gas) transport. An ECT test system has been used to monitor the pneumatic transport of rape seeds(52). Others, Sundaresan et al.(53), have addressed the problem of pneumatic conveying of granular solids in vertical and inclined risers using electrical capacitance tomography. Recently, pneumatic conveying (a model system of plastic pellets) has been studied using dual-plane ECT and an electrodynamic sensor(54). Paste extrusion has also been studied using EIT, in a work of William et al.(55). An ERT system was used to visualise swirling flows in a conveying pipe(30). The internal flow structure within fluidised beds of different sizes has been studied using ECT(56) in order to better understand the hydrodynamics of these systems(57). Capacitance computed tomography techniques were also used to visualise particle movement in the draft tube of a spouted fluidised bed for the coating process of drug production(58). ERT has been used as well to enhance the performance of a differential pressure flowmeter (Venturi type) in two-phase flow measurements(59).

Foams are also an important issue in a variety of industrial processes including mineral production processes such as froth flotation. Applying electrical capacitance tomography to low water fraction foams (<0.05) was addressed by William et al. (60). Kourunen et al. used electrical impedance tomography to image the mixing of two miscible liquids in a turbulent flow, using the trump-jet mixing system of papermaking chemicals and additives(61).

Electrical capacitance tomography has been adapted to characterise combustion phenomena in a scaled model of an internal combustion engine by Vilar et al. (62): it was thus possible to locate flame position, measure flame size and to monitor the effect of varied air/fuel ratio. Electrical resistance tomography was applied for the study of three-dimensional imaging of concrete(63). ERT has also been used recently for multivariate process control of a sunflower oil/water emulsion process(64). In a similar way, the applicability of electrical resistance tomography to pharmaceutical chemicals development has been considered: vessel/stirrer configurations designed to mimic typical plant reactor geometries were investigated in connection with multiphase processes typical of the pharmaceuticals industry(65). Electrical impedance tomography was also adapted to monitor drug release three-dimensionally as a function of time(66). EIT was also used for imaging the electrical conductivity distribution within a two-dimensional cell culture, in a work by Morgan et al. (67).

Two-phase flow tomography by EIT: current developments

The authors have also been working on the improvement of EIT applied to image acquisition of two-phase flows (solid/liquid) with the aim of CFD model validation(34). The EIT system developed by them measures the differences in both the real and imaginary parts of the impedance, so no data is lost. This EIT system is a portable one, to be transported easily to any location where an electrode ring is present and can be used for 16-electrode or 32-electrode rings. To circumvent difficulties and costs of designing a current source, a choice was made to depart from traditional EIT systems, and instead a voltage source was designed. It has been demonstrated that using a voltage source for stimulating the domain instead of a current source allows surpassing the limitations found when studying more conductive media(27). This EIT system has already been described elsewhere(34): however, for the sake of a better understanding, a brief description is given here. A series of USB-type devices is used for purposes of interfacing between the EIT system and the PC (DAQ boards). The devices are used to read the electrical potentials by means of the analogue input channels. The EIT system designed has an image acquisition frame rate that can achieve up to 4000 frames per second and 1000 frames per second for the 16- and 32-electrode measurement rings, respectively. A programmable frequency voltage waveform generator with an output frequency up to 25 MHz was implemented. Two additional signals, both with unitary magnitude, one in phase and the other 90 degrees out of phase with the excitation signal, are generated simultaneously. Then the electrical potential voltages read at the electrodes are multiplied by these two unitary signals. The signals resulting from the multiplications go through low-pass filters: this allows isolation of the constant terms needed to determine the impedance of the domain. The routing of the excitation signal and of the electrode potentials to the multipliers is done using analogue multiplexers: the addressing of the multiplexers is accomplished through the digital outputs of the DAQ boards.

Tomographic images of solid-liquid suspensions

The experiments were conducted in a pilot rig described elsewhere[34, 68]. In short, the test section consisted of a horizontal PVC tube, 7.5m in length and 100 mm in internal diameter. The flow rate was measured by an electromagnetic flowmeter and the pressure drop was measured by a differential pressure transducer whose pressure taps were 4 metres apart. Appropriate lengths were inserted before and after the test section to account for entrance and exit effects. The electrodes were mounted equally spaced around the circumference of Perspex tubes, and the tubes were inserted in the test section between the pressure taps. For the tests depicted here, an adjacent injection strategy was adopted with the 16-electrode system, with a frame acquisition rate of 4000 frames per second, while the voltage source was configured to produce a sinusoidal waveform of 2 kHz frequency and 1.5 V of amplitude. With this set-up, a 90 μA current amplitude was applied to the domain. The tests were performed using solid/liquid suspensions of spherical glass beads in a diluted aqueous solution of NaCl (conductivity of 663 μS/cm) flowing in the system. The bead sizes ranged from 400 to 600 μm in diameter. For image reconstruction, the open source software EIDORS[39], under consideration of direct differential measured voltages, was used (two meshes were tested: mesh 1 with 2304 linear elements and 1201 nodes, a structured mesh, and mesh 2 which is a non-structured one with 415 linear elements and 241 nodes). This software implements a non-linear back-projection method using a regularised algorithm (Tikhonov regularisation). To solve the forward problem, the Complete Electrode model (CEM)[69] was chosen: this model incorporates the shunt effect and the contact impedance in the electrode/domain interface[39]. Tests were performed at different flow rates, from 0 up to 52 m^3/h. At very low flow rates, the particles were not moving and remained as a fixed bed sedimented on the bottom of the tube. But once the flow was increased enough to fluidise the bed, the particles started moving, and as the flow rate continued to increase, the amount of sedimented particles decreased and these became more and more dispersed in the conveying medium until a quasi-uniform distribution was reached. This is evident in **Fig. 3** where each row refers to a value of the flow rate: 0, 13, 33 and 52 m^3/h; the first column shows photographs of the conveying suspension inside the tube, the second and third columns show the reconstructed images using mesh 1 and mesh 2, respectively, once again considering direct differential measured voltages. For all images depicted in the middle and right columns of **Fig. 3**, dark blue identifies a higher impedance state and dark red a lower impedance state (in a linear transition scale).

When the system was stationary (the pump was switched off) the particles were sedimented in the lower region of the pipe and the gradient of conductivity was high (first row); when the flow rate was 13 m^3/h, the particles were already moving but generally were dragged by the water into the lower region of the pipe which clearly looks like a deposit at the bottom where the conductivity gradient is high (second row). For the highest flow rate, 52 m^3/h, the particles were almost completely distributed all over the entire cross-section of the pipe, therefore a very small gradient of conductivity exists, the image corresponding to the red colour, with some slightly higher concentration near the bottom, as is evident in the 4th row of **Fig. 3**.

7. Future Trends

Electrical tomography has been evolving over the years, becoming more accurate, retrieving images with better resolution, becoming faster and acquiring new functionalities. These upgrades result either from new sensor configurations, new injection strategies, upgrading of the acquisition system, better and/or faster reconstruction algorithms, etc.

The ring electrodes developed for bubbly systems represent a step forward in the use of electrical tomography for such systems, including processes involving foams[26]. Linear sensors, constructed from printed circuit boards (PCBs) are also now being used to better visualise non-circular vessels or ducts[70]. Additionally, a recently added feature to electrical tomography is the data acquisition feature using a dual-electrode device, in order to obtain in-

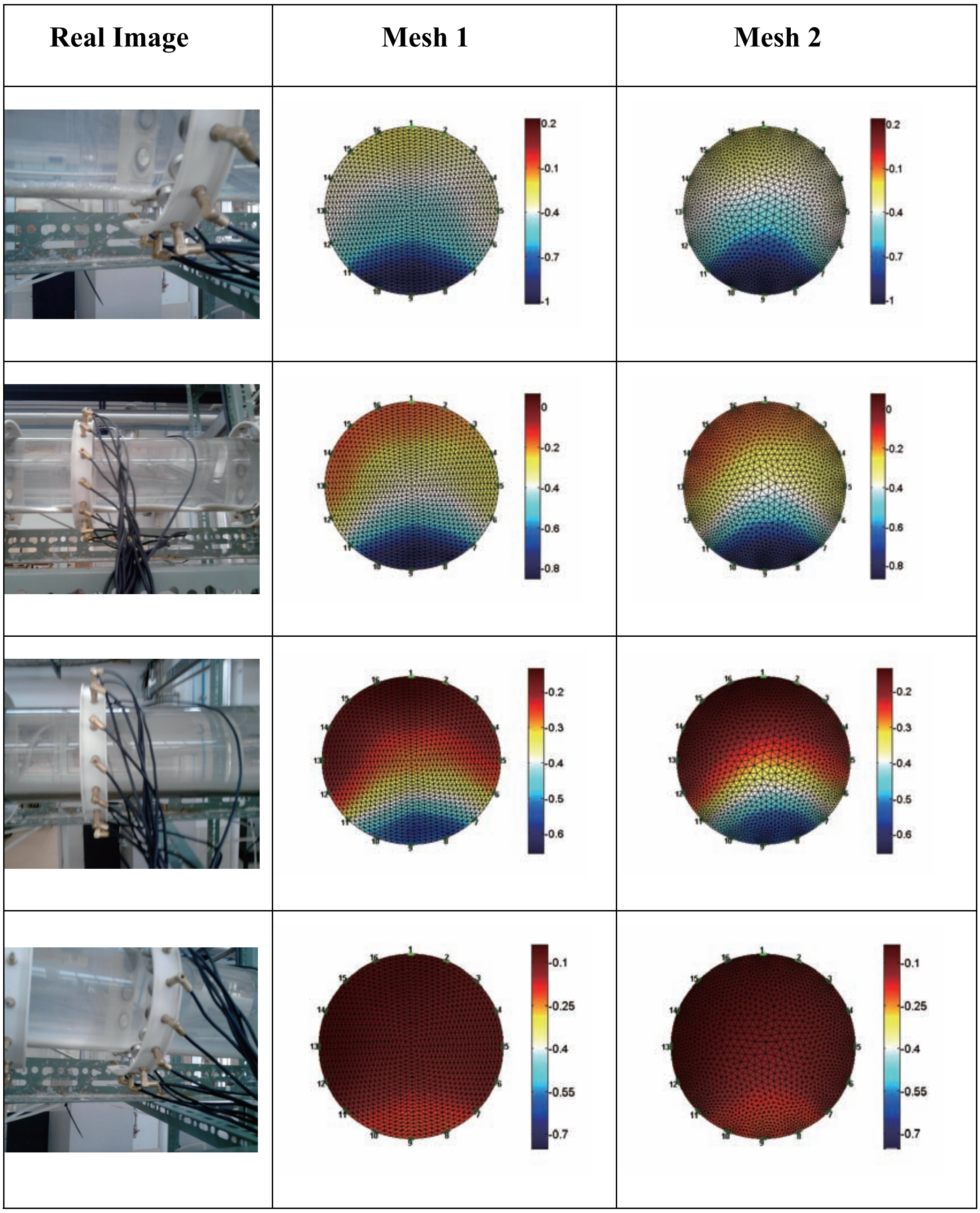

Fig. 3 Solid-liquid suspension tests carried out with an average particle concentration of 3.9 g/l for flow rates of 0, 12, 33 and 52 m^3/h, respectively, from top to bottom (left column contains pictures of the section under study, middle column images obtained using mesh 1 and the right column images obtained using mesh[2] (reproduced from[34]).

formation about the velocity profile in the process through cross-correlation of the signals acquired[26, 30]. This functionality is expected to be further developed in the future. In this case, ERT can be used coupled with other measuring techniques to improve the accuracy of traditional flowmeters used for multiphase systems[59].

On the other hand, the injection strategy can be an important parameter to be controlled when applying electrical tomography to real industrial processes. Voltage sources have proved to be a better option in the case of highly conductive fluids[27, 34]. Temperature compensation of the reference profiles is also a good strategy when dealing with conductive fluids[30].

Finally, and regarding the hardware of electrical tomography, modularity has become an important characteristic, mainly when industrial application is envisaged[71]. Moreover, multi-modal process tomography, exploiting multiple sensors and allowing the integration of their data[72], will be pursued in the future.

Another domain where a lot of work is being done is image reconstruction algorithms. In fact, improving this step can contribute a lot to the better resolution of the final images and, additionally, faster reconstruction algorithms are needed if on-line applications are targeted. Work is being done in order to minimise the influence of small perturbations in the measured data, on the inverse solution. This is, for instance, the case of the standard Tikhonov regularisation (STR), which is now being applied for online reconstruction[73] included in a semi-parametric model reconstruction algorithm. Further coupling of STR with maximum entropy regularisation (MER) can additionally reduce the artefacts of the reconstructed images[74]. This technique is particularly well suited for 3D reconstructions. Heuristic methods are another route for on-line reconstruction[49].

Regarding the applications, besides its use for model validation in particulate processes, nowadays in connection with sophisticated CFD models[44], the application of electrical tomography for the online control of the process is now being pursued. Traditionally, electrical tomography was used in the industrial process to inspect abnormalities in the equipment. Recent studies show that it is now possible to use ERT for multivariate statistical process control, where it is used to predict the probability of the process monitored being in a normal or abnormal operational state[64]. Another important vector which has been pursued for years, but still needs further development, is the conversion of the reconstructed permittivity/conductivity images to adequate physical values for each particular application[36].

Acknowledgments

The authors are grateful for the financial support of FCT (Fundação para a Ciência e Tecnologia) to their project, contract PTDC/EQU-EQU/66670/2006.

References

1) Torczynski, J.R., O'Hern, T.J., Adkins, D.R., Jackson, N.B. and Shollenberger, K.A. (1997): Advanced Tomographic Flow Diagnostics for Opaque Multiphase Fluids, Sandia Report SAND97-1176 • UC-406, Sandia National Laboratories, Albuquerque, New Mexico, USA.
2) Abel, N.H. (1826): Resolution d'un probleme de mecanique, J. Reine Agnew. Math., 1, pp.311-389.
3) Radon, J. (1917): Über die Bestimmung von Funktionen durch ihre Integralwerte längs gewisser Mannigfaltigkeiten, Ber. Saechs. Akad. Wiss. 69, pp.262-278.
4) Seeram, E. (2000): "Computed Tomography: Physical Principles, Clinical Applications, and Quality Control" , W.B Saunders Comp.
5) Plakowski, A., Beck, M.S., Thorn, R. and Dyakowski, T. (1995): "Imaging Industrial Flows" , IOP Publishing, Bristol.
6) Williams, R.A. and Beck, M.S. (1995): "Process Tomography — Principles, Techniques and Applications" , Butterworth-Heinemann, Oxford.
7) Mewes, D. and Schmitz, D. (1999): Tomographic methods for the analysis of flow patterns in steady and transient flow, Proceedings of the Second International Symposium on Two-Phase Flow Modelling and Experimentation, Rome, Italy, 23-26 May (1999), pp.29-42.
8) Chaouki, J., Larachi, F. and Dudukovic, M. P. (1997): Non-invasive tomographic and velocimetric monitoring of multiphase flows, Ind. & Eng. Chem. Research, 36 (11), pp.4476-4503.
9) Williams, R.A. and Xie, C.G. (1993): Tomographic techniques for characterizing particulate processes, Part. & Part. Systems Characterization, 10 (5), pp.252-261.
10) Brown, G.J., Reilly, D. and Mills, D. (1996): Development of an ultrasonic tomography system for application in pneumatic conveying. Meas. Sci. Technol, 7, pp.396-405.
11) Rahim, R.A., Green, R.G., Horbury, N., Dickin, F.J., Naylor, B.D. and Pridmore, T.P. (1996): Further development of a tomographic imaging system using optical fibres for pneumatic conveyors. Meas. Sci. Technol, 7, pp.419-422.
12) Green, R.G., Rahim, R.A., Evans, K., Dickin, F.J., Naylor, B.D. and Pridmore T.P. (1998): Concentration profiles in a gravity chute conveyor by optical tomography measurement. Powder Technol. , 95 (1), pp.49-54.
13) Uchiyam,a H., Nakajima, M. and Yuta, S. (1985): Measurement of flame temperature distribution by IR emission computed tomography. Appl. Opt., 24, pp.4111-4116.
14) Xie, C.G., Reinecke, N., Beck, M.S., Mewes, D., Williams, R.A. (1995): Electrical tomography techniques for process engineering applications, The Chem. Eng. J., 56, pp. 127-133.
15) Yu, Z.Z., Peyton, A.T., Beck, M.S., Conway, W.F. and Xu, L.A. (1993): Imaging system based on Electromagnetic Tomography, Electronic Letters, 29, pp.625-626.
16) Wilkinson, A.J., Randall, E.W., Long, T.M. and Collins, A. (2006): The design of an ERT system for 3D data acquisition and a quantitative evaluation of its perfor-

mance, Meas. Sci. Technol., 17, pp.2088-2096.

17) Maxwell, J.C. (1873): “A Treatise on Electricity and Magnetism vol. I” , Clarendon Press, Oxford.

18) Morse, T. D. and Ballou, C. O. (1951): The uniformity of fluidisation, its measurement and use, Chem. Eng, Progress. 47, pp.199-211.

19) Geldart, D. and Kelsey, J.R. (1972): The use of capacitance probes in gas fluidised beds, Powder Tech., 6, pp.45-50.

20) Abouelwafa, M.S.A. and Kendall, E.J.M. (1979): Analysis and design of helical capacitance sensors for volume fraction determination, Rev. Sci. Instrum., 50 (7), pp.872-878.

21) Dyakowski, T., Jeanmeure, L.F.C. and Jaworski, A.J. (2000): Applications of electrical tomography for gas-solids and liquid-solids flows - a review, Powder Tech., 112, pp.174-192.

22) Dyakowski, T., Johansen, G.A., Hjertaker, B.T., Sankowski, D., Mosorov, V. and Wlodarczyk, J. (2006): A Dual Modality Tomography System for Imaging Gas/Solids Flows, Particle & Particle Systems Characterization, 23, pp.260-265.

23) Yang, W. (2007): Tomographic Imaging based on Capacitance Measurement and Industrial Applications, IEEE International Workshop on Imaging on Systems and Techniques, 2007, pp.1-6.

24) Azzopardi, B.J., Abdulkareem, L.A., Zhao, D., Thiele, S., da Silva, M.J., Beyer, M. and Hunt, A. (2010): Comparison between Electrical Capacitance Tomography and Wire Mesh sensor for air/silicone oil flow in a vertical pipe, Ind. & Eng. Chem. Research, 49, pp.8805-8811.

25) Grootveld, C. J. (1996): “Measuring & Modelling of concentrated settling suspensions using Electrical Impedance Tomography” , PhD thesis, , Univ. of Delft, Delft, Holland.

26) Wang, M. (2005): Impedance Mapping of Particulate Multiphase Flows, Flow Measurement and Instrumentation, 16, pp.183-189.

27) Jia, J., Wang, M., Schlaberg, H. I. and Li H. (2010): A Novel Tomographic Sensing System for High Electrically Conductive Multiphase Flow Measurement, Flow Measurement and Instrumentation, 21(3), pp.184-190.

28) Henderson, R.P. and Webster, J.G. (1978): An Impedance Camera for Spatially Specific Measurements of the Thorax. IEEE Transactions on Biomedical Engineering, 25 (3), pp.250-254.

29) Barber, D.C. and Brown, B.H. (1984): Applied Potential Tomography, Journal of Physics E: Scientific Instruments, 17 (9), pp.723 - 733.

30) Wang, M., Jones, T.F. and Williams, R.A. (2003): Visualization of Asymmetric Solids Distribution in Horizontal Swirling Flows Using Electrical Resistance Tomography, Chemical Engineering Research and Design 81 (8), pp.854-861.

31) Malmivuo, J. and Plonsey, R. (1995): “Bioelectromagnetism: Principles and Applications of Bioelectric and Biomagnetic Fields” , Oxford University Press, New York - Oxford.

32) Pakzad, L., Ein-Mozaffari, F. and Chan, P. (2008): Using Electrical Resistance Tomography and Computational Fluid Dynamics Modelling to Study the Formation of Cavern in the Mixing of Pseudoplastic Fluids Possessing Yield Stress, Chemical Engineering Science, 63 (9), pp.2508-2522.

33) Razzak, S.A., Barghi, S., Zhu, J.-X. (2009): Application of electrical resistance tomography on liquid-solid two-phase flow characterization in an LSCFB riser, Chemical Engineering Science, 64 (12), pp. 2851-2858.

34) Faia, P.M., Ferreira, A.R., Santos, M.J., Santos, J.B., Silva, A.P.R., Rasteiro, M.G. and Garcia, F.A.P.: Imaging particulate two-phase flow in liquid suspensions with Electric Impedance Tomography, Particulate Science and Technology, in press.

35) Karapantsios, T.D. and Papara, M. (2008): On the design of electrical conductance probes for foam drainage applications. Assessment of ring electrodes performance and bubble size effects on measurements, Colloids & Surfaces A: Physicochem. Eng. Aspects 323, pp.139-148.

36) Wang, M., Mann, R. and Dickin, F.J. (1999): Electrical resistance tomography sensing systems for industrial applications, Chem. Eng. Comm. 175, pp.49-70.

37) Lucas, G.P., Cory, J., Waterfall, R.C., Loh, W.W. and Dickin, F.J. (1999): Measurement of the solids volume fraction and velocity distributions in solids-liquids flows using dual-plane electrical resistance tomography, Flow Measurement Instrumentation 10, pp.249-258.

38) Wang, M. and Yin, W. (2001): Measurements of concentration and velocity distribution in miscible liquid mixing using electrical resistance tomography, Trans. Chemical Engineering Research and Design, 79 (A8), pp.883-886.

39) Polydorides, N. and Lionheart, W.R.B. (2002): A Matlab toolkit for three-dimensional electrical impedance tomography: a contribution to the Electrical Impedance and Diffuse Optical Reconstruction Software project, Measurement Science and Technology, 13(12), pp.1871-1883.

40) Kotre, C.J. (1994): EIT image reconstruction using sensitivity weighted filtered backprojection. Phys. Meas., A 15, pp.125-136.

41) Yang, W. Q., Gamio, J.C. and Beck, M.S. (1997): A fast iterative image reconstruction algorithm for capacitance tomography, Sensors and their Applications, vol. III, IOP Pub., pp.47-52.

42) Lionheart, W.R.B. (2001): Reconstruction algorithms for permittivity and conductivity imaging, Proceedings of the Second World Congress on Industrial Process Tomography, Hannover, Germany, 29-31 August, 2001, pp.4-11.

43) Yorkey, T.J., Webster, J.G. and Tompkins, W. (1987): Comparing reconstruction algorithms for electrical impedance tomography, IEEE J. Bio-Med. Eng., 34, pp.843-852.

44) Parvareh, A., Rahimi, M., Alizadehdakhel, A. and Alsaifari, A.A. (2010): CFD and ERT investigations on two-phase flow regimes in vertical and horizontal tubes, Int. Comm. Heat & Mass Transfer, 37, pp.304-311.

45) Molinari, M., Cox, S.J., Blott, B.H. and Daniell, G.J. (2001): Efficient non-linear 3D electrical tomography reconstruction, Proceedings of the Second World Congress on Industrial Process Tomography, Hannover, Germany, 29-31 August 2001, pp.424-432.

46) Cho, K.H., Kim, S. and Lee, Y.J. (1999): A fast reconstruction method for the two phase flow visualization, Int. Comm. Heat & Mass Transfer, 26 (5), pp.637-646.

47) Tapp, H.S. and Wilson, R.H. (1997): Developments in low-cost electrical imaging techniques, Process. Contr. Qual. 9, 1997, pp.7-16.

48) Sun, T.D., Mudde, R., Schouten, J.C., Scarlett, B. and Bleek, C.M. (1999): Image reconstruction of an electrical capacitance tomography system using an artificial neural network, Proceedings of the First World Congress on Industrial Process Tomography, Buxton, UK, April 1999, pp.174-180.

49) Mohamad-Saleh, J., Hoyle, B.S., Podd, F.J.W. and Spink, D.M. (2001): Direct flow process estimations from tomographic data using artificial neural systems, Proceedings of the Second World Congress on Industrial Process Tomography, Hannover, Germany, 29-31 August 2001, pp.751-758.

50) Hamidipour, M. and Larachi, F. (2010): Characterizing the liquid dynamics in concurrent gas-liquid flows in porous media using twin-plane electrical capacitance tomography, Chemical Engineering Journal, 165 (1):15, pp.310-323.

51) Meng, S., Shi, L., Zhihong, L. and Jing, L. (2008): Application of Electrical Capacitance Tomography to the Concentration Measurement in a Cyclone Dipleg, Chinese Journal of Chemical Engineering, 16 (4), pp.635-639.

52) Brodowicz, K., Maryniak, L. and Dyakowski, T. (1993): Application of capacitance tomography to pneumatic conveying processes, “Tomographic Techniques for Process Design and Operation” , Computational Mechanics Publications, Southampton and Boston, pp.361-368.

53) Zhu, K., Rao, S. M., Wang, C. and Sundaresan, S. (2003): Electrical capacitance tomography measurements on vertical and inclined pneumatic conveying of granular solids, Chemical Engineering Science, 58 (18), pp.4225-4245.

54) Arko, A., Waterfall, R.C., Beck, M.S., Dyakowski, T., Sutcliffe, P. and Byars, M. (1999): Development of electrical capacitance tomography for solids mass flow measurement and control of pneumatic conveying systems, in: Proceedings of the First World Congress on Industrial Process Tomography, Buxton, UK, 14-17 April 1999, pp.140-146.

55) West, R.M., Wu, Y., Scott, D.M., Sunshine, G., Hoyle, B.S., Kostuch, J., McLeod, C.N. and Williams, R.A. (2001): Electrical impedance imaging of paste during extrusion, Proceedings of the Second World Congress on Industrial Process Tomography, Hannover, Germany, 29-31 August 2001, pp.300-306.

56) White, R.B., and Zakhari, A. (1999): Internal structures in fluid beds of different scales: an application of electrical capacitance tomography, Proceedings of the First World Congress on Industrial Process Tomography, Buxton, UK, 14-17 April 1999, pp.39-46.

57) Makkawi, Y.T. and Wright, P.C. (2001): Application of process tomography as a tool for better understanding of fluidization quality in a conventional fluidized bed, Proceedings of the Second World Congress on Industrial Process Tomography, Hannover, Germany, 29-31 August 2001, pp.324-338.

58) Takei, M., Zhao, T. and Yamane, K. (2009): Measurement of particle concentration in powder coating process using capacitance computed tomography and wavelet analysis, Powder Technology, 193 (1), pp.93-100.

59) Meng, Z., Huang, Z., Wang, B., Ji H. and Yan, Y. (2010): Air-water two-phase flow measurement using a Venturi meter and an electrical resistance tomography sensor, Flow Measurement Instrumentation, 21, pp. 268-276.

60) Bennett, M.A., West, R.M., Luke, S.P. and Williams, R.A. (2002): The investigation of bubble column and foam processes using electrical capacitance tomography, Minerals Engineering, 15 (4), pp. 225-234.

61) Kourunen, J., Käyhkö, R., Matula, J., Käyhkö, J., Vauhkonen, M. and Heikkinen, L.M. (2008): Imaging of mixing of two miscible liquids using electrical impedance tomography and linear impedance sensor, Flow Measurement and Instrumentation 19 (6), pp.391-396.

62) Vilar, G., Williams, R.A., Wang, M. and Tweedie, R.J. (2008): On line analysis of structure of dispersions in an oscillatory baffled reactor using electrical impedance tomography, Chemical Engineering Journal, 141 (1-3), pp.58-66.

63) Karhunen, K., Seppänen, A., Lehikoinen, A., Monteiro, P.J.M. and Kaipio, J.P. (2010): Electrical Resistance Tomography imaging of concrete, Cement and Concrete Research, 40 (1), pp.137-145.

64) Boonkhao, B., Li, R. F., Wang, X. Z., Tweedie, R. J., Primrose, K. (2010): Making use of process tomography data for multivariate statistical process control, AIChE J., doi 10.1002/aic.12443,.

65) Ricard, F., Brechtelsbauer, C., Xu, X.Y. and Lawrence, C.J. (2005): Monitoring of Multiphase Pharmaceutical Processes Using Electrical Resistance Tomography, Chemical Engineering Research and Design, 83 (7), pp.794-805.

66) Rimpiläinen, V., Kuosmanen, M., Ketolainen, J., Järvinen, K., Vauhkonen, M. and Heikkinen, L.M. (2010): Electrical impedance tomography for three-dimensional drug release monitoring, European Journal of Pharmaceutical Sciences, 41 (2), pp.407-413.

67) Sun, T., Tsuda, S., Zauner, K. and Morgan, H. (2010):

On-chip electrical impedance tomography for imaging biological cells, Biosensors and Bioelectronics, 25 (5), pp.1109-1115.

68) Ventura, C., Garcia, F.A.P., Ferreira, P. and Rasteiro, M.G. (2007): Flow Dynamics of pulp fiber suspensions, Tappi Journal, 7 (8), pp.20-26.

69) Cheng, K.S., Isaacson, D., Newell, J.C. and Gisser, D. G. (1989): Electrode Models for Electric Current Computed Tomography, IEEE Transactions on Biomedical Engineering, 36 (9), pp.918-924.

70) Schlaberg, H. I., Baas, J. H., Wang, M., Best, J. L., Williams, R. A. and Peakall, J. (2006): Electrical resistance tomography for suspended sediment measurements in open channel flows using a novel sensor design, Part. Part. Syst. Charact., 23, pp.313-320.

71) Wang, M., Ma, Y., Holliday, N., Dai, Y., Williams, R. A. and Lucas G. (2005): A high performance EIT system, IEEE sensors J., 5 (2), pp.289-299.

72) Hoyle, B. S., Jia, X., Podd, F. J. W., Schlaberg, H. I., Tan, H. S., Wang, M., West, R. M., Williams, R. A., and York T. A. (2001): Design and application of a multimodal process tomography system, Meas. Sc. & Tech., 12, pp.1157-1165.

73) Lei, J., Liu, S., Guo, H. H., Li, Z. H., Li, J. T. and Han, Z. X. (2011): An image reconstruction algorithm based on semiparametric model for electrical capacitance tomography, Computers & Mathematics with Applications, 61, pp.2843-2853.

74) Fan, W. R. and Wang H. X. (2010): Maximum entropy regularization method for electrical impedance tomography combined with a normalized sensitivity map, Flow Meas. & Instr., 21, pp.277-283.

Author's short biography

M. G. Rasteiro

Maria da Graça Rasteiro graduated in Chemical Engineering at the University of Coimbra, did post graduate studies in Loughborough University, UK, and obtained a PhD in Chemical Engineering/Multiphase Processes, in 1988, in the same university, under the co-supervision of Professor Brian Scarlett. She is presently an Associate Professor in the Chemical Engineering Department of the University of Coimbra in Portugal. She was a member of the working group on Particle Characterization of the European Federation of Chemical Engineering, and is presently a member of the Portuguese Engineers Association and a founding member of the Portuguese Society for Engineering Education (SPEE). Her research interests have always been in the field of Particle Technology and she started the first Portuguese laboratory on particle characterization. Presently, she has got research interests in the field of particle aggregation, rheology of particle suspensions, solid/liquid flow modelling including fibre flow modelling, and on experimental techniques for flow visualization including tomographic techniques.

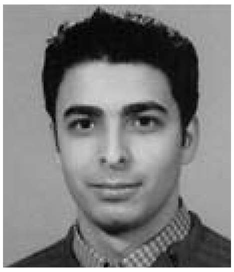

R. Silvae

Rui César Costa da Silva received his degree in Chemical Engineering from the University of Porto in 2006, In 2009, received his Master Degree in Chemical Engineering from the University of Coimbra. He is presently a Ph.D. student at the research group of Particle Technology and Multi-Phase Systems in the University of Coimbra. His research interests are in Multiphase Systems, Process Tomography and Computational Fluid Dynamics.

F. A. P. Garcia

Fernando A. P. Garcia was graduated as a chemical engineer in the Instituto Superior Técnico of the Technical University of Lisbon. He obtained a Master degree in Biological Engineering in Chemical Engineering and then a PhD degree in Chemical Engineering in the University of Birmingham, UK. He started his academic career in the University of Coimbra, first as an assistant demonstrator in the areas of fluid dynamics and transport phenomena. After his doctorate he became an assistant professor and latter an associate professor. Apart from the transport phenomena, his main interests are in the area of biocatalysis and downstream operations of fermentation processes and in treatment of industrial effluents. He is a member of several scientific institutions. He served as secretary of the ESAB, the European Section Applied Biocatalysis of the European Federation of Biotechnology and more recently as a member of the Executive Board, remaining as member of the Scientific Board.

P. M. Faia

Pedro M. Faia received is degree in Electrical Engineering (1990), is M.S. in Automation (1994) and is Ph.D in Electronic Materials (2003) from the University of Coimbra. He is an Auxiliary Professor at the Department of Electrical Engineering and Computers of the University of Coimbra where is research interests concern the research and development of solid state chemical sensors, sensor integration techniques, Electrochemical sensor and biosensors, Impedance Spectroscopy technique and applications. He is a member of the Portuguese Materials Society.

Modeling and Validation of Percolation Segregation of Fines from Coarse Mixtures during Shear Motion[†]

A.K. Jha and V.M. Puri*
Materials Research Institute, Department of Agricultural and Biological Engineering, The Pennsylvania State University[1]

Abstract

Segregation negatively impacts the product quality and depends on physical and mechanical properties of particulate materials. Size is the most dominant parameter contributing towards fines percolation segregation from mixtures with size distribution. A continuum theory-based convective and diffusive model was developed and validated to study time-dependent percolation segregation of fines. In addition, to scale-up the results, a mechanistic theory-based dimensional analysis approach was used to incorporate physical and mechanical properties of particulates in a time-independent model. In dimensional analysis model, size, shape, density, size ratio, mixing ratio, strain rate, strain, and bed depth were included.

The results showed that the time-dependent convective and diffusive model predicted the segregated mass of fines within the 95% confidence interval of measured fines for size ratios 2.4:1.0 and 1.7:1.0 at strains of 6% and 10%. Dimensional analysis results showed that the Coefficient of Variation (CoV) of the modeled values with respect to the experimental values were 18%, 15%, and 11%, respectively, for binary mixtures of urea and potash at strains of 2%, 6%, and 10% and strain rate of 0.25 Hz.

Keywords: Percolation segregation, constitutive models, dimensionless analysis, geometrical similitude, convective/diffusive, validation, scale-up

1. Introduction

Particulate materials are handled, stored, mixed, and processed in various industries such as agriculture, cosmetic, food, metal and metallurgy, nutraceutical, and pharmaceutical. Segregation occurs in particulates during the mentioned unit operations and negatively impacts the quality of products. Segregation in particulate materials occurs due to differences in the constituents' physical and mechanical properties (Rosato et al., 2002). Although segregation is governed by several parameters; however, simultaneously studying the effects of all parameters is not feasible due to the lack of fundamental understanding of their complex and nonlinear interactions. To gain greater and deeper insights, dominant variables should be identified and studied for different process parameters. Bridgwater and co-workers were the pioneers in identifying the dominant parameters and mechanisms of segregation and reported that size is the dominant parameter (Bridgwater et al., 1978 and Bridgwater, 1994). In practice, segregation has been quantified using coefficients, described using mechanisms, and analyzed using models (Rosato and Blackmore, 2000). Of the three, to model the segregation process for a specific mechanism is preferred so that the model could be applied to different operating conditions. To date, thirteen segregation mechanisms have been identified based on different operating conditions, i.e., trajectory, air current, rolling, sieving and sifting, impact, embedding, angle of repose, push-way, displacement or floating, percolation, fluidization, agglomeration, and, concentration driven displacement (Mosby et al., 1996; Salter, 1998; de Silva et al., 2000). Of the thirteen, percolation segregation is widely observed when materials are han-

---

[†] Accepted: July 8th, 2011

[1] University Park, PA 16802, USA

[*] Corresponding author:
E-mail: anjani.k.jha@gsk.com
TEL: (+1) 919-404-6404 FAX: (+1) 919-404-6197

ⓒ 2011 Hosokawa Powder Technology Foundation

dled, stored, mixed, and conveyed in various industries. Percolation segregation in particulate materials during various operations has been modeled when size, shape, and density of particulate were included. Percolation segregation in particulates is also affected by the mechanical conditions under which materials are handled (Tang and Puri, 2005 and Jha and Puri, 2009). Percolation segregation is defined as the migration of fine particles through a bed of coarse particles during gravity, shear, and vibration motions when subjected to dynamic conditions (Vallance and Savage, 2000). However, most of the studies were conducted for specific operating conditions using ideal materials (glass beads) and a few real-world materials (commonly used in industries) (Tang, 2004), few models were also developed for time-dependent process using ideal and real-world materials (Duffy and Puri, 2002). Tang and Puri, and Duffy and Puri used point feed and a layer of feed of fines in the coarse particle bed, respectively. Tang and Puri (2005) used point feed of fines in the coarse particle bed using real-world materials (poultry feed), which is not the common approach to handle particulates in industries. To overcome the limitations of previous studies, percolation segregation during shear motion was selected for modeling due to its wide application in industries. Segregation in particulates can be modeled by three approaches: continuum models, kinetic theory models, and discrete models (Moakher et al., 2000). Each modeling approach has advantages and disadvantages, continuum models consider the conservation principles of mass, momentum, and energy but neglect the discrete nature of particles; kinematic models consider the principle of interacting grains and colliding molecules in a dense gas but it is limited to the surface of an agitated granular mass; and discrete models consider the constituent grains to be distinct and apply the prescribed rules but limited to relatively small systems (Khakhar et al., 2001).

Tang (2004) developed a mechanistic theory which included the advantages of all the three mentioned modeling approaches. Mechanistic theory incorporated the continuum and discrete element theory by including the segregation potential of fines sizes and kinetic theory by studying the falling path of fines in larger size ratios.

Based on the literature review, application of the convective-diffusive model developed by Duffy and Puri is limited to large size ratios and ideal materials. To overcome this limitation, the model proposed and developed in this paper is for small size ratios, which includes resistance offered by the screen placed at the bottom; a common situation in modern day industrial practices. Dimensional analysis model developed by Tang (2004) is limited to binary mixtures and limited number of mechanical conditions. To improve the capability of mechanistic theory based dimensional analysis model, numbers of size components were increased and several operating conditions were included. As a result, the dimensional analysis model is more robust and applicable for scale-up of process from bench-scale to other relevant scales. The developed dimensional analysis model includes size, shape, density, size ratio, mixing ratio, strain rate, strain, and bed depth.

2. Materials and Methods

The Primary Segregation Shear Cell (PSSC-II) described sufficiently in Tang and Puri (2005 and 2007) and modified by Jha and Puri (2009) was used in this study. Since binary size mixture is considered to be the foundation of multi-size and continuous mixtures; a time-dependent convective and diffusive model is presented for binary mixtures (Jha, 2008). Nine different binary size ratios of potash and six different size ratios of urea in different mixing ratios were used in modeling studies. Mechanistic theory based time-independent model includes size, shape, density, size ratio, mixing ratio, strain rate, strain, and bed depth. Dimensional analysis model is suitable for process scale-up.

2.1 Test material selection and parameter determination

Urea and potash were selected for studying percolation segregation due to their extreme shape and density among the three major raw ingredients: urea, potash, and phosphate, used in the manufacture of different fertilizer blends (Jha and Puri, 2009 and Jha et al., 2008). For segregation study, three parameters including material bed depth, particle bed strain, and strain rate were selected for operating PSSC-II based on published results (Tang and Puri, 2005 and 2007). Bed depth of 85 mm (shear box height = 100 mm) was used to represent percolation of fines within bagged fertilizers in normal orientation, i.e., depth direction along gravity, during conveying, handling, and transportation. The selected strain of 2%, 6%, 10% and strain rates of 0.25, 0.5, 1.0 Hz represent the unfilled bag volume (≤15%) and intensity of motion, respectively, experienced by the blend in the bag during processing operations (<10 Hz) (Vursavus and Ozguven, 2004). The tests at strain rate of 1.0 Hz were conducted only at strain of 6% for binary mixtures of urea and potash due to limitation of operation of PSSC-II at high shear rate. Based on plant visits, strains higher than 6% at shear rate of 1.0 Hz seemed high for the operation of fertilizer blend manufacturing and conveying (Jha, 2008).

Different coarse and fine particle size ranges of the test material were obtained using US standard sieve of $(2)^{1/4}$ series. Potash and urea were received from local fertilizer blend plant facilities. Three size ranges (3,350-4,000; 2,800-3,350; and 2,360-2,800 µm) were designated as coarse and while three smaller size ranges (2,000-2,360; 1,700-2,000; and 1,400-1,700 µm) were designated as fines in the present study (**Table 1**). Since size spread of urea was small compared with potash, fines size range 1,400-1,700 µm were not found in sufficient quantity, therefore, this fine size was not included in the segregation study of urea. Size ratio of binary mixture was defined as the ratio of mean size of coarse particles to mean size of fine particles. For convective and diffusive model development using potash, two size ratios for each coarse sizes 3,675 µm, 3,075 µm, and 2,580 µm were used: 2.4:1.0, 1.7:1.0; 2.0:1.0, 1.4:1.0; and 1.7:1.0, 1.2:1.0, respectively, (**Table 1**). For urea, two size ratios for coarse size 3,675 µm, 3,075 µm, and 2,580 µm were used: 2.0:1.0, 1.7:1.0; 1.7:1.0, 1.4:1.0; and 1.4:1.0, 1.2:1.0, respectively (**Table 1**). Multi-size mixtures were used for dimensional analysis model development in addition to the materials used for convective diffusive model (**Tables 1 and 2**). For validation of convective and diffusive model, the size ratio 2.0:1.0 of potash was used at strains of 2%, 6%, and 10% and two strain rates of 0.25 and 0.5 Hz. For urea, two size ratios for coarse size 3,675 µm, 3,075 µm, and 2,580 µm used were 2.0:1.0, 1.7:1.0; 1.7:1.0, 1.4:1.0; and 1.4:1.0, 1.2:1.0, respectively, at strains of 2%, 6%, and 10% and strain rate of 0.5 Hz (**Table 3**). Conditions used for validation of dimensional analysis model are given in **Table 4**. Different mixing ratios (MR) were used for different size ratios based on weight proportion of different size (**Tables 1, 2, 3, and 4**) distributions found in low analysis such as 10-10-10 fertilizer samples collected from Commonwealth of Pennsylvania blend plants (Jha, 2008).

2.2 Test condition and experimental design

Coarse size particles were mixed with fine size particles in a 225-W six-speed bench-top mixer (Model-106772N, Type-M27, General Electric, Marketed by Wal-Mart Stores Inc., Bentonville, AR). Initial tests showed that 30 s at lowest rpm was sufficient to uniformly mix the binary, ternary, and quaternary size samples within the 95% confidence interval. Mixed samples were placed in shear box of the PSSC-II very gently with a scoop to avoid segregation. From statistical analysis of data, a separate experimental design was considered for binary, ternary and quaternary mixtures including dissimilar amount of fines (**Tables 1, 2, 3 and 4**). Based on published results (Duffy and Puri, 2002, and Tang and Puri, 2005), and preliminary testing with fertilizer blends, six replications were done for each set of experiments for testing percolation segregation using PSSC-II. A complete block design was selected for data analysis. A set of coarse particles was considered as a block of ex-

Table 1 Experimental design for binary size mixtures for potash and urea*

Material	Strain Rate (Hz)	Coarse size (µm)	Fine Size (µm)	Size Ratio	Mixing Ratio	Number
Potash	0.25 1.00**	3,675	1,550	2.4 : 1.0	50 : 50	6
			1,850	2.0 : 1.0	37 : 63	
			2,180	1.7 : 1.0	37 : 63	
Potash	0.25 1.00**	3,075	1,550	2.0 : 1.0	63 : 37	6
			1,850	1.7 : 1.0	50 : 50	
			2,180	1.4 : 1.0	50 : 50	
Potash	0.25 1.00**	2,580	1,550	1.7 : 1.0		6
			1,850	1.4 : 1.0	60 : 40	
			2,180	1.2 : 1.0	60 : 40	
Urea	0.25 1.00**	3,675	1,850	2.0 : 1.0	37 : 63	4
			2,180	1.7 : 1.0	37 : 63	
Urea	0.25 1.00**	3,075	1,850	1.7 : 1.0	37 : 63	4
			2,180	1.4 : 1.0	37 : 63	
Urea	0.25 1.00**	2,580	1,850	1.4 : 1.0	37 : 63	4
			2,180	1.2 : 1.0		
Total (replications)						30 × 3 × 6 = 540

*Strains of 2%, 6% and 10%

**Strain rate only at strain of 6%

Table 2 Experimental design for multi-size mixtures for potash and urea*

Material	Strain Rate (Hz)	Coarse size (μm)	Fine Size (μm)	Size Ratio	Mixing Ratio	Number
Potash	0.25	3,675+3,075	1,550	2.4:2.0:1.0	28:44:28	6
	0.50		1,850	2.0:1.7:1.0	22:39:39	
			2,180	1.7:1.4:1.0	22:39-39	
Potash	0.25	3,075+2,580	1,550	2.0:1.7:1.0	33:46:21	4
	0.50		1,850	1.4:1.4:1.0	29:42:29	
Potash	0.25	3,675+3,075+ 2,580	1,550	2.4:2.0:1.7:1.0	17:28:38:17	4
	0.50		1,850	2.0:1.7:1.4:1.0	13:25:37:25	
Urea	0.25	3,675+3,075	1,850	2.4:2.0:1.0	22:39:39	4
	0.50		2,180	2.0:1.7:1.0	22:39:39	
Urea	0.25	3,075+2,580	1,850	2.0:1.7:1.0	29:42:29	2
Urea	0.25	3,675+3,075+ 2580	1,850	2.0:1.7:1.4:1.0	13:25:37:25	2
Total (six replications)						22×6×3 = 396

*Strains of 2%, 6%, and 10%

Table 3 Validation design for binary size mixtures for potash and urea*

Material	Strain Rate (Hz)	Coarse size (μm)	Fine Size (μm)	Size Ratio	Mixing Ratio	Number
Potash	0.25	3,675	1,850	2.0:1.0	37:63	2
	0.50					
Potash	0.25	3,075	1,850	1.7:1.0	50:50	2
	0.50					
Potash	0.25	2,580	1,850	1.4:1.0	63:37	2
	0.50					
Urea	0.25	3,675	1,850	2.0:1.0	37:63	2
	1.00		2,180	1.7:1.0	37:63	
Urea	0.25	3,075	1,850	2.0:1.0	50:50	2
	1.00		2,180	1.7:1.0	50:50	
Urea	0.25	2,580	1,850	2.0:1.0	60:40	2
	1.00		2,180	2.0:1.0	60:40	
Total (three replications)						12×3×3 = 108

*At strains of 2%, 6%, and 10%

Table 4 Validation design for binary size mixtures for potash and urea*

Material	Strain Rate (Hz)	Coarse size (μm)	Fine Size (μm)	Size Ratio	Mixing Ratio	Number
Potash	0.5	3,675	1,550	2.4:1.0	50:50	3
			1,850	2.0:1.0	37:63	
			2,180	1.7:1.0	37:63	
Potash	0.5	3,075	1,550	2.0:1.0	63:37	3
			1,850	1.7:1.0	50:50	
			2,180	1.4:1.0	50:50	
Potash	0.5	2,580	1,550	1.7:1.0	67:33	3
			1,850	1.4:1.0	60:40	
			2,180	1.2:1.0	60:40	
Urea	0.5	3,675	1,850	2.0:1.0	37:63	2
			2,180	1.7:1.0	37:63	
Urea	0.5	3,075	1,850	1.7:1.0	37:63	2
			2,180	1.4:1.0	37:63	
Urea	0.5	2,580	1,850	1.4:1.0	60:40	2
			2,180	1.2:1.0	60:40	
Total (six replications)						15*6 = 90

*Strain of 6%

periment. Within each block, all treatments (replicate = 1 × 6 = 6) were randomly assigned. Convective and diffusive model was validated with binary mixtures of urea and potash (**Table 3**). Developed dimensional analysis model was validated for binary size mixtures of urea and potash (**Table 4**). Ternary and quaternary size ratios were not available in the sufficient quantity; therefore, these were not included in validation in the present study, i.e., deferred to a future study. All tests were conducted in an environment-controlled laboratory with average temperature of 22 degree C ± 3 degree C and relative humidity less than 40%.

2.3 Convective and diffusive model development

Binary mixtures of different size ratios of urea and potash were filled in the shear box up to 85 mm (the height of the shear box is 100 mm, dimension 150 mm × 76 mm × 100 mm). This is consistent with the height of bagged blended fertilizers (Jha, 2008). Based on size of coarse and fine particles, the bed of binary mixture of 85 mm height was divided into twelve slabs, i.e., 11 interfaces and two faces (1 to

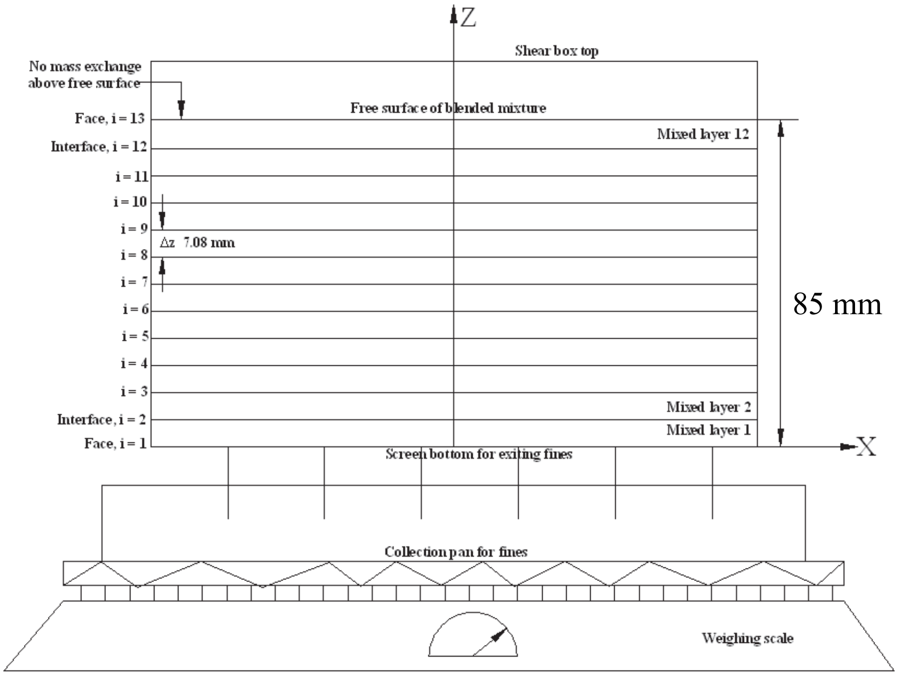

Fig. 1 Binary mixtures in shear box showing 12 equal size layers for model development.

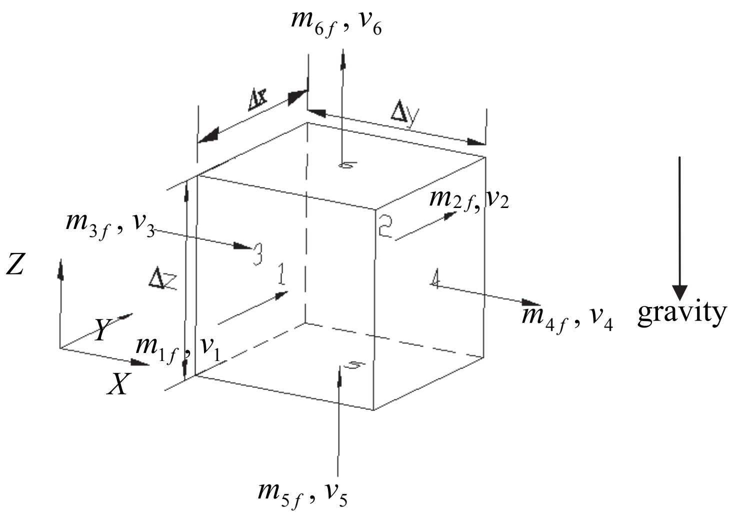

Fig. 2 Three-dimensional mass balances in the shear box.

13 levels) (**Fig. 1**). Mass balance of fines along the three principal directions is given in **Fig. 2**.

The main driving forces acting on binary mixtures in the shear box were gravity and shear (to-and-fro) motion of the box. Based on the nature of driving forces, the following two assumptions were made

1) velocity of fines along gravity (z-direction) can be represented by a mean effective value,
2) there is negligible concentration and velocity gradients along x and y directions compared with z-direction.

Based on the above, the governing convective-diffusive model is:

$$\frac{\partial m_f}{\partial t} = -\bar{v}\frac{\partial m_f}{\partial z} + \bar{D}\frac{\partial^2 m_f}{\partial z^2} \quad 0 < z < h = 85 \tag{1}$$

Here, $\bar{v}$ and $\bar{D}$ are the fundamental material parameters and represent the convective or demixing and diffusive or mixing components, respectively. The units of $\bar{v}$ and $\bar{D}$ are mm/min (dimension, L/T) and mm^2/min (dimension, L^2/T), respectively. The binary mixture in the shear box was filled to height of 85 mm.

Based on nature of the problem, it was assumed that binary mixtures were well mixed when placed in shear box (Jha and Puri, 2009). The following initial condition and two boundary conditions are used to describe segregation attributed to the percolation mechanism, i.e., solve differential equation (1):

$$m_{f0}(z, t=0) = m_{f0},\ 0 \le z \le 85 \tag{2}$$

There is a screen of opening size 2,360 μm at the bottom of the shear box, the preliminary experiments showed that there is no mass accumulation on the screen but some resistance was offered by screen bottom. The resistance "R" was included in the boundary condition at the screen bottom given in equation (3). Although top surface of binary mixture was slightly convex during the test (largest noted mound angle was ≤5°); therefore, for simplicity it was assumed that the top surface remains flat. With the help of above two conditions, two boundary conditions were formulated as given in equations (3) and (4). Crank and Nicolson (1947) proposed method that combines implicit and explicit method was used. Central difference method was for solving the differential equation.

$$\left(R\frac{\partial m_f}{\partial z}\right)_{z=1} = \left(m_f\right)_{z=1}$$

$$z = 85, t > 0,\ \text{Resistance offered by screen} \tag{3}$$

$$\frac{\partial m_f}{\partial z} = 0 \quad z = 0, t > 0, \text{No mass flux out of free surface} \tag{4}$$

Crank and Nicolson method reduces the number of calculations and results in a difference form that is valid (i.e., convergent and stable) for all finite values. For most stable results, Crank-Nicolson scheme takes average of explicit and implicit methods. The final form of equation using Crank and Nioloson method is given in equation 5. Details of solving equation is given in Jha (2008):

$$m_{f_i}^{j+1} - m_{f_i}^{j} = -\frac{\bar{v}\Delta t}{2\Delta z}\left(m_{fi-1}{}^{j+1} - m_{fi+1}{}^{j+1} + m_{fi-1}{}^{j} - m_{fi+1}{}^{j}\right)$$

$$+\frac{\bar{D}\Delta t}{2\Delta z^2}\begin{pmatrix} m_{fi-1}{}^{j+1} - 2m_{fi}{}^{j+1} + m_{fi+1}{}^{j+1} + \\ m_{fi-1}{}^{j} - 2m_{f_i}^{j} + m_{fi+1}{}^{j} \end{pmatrix} \tag{5}$$

Consider

$$\mu = \frac{\bar{v}\Delta t}{2\Delta z}, \text{ a dimensionless parameter}$$

$$\delta = \frac{\bar{D}\Delta t}{2\Delta z^2}, \text{ a dimensionless parameter}$$

The physical interpretations of μ and δ are mass-balance and concentration-gradient related parameters that represents the fraction of material leaving a given location. Solving for implicit and explicit parameters after incorporating μ and δ. Rearranging equation (5) leads to equation 6.

$$2(m_{f_i}^{j+1} - m_{f_i}^{j}) = -\mu\left((m_{f_i}^{j+1} - m_{f_{i-1}}^{j+1}) + (m_{f_i}^{j} - m_{f_{i-1}}^{j})\right)$$

$$+\delta\begin{pmatrix} (m_{f_{i+1}}^{j+1} - 2m_{f_i}^{j+1} + m_{f_{i-1}}^{j+1}) \\ +(m_{f_{i+1}}^{j} - 2m_{f_i}^{j} + m_{f_{i-1}}^{j}) \end{pmatrix} \tag{6}$$

The final form of equation (6) is given in equation (7)

$$-(\mu+\delta)m_{f_{i-1}}^{j+1} + (2+\mu+2\delta)m_{f_i}^{j+1} - \delta m_{f_{i+1}}^{j+1}$$

$$= (\mu+\delta)m_{f_{i-1}}^{j} + (2-\mu-2\delta)m_{f_i}^{j} + \delta m_{f_{i+1}}^{j} \tag{7}$$

Incorporating the two boundary conditions, a program was written in MATLAB (Mathworks Inc, Natick, Massachusetts) to solve the finite difference equations with the given boundary and initial conditions (Jha, 2008). The precision of μ and δ was kept to two decimal places to be consistent with variations in experimental data. Equation (8) represents the

RMSE between experimental and modeled data. The values of μ and δ that produced the smallest error were taken as the material parameter for a given set of operating conditions. The df is the degree of freedom. The two independent variables μ and δ are calculated so that the degree of freedom is 2. In equation (8), $\hat{m}_i$ and m_i represent the experimentally measured and modeled mass values in the layer i.

$$Root\ mean\ square\ error\,(RMSE) = \sqrt{\frac{\sum_{i=1}^{n}(\hat{m}_i - m_i)^2}{n - df}} \quad (8)$$

where, n = number of observations

2.4 Dimensional analysis model development

Based on the physics of the problem and to correctly apply Fourier's principle of dimensional homogeneity without omitting significant variables (Streeter et al., 1996, Murdock, 1993), percolation segregation in bagged fertilizer was assumed to be affected by size, shape, density, and mixing ratio, relative movement (strain), intensity of movement (strain rate), and fill height of bagged blended fertilizers. As mechanistic theory states that a mathematical relationship exists between percolation segregation in particulate materials (e.g., fertilizer) and physical and mechanical properties of the particulates. In the case of fertilizer, physical property includes size (as Size Guide Number, SGN, which is defined as size in millimeters multiplied by 100), size ratio (as Uniformity Index, UI, which is the ratio of 100 times (size of 10 percentile particle divided by 95 percentile particle), shape, density, and mixing ratio and mechanical property includes strain (displacement), strain rate (intensity of to-and-fro motion), and bed depth. However, there are other physical parameters that indirectly affect segregation such as surface texture, surface composition, and electrostatics; their effect being secondary compared with the gravitational force, were not included. The physical and mechanical parameters used in this model are defined below for the better understanding.

Buckingham Pi theorem was to be used to develop dimensional analysis model but the number of variables were not sufficient to make proper dimensionless grouping. Based on fertilizer blend plant visits, experimental data, and previous experiences of Tang and Puri (2007), the physical and mechanical parameters that significantly affect percolation segregation are included in the mechanistic theory and grouped in such a fashion that each term is dimensionless. Based on these considerations, a dimensional analysis model was proposed and is given below in equation (9).

$$\frac{NSR}{Strain\,Rate} = c\,(Shp)^l \left(\frac{Coarse\ size}{Bed\ Depth}\right)^m (Mixing\ Ratio)^n (Strain)^o (Size\ Ratio)^p \quad (9)$$

where,
NSR = Segregated fines/fines in the mixture/Total time of PSSC-II operation, kg/kg-s
Strain Rate = intensity of movement of bagged fertilizer, Hz
Shp = shape and density of fertilizer, dimensionless
Coarse Size = size guide number (SGN) or size of particle, mm*100
Bed Depth = depth of fertilizer in the bag, mm
Mixing Ratio = ratio of mass of coarse to mass of fines*100, dimensionless
Displacement = relative displacement two side walls (length wise) of bagged fertilizer, %
Size Ratio = defined via Uniformity Index, UI, which is defined as 100 times the (size of 10 percentile particle divided by 95 percentile particle),, dimensionless
l = power, indicates the contribution of shape and density to NSR/Strain rate
m = power, indicates the contribution of coarse size and number of layers of coarse in the bed depth to NSR/Strain rate
n = power, indicates the contribution of mixing ratio to NSR/Strain rate
o = power, indicates the contribution of strain to NSR/Strain rate
p = power, indicates the contribution of size ratio to NSR/Strain rate

The constant c and exponents l, m, n, o, and p were calculated by taking logarithm of equation (6) followed by linear regression analysis. Their physical meaning is needed to understand the dimensional analysis model well. Segregation under shear motion is contributed by the difference in physical and mechanical properties of particulates. On the left side, the model has two parameters, normalized segregation rate (NSR) and strain rate. The segregation measuring parameter NSR was developed to make segregation rate independent of amount of initial fines in the material mixtures. The NSR contains two fundamental dimensions, mass (M) and time (T). The second parameter strain rate is the operating parameter of the PSSC-II and it has the unit of time

(T). These two parameters make the left side of the above equation dimensionless. Thus, the ratio of NSR to strain rate $\left(\frac{NSR}{Strain\ Rate}\right)$ is a dimensionless quantity, which, physically, is an index to determine the segregation potential of the test material.

On the right side of the equation, the dominant physical and mechanical parameters of materials are included. The dominant parameters for the PSSC-II under shear motion contributing to segregation included coarse size, shape, mixing ratio, strain, size ratio, and bed depth. As used, the use of porosity may not be nearly as accurate as using individual particle shape using dimensions (length, width) or index compared with spherical-shaped particle (Gotoh, 1997). How these parameters have affected the segregation of fines in the test materials must be understood before creating sets for making dimensionally homogenous equation. The segregation potential of binary size mixtures is proportional to the coarse size, size ratio, strain, mixing ratio, and shape and inversely proportional to bed depth. The physical and mechanical parameters were grouped in such a way that the right side of the equation must be dimensionless to make the dimensionally homogeneous equation. Both bed depth and coarse size have the same dimension, length (L). The shape, mixing ratio, strain, and size ratio are dimensionless.

The size of coarse particle and size ratio were among the main contributors to the magnitude of NSR. Furthermore, in binary mixtures below size ratio 2.5, NSR exponentially increased with the size ratio. The NSR also increased with the increase in coarse size in binary mixtures (Jha et al., 2008). Therefore, a dimensionless equation after taking natural logarithm on both sides based on Buckingham Pi theorem is given below in equation (10):

$$\ln\left[\frac{NSR}{Strain\ Rate}\right] = l\ln(Shape) + m\ln\left(\frac{Coarse\ size}{Bed\ Depth}\right) + n\ln(Mixing\ Ratio) + p\ln(Strain) + p\ln(Size\ Ratio) \quad (10)$$

The physical and mechanical parameters were obtained from the experimental data and NSR was also calculated individually for these parameters. The size ratio rounded off to the first decimal place was used for data collection. The root-mean square error (RMSE) and the coefficient of variation (CoV) were calculated to evaluate the accuracy of the model through equations (11) and (12).

$$RMSE = \sqrt{\frac{\sum_{i=1}^{N}(P_i - R_i)^2}{N}} \quad (11)$$

RMSE = root-mean square error

P_i= ith fitted value corresponding to the ith observation

R_i= ith observation

N= number of observation

$$CoV = \frac{RMSE}{Experimental\ mean} \times 100\% \quad (12)$$

3. Results and Discussion

Results of the convective and diffusive segregation model and dimensional analysis model development and validation are presented and discussed in the following sections.

3.1 Convective and diffusive segregation model development

The measured and modeled segregated mass versus time relationships for potash and urea are given in **Fig. 3**. **Fig. 3a** shows the segregated mass vs. time relationship for size ratio 2.4:1.0 of potash at strain of 6% and strain rate of 0.5 Hz. The cumulative segregated mass increased with time. For size ratio 2.4:1.0, convective and diffusive segregation model values were within the 95% confidence interval (CI) of measured values. For size ratio 1.7:1.0, the modeled segregated mass values were always lower than the measured segregated mass values but within the 95% confidence interval (**Fig. 3b**). **Fig. 3c** shows the segregated mass vs. time relationship for size ratio 2.4:1.0 of potash at strain of 10% and strain rate of 0.5 Hz. For size ratio 2.4:1.0, convective and diffusive segregation model represents the measured values are also within the 95% confidence interval. For size ratio 1.7:1.0, the modeled segregated mass values were initially higher and after 25 minutes lower than the measured segregated mass values (**Fig. 3d**). The initial over prediction and later under prediction of segregated mass were observed because at higher strain of 10%, time was not enough for fine particles to percolate through the void spaces of coarse particles and also due to bridges formed in the binary mixtures. At later stage (after 25 minutes), bridges very likely collapsed and fine particles found the way through void spaces of coarse particles because of less fines in binary mixtures. The initial modeled segregated mass upto 10 minutes of PSSC-II operation was not within the 95% confidence interval of the measured segregated mass. For size ratio 2.4:1.0 and 1.7:1.0 of potash, convective and diffusive segregation model segregated mass values were not within the 95% confidence interval at strain of 2% and strain rate of 0.5 Hz. At strain of 2% and strain rate of 0.5 Hz, the input energy was not sufficient to create large void spaces so that fines could percolate and bridges might have formed within the binary size mixtures of potash. Similar results were obtained at three strains of 2%, 6%, and 10% and strain rate of 0.25 Hz for size ratios 2.4:1.0 and 1.7:1.0; also for size ratios 2.0:1.0 and 1.4:1.0 when the coarse size was 3,075 μm. The modeled segregated mass was not within the 95% confidence interval for size ratios 1.7:1.0 and 1.4:1.0 when the coarse size was 2,580 μm.

At strain rate of 0.25 Hz and stain of 6%, convective and diffusive segregation modeled segregated urea mass was not within the 95% confidence interval; however, model under-predicted in the initial phase upto 13 minutes and thereafter over-predicted. At strain rate of 1.0 Hz, the modeled segregated mass values were not within the 95% confidence interval and under-predicted in the initial phase upto 22 minutes and thereafter over-predicted. In the case of urea over and under prediction of were observed in binary mixtures for the size ratio 2.0:1.0 at different times. The shape of urea was spherical and density was lower than that of potash. Gravity is the dominant force for material separation in binary mixtures, the combined effect of size, shape, and density was more in the case of potash compared with urea. The bridges very likely formed and energy supplied by the shear box and dominant gravity force was not sufficient to break those bridges initially and also time was not sufficient for fines to percolate through void spaces of coarse particles bed.

If energy imparted by shear box was sufficient to break bridges, then fines particles percolated through coarse particles bed. With increasing time, proportion of fines decreased that increased the rate of segregation causing model to under-predict segregated mass. Similar results were obtained for size ratio 1.7:1.0 at strain rates of 0.25 Hz and 1.0 Hz and for size ratios 2.0:1.0 and 1.7:1.0 at strains of 10% and 2% for strain rates of 0.25 Hz and 0.5 Hz. The convective and diffusive model well represented the measured segregated mass values of binary size ratios when the size ratios were higher than 1.4:1.0 and coarse size was larger than 2,580 μm. The accuracy of the model was the highest at strain of 6% because void space created in the coarse particles bed and time available to percolate for fine particles was sufficient. The under and over predictions of modeled

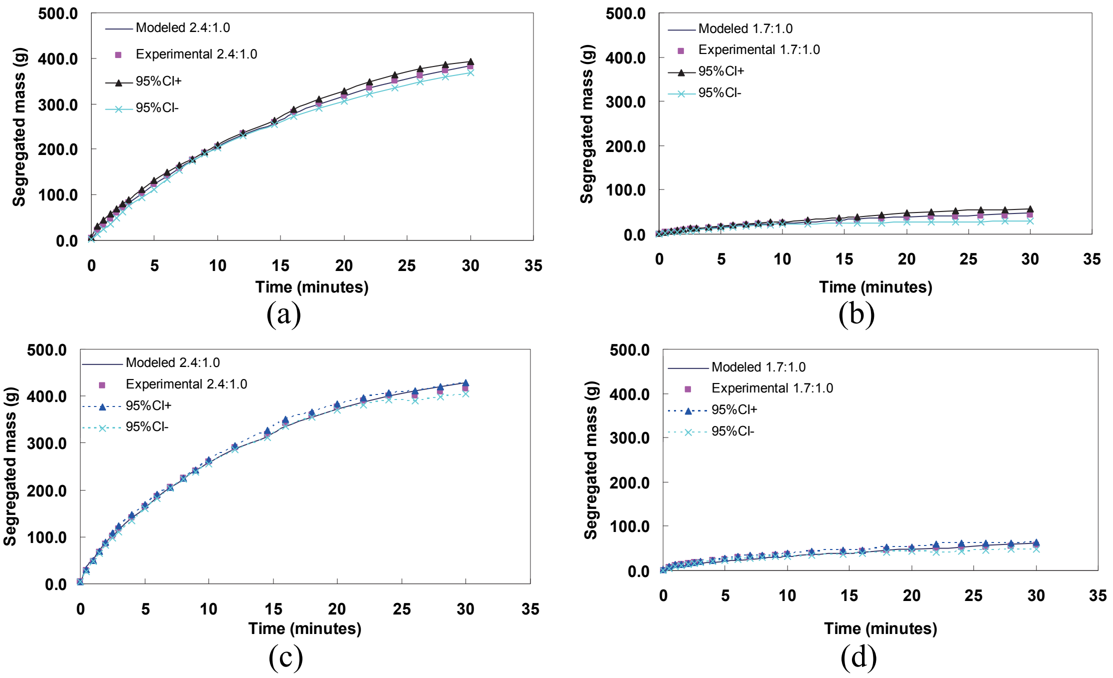

Fig. 3 Modeled and experimental data of potash at strain rate of 0.5 Hz (a) size ratio 2.4:1.0 at strain of 6%, (b) size ratio 1.7:1.0 at strain of 6%, (c) size ratio 2.4:1.0 at strain of 10%, (d) size ratio 1.7:1.0 at strain of 10%.

segregated mass might also have been observed because of other physical properties involved such as surface texture, and surface property. These properties cannot be studied with the discussed continuum theory based model. To overcome the limitation of continuum theory model, a hybrid model comprising continuum and discrete element theories (including multiscale formulations) needs to be developed, i.e., combines the advantages of continuum and discrete element models (including multiscale formulations) to explain segregation at particle-particle level and secondary and tertiary level structures.

4. Dimensional Analysis Model

The exponents l, m, n, o, and p were determined using linear regression. Equation (10) was linearly regressed using data for binary mixtures of urea and potash and binary mixtures when urea and potash were taken together. Equation (10) was also regressed using data of ternary mixtures of urea and potash. Quaternary mixtures were not used individually for linear regression because only limited (three) number of quaternary mixtures were available. Finally equation (16) was linearly regressed when binary, ternary, and quaternary mixtures of urea and potash were taken together. For multi-size mixtures, the equation was regressed in two different ways. In the first case, the average shape or porosity (53%) was considered when the porosity of urea and potash mixtures was 51% and 55%, respectively so that porosity could be treated as constant to eliminate a term from the final equation. In the second approach, the actual porosity of urea and potash was used for determining the coefficient l, m, n, o, and p.

4.1 Determination of exponents l, m, n, o, and p for multi-size mixtures

Regression-based variance of analysis for binary mixtures of potash showed that all five terms, Constant, ln(Size Ratio), ln(Coarse Size/Bed Depth), ln(Mixing Ratio), and ln(Strain) had significant effect on NSR/Strain Rate ($p<0.05$). The values of these five exponents l, m, n, o, and p (14.6, 7.17, -8.02, -1.28, and 1.63, respectively) were obtained through regression analysis and equation is summarized below (13).

$$\ln\left(\frac{NSR}{Strain\ Rate}\right) = 14.6 + 7.17\ln(Size\ Ratio) \\ - 8.02\ln\left(\frac{Coarse\ size}{Bed\ depth}\right) - 1.28\ln(Mixing\ Ratio) \\ +1.63\ln(Strain) \qquad (13)$$

The porosity of binary mixture of potash was constant (55%) and was incorporated into constant "c" in the linear regression analysis. The contributions of Size Ratio and Strain were proportional to NSR/Strain Rate, whereas contributions of Coarse Size/Bed Depth and Mixing Ratio were inversely proportional. Positive constant l and exponents p and o represent that the effect of porosity, Size Ratio, and Strain are proportional to NSR/Strain Rate, i.e., increase in porosity, Size Ratio, and Strain will increase the NSR/Strain Rate. The negative exponents m and n represent Coarse Size/Bed Depth and Mixing Ratio showed inverse relation with NSR/Strain Rate, i.e., increase in Coarse Size/Bed Depth and Mixing Ratio will decrease NSR/Strain Rate.

Regression-based variance of analysis for ternary potash mixtures showed that all five terms, Constant, ln(Size Ratio), ln(Coarse Size/Bed Depth), ln(Mixing Ratio), and ln(Strain) had significant effect on NSR/Strain Rate ($p<0.05$). Values of these five parameters l, m, m, o, and p (22.6, 8.64, -9.12, -2.47, and 1.88, respectively) were obtained through regression analysis and are given in **Table 5** with R2 = 0.943. The R-square value for ternary size mixtures (0.943) was higher than the binary size mixture (0.90) because coarse size 2,580 μm was included only twice compared with 5 times in the binary mixtures.

The porosity of ternary mixture of potash was constant (55%) and incorporated into constant "c" in the linear regression analysis. The contribution of Constant, Size Ratio, Coarse Size/Bed Depth, Mixing Ratio, and Strain was larger for ternary mixtures vs. binary mixtures when the regression equation was developed. Experimental design for binary and ternary mixtures showed that ternary mixtures had used coarse size 2,580 μm used twice vs. three times with binary mixtures (**Tables 1 and 2**). Exponents of Size Ratio and Coarse Size/Bed Depth were higher compared with Mixing Ratio and Strain. It means Size Ratio and Coarse Size/Bed Depth contributed more to NSR/Strain Rate compared with Mixing Ratio and Strain. Also the effect of Coarse Size/Bed Depth was the highest among five variables followed by Size Ratio. Results showed that size was the most dominant variable contributing towards segregation of fines from well mixed systems.

4.2 Validation of convective and diffusive segregation model

The convective and diffusive model was validated for size ratios 2.0:1.0 at strains of 2%, 6%, and 10% and strain rates of 0.25 Hz and 0.5 Hz (**Table 3**). The convective and diffusive parameters were estimated using linear interpolation from size ratios 2.4:1.0 and 1.7:1.0 for potash and strain rates of 0.25 and 1.0 Hz for urea at strains of 2%, 6%, 10%. The goal of interpolation was to determine convective, diffusive, and resistance parameters to predict segregated mass for potash and urea of size ratio 2.0:1.0. **Fig. 4** shows the graphical representation of modeled data and experimental data. With the help of interpolated convective, diffusive, and resistance values, the segregated mass values were calculated but the modeled segregated mass values under predicted the measured segregated mass values at strains of 2%, 6%, and 10%. For size ratio of 2.0:1.0 of potash, at the strain of 6% and strain rate of 0.5 Hz after 30 minutes, the actual modeled segregated mass was 7.3 g, which is higher than the experimental segregated mass. Whereas, the segregated mass calculated from the model operating parameters convective, diffusive, and resistance obtained from linear interpolation was 45.3 g higher than experimental segregated mass. The modeled segregated mass was within the 95% confidence interval of the experimental values. The modeled convective, diffusive, and resistance parameters were 0.28 mm/min, 74.18 mm2/min, and 17 mm, respectively. Whereas these parameters calculated from linear interpolation were 0.85 mm/min, 45.11 mm2/min, and 6.75 mm, respectively.

The convective parameter was higher in the case of linear interpolation but diffusive and resistance parameters were higher in the modeled case. In the case of linear interpolation convective parameter responsible for segregation was overestimated but the other two parameters responsible for mixing (diffusive) and resistance responsible for offering resistance in binary mixture due to bridging were underestimated. The convective parameter is dominant because of dominant gravity driving force on larger fines size that resulted in over estimation of the segregated mass. The interpolation of convective, diffusive, and resistance parameters is not the best approach because the NSR is not linearly dependent on (ln(NSR) = m ln(size ratio). Where m is the exponent of size ratio and varies with size ratio and type of material.

For size ratio of 2.0:1.0 of potash, at strain of 10% and strain rate of 0.5 Hz after 30 , the modeled segregated mass was 8.4 g (643.2g) higher than the experimental segregated mass. Whereas, the segregated mass calculated from the model operating parameters convective, diffusive, and resistance obtained from linear interpolation was 24.5grams (643.2g) higher than experimental segregated mass. The modeled segregated mass was within the 95% confidence interval of the experimental values. The modeled convective, diffusive, and resistance parameters were 0.99mm/min, 98.24mm^2/min, and 13.00mm, respectively. Whereas these parameters calculated from linear interpolation were 1.20 mm/min, 42.61 mm^2/min, and 2.75mm, respectively. For size ratio of 2.0:1.0 of urea, at the strain of 6% and strain rate of 0.5Hz after 30minutes, the modeled segregated mass was 2.3g higher (469.0g) than the experimental segregated mass. Whereas, the segregated mass calculated from the model operating parameters convective, diffusive, and resistance obtained from linear interpolation was 15.4g (469.0g) lower than experimental segregated mass. The modeled segregated mass was not within the 95% confidence interval of the experimental values. The modeled convective, diffusive, and resistance parameters were 0.00mm/min, 21.05mm^2/min, and 1mm, respectively. Whereas these parameters calculated from linear interpolation were 0.00 mm/min, 16.54mm^2/min, and 1mm, respectively. Sufficient number of size ratios was not available so that a definite relationship between NSR and size ratio

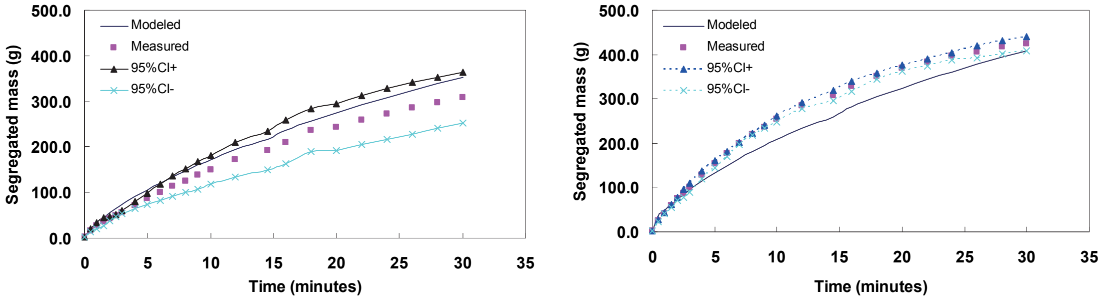

(a) (b)

Fig. 4 Validation at strain rate of 0.5 Hz for size ratio 2.0:1.0 (a) potash-6%, and (b) potash-10%, 95%CI+ and 95%CI- upper and lower limits of CI.

could be deduced. The segregation behavior of urea at strain of 6% and strain rates of 0.25 and 1.0Hz could not be used to explain the segregation behavior at intermediate strain rate 0.5Hz accurately. To explain the segregation behavior of fines in urea at strain intermediate strain of 0.5Hz and smaller size ratios of potash (<1.7:1.0), a hybrid model (as mentioned previously) which combines the principles of continuum and discrete element theories needs to be used.

5. Validation of the dimensional analysis segregation model

Accuracy of the model developed using binary mixtures of potash was determined through the comparison of experimental values to modeled values for binary mixtures of potash and urea. When equation (10) was used for validation purposes, the CoV, RMSE, and overall mean of the modeled values when compared with the experimental values were 18%, 0.63, and 2.85, respectively, for binary mixtures of urea and potash at strain of 2% and strain rate of 0.25Hz. The CoV, RMSE, and overall mean of the modeled values when compared with the experimental values were 15%, 0.82, and 4.64, respectively, for binary mixtures of urea and potash at strain of 6% and strain rate of 0.25Hz. Whereas, at strain of 10% and strain rate of 0.25Hz, the CoV, RMSE, and overall mean of modeled values when compared with experimental values were 11%, 0.58, and 5.47, respectively. However, the overall mean of the NSR for binary mixtures increased with the increase in strain from 2% to 10% although CoV for binary mixtures of urea and potash decreased with the increase in strain from 2% to 10% for the same size ratios.

To validate the model, comparison between the modeled data and experimental values was performed for the size ratios for which model was developed but at intermediate strain rate. When equation (7) was used for validation purposes, the CoV, RMSE, and overall mean of the modeled values to the experimental values were 9.1%, 0.47, and 4.48, respectively (**Fig. 5**). To validate the model, comparison between the modeled data and experimental values was performed for size ratios for which model was developed but at intermediate strain rate of 0.5Hz.

6. Conclusions

Percolation segregation in binary, ternary, and quaternary mixtures of urea and potash was modeled by convective and diffusive segregation model and dimensional analysis scale-up enabling model. Convective and diffusive model included binary size ratios of urea and potash for both model development and validation. Model over-predicted for small size ratios and under-predicted large size ratios but data were within 95% confidence interval. Dimensional analysis model included the range of variables size ratio, shape, density, strain rate, and strain to predict NSR.

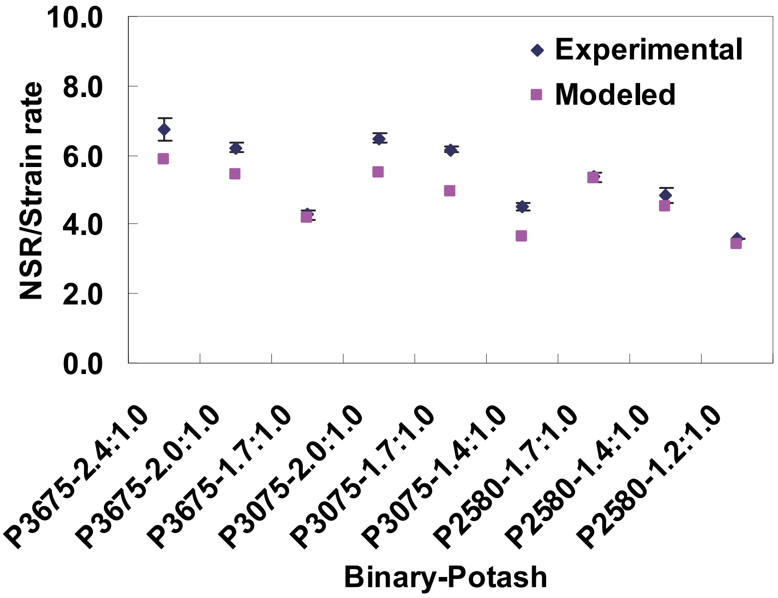

Fig. 5 Validation of dimensional analysis model by comparison of modeled values to experimental values for potash at strain rate of 0.5Hz, with ± SD as error bars (P-potash, first four number after P is mean size of coarse particles followed by binary size ratio corresponding to coarse mean size).

Developed dimensional analysis model was validated for binary mixtures of urea and potash. Furthermore, all the binary, ternary, and quaternary mixtures were combined with and without keeping porosity constant but found not be the representative of experimental data. Based on results, the following conclusion can be drawn:

1) For size ratio of 2.0:1.0 of urea, at the strain of 6% and strain rate of 0.5Hz after 30 minutes, the modeled segregated mass was 2.3g higher than the experimental segregated mass. Whereas, the segregated mass calculated from the model operating parameters convective, diffusive, and resistance obtained from linear interpolation was 15.4g lower than experimental segregated mass. The modeled segregated mass was not within the 95% confidence interval of the experimental values.
2) At the strain of 10% and strain rate of 0.5 Hz after 30 minutes, for size ratio 2.0:1.0 of urea, the modeled convective, diffusive, and resistance parameters were 0.00mm/min, 21.05mm^2/min, and 1.00mm, respectively. Whereas these parameters calculated from linear interpolation were 0.00mm/min, 16.54mm^2/min, and 1.00 mm, respectively.
3) For size ratio of 2.0:1.0 of potash, at the strain of 6% and strain rate of 0.5Hz after 30 minutes, the modeled segregated mass was 7.3g higher than the experimental segregated mass. Whereas, the segregated mass calculated from the model operating parameters convective, diffusive, and resistance obtained from linear interpolation was 45.3g higher than experimental segregated mass. The modeled segregated mass was within the 95% confidence interval of the experimental values.
4) At the strain of 10% and strain rate of 0.5Hz after 30 minutes, for size ratio 2.0:1.0 of potash, the modeled convective, diffusive, and resistance parameters were 0.99mm/min, 98.24mm^2/min, and 13.00mm, respectively. Whereas these parameters calculated from linear interpolation were 1.20mm/min, 42.61mm^2/min, and 2.75mm, respectively..
5) When equation (5) was used for validation purposes, the CoV of the modeled values to the experimental values were 18%, 15%, and 11% for binary mixtures of urea and potash at strains of 2%, 6%, and 10% and strain rate of 0.25Hz.
6) The dimensional analysis model developed by the binary mixtures of potash was sufficient to represent the binary, ternary, and quaternary mixtures of urea and potash.

This study showed the strengths and revealed limitations of continuum theory-based segregation model. To overcome the limitations, multiscale formulations that combine the principles of continuum and discrete element theories (involving multi-scale formulations) need to be developed to better model the segregation of fines; for not only smaller size ratio, but one that spans all size ratios.

7. References

Bridgwater, J., M. H. Cooke, and A. M. Scott (1978): Interparticle percolation: equipment development and mean percolation velocities. Institution of Chemical Engineers, 56, pp. 157-167.

Bridgwater, J. (1994): Mixing and segregation mechanisms in particle flow. Ed.: Mehta, A. Granular material-an interdisciplinary approach, pp. 161-193. Springer-Verlag New York, Inc.

Crank, J., and P. Nicolson (1947): A practical method for numerical evaluation of solutions of partial differential equations of the heat-conduction type. Proceedings of the Cambridge Philosophical Society, 43, pp. 50-67.

de Silva, S., A. Dyroy, and G. G. Enstad (2000): Segregation mechanisms and their quantification using segregation testers. Eds: Rosato, A. D. and D. L. Blackmore. IUTAM Symposium on Segregation in Granular Flows, pp. 11-29. Kluwer Academic Publishers.

Duffy, S. P. and V. M. Puri (2003). Development and validation of a constitutive model for size-segregation during percolation. KONA Powder and Particle Journal, 21, pp. 151-162.

Jha, A. K. (2008): Percolation segregation in multi-size and multi-component particulate mixtures: Measurement, sampling, and modeling, PhD Dissertation, Pennsylvania State University.

Jha, A. K., J.S. Gill, and V.M. Puri (2008): Percolation segregation in binary size mixtures of spherical and angular-shaped particles of different densities, Part. Sci. Technol., Int. J. 26 (5), pp. 482–493.

Jha, A. K. and V.M. Puri (2009): Percolation segregation of binary mixtures under periodic movement, Powder Technology, 195(2), pp. 73–82.

Gotoh, K. (1997): Particle shape characterization. Ed: Gotoh, K., H. Masuda, and K. Higashitani. Powder Technology Handbook (2nd Ed.). Marcel Dekker Inc.

Khakhar, D. V., A. V. Orpe, and J. M. Ottino (2001): Continuum model of mixing and size segregation in a rotating cylinder: concentration-flow coupling and streak formation. Powder Technology, 116, pp. 232-245.

Moakher, M., T. Shinbrot, and F. J. Muzzio (2000): Experimental validated computations of flow, mixing and segregation of non-cohesive grains in 3D tumbling blenders. Powder Technology, 109, pp. 58-71.

Mosby, J., S. R. de Silva, and G. G. Enstad (1996): Segregation of particulate materials-mechanisms and testers. KONA Powder and Particle Journal, 14, pp. 31-42.

Murdock, J. W. (1993): Fundamental fluid mechanics for the practicing engineer, Marcel Dekker, Inc. New York, NY.

Rosato, A. D. and D. L. Blackmore (2000): Segregation in granular flows. Proceedings of the IUTAM Symposium held in Cape May, NJ, June 5-10, 1999. Kluwer Academic Press, Boston, MA. Pp. 342.

Rosato, A. D., D. L. Blackmore, N. Zhang, and Y. Lan (2002): A perspective on vibration induced size segregation of granular materials, Chemical Engineering Science, 57, pp. 265-275.

Salter, G. F. (1998): Investigations into the segregation of heaps of particulate materials with particular reference to the effects of particle size, Ph.D. diss., University of Greenwich.

Shinohara, K. and B. Golman (2002): Particle segregation of binary mixture in a moving bed by penetration model. Chemical Engineering Science, 57, pp. 277-285.

Streeter, R. L., G. Z. Watters, and J. K. Vennard (1996): "Elementary fluid mechanics", John Wiley & Sons, Inc.

Tang, P. (2004): Percolation and sieving segregation patterns-Quantification, mechanistic theory, model development and validation, and application, Ph.D. diss. The Pennsylvania State University, University Park, PA.

Tang, P. and V. M. Puri (2005): An innovative device for quantification of percolation and sieving segregation patterns – Single component and multiple size fractions. Particulate Science and Technology, An International Journal, 23 (4), pp. 335-350.

Tang, P. and V. M. Puri (2007): Segregation Quantification of Two Component Particulate Mixtures – Effect of Particle Size, Density, Shape, and Surface Texture, Particulate Science and Technology, An International Journal, 25(6), pp. 571-588.

Vallance, J.W. and S.B. Savage (2000): Particle segregation in granular flows down chutes. Eds: Rosato, A.D. and D.L. Blackmore. IUTAM Symposium on Segregation in Granular Flows, pp. 31-51. Kluwer academic Publishers.

Vursavus, K. and F. Ozguven (2004): Determining the effects of vibration parameters and packaging method on mechanical damage in golden delicious apples. Turkey Journal of Agriculture, 28, pp. 311-320.

Author's short biography

Virendra M. Puri

Virendra M. Puri, University Distinguished Professor, has been involved in research in the field of powder science, engineering, and technology for over three decades. He has served as the Acting Director of the NSF/IUCRC (Industry University Cooperative Research Center) – the Particulate Materials Center. Professor Puri has co-authored numerous publications. In addition, he is co-inventor and holder of patents in the area of powder flow, deposition and compaction. Professor Puri has a Copyright for multi-purpose computational software dealing with powder processing applications. He has been invited to serve on Editorial Boards, International Advisory Boards, and Chairpersons of several bulk solids-related publications and professional activities. Professor Puri is Co-Editor-in-Chief of Particulate Science and Technology, An International Journal. He regularly offers seminars, courses, and workshops in powder mechanics to industry and academia. Professor Puri has received several teaching and research awards.

Dr. Anjani Jha

Currently, Dr. Anjani Jha is a Product Owner MDPI in the Technical Department at GlaxoSmithKline, Zebulon, NC, USA. Before joing GlaxoSmithKline, Dr. Jha worked as a postdoctoral associate in the Chemical Engineering Department at Massachusetts Institute of Technology. He is heavily involved in the area of particulate science and technology research and results implementation in downstream processing of solids. The reported work was completed during Dr. Jha's PhD research

Na-Bentonite and MgO Mixture as a Thickening Agent for Water-Based Paints[†]

F. Karakaş[1], G. Pyrgiotakis[2], M.S. Çelik[1] and Brij M. Moudgil[2]
Istanbul Technical University, Mineral Processing Engineering Dept.[1]
Particle Engineering Research Center, University of Florida[2]

Abstract

Rheology plays a major role both in production and application stages of paints. Na-Bentonite, clay based thickening agent, is generally used to modify the viscosity of paints, since it is more economical and environmentally friendly compared to polymer based thickening agents. In solvent based systems bentonite is generally modified with quaternary ammonium salt to obtain appropriate polarity. However it is necessary to improve its thickening character to obtain optimum performance in water based paints. It has been reported that its flow behavior and stability can be improved by additives like MgO and LiCl for use in water based system.

In this paper, Na-Bentonite and MgO mixture was evaluated as an additive in water-borne paints. Standard paint tests such as viscosity, density, opacity, gloss, and Bucholz hardness were conducted to characterize the paint quality. It is determined that the bentonite – Mgo mixture can perform as well, or better than other thickening agents tested in this study.

Keywords: Thickening agent, Na-Bentonite, paint.

1. Introduction

Environmental regulations by EPA and European Union Commission are driving a shift from solvent-based to water-borne paints. However, it is a challenge to achieve the satisfactory service properties in water borne paints as compared to solvent based systems. Water borne paints generally show inferior properties in terms of leveling and open time compared to solvent-borne paints. This is because of relatively high evaporation rate of water and difficulty in adjusting viscosity to appropriate level. Additives are known to play a major role in determining paint service properties. Additionally, they also have considerable influence on hazardous components of paints, such as Volatile Organic Compounds (VOCs) and Alkylphenolethoxylates (APEOs). Consequently, "green" additives are being increasingly sought by the paint industry Thickeners; for instance, represent one of the main groups of these additives.

Bentonite, which is generally used as a thickening agent in paints, is nontoxic natural material and cheaper compared to polymer based thickeners. Modification of bentonite with inorganic or organic materials converts it into a gel like structure which is appropriate for use as a thickening agent in water borne paints.

Bentonite, the commercial name for more than 80 wt% montmorillonite, is an aluminum phyllosilicate clay. Major impurities of bentonite are quartz, calcite, feldspar and biotite. Bentonites are used in a variety of diverse industries including thickeners and extenders for paints; their unique rheological properties render them to be particularly useful raw materials in foundry sand and drilling mud production[1-2)].

Bentonite structure can be modified to manipulate their properties. A number of studies have utilized activation and modification, using different reagents and techniques, to change the structure of bentonite[3-7)]. Activation process may involve ion exchange and ion adsorption. In modification process on the other hand, the main target is to expand the basal spacing of the bentonite by introducing larger cat-

---

[†] Accepted: July 8th, 2011

[1] Ayazağa, Istanbul, Turkey
[2] 205 Particle Science and Technology, Gainesville, FL 32611, USA
[*] Corresponding Author: Brij M. Moudgil
E-mail: bmoudgil@perc.ufl.edu
TEL: (+1) 352-8461194 FAX: (+1) 352-8461196

ⓒ 2011 Hosokawa Powder Technology Foundation

ions. Bentonites are generally modified to change their wettability character from hydrophilic to hydrophobic for use in solvent based applications.

Activation of bentonite with sodium increases the number of thin hexagonal laminar particles. Ion type is an important parameter, for example, Ca^{2+} ions cause "band structure" while Mg^{2+} ions cause "network structure". Anionic clay particles serving as cation activators secure the formed networked "band structure" [8].

Thickener additives not only behave like rheology modifiers but also affect some physical properties such as gloss and hiding power of paint by modifying dispersion of primary pigments and extenders in paint formulations. Thus close attention must be paid to dispersant, thickener and pigment types to achieve optimum paint properties[9].Hydrophobically modified ethoxylated urethane [HEUR] and hydroxyethyl cellulose (HEC), which are used in water based paints have considerable effect on paint rheology. In particular different spray angles and nozzle geometries[10] dictate the type and amount of thickeners. The interaction of associative (HEUR type) and non-associative thickeners (HEC) with the rest of additives in paints emphasizes the role of latex particle size, surfactant type, amount and type of the thickener used in the water borne paint systems[11-14]. While they are very important in achieving appropriate viscosity profile across the entire shear range encountered in paint applications, they might also introduce some adverse effects. For example, associative thickener additives (HEUR) improve the open time and the leveling behavior of water-borne paints by providing an increase of network viscosity and a reduction of dispersion viscosity; they decrease the filling capacity and enhance water sensitivity problems[15]. Paint viscosity is a crucial paint property and needs to be taken into consideration in each step of the process; production, storage and application since each step demands dramatically different viscosity values.

In this study bentonite -based thickener for water borne architectural paint was produced. Role of MgO- a cheap and less hazardous inorganic additive was investigated to achieve a gel (network) structure. Bentonite - MgO interactions were assessed by rheological and electrokinetic measurements. Performance of the optimum thickener formulation developed using bentonite - MgO mixture was compared with two commercial clay based thickeners.

2. Experimental

2.1. Materials and methods

2.1.1. Production of Na-Bentonite

TiO_2 was received from DuPont (TiPure902) and Calcite from Mississippi Corporation General properties of TiO_2 and calcite are given in **Tables 1** and **2**, respectively. Na-Bentonite used in the study was obtained from Wyoming region of the USA. Typical properties of Na-Bentonite are given in **Table 3**.

Magnesium oxide (MgO) used in the experiments was supplied by Oerac Incorporated with the properties shown in **Table 4**. Distilled and tap water were used in the production of Na-bentonite based thickener and paint, respectively. Rest of the ingredients such as dispersant, wetting agent and defoamer are commercial grade additives.

Table 1 General properties of TiO_2 pigment

TiO_2, wt%, min.	93
Alumina	yes
Amorphous Silica	yes
Specific Gravity, g/cm^3	4.0
Bulking Value, L/kg	0.25
Organic Treatment	yes
Color CIE L*	99.6
Median Particle Size, μm	0.405
Oil Absorption, ml/100g	16.2
pH	7.9
Resistance at 30℃ (86°F) (1,000 ohm)	8.1
Carbon Black Undertone	11.7

Table 2 General properties of paint grade calcite

Specific Gravity, g/cm^3	2.7
Refractive Index	1.58
Whiteness, (D 65/10) Elrepho 450 X (L, a, b)	98 ± 1
Hardness (Mohs Scale)	3
Oil Absorption, ml/100g	17 ± 2.00

Table 3 Physical properties of Na-bentonite

Screen analysis	
Dry screen, % minus 200 mesh	99.9
Dry screen, % minus 325 mesh	97.1
Wet screen, % plus 325 mesh	0.3
Slurry Properties (6% by wt. suspension)	
Viscosity, FANN® Viscometer 600 rpm	19
Apparent viscosity, cps	9.5
Plastic viscosity (PV)	7
Yield point, lb./100 ft^2	2
Filtrate, 30 minutes @ 100 psi, ml	15
Industrial Properties	
Moisture, %	9
Base exchange capacity meq/100 g	105
Swell index, ml	28
Plate water absorption, wt % @ 20℃ /18 hr	900
Oil absorption, ml/100 g	41.3
Surface area, m^2/gram (N_2 absorption)	20
pH, 6% suspension	9.5
Bulk density, g/cm^3 uncompacted	2.37
Bulk density, g/cm^3 compacted	3.62

Table 4 General properties of MgO

Particle Size, μm	44
Median Particle Size, μm	1.29
MgO Purity	Typically 99.95%
Spectrographic Analysis	
B	<0.0001
Ca	0.0007
Cd	<0.0007
Cr	<0.0002
Cu	<0.0001
Fe	0.0006
Mn	<0.0002
Pb	<0.0001
Sr	<0.0005
Zn	<0.0006

Table 5 presents some physical properties of two commercial thickening agents used in water based paints, Bentone EW and Optigel CK.

Thickeners can be added both in the form of powder or paste. In this study, bentonite paste was prepared with appropriate amounts of MgO and water. In order to find out the effect of MgO dosage on the final product, 7 different mixtures of Na-Bentonite-MgO were prepared. Na-Bentonite and MgO were mixed dry and then sufficient water was added to make up 5 % solids by wt. The suspension was stirred at 6.000 rpm with a high speed "Sheen" brand laboratory disperser for 10 minutes. The suspensions were characterized by pH and viscosity profile determinations a function of time and MgO dosages. Zeta potential profile as a function of MgO dosage was also obtained for understanding the interaction of MgO with clay particles.

"Brookfield LVDV-II+ Visco-meter" with LV type spindles at 30 rpm was used for viscosity measurements. These spindles can measure fluid viscosities from 15 to 2,000,000 mPas. Zeta potential measurements were performed with "Brookhaven ZetaPlus" which measures zeta potential by Doppler shift analysis. The instrument can measure particle size rang-

Table 5 Physical properties of Bentone EW and Optigel CK

Property	Bentone EW	Optigel CK
Composition	Highly beneficiated smectite clay	Activated bentonite product
Color	Milky-white	White
Form	Soft powder	Soft powder
Density, g/cm^3	2.5	2.5
Moisture, %	10 max	8-13 max

ing from 2 nm to 30 microns. Zeta potential values were calculated using the Smoluchowski equation.

2.1.2. Production and analyses of paint with thickeners

Paint Production: Paint employed in the study was formulated according to a commercial paint recipe using ingredients listed in **Table 6**. Optimum bentonite addition established in a previous study, and two different commercial water based thickeners were separately used in this investigation. A total of 9 paints were produced with triplicates for each recipe.

Paint production process involves three main stages. At the first stage, additives such as wetting agents, dispersants, defoamer and biocides are added. The basic purpose of this stage is to provide a favorable environment for wetting and dispersion of particles. In this stage, 22.5g of additives were added to 185ml of water based on paint formula shown in **Table 6**. This mixture was stirred using a high speed stirrer for about 15minutes with 2000rpm, which is equal to a peripheral speed of 5.2m/s. In the second stage, also called as "Millbase", pigments and extenders are dispersed in one of a number of mills depending on the type of paint to be prepared ranging from ball mills to cavitation mixers and attritors. Immediately after dispersion, the "Hegman grind" is measured as per the established standards[16].In our case, pigment and extenders in varying amounts, given in **Table 6**, were dispersed in the mixture formed in the first stage. The stirrer speed in the millbase stage was kept at 6000 rpm, which corresponds to a peripheral speed of 15.7m/s and the mixture was stirred for another 15minutes. During the production stage, size distributions of the paints were checked by Hegman gauge to ensure completion of the dispersion process.

In millbase, binder was not added to avoid its structural deformation under the high mechanical forces. Finally binder (370g) plus rest of the additives used in the first stage (42.5g) were mixed with 15ml water at 2000rpm that is equivalent to 5.2m/s in terms of the peripheral speed to yield a solids loading of 36.9% by weight. This stage is called "Letdown"[17]. In this stage mixture was stirred at 2000 rpm for another 15 minutes. The final pH of the paint was measured to be 8.6. 1kg of paint was produced for each formulation. Energy losses in the mill base are minimized by adding thickeners before the dispersion stage of the production process[18].

Performance Evaluation: In order to evaluate the quality of the paints produced, standard paint analyses such as density[19], viscosity[20], opacity[21], gloss[22], hardness[23] and stability[24, 25] of the paint films were measured. The paints were applied wet onto opacity charts (15 × 10cm), aluminum panels (15 × 7.5cm) and glass panels (15 × 10cm) using automatic film applicator with 4-sided cylinder applicators and applicator frame. Both of them have 4 sides with different application thickness. Applicator frame and 4-sided cylinder applicators are capable of forming. 50-100-150- 200μm and 30-60-90-120μm wet film thickness respectively. Panels and charts were attached to automatic film applicator using vacuum. Application speed was kept at 150mm/s to provide sufficient accuracy.

Viscosity of paints was determined by Krebs Viscometer at a constant revolution speed of 200rpm. For opacity measurements, wet paints were applied onto an opacity chart with the wet film thickness of 200μm using 200μm side of applicator frame and automatic film applicator and cured under atmospheric conditions for two days to obtain a dry paint film. Opacity, which is one of the most important properties for both water and solvent-borne paints, was determined based on the contrast ratio of paint.

Wet paints with wet thickness of 90μm were applied on glass panels using 90μm side of 4-sided cylinder applicator and automatic film applicator and were cured for 2 days under atmospheric conditions. Gloss measurements were performed with three different incidence angles of 20°, 60° and 85°. Aluminum panels with wet paint of 200 μm in thickness were cured for 2 days under atmospheric conditions and used for determining hardness of paint. Bucholz Hardness apparatus used for determining the hardness of paint film is capable of applying 5 Newton forces.

3. Results and Discussion

3.1. Production of Na-Bentonite

All the measurements were repeated at least 3 times. Viscosity, pH and zeta potential values of bentonite as a function of seven different MgO dosages, provided in **Table 7**, indicate that the pH of the suspensions is increasing with increasing amounts of MgO up to a maximum pH of 11, and remains constant with further increase in the MgO content. Experimental fluctuation for pH, zeta potential and viscosity are ± 0.1, ± 1.5mV and ± 50cP respectively.

The variation of pH values with different amounts of MgO versus time are shown in **Fig. 1**. The measurements were taken one hour apart. Upon interacting Na-Bentonite with MgO, the pH values of the sus-

Table 6 Paint recipes with three different thickeners.

Stages	Material	Quantity, %		
		Bentonite+1.5 %MgO*	Bentone EW*	Optigel CK*
First	Water	18.5	18.5	18.5
	Antifreeze	0.8	0.8	0.8
	Biocide	0.15	0.15	0.15
	Thickener	0.2	0.2	0.2
	Dispersant	0.2	0.2	0.2
	Wetting Agent	0.3	0.3	0.3
	Defoamer	0.2	0.2	0.2
	pH adjuster	0.2	0.2	0.2
	Thickener*	0.2	0.2	0.2
Mill base	TiO_2	28.0	28.0	28.0
	Calcite D1.7	8.5	8.5	8.5
Letdown	Styrene Acrylic Binder	37.0	37.0	37.0
	Silicone	0.1	0.1	0.1
	Film forming agent	0.8	0.8	0.8
	Synthetic thinner	1.6	1.6	1.6
	Defoamer	0.2	0.2	0.2
	Biocide	0.15	0.15	0.15
	Antibacterial	0.3	0.3	0.3
	Butyl Glycol	0.8	0.8	0.8
	Anti-settling agent	0.3	0.3	0.3
	Water	1.5	1.5	1.5
	TOTAL	**100.0**	**100.0**	**100.0**

pensions changed considerably in the first 5 hours and much slower thereafter indicating approaching an equilibrium.

The viscosity of Na-Bentonite suspension in the absence of MgO is 1352.5 cP. An increasing trend in viscosity with the addition of MgO was observed (see **Fig. 2**). However, at 2.5wt% MgO addition, the viscosity peaked with a value of 17126.24 cP indicating formation of a gel structure. The pH and viscosity values correlate with each other and suggest approaching an equilibrium condition in Na-Bentonite-MgO system after 5 hours.

All Bentonite+MgO suspensions yielded pseudoplastic flow behavior, i.e. their viscosity values decreased with increasing shear rate. Their viscosity also decreased with time indicating a typical thixotropic flow behavior. Such flow properties make these additives compatible to paints in terms of viscosity requirement. Viscosity of paints can be easily adjusted to desired values utilizing both pseudodplastic and thixotropic flow behavior of these additives during storage, transport and application stages.

Table 7 pH, viscosity and zeta potential values of Na-bentonite+MgO suspensions

MgO,%	pH	Viscosity, cP	Zeta Potential, mV
0.0	10.05	1352.5	-47.55
0.5	10.68	3805.1	-44.82
1.0	10.71	7496.1	-37.40
1.5	10.81	12965.0	-35.14
2.0	10.99	14998.8	-33.48
2.5	11.02	17126.2	-15.54
3.0	11.2	15987.4	-10.56

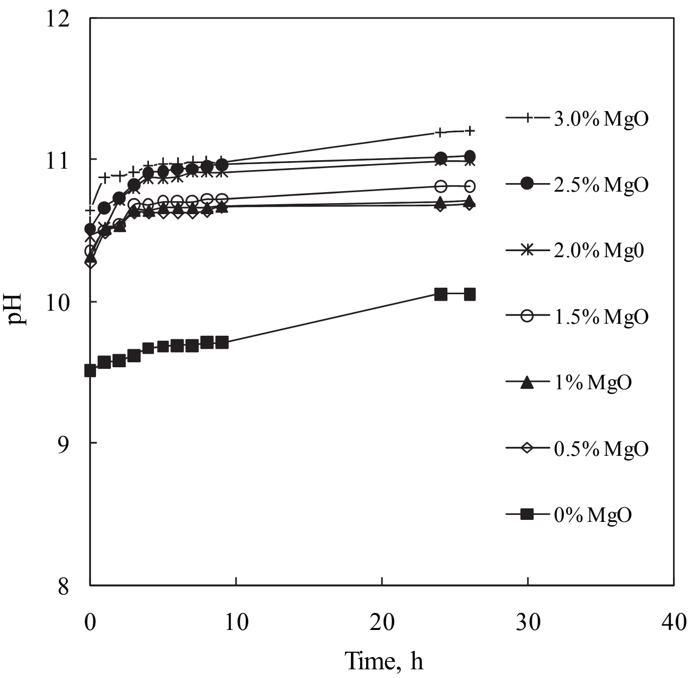

Fig. 1 Variation of pH with time for Na-Bentonite+MgO suspensions at different MgO additions.

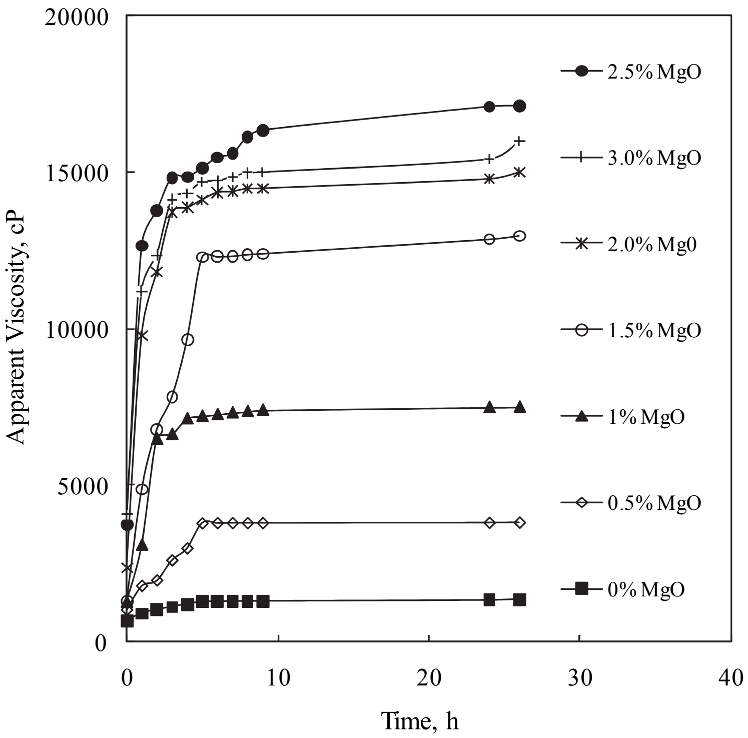

Fig. 2 Variation of viscosity with time for Na-Bentonite+MgO suspensions at different MgO additions (LV2-30 rpm).

Zeta potential of Na-Bentonite suspensions was also studied as a function of MgO dosage. Dependence of viscosity and zeta potential on MgO addition is shown in **Fig. 3**. As expected, increasing MgO dosage renders zeta potential values more positive. It should be noted that the zeta potential of the pure Na-Bentonite was found to be - 47.55 mV and increased to -10.56 mV with the addition of 3 % MgO. It is well known that Mg ions released from MgO can form $MgOH^+$ complexes in solution and these hydoxy complexes can adsorb onto bentonite and make it more positively charged[3, 27]. Heterocoagulation of bentonite with MgO particles becomes conducive most probably at zeta potentials in the vicinity of -15 mV where viscosity values exceed 12,000 cP. There appears to be a critical point at which the network structure breaks down. Stability experiments of paint pastes conducted in Ishakol Paint Company laboratories revealed that upon aging high viscosity suspensions are not stable upon prolonged exposure to UV light and thus moderate viscosity levels must be maintained for achieving stable paint formulations.

pH and viscosity measurements, along with stability analysis of suspensions, reveal optimal performance at, 1.5 % MgO dosage.

3.2. Comparison of Na-Bentonite + MgO with commercial clay based thickneres

The same paint recipe was repeated three times for reproducibility of analysis. Differences among them are acceptable in terms of related standards[19-25]. Viscosity, density, contrast ratio (opacity), gloss and hardness of the paint produced with different clay based thickeners are summarized in **Table 8**. Hardness is represented by indentation resistance according to the related standard.

As apparent from **Table 8**, there is no significant difference in the density of paints with different clay based thickeners. The main evaluating test for thickener effectiveness in paint is the stabilization test. After performing the physical tests on the freshly prepared paint, the remaining paint was stored (covered) in an oven at 52℃±2 for 1 month. After a month, the viscosity was measured again and compared to those measured immediately after initial production. Any settling after storage was assessed. Stored paint samples were carefully mixed by hand in order to observe settling of any pigment or extender caused by agglomeration or lack of network structure.

All the paints listed in **Table 8** fall within the technical requirement range (124 ± 15 KU) in terms of

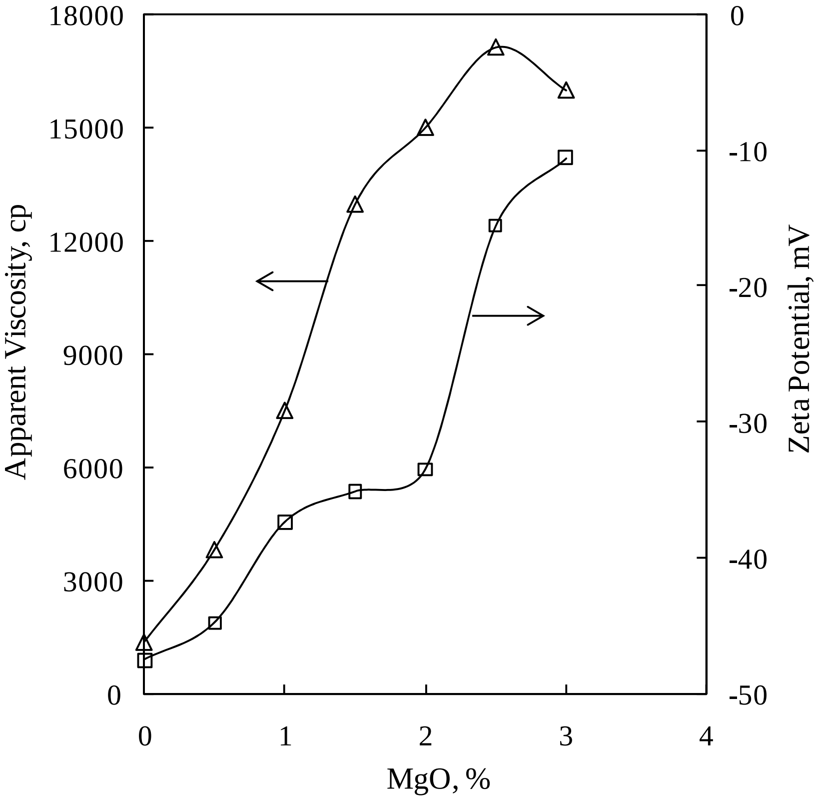

Fig. 3 Dependence of viscosity and zeta potentials on MgO dosage.

Table 8 Key physical properties of paints using different thickeners

Property		Bentonite +1.5 %MgO	Bentone EW	Optigel CK
Density, g/cm^3		1.32	1.35	1.37
Viscosity, KU Initial-Final		118.4-121.2	113.1-116.7	115.3-104.8
Contrast Ratio, %		98.2	97.65	97.2
Gloss	20°	1.5	1.5	1.65
	60°	10.65	9.15	12.75
	85°	59.40	54.80	50.95
Indentation Resistance, α B		58.8	52.6	58.8

initial viscosity values. After a month under the oven conditions (52℃ ± 2), the viscosity value of paint with Optigel CK dramatically decreased while the other two paints with Bentonite+1.5%MgO and Bentone EW remained practically the same. Decrease in viscosity is an indication of pigment settling or breakdown of network structure. This is usually triggered by the lack of dispersion and agglomeration. Network structure necessary for avoiding settling of particles is provided by appropriate thickeners.

In terms of hardness (indentation resistance) value, Bentonite+1.5 % MgO and Optigel CK are almost the same and better than Bentone EW. In fact, the dominant parameters that determine the hardness value of paint are the binder type and its amount. Type of pigment and extender and amount and particle size also impact hardness. Thickeners might have an auxiliary role on hardness values through modifying particle size distribution or interaction between binder and particles.

Paints with a contrast ratio between 95% and 98% are classified as the third class paint and over 98% are considered as the first class. Therefore, the paint recipe with Bentonite+ 1.5% MgO is better than the other paints. There is no any appreciable difference among Gloss values of all the paints and all fall into the second class category.

Opacity strictly depends on dispersion of particles in the paint systems. Dispersion process has three main stages. The first one is the wetting of pigment and extender particles. In this stage, particles agglomerated due to their hydrophobic nature or resistant to wetting are made hydrophilic through with surface active agents. After the pigment particles have been partially wetted, agglomerates are broken into smaller particles by mechanical forces (high speed dissolvers, mills). Peripheral speed of a dissolver should be 18-20 m/s for millbase. Last stage of the dispersion process is the stabilization of dispersed particles. Brownian movement results in continues collisions between the pigment particles of dispersed systems. Insufficient stabilization of the particle can therefore result in reflocculation[17].

Dispersion agents can modify the electric charge on the surface and introduce steric barriers that increase the stability. They can also alter the adsorption characteristics of the surface to increase the adsorption of polymeric materials or thickeners, thus increasing the barrier to flocculation[18]. Therefore, the ability of thickeners to form a good network structure directly affects dispersion by preventing reflocculation. In this case, Bentonite + 1.5 % MgO thickener provides much higher opacity than its counterparts indicating more robust dispersion behavior.

4. Conclusions

MgO was successfully used to produce bentonite based water borne thickener from natural sources. Production of water borne paint is more complicated than solvent borne systems because more special additives such as wetting agents, dispersants and defoamers must be used to obtain at least a similar quality to the solvent one. Interaction of paint components in water based systems requires the use of an appropriate thickener type and amount to avoid any adverse effect deteriorating the paint quality. Na-Bentonite and MgO mixture performed as well or better than two commercially available clay based thickening agents. Optimal paint properties were achieved at a MgO dosage of 1.5 wt. %. Higher opacity and paint stability with Na-Bentonite and MgO mixture indicated higher resistance to reflocculation, or more robust dispersion of particles.

5. Acknowledgements

This work was supported by the scholarship program of "The Scientific and Technological Research Council of Turkey (TUBITAK)". Authors acknowledge the financial support of the TUBITAK. Partial financial support of the Particle Engineering Research Center and the Center for Particles and Surfactant Systems – a NSF I/UCRC is also acknowledged.

References

1) McMurry, R. C., (1992): "Organic Chemistry", Cornell University, U.S.A.
2) Allo, W.A., Murray, H.H., (2004): Mineralogy, chemistry and potential applications of a white bentonite in San Juan province, Argentina, Applied Clay Science, 25, pp. 237– 243.
3) Karagüzel, C., Çetinel T., Boylu F., Çinku K., Çelik M.S., (2010): Activation of (Na, Ca)-bentonites with soda and MgO and their utilization as drilling mud, Applied Clay Science, 48, pp. 398–404.
4) Rawajfih, Z., Nsour, N., (2006): Characteristics of phenol and chlorinated phenols sorption onto surfactant-modified bentonite, Journal of Colloid and Interface Science, 298, pp. 39–49.
5) Rodriguez-Sarmiento, D.C., Pinzo´n-Bello J.A, (2001): Adsorption of sodium dodecylbenzene sulfonate on organophilic bentonites, Applied Clay Science, 18Ž, pp. 173–181.
6) Bojemueller, E., Nennemann, A., Lagaly G., (2001): Enhanced pesticide adsorption by thermally modified bentonites, Applied Clay Science, 18Ž, pp. 277–284.
7) Li J., Zhua, L., Cai, W., (2006) : Characteristics of organobentonite prepared by microwave as a sorbent to organic contaminants in water, Colloids and Surfaces A: Physicochem. Eng. Aspects, 281, pp. 177–183.
8) Radojevi´c, Z., Mitrovi´c, A., (2007): Study of montmorillonite and cationic activators sistem rheological characteristic change mechanism, Journal of the European Ceramic Society, 27, pp. 1691–1695.
9) Kostansek, E., (2007): Controlling particle dispersion in latex paints containing associative thickeners, J. Coat. Technol. Res., 4 (4), pp. 375–388.
10) Elliott, P.T., Mahli, D.M., Glass, J.E., (2007): Spray applications: Part IV. Compositional influences of HEUR thickeners on the spray and velocity profiles of waterborne latex coatings, J. Coat. Technol. Res., 4 (4), pp. 351–374.
11) Mahli, D.M., Wegner, J.M., Glass, J.E., Phillips D.G., (2005): Waterborne Latex Coatings of Color: II. Surfactant Influences on Color Development and Viscosity, JCT Research, 2, 8.
12) Mahli, D.M., Wegner, J.M., Glass, J.E., Phillips D.G., (2005): Waterborne Latex Coatings of Color: I. Component Influences on Viscosity Decreases, JCT Research, 2, 8.
13) Mahli, D.M., Wegner, J.M., Glass, J.E., Phillips D.G., (2007): Waterborne latex coatings of color: III. Triblock polyether influences on color development and viscosity J. Coat. Technol. Res., 4 (1), pp. 31–41.
14) Eme´lie, B., Schuster, U., Eckersley, S., (1998): Interaction between styrene/butylacrylate latex and water soluble associative thickener for coalescent free wall paints, Progress in Organic Coatings, 34, pp. 49–56.
15) Reuvers, A.J., (1999): Control of rheology of waterborne paints using associative thickeners, Progress in Organic Coatings, 35, pp. 171–181.
16) ASTM-D 1210 – 05, (1995): Standard Test Method for Fineness of Dispersion of Pigment-Vehicle Systems by Hegman-Type Gage.
17) "Paint and Surface Coatings: Theory and Practice", Edited by R.Lambourne, (1987), 850 pages, Ellis Horwood Ltd.
18) "Additive for Coatings", Edited by Johan Bieleman, WILEY-VCH, (2000). 372 pages.
19) ISO 2811-1, (2002): Paint and varnishes- Determination of density Part 1: Pyknometer method.
20) ASTM D562-01(2005): Standard Test Method for Consistency of Paints Measuring Krebs Unit (KU) Viscosity Using a Stormer-Type Viscometer
21) ASTM-D 2805 – 96a, (1996): Standard Test Method for Hiding Power of Paints by Reflectometry.
22) ISO 2813, (2002): Paints and varnishes - Determination of specular gloos of non-metallic paint films at 20, 60 and 85.
23) ISO 2815, (2005): Paints and varnishes – Buchholz indentation test.
24) ASTM D1849 – 95 (2008): Standard Test Method for Package Stability of Paint.
25) ASTM D869 – 85 (2004): Standard Test Method for Evaluating Degree of Settling of Paint.
26) Çinku K. : "Investıgatıon of water based rheologıcal agent productıon from bentonıtes by use of actıvatıon methods", PhD thesis (in Turkish), Istanbul University, Turkey.
27) Çelik, M.S., Yasar, E. and El-Shall, H., (1998): Flotation of Heterocoagulated Particulates in Ulexite/SDS/Electrolyte System, J. Colloid and Interface Science, 203, pp. 254-259.

Author’s short biography

Dr Fırat Karakaş

Fırat Karakaş received his B.S and M.S.degrees in mineral processing division of mining engineering from Istanbul Technical University (ITU), in 2004 and 2006 respectively. He also received his Ph.D. degree in surface chemistry from Institute of Science and Technology of ITU under the supervision of Dr.M.S.Çelik in 2011.
He got the scholarship named as “Iz Birakanlar” from Turkish Cement Manufacturers’ Association” in 2005. He studied for 6 months in “Particle Engineering Research Center” of University of Florida, during his Ph.D. and worked under the guidance of Dr.B.M.Moudgil that was supported by “The Scientific and Technological Research Center Council of Turkey”
His research activity concerns the use of mineral particles as a pigment, filler or an additive, and optimizing the paint formulations including dispersion and stabilization phenomena based on surface chemistry.

Dr. Mehmet Sabri Çelik

Mehmet Sabri Çelik received his B.S., M.S. and Ph.D. degrees from Istanbul Technical University (ITU, Turkey), Pennsylvania State University (USA) and Columbia University (USA), respectively. He is presently working as a professor of Mineral Processing Engineering in ITU. His current areas of interests include surface and colloid chemistry of flotation processes, development of commercial products out of industrial minerals, particle-particle interactions in aqueous and nonaqueous media, production and characterization of micro and nano particles related to paint, coating and plastics.

Dr. G. Pyrgiotakis

Dr. Pyrgiotakis has a BS degree in Physics from the University of Crete since 1995. In 2003 he obtained his MS degree from the University of Florida, in Materials Science and Engineering with specialty on Electronic Materials. Following, in 2006 he obtained his PhD in Materials Science and Engineering with specialty on Ceramic Materials. His dissertation was dealing with the synthesis of an advanced photocatalytic particle that consist on a Carbon Nanotubes core and a titania coating. Since then he was appointed as a postdoctoral research associate at the Particle Engineering Research. His research aim is to investigate toxicity of nanoparticles and how it correlates to their properties, such size, surface morphology, shape, porosity etc. He has served as the president of KERAMOS Florida Chapter, from 2004 to 2006.

Author's short biography

Brij M. Moudgil

Brij Moudgil is a Distinguished Professor of Materials Science and Engineering at the University of Florida where he currently holds the Alumni Chair in Materials Science and is also the Director of the Particle Engineering Research Center. He served as the president of the Society for Mining, Metallurgy, and Exploration (SME) for the year 2006-2007. His research interests are in polymer and surfactant adsorption, dispersion and aggregation of fine particles, nanotoxicity, multifunctional nanoparticles for bioimaging, diagnosis, and therapy, nanoparticulate processing and separation technology for enhanced performance in mineral, chemical, microelectronics, pharmaceutics, advanced materials, and resource recovery & waste disposal applications. He received his B.E degree in Metallurgical Engineering from the Indian Institute of Science, Bangalore, India and his M.S and Eng. Sc.D degrees in Mineral Engineering from the Columbia University. In 2002 he was elected as a member of the U.S National Academy of Engineering for his contributions to mineral processing and professional leadership in the particle community. He can be reached at bmoudgil@perc.ufl.edu.

Estimation of Particle Deposition in the Airways From Different Inhaler Formulations Using an In Silico Model[†]

Smyth, H.D.C.*[1], Martonen, T.B.[2], Isaacs, K.K.[3], Hickey, A.J.[4]
College of Pharmacy, University of Texas at Austin[1]
CyberMedicine, Inc.[2]
United States Environmental Protection Agency[3]
Eshelman School of Pharmacy, University of North Carolina at Chapel Hill[4]

Abstract

The objective of these studies was to evaluate the use of an in silico model for predicting lung deposition of inhaled therapeutic aerosols. A range of input data derived from our own in vitro data and published clinical studies was utilized. The in silico model ran simulations for these propellant driven metered dose inhaler formulations across a range of conditions. Firstly, a range of pressurized metered dose inhaler formulations were evaluated in the in silico model and compared to the in vitro aerosol performance data. Limitations of using in vitro cascade impaction data were observed. Then, using in vivo data from healthy human subjects using metered dose inhalers, lung deposition profiles were compared with the in silico model predictions. Despite differences in oropharyngeal deposition the model predicted lung deposition accurately. We conclude that the in silico model can be applied to various conditions for particulate based inhalation aerosol systems.

Keywords: Aerosol, Metered dose inhalers, hydrofluoroalkane, pMDI, in silico, prediction

1. Introduction

The efficacy of aerosolized drugs would be enhanced if they could be selectively deposited (i.e. targeted) at appropriate sites within the human respiratory system. This targeting may be interpreted from a macro-scale (regional lung targeting) to a micro-scale (cellular or receptor targeting). To achieve selective regional deposition within the airways, aerosol administration has traditionally been achieved using nebulized liquids, propellant driven aerosols, or dry powder inhaler systems. As these technologies have advanced, their efficiencies have improved but little has been intentionally introduced to effect more selective targeting of different regions of the airways. This is despite recent evidence from clinical studies that indicate improved therapeutic efficacy when laboratory engineered mono-dispersed aerosols were delivered to asthmatics (Usmani et al., 2003).

Of the current aerosol delivery systems, propellant driven metered dose inhalers (pMDIs) predominate, with sales that reached an estimated 4.6 billion dollars in 2007. These systems have also witnessed significant change in recent years due to the transition from chloroflorocarbon (CFC) based propellants to hydrofluorocarbon (HFC) based propellants as required by international agreements[2,3)]. The redesign of pMDIs led to significant changes in the formulation of new and existing inhaled drug products[4)]. Most notably, lung deposition patterns were significantly altered due to the different formulations and the physicochemical properties of the propellants that drive the atomization process[3)]. As a consequence of the change in performance, prediction and extrapolation of lung deposition profiles has been challenging. In particular, those wishing to match the performance of the predecessor CFC-based systems to a reformulated HFA-based system requires large design of experiment studies so that equivalence between the two could be achieved. Alternatively, utilizing formulations to more appropriately target therapeutic agents within the airways appears a logi-

---

[†] Accepted: July 8th, 2011

[1] Austin, TX 78712, USA
[2] Laguna Beach, CA92651, USA
[3] Research Triangle Park, NC27711, USA
[4] NC, USA
[*] Corresponding author
E-mail: hsmyth@mail.utexas.edu
TEL: (+1) 512-4713383 FAX: (+1) 512-4717474

ⓒ 2011 Hosokawa Powder Technology Foundation

cal approach. However, as mentioned earlier, little work has been performed linking formulation design to specific lung deposition patterns. Indeed, in these studies we show the limitations of using in vitro data to predict lung deposition patterns.

In particular, we previously reviewed the significant differences in HFA propellant characteristics that give rise to major changes in pMDI performance compared to the CFC predecessor devices[4]. In addition, we reported in vitro performance data on the effect of spacer devices used with solution HFA 134a pMDIs[5]. Interestingly, in these studies, spacer devices had little effect on in vitro performance of HFA 134a solution pMDIs. We also extended these findings by applying the currently described in silico model to further elucidate the implications of both formulation changes and the utility of spacers with these newer HFA 134a based pMDIs (Smyth et al., 2010). It was shown that using a validated model of airway deposition in vitro observations corresponded to in silico equivalence in regional lung deposition. However, oropharyngeal deposition predictions were likely to be inaccurate due to the bias introduced into particle size information obtained by in vitro cascade impaction studies that does not represent the human physiology.

In the present studies we employed an in silico model to study the effects of formulation design on lung deposition and evaluate the in silico – in vitro, and in silico – in vivo correlations. Specifically, to study the effects of the factors addressed in our work (e.g HFA versus CFC based pMDI systems) we employed an *in silico* aerosol dosimetry model and compared the results of in silico predictions to experimentally determined data in both in vitro cascade impactors and human subjects. The in silico model had been previously tested extensively via comparisons of its predictions with in vivo data from human subject experiments. The validated *in silico* model allowed us to consider drug delivery conditions and inhaler performance where in vitro data are not currently available extrapolating to new situations.

2. Methods

The mathematical calculations and computer simulations performed in this study used the in silico dosimetry model which has evolved through the works of Martonen[7] and Martonen et al.[8,9]. The in silico model was tested by comparing its theoretical predictions with in vivo data from the work of Heyder et al.[10]. The excellent agreement between theory and experiment over the wide range of conditions validate the in silico model and support its use for extrapolation purposes in our analyses.

For orientation we shall provide a few salient details in this METHODS section. However, a comprehensive review of the theoretical concepts and related software development is beyond the scope of this text. The mathematical techniques and computational protocols can be found in the aforementioned citations.

The behavior and fate of inhaled particles (i.e. micronized powders and atomized droplets) can be formulated in terms of three families of variables which describe respiratory system morphology, ventilation parameters, and aerosol characteristics. Let us consider these factors, albeit briefly.

Respiratory System Morphology

This topic considers the shapes and dimensions of individual airways and their spatial arrangement in a 3D branching network. In this work we shall employ the morphometric data published by Soong et al.[11], as augmented by clinical studies from our laboratory[12]. To produce an anatomically realistic system, the tubular network was positioned within patient-specific left and right lungs whose boundary surfaces were generated via computer reconstructions of magnetic resonance images[13]. The lungs were coupled with extrathoracic data describing the head and throat from high resolution computed tomography to produce a 3D computer depiction of the complete respiratory system from the nose and mouth to the alveoli[14]. The resulting contiguous system is presented in **Fig. 1**.

Ventilatory Parameters

To describe breathing conditions during the administration of aerosolized drugs the salient parameters are tidal volume (TV), breathing frequency (f), and breath-hold time (Dt). The differences in these factors pertaining to spontaneous versus controlled breathing regimens have been addressed in an earlier work (see **Fig. 8.6** of reference 9) and related text). We shall employ ventilatory parameters consistent with the outpatient use of MDIs and the details of which are included for each simulation below in the results section.

Aerosol Characteristics

The size distribution of an aerosolized drug may be defined by the mass median aerodynamic diameter (MMAD) and geometric standard deviation (GSD)

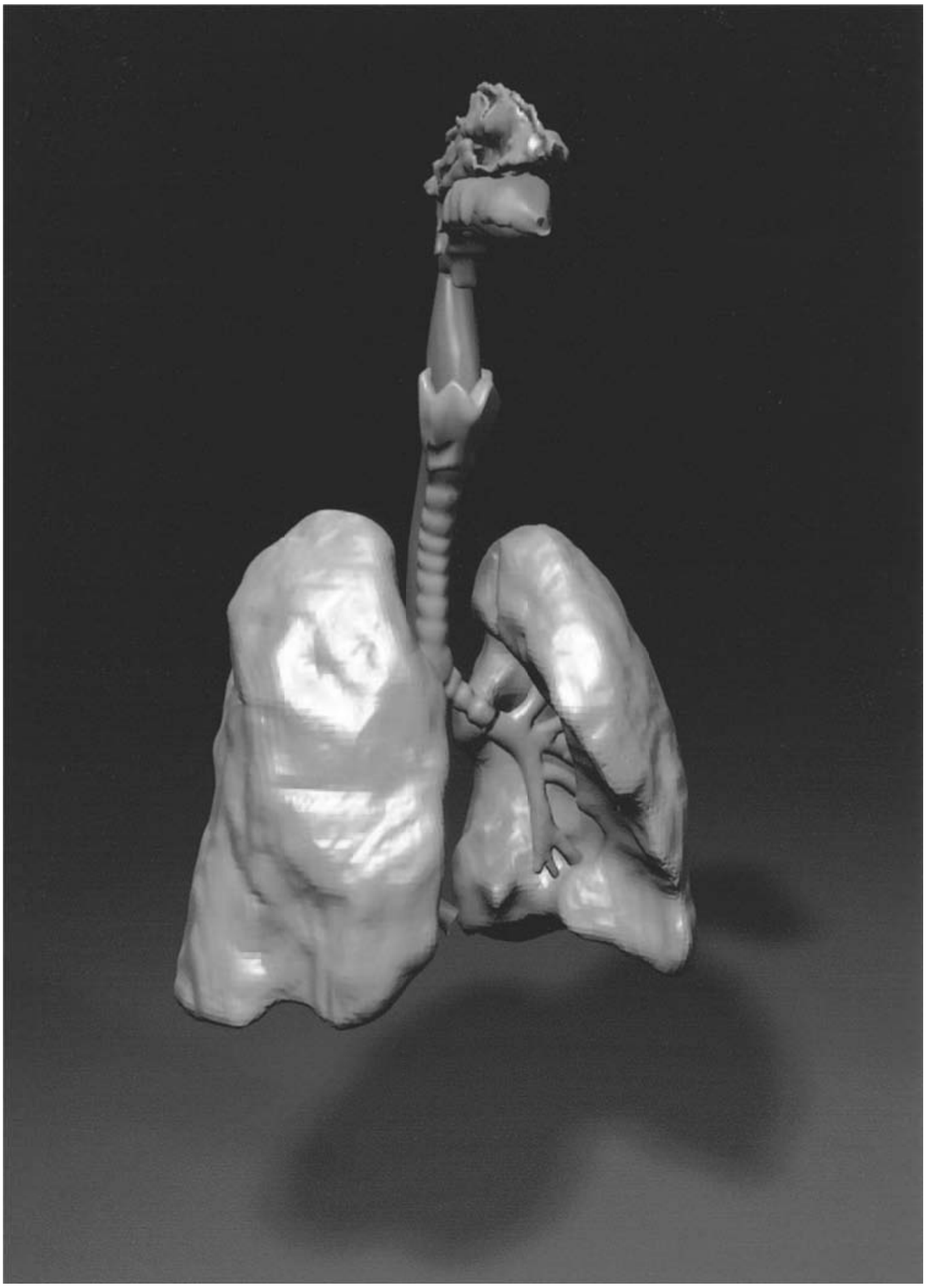

Fig. 1 Three-dimensional computer reconstruction of the entire human respiratory system. With permission (14).

of its constituent particles. Herein, practical MMAD and GSD values were considered; that is, representative values used in particle dosimetry simulations will be within the range of commercially available inhalers. The details for each simulation performed are described below in the results section.

We shall now demonstrate how the three families of variables outlined above may be integrated to create a biologically realistic in silico aerosol dosimetry model.

In Silico Dosimetry Model

The factors (TV, f, and Δt) are used with airway dimension measurements to calculated airstream velocity values which, in turn, are used in published formulas to determine particle deposition probabilities within the respiratory system. Particle deposition is described by the processes of inertial impaction, sedimentation, and diffusion which simulate particle trajectories due to momentum, gravity, and Brownian motion, respectively. The three deposition mechanisms are shown in **Fig. 2**. A comprehensive review of various deposition probability formulae has been conducted by Isaacs et al.[9]. We shall use the coupled (i.e. mathematically consistent) system of equations derived by Martonen[15].

To simulate the behavior and fate of aerosolized drug produced by a particular device, its MMAD and GSD values are used as input to the aforementioned deposition probability equations. The deposition values within individual airways are computed, which can then be summed appropriately to describe deposition patterns to desired levels of spatial resolution. For example, output can be presented for total lung deposition, compartmental (ie. tracheobronchial (TB) and pulmonary (P)) deposition fractions of the total, and generation-by-generation deposition fractions of the total.

For our purposes, the aforementioned particle deposition fractions are acceptable computational endpoints. However, in future drug efficacy studies aerosol dose delivered values may be the desired computational endpoints. It may be incumbent on us, therefore, to explain how to make the conversion from particle deposition fractions to aerosol dose delivered. The *in silico* model predicts the number of particles of a prescribed size deposited in a specified region, for example, in a given airway generation. That number can be normalized in a manner selected by the investigator. For instance, a clinician may elect to normalize the deposition to the number entering the trachea. This would actually be the standard technique because experimental data have been routinely based on TB and P clearance measurements which are inherently related to the quantity entering the lungs. When the MMAD and GSD of an aerosolized drug are known, particle deposition fractions can be converted to corresponding particle mass values in a straightforward manner. For a prescribed size distribution of constituent particles the aerosol mass deposition fraction can then be determined. The aerosol dose delivered can then be calculated using the computational endpoint desired by the investigator. For instance, when the aerosol mass deposited is divided by the cumulative airway surface area in a generation the aerosol dose delivered units would be $\mu g/cm^2$.

In this METHODS section, we would be remiss if the subject matter of computational fluid dynamics (CFD) was not recognized. Several third party CFD packages are commercially available and permit particle trajectories to be mapped within branching networks. We have utilized such CFD codes, and although they allow localized deposits to be discerned in networks containing only a limited number of airways, they are not of practical application when considering complete lungs which, obviously, must be addressed in the medical arena[16, 17, 18].

Isaacs et al.[19] compared the *in silico* aerosol dosimetry model with CFD techniques. The respective outputs of the two approaches were compared with particle deposition data from experiments with human replica casts[20]. Whereas the *in silico* model accurately predicted airway surface-average values the deterministic manner in which computations are performed did not allow it to produce the hot-spots at airway bifurcations detected by CFD analyses. It

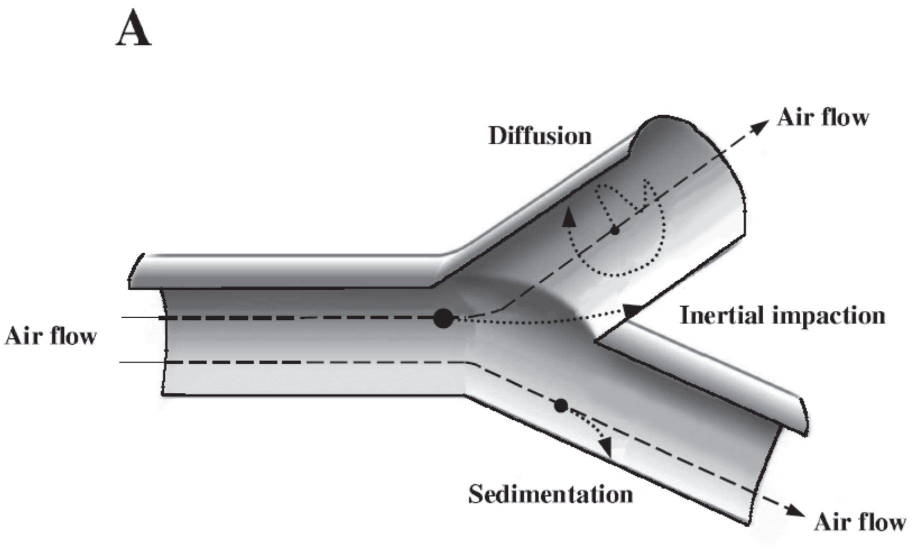

Fig. 2 Mechanisms of particle deposition in the human airways are schematically illustrated. With permission (9).

must be emphasized that, pertaining to the in vivo delivery of aerosolized drugs to patients, the in vitro data from replica casts are obviously of a much finer degree of spatial resolution than can be measured within human lungs *per se*. CFD analyses of are of limited practical use at this time simply because they cannot be reasonably used for complete lungs consisting of several millions of individual airways. For instance, the Soong et al. geometry used in this work consists of approximately 17 × 10^6 airways. The *in silico* model , therefore, is the most viable alternative for implementation in drug delivery studies.

Finally, we shall note that Martonen et al.[21] have recently evaluated the methodology of the *in silico* model using single photon emission computed tomography (SPECT) observations as benchmark testing criteria. The findings support the *in silico* model' s use in the medical arena.

3. Results and Discussion

In vitro – in silico correlations

In **Fig. 3**, the fine particle fraction (FPF) as determined by Andersen Cascade impaction studies and laser diffraction, is shown for four HFA 134a formulations with increasing concentrations of added ethanol (2.5% to 50% w/w). Previously we had shown that multimodal particle size distributions are generated from these solution based HFA 134a systems[22]. Increasing ethanol concentrations did not lead to a shift in the particle size distributions such that the distribution modes were changed. Rather, the particle populations in either the "respirable" (less than 5 microns) or "non-respirable" (distribution mode at around 10 microns) would be increased or decreased according to the formulation composition. This is reflected in **Fig. 3** where increasing the ethanol concentration in the formulation leads to a decrease in the fine particle fraction emitted from the inhaler. The performance of these formulations were then assessed using the in silico model.

In **Fig. 4** the predicted deposition patterns for the four HFA 134a/ethanol formulations is shown. The in silico model calculates the deposition fractions for oropharyngeal, total lung, central and peripheral lung zones. For oropharyngeal and central airway deposition the model predicts an increase in deposition with an increase in ethanol concentration in the formulation. However, for total lung and peripheral lung deposition the model predicts that maximal deposition will be achieved using the 20% ethanol formulation. Peripheral deposition was reduced in both the highest ethanol concentration (50% w/w) and the lowest (2.5% w/w).

Comparing the in silico and in vitro results several areas of agreement and disparity were identified and can be observed in **Fig. 5**. In **Fig. 5** the predicted deposition fraction is plotted against the in vitro determined fine particle fraction for each of the different pulmonary regions calculated by the model. Correlations are generally not good for in vitro determined data. Maximum peripheral deposition was predicted for the 20% and 10% w/w ethanol HFA formulations, whereas the in vitro cascade impactor and laser diffraction studies indicate that maximal deposition should be attained when ethanol concentrations

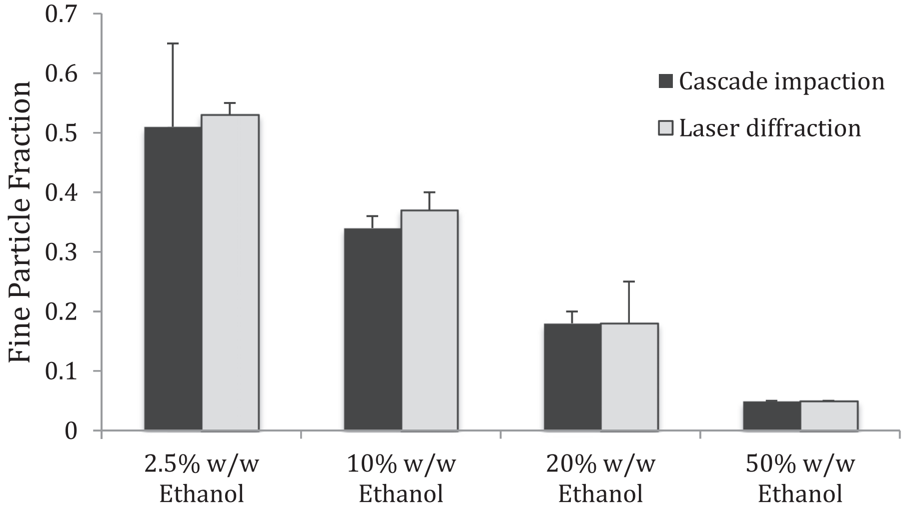

Fig. 3 Effect of ethanol concentration on the fine particle fraction (fraction of particles less than 5 microns) in HFA 134a metered dose inhaler aerosols.

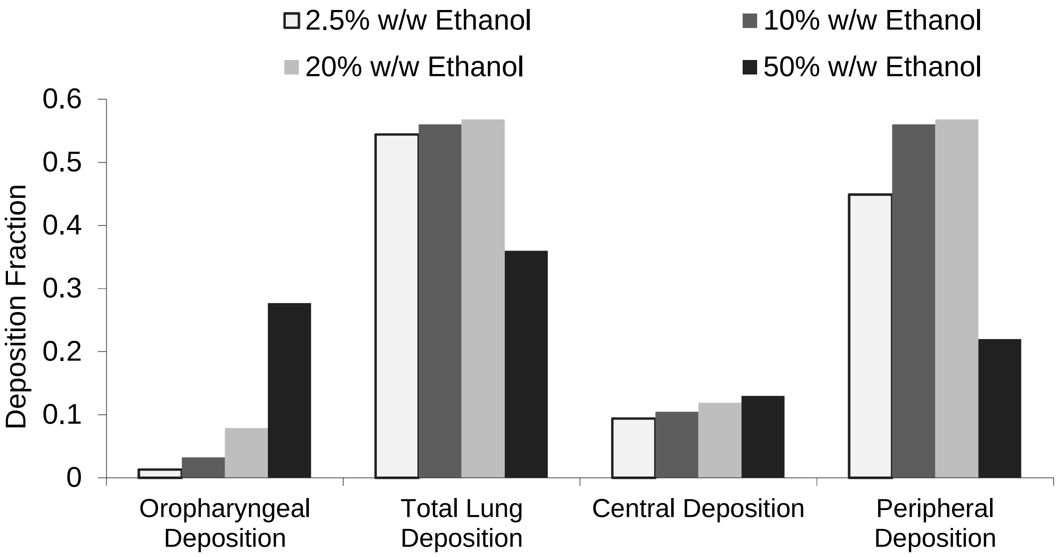

Fig. 4 Predicted deposition patterns for the four different HFA –ethanol formulations obtained using in vitro sizing data.

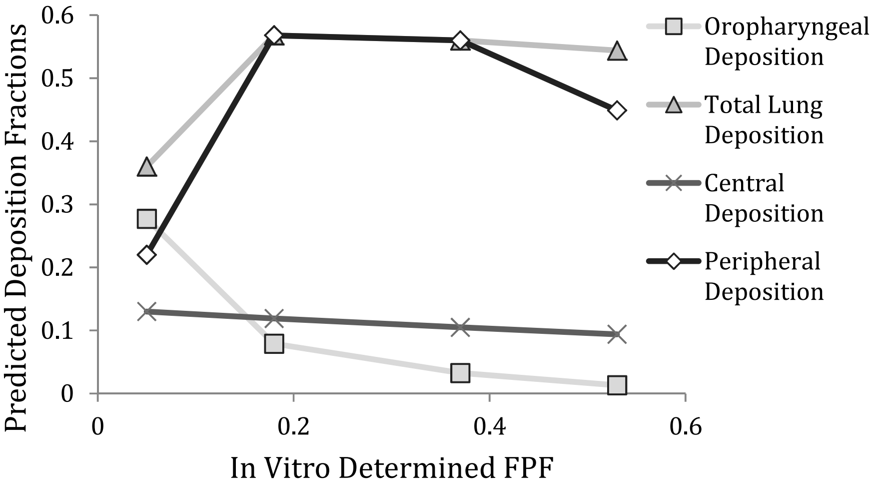

Fig. 5 Relationships between the in vitro determined fine particle fractions and the in silico predicted deposition patterns using HFA 134a/ethanol pMDI formulations.

are minimized and only 2.5% ethanol is present. The disparities between the data sets are derived from the more realistic in silico breathing model, whereby the high proportion of extra fine particles present in these aerosols are governed by diffusion based lung deposition mechanisms and, therefore, are more susceptible to exhalation. Exhaled particles are generally not accounted for when performing analysis on cascade impaction data and therefore are counted as respirable despite their propensity for avoiding lung deposition without a breath hold during inhalation. The in vitro fine particle fractions did appear to correlate with central deposition predictions (linear negative correlation) and oropharyngeal deposition (negative correlation). The model may be useful in directing formulation studies to achieve desired deposition profiles, that are perhaps more meaningful than standard cascade impaction or laser diffraction studies. To determine the potential for prediction of deposition for these inhaler types in humans, we used data obtained from clinical lung imaging dosimetry studies in the next part of the study.

In vivo – in silico Correlations

Four additional simulations were performed, using the data presented in a paper by Leach et al.[23] in which in vitro and in vivo data were obtained for CFC and HFA based inhaler systems. In these studies, four experimental groups were assessed in normal subjects:

1) HFA-BDP-50 (HFA-BDP, 50 microgram shot)
2) HFA-BDP-100 (HFA-BDP, 100 microgram shot)
3) CFC-BDP-50 (CFC-BDP, 50 microgram shot)
4) CFC-BDP-250 (CFC-BDP, 250 microgram shot)

The model input parameters were derived from the data published in the paper by Leach et al. Specifically, the input particle size distributions are shown in **Fig. 6** for both the HFA and CFC based systems. **Table 1** shows the physiological parameters input into the in silico model. The flow profile for both propellants was assumed parabolic. Airway morphology was assumed to be represented by Weibel Symmetric A, adult model.

Model predictions over estimated performance of the CFC-based inhaler formulations used in these experiments (**Fig. 7**). Experimentally determined oropharyngeal deposition was underestimated significantly and, therefore, total lung deposition was over estimated. This was similar to the findings for the HFA formulations (also a HFA-ethanol based solution formulation) where the model also underestimated oropharyngeal deposition. Despite this, the model accurately predicted total lung deposition.

The oropharyngeal predictions are likely to underestimate deposition due to limitations in the input data. In particular, input data is derived from measures of the particle size distributions of the inhaled aerosols. In most cases this is obtained from cascade impaction studies which truncates the particle size distribution as its upper particle size limit is around 10 microns. This truncation likely leads to underestimation of the emitted particle size and, therefore, underestimates the aerosol potential for inertial impaction on the orophartnyx.

The good agreement between total lung deposition predicted and that experimentally measured confirms earlier research using this model in other systems that showed good predictability. **Fig. 8** shows that HFA solution based systems are predicted to yield much greater peripheral deposition than central

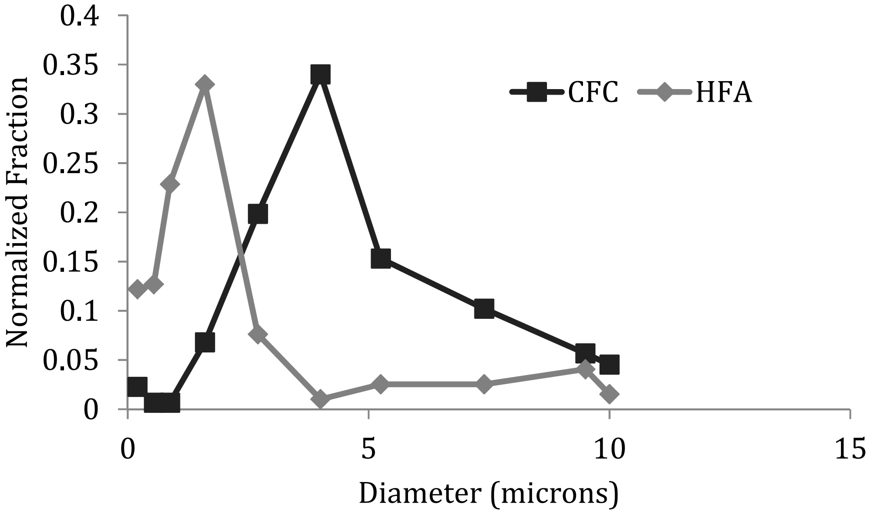

Fig. 6 Particle size distributions used as input data for the in silico model predictions of lung deposition.

Table 1 Physiological parameters measured during the in vivo lung deposition studies comparing HFA and CFC formulations

Formulation	Tidal Volume	Inspiration/ Expiration Time	Breath-Hold Time
HFA-BDP-50	5295 ml	3.1 sec	10.4 sec
HFA-BDP-100	4503 ml	3.4 sec	10.0 sec
CFC-BDP-50	5388 ml	3.2 sec	10.3 sec
CFC-BDP-250	5190 ml	3.1 sec	10.2 sec

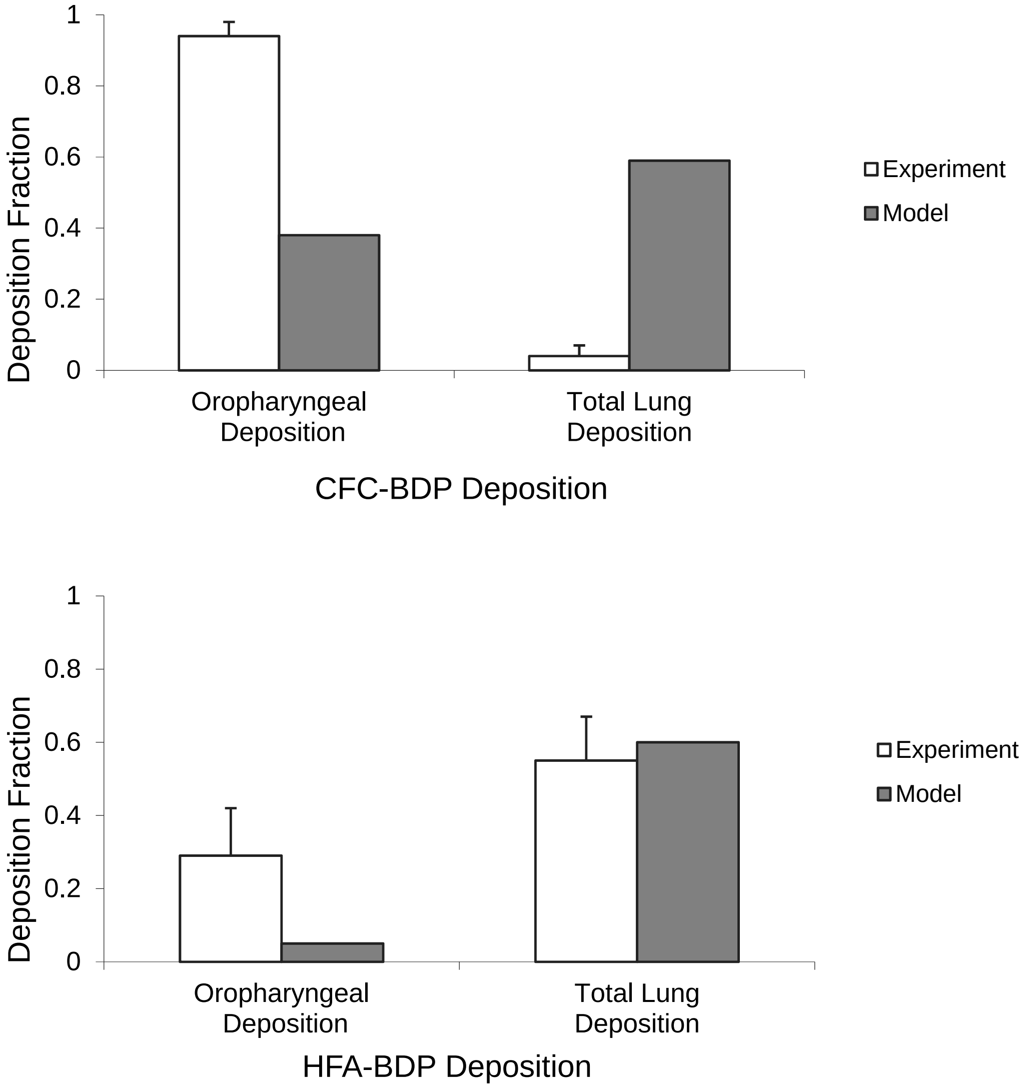

Fig. 7 Comparison of the model predictions of lung deposition to the in vivo experimentally determined lung deposition fractions for CFC based inhalers (upper graph) and HFA based inhalers (lower graph).

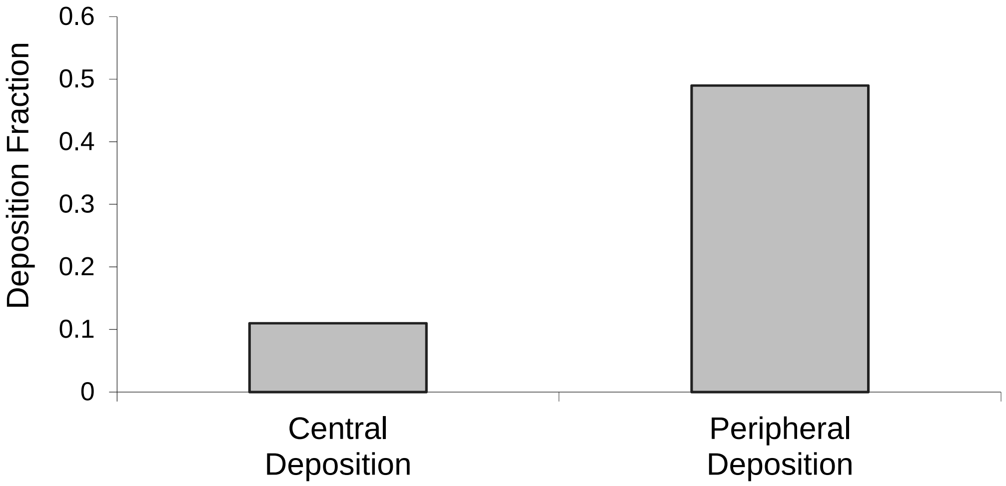

Fig. 8 Central versus peripheral lung deposition fractions for HFA based metered dose inhalers as predicted by the in silico model.

airway deposition. This is confirmed in other studies using HFA 134a solution based systems where lung imaging has shown significantly more peripheral deposition in human subjects[23, 24, 25].

4. Conclusion

We believe the validated *in silico* aerosol dosimetry model used in this work is a valuable research tool. It can be employed in a complimentary manner with technological (e.g., inhaler design and development) and medical (e.g., targeted drug delivery) issues of importance to inhalation therapy. Additional studies designed specifically to address the limits of the model with respect to input data for the major categories of inhaler (pMDI, dry powder inhaler and nebulizer) and implications for clinical impact would be desirable.

Acknowledgements

Disclaimer: K.K. Isaacs was supported by NHEERL-UNC DESE Cooperative training agreement in Environmental Sciences Research, EPA CT829471. The information in this document has been funded wholly (or in part) by the U.S. Environmental Protection Agency. Its contents are solely the responsibility of the authors and do not necessarily represent official views of the agency. The paper has been subjected to the agency's review process and has been approved for publication. Mention of trade names or commercial products does not constitute an endorsement or recommendation for use..

References

1) Usmani, O. S., Biddiscombe, M. F., Nightingale, J. A., Underwood, S. R. and Barnes, P. J. (2003): Effects of bronchodilator particle size in asthmatic patients using monodisperse aerosols, J Appl Physiol, 95, pp. 2106–2112.
2) Smyth, H. D. C. and Leach, C. L. (2006): Alternative Propellant Aerosol Delivery Systems, Critical Reviews™ in Therapeutic Drug Carrier Systems, 22(6), pp.493-534
3) Smyth, H. D. C. (2005): Propellant-Driven Metered-Dose Inhalers For Pulmonary Drug Delivery, Expert Opinion on Drug Delivery, 2(1), pp.53 – 74,
4) Smyth H. D. C. (2003): The Influence Of Formulation Variables On The Performance Of Alternative Propellant-Driven Metered Dose Inhalers, Advanced Drug Delivery Reviews, 55(7), pp. 807-828
5) Smyth H. D. C., Beck V.P., Williams D. and Hickey A. J. (2004): The Influence Of Formulation And Spacer Device On The In Vitro Performance Of Solution Chlorofluorocarbon-Free Propellant-Driven Metered Dose Inhalers, AAPS PharmSciTech, 5(1), Article 7
6) Smyth, H. D. C., Isaacs, K., Martonen, T. and Hickey, A. J. (2008): In Silico Predictions of Lung Deposition for Solution HFA 134a pMDIs with Spacers, Respiratory Drug Delivery 2008, Vol 3, pp 873-876.
7) Martonen, T. B. (1993): Mathematical model for the selective deposition of inhaled pharmaceuticals, J. Pharm. Sci., 82, pp.1191-1199.
8) Martonen, T., Fleming, J., Schroeter, J., Conway, J. and Hwang, D. (2003) : In silico modeling of asthma, *Adv. Drug Deliv. Rev*., Jul 18, 55(7), pp. 829-49.
9) Martonen, T. B., Rosati, J. and Isaacs, K. K. (2004): Modeling particle deposition in human airways, In: Aerosols Handbook, Measurement, Dosimetry, and Health Effects, Ruzer, L. and Harley, N. editors. CRC Press,.
10) Heyder, J., Gebhardt, J., Rudolf, G., Schiller, C.F. and Stahlhofen, W. (1986): Deposition of particles in the human respiratory tract in the size range 0.005–15 μm, *J. Aerosol Sci*., 17, pp. 811-825,.
11) Soong, T. T., Nicolaides, P., Yu, C. P. and Soong, S. C. (1979): A statistical description of the human tracheobronchial tree geometry, Respir. Physiol., 37, pp. 161-172.
12) Schroeter, J. D., Fleming, J. S., Hwang, D. and Martonen, T. B. (2002): A computer model of lung morphology to analyze SPECT images, Comput. Med. Img. Graph., 26, pp. 237-246,.
13) Burton, R., Isaacs, K. K., Fleming, J. and Martonen, T. B. (2004): Computer reconstruction of a human lung boundary model from magnetic resonance images. *Respir. Care*. 49(2), pp.180-185,.
14) Martonen T. B., Smyth H.D., Isaacs K. K. and Burton R. T. (2005): Issues in drug delivery: concepts and practice. *Respir Care*. Sep.50(9), pp.1228-52.
15) Martonen, T. B. (1982): Analytical model of hygroscopic particle behavior in human airways, *Bull. Math. Biol*., 44, pp. 425-442,.
16) Martonen, T. B. and Guan, X. (2001): Effects of tumors on inhaled pharmacologic drugs. I. Flow patterns, Cell Biochem. Biophys., 35, p. 233,.
17) Martonen, T. B. and Guan, X. (2001): Effects of tumors on inhaled pharmacologic drugs. II. Particle motion, Cell Biochem. Biophys., 35, pp. 233-243,.
18) Martonen, T. B., Zhang, Z., Yue, G. and Musante, C. J. (2002): 3-D particle transport within the human upper respiratory tract, J. Aerosol Sci., 33, pp. 1095-1110..
19) Isaacs, K. K., Martonen, T. B. and Schlesinger, R. (2006): Three-dimensional computational fluid dynamics simulations of particle deposition in the tracheobronchial tree. *J Aerosol Med*.,19(3), pp. 344-52.
20) Schlesinger, R. B., Gurman, J. L. and Lippmann, M. (1982): Particle deposition within bronchial airways: comparisons using constant and cyclic inspiratory flows. Ann. Occup. Hyg. 26, pp.47–64.

21) Martonen, T. B, Schroeter, J. D. and Fleming, J. S. (2007): 3D in silico modeling of the human respiratory system for inhaled drug delivery and imaging analysis. J Pharm Sci. , 96(3), pp. 603-17.

22) Smyth, H. D.C, Hickey, A. J. (2003): Multimodal Particle Size Distributions Emitted From HFA-134a Solution Pressurized Metered-Dose Inhalers, AAPS PharmSciTech, 4(3), article 38

23) Leach, C. L., Davidson, P. J. and Boudreau, R. J. (1998): Improved airway targeting with the CFC-free HFA-beclomethasone metered-dose inhaler compared with CFC-beclomethasone. Eur. Resp. J., 12(6), pp. 1346-1353.

24) Leach, C. L., Davidson, P. J., Hasselquist, B. E. and Boudreau, R. J. (2002): Lung Deposition of Hydrofluoroalkane-134a Beclomethasone Is Greater Than That of Chlorofluorocarbon Fluticasone and Chlorofluorocarbon Beclomethasone : A Cross-over Study in Healthy Volunteers, Chest, 122(2), pp. 510-516

25) Nave, R., Zech, K. and Bethke, T. D. (2005): Lower oropharyngeal deposition of inhaled ciclesonide via hydrofluoroalkane metered-dose inhaler compared with budesonide via chlorofluorocarbon metered-dose inhaler in healthy subjects, European Journal of Clinical Pharmacology, 61(3), pp. 203-208,

Author's short biography

Hugh DC Smyth, Ph.D

Hugh DC Smyth, Ph.D., Dr Hugh Smyth is currently Assistant Professor of Pharmaceutics at the University of Texas at Austin, College of Pharmacy. He is also Adjunct Associate Scientist at Lovelace Respiratory Research Institute in Albuquerque, New Mexico. He received his Ph.D. in Drug Delivery from the University of Otago in New Zealand, in collaboration with GlaxoWellcome Inc. in Research Triangle Park, North Carolina. He did a postdoctoral fellowship at the University of North Carolina at Chapel Hill. Following two years as a Research Assistant Professor at this same institution he took a faculty position at the University of New Mexico (2005) prior to moving to Texas in 2009. He serves on several advisory boards for professional societies and international journals. He has published over 40 scientific peer-reviewed manuscripts, has 12 patent applications pending, and is editor of two books and author of 8 book chapters. In 2007, he was awarded the 2007 AAPS New Investigator Award in Pharmaceutics and Pharmaceutical Technologies, and also the 2007 Pharmaceutical Research and Manufacturers Association New Investigator award.

Author's short biography

Ted Martonen, Ph.D

Ted Martonen, Ph.D., is a research physicist. His research has primarily focused on the development of mathematical models which describe the behavior and fate of inhaled substances for risk assessment. Through his collaborations with pharmaceutical scientists, Dr. Martonen has shown that there is a great commonality between the fields of toxicology and medicine. Specifically, he realized that dosimetry models for air pollutants, since they quantitate the toxic particulate matter delivered to airway cells, could be integrated into the treatment of airway diseases caused or exacerbated by those same air pollutants.

Kristin Isaacs, Ph.D

Kristin Isaacs, Ph.D., Dr. Isaacs received a PhD in biomedical engineering from Vanderbilt University (Nashville, TN) in 2002. From 2002 to 2005 she was a postdoctoral fellow at the U.S. EPA's National Health and Environmental Effects Research Laboratory in Research Triangle Park, NC. Currently she is a Research Physical Scientist in EPA's National Exposure Research Laboratory. Her research interests include analysis of human activity patterns, stochastic human exposure modeling of air pollutants and multimedia chemicals, and particulate matter lung dosimetry.

Anthony J Hickey, Ph.D

Anthony J Hickey, Ph.D., Dr. Hickey is Emeritus Professor of Molecular Pharmaceutics of the Eshelman School of Pharmacy, and Adjunct Professor Biomedical Engineering of the School of Medicine, at the University of North Carolina at Chapel Hill (Professor, 1993-2010). He obtained Ph.D. (1984) and D.Sc. (2003) degrees in pharmaceutical sciences from Aston University, Birmingham, UK. Following postdoctoral positions, at the University of Kentucky (1984-1988) Dr. Hickey joined the faculty at the University of Illinois at Chicago (1988-1993). In 1990 he received the AAPS Young Investigator Award in Pharmaceutics and Pharmaceutical Technology. In 1993 he joined the faculty of the School of Pharmacy, UNC-CH. He is a Fellow of the UK Society of Biology (2000), the American Association of Pharmaceutical Scientists (2003) and the American Association for the Advancement of Science (2005). He has published numerous papers and chapters in the pharmaceutical and biomedical literature, one of which received the AAPS Meritorious Manuscript Award in 2001. He has edited five texts on pharmaceutical inhalation aerosols and co-authored others on Pharmaceutical Process Engineering, Particulate Science and Pharmaco-complexity. He is founder, President and CEO of Cirrus Pharmaceuticals, Inc. (since 1997), founder (2001, and formerly CSO, 2002-2007) of Oriel Therapeutics, Inc, which was acquired by Sandoz in 2010, member of the Pharmaceutical Dosage Forms Expert Committee of the United States Pharmacopeia (2010?2015) and formerly Chair of the Aerosols Expert Committee of the United States Pharmacopeia (2005-2010). Dr. Hickey conducts a multidisciplinary research program in the field of pulmonary drug and vaccine delivery.

Comparison of Wall Friction Measurements by Jenike Shear Tester and Ring Shear Tester[†]

Ting Han[*]
The Dow Chemical Company

Abstract

For a silo design, it is very important to understand the friction characteristics of bulk solids with silo walls. This so-called wall friction angles were measured in this study with two different testers: Jenike shear tester and Schulze ring shear tester (RST). Soft PE plastic pellets A was used as the tested bulk solids while stainless steel SS 304 and aluminum Al 6061were selected as wall plates.

It was found that the most important parameter in this study is wall roughness. With decreasing wall roughness, wall friction angles decrease no matter which tester was used. Wall friction angles for both testers were similar if wall roughness was similar. The only exception is under the testing condition of the low pressure (500 Pa) on a wall plate. In addition, the impact of testing temperatures (22 and 37 °C) has been described in this study.

Keywords: Wall friction measurement, Jenike shear tester, ring shear tester, wall friction angle, wall roughness

1. Introduction

Wall friction of bulk solids is a critical parameter when designing a mass flow silo/hopper. A translatory shear tester, the Jenike shear tester, is widely used in measuring the wall friction of bulk solids. However, the Jenike shear tester is not an automated apparatus, and its testing results are operator dependent[1]. Schulze et. al.[2] developed a new ring shear tester, which can be used to measure the wall friction of bulk solids automatically. Schwedes et. al.[3] reviewed developments in the design of several shear testers, including Jenike shear tester and ring shear tester. They considered these two testers as the simpler testers to permit straightforward measurement of the flow properties used for practical applications.

In this work, the wall friction of the soft PE plastic pellets A was measured with a) the Schulze ring shear tester RST-01, and b) the Jenike shear tester. The effect of elasticity of products was not investigated in this paper.

2. Testing Methods and Materials

2.1 Ring Shear Tester (RST)

The wall friction cell of the Schulze ring shear tester is shown in **Fig. 1**[4]. To measure the wall friction using the RST, the distance between the upper surface of the wall material sample and the upper edge of the shear cell should be about 8 to 10 mm. The details on the operating procedure of RST could be found in the reference[4].

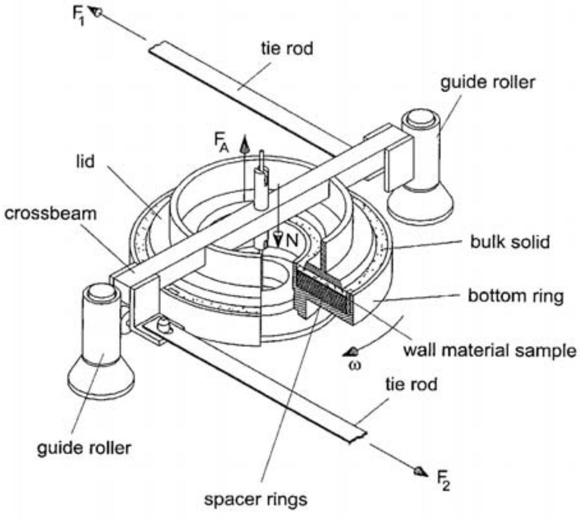

Fig. 1 Jenike-Schulze Wall Friction Cell [4].

[†] Accepted: July 8th, 2011
[1] Midland, MI, USA
[*] Corresponding author
E-mail: than@dow.com
TEL: (+1)989-633-1166; FAX: (+1)989-636-4019:

ⓒ 2011 Hosokawa Powder Technology Foundation

Fig. 2[4] shows where the shear force Sw is plotted vs the shear travel measured by a ring shear tester. Relating the shear force to the normal force N_w, the Wall Yield Loci (WYL) can be calculated (**Fig. 2** right). Typically the WYL is convex-upward. The wall friction angle, φ_w, then is, defined as:

When tests are to be conducted at elevated temperature, the solids and shear cells are heated to test temperature in an oven prior to conducting the shear test. The heated shear cell and solids are removed from the oven and placed on the ring shear tester to measure the flow properties. During a shear test, Infrared lamps are arranged around the shear cell to prevent the cooling of the shear cell during the test. At the end of each shear test, the temperature of the solids in the shear cell is checked to ensure that the temperature of the solids and the wall friction sample remained constant during the shear test.

2.2 Jenike Shear Tester

A sketch of the Jenike shear tester is presented in **Fig. 3** and the procedure to measure the wall friction angle with the Jenike shear tester could be found in the reference[5].

The recorded values of normal loads, N_w, and shear stress, S_w, (**Fig. 3**) from Jenike shear tester could be plotted as shown in **Fig. 2** right (the same as for the RST). Then the wall friction angle, φ_w, can be obtained by Eq. (1). Since a wall yield locus is usually represented by a curved line, the wall friction angle varies and is a function of the pressure at the wall.

2.3 Wall Roughness Tester

A Taylor Hobson manufactured wall roughness tester (model: Surtronic™3+) was used to measure the wall roughness, Ra, for all wall plates. The typical relationship of the finishing process vs approximate range of Ra values was listed in **Table 1**[6].

$$\tan\varphi_w = \frac{S_w}{N_w} \tag{1}$$

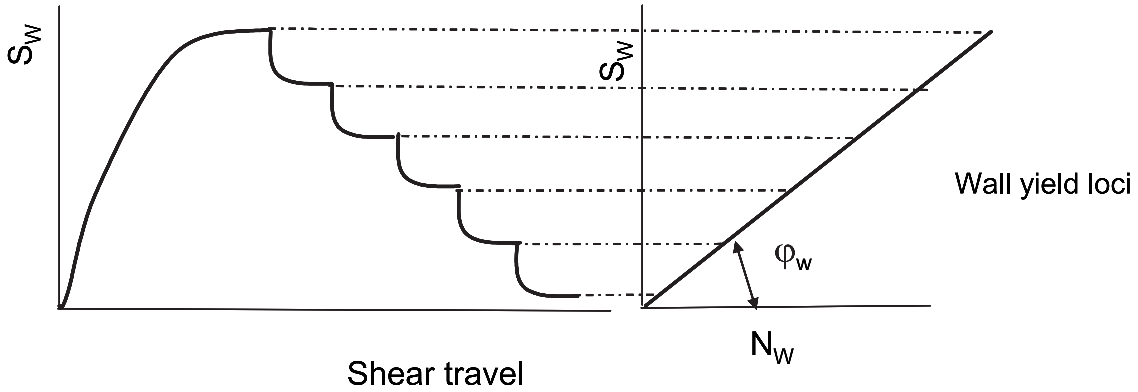

Fig. 2 Wall Yield Locus (WYL) Obtained by the Ring Shear Tester [4].

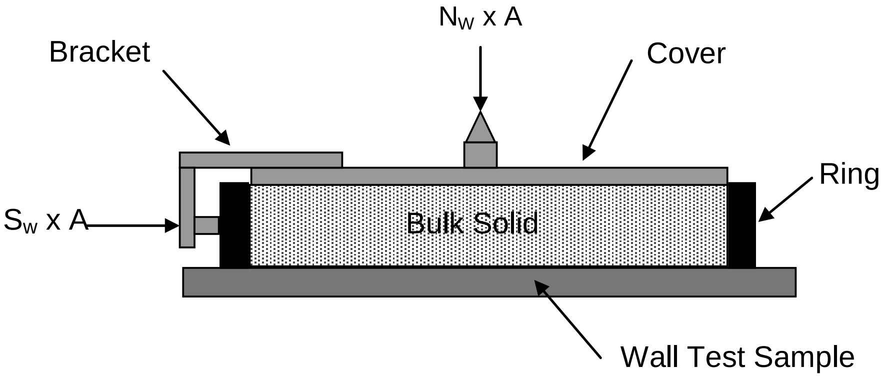

Fig. 3 A Sketch of Jenike Shear Tester.

Table 1 Finishing process vs approximate range of Ra values [6)]

Finishing Process	Ra, μ m	Finishing Process	Ra, μ m
Super-finishing	0.05 – 0.2	Boring	0.4 – 6.3
Lapping	0.05 – 0.4	Drawing	0.8 – 3.2
Diamond turning	0.1 – 0.4	Broaching	0.8 – 3.2
Honing	0.1 – 0.8	Extruding	0.8 – 3.2
Grinding	0.1 – 1.6	Milling	0.8 – 6.3
Turning	0.4 – 6.3	Shaping	1.6 – 12.5

2.4 Bulk Solids

In this work, soft PE plastic pellets A was used as the tested bulk solids.

2.5 Wall Plates

In this work, 4 different wall surfaces were tested:

1. Stainless Steel SS304 polished
2. Stainless Steel SS304 non-polished
3. Aluminum Al6061 polished
4. Aluminum Al6061 non-polished

The wall roughness, Ra, for each plate has been measured with Surtronic 3+ and shown in **Table 2**. RST uses a round wall plate and only one orientation's roughness is measured. However, Jenike shear tester uses a square wall plate. Square wall plates can have different wall roughness in the different orientation due to the manufacturing process. Therefore, the wall roughness on the different orientations (along with grain and against grain) was measured for each square wall plate (apply for Jenike shear tester only).

3. RESULTS AND DISCUSSION

3.1 Comparisons of Wall Friction Measurement by RST and Jenike Shear Tester

The wall friction angles can be affected by wall surface conditions and bulk solids characteristics[7)]. For the purpose of comparing the results of the RST and the Jenike shear tester, only soft plastic pellets A was chosen to be tested by these two methods separately with the same testing conditions besides the wall plates. Here, two wall materials (SS 304 & Al 6061), and two wall surface conditions (polished and non-polished) were tested for the soft plastic PE pellets A. **Fig. 4** shows the wall friction angles of soft plastic PE pellets A measured on different SS 304 wall plates with different wall roughness by Jenike shear tester and Schulze ring shear tester. The tests were carried out at 22℃ & 37℃, respectively. It can be seen from **Fig. 4 (a)** and **(b)** that the wall friction angles are similar if the wall roughness is similar, no matter if the Jenike shear tester was used or Schulze ring shear tester was used.

If the wall roughness is significantly different, **Fig. 4** further shows wall friction angles increase with in-

Table 2 Wall roughness of wall plates

Wall Material	Tester/Orientation	Surface Condition	Ra, μ m
SS 304	Jenike-Against Grain	Non-Polish	1.71
SS 304	Jenike-Along Grain	Non-Polish	1.45
SS 304	RST	Non-Polish	1.09
Al 6061	Jenike-Against Grain	Non-Polish	0.79
Al 6061	Jenike-Along Grain	Non-Polish	0.57
Al 6061	RST	Non-Polish	0.36
SS 304	Jenike-Against Grain	Polish	0.34
SS 304	Jenike-Along Grain	Polish	0.28
SS 304	RST	Polish	0.11
Al 6061	Jenike-Against Grain	Polish	0.50
Al 6061	Jenike-Along Grain	Polish	0.39
Al 6061	RST	Polish	0.13

creasing wall roughness independent of wall surface conditions (polished or non-polished) and testing methods (RST or Jenike shear tester). Comparing the wall friction angles in **Fig. 4 (a)** and **(b)**, it also could be found that wall friction angles have no significant changes under the different testing temperature conditions (22℃ and 37℃).

3.2 Wall Friction Angle vs Wall Roughness

Fig. 5 and **6** show wall friction angle vs. wall roughness under 22℃ for RST and Jenike shear tester, respectively. It might be concluded from **Fig. 5** and **6** that wall roughness of a wall plate is the key parameter to control wall friction angles of soft PE plastic pellets A. The trends in **Fig. 5** and **6** predict

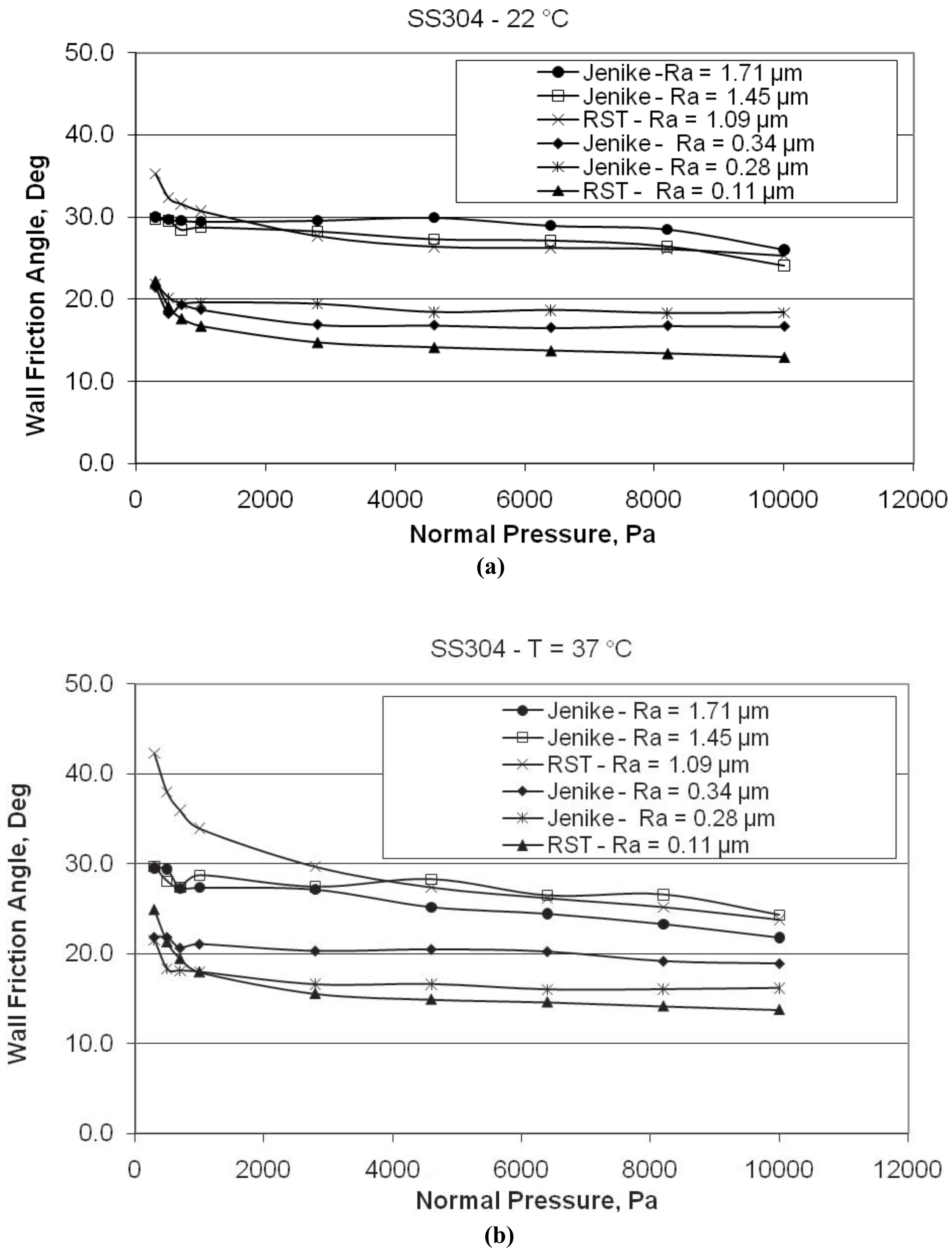

(a)

(b)

Fig. 4 Wall Friction Angles of Pellets A against Different Surfaces at 22℃ & 37℃.

that with increasing wall roughness the wall friction angles increase. It also could be seen from **Fig. 5** and **6** that wall friction angles increase with decreasing normal pressure on walls.

Furthermore, it was observed from **Fig. 5** and **6** that under high normal pressures (4,600 Pa and 10,000 Pa), wall friction angles only depend on wall roughness, no matter which testing method was used. However, for the low normal pressure (500 Pa), wall friction angles measured by RST are much larger than those measured by Jenike shear tester.

The reason for the difference at low normal pressure is not clear, and also it could not be explained which one is more accurate. However, the low pressure on walls is usually found close to the silo outlet during discharge. If the critical wall friction angle located at the low pressure when designing a silo/hopper, the larger wall friction angle from RST will give

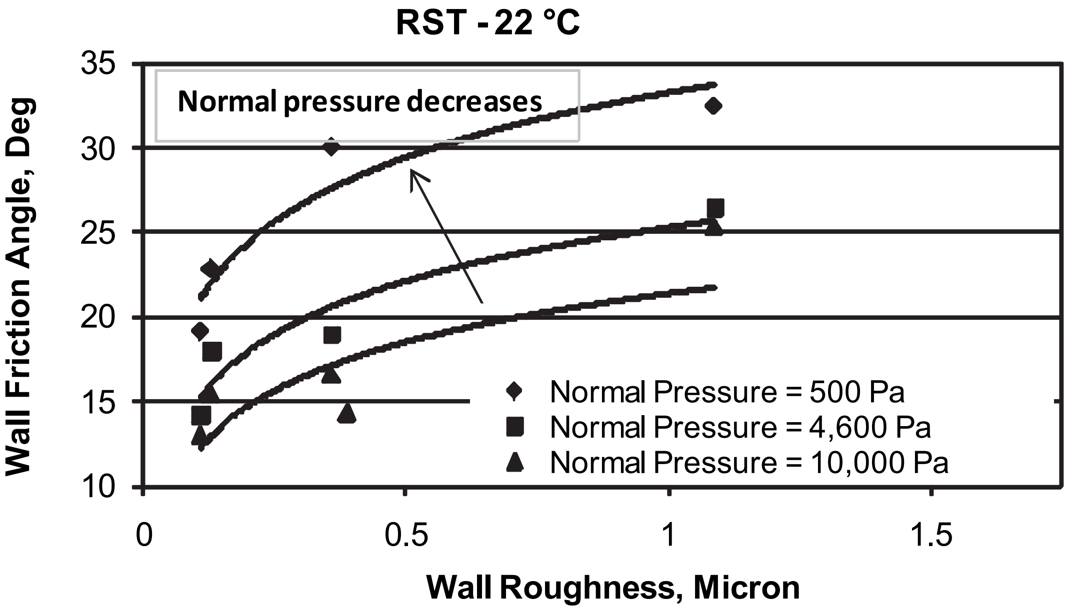

Fig. 5 Wall Friction Angle vs. Wall Roughness (RST at 22℃).

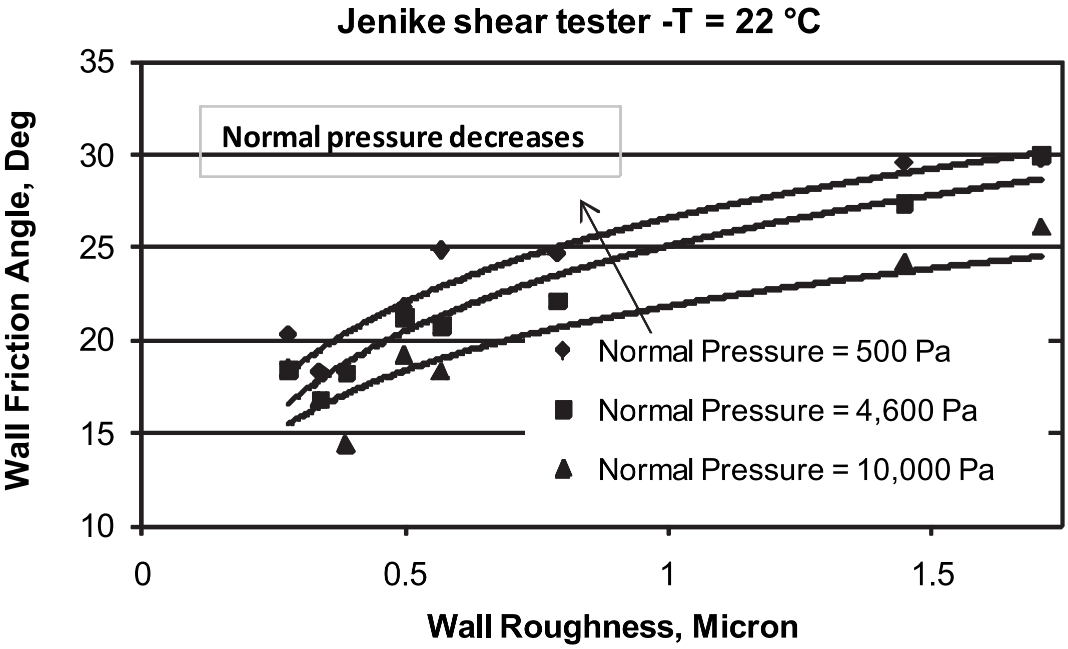

Fig. 6 Wall Friction Angle vs. Wall Roughness (Jenike Shear Tester at 22℃).

a more conservative design to avoid the potential of funnel flow. However, a steeper hopper increases total construction cost.

It was derived[1)] that an increase in the wall friction angle of φ_w of 1 degree, roughly leads to a decrease in the half hopper angle (measured from the vertical) of 1.3 degree. Therefore, the difference of several degrees of wall friction angles will also significantly impact the evaluation of a silo/hopper for a given bulk solids. The similar relationship of wall friction angle vs. wall roughness was also applied for the higher testing temperature (37℃). The results have been shown in **Fig. 7** and **8**. By further comparing the curves in **Fig. 7** and **8**, we can conclude that no significant difference was found between these two testing temperatures.

4. Conclusions

It was found that the most important parameter in this study is wall roughness. With decreasing wall

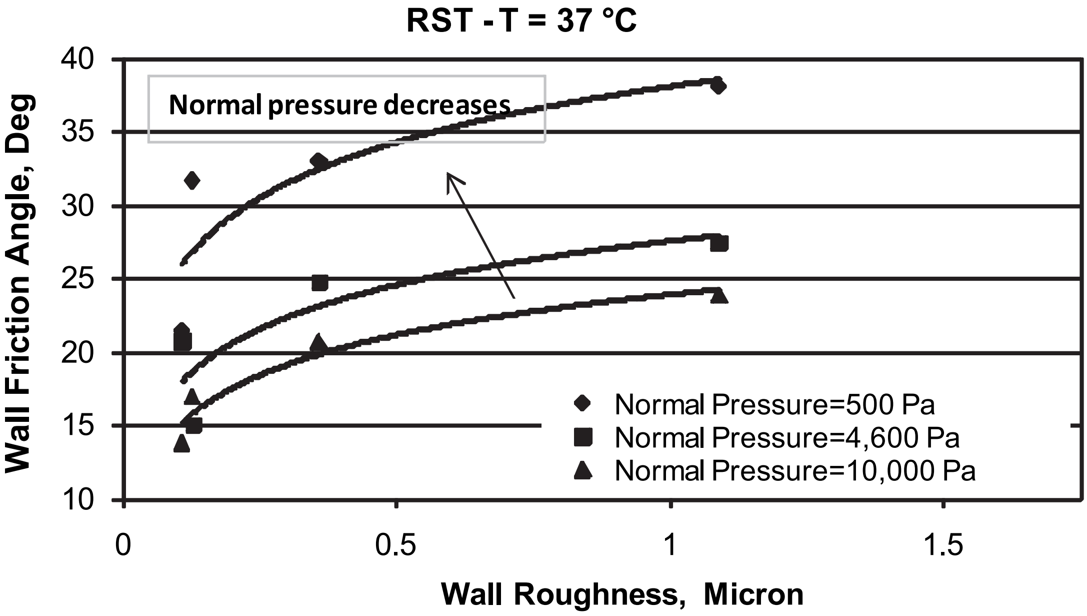

Fig. 7 Wall Friction Angle vs. Wall Roughness (RST at 37℃).

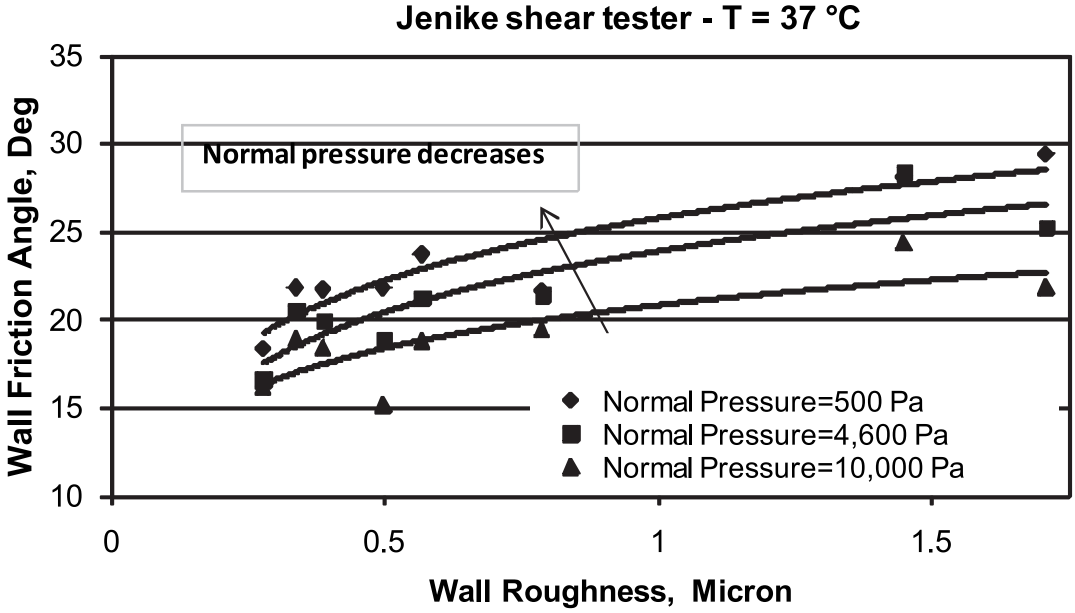

Fig. 8 Wall Friction Angle vs. Wall Roughness (Jenike shear tester at 37℃).

roughness, wall friction angles decrease no matter which tester was used. Wall friction angles for both RST and Jenike shear tester were similar if wall roughness was similar. The only exception is under the testing condition of the low pressure (500 Pa) on a wall plate, while Schulze ring shear tester gave larger wall friction angles than Jenike shear tester did. In addition, wall friction angles have no significant changes under the different testing temperature conditions (22℃ and 37℃).

Acknowledgement

Jorg Theuerkauf was appreciated on discussion of this study. Tieying Gong and Bing Du's contributions on the testing parts were very useful and aided its completion.

References

1) Haaker, G. (1999): Wall Friction Measurement on Bulk Solids: Results of Comparative Measurements on 9 Bulk-Solid/Wall Combinations from 13 Laboratories Using the Jenike Sheartester, Powder Handling & Processing, 11(1), pp. 19-26.

2) Behres, M. Klasen, C.J. and Schulze, D. (1998): Development of a Shear Cell for Measuring the Wall Friction of Bulk Solids with a Ring Shear Tester, Powder Handling & Processing, 10(4), pp. 405-412.

3) Schwedes, J. and Schulze, D. (1990): Measurement of Flow Properties of Bulk Solids, Powder Technology, 61, pp. 59-68.

4) Dietmar, S. (1999): Ring Shear Tester RST-01.pc Operating Instructions.

5) Jenike, A. W. (1989): Storage and Flow of Solids, Bulletin No. 123, Utah Engineering Experiment tation, University of Utah, Salt Lake City, Utah, Thirteenth Printing, April, 1989.

6) Surtronic 3+ (1997): Operator's Handbook, Taylor Hobson.

7) Prescott, J.K. Ploof, D.A. Carson, J.W. (1999): Developing a Better Understanding of Wall Friction, Powder Handling & Processing, 11(1), pp. 27-35.

Author's short biography

Dr. Ting Han

Dr. Ting Han received B.S. and M.S. degrees in Metallurgical Science and Engineering from Northeastern University (China). He received Ph.D. degree in Mechanical Engineering from Ben-Gurion University, Israel. He was a postdoc fellow in Chemical Engineering, Carnegie Mellon University, USA. After he joined in the Dow Chemical Company, he worked in solids processing group of Dow Corporation R&D at Freeport, TX for 4 years. Right now he is working in Energy Storage Device Material (ESDM) R&D at Dow Midland, MI, on solids processing, including powder coating, milling and particle characterization.

Classification of Particles Dispersed by Bead Milling with Electrophoresis[†]

Tetsuya Yamamoto*, Yoshitaka Harada, Takayuki Tsuyama, Kunihiro Fukui and Hideto Yoshida
Department of Chemical Engineering, Hiroshima University[1]

Abstract

The purpose of the present study is to develop a new particle classification technique and apparatus to replace centrifugal separation method, where continuous operation for classification is impossible because of the deposition of the coarse particles on the wall of the separator. In our recent research, it was clear that the zeta potential of the silica particles dispersed by a bead mill had size dependency. Hence, the particles were classified using an electrical field flow fractionation (EFFF) system under the condition that the zeta potential of the smaller particles was more negative than that of larger particles. Previous EFFF apparatus utilized horizontal field flow; however, the apparatus designed in this study had vertical field flow and cylindrical channel with length of 350 mm and radius width of 6 mm to reduce the running cost and operation time for classification of particles. About the classification performance of this apparatus, it was found that the silica particles with the size from 50 nm to 400 nm were classified using a low applied voltage. This method prevented deposition of particles on the wall of the apparatus and allowed continuous operation. Results of theoretical calculations supported qualitatively the experimental results obtained in this research.

Keywords: Zeta Potential, Classification, Electrophoresis, EFFF

1. Introduction

One of the current industrial requirements is technique of separation and classification for nanoparticles because their applications become widespread. So far, we have developed particle-classification techniques using electrical field flow fractionation[1-3] and beads mill dispersion. Bead mills have been widely used for the dispersion of particles in suspension[4]. In recent studies, a bead mill capable of nanoparticle dispersion was developed[5], the surface potential of silica particles treated with a bead mill demonstrated size dependency — smaller particles had a more negative zeta potential. It was found that the mechanism for size dependency was related with the collision and frictions between particles and beads in the beads mill[6,7].

This technique effectively classifies nano-sized particles using vertical or horizontal electrophoresis[8-10]. The purpose of the present study is to develop compact classification apparatus with electrophoresis and to evaluate its classification performance.

2. Experimental

2.1 Measurement of particle size distribution and zeta potential

Particle size distribution of the slurries was measured using dynamic light scattering (DLS; LB-550, HORIBA Co., Ltd.). For the DLS measurements, the particle concentration of the slurry was adjusted so that the intensity of the scattered light would be detectable using the DLS apparatus. Because the DLS measurement of nanoparticle distribution included error, the parameters of the DLS measurements were modified to reduce the difference between the size distributions obtained using DLS and transmission electron microscopy. Modification of the DLS parameters allowed for a nearly accurate measurement of the nanoparticle size distribution[11].

[†] Accepted: July 26th, 2011

[1] 1-4-1,Kagamiyama, Higashi-Hiroshima-shi, Hiroshima 739-8527, Japan
* Corresponding author
E-mail: ytetsuya@hiroshima-u.ac.jp
TEL: (+81) 82-424-7853 FAX: (+81) 82-424-5494

ⓒ 2011 Hosokawa Powder Technology Foundation

Zeta potentials of the slurries were measured using a ZETASIZER (ZETASIZER 2000, MALVARAN Co., Ltd.).

2.2 Properties of the particle dispersed by a bead mill

Silica powder (DENKA FUSED SILICA, Denki Kagaku Kogyo, Co., Ltd.) with a specific surface area of 22.4～24.1 m^2/g was used as the test powder in the present study. Glass beads (Plasma Beads, Neturen Co., Ltd.) ranging in size from 100 μm to 150 μm were selected for use in the bead mill (UAM-015, Kotobuki Industries Co., Ltd.), because their composition was almost identical to that of the test powder.

A bead mill was used to disperse the silica powder in water that had been deionized using an ion-exchanged resin. The resulting slurry was subsequently used for nanoparticle classification by EFFF. The bead mill was operated using the following procedures and conditions. First, the silica powder was added to 1.25 L of deionized water with gentle stirring at a final concentration of 2 wt% of the slurry mass. Then, the slurry was circulated from the slurry tank to the bead mill at a flow rate of 3.33×10^{-3} L/s using a pump. The peripheral speed of the bead mill rotor was 6.24 m/s and the glass beads occupied 60% of the chamber volume of the bead mill. After the milling operation for 30 min, the dispersed slurries were prepared. The size distribution of the tested silica particles was shown in **Fig. 1a**. Each size of particle obtained as a result of bead milling was characterized. The dispersed slurry prepared using the bead mill was separated into different sized particles using a centrifugal separator (Kansai Centrifugal Separator Mfg. Co., Ltd.), and then the zeta potential of the each sized particles were measured by the ZETASIZER. The relationship between zeta potential and median size was shown in **Fig. 1b**, which indicated that the zeta potential of the slurry had size dependency; the zeta potential of the smaller particles was more negative than that of the larger particles. The mechanism of which has been investigated elsewhere[5]. The relationship between the zeta potential and the particle diameter is shown in Eq. (1).

$$\zeta = 0.08390\, D_P - 53.68 \tag{1}$$

Also, the sedimentation balance method[12] was used to clarify the relationship between zeta potential and the specific size of the particle dispersed by the beads mill instead of the centrifugal classification. Here, the conventional sedimentation balance apparatus was equipped with vertical electrophoresis. And then, the result was shown in the following equation calculating differences of the sedimentation curves before and after applying voltage at the electrical potential. This equation was applied to the silica particles with the size from 30 nm to 500 nm.

$$\zeta = -640.4\, D_P^2 + 452.7\, D_P - 99.07 \tag{2}$$

2.3 Classification of particles by the channel with electrophoresis

As shown in **Figs. 2**, an EFFF system was used to separate fine particles from the dispersed slurry produced by bead milling. A double cylindrical channel with length of 350 mm and a radius width of 6 mm stood vertically, as shown in **Fig. 2b**. The slurry was stirred in the slurry tank where the temperature and concentration of the slurry were controlled to be 30 ℃ and 0.2 wt%, respectively. There were three inlets in the top of the EFFF channel. One inlet was located at the nearest center of the apparatus and was used to supply the dispersed slurry from the slurry tank, and the others were used to supply the deionized water from the water tank.

The flow rates of the slurry and deionized water could be controlled at their respective inlets. The linear velocities of the slurry and deionized water were equivalent, and the total flow rate was from 200 to 500 mL/min to create laminar flow in the channel. The outside wall of the channel was the positive electrode and the inside cylinder served as the negative electrode. A DC electric field was generated perpendicular to the direction of fluid flow in the channel. Therefore, negatively charged silica particles moved towards the wall of the channel. A thin plate was placed at the bottom outlet for separation of particles in the outlet flow.

Partial separation efficiency, $\Delta\eta$, which is defined by Eq. (3), was used to evaluate classification performance of the present apparatus. The mass of the dried powders from the fine silica and coarse particle slurries were measured. Sample of each slurry was collected by sample bottle, and the size distribution of each sample was determined by DLS.

$$\Delta\eta = \frac{m_c f_c\left(D_p\right)\Delta D_p}{m_f f_f\left(D_p\right)\Delta D_p + m_c f_c\left(D_p\right)\Delta D_p} \tag{3}$$

In the above equation, m_c and m_f represent the mass of the coarse silica powder and the separated fine powder, while f_c and f_f represent the size distributions of the coarse silica powder and the separated fine powder, respectively.

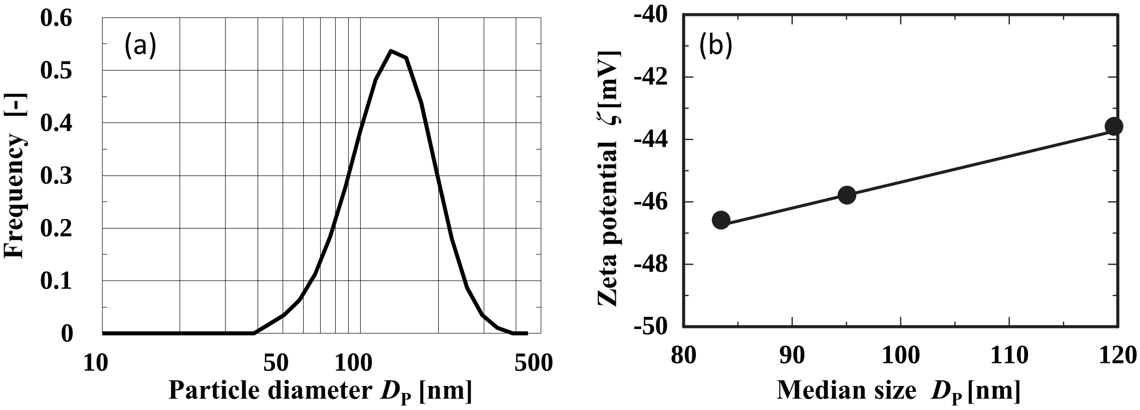

Fig. 1 Properties of the tested silica particle: (a) size distribution; (b) zeta potential with median size.

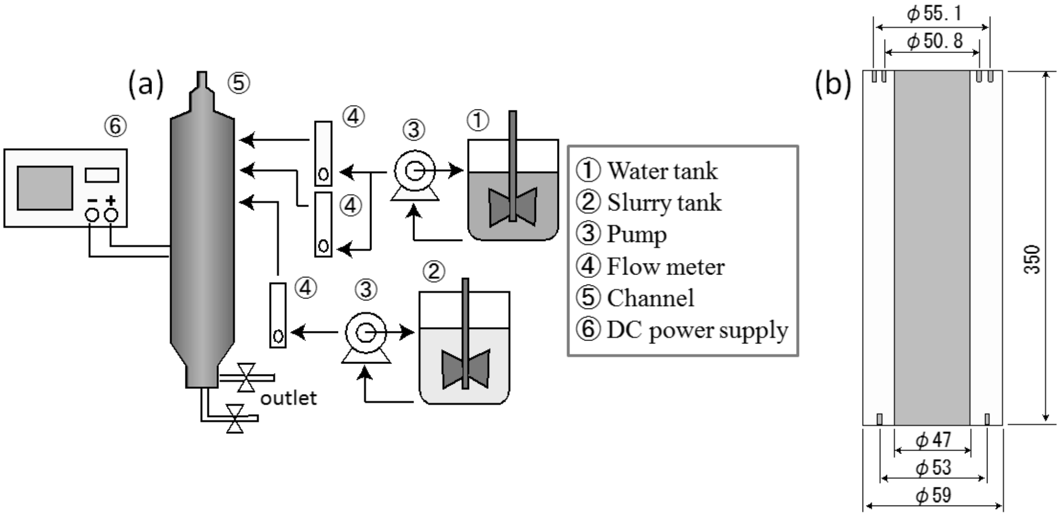

Fig. 2 Experimental apparatus: (a) experimental system; (b) sectional details of the channel.

3. Theoretical Calculations

v_g and v_e represent the Stokes sedimentation velocity and the velocity of electrophoresis, which are determined by Eqs. (4) and (5), respectively[13].

$$v_g = \frac{(\rho_P - \rho_f)\, D_P^2 g}{18\mu} \tag{4}$$

$$v_e = \frac{\varepsilon \zeta E}{\mu} \tag{5}$$

The velocity distribution of channel flow was calculated using the control volume method, the *r-z* two-dimensional grid portion of the channel shown in **Fig. 3** on the assumption of axial symmetry, the equation of continuity, Navier-Stokes equations, and diffusion equation, as shown Eqs. (6) – (9).

$$\frac{\partial \rho}{\partial t} + \frac{1}{r}\frac{\partial \rho r u_r}{\partial r} + \frac{\partial \rho u_z}{\partial z} = 0 \tag{6}$$

$$\rho\left(\frac{\partial u_r}{\partial t} + u_r\frac{\partial u_r}{\partial r} + u_z\frac{\partial u_r}{\partial z}\right) = -\frac{\partial p}{\partial r} + \mu\left[\frac{\partial}{\partial r}\left(\frac{1}{r}\frac{\partial r u_r}{\partial r}\right) + \frac{\partial^2 u_r}{\partial z^2}\right] \tag{7}$$

$$\rho\left(\frac{\partial u_z}{\partial t} + u_r\frac{\partial u_z}{\partial r} + u_z\frac{\partial u_z}{\partial z}\right) = -\frac{\partial p}{\partial z} + \mu\left[\frac{1}{r}\frac{\partial}{\partial r}\left(r\frac{\partial u_z}{\partial r}\right) + \frac{\partial^2 u_z}{\partial z^2}\right] + \rho g \tag{8}$$

$$\frac{\partial rC}{\partial t} + \frac{\partial rCv_r}{\partial r} + \frac{\partial rCv_z}{\partial z} = D\left[\frac{\partial}{\partial r}\left(r\frac{\partial C}{\partial r}\right) + \frac{\partial}{\partial z}\left(r\frac{\partial C}{\partial z}\right)\right] \tag{9}$$

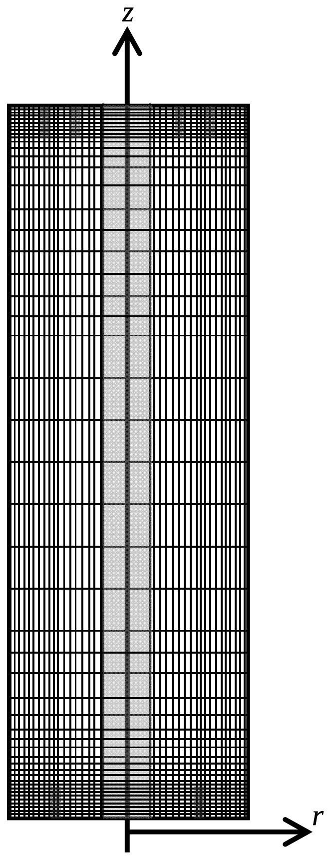

Fig. 3 Grid of the channel.

Pressure was calculated using the SIMPLE (Semi-Implicit Method for Pressure-Linked Equations) method. Particle trajectories and partial separation efficiency were calculated by numerical integration of the motion equations below, where u_r and u_z are fluid velocities in the r and z directions.

$$\frac{\mathrm{d}r}{\mathrm{d}t} = u_\mathrm{r} + v_\mathrm{e} \qquad \frac{\mathrm{d}z}{\mathrm{d}t} = u_\mathrm{z} + v_\mathrm{g} \tag{10}$$

4. Results and Discussion

4.1 The influence of applied voltage on partial separation efficiency curve

Figs. 4 show the influence of applied voltage on partial separation efficiency at the total flow rate of 300 mL/min by the experiments and theoretical calculations, where it was assumed that zeta potential, ζ, in Eqs (5) was represented by Eq. (1). The experimental and theoretical results were qualitatively consistent with each other. As the applied voltage decreased, the partial separation efficiency curve shifted towards small particles. This result indicated that the larger particles also moved to the fine outlet side, which was near the outside wall, by higher applied voltage according to the relationship between zeta potential and median size in **Fig. 1(b)**. For example, in the case of 300-nm particles, all of them cannot be collected by the fine side at the applied voltage 4 V, however, all of the particles were collected by the fine side when the applied voltage was 7 V as shown in **Figs. 5**.

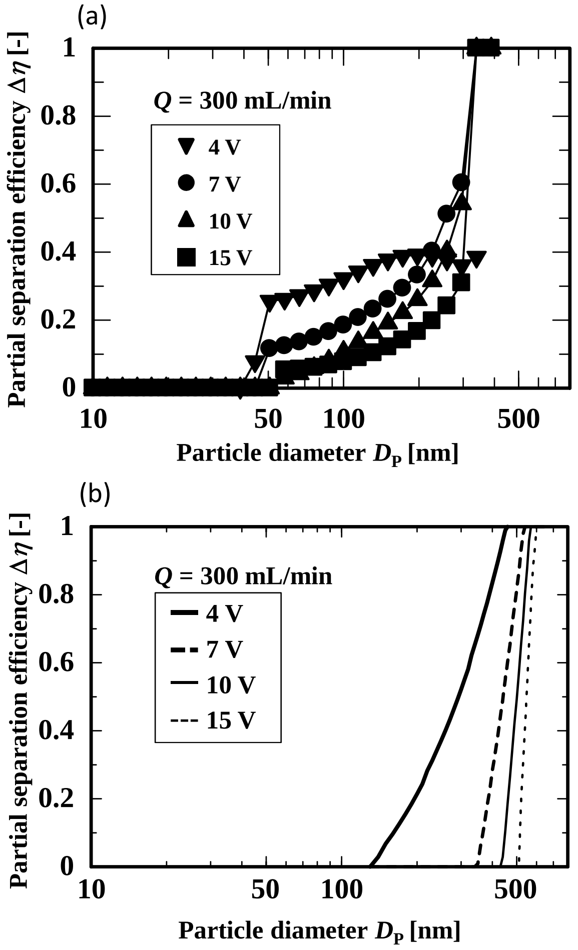

Fig. 4 Effect of applied voltage on partial separation efficiency curves at Q = 300 mL/min by: (a) experiment; (b) numerical simulation.

Thus, partial separation efficiency curve was controlled by changing the applied voltage; however, collection ratio as defined by Eq. (11) was decreased with the applied voltage increasing as shown in **Fig. 6**.

$$E_\mathrm{c} = \frac{m_\mathrm{f} + m_\mathrm{c}}{m_\mathrm{o}} \tag{11}$$

The reason of this result is the amount of particles collected by the wall increased. For example, in the case of the particles with the size of 120 nm, the

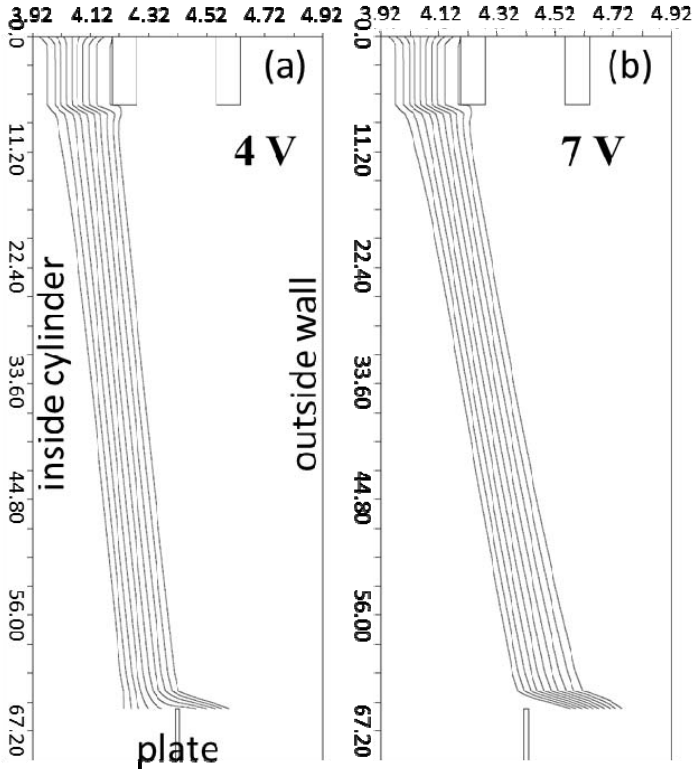

Fig. 5 Calculated 300 nm-particle trajectories in the apparatus at the flow rate of 300 mL/min and the applied voltage of: (a) 4 V; (b) 7 V.

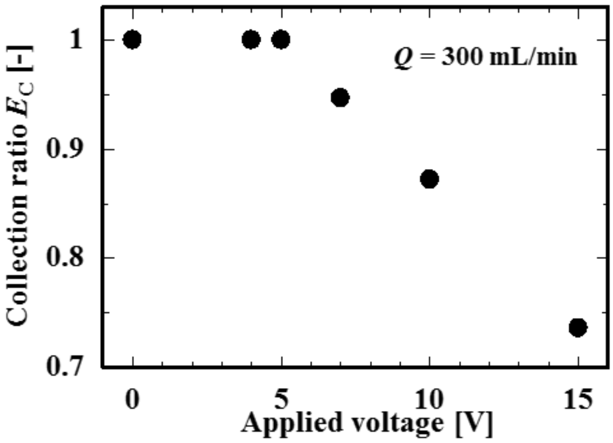

Fig. 6 Relationship between collection ratio and applied voltage at the total flow rate of 300 mL/min.

particle trajectories in the channel were shown in **Figs. 7.** It was clear that particles were collected not by the fine side but by the outside wall when the applied voltage was 15 V. The amount of the particles collected by the outside wall was not included in the masses of dried fine and coarse powders. Hence, collection ratio was decreased when the applied voltage was over 15 V.

4.2 The influence of flow rate on partial separation efficiency curve

Fig. 8 (a) and **(b)** show the influence of flow rate on partial separation efficiency at the applied voltage of 15 V and the results of theoretical calculation according to Eq. (1). When the total flow rate was increased, the residence time for particles in the apparatus became short. Thus, partial separation efficiency curve was shifted towards smaller particles

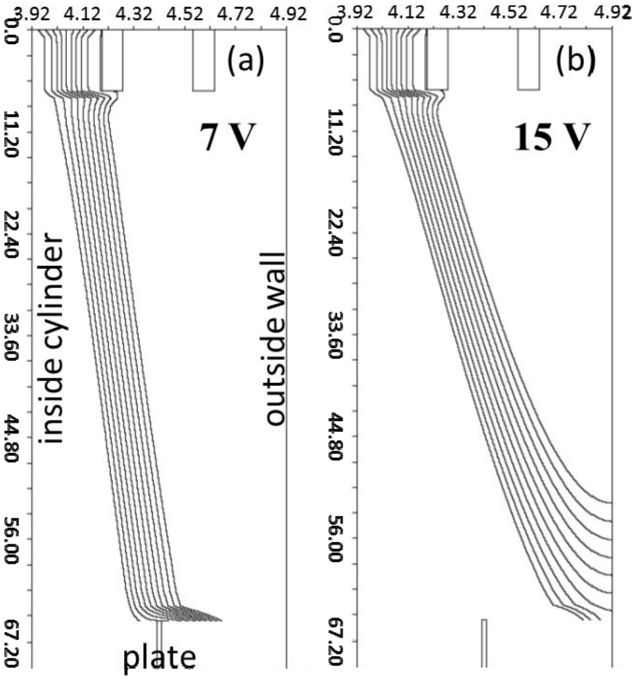

Fig. 7 Calculated 120 nm-particle trajectories in the apparatus at the flow rate of 300 mL/min and the applied voltage of: (a) 7 V; (b) 15V.

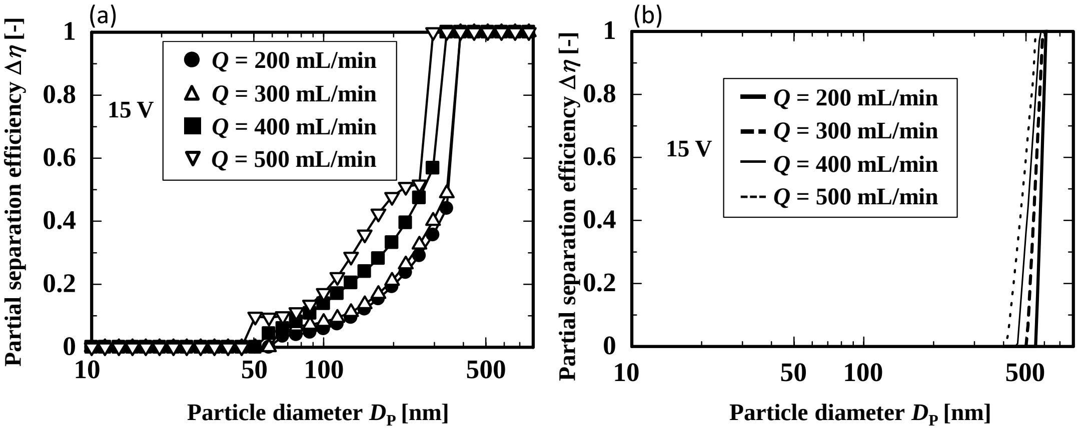

Fig. 8 Effect of flow rate on partial separation efficiency curves at the applied voltage of 15 V by: (a) experiment; (b) numerical simulation according to Eq.(1).

because of larger influence on the smaller particle by electrophoresis. However, the difference between experimental and calculated values was large probably because Eq.(1) did not show the relationship between zeta potential and particle size accurately. Then, numerical calculations were carried out under the condition of Eq.(2) on the basis of the sedimentation balance method. The differences were remained because the slurry and water might not flow in the apparatus as simulated, but the calculated curves approached the experimental curves as shown in **Fig. 9**. Hence, it was possible to think that Eq.(2) was more precise to express size dependency of zeta potential than Eq.(1). The sedimentation method was effective for investigation of the relationship between zeta potential and particle size.

4.3 Relationship between collection ratio and flow rate

Fig. 10 represents the relationship between collection ratio and flow rate at various applied voltages. As flow rate increased, the collection ratio was in-

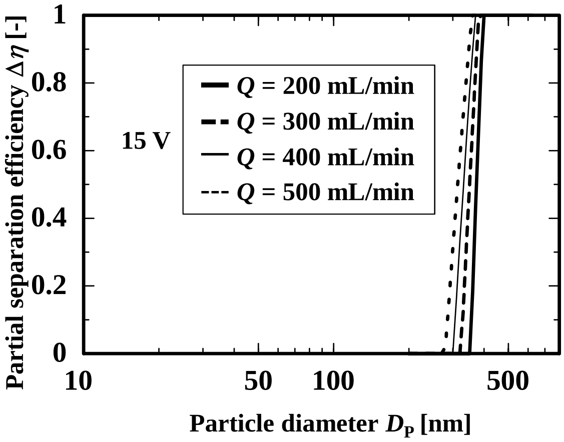

Fig. 9 Effect of flow rate on partial separation efficiency curves at the applied voltage of 15 V calculated according to Eq.(2).

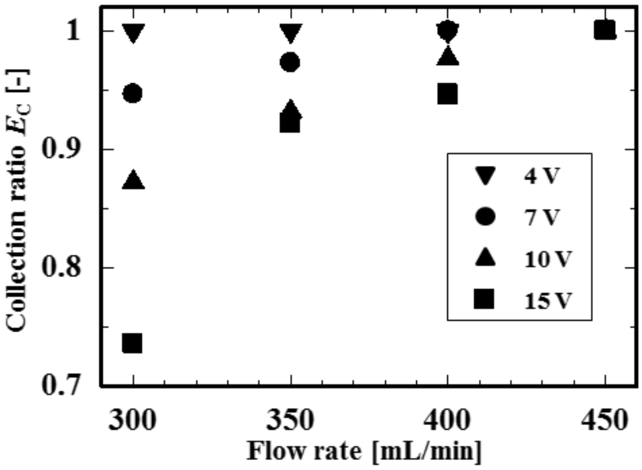

Fig. 10 Relationship between collection ratio and applied voltage.

creased because the residence time became shorter so that the particles were not easy to be collected by the outside wall of the apparatus. And also, the collection ratio was decreased with the applied voltage increasing because high collection of particles by the outside wall resulting from larger electrophoresis mobility as described in the section of 4.1. Hence, to keep high collection ratio for classification, the operating conditions of flow rate and applied voltage must be selected carefully.

5. Conclusions

The purpose of the present study is to develop a compact nanoparticle-classification apparatus with easy operation using EFFF. The channel of the apparatus was double cylinder with the length and diameter of 350 mm and 59 mm, respectively. The outside wall and inside cylinder of the channel served as positive and negative electrodes, respectively. Using a low-applied potential, the silica particles with the size from 50 to 400 nm were classified. This method prevented deposition of negatively charged silica particles with low applied voltage and high flow rate, and allowed both low-energy and continuous operation. Results of theoretical calculations qualitatively supported the experimental results obtained in this study.

Nomenclature

C	concentration	[wt%]
D	diffusion coefficient	[m^2 s^{-1}]
D_p	particle diameter	[m]

ΔD_p	small difference in particle diameter	[m]
E	electric field strength	[V m-1]
E_c	collection ratio	[-]
$f_c(D_p), f_f(D_p)$	particle size distributions of the coarse silica and classified fine particles, respectively	[-]
g	acceleration due to gravity	[m s^{-2}]
m_c, m_f , m_o	mass of the collected coarse, classified fine, and original particles, respectively	[g s^{-1}]
p	pressure	[Pa]
Q	total flow rate	[m^3/s]
t	time	[s]
u_r, u_z	fluid velocity in the r and z directions, respectively	[m s^{-1}]
v_r, v_z	particle velocity in the r and z directions, respectively	[m s^{-1}]
v_g, v_e	Stoke's sedimentation velocity and electrical migration velocity, respectively	[m s^{-1}]
r, z	coordinates of r and z directions, respectively	[m]
ε	dielectric constant	[F m^{-1}]
$\Delta\eta$	partial separation efficiency	[-]
μ	fluid viscosity	[Pa s]
$,\ {}_{p}$	fluid and particle density, respectively	[kg m^{-3}]
ζ	zeta potential	[V]

Literature Cited

1) Caldwell, K. D., L. F. Kesner, M. N. Mayers and J. C. Giddings (1972): Electrical Field-Flow Fractionation of Proteins, Science, 176, pp.296 – 298.
2) Caldwell, K. D. and Y.-S. Gao (1993): Electrical Field-Flow Fractionation in Particle Separation. 1. Monodisperse Standards, Anal. Chem., 65, pp.1764 – 1772.
3) Palkar, S. A. and M. R. Schure (1997): Mechanistic Study of Electrical Field Flow Fractionation. 1. Nature of the Internal Field, Anal. Chem., 69, pp.3223 – 3229.
4) Kwade, A. (1999): Wet Comminution in Stirred Media Mills — Research and its Practical Application, Powder Technol., 105, pp.14 – 20.
5) Inkyo, M., T. Tahara, T. Iwaki, F. Iskandar, C. J. Hogan and K. Okuyama (2006): Experimental Investigation of Nanoparticle Dispersion by Beads Milling with Centrifugal Bead Separation, J. Colloid Interface Sci., 304, pp.535 – 540.
6) Yamamoto, T., Y. Harada, K. Fukui and H. Yoshida (2010): AFM investigation of the surface properties of silica particles dispersed by bead milling, Colloids and Surfaces A: Physicochemical and Engineering Aspects, 362, pp.97 – 101.
7) Alex, T. C., R. Kumar, S. K. Roy and S. P. Mehrotra (2008): Stirred Bead Mill Grinding of Gibbsite: Surface and Morphological Changes, Adv. Powder Technol., 19, pp.483 – 491.
8) Yoshida, H., K. Fukui, T. Yamamoto, A. Hashida and N. Michitani (2009): Continuous fine particle classification by water elutriator with applied electro-potential, Adv. Powder Technol., 20, pp.398 – 405.
9) Yamamoto, T., Y. Harada, K. Fukui and H. Yoshida (2009): Classification of Particles Dispersed by Bead Milling using Electrical Field-Flow Fractionation, Journal of Chemical Engineering of Japan, 42, pp.720 – 727.
10) Yamamoto, T., Y. Harada, K. Fukui and H. Yoshida (2011): Enhancement of the Classification Performance of Electrical Field-Flow Fractionation Using Horizontal Electrophoresis, Journal of Chemical Engineering of Japan, 44, pp.398 – 404.
11) Yamamoto, T., N. Watanabe, K. Fukui and H. Yoshida (2009): Effect of Inner Structure of Centrifugal Separator on Particle Classification Performance, Powder Technol., 192, pp.268 – 272.
12) Fukui, K., H. Yoshida, M. Shiba, Y. Tokunaga (2000): Investigation about data reduction and sedimentation distance of sedimentation balance method, Journal of Chemical Engineering of Japan, 33, pp.393 – 399.
13) Goto, K., H. Masuda and K. Higashitani (1997): "Powder Technology Handbook, 2nd ed.", pp.123 – 132, Marcel Dekker, Inc., New York, USA.

Author's short biography

Tetsuya Yamamoto

Dr. Tetsuya Yamamoto is an Assistant Professor of Department of Chemical Engineering at Hiroshima University. He received a Ph. D. in Department of Chemical Engineering from Kyoto University in 2005. His major research interests are development of classification technique for nano particles using electrophoresis, synthesis of polymeric particles via polymerization, and measurement of surface forces and imaging using AFM.

Yoshitaka Harada

Yoshitaka Harada received B.S. and M.S. degrees from Department of Chemical Engineering at Hiroshima Universtiy, in 2009 and 2011, respectively. He has been working in NOF Corporation since 2011.

Takayuki Tsuyama

Takayuki Tsuyama is a undergraduate student at Faculty of Engineering Cluster III at Hiroshima University in 2011.

Kunihiro Fukui

Dr. Kunihiro Fukui is a Professor of Department of Chemical Engineering at Hiroshima University. He received a Ph. D. in Department of Chemical Engineering from Kyoto University in 1998. His major research interests are accurate size classification of fine particles, the advancement of powder handling process with microwave heating technique, and the recycling technology of particular wastes.

Hideto Yoshida

Dr. Hideto Yoshida has been a Professor of Department of Chemical Engineering at Hiroshima University since 1994. He received a Ph. D. in Department of Chemical Engineering from Kyoto University in 1979. His major research interests are fine particle classification, numerical simulation of cyclone separator, cut size control of dry and wet cyclones, development of particle size distribution with automatic liquid sedimentation method and recycling of fly ash particles.

Synthesis and Characterization of Nickel Particles by Hydrogen Reduction Assisted Ultrasonic Spray Pyrolysis(USP-HR) Method[†]

Burçak Ebin, Sebahattin Gurmen*
Metallurgical & Materials Eng. Dept., Istanbul Technical University[1],

Abstract

Spherical nickel particles were prepared by hydrogen reduction assisted ultrasonic spray pyrolysis (USP-HR) method using nickel chloride solution without any additives. Thermodynamic of the hydrogen reduction of the nickel chloride were studied by FactSage software. Particles were obtained at 800℃ reaction temperature by hydrogen reduction of aerosol droplets under H_2 flow. The effects of the precursor concentration on the particle size and morphology were investigated by scanning electron microscopy. Results showed that nickel particle sizes were decreased from 630 to 270 nm by reducing solution concentration, and also narrower size distribution was obtained using lower concentrated precursor. Nickel particle sizes were theoretically calculated and results indicated that there was a slight difference in the particle sizes compared to experimental values.

Keywords: nickel particles, nanocrystalline, ultrasonic spray pyrolysis, hydrogen reduction

1. Introduction

Fine powders of the transition metals especially iron, cobalt, nickel, copper and their alloys have been drawn increasing attention for several years due to their novel magnetic, electrical and catalytic features. In the case of nickel particles, the relation between the grain size of Ni nano-crystals and their magnetic properties has been studied in the past decade. The reason of the attention on nickel fine particles is the effect of particle/crystalline size on their physical properties which providing an opportunity to use them in various practical applications such as catalysts, electrodes in electronic products, magnetic fluids and high density recording media1-6).

Various techniques have been developed for the synthesis of submicron particles such as mechanical alloying which is the well known top down method, beside that microemulsion methods, polyol process, chemical vapor deposition, laser pyrolysis, gas deposition, microwave plasma, flame spraying, and spray pyrolysis are chemical base bottom up methods4-9). Among them, ultrasonic spray pyrolysis (USP) method is used for preparation of spherical non-agglomerated ultra fine particles in controlled chemical composition, size and crystallinity, which are suitable for direct application or fabrication of high technology materials10-12). It is a versatile method to produce metallic, alloy and metal oxide particles in various size and morphology. In USP method, spraying is performed by applying high frequency ultrasound to the precursor solution that forms aerosols with constant droplet size, which depends on the characteristic of the liquid and the frequency of the atomizer. Particle formation occurs from the reduction or thermal decomposition of the aerosol droplets12-16). Although several studies were reported on the metallic particle production by USP method such as Co12), Fe14), FeNi15), FeCo16) and Ag17), there is still a lack of nickel particle production, which is an important industrial material.

Stopic et al.18) prepared nickel powders by USP method using aqueous solutions of $NiCl_2$ at 900 and 1000℃ under H_2-N_2 (1:5) mixture gas atmosphere. They reported that pure Ni particles could only be produced at 1000℃ with H_2-N_2 gas mixture under 20 sec droplet residence time conditions. Also they observed NiO traces in Ni particles obtained at 900 ℃. Besides, Stopic and co-workers19) investigated

---

[†] Accepted: July 27th, 2011

[1] Ayazaga Campus, 34469 Istanbul-Turkey

[*] Corresponding author
E-mail: gurmen@itu.edu.tr
TEL: + 90 212 285 68 62; FAX: + 90 212 285 34 27

© 2011 Hosokawa Powder Technology Foundation

the influences of additives (0.1 mass% of Cu, Pd, Ni) in the $NiCl_2$ aqueous solution on Ni particle properties. They indicated that Ni particles obtained by USP method at 900℃ under H_2-N_2 (1:3) gas mixture contained $NiCl_2$ and $NiCl_2.2H_2O$ phases, indicating an incomplete reduction of the starting material at given temperature. Also, they could produce pure spherical non-agglomerated Ni particles at 900℃ by the addition of 0.1 mass% Cu, Pd or Ni particles into the solution. Xia et al.[20] reported the preparation of Ni particles by USP using $NiCl_2.6H_2O$ precursor containing aqueous ammonia and ammonium bicarbonate. They suggested that that the addition of $NH_3.H_2O$ and NH_4HCO_3 to $NiCl_2.6H_2O$ precursor changes the reaction pathway of Ni formation. Kim et al.[21] synthesized Ni particles by USP method from nickel nitrate solution using hydrogen and argon gas mixture at a residence time of 19 sec. They showed that obtained nickel particles had not spherical morphology and fully densified until 850℃. Recently, Yung et al.[22] reported the production of spherical Ni particles by a large scale spray pyrolysis process with two continuous reactors from nickel nitrate and nickel acetate as a starting material using nitrogen gas containing 10% H_2. In their process, the temperature of the first reactor was changed from 300 to 900℃, and the temperature of the second reactor was controlled at the range 900 to 1400℃.

In this research, we investigated the production of the nanocrystalline nickel particles by a simple process using nickel salt without any additives. Spherical and dense Ni particles were prepared by hydrogen reduction assisted ultrasonic spray pyrolysis (USP-HR) technique using nickel chloride aqueous solution at 800℃ under only H_2 flow. Also, effects of the corresponding solution on the particle size and morphology were studied and compared with theorical values.

2. Experimental

Ni particles were synthesized by hydrogen reduction assisted ultrasonic spray pyrolysis method using nickel chloride as a starting material. Nickel chloride hexahydrate ($NiCl_2.6H_2O$) was dissolved in distilled water in desired amounts to prepare precursor solutions and concentrations of the solutions were 0.8, 0.4 M and 0.04 M. Nitrogen with 1.0 L/min flow rate was used to create an inert atmosphere prior to and after the reduction process due to the safety regulations. Corresponding solution was atomized a high frequency ultrasonic nebulizer Pyrosol 7901 (Ramine Baghai Instrumentation, with a frequency of 1.3 MHz). Then, the obtained aerosol droplets were carried into the horizontal quartz reactor by gas flow. Hydrogen was used without mixing any inert gas in the experiments as a carrier/reducing agent in 1.0 L/min gas flow rate. Reduction process took place in the quartz reactor (0.25 m heated zone, and 0.02 m diameter) occupied in the electrically heated furnace (Nabertherm, Germany) at 800℃. The residence time of the droplet/particle was about 4.7 sec, which was calculated by taking into account the ratio of the volume of the reaction zone and the carrier gas flow rate. Reaction products were collected in the washing bottles which connected to the outlet of the quartz reactor.

X-ray diffraction (XRD) pattern was recorded by Siemens D5000 X-ray diffractometer with Cu Kα radiation (λ= 1.54187 Å, 2θ range 30-80°, 2θ step of 0.016 ℃ and time per step 0.2 sec) to determine the crystal structure of the particles. XRD data was also used to calculate the crystalline size of the particles by Scherrer formulation. Scanning electron microscopy (SEM) images of the products were taken by Jeol JSM 7000F FE-SEM. Particle size and size distribution were determined from SEM images by Leica Image Manager. All the clearly observed particles on the SEM images were taken into account in these analyses.

3. Results

3.1 Thermodynamic analysis of hydrogen reduction

The reaction for the formation of metallic nickel from nickel chloride described as in Eq. 1. The thermodynamic analysis was done using Fact Sage™ software in the temperature range of 50 - 1200 ℃, shown in **Fig. 1**.

$$NiCl_2 + H_2 \rightarrow Ni + 2HCl \qquad (1)$$

The values of Gibbs free energy ($\Delta G°$) for the Eq. 1 at the temperature range up to 1000 ℃ confirm the possibility of formation of nickel from $NiCl_2$ by hydrogen reduction. Although Gibbs free energy is always negative between the 0 - 1200℃ temperature range, it increases through the positive values at elevated temperatures. It was supposed that determined reaction time was sufficient for the transformation of droplets to metal particle in the hydrogen atmosphere.

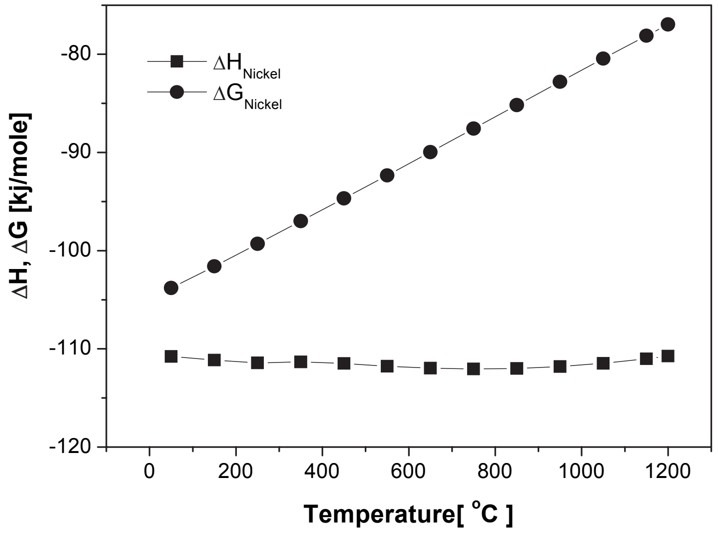

Fig. 1

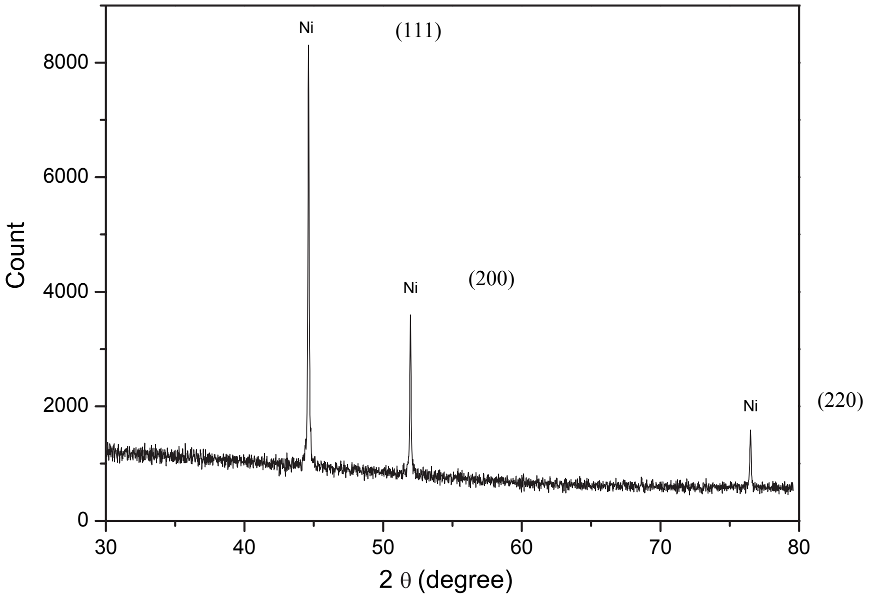

Fig. 2

3.2 X-ray analysis of nickel powder

XRD pattern of the nickel particles produced from 0.8 M solution is shown in **Fig. 2**. The peaks at 44.61°, 51.78° and 76.80° were referred to (111), (200) and (220) diffraction planes of nickel, respectively. Results showed that pure nickel in face centered cubic crystal structure were produced without oxidation. Also, any peaks due to the incomplete reduction of the starting material such as $NiCl_2$ was not observed. Crystalline size of the sample was calculated by Scherrer Equation using XRD data,

$$t = \frac{K.\lambda}{B.\cos\theta} \tag{2}$$

Eq. 2 defines a simple relationship between crystalline size, and peak width. In this equation K is constant, the value of which is between 0.85, and 0.9; λ is the wavelength of the X-ray (Cu $K\alpha_1$ = 1,541874 Å); B is the width (in radians) of the peak due to size effect; θ is the Bragg angle; and t is the particle size. In the crystallite size calculation instrumental broadening was taken into account to obtain accurate size. The crystallite size of nickel particles prepared using 0.8 M precursor solutions was 89 nm.

3.3 Effect of the precursor solution concentration

SEM images were used to investigate the effects of the precursor concentration ranged 0.04, 0.4, and 0.8 M on the particle size and morphology. SEM images of the nickel particles are given in **Fig. 3**. Particles prepared in all concentrations had spherical shape morphology and smooth surface. Ni particles sizes showed reducing trend by decreasing of the corresponding solution concentration. The mean particle sizes for nickel powders produced using 0.8, 0.4 and 0.04 M solutions were 630, 495 and 270 nm, respectively. Moreover the decreasing of the solution concentration increased the size uniformity of the products and narrower particle size distribution was obtained by lessen of the precursor concentration. Although particle size range was between 100 and1130 nm for particles obtained using 0.8 M solution, size distribution was narrowed between 50 and 550 nm using 0.04 M precursor solution.

3.4 Theoretically particle diameter

The relation between the droplet diameter and the frequency of the ultrasound source was studied by Jokanovic et al. 23). The mean diameter of the aerosol droplets can be determined by the given equation.

$$D = 0.34\,(8 \cdot \pi \cdot \gamma / \rho \cdot f^{2})^{1/3} \qquad (3)$$

In Eq. 3, D is the mean droplet diameter; γ is the surface tension of the solution; ρ is the density of the solution; and f is the frequency. Thus, droplet diameter was calculated 3.49 μm by Eq. 3 using the parameters of this study (γ:72.9·10^{-3} Nm^{-1}; ρ:1 g cm^{-3}; f: 1.3 MHz). The nickel particles diameters produced by USP-HR

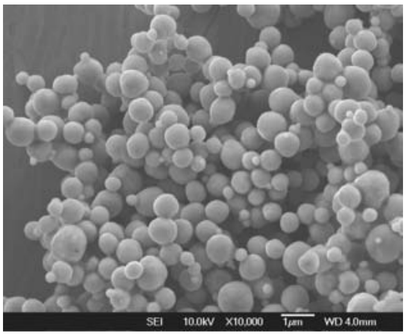

Fig. 3a

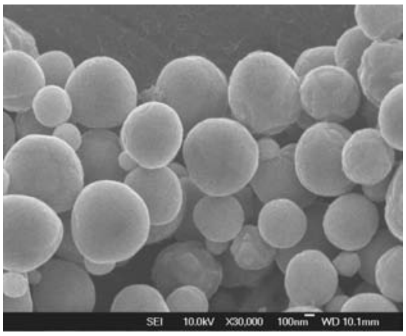

Fig. 3b

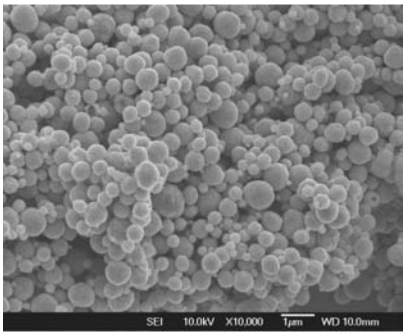

Fig. 3c

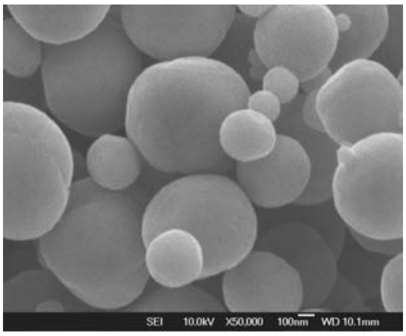

Fig. 3d

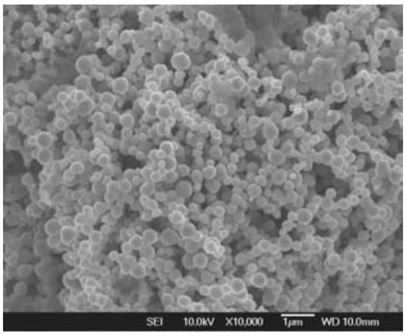

Fig. 3e

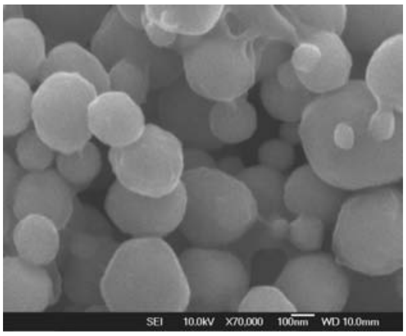

Fig. 3f

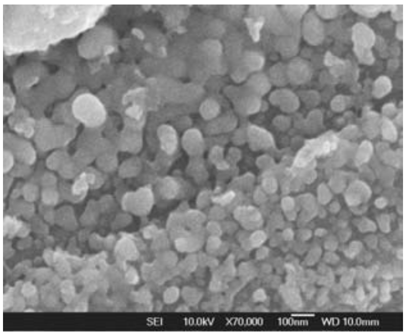

Fig. 3g

Fig. 3

method were determined by Eq. 4. For Eq. 4, these were assumed that precursor concentration was homogeneous in all droplets and the aerosol droplets transformed to fully dense nickel particles.

$$D_p=D(C_{precursor} \,.\, M_{Ni} \,/\, M_{precursor} \,.\, \rho_{Ni})^{1/3} \tag{4}$$

In Eq. 4, D_p is the particle diameter; D is the droplet diameter; $C_{precursor}$ is the concentration of the solution, ρ_{Ni} is the density of nickel, M_{Ni} is the atomic weight of nickel and $M_{precursor}$ is the molecular weight of the precursor. **Fig. 4** shows the change of the calculated particles sizes by the increasing concentration. The theoretical particle diameters for 0.8, 0.4 and 0.04 M precursor were calculated as 611, 480 and 220 nm, respectively.

4. Discussion

The experimental obtained mean particle sizes and theoretical calculated particle sizes are given in **Table 1**. The possible reason, why the experimental particle sizes were slightly bigger than the theoretical calculated values, was the insufficient sintering and densification of the particles due to less residence time. Also, the highest size difference between theoretical and experimental results was observed for particles obtained by 0.04M solution. It showed that the particles produced using lower precursor concentration had slower densification rate probably due to the less amount of nickel content in the same droplet size.

The active particle formation mechanism for nickel particle production by USP-HR method was one droplet to one particle transformation as proposed in Co particles production by Gurmen et al[12] and in our previous study about the iron particles production[14]. The steps of the one droplet to one particle mechanism for nickel particle production were shrinkage of the droplets due to the evaporation of the solvent in the entrance of the heated zone, reduction reaction of metal salt by hydrogen and nucleation of primary particles (nanoparticles), and finally secondary particles (submicron range particles) formed by sintering and densification of the nickel nanoparticles. The explained mechanism is well suited with theoretical approach and experimental obtained mean particle sizes. Besides, determined crystallite size of the nickel particles (89 nm) confirmed the formation of primary particles.

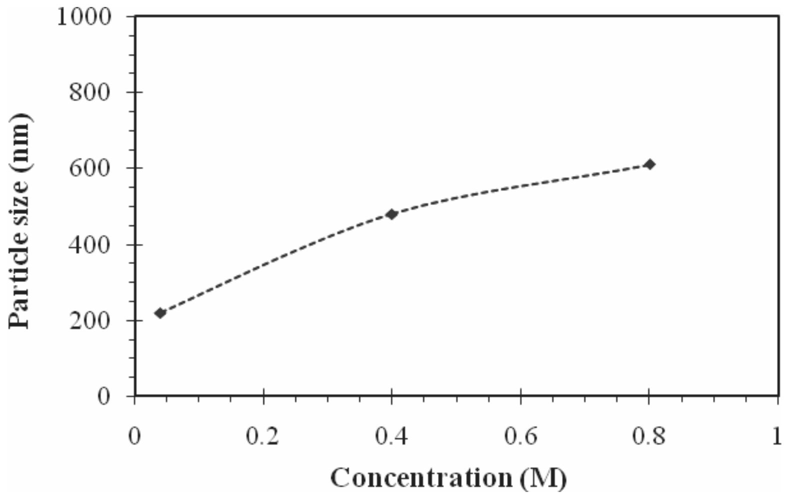

Fig. 4

Table 1 Comparison of the experimental obtained and calculated particle sizes

Concentration (M)	Experimental Mean Particle Size (nm)	Theoretical Calculated Particle Size (nm)
0.04	270	220
0.4	495	480
0.8	630	611

On the other hand, one droplet to one particle mechanism has a lack to explain the existence of the smaller/nanoparticles. The one of the possible reasons is the fragmentation of the droplets after nucleation of the primary particles due to collisions. Thus, nanoparticles dispersed and some of them sintered with each other or other droplets which cause the formation of the smaller and bigger particles.

5. Conclusion

Ni particles were produced by hydrogen reduction assisted ultrasonic spray pyrolysis (USP-HR) method using nickel chloride salt as a starting material without any additives. Ni particles were prepared in the submicron size range in spherical morphology at 800 ℃ reaction temperature. Results showed that decreasing of the corresponding solution concentration caused to not only reduce the mean particle size from 630 to 270 nm, but also narrow the size distribution.

Acknowledgments

This study was supported by The Scientific and Technological Research Council of Turkey (TUBITAK) under Grant No. 105M063.

References

1) Huber, D. L. (2005): Synthesis, Properties, and Applications of Iron Nanoparticles, Small, No.1, pp.482-501.
2) Shao H., Huang, Y., Lee, H. S., Suh, Y. J. and Kim, C. O. (2006): Cobalt Nanoparticles Synthesis from $Co(CH_3COO)_2$ by Thermal Decomposition, Journal of Magnetism and Magnetic Materials, No.304, pp.e28-e30.
3) Duan, Y. and Li, J. (2004): Structure Study of Nickel Nanoparticles, Materials Chemistry and Physics, No.87, pp.452-454.
4) Sakai, T., Tsukahara, N., Tanimoto, H., Ota, K., Murakami, H. and Kita, E. (2001): Magnetic Anistoropy of Ni Nano-crystals Prepared with Gas-Deposited Method, Scripta Materialia, No.44, pp.1359-1363.
5) Rosenband, V. and Gany, A. (2004): Preparation of Nickel and Copper Submicrometer Particles by Pyrolysis of Their Formates, Journal of Materials Processing Techonolgy, No.153-154, pp.1058-1061.
6) Uhm, Y. R., Park, J. H., Kim, W. W., Cho, C. H. and Rhee, C. K. (2004): Magnetic Properties of Nano-Size Ni Synthesized by the Pulsed Wire Evaporation (PWE) method, Materials Scienc and Engineering B, No.106, pp.224-227.
7) He, Y., Li, X. and Swihart, M. T. (2005): Laser-Driven Aerosol Synthesis of Nickel Nanoparticles, Chemistry of Materials, No.17, pp.1017-1026.
8) Swihart, M. T. (2003): Vapor-phase Synthesis of Nanoparticles, Current Opinion in Colloid & Interface Science, No.8, pp.127-133.
9) Goh, C. F., Yu, H., Yong, S. S. Mhaisalkar, S. G. Boey, F. Y. C. and Teo, P. S. (2006): The Effect of Annealing on the Morphologies and Conductivities of Submicrometer Sized Nickel Particles Used for Electrically Conductive Adhesive, Thin Solid Films, No.504, pp.416-420.
10) Taniguchi, I., Lim, C. K., Song, D. and Wakihara, M. (2002): Particle Morphology and Electrochemical Performances of Spinel $LiMn_2O_4$ Powders Synthesized Using Ultrasonic Spray Pyrolysis Method, Solid State Ionics, No.146, pp.239-247.
11) Shi, X., Wang, S. Duan, X. and Zhang, Q. (2008): Synthesis of Nano Ag Powder by Template and Spray Pyrolysis Technology, Materials Chemistry and Physics, No.112, pp.1110-1113.
12) Gurmen, S., Stopic, S. and Friedrich, B. (2006): Synthesis of Nanosized Spherical Cobalt Powder by Ultrasonic Spray Pyrolysis, Materials Research Bulletin, No.41, pp.1882-1890.
13) Wang, W. N., Itoh, Y., Lenggoro, I. W. and Okuyama, K. (2004): Nickel and Nickel Oxide Nanoparticles Prepared from Nickel Nitrate Hexahydrate by a Low Pressure Spray Pyrolysis, Materials Science and Engineering B, No.111, pp.69-76.
14) Ebin, B. and Gurmen, S. (2011): Aerosol Synthesis of Nano-crystalline Iron Particles from Iron (II) Chloride Solution, Metall-Forschung, No.65/4, pp.151-154.
15) Gurmen, S., Ebin, B., Stopic, S. and Friedrich, B. (2009): Nanocrystalline Spherical Iron–Nickel (Fe–Ni) Alloy Particles Prepared by Ultrasonic Spray Pyrolysis and Hydrogen Reduction (USP-HR), Journal of Alloys and Compounds, No.480, pp.529-533.
16) Gurmen, S., Guven, A., Ebin, B., Stopic, S. and Friedrich, B. (2009): Synthesis of Nano-crystalline Spherical Cobalt–Iron (Co–Fe) Alloy Particles by Ultrasonic Spray Pyrolysis and Hydrogen Reduction, Journal of Alloys and Compounds, No.481, pp.600-604.
17) Pingali, K. C., Rockstraw, D. A. and Deng, S. (2005): Silver Nanoparticles from Ultrasonic Spray Pyrolysis of Aqueous Silver Nitrate, Aerosol Science and Technology, No.39, pp.1010-1014.
18) Stopic, S., Ilic, I. and Uskokovic, D. (1995): Structural and Morphological Transformations during NiO and Ni Particles Generation from Chloride Precursor by Ultrasonic Spray Pyrolysis, Materials Letters, No.24, pp.369-376.
19) Stopic, S., Nedeljkovic, J., Rakocevic, Z. and Uskokovic, D. (1999): Influence of Additives on the Properties of Spherical Nickel Particles Prepared by Ultrasonic Spray Pyrolysis, Journal of Materials Research, No.14, pp.3059-3065.
20) Xia, B., Lenggoro, I. W. and Okuyama, K. (2001): Preparation of Ni Particles by Ultrasonic Spray Pyrolysis of $NiCl_2.6H_2O$ Precursor Containing Ammonia, Journal

of Materials Science, No.36, pp.1701-1705.

21) Kim, K. N. and Kim, S.-G. (2004): Nickel Particles Prepared from Nickel Nitrate with or without Urea by Spray Pyrolysis, Powder. Techology, No.145, pp.155-162.

22) Jung, K. Y., Lee, J. H., Koo, H. Y., Kang, Y. C. and Park, S. B. (2007): Preparation of the Solid Nickel Particles by Large-scale Spray Pyrolysis of $Ni(NO_3)_2.6H_2O$: Effects of Temperature and Nickel Acetate on the Particle Morphology, Materials Science and Engineering B, No.137, pp.10-19.

23) Jokanovic, V., Spasic, A. M., and Uskokovic, D. (2004): Designing of Nanostructured Hollow TiO_2 Spheres Obtained by Ultrasonic Spray Pyrolysis, Journal of Colloid and Interface Science, No.278, pp.342-352.

Author's short biography

Burçak Ebin

Burçak Ebin receieved a bachelor degree in Metallurgical and Material Engineering (2006) and followed by a M.Sc. (2008) in Material Science and Engineering at Istanbul Technical University in Turkey. He has been working as a research assistant since 2006 at the same university. As a part of his M. Sc. and Ph.D., he studied on metallic, alloy and ceramic nano/submicron size particle production and characterization. Currently, he continues his Ph.D. in the field of new cathode materials production for lithium-ion batteries with Dr. Sebahattin Gürmen at Istanbul Technical University.

Dr. Sebahattin Gürmen

Sebahattin Gürmen studied Metallurgical and Material Engineering at Istanbul Technical University in Turkey, where he got Ph.D. with thesis about production of tungsten powder from scheelite concentrate, in 1999. He then spent two years as a post-doctoral fellow (Alexander von Humboldt Foundation) at RWTH-Aachen in Germany with Professor Bernd Friedrich undertaking particle production research. Research fields are extractive metallurgy, recycling and nano/submicron particle production. He is a professor and the vice-chairman in Metallurgical and Material Engineering Dept. at Istanbul Technical University.

Liquid-phase Synthesis of CaF$_2$ Particles and Their Low Refractive Index Characterization[†]

Asep Bayu Dani Nandiyanto,[1] Takashi Ogi,[1,*] Akihiro Ohmura,[1] Eishi Tanabe[2] and Kikuo Okuyama[1]
Department of Chemical Engineering, Graduate School of Engineering, Hiroshima University[1]
Hiroshima Prefectural Institute of Industrial Science and Technology[2]

Abstract

The purpose of the present study was to reveal the details of the preparation of CaF$_2$ particles with controllable size (30-900 nm) and shape (spherical, hexagonal, and cubical forms) using a liquid-phase synthesis method, and to demonstrate that a change in the composition of the reactants and crystalline structure of the CaF$_2$ product could improve material performance. The particles were synthesized from the reaction of CaCl$_2$ and NH$_4$F in an aqueous solution in the absence of any additional components (e.g., chemicals, surfactants). Monodispersed particles were achieved by the optimization of the reaction condition parameters: temperature, mixing rate, and reaction time. Control of the particle size was accomplished mainly by changing the concentration of the reactants, which is qualitatively explained by the conventional nucleation theory. Flexibility of the process in controlling particle morphology, from a spherical to a hexagonal and/or a cubical form, was predominantly achieved by varying the concentration of CaCl$_2$. Since the identical XRD pattern was detected in particles with varying morphologies, the shape transformation was due to changes in particle growth. A theoretical background to support how the particles changed was also added and was compared with an analysis of the number of nuclei. In addition, sufficient adjustment of the reactant compositions made it possible to produce a material with an ultralow refractive index (n_{CaF2} was near to $n_{theoretical\ CaF2}$), which was confirmed by the measurement of the refractive index and the material crystallinity.

Keywords: calcium fluoride particles, nucleation theory, particle growth, morphological control, low refractive index material, crystal size

1. Introduction

Calcium fluoride (CaF$_2$) is an attractive material due to its excellent properties: low refractive index, corrosion-resistance, thermal stability, and significant hardness. Excellent performance makes this material useful for applications, from catalytic support, protective-coating materials, to anti-reflective lenses.1)

Several approaches to the synthesis of this alkaline-earth metal fluoride material have been developed, which include physical and chemical methods.2) Although the current synthesis methods have shown potential for industrial applications, several disadvantages have been noted: (i) most of the processes require high-temperature processing, specific and complicated synthetic equipment, and rigid conditions;1) (ii) most require the use of harmful and difficult-to-handle chemicals (e.g., hydrofluoric acid (HF)1), trifluoroacetate (TFA)3), etc.), creating conflicts with safety and environmental regulations in industrial applications;4) (iii) most conduct in an anhydrous synthesis system1) (either oil-phase, alcohol, or sol-gel synthesis), which would be inflexible for further developments; (iv) most have been applied for the production of film material only, with only a few reports published on work on the synthesis of particles;3) and, (v) most reports have focused on only the fabrication of the material with no emphasis on actual applications.

[†] Accepted:August 6th, 2011

[1] 1-4-1 Kagamiyama, Higashi Hiroshima 739-8527, Japan

[2] 3-10-32, Kagamiyama, Higashi-Hiroshima 739-0046, Japan

[*] Corresponding author:
E-mail: ogit@hiroshima-u.ac.jp
TEL: (+81) 82-424-7850 FAX: (+81) 82-424-7850

ⓒ 2011 Hosokawa Powder Technology Foundation

To circumvent the current problems described above, several alternative methods have been suggested. Methods that are conducting a reaction system in an aqueous solution and changing the type of raw materials have been suggested. Franklin reported employment of the aqueous-solution reaction system and the use of NH_4F as a fluoride source,5) which successfully produced CaF_2 particles with controllable size. However, no precise information exists concerning the minimum size that can be produced. Page et al.6) reported the synthesis of CaF_2 using alkaline metal fluoride (KF) as an F source. Particles in the range of 15 to 80 nm were effectively produced; unfortunately, the use of KF affected the production of fluoro-perovskite materials (materials with K, Ca, and F components ($KCaF_3$)).7) Further, there is no mention included on the feasibility for the control of particle morphology, as well as their material performances. Fujiwara et al.8) and Grob et al.1) reported a development in the synthesis of fluoride material. Optical properties were also reported. However, synthesis of CaF_2 was not their main focus, and the control of particle morphology was not reported. In fact, nanometer-sized particles with controllable morphology are important because the change of morphology exhibits unique properties (e.g., optical transparency).4,9) For this reason, the purpose of the present study was to reveal the details of the preparation of CaF_2 particles with controllable size and shape and to demonstrate that a change in the composition of the reactants could improve material performance (i.e., refractive index).

In our initial studies, we reported the preparation of porous silica nanoparticles (namely, Hiroshima Mesoporous Materials; HMM)9,10) and MgF_2 nanoparticles4) with controllable size and morphology using a liquid-phase synthesis method. Experimental results in the control of particle size and morphology were investigated and compared with theoretical explanations. Besides, we also successfully developed a process for the synthesis of particles with controllable size and morphology using a spray method.11-24) Here, we report the synthesis of CaF_2 particles with controllable size and morphology using the liquid-phase synthesis method. Different from other CaF_2 synthesis methods, the synthesis was based on the reaction of Ca^{2+} and F^- ions in an aqueous solution in the absence of additional components (polymers, surfactants, chemicals, etc.). As the fluorine source, we used ammonium fluoride (NH_4F), which was easier to handle than either HF or TFA.4) Monodispersed particles could be achieved through the optimization of reaction condition parameters: temperature, mixing rate, and reaction time. The ability to control size (from 30 to 900 nm) and morphology (spherical, hexagonal, and cubical forms) was achieved by changing the NH_4F:$CaCl_2$ ratio, in which to the best of our knowledge, this is the first documented preparation of well-controlled particle size (from several tens nanometers) and morphology. A theoretical explanation of the control of particle size and the morphological control, as well as the particle formation phenomenon, was added to support our synthesis method. Furthermore, the relationship of particle diameter and morphology with concentration of the reactants was investigated in detail, both experimentally and theoretically. The effect of reactant composition on material performance (i.e. refractive index) was also investigated, along with an analysis of crystallinity. The results provided evidence that the present particles had a low refractive index value (approaching that of the theoretical monocrystalline CaF_2 monolayer). We believe that this information is important for further developments in the synthesis of low refractive index materials.

2. Fundamental Theory of Particle Formation

The LaMer and Dinegar theory is typically used as a qualitative model to comprehend particle-formation phenomena.25) This theory describes monomer formation, the nucleation step, and the growth process. To apply this theory to the present particle formation, several conditions should be assumed:4) (i) The monomer is supplied only from the chemical reaction; (ii) Critical supersaturation (C_{crit}) is a minimal requirement for the nucleate to be discernible; (iii) As the monomer concentration is lowered below the C_{crit} level, nucleus formation ceases and the nucleus then starts to consume monomers to increase its weight (growth-step process); and, (iv) during the growth-step process, processing conditions can interfere with particle shape transformation.

An example of time-dependent particle formation illustrating the LaMer and Dinegar theory is depicted in **Fig. 1**. Two conditions in different monomer formation rates are selected as a comparison parameter because its discrepancies can be easily distinguished. Particle-formation models in high and low monomer formation rates are presented in **Fig. 1** in condition lines 1 and 2, respectively. A high rate means the rapid progress to the step of nucleus formation, while a low rate is the low rate in the formation of monomer that makes creation of nuclei slower.

When the chemical reaction occurs, monomers are formed. This causes an increase in monomer concentrations with time. At a high rate (condition 1), the higher monomer formation rate allows the monomer concentration to get C_{crit} in a short time; however, a low rate (condition 2) slows the monomer formation rate, consequently taking a longer amount of time for the monomer concentration to reach C_{crit}.

After C_{crit} is reached, nuclei start to form. During nuclei construction, available monomers in the solution are consumed, resulting in a deceleration of monomer concentration. When there is no consumption of monomers, monomer concentration is steady (illustrated by the striped line). With a longer time period, nuclei formation causes the monomer concentration to promptly decrease. Between these two conditions, dissimilarity in the areas above C_{crit} (nucleation area) can be obtained, informing different particle phenomenon characteristics (i.e., numbers of nuclei). In condition 1, a wide nucleation area (in the blue, vertical-line textured area) can be obtained. The increase in reactant conversion causes a rapid conversion of reactants into monomers, which accelerates nuclei formation but retards particle growth. Conversely, in condition 2, a narrow nucleation area (in the red, horizontal-line textured area) can be obtained. A lower monomer formation rate is found. As a consequence, a short-nucleation stage occurs, resulting in the production of fewer nuclei and allowing the nuclei to catch more monomers and increase their weight during the particle growth stage.

When the monomer concentration collapses to below C_{crit}, the nuclei growth stage starts. The monomers tend to coalesce with formed nuclei to increase nuclei weight, rather than forming new nuclei. The growth stage continues until the concentration of monomer reaches a stable condition (C_{stable}).

3. Experimental Method

CaF_2 particles were prepared using the liquid-phase synthesis method with a simple reaction between calcium and fluoride sources ($CaCl_2 + 2\ NH_4F \rightarrow CaF_2 + NH_4Cl$). Each reactant (i.e., $CaCl_2$ (Kanto Chemical Co., Inc., Japan) and NH_4F (Aldrich, US)) was diluted in an aqueous solution. Both diluted reactants (each fixed at 40 mL) were added into a reactor system, in which the reactor system itself was comprised a batch glass reactor (300 mL of a four-necked reactor), a magnetic stirrer, a mantle heater, a condenser, and a nitrogen gas inlet. The concentration of reactants varied from 1 to 1000 mmol/L. Detailed variations of reactant concentrations are listed in **Table 1**.

The mixed reactants were vigorously mixed for several minutes to reach a homogenous condition. The homogenous mixtures were then heated to a specific temperature and kept at this temperature for

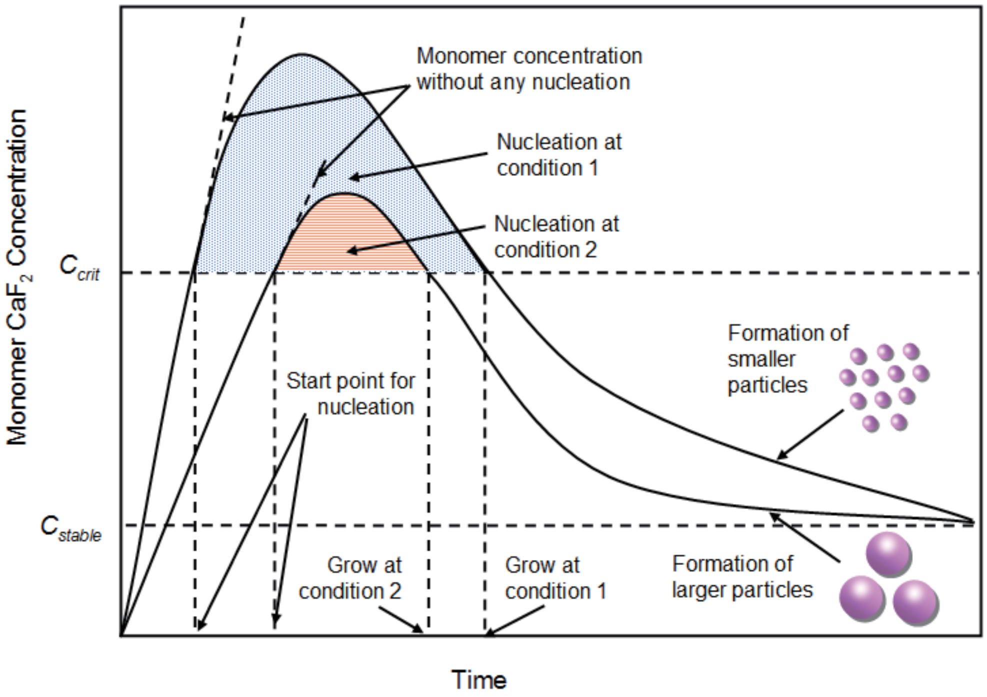

Fig. 1 Illustration of the Lamer and Dinegar theory as a function of reaction time.

up to 4 hours under a nitrogen atmosphere. Next, the reacted solutions were cooled to room temperature. In order to collect the prepared particles and remove un-reacted reactants and impurities, the cooled solutions were purified using a centrifugation process (15,000 rpm; 30 minutes; washing by ethanol).

The purified particles were then characterized using a scanning electron microscope (SEM, Hitachi S-5000 operated at 20 kV) and a transmission electron microscope (TEM; JEM-3000F, JEOL, operated at 300 kV) to examine the size, morphology, and structure of the particles. The crystallinity of the samples was measured by an X-ray diffraction (XRD; Rigaku Denki RINT2000, with Cu Kα radiation, with angular domain between 20 and 80° (2θ)). Elemental mapping and chemical composition of the prepared particles were evaluated using a scanning transmission electron microscope (STEM) equipped with an energy-dispersive X-ray spectroscopy (EDS).

To determine the effect of reactants composition and CaF_2 particle crystallinity on material performance (i.e., refractive index), the following experimental procedure was conducted: First, the purified particles were dried at 80 ℃ to ensure a solvent-free condition. The dried particles were then diluted by an aqueous standard solution and used as a precursor. The precursor was deposited onto a substrate (prism glass grids), which was attached to a refractive index measurement system (DR-M2, Atago Co. Ltd., Tokyo, Japan). The precursor was then measured using a visible light (589 nm) at 25 ℃. In addition, prior to using, the substrate was washed using an ethanol solution and left for several minutes. For a standard comparison, we prepared the precursor with no additional particles. The duration time for the measurement was no more than 1 minute to minimize the evaporation of precursor's solvent. The measurements were repeated three times to ensure the results.

4. Results and Discussion

4.1. Synthesis of CaF_2 particles

The present work was primarily directed towards investigation of the effect of several reaction parameters on the synthesis of monodispersed CaF_2 particles. This study used a single-step process, which was performed in the absence of any additional components (e.g., chemicals, surfactants, etc). This study demonstrated the possibility of production of monodispersed particles with controllable size and morphology through suitable changes in reaction parameters: temperature, reaction time, mixing rate, and composition of reactants.

Fig. 2 shows the SEM images of prepared particles as a function of reaction time. The particles were prepared at 70℃ using a ratio concentration of NH_4F:$CaCl_2$ of 54:450 and a mixing speed of 400 rpm. A slight difference in size was obtained with different reaction times. Particles with a size of 110 nm were formed at a relatively short reaction time (0.5 hours) (**Fig. 2a**). By adding longer reaction time, an increase in particle size could be obtained (**Fig. 2b**).

Table 1 A summary of CaF_2 particles prepared under different conditions

Sample code	Reactant concentration (mmol/L)			d_p (nm)	St_{dev} (nm)	Particle morphology
	C_{NH_4F}	C_{CaCl_2}	$NH_4F/CaCl_2$			
A	27	18	1.50	400	77	Spheres
B	54	18	3.00	222	32	Spheres
C	108	18	6.00	118	27	Spheres
D	216	18	12.00	59	16	Spheres
E	54	9	6.00	842	137	Spheres
F	27	36	0.75	305	89	Hexagonal
G	27	90	0.30	121	26	Hexagonal
H	27	180	0.15	133	35	Cubes
I	27	360	0.08	81	18	Cubes
J	54	900	0.06	62	15	Cubes
K	108	900	0.12	45	13	Cubes
L	216	900	0.24	32	9	Cubes
M	108	36	3.00	80	23	Mixed spherical and cubical form
N	108	180	0.60	73	20	Hexagonal
O	108	360	0.30	70	20	Mixed spherical, hexagonal, and cubical form

A longer reaction time allows the nucleus to adsorb more monomers, gaining weight, and resulting in larger particles. However, when applying further increasing reaction time (**Fig. 2c**), almost no change in the particle size was detected. The size of the prepared particles at further longer reaction time (time > 2 hours) was identical. The particle size increased gradually only when the reaction time was up to 2 hours, confirming that the particle growth process occurred during this period. The particle growth would not happen when the reaction time is above the certain value, confirming the concept of C_{stable} in the Lamer and Dinegar theory in **Fig. 1**.

Fig. 3 shows the effect of mixing speed on particle size and size distribution. Various particle sizes with different size distributions could be obtained. At a low-rate mixing speed, particles with a size of 130 nm could be produced (**Fig. 3a**). An increase in mixing speed caused the decreases in the particle size and the size distribution (**Fig. 3b** and **c**). However, further additional speed made no impact on the decrease of particle size. When increasing the mixing rate, a high interaction among the reactants happened, followed by a rapid conversion of the reactants into a monomer. This led to faster progress in the creation of nucleus and growth process. However, for some cases, a high interaction sometimes creates an inhomogeneous state in the particle-formation phenomenon, with the exception of the Ostwald-ripening theory. Some particles can grow and be constructed faster, while the others are still in an unstable condition (e.g. un-interacted reactant and incomplete particle growth). This condition allowed the formation of particles with a broad size distribution, which was avoided for the obtainment of monodispersed particles. From these results, an optimum mixing speed that would result in the formation of relatively monodispersed particles was 800 rpm.

Fig. 4 shows the effect of temperature on particle size and size distribution. An increase of temperature can lead to high interaction between reactants and good progress in particle formation. Nanoparticles could be obtained when processing at a temperature of 25℃ (**Fig. 4a**). By increasing temperature, the creation of larger particles could be obtained (**Fig. 4b-d**). The fundamental reason for this phenomenon is that increasing temperature allows a high contact and interaction among the reactants, which results in a rapid particle formation. However, with this high contact and interaction phenomenon, increases in the particle size distribution cannot be avoided. Inhomogeneous particle growth was obtained for the case of too high temperature process, making size distribution broader. Some nuclei could catch more

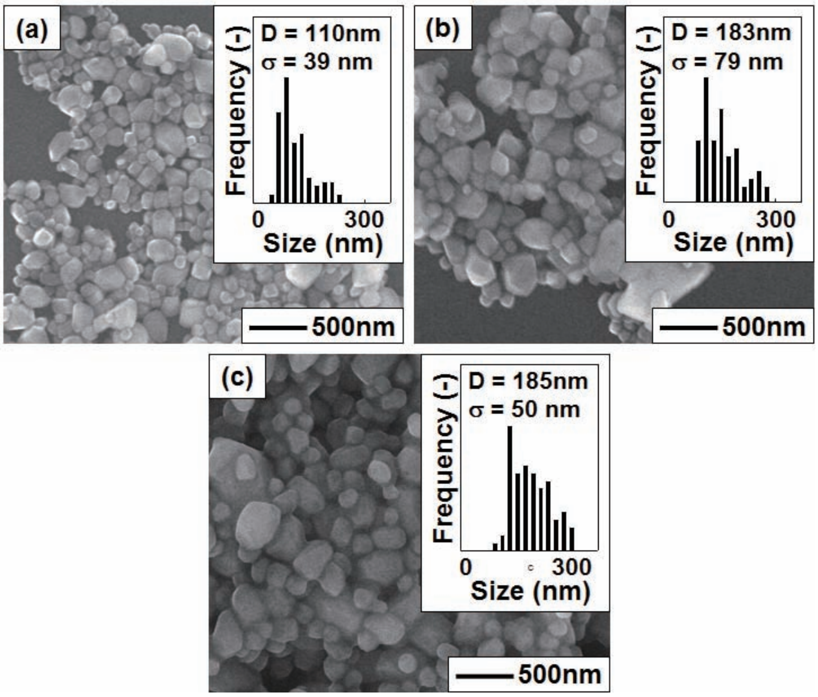

Fig. 2 SEM images of prepared particles conducted at different reaction times (0.50 (a), 2.00 (b), and 4.00 hours (c)). All samples were prepared at 70 ℃ using NH_4F and $CaCl_2$ compositions of 54 and 450 mmol/L, respectively. The mixing speed used to synthesize samples was 400 rpm.

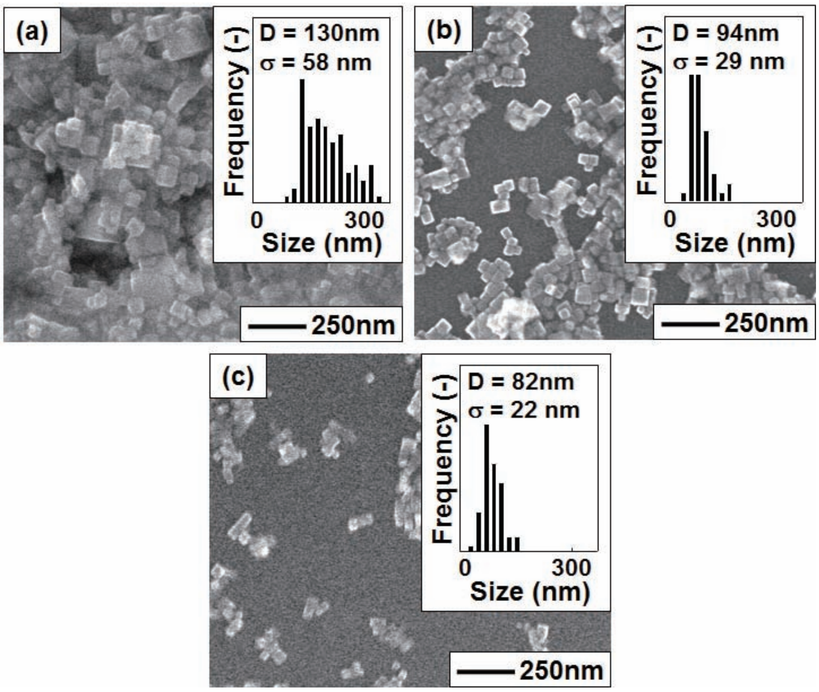

Fig. 3 SEM images of prepared particles conducted at different mixing speeds (400 (d); 800 (e); and 1000 (f)). All samples were prepared at 70 ℃ using NH_4F and $CaCl_2$ compositions of 54 and 450 mmol/L, respectively. Samples were conducted at 2 hours.

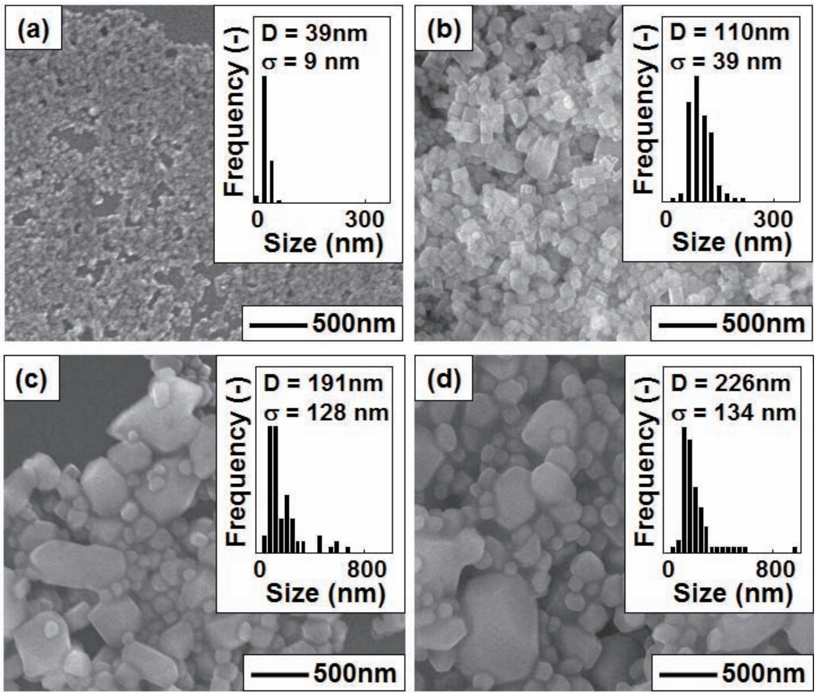

Fig. 4 SEM images of prepared particles conducted during different temperature processes: (a) 25, 50, 70, and 80 ℃. All samples were prepared at 400 rpm using a NH_4F and $CaCl_2$ composition of 54 and 450 mmol/L, respectively.

monomers and grow faster, while the others were not. From **Fig. 4a-d**, an optimum temperature to gain particles with a relatively narrow size distribution was 50 ℃.

A reactant composition can also be selected as a comparison parameter. By varying the composition of the reactants under the optimum reaction conditions (i.e., temperature, mixing speed, and reaction time), the control of particle size and morphology can be achieved, but the process can maintain the production of particles in the monodispersed range. For this reason, the effect of the composition of reactants on the particle size and morphology was investigated.

Fig. 5 shows the effect of NH_4F concentration on particle size. **Fig. 5a-c** correspond to the SEM micrographs of CaF_2 particles; while **Fig. 5d** shows the relationship between particle diameter and reactants composition. The SEM analysis shows that spherical particles with nearly monodispersed were obtained. A strong relationship between particle diameter and reactant composition was revealed. Submicron particles were formed when a fluorine ion concentration of about 50 mmol/L was employed (**Fig. 5a**). The addition of anion allowed the production of smaller particles (**Fig. 5b**). Further increases in the anion composition (fluorine ion concentration of more than 200 mmol/L) resulted in the formation of nanoparticles (**Fig. 5c**). In order to confirm the correlation between particle diameter and reactant composition, simple data regressions of final particle diameters as a function of the NH_4F concentration, when performed at $CaCl_2$ concentrations of 4.5; 45, 90, and 450 mmol/L, are plotted in **Fig. 5d**. The regressed data showed that for all variations, the final size of the particles decreased with increasing concentrations of calcium and fluoride sources.

The results of the reactant compositions in **Fig. 5** were in a good agreement with the Lamer and Dinegar theory (**Fig. 1**). High reactant composition meant high contact and interaction among the reactants, resulted in a rapid conversion of reactants into monomers (**Fig. 1, condition 1**). This rapid conversion allowed the acceleration of nuclei formation but retarded particle growth, resulting in the production of smaller sized particles. Conversely, when using a low reactant composition, the condition as described in **Fig. 1, condition 2** could be achieved.

To confirm our hypothetical study in the particle formation, we approximated the final particle number (n) from the experimental results as a quantifier of nucleation.[4] The n is calculated by dividing the mass of total formed particles (m_o) by the mass of an apparent single particle (m_p). The equation of n can be

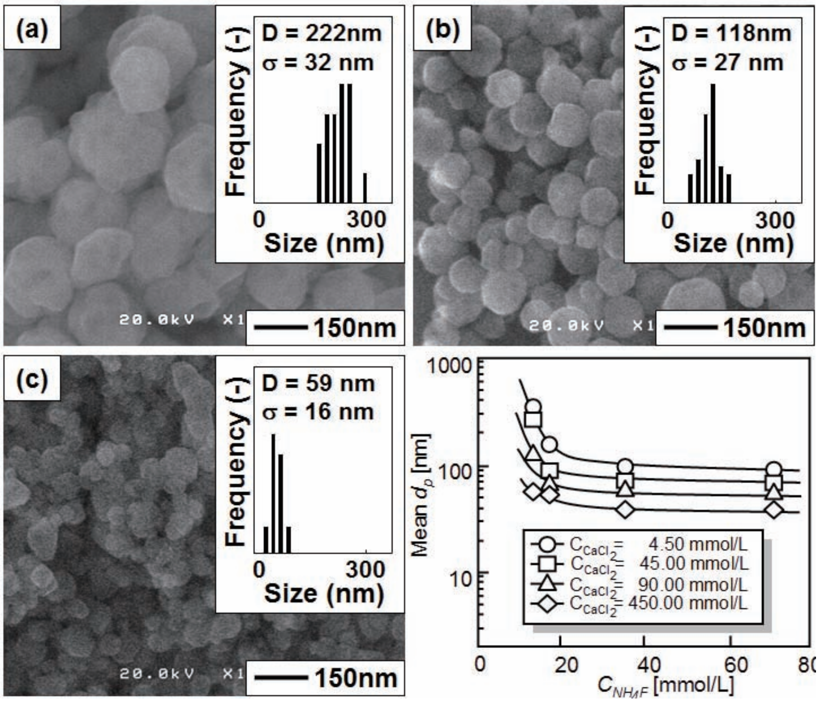

Fig. 5 SEM images of prepared particles with NH_4F:$CaCl_2$ composition ratios (in mmol/L) of 54:18 (Sample B) (a), 108:18 mmol/L (Sample C) (b), and 216:18 (Sample D) (c). Fig. (d) shows average particle size as a function of NH_4F and $CaCl_2$ concentrations.

derived as $n = \frac{m_o}{m_p}$. Obviously, the approximation of the value of m_o came from the stoichiometrical calculation, while the value of m_p was from the multiplication of particle density (ρ) and volume of a particle (V_s). The value of ρ was fixed using a standard bulk density of CaF_2 (3,180 kg/m^3) to simplify the calculation of m_p. To simplify the calculation, the particles are assumed to be spherical particles and the V_s is approximated using $V_s = \frac{1}{6}\pi \cdot d_p^3$; where d_p is the apparent particle size from SEM images.

Fig. 6 shows the number of nuclei generated (n) as a function of NH_4F concentration, carried out at $CaCl_2$ concentrations of 4.50, 45.00, 90.00, and 450.00 mmol/L. The number of nuclei increased from 10^{12} to 10^{17} with the changes in reactant composition, in which the results were in a good agreement with our theoretical hypothesis. The increase in the concentrations of the reactants caused a rapid conversion of reactants into monomers. Reactants were joined to create a monomer and a nucleus rather than simply combining reactants with a formed nucleus to increase the weight. Because most of the reactants/monomers were consumed for the nucleus construction, retardation in the particle growth was found. Conversely, the decrease in reactant concentration resulted in fewer monomers. As a consequence, a short-nucleation stage occurred (resulting in the production of fewer nuclei), which allowed the nuclei to catch more monomers and increase their weight in the next step (the particle growth stage).

Fig. 7 shows the effect of various calcium ion amounts on particle morphology at a low reactant ratio. Relatively monodispersed particles with a specific morphology were examined. A strong relationship between reactant composition and particle shape was obtained. Submicrometer particles with a spherical shape were formed when a calcium amount of 9 mmol/L was employed (**Fig. 7a**). The increase in calcium concentration in the same concentration of a fluorine source allowed the production of smaller particles with a hexagonal shape (**Fig. 7b**). A further increase in calcium composition resulted in the formation of other morphologies: cubical form particles (**Fig. 7c**). However, in the case of changing anion concentration but in the same concentration of calcium (as resulted in **Fig. 7c**), the production of smaller particles with size of down to nanometer range was found (**Fig. 7d**). Ferret analysis showed that the particles with NH_4F:$CaCl_2$ molar ratios (in mmol/L) of 9:27; 90:27; 900:55; and 900:100 had sizes of 400, 305, 62, and 45 nm, respectively.

TEM images of particles with different morphologies are shown in **Fig. 8**. Dense particles were observed for all cases. Particles with hexagonal and cubical shapes were observed clearly in **Fig. 8a** and **c**, respectively. The low magnification of TEM images presented a group of identical particles, confirming that the morphology and dimensions of all particles

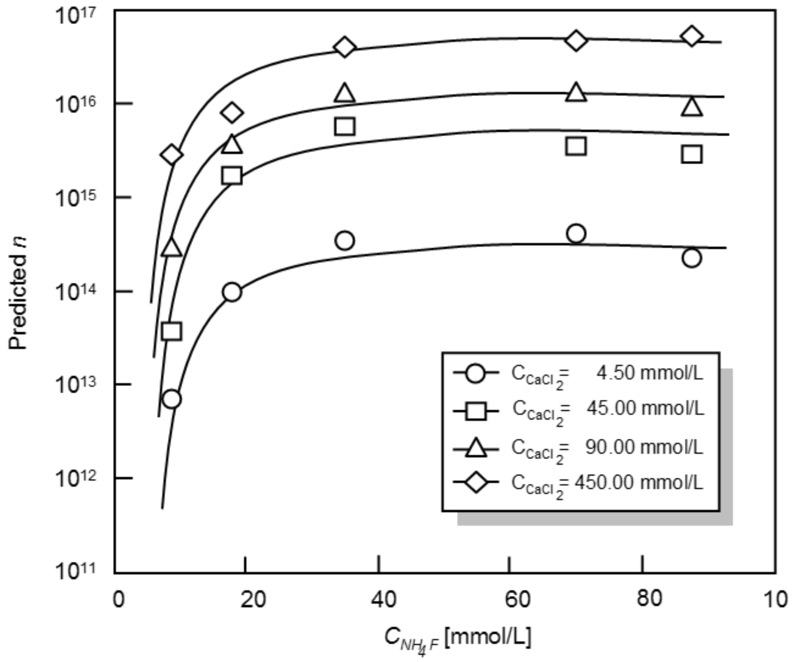

Fig. 6 The predicted number of nuclei (n) as a function of $CaCl_2$ and NH_4F concentrations.

under identical procedural conditions are similar. The sizes and morphologies of particles, as assessed by TEM, were in a good agreement with the SEM results (in **Fig. 6c**). To verify the structure of the particle, high magnification of TEM was conducted, as shown in **Fig. 8b** and **d**. This TEM analysis indicated

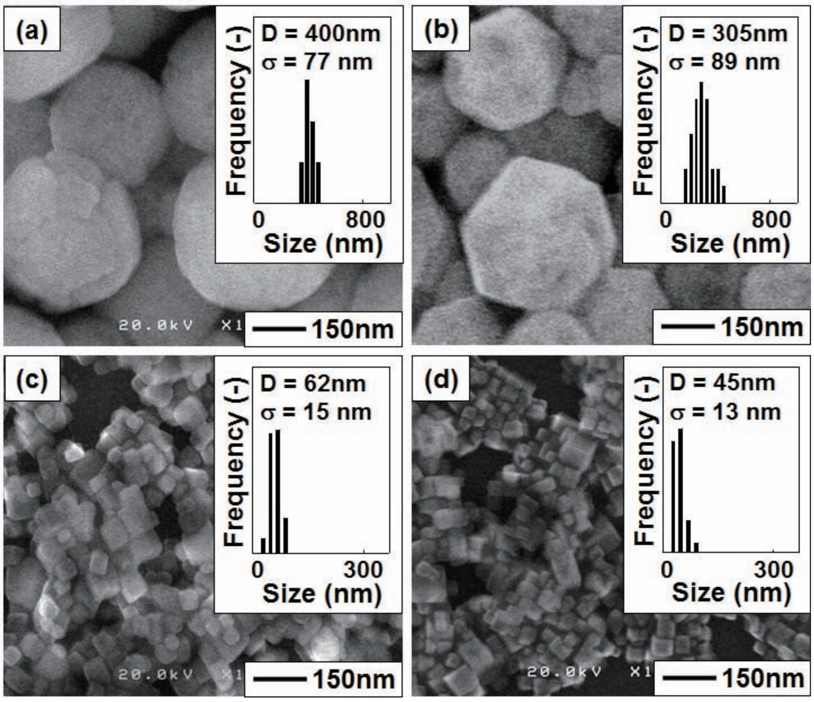

Fig. 7 SEM images of prepared particles with $NH_4F/CaCl_2$ composition ratios (in mmol/L) of 27:9 (Sample A) (a), 27:90 (Sample F) (b), 54:900 (Sample J) (c), and 108:900 (Sample K) (d).

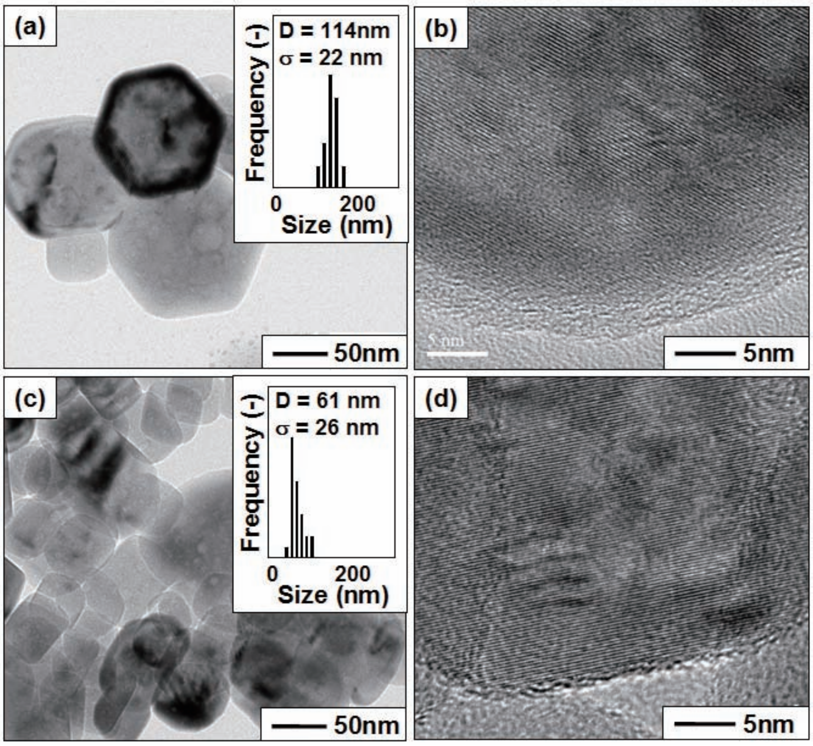

Fig. 8 TEM images of hexagonal- (Sample G) and cubical-shaped particles (Sample K).

that the particles contained high crystallinity for both morphologies.

STEM with elemental analysis of particles with a cubical morphology is shown in **Fig. 9**. Dense particles with an identical shape (i.e., cubical shape) were observed (**Fig. 9a**). Elemental mapping analysis showed that the particles had different components: one was calcium (**Fig. 9b**) and the other was fluoride (**Fig. 9c**). Calcium and fluoride were well-distributed inside the nanoparticles as prepared, confirming that the particles consisted of calcium-fluoride compounds.

Fig. 10 presents the XRD patterns of prepared particles with different morphologies. The results showed that although different reactant ratios can possibly lead to changes in material sizes and shapes, identical patterns as a CaF_2 compound were detected in all cases. The main diffraction peaks of 2θ were observed at 27.94, 46.68, 55.42, and 68.54. These peaks corresponded to the (110), (220), (311), (400) planes, which could be indexed to the CaF_2 compound.[3] No impurity peaks were observed, indicating that the particles prepared by the present method were pure in both chemistry and in the crystalline phase. The only difference appeared to be the intensity of the peaks describing dissimilar crystal sizes. The peak intensities increased with a change in the morphology from spherical to cubical shapes. The lowest intensity was observed in the spherical particles, indicating a low degree of crystallinity. However, for the case of cubical shape particles, the highest intensity was obtained, implying that the particles had a high degree of crystallinity. This result also verified that this shape was the most stable crystal in the CaF_2. According to the Scherer equation, the crystal sizes of spherical- (size of 222 nm), hexagonal- (size of 114 nm), and cubical-shaped particles (size of 62 nm) were 71.22, 47.48, and 44.99 nm, respectively. These results also implied that a significant reactant ratio changed only the size of the crystalline particles (formation of a very small crystalline) but did not substantially contribute to a change in the material phase and pattern. The spherical particles had a polycrystalline structure, but the structure of the cubic particles was relatively monocrystalline.

The transformation of particle shapes from spherical into hexagonal and/or cubical form was observed (**Fig. 7**), but the XRD patterns for all shapes were the same (**Fig. 10**). This result illustrated that the fundamental reason behind the shape transformation

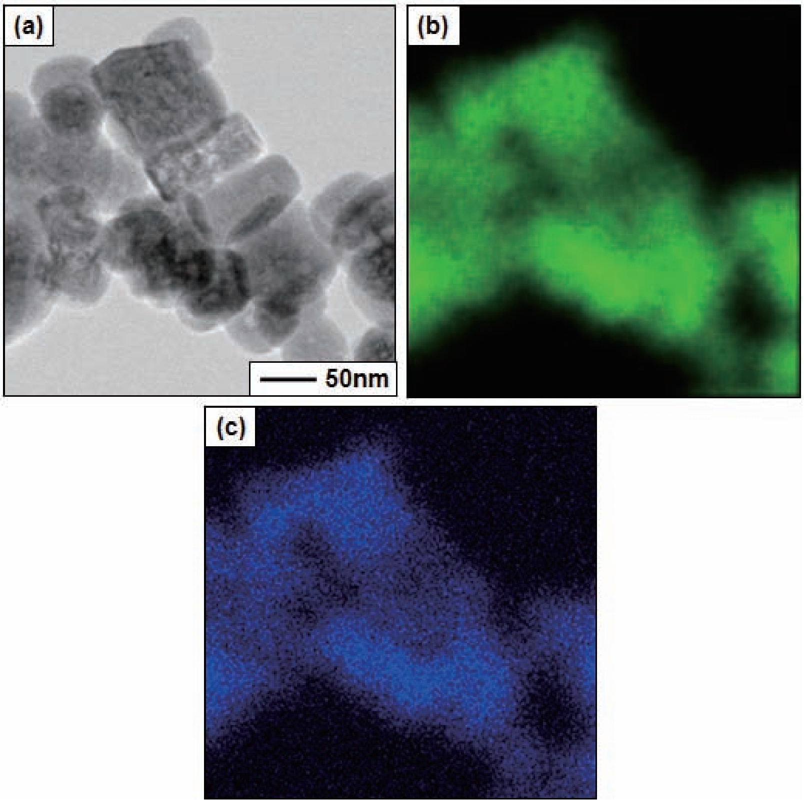

Fig. 9 STEM image (a) with elemental mapping analysis (calcium (b) and fluorine (c)) of cubical-shaped particles (Sample K).

was not changes in material patterns or chemical structures. To confirm this theoretical explanation, a modification of the Lamer and Dinegar theory should be included to describe the shape transformation phenomenon.[26] This modification theory described that some conditions can change other energies (e.g., surface free energy) during particle growth formation, causing the transformation of particle shape.[4] When the ratio of NH_4F:$CaCl_2$ was very low, a limited amount of monomer was formed. This condition caused the retardation of the particle growth rate, changing the surface potential adsorption of monomers in the nuclei, and resulting in the growth of particles into their stable and original form. This confirmed that cubical particles had a high crystallinity and was near to monocrystalline-type structure (**Fig. 8**). However, when the ratio was high, the number of reactants also should have been high. As the excess amount of reactants increased, monomers were rapidly produced, allowing faster nuclei and crystal formation (very small crystalline generation). This condition makes the monomer to be sufficient to change specific surface energy, enhancing particle growth from all particle surface faces. As a result, spherical particles could be formed (**Fig. 7a**). Evidence in the generation of very small crystallinity in the spherical particles is shown in **Fig. 10**. The low peak intensities were observed in the case of spherical particles, confirming that this type of particle had a low degree of crystallinity, containing polycrystalline structure. This result also implied that the pattern was nearly amorphous.

Based on all experimental results, a summary of the effect of the composition of the reactants on particle size and morphology is described in **Fig. 11**. The ratio of the reactants could be used as a parameter to control particle size and morphology. Some combinations of this composition resulted in the successful formation of particles with a spherical shape, while other combinations produced various morphologies (i.e., cubical and hexagonal shapes). When the ratio of NH_4F:$CaCl_2$ was relatively less than 0.33, cubical particles could be prepared (dark-blue-patterned area). An increase in the ratio allowed the production of hexagonal-shaped particles (sky-blue-patterned area). However, a further increase in the ratio permitted the production of spherical-shaped particles (clear-pattered area). For all shapes, particle size could be easily controlled by changing the amounts of the reactants, as illustrated by the red and dashed line (namely, the "dp trend" line). Nanoparticle synthesis lies above the dp trend line, while the submicrometer is below the line. In addition, because recognition of the present study came from the experimental results, in which the variation was within strictly specified concentrations (reactant concentration = 1–1000 mmol/L), the preparation of CaF_2 particles that are controllable for size and morphology underscores the need for further studies.

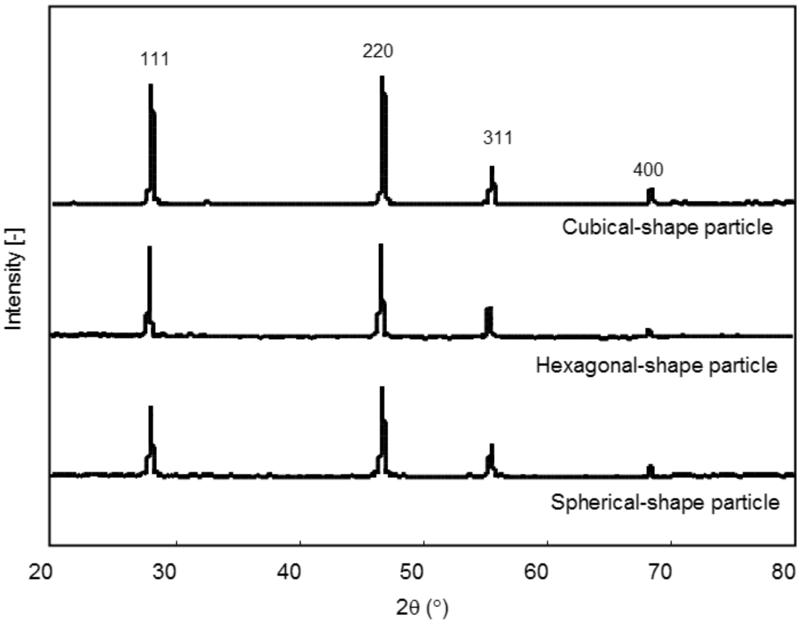

Fig. 10 X-ray diffraction patterns of spherical- (Sample B), hexagonal- (Sample G), and cubical-shaped particles (Sample K).

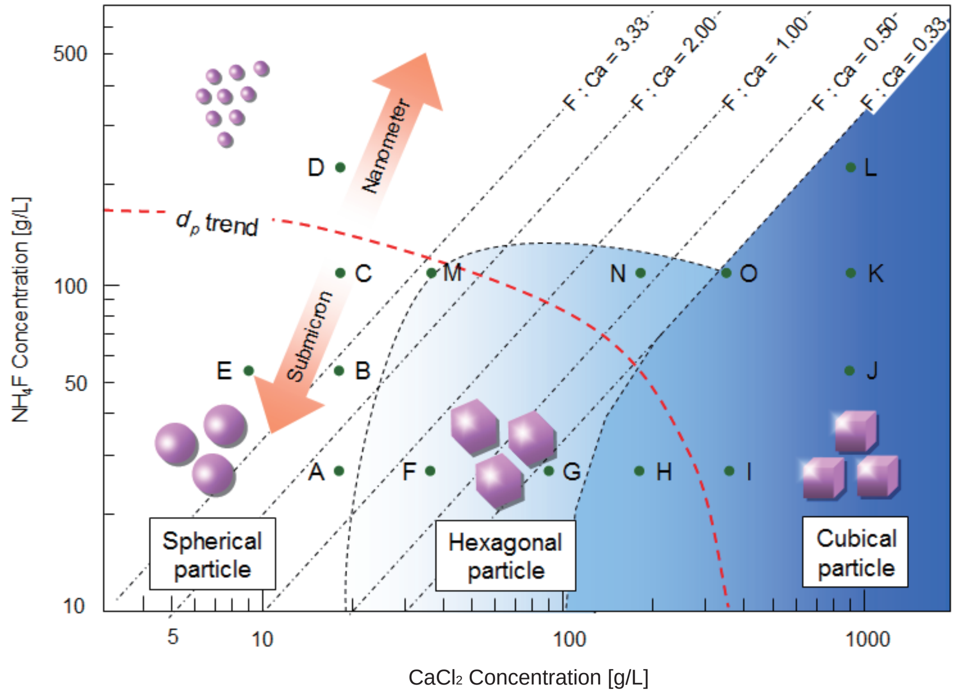

Fig. 11 Summary of the effect of variations of $CaCl_2$ and NH_4F concentrations on CaF_2 particle size and morphology.

4.2. Analysis of refractive index of CaF_2 particles

Because the creation of the excellent properties of the material can be attained by the change of particle size and morphology,[18] it should be interest to demonstrate and compare the material properties for the various particles. To characterize the properties of materials, a specific analytical measurement is typically used. However, in the present study, a refractive index based on a simple measurement system was used. Refractive index material is relatively sensitive, depending on the elemental structure and the material morphology.[27,28] This reason makes that the analysis of refractive index is the best to confirm the effect of reactant composition, size, and morphology on material properties.[14]

To measure the refractive index value, the conventional Lorenz-Lorentz theory is typically used[29]:

$$\frac{n_{tot}^2-1}{n_{tot}^2+2} = \varphi_m \frac{n_m^2-1}{n_m^2+2} + \varphi_p \frac{n_p^2-1}{n_p^2+2}$$

; where n_{tot}, n_m, and n_p are the refractive index of precursor, medium, and particles, respectively. The symbols φ_m and φ_p are, respectively, the volume fractions of the medium and particles.

Table 2 shows the result of the refractive index of CaF_2 particles calculated using the conventional Lorenz-Lorentz theory. To simplify the investigation, samples used in this analysis contained particles with identical size and shape (cubical structures; size of about 60 nm). The solution with no additional particles showed the lowest refractive index (n = 1.333). Adding particles resulted in an increase in the refractive index value. Impact from the change of particle type to the material performance was confirmed.[14] An increase in the calcium amount would increase the refractive index of the precursor. The particles with a Ca:F ratio of 1:2 had the lowest value of refractive index value (close to the theoretical refractive index of a single crystalline CaF_2 monolayer (1.433[30])), while particles with a ratio of 15:1 had the highest. The size and shape of the characterized particles were almost the same, informing these factors had no effect on the change in the refractive index value. Differences in the refractive index are probably caused by differences in the crystallinity of the characterized particles. The results of the refractive index were 1.43, 1.64, and 1.89, corresponding to particles prepared from Ca: F ratios of 1:2, 5:1, and 15:1, respectively.

Fig. 12 shows the effect of the degree of crystallinity on the refractive index. The size of the crystal ($d_{crystal}$) was measured using the Scherer method from XRD (XRD not displayed), while the particle size (d_p) was determined from the SEM images using the Ferret analysis. As expected, the effect of the crystallin-

Table 2 Analysis comparison of an average CaF_2 refractive index as a function of calcium and fluorine ion composition

No	$CaCl_2/NH_4F$	Refractive index
1	Standard solution	1.333
2	1 : 2	1.433
3	5 : 1	1.645
4	10 : 1	1.892
5	Theoretical CaF_2	1.433

Note: Samples were characterized at a visible light at a wavelength of 589 nm and measured at 25℃. Theoretical value of CaF_2 was adapted from a reference[30]. $d_{crystal}$ and d_p are the size of crystal (measured using Scherer method) and the particle size (measured from SEM images using Ferret analysis), respectively.

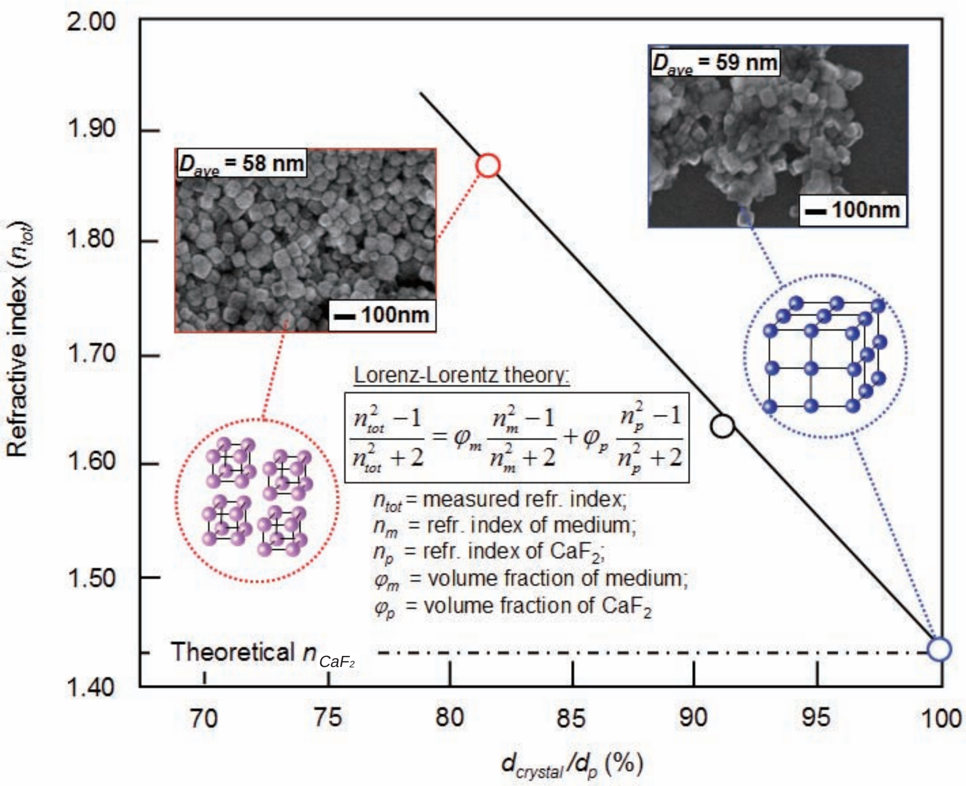

Fig. 12 Effect of crystalline size on refractive index. $d_{crystal}$ and d_p are the size of crystal (measured using the Scherer method) and the particle size (measured from SEM images using the Ferret analysis), respectively. A theoretical CaF_2 value was adapted from a reference.[30]

ity of the material on the refractive index value was verifiable. An increase in the ratio of $d_{crystal}$: d_p seemed to have an impact to the increase of refractive index value. When the particles with a relatively monocrystalline structure ($d_{crystal}/d_p$=100%) were applied, a low refractive index performance could be obtained; the particles with polycrystalline and a lower degree of crystallinity resulted in a high refractive index value.

The characterization and measurement was directly measured by the visual refractive index analysis of the dispersed particles in the solution. Therefore, there was a concern that an error might have been created by the measurement of agglomerated and precipitated particles in the suspension. The additional functionalization of particles should be the best for homogenizing particles in the standard solution;[23] however, it can produce misleading results because some functionalization techniques use a high energy/pressure to disperse particles (e.g., ultrasonic, beads mills process, etc.) and employ other components/

chemicals as coupling agents, which doesn't allow particles to retain their original morphology (as-synthesized shape).[9] For this reason, additional studies are required to verify the actual material properties (e.g., refractive index). However, we believe that insights gained from this type of research will contribute to more fabrication innovation, particularly with respect to the synthesis of ultralow refractive index materials.

5. Conclusions

CaF_2 particles with controllable size (from 30 to 900 nm) and morphology (spherical, hexagonal, and cubic forms) were successfully prepared using a liquid-phase synthesis method. The effectiveness of this method in producing monodispersed particles relied on the optimization of several reaction parameters: temperature, mixing speed, and reaction time, which were qualitatively verified using conventional nucleation theory. The ability to create particles with various sizes and morphologies was due to changes in the NH_4F:$CaCl_2$ molar ratios. Particles in the size of several tens nanometer could be synthesized when a high concentration of reactants was employed, while the submicrometer particles were due to low concentrations of reactants. In the case of particle morphology, 3 types of particles could be created: spherical, hexagonal, and cubical. Cubical particles were prepared when the ratios were less than 0.33. When the ratios increased, the process led to the production of particles with a hexagonal shape. Further increases in ratio permitted to the synthesis of particles with a spherical morphology. No change in the XRD phase and pattern was found, confirming that the shape transformation was due to change in the particle growth orientation. A theoretical background to support how the particles were changing was also added, compared with an analysis of the number of nuclei. The effect of the composition and crystalline structure of particles of reactants on material performance (i.e. refractive index) was investigated in this paper, opening the door for the future synthesis of material with a low refractive index. Due to simple preparation procedures, use of relatively low-temperature processing, and employment of easy-to-handle chemicals, we believe that the present study provides important new information for the field of chemical and material science and engineering.

6. Acknowledgements

A fellowship provided for A.B.D.N. by the Japan Society for the Promotion of Science (JSPS) is gratefully acknowledged. We also thank the Hosokawa Powder Technology Foundation for providing a research support grant for A.B.D.N. This work was supported by (MEXT)-KAKENHI Grant-in-Aid for Scientific Research A (No. 22246099).

7. References

1) U. Groß, S. Rüdiger, E. Kemnitz (2007): Alkaline earth fluorides and their complexes: A sol-gel fluorination study, Solid State Sci, No. 9, pp. 838-842.

2) S.V. Kuznetsov, V.V. Osiko, E. Tkatchenko, P.P. Fedorov (2006): Inorganic nanofluorides and related nanocomposites, Russ Chem Rev, No. 75, pp. 1065.

3) Z. Quan, D. Yang, P. Yang, X. Zhang, H. Lian, X. Liu, J. Lin (2008): Uniform colloidal alkaline earth metal fluoride nanocrystals: nonhydrolytic synthesis and luminescence properties, Inorg Chem, No. 47, pp. 9509-9517.

4) A.B.D. Nandiyanto, F. Iskandar, T. Ogi, K. Okuyama (2010): Nanometer to Submicrometer Magnesium Fluoride Particles with Controllable Morphology, Langmuir, No. 26, pp. 12260–12266.

5) R.J. Franklin (1967): US Patent, 3529929.

6) E.J. Page, T.R. White (1970): US Patent, 3529929.

7) W.L.W. Ludekens, A.J.E. Welch (1952): Reactions between metal oxides and fluorides: some new double-fluoride structures of type ABF3, Acta Crystallog, No. 5, pp. 841-841.

8) S. Fujihara, K. Tokumo (2009): Chemical processing for inorganic fluoride and oxyfluoride materials having optical functions, J. Fluorine Chem, No. 130, pp. 1106-1110.

9) A.B.D. Nandiyanto, S.G. Kim, F. Iskandar, K. Okuyama (2009): Synthesis of spherical mesoporous silica nanoparticles with nanometer-size controllable pores and outer diameters, Micropor Mesopor Mat, No. 120, pp. 447-453.

10) A.B.D. Nandiyanto, Y. Kaihatsu, F. Iskandar, K. Okuyama (2009): Controllable Mesopore-size and Outer Diameter of Silica Nanoparticles Prepared by a Novel Water/Oil-Phase Technique, MRS Proceedings, No. 1220, pp. 11-17 (doi:10.1557/PROC-1220-BB1504-1505).

11) F. Iskandar, S.G. Kim, A. Bayu, D. Nandiyanto, Y. Kaihatsu, T. Ogi, K. Okuyama (2009): Direct synthesis of hBN/MWCNT composite particles using spray pyrolysis, J. Alloy Compd, No. 471, pp. 166-171.

12) F. Iskandar, A.B.D. Nandiyanto, W. Widiyastuti, L.S. Young, K. Okuyama, L. Gradon (2009): Production of morphology-controllable porous hyaluronic acid particles using a spray-drying method, Acta Biomater, No. 5, pp. 1027-1034.

13) F. Iskandar, A.B.D. Nandiyanto, K.M. Yun, C.J. Hogan, K. Okuyama, P. Biswas (2007): Enhanced photocatalytic performance of brookite TiO_2 macroporous particles prepared by spray drying with colloidal templating, Adv. Mater, No. 19, pp. 1408-1412.
14) A.B.D. Nandiyanto, N. Hagura, F. Iskandar, K. Okuyama (2010): Design of a highly ordered and uniform porous structure with multisized pores in film and particle forms using a template-driven self-assembly technique, Acta Mater, No. 58, pp. 282-289.
15) A.B.D. Nandiyanto, F. Iskandar, K. Okuyama (2008): Nanosized Polymer Particle-facilitated Preparation of Mesoporous Silica Particles Using a Spray Method, Chem Lett, No. 37, pp. 1040-1041.
16) A.B.D. Nandiyanto, F. Iskandar, K. Okuyama (2009): Macroporous anatase titania particle: Aerosol self-assembly fabrication with photocatalytic performance, Chem Eng J., No. 152, pp. 293-296.
17) A.B.D. Nandiyanto, Y. Kaihatsu, F. Iskandar, K. Okuyama (2009): Rapid synthesis of a BN/CNT composite particle via spray routes using ferrocene/ethanol as a catalyst/carbon source, Mater Lett, No. 63, pp. 1847-1850.
18) A.B.D. Nandiyanto, K. Okuyama (2011): Progress in Developing Spray-drying Methods for the Production of Controlled Morphology Particles: From the Nanometer to Submicrometer Size Ranges, Adv. Powder Technol., No. 22, pp. 1-19.
19) K. Okuyama, K. Ohshima, K. Tsuto (1991): Preparation of micro controlled particles using aerosol process technology, KONA Powder and Particle Journal, No. 9, pp. 79-93.
20) K. Okuyama, W. Wang, F. Iskandar (2007): Technology innovation in the nanoparticle project-synthesis of nanoparticles and nanocomposites, KONA Powder and Particle Journal, No. 25, pp. 237-243.
21) K. Okuyama (1991): Preparation of micro-controlled particles usingaerosol process, J. Aerosol Sci., No. 22, pp. S7-S10.
22) K. Okuyama, I. Lenggoro, S. Tamaki, N. Tohge (1997): The formation of ultrafine particles of metal sulfide by the electrostatic spray pyrolysis method, KONA Powder and Particle Journal, No. 15, pp. 227-234.
23) A.B.D. Nandiyanto, T. Ogi, F. Iskandar, K. Okuyama (2010): Highly ordered porous monolayer generation by dual-speed spin-coating with colloidal templates, Chem Eng J., No. 167, pp. 409-415.
24) K. Ohshima, Y. Torimoto, K. Tsuto, K. Okuyama, R. Ushio, Y. Kousaka (1991): Experimental control of preparation of thin film and fine particles by CVD, KONA Powder and Particle Journal, No. 9, pp. 59- 70.
25) T. Sugimoto (2001): "Monodispersed Particles", Elsevier, Amsterdam.
26) Z. Peng, S. Yang, H. Yang, (2009): Approaches to the synthesis and characterization of spherical and anisotropic platinum nanomaterials, in: C.S.S.R. Kumar (Ed.) "Metallic nanomaterials", Wiley, Weinheim, pp. 357-401.
27) J.P. Mitchell (2000): Particle standards: their development and application, KONA Powder and Particle Journal, No. 18, pp. 41-59.
28) H. Chang, K. Okuyama (2002): Optical properties of dense and porous spheroids consisting of primary silica nanoparticles, J. Aerosol Sci., No. 33, pp. 1701-1720.
29) W. Heller (1945): The determination of refractive indices of colloidal particles by means of a new mixture rule or from measurements of light scattering, Physical Review, No. 68, pp. 5-10.
30) R.H. Perry, D.W. Green (1984): "Perry's chemical engineers' handbook 8th ed", McGraw-Hill New York.

Author's short biography

Asep Bayu Dani Nandiyanto

Asep Bayu Dani Nandiyanto is a JSPS (the Japan Society of Promotion Science) researcher at Hiroshima University. He received his Sarjana Teknik (equivalent to B.Eng.) in 2005 in microparticle synthesis from Department of Chemical Engineering at Institut Teknologi Bandung (ITB). He received M.Eng (2008) and Dr.Eng (2011) from Department of Chemical Engineering at Hiroshima University. He received numerous awards and scholarships, including the grant and student awards by the Supersemar, the P.T. Sanbe Farma, the Ministry of Education of Japan (MEXT), the Kawamura foundation, and the Hosokawa Micron Foundation. His research is in the area of particle technology focused on production of fine and ultrafine particles, starting from gas, aqueous, organic, or colloidal precursor via aerosol routes and liquid-phase synthesis, and their applications to the development materials (e.g. optical, medical, catalyst, energy, and environmental technologies).

Takashi Ogi

Takashi Ogi is an assistant professor in Chemical Engineering at Hiroshima University. He received his PhD degree in Chemistry and Chemical Engineering in 2008 from Hiroshima University. He was a JSPS researcher from 2006 to 2008 and an assistant professor at Osaka Prefecture University from 2008–2010. His current research interests include synthesis of nanoparticles materials via liquid phase, spray, microbial method. Especially, he focus on the development of alternative materials for rare earth, and the application of his research are visible light-sensitive photocatalysts, rare-earth free phosphors, and catalysts for fuel cell. Furthermore, he also engaged in the research on recovery of rare-earth.

Akihiro Ohmura

Akihiro Ohmura is a master student at Hiroshima University supervised by Prof. Kikuo Okuyama. His research is in the area of particle technology focused on production of nanoparticles using a liquid-phase synthesis method. Now, he is working in the synthesis of low-refractive index materials and their functionalization (e.g. optical lens, film, etc)

Eishi Tanabe

Eishi Tanabe is an associate senior researcher at Hiroshima Prefectural Technology Research Institute, West Region Industrial Research Center, Hiroshima. He received M.Sc. (1995) in Department of Material Science at Hiroshima University and PhD (2005) at Department of Materials Creation and Circulation Technology at Shimane University. His current research interests include electron energy loss spectroscopy of catalyst and 3D electron tomography of nano composite.

Author's short biography

Kikuo Okuyama

Kikuo Okuyama is a Professor of Chemical Engineering at Hiroshima University. He received his doctoral degree in 1978 in chemical engineering at Osaka Prefecture University. His research has touched many aspects of aerosol science and technology, from fundamental investigations on aerosol dynamic behavior to the development of aerosol measurement equipments with a recent focus on nanomaterial synthesis. Prof. Okuyama has received numerous honors and awards, including the Fuchs Memorial Award in 2002, and KONA Award in 2007. He has coauthored more than 420 scientific papers, 120 review papers, 50 books/chapters, and 70 patents.

Attachment Efficiency of Polydisperse Nanoparticles Wall-Deposition†

Yuming Wang[1] **and Jianzhong Lin**[1, 2*]
Institute of Fluid Mechanics, China Jiliang University[1]
State Key Laboratory of Fluid Power Transmission and Control, Zhejiang University[2]

Abstract

The attachment efficiency when nanopartiles contact with a flat smooth wall is investigated by taking the elastic deformation force, van der Waals force and Stokes resistance into account. The equations of interactions between particle and wall are derived and solved numerically to obtain the attachment efficiency for dioctyl phthalate nanoparticles with diameter changing from 100nm to 800nm and for different initial angle of attack. The results show that it is more difficult to attach onto the wall for the particles which attack the wall vertically. The attachment efficiency decreases overall with increasing particle diameter. There exists an abrupt increase in the attachment efficiency when the particle diameter is around 550nm. The attachment efficiency is different with or without considering the elastic deformation force. The difference in the values of attachment efficiency for vertical and horizontal walls is negligible. A new formula for the attachment efficiency is presented to express the relationship between the attachment efficiency and the particle diameter as well as the initial angle of attack.

Keywords: nanoparticles, contact with wall, attachment efficiency, numerical simulation

1. Introduction

Nanoparticles deposition to the walls is a common phenomenon in nature and of importance in many industrial processes, for example, granular filtration1), chromatographic separation2), heat transfer3), atmospheric pollution and cell transport in living systems4,5). Deposition rate of nanoparticles is primarily controlled by Brownian diffusion, gravitational settling and turbulent diffusion.

Over the past several decades, the nanoparticle deposition in flows has received much attention. Davies6) and Ingham7) made some analysis on the Brownian deposition and gravitational sedimentation of nanoparticles in a long channel. Fuchs8) studied the particle deposition in laminar flow and calculated the deposition rate. Jia and Williams9) and Van de Ven10) considered particle deposition in detail including many physicochemical interactions such as van der Waals force and electrostatic interactions. Shams et al.11) studied particle deposition from 10 nm to 50 μm in turbulent duct flows, and the effects of flow shear velocity on the deposition rates of different size particles are given. Lai and Nazaroff12) applied the results of near-surface turbulence to produce an analogous model for particle deposition onto indoor surfaces. The model accounts for the effects of Brownian and turbulent diffusion and gravitational settling, and predicts deposition to smooth surfaces as a function of particle size and density. Zhang and Kleinstreuer13) studied airflow structures and nanoparticle deposition in a human upper airway model and found that the total particle deposition fractions for cyclic inspiratory flow are not significantly different from those for steady flow, and particle deposition distributions vary with airway segment, particle size, and inhalation flow rate. Zhang et al.14) made a comparison of micro- and nano-size particle depositions in a human upper airway model and illustrated that the deposition distributions are much more uniform for nanoparticles. Chein and Liao15) numerically studied particle deposition with diameters of 3, 5, and 10 nm

---

[†] Accepted: August 20th, 2011
[1] Hangzhou 310018 P.R. China
[2] 310027, China
[*] Corresponding author
E-mail: JZLIN@ZJUEM.Z.JU.EDU.CN
TEL: (+86)571-86836009 FAX: (+86)571-86914401

ⓒ 2011 Hosokawa Powder Technology Foundation

in a finite-length heated channel flow under both molecular diffusion and thermophoretic effects, it is found that, for a finite channel length, higher particle deposition can be obtained for the various inlet temperature and fixed wall temperature cases. Winkler et al.[16] studied the deposition of dense solid particles in a downward, fully developed turbulent square duct flow, and it is observed that the deposition rates in a square duct are greater than those in a pipe flow, especially for the low Stokes number particles. Zamankhan et al.[17] numerically studied the flow and nanoparticle transport and deposition in a realistic human nasal passage. Based on the simulated results, a semi-empirical equation for the capture efficiency of the nasal passage for nanoparticles was fitted in terms of Peclet number. Lantermann and Hanel[18] presented a numerical solution concept for simulating the transport and deposition to surfaces of discrete nanoparticles. They included the interaction between the deposited particle layer and the fluid field or the external forces recomputing of these fields with changed boundaries, the results showed the influence of different effects on the particle motion and deposition. Tian and Ahmadi[19] conducted a series of numerical simulations to study the transport and deposition of nanoparticles in a turbulent duct flow using different turbulence models, it was shown that when sufficient care was given to the modeling effort, the particle deposition rates could be predicted with reasonable accuracy. Asgharian and Price[20] developed a mathematical model of nanoparticle transport by airflow convection, axial diffusion, and convective mixing in realistic stochastically generated asymmetric human lung geometries. It is found that particles below 10 nm in diameter were effectively removed from the inhaled air in the tracheobronchial region with little or no penetration into the pulmonary region. Lin and Lin[21] studied nanoparticle transport and deposition in bends with circular cross-section for different Reynolds numbers and Schmidt numbers, the results showed that particle deposition is the most intensive at the outside edge and weakest at the inside edge. Curvatures of tube, Reynolds number, and Schmidt number have second-order, forth-order, and first-order effects on the relative deposition efficiency, respectively. Zhang[22] simulated nanoparticle deposition at the bottom surface in a room-scale chamber with particle injection, and plotted distributions of particle-number density at different times in several viewing planes to facilitate discussion of the particle-distribution patterns. Lin et al.[23] studied the nanoparticles transport and deposition in a rotating curved pipe, the results showed that when the Schmidt number is small, the nanoparticle distributions are mostly determined by the axial velocity. When the Schmidt number is many orders of magnitude larger than 1, the secondary flow will dominate the nanoparticle distribution. When the pipe co-rotates, the distribution of nanoparticle mass fraction is similar to that for the stationary case. Zhang and Kleinstreuer[24] made computational analysis of airflow and nanoparticle deposition in a combined nasal-oral-tracheobronchial airway model, it was found that the change in breathing route not only significantly influences nanoparticle deposition in the regions of nasal and oral cavities, nasopharynx and oropharynx, but also measurably affects depositions from pharynx to bronchial airways for tiny nanoparticles. Moghadas et al.[25] numerically simulated the septal deviation effect on deposition of nanoparticles in human nasal passage, the results showed that the flow field and particle deposition strongly depend on the passage geometry especially for micro particles.

Despite the relatively large number of works on nanoparticle deposition in flows, there is a lack of information on the attachment of particles on the wall because the previous works almost assumed that the particles which contact with wall surface will attach onto the wall. Actually some particles will spring-back from the wall for the existence of material elasticity of the wall and the particles. For the elastic collision between two spherical nanoparticles, Feng and Lin[26] built the model of the collinear central collision of two nanoparticles with same diameter undergoing van der Waals force and elastic deformation force, and then calculated the collision efficiency. Wang et al.[27-29] extended Feng and Lin's work to the oblique collision of two nanoparticles with different diameter by taking the electrostatic force into account. Chen and You[30] used another method to calculate the collision efficiency in the presence of hydrodynamic interactions. However, the research on the elastic collision between nanoparticles and wall as well as the attachment efficiency has yet not been found in literature. In the present study, therefore, we focus our attentions to the attachment efficiency when nanopartiles contact with a flat smooth wall by considering the elastic deformation force, van der Waals force and Stokes resistance.

2. Forces Exerted on Nanoparticles

There are some forces exerted on nanoparticles in the process of elastic collision between nanoparticles and wall, for example, van der Waals force, Stokes resistance, elastic deformation force and gravitational force. The previous works[31,32] showed that the van der Waals force and elastic force are the most dominant forces after the particles touch the wall, while the Stokes resistance is of important only when the particles move near a wall.

2.1 Van der waals force

The van der Waals force is aroused from the electropolar effect and plays an important role on the collision when the distance between particle and wall is less than 1 μm, The van der Waals forces between two flat smooth walls and between particle and wall are, respectively[33]:

$$F_{vdw1} = \frac{A}{6\pi Z_0^3}, \tag{1}$$

$$F_{vdw2} = \frac{Ad_p}{12Z_0^2}, \tag{2}$$

where d_p is the particle diameter, Z_0 is the distance at which the van der Waals force comes to exert, which is typically taken as 16.5-40 nm, A is the Hamaker constant[34]:

$$A = \frac{3}{4}kT\left(\frac{\varepsilon_1 - \varepsilon_3}{\varepsilon_1 + \varepsilon_3}\right)^2 + \frac{3hv_e}{16\sqrt{2}}\frac{\left(n_1^2 - n_3^2\right)^2}{\left(n_1^2 + n_3^2\right)^{3/2}}, \tag{3}$$

where k is the Boltzmann constant, T is the absolute temperature, h is Planck's constant, v_e is the plasma frequency of the free electron gas, which is typically taken as $3.0 \times 10^{15} \mathrm{s}^{-1}$, n_1 and ε_1 are the index of refraction and dielectric constant for the particles, respectively, and n_3 and ε_3 are the corresponding values for the suspending medium, respectively.

During the collision between particle and wall, the touch model will change from the point-touch to the surface-touch because the deformation of the particle. Thus, the expression for the van der Waals force in the collision is[35]

$$F_{vdw} = \frac{Ad_p}{12Z_0^2} + s\left(d_p - s\right)\frac{A}{6\pi Z_0^3}, \tag{4}$$

where s is the displacement of particle deformation as shown in **Fig. 1**.

2.2 Elastic deformation force

The elastic particle will deform when it collides with wall, and the elastic deformation force is given according to the Hooke's law. The collision process is composed of compression and spring-back. The compression process is finished when the relative velocity between particle and wall is 0 and s is equal to the maximum s_m. Feng and Lin[26] gave out the expression for the elastic deformation force in the stage of compression:

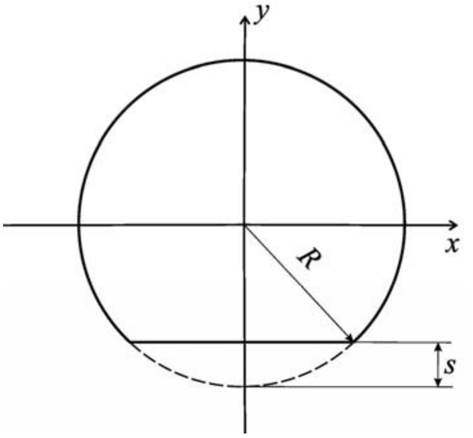

Fig. 1 The displacement of particle deformation.

$$F_e = \pi k_0\left(\frac{s^3}{3} - \frac{d_p}{2}s^2\right), \tag{5}$$

where k_0 is the stiffness of material and dependent on the material characteristics and particle diameter. Considering the loss of mechanical energy, the elastic deformation at the stage of spring-back is different from that at the stage of compression. The elastic deformation force at the stage of spring-back is:

$$F_e' = \begin{cases} \pi k_0\{\frac{d_p}{2}[s_m - \frac{1}{e}(s_m - s)]^2 - \frac{1}{3}[s_m - \frac{1}{e}(s_m - s)]^3\} & s \in ((1-e)s_m, s_m] \\ 0 & s \in [0, (1-e)s_m] \end{cases}, \tag{6}$$

where e is the coefficient of restitution.

2.3 Stokes resistance

The Stokes resistance is the force exerting on the particle by fluid when the particle moving in the fluid. For the particles less than 1 μm the Stokes resistance should be modified by considering the non-continuum effects:

$$F_{stokes} = \frac{3\pi\mu v d_p}{C}, \tag{7}$$

where μ is the fluid viscosity, v is the relative velocity between the particle and the fluid, the Cunningham correction factor is[36]:

$$C = 1 + \frac{\lambda}{d_p}\left(2.34 + 1.05\exp\left(-0.39\frac{d_p}{\lambda}\right)\right), \tag{8}$$

where λ is the mean free path of the molecules.

3. Collision between Particle and Vertical Wall

The process of collision between particle and wall begins when the particle contacts with the wall surface in one point and ends with particle separation or attachment. In the process the particle undergoes two stages, i.e. compression and spring-back.

3.1 The stage of the compression

At the beginning of the compression a particle contacts with a flat smooth wall with an initial velocity v_0 and an initial angle θ_0 as shown in **Fig. 2**, this moment the displacement of particle deformation is zero. After that s increases while the particle velocity v decreases under the effects of various forces. In the end of compression the particle velocity v reduces to 0 while s attains its maximum s_m. The equations during the compression process are:

$$\frac{ds}{dt} = -v_x, \tag{9}$$

$$\frac{dv_x}{dt} = \frac{F_e - F_{vdw} - F_{stokes}}{m}, \tag{10}$$

where v_x ($=v\cos\theta$) is the collision velocity between particle and wall because only the x component of velocity affects the attachment efficiency, and m is the mass of the particle. The initial conditions are:

$$s|_{t=0} = 0, \tag{11}$$

$$v_x|_{t=0} = v_0 \cos\theta_0. \tag{12}$$

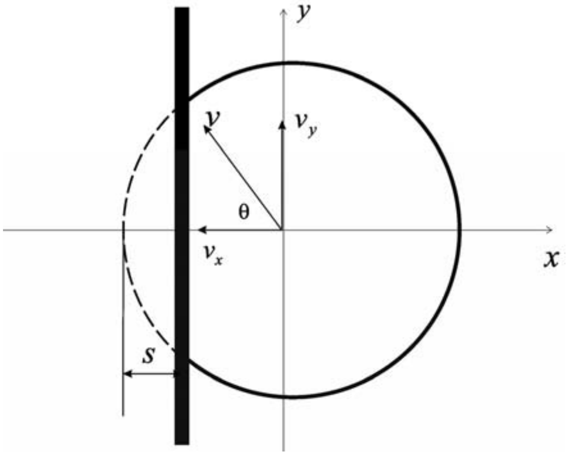

Fig. 2 Model of particle collision to the vertical wall.

Eqs.(9)-(10) are solved to give the maximum s_m which is used to judge whether attachment occurs or not.

3.2 The stage of the spring-back

At the stage of the spring-back s decreases while the particle velocity v increases from 0. Attachment does not happen when the deformation displacement, s, at the spring-back stage is returned to zero, meanwhile, the particle velocity v is still larger than zero. The equations during the spring-back process are:

$$\frac{ds}{dt} = -v_x, \tag{13}$$

$$\frac{dv_x}{dt} = \frac{F'_e - F_{vdw} - F_{stokes}}{m}, \tag{14}$$

and the initial conditions are:

$$s|_{t=0} = s_m, \tag{15}$$

$$v_x|_{t=0} = 0. \tag{16}$$

3.3 Attachment efficiency

Particle attachment on the wall occurs if the particle velocity is reduced to zero before the spring-back is accomplished. Otherwise, the particle will spring-back from the wall. By determining the critical velocity with which the attachment occurs, we can refer to Maxwell velocity distribution to find a corresponding probability. This probability is the attachment efficiency.

Based on Eqs.(13) and (14), the relationship between s, v_x and t can be built. In the function of $v_x(t)$, we can obtain non-zero root t_1 for which $v_x(t)$ has a minimum value, then search the value of $s(t_1)$. $s(t_1) \geq 0$ means that the particle has not left the wall when the particle velocity is reduced to zero. Then, we can obtain critical velocity v_{cr} with which the attachment occurs. After substituting v_{cr} into the Maxwell velocity distribution, we can obtain the attachment efficiency:

$$\alpha = \int_0^{-v_{0cr}} 4\pi \left(\frac{m}{2\pi kT}\right)^{3/2} e^{\frac{mv^2}{2kT}} v^2 dv, \tag{17}$$

where v_{0cr} is the critical value of v_0.

4. Results and Discussions

4.1 Method and parameter

Equations (9), (10), (13), (14) are solved numerically using the fourth-order Runge-Kutta method. The dioctyl phthalate nanoparticles are chosen as the objects. Some parameters of the dioctyl phthalate particles are listed in **Table 1**. The particle diameter is within 100-800nm. The relationship between k_0 and d_p is given based on the experimental data[37,38]:

$$\ln\left(\frac{k_0}{10^7}\right) = 15d_p^3 + 33d_p^2 - 29d_p + 6.3$$
$$d_p \in [100\text{nm}, 800\text{nm}]. \tag{18}$$

Table 1 Some parameters of dioctyl phthalate nanoparticles

A	Z_0	k_0	ρ	λ	e
6.8×10^{-20}	d_p	$f(d_p)$	0.982kg/m^3	65nm	0.7

4.2 Relationship between S_m and v_0 at the stage of compression

The relationship between s_m and v_0 for d_p=400nm and different initial angle of attack, θ_0, at the stage of compression is shown in **Fig. 3**. It is obvious that s_m is directly proportional to v_0 and in inversely proportional to θ_0. The polynomial for the curves in **Fig. 3** is:

$$s_m = -4.5678 \times 10^{-20} (v_0 \cos\theta_0)^3 + 7.2695 \times 10^{-7} (v_0 \cos\theta_0)^2$$
$$-1.2431 \times 10^{-9} (v_0 \cos\theta_0) + 8.8217 \times 10^{-8}$$
$$\theta_0 \in \left[0, \tfrac{\pi}{2}\right). \tag{19}$$

4.3 Relationship between S_m and S_f at the stage of spring-back

Substituting s_m calculated at the stage of compression to Eqs.(14)-(15) we can obtain the relationship between s_m and s_f at the stage of spring-back as shown in **Fig. 4** where s_f is the displacement of particle deformation corresponding to that the particle velocity is zero. In the figure s_f decreases from positive values to negative ones with the increasing of s_m. The polynomial for the curves in **Fig. 4** is:

$$s_f = -4.5145 \times 10^{14} s_m^3 + 2.2193 \times 10^8 s_m^2$$
$$-37.846 s_m + 2.2616 \times 10^{-6}. \tag{20}$$

4.4 Particle attachment efficiency

Substituting v_{0cr} to Eq.(17) we can obtain the attachment efficiency for d_p=400nm and θ_0=0°:

$$\alpha = \int_0^{0.4403} 4\pi \left(\frac{m_{400nm}}{2\pi kT}\right)^{3/2} v^2 dv = 0.3271, \tag{21}$$

where $m_{400nm} = \frac{4}{3}\rho\pi\left(\frac{400 \times 10^{-9}}{2}\right)^3$.

Equation (21) is obtained for the particles with diameter of 400nm. We also can calculate the attachment efficiencies for the particles with diameter changing from 100nm to 800nm and for different initial angle of attack with the same manner. The calcu-

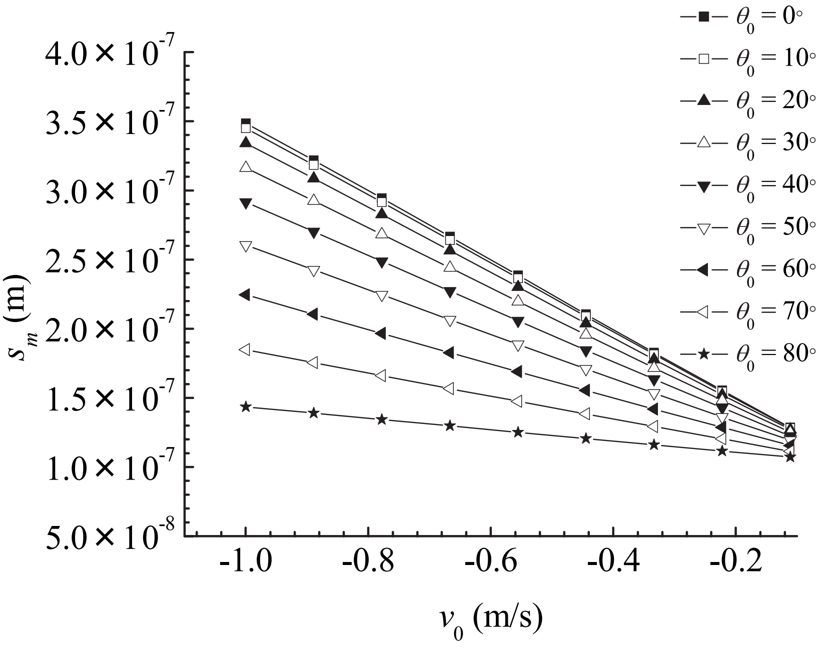

Fig. 3 Relationship between s_m and v_0 at the stage of compression.

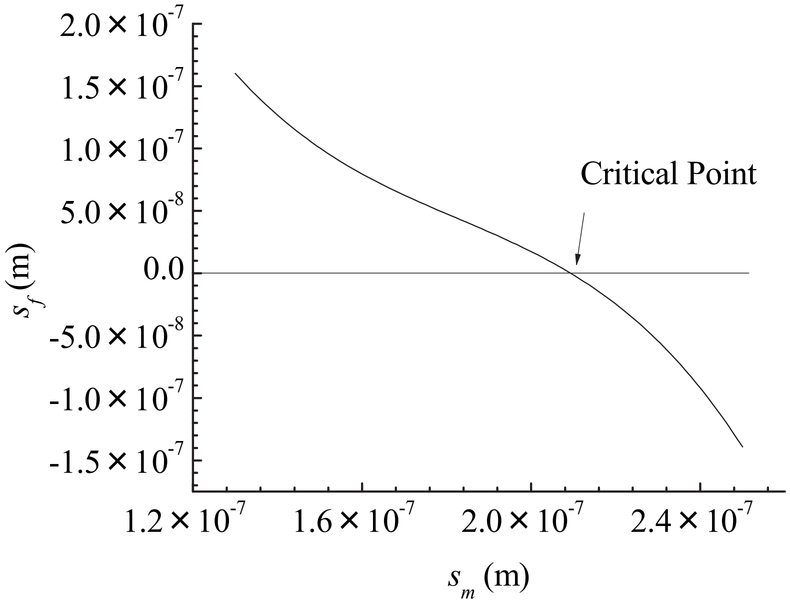

Fig. 4 Relationship between s_m and s_f at the stage of spring-back

lated results are shown in **Fig. 5**. We can see that the attachment efficiency is directly proportional to θ_0, i.e., it is more difficult to attach onto the wall for the particles which attack the wall vertically. The attachment efficiency decreases with increasing particle diameter in the range of 100-500nm. There is a small peak of attachment efficiency around d_p=550nm. The effect of van der Waals force on the particle attachment becomes weak with increasing particle diameter. If elastic deformation force is not considered, the attachment efficiency will decrease monotonously with the increase of particle diameter under the effect of van der Waals force. Therefore, the appearance of a small peak of attachment efficiency is related to the elastic deformation force. When particle diameter is less than 500nm, the van der Waals force is predominant, so attachment efficiency decreases with increasing particle diameter. For the particles with d_p>500 the function of elastic deformation force becomes strong. However, the elastic deformation force does not change with the particle diameter monotonously according to Eqs.(5)-(6), there exists a maximum which occurs around d_p=550nm as shown in **Fig. 5**. It is obvious that the attachment efficiency is different with or without considering the elastic deformation force. Therefore, the elastic deformation force can not be neglected in the computation of particle attachment efficiency. From figure 5 we can built polynomial between α and d_p, θ_0 as follows:

$$
\begin{aligned}
\alpha = &\left(-5.2240\theta_0^3 + 11.690\theta_0^2 - 2.6155\theta_0 - 4.6215\right) \times 10{d_p}^3 \\
&+ \left(5.6912\theta_0^3 - 12.665\theta_0^2 + 2.8402\theta_0 + 4.9376\right) \times 10{d_p}^2 \\
&- \left(1.8680\theta_0^3 - 4.2230\theta_0^2 + 0.9577\theta_0 + 1.7012\right) \times 10d_p \\
&+ \left(1.3489\theta_0^3 - 3.0706\theta_0^2 + 0.6963\theta_0 + 2.2430\right) \\
&d_p \in [0.1\mu\text{m}, 0.5\mu\text{m}]\ ,
\end{aligned}
\tag{22}
$$

$$
\begin{aligned}
\alpha = &\left(-2.0925\theta_0^2 + 1.3061\theta_0 + 1.1090\right) {d_p}^2 \\
&- \left(-3.7954\theta_0^2 + 2.8282\theta_0 + 1.8723\right) d_p \\
&+ \left(-1.0413\theta_0^2 + 1.2289\theta_0 + 1.0296\right) \\
&d_p \in [0.55\mu\text{m}, 0.75\mu\text{m}]\ .
\end{aligned}
\tag{23}
$$

4.5 Collision between particle and horizontal wall

We also calculate the particle attachment efficiency when particle contacts with the flat smooth horizontal wall. The forces exerted on the particle are same with that in Chapter 3 except for the gravity. The similar equations with Chapter 3 are derived by taking the gravity into account. **Table 2** is a comparison of particle attachment efficiency in vertical and horizontal walls. It can be seen that the difference in the values of attachment efficiency for vertical and horizontal walls is negligible.

5. Conclusion

The attachment efficiency when nanopartiles contact with a flat smooth wall is investigated by con-

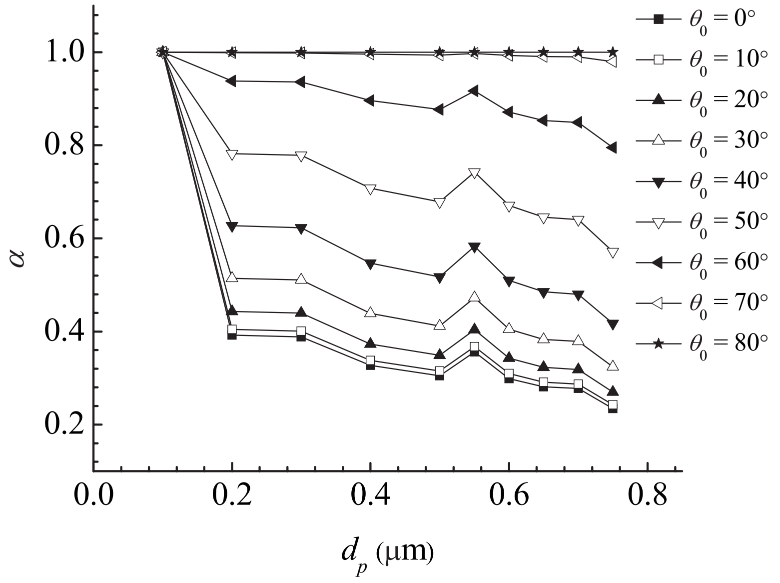

Fig. 5 Attachment efficiency for different particle diameter and initial angle of attack.

Table 2 Comparison of attachment efficiency in vertical and horizontal walls

Particle diameter	vertical wall	horizontal wall
200nm	0.3922	0.3922
300nm	0.3886	0.3900
400nm	0.3271	0.3271
500nm	0.3046	0.3047
600nm	0.2989	0.2991
700nm	0.2773	0.2773

sidering the elastic deformation force, van der Waals force and Stokes resistance. First the equations of interactions between particle and wall at the stages of the compression and spring-back are derived, and then the equations are solved using the fourth-order Runge-Kutta method to obtain the attachment efficiency for dioctyl phthalate nanoparticles with diameter changing from 100nm to 800nm and for different initial angle of attack. The results show that it is more difficult to attach onto the wall for the particles which attack the wall vertically. The attachment efficiency decreases overall with increasing particle diameter. There exists an abrupt increase in the attachment efficiency when the particle diameter is around 550nm. The attachment efficiency is different with or without considering the elastic deformation force. Therefore, the elastic deformation force can not be neglected in the computation of particle attachment efficiency. The difference in the values of attachment efficiency for vertical and horizontal walls is negligible. Finally a new formula for the attachment efficiency when nanopartiles contact with a flat smooth wall is presented to express the relationship between the attachment efficiency and the particle diameter as well as the initial angle of attack.

Acknowledgement

This work was supported by the Major Program of the National Natural Science Foundation of China with Grant No. 11132008.

List of symbols

A	Hamaker constant
C	Cunningham correction factor
d_p	particle diameter
e	coefficient of restitution
F_e	elastic force
F_{stokes}	Stokes resistance
F_{vdw}	van der Waals force
h	Planck's constant

k	Boltzmann constant
k_0	stiffness of material
m	mass of the particle
n_1	index of refraction for the particles
n_3	index of refraction for the suspending medium
s	displacement of particle deformation
s_f	displacement of particle deformation corresponding to that the particle velocity is zero
s_m	maximum of s
T	absolute temperature
v	relative velocity between the particle and the fluid
v_{cr}	critical velocity
v_e	plasma frequency of the free electron gas
v_x	component of v
v_0	initial velocity
Z_0	distance at which the van der Waals force comes to exert

Greek symbols

α	attachment efficiency
ε_1	dielectric constant for the particles
ε_3	dielectric constant for the suspending medium
θ	contact angle
θ_0	initial contact angle
λ	mean free path of the molecules
μ	fluid viscosity

References

1) Tien C.Granular Filtration of Aerosols and Hydrosols (Butterworth, Stoneham, MA, 1989).
2) Small, H.(1847): Hydrodynamic chromatography a technique for size analysis of colloidal particles, Journal of Colloid and Interface Science, Vol.48, No.1, pp147-161.
3) Yiantsios, S.G. and Karabelas, A.J.(1998): The effect of gravity on the deposition of micron-sized particles on smooth surfaces, International Journal of Multiphase Flow, Vol.24, No.2, pp283-293.
4) Mura-Galelli, M.J., Voegel, J.C., Behr, S., Bres, E.F. and Schaaf, P. (1991): Adsorption/desorption of human serum albumin on hydroxyapatite: a critical analysis of the Langmuir model, Proceedings of the National Academy of Sciences, Vol.88, pp5557-5561.
5) Prime, K.L. and Whitesides, G.M.(1991): Self-assembled organic monolayers: model systems for studying adsorption of proteins at surfaces, Science, Vol.252, pp1164-1167.
6) Davies, C.N.(1973): Diffusion and sedimentation of aerosol particles from Poiseuille flow in ducts, Journal of Aerosol Science, Vol.4, pp317-328.
7) Ingham, D.B.(1976): Simultaneous diffusion and sedimentation of aerosol particles in rectangular tubes, Journal of Aerosol Science, Vol.7, pp373-380.
8) Fuchs, N. A.: The Mechanics of Aerosols (Dover Publications, New York, 1989).
9) Jia, X. and Williams, R.A.(1990): Particle deposition at a charged solid/liquid interface, Chemical Engineering Communications, Vol.91, pp127-198.
10) Van de Ven: Colloidal Hydrodynamics (Academic Press, London, 1989).
11) Shams, N., Ahmadi, G. and Rahimzadeh, H.(2000): A sublayer model for deposition of nano- and microparticles in turbulent flows, Chemical Engineering Science,Vol.55, pp6097-6107.
12) Lai, A.C.K. and Nazaroff, W.W.(2000): Nazaroff. Modeling indoor particle deposition from turbulent flow onto smooth surfaces, Journal of Aerosol Science, Vol.31, pp463-476.
13) Zhang, Z. and Kleinstreuer, C.(2004): Airflow structures and nano-particle deposition in a human upper airway model, Journal of Computational Physics, Vol.198, pp178-210.
14) Zhang, Z., Kleinstreuer, C. and Donohue, J.F. (2005): Comparison of micro- and nano-size particle depositions in a human upper airway model, Journal of Aerosol Science, Vol.36, pp211-233.
15) Chein, R.Y. and Liao, W.Y.(2005): Thermophoretic effects on nano-particle deposition in channel flow, Heat and Mass Transfer, Vol.42, pp71-79.
16) Winkler, C.M., Rani, S.L. and Vanka, S.P.(2006): Vanka. A numerical study of particle wall-deposition in a turbulent square duct flow, Powder Technology, Vol.170, pp12-25.
17) Zamankhan, P., Ahmadi, G. and Wang, Z.C.(2006): Airflow and deposition of nano-particles in a human nasal cavity, Aerosol Science and Technology, Vol.40, pp463-476.
18) Lantermann, U. and Hanel, D.(2007): Particle Monte Carlo and lattice-Boltzmann methods for simulations of gas-particle flows, Computers & Fluids, Vol.36, pp407-422.
19) Tian, L. and Ahmadi, G.(2007): Particle deposition in turbulent duct flows - comparisons of different model predictions, Journal of Aerosol Science, Vol.38, pp377-397.
20) Asgharian, B. and Price, O.T.(2007): Deposition of ultrafine (NANO) particles in the human lung, Inhalation Toxicology, Vol.19, pp1045-1054.
21) Lin, P.F. and Lin, J.Z.(2009): Prediction of nanoparticle transport and deposition in bends, Applied Mathematics and Mechanics, Vol.30, pp957-968.
22) Zhang, N., Zheng, Z.C. and Glasgow, W.L.(2010): Simulation of particle deposition at the bottom surface in a room-scale chamber with particle injection, Advanced Powder Technology, Vol.21, pp256-267.
23) Lin, J.Z., Lin, P.F. and Chen, H.J.(2009): Research on the transport and deposition of nanoparticles

in a rotating curved pipe, Physics of Fluids. Vol.21, pp122001.

24) Zhang, Z. and Kleinstreuer, C.(2011): Computational analysis of airflow and nanoparticle deposition in a combined nasal-oral-tracheobronchial airway model, Journal of Aerosol Science, Vol.42, pp174-194.
25) Moghadas, H., Abouali, O. and Faramarzi, A.(2011): Numerical investigation of septal deviation effect on deposition of nano/microparticles in human nasal passage, Respiratory Physiology & Neurobiology, Vol.177, pp9-18.
26) Feng, F. and Lin, J.Z.(2008): The collision efficiency of spherical dioctyl phthalate aerosol particles in the Brownian coagulation, Chinese Physics B, Vol.17, pp4547-4553.
27) Wang, Y.M., Lin, J.Z. and Feng, Y.(2010): The central oblique collision efficiency of spherical nanoparticles in the Brownian coagulation, Modern Physics Letters B, Vol.24, pp1-9.
28) Wang, Y.M. and Lin, J.Z.(2011): The oblique collision efficiency of nanoparticles at different angles in Brownian coagulation, Computers and Mathematics with Applications, Vol.61, pp1917-1922.
29) Wang, Y.M., Lin, J.Z. and Chen, Z.L.(2011): Properties of the collision efficiency of nanoparticles in Brownian coagulation, Chinese Physics Letters, Vol.28, pp014702.
30) Chen, Z.L and You, Z.J.(2010): New expression for collision efficiency of spherical nanoparticles in Brownian coagulation, Applied Mathematics and Mechanics, Vol.31, pp851-860.
31) Seville, J. P. K., Willett, C.D. and Knight, P.C.(2000): Interparticle forces in fluidization: a review, Powder Technology, Vol.113, pp261-268.
32) Zhou, T. and Li, H.Z.(1999): The calculation model of agglomerate sizes in fluidized beds of cohesive particles, Chemical Reaction Engineering and Technology, Vol.15, pp44-51.
33) Israelachvili, J.N.:Intermolecular and Surface Science (Second Edition) (Academic Press, San Diego, 1991).
34) Chun, J. and Koch, D.L(2006): The effects of noncontinuum hydrodynamics on the Brownian coagulation of aerosol particles, Journal of Aerosol Science, Vol.34, pp471-482.
35) Zhang, W. B., Qi, H. Y., You, C. F. and Xu, X. C.(2002): Mechanical analys is of agglomeration and fragmentation of particles during collisions, Journal of Tsinghua University (Science & Technology), Vol.42, pp1639-1643.
36) Kamiadakis, G.E.: Micro Flows: Fundamentals and Simulation (Springer, New York, 2001).
37) Devir, S.E.(1963): On the coagulation of aerosols (part I), Journal of Colloid and Interface Science, Vol.18, pp744-756.
38) Devir, S.E.(1967): On the coagulation of aerosols III: effect of weak electric charges on rate, Journal of Colloid and Interface Science, Vol.21, pp80-89.
39) Hinds, W.C.: Aerosol Technology: Properties, Behavior, and Measurement of Airborne Particles (Wiley-Interscience, New York, NY, 1982).

Author's short biography

Yuming Wang

WANG Yuming graduated in Fluid Dynamics at China Jiliang University where he conducted numerical simulation of multiphase flow. Now he is a graduated student. Recent two years, ha has published five papers on nanoparticle dynamics.

Jianzhong Lin

LIN Jianzhong is a professor of fluid mechanics in China Jiliang University and Zhejiang University. Now he is president of China Jiliang University. His research fields include multiphase flows, dynamics of fiber suspensions, pneumatic conveying and microfluid dynamics. Recent three years, his group has published more than 80 papers. Presently, he serves as associate editor of the International Journal of Multiphase Flow, and as an editorial board member of many journals including Engineering Applications of Computational Fluid Mechanics, Journal of Computational Multiphase Flows, Journal of Hydrodynamics, Applied Mathematics and Mechanics and so on.

Kinetics of Dissolution and Recrystallization of Sodium Chloride at Controlled Relative Humidity[†]

Marina Langlet[1]*, Frederic Nadaud[2], Mohamed Benali[1], Isabelle Pezron[1], Khashayar Saleh[1], Pierre Guigon[1], Léa Metlas-Komunjer[1]
UTC/ESCOM, Équipe d'Accueil "Transformations Intégrées de la Matière Renouvelable" (EA 4297)[1]
UTC/ESCOM, Service d'Analyses Physico-Chimique[2],

Abstract

Both producers and users of divided solids regularly face the problem of caking after periods of storage and/or transport. Particle agglomeration depends not only on powder water content, temperature and applied pressure, but also on the interactions between the solid substance and water molecules present in the atmosphere, i.e. on relative humidity (RH) at which the product is stored. Ambient humidity plays an important role in most events leading to caking: capillary condensation of water at contact points between particles, subsequent dissolution of a solid and formation of a saturated solution eventually followed by precipitation of the solid during the evaporation of water. Here, we focus on the kinetics of dissolution followed by evapo-recrystallization of a hygroscopic sodium chloride powder under controlled temperature and RH, with the aim of anticipating caking by predicting rates of water uptake and loss under industrial conditions. Precise measurements of water uptake show that the rate of dissolution is proportional to the difference between the imposed RH and deliquescence RH, and follows a model based on the kinetic theory of gases. Evaporation seems to be governed by more complex phenomena related to the mechanism of crystal growth from a supersaturated salt solution.

Keywords: Sodium chloride, hygroscopy, Knudsen law, vapor sorption, caking

1. INTRODUCTION

Water being ubiquitous in the atmosphere, the influence of moisture on the chemical and physical stability of many dispersed systems and its impact on product manufacturability, quality and shelf-life is of great concern. In particular, the presence of water in an atmosphere where formulated products containing deliquescent hygroscopic substances are manipulated can have a pronounced effect on their end-use properties such as particle aggregation and ability of powder to flow. Many industrial formulations, especially food products, contain sodium chloride, a deliquescent substance with a deliquescence relative humidity, *DRH*, of 75% at 25℃. Examples of systems at risk include also cosmetics, agricultural chemicals, explosives and pharmaceuticals. Caking of such powders is generally strongly influenced by dissolution followed by recrystallization of the hygroscopic solid substance present. A crystalline substance is said to deliquesce if it forms an aqueous solution when the ambient relative humidity reaches a certain threshold value. Below this critical *RH*, crystal surrounded by water vapor is thermodynamically favorable[1,2] while above the critical *RH*, the aqueous solution is the thermodynamically favored phase. It is of fundamental interest to understand events taking place when particles containing a hygroscopic substance are exposed to the atmosphere containing water vapor. For example, it is well known that adsorbed water cannot cause the dissolution of the solid substrate while condensed liquid water can. Capillary condensation of water vapors leads to the formation of pendular liquid bridges at the contact points between particles. This liquid water is likely to dissolve deliquescent crystalline substances present in the particles. Disso-

---

[†] Accepted : September 10th, 2011

[1] Rond-Point Guy Deniélou, 60200 Compiègne, France
[2] Rond-Point Guy Deniélou, 60200 Compiègne, France
[3] 1 allée du réseau Jean-Marie Buckmaster, 60200 Compiègne, France
* Corresponding author:
E-mail: marina.langlet@utc.fr
TEL: (+33)344 234 744

© 2011 Hosokawa Powder Technology Foundation

lution gives rise to the formation of a saturated solution from which recrystallization of solute follows if water is evaporated, for example due to the changes of ambient conditions of relative humidity and/or of temperature. Usually the re-crystallized solid bridges mechanically bind the particles in contact more efficiently than the pendular liquid bridges between them. The mechanical strength of solid bridges depends not only on temperature, humidity and pressure, but it depends also on the mass transfer, the solubility of the powder in water and the number of contact points, i.e. on the coordination number of particles in the powder bed[3].

A schematic representation of the adsorption of water molecules followed by capillary condensation and dissolution of the solid phase is proposed in **Fig. 1**. The time sequence of phenomena taking place when hygroscopic crystals are brought in contact with an atmosphere containing water vapor is the following: adsorption of water molecules on the solid surface at low vapor pressure (steps 1 and 2), followed by the multilayer formation and capillary condensation at contact points/lines/surfaces at intermediate vapor pressures (step 3). In the case of good wetting of the solid by liquid water, capillary condensation can occur at quite low vapor pressures, i.e. at low *RH*, but the quantity of liquid water, determined by the so-called Kelvin radius, will remain small. At higher *RH*, both Kelvin radius and the corresponding quantity of liquid water will increase rapidly. Deliquescence of the solid takes place if *RH* becomes equal or higher than *DRH*, i.e. when the ambient vapor pressure becomes equal or higher than the vapor pressure of the saturated solution of NaCl (steps 4 to 6). When a mixture of small individual particles and agglomerates of a hygroscopic substance is subjected to high *RH*, small particles might completely dissolve long before large agglomerates are dissolved (as presented in step 5). This means that not all parts of the solid sample are in equilibrium with their environment. In order to better understand the kinetics of the deliquescence of hygroscopic substances under well-controlled ambient conditions, we propose the use of Dynamic Vapor Sorption (DVS) apparatus. We examine dissolution of a solid followed by its recrystallization via the precise measurements of water uptake and water loss at variable conditions of ambient relative humidity. In such a way we provide an original method for the precise determination of deliquescence relative humidity. Modeling the dissolution of a solid and the evaporation of water from a solution so obtained is tempting on the basis of the kinetic theory of gases with the aim of predicting the corresponding kinetics at different ambient conditions of *RH* similar to those met in industrial applications.

This work will focus on the partial dissolution and recrystallization of sodium chloride, a classic model hygroscopic solid. Sodium chloride is present in atmospheric aerosols where it represents the majority of solid particles[1]. For that reason, a significant quantity of highly reliable data concerning NaCl-water binary systems, as well as various other mixtures relevant to atmosphere science, has been published in the last few decades[1,4,5]. Moreover, salt dissolution in water is of particular interest also because of its occurrence in food and other industrial products. Yet these formulations are often complex mixtures of ingredients influencing each other's behavior. Issues

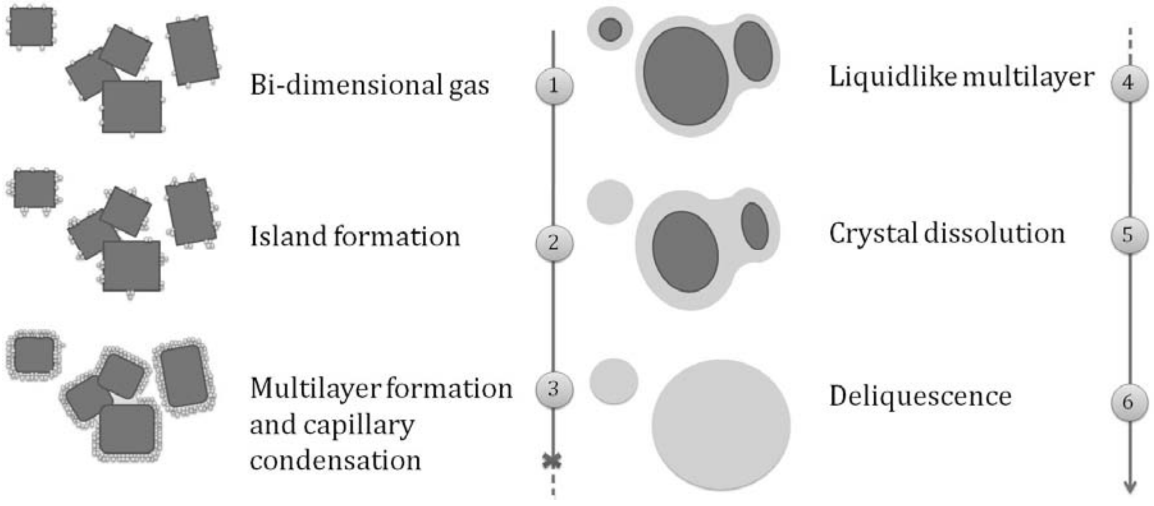

Fig. 1 Hygroscopic crystals in water vapors: adsorption of water vapor and condensation of liquid water followed by dissolution of a solid (adapted from Peters[4], Zasetsky[5] and Mauer[2]).

concerning caking phenomena in multi-component systems are currently under study in our laboratory.

In **Fig. 2**, one can find the well-known P-T diagram for pure water in the temperature range between 0℃ and 30℃ (in dark continued line). It is completed by an analogous curve for a saturated solution of NaCl in water (in light continued line). One can verify that the NaCl curve closely follows the shape of the pure water curve, and that the vapor pressure of the saturated solution of NaCl is approximately 75% to 76% of vapor pressure for pure water for this temperature range in accordance with *DRH* values for sodium chloride cited in literature. The curves of vapor pressure for pure water and the aqueous solution of NaCl are completed by the vapor pressures corresponding to 60, 70, 80 and 90% *RH* (dotted lines). These conditions of *RH* are chosen for their relevance in powder caking. One can also note that in this temperature range, moderate variations of vapor pressure permit setting up conditions for the dissolution of NaCl (when *RH*>*DRH*) and its recrystallization (when *RH* <*DRH*).

Theoretical background

We propose to describe the dissolution and crystallization of NaCl on the basis of a simple model taken from the kinetic theory of gases which was already successfully applied to another hygroscopic salt, ammonium nitrate[8,9]. The well-known Knudsen formula links the flux of molecules impinging on the surface of a condensed phase with the pressure of the ambient gas, *P*, linearly. The proportionality coefficient is dependent on temperature, molar mass of the condensed phase and exchange surface. It is represented by a "Knudsen coefficient", $K_{Knudsen}$. If we define the sticking-coefficient as the probability for a water molecule to remain at the surface after impact, and considering that the condensed phase has a non-negligible pressure, p_s, the net flux of molecules, *dm/dt*, entering the condensed phase is:

$$\frac{dm}{dt} = K_{Knudsen}(P - p_s) \qquad Eq.\ (1)$$

Moreover, as *P* corresponds to the relative humidity and p_s corresponds to the deliquescence relative humidity, one can write:

$$\frac{dm}{dt} = \frac{K_{Knudsen}P_0}{100}(RH - DRH) \qquad Eq.\ (2)$$

or,

$$\frac{dm}{dt} = K_{Knudsen}P_0(a_w - a_w^*) \qquad Eq.\ (3)$$

where a_w is the water activity of the substance in solution and a_w the water activity of the saturated solution of the same substance at the same conditions of pressure and temperature. Note that water activity is linked to relative humidity: $a_w = \frac{RH}{100}$ and to the imposed vapor pressure, *P*, via the saturated pressure of pure water P_0

$$a_w = \frac{P}{P_0}$$

Accordingly, the rate of uptake of water molecules from the vapor phase should be proportional to the water activity of the binary mixture water-NaCl.

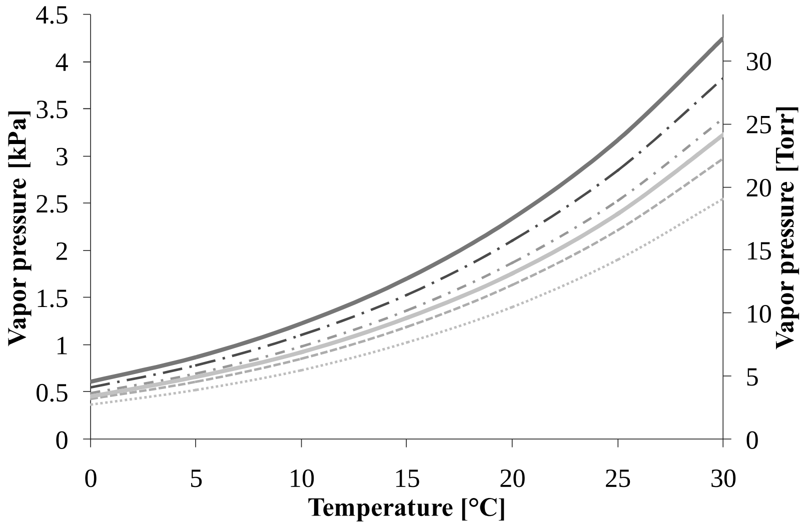

Fig. 2 Pressure-Temperature diagram of water (in dark continued line) (data from Mullin's book[6]) and of saturated aqueous NaCl solution (in light dotted line) (data are adapted from Apelblat and Korin[7]). Curves of water vapour pressure at 90%, 80%, 70% and 60% *RH* are represented in dotted lines from top to bottom, respectively.

2. EXPERIMENTAL

Dynamic Vapor Sorption (DVS)

Sodium chloride crystals of about millimeter in size and a purity of 99.5% were used as provided by Merck. Samples, typically of 8 to 25 mg, were submitted to the continuous gas flow of 200 cm^3/min containing pure nitrogen and water-vapor-saturated nitrogen in proportion corresponding to the desired relative humidity. Mass variations due to the uptake of water from the gas phase were measured by an accurate microbalance system (DVS, Surface Measurement Systems) with a precision of 0.1 μg**; its variation with respect to time**, *dm/dt*, was calculated on a lapse of time of 10 min with an acquisition every minute. Temperature and humidity were controlled to 0.1℃ and 0.5% RH, respectively.

A schematic representation of the apparatus is shown in **Fig. 3**.

Environmental Scanning Electronic Microscopy

The Environmental Scanning Electron Microscopy (ESEM) instrument allows the examination of particles under moderate vacuum (up to 50 Torr for low magnifications). In addition, the sample observation can be carried out in an environment of controlled temperature, pressure and humidity, allowing observation of wetting and drying, with no damage to the material and no need for any special preparation or metal coating.

As one can see from **Fig. 2**, by keeping the temperature at 2℃ and by varying the pressure of the water vapor between about 3 and 5 Torr (400 and 666 Pa), significant variations of RH can be imposed in the observation chamber. Under such conditions, dissolution of NaCl crystals can be observed if the imposed *RH* is greater than 75% *RH*, while recrystallization can be observed when the pressure of water vapor is lowered to the values corresponding to *RH*< 75% *RH*.

3. RESULTS AND DISCUSSION

Dissolution mechanism

The images in **Fig. 4** illustrate the phenomenon of capillary condensation at the contact area between two crystals at *RH* close to *DRH*. **Fig. 4a** shows two NaCl crystals in contact at 72% *RH*, i.e. *RH*<*DRH*. Even if liquid water condenses at the contact area, its volume is too small to be observed at micrometric scale. However, when *RH* is elevated to 83% *RH*, *a* significant volume of condensed liquid water is observed at the contact surface (**Fig. 4b**). The shape of the liquid/vapor interface indicates that the solid substrate is well wetted by liquid water, which is to be expected for high-affinity substances such as hygroscopic solids and water. Such events constitute the starting point of caking phenomena: the solid phase dissolves into liquid bridges formed by the condensation of water, and a saturated solution embedding solid particles is formed, as can be observed in **Fig. 4b**.

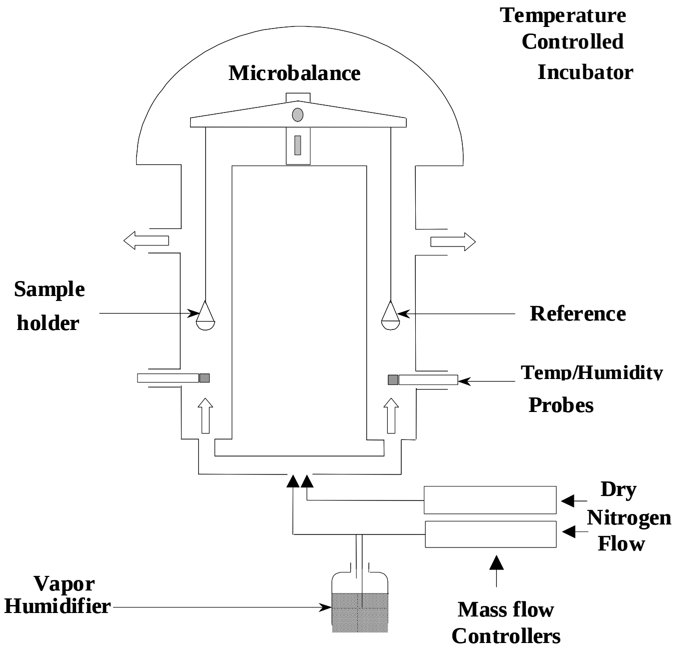

Fig. 3 Schematic representation of the Dynamic Vapor Sorption apparatus.

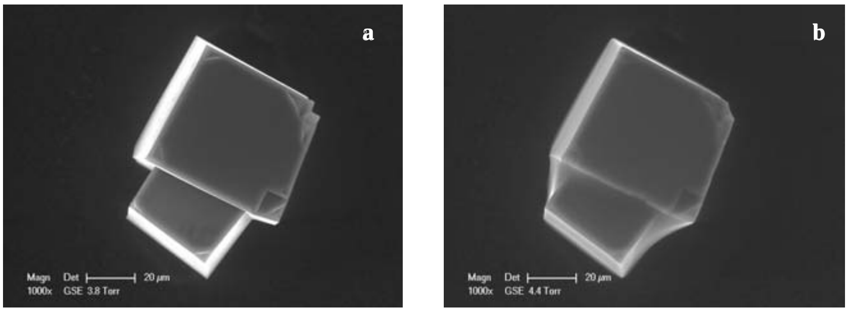

Fig. 4 Capillary condensation of water on NaCl crystal.

The dissolution of an ensemble of NaCl crystals in condensed water can be observed in **Fig. 5**. Images are acquired by ESEM at *RH*>*DRH* by progressively increasing the vapor pressure in the observation chamber to the values corresponding to *RHs* between 75% *RH* and 80% *RH*. In **Fig. 5a** one can observe one individual crystal of approximately 30 by 50 µm in size in the upper part of the figure and two aggregates of unequal size of a few hundred µm in the lower left-hand corner. The dissolution starts by a smoothing of the surfaces until the individual crystal disappears and a perfectly circular drop of aqueous solution is formed (**Fig. 5c**). Simultaneously, on the surface of the aggregates, one can see that water spreads over the surface and a rounding of crystals composing the aggregate can be observed, the quantity of the liquid phase progressively increases from **Fig. 5d** to **Fig. 5f**, but traces of the solid phase are still visible in the lower left corner of **Fig. 5f**.

Although ESEM images illustrate what is happening under industrially relevant conditions very well, one should keep in mind that they are qualitative observations and not representative of the kinetics of dissolution mechanism. Consequently, a quantitative study is necessary to complete the description of phenomena taking place. The quantity of water taken by the powder during the chosen time can be determined experimentally by weighing the sample. As shown earlier for highly hygroscopic ammonium nitrate[8)], the same quantity can be obtained from the Knudsen formula: by integrating **Eq. (2)** under the assumption that the exchange area and sticking coefficient remain constant, one can calculate the number of water molecules taken by the sample as a function of time for each imposed *RH* [see ref. 8) for details]. Experimental verification of the model was provided by the DVS technique.

Quantitative DVS experiments of the present work consist of exposing a NaCl powder sample during a fixed period (4 hours) to a chosen constant *RH*>

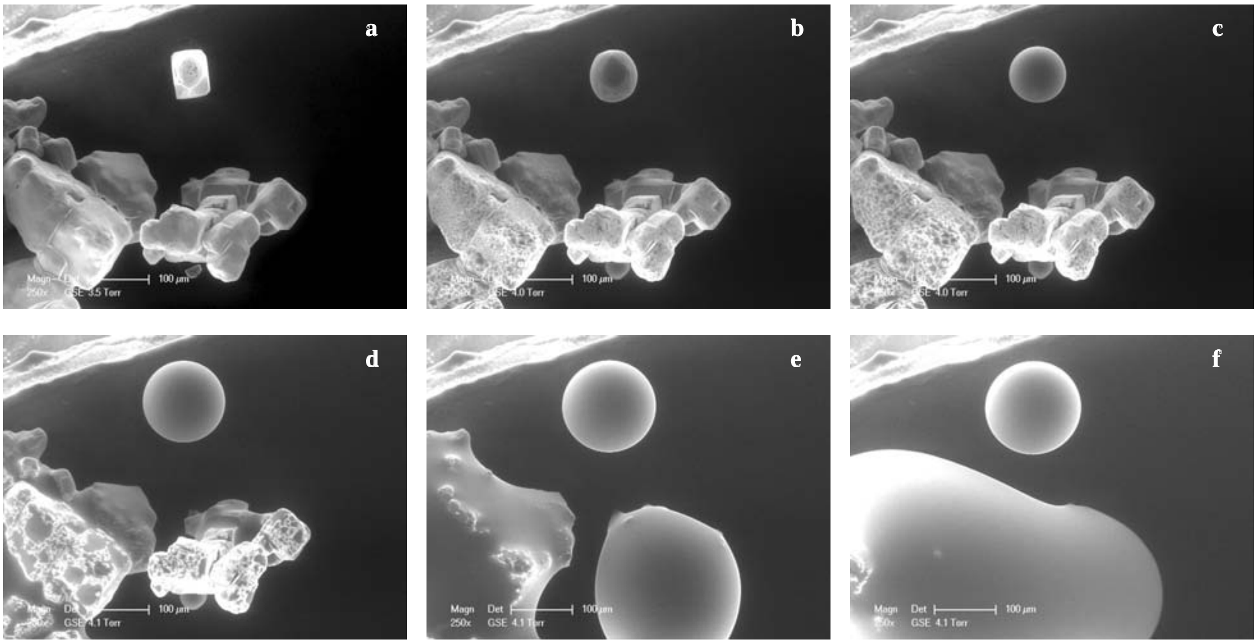

Fig. 5 Time sequence of ESEM images of the dissolution of NaCl at *RH*>*DRH* (a to f); size bar is 100µm in all images.

DRH and measuring the increase of sample mass due to the absorption of water. Subsequently, the same sample is exposed during the same period of time to a chosen constant $RH<DRH$. This gives rise to evaporation of absorbed water and recrystallization of the solid substance. **Fig. 6** shows the quantity of water measured as a function of time: left-hand side of the graph corresponds to water absorption at three different $RH>DRH$, while the right-hand side corresponds to the evaporation and recrystallization of the solid at three different $RH<DRH$. Several samples containing between 12.5 and 13.5 mg of NaCl were analyzed.

First of all, one can notice that except at the very end of the evaporation step, i.e. the last 2 000 to 3 000 s of each experiment, both the water uptake and water loss seem to be directly proportional to the time of exposure to water vapors. Moreover, the dissolution rate, i.e. the slope of absorbed quantity versus time curve, increases at increasing relative humidities while the evaporation rate increases at decreasing relative humidity. One can also note that the quantity of water absorbed during 4 hours (14 400s) is strongly influenced by the imposed *RH*: it amounts to 4.46 mg for 85% *RH*, 7.76 mg for 90% *RH* and 10.76 mg for 95% *RH* for a comparable initial mass of NaCl.

Moreover, the kinetic curves of water uptake and water loss look approximately symmetrical with respect to the axis *t=14 400s*, suggesting the linearity between water uptake or loss and the difference between the imposed relative humidity and the deliquescence point, *RH-DRH*, in accordance with the prediction of the Knudsen law (see **Eq. (2)**). The imposed *RHs* were chosen so that the differences between *RH* and *DRH* are identical (in absolute value) during dissolution of a solid and solution evaporation.

From the data presented in **Fig. 6** and from similar measurements at other imposed relative humidities, the rate of water uptake or water loss is calculated for different samples of the order of 12.5 to 13.5 mg of NaCl. The obtained values corresponding to water absorption (2 points situated on the right-hand side of point M at *75% RH*) and evaporation (7 points situated on the left-hand side of point M) are shown in **Fig. 7**.

The unquestionable linearity between the rate of water uptake or water loss and the imposed relative humidity is in agreement with the Knudsen law. It allows the determination of an experimental value of $K_{Knudsen}$ equal to 1.30 10^{-12} kg.s^{-1}.Pa^{-1} with a relative error inferior to 10^{-2}. By taking the rate of water uptake equal to zero one can determine the deliquescence point at 76% *RH* (with an accuracy of 0.5% *RH*), which is in good agreement with literature data. Graphically, the same result can be obtained by two means. The easy way is to take the abscissa for the null rate because it corresponds to the point where equilibrium is reached. Otherwise, as the Knudsen coefficient can be obtained from the slope of water uptake *versus* *RH* curve (proportionality coefficient of the graph), which is $\frac{K_{Knudsen}P_0}{100}$, one can deduce the *DRH* point by means of the ordinate at the origin, which corresponds to $\frac{K_{Knudsen}P_0 DRH}{100}$.

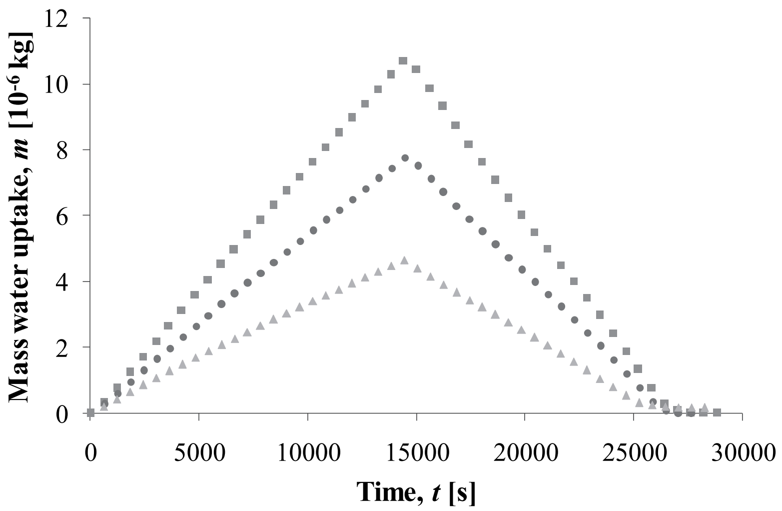

Fig. 6 Water uptake for samples containing between 12.5 and 13.5 mg of NaCl exposed to 95% *RH* (■), 90% *RH* (●) and 85% *RH* (▲) and water loss at 55% *RH* (■), 60% *RH* (●) and 65% *RH* (▲) at 25℃

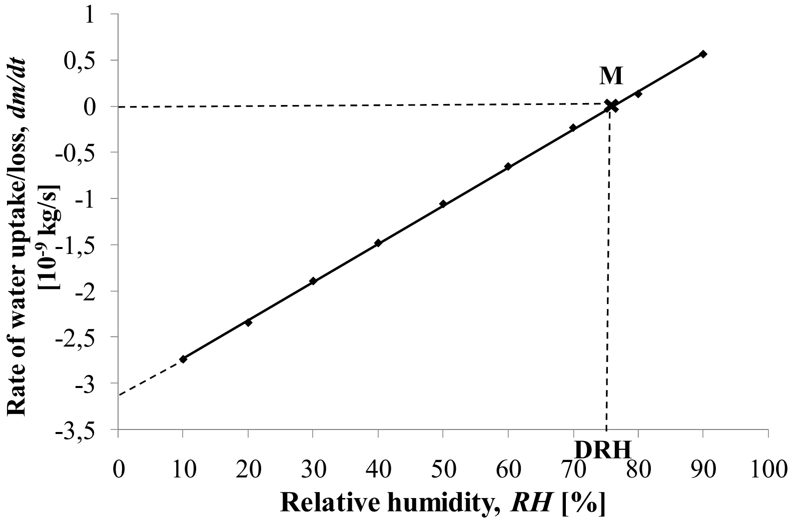

Fig. 7 Water uptake/loss rate at different constant relative humidities at 25℃ during partial dissolution followed by recrystallization of NaCl; point M corresponds to *DRH*.

Experimental data suggest that, in the case of partial dissolution followed by evaporation; both processes can be described by a simple model: water uptake/loss is dependent on the difference between the imposed relative humidity and the deliquescence relative humidity, *RH-DRH*. Moreover, according to ESEM observations at high relative humidity, dissolution seems to be a homogeneous process where all particles, individual crystals as well as aggregates, take up water simultaneously. However, detailed study of recrystallization after partial dissolution will show the complexity of the mechanism at issue. In particular, ESEM observations provided the proof of the existence of two perceptible successive stages during recrystallization.

Keeping in mind practical aspects of the present study, one can use the measured rates of dissolution/recrystallization to determine the amount of hygroscopic powder dissolved or the time required for its caking by recrystallization. For example, let us imagine a product containing NaCl which is stored during four days of rainy weather followed by a period of dry weather. In this case (and by taking the simplifying assumption that there is no interaction with other constituents present in the product), the amount of dissolved NaCl and the required time for recrystallization as a function of relative humidity can be calculated. Some values are reported in **Table 1**:

Recrystallization at *RH<DRH*

In order to better understand the phenomena taking place during recrystallization of the solid phase, ESEM observations at imposed *RH<DRH* were also performed. After partial dissolution shown in the sequence in **Fig. 5**, two partially dissolved aggregates (lower left-hand side of **Fig. 8a**) bathing in a large non-spherical drop and the spherical drop issued from dissolution of small individual crystals (upper right-hand side of **Fig. 8a**) can be observed. The recrystallization of the large aggregate of crystals can be witnessed from **Fig. 8a** to **Fig. 8d**, where water is

Table 1 Percentage of NaCl dissolved (**1a**) and time needed for complete recrystallization (**1b**) as a function of imposed *RH* at 25℃ (mass of NaCl: 0.1g)

1a Amount of dissolved NaCl after 4 days at indicated *RH* at 25℃

RH [%]	**Percentage dissolved**
80	25.5%
85	57.3%
90	80.3%

1b Required time for recrystallization at indicated *RH* at 25℃ if 57.3% of NaCl was dissolved

RH [%]	**Time for recrystallization**
60	3 days
45	1.5 days
30	1 day

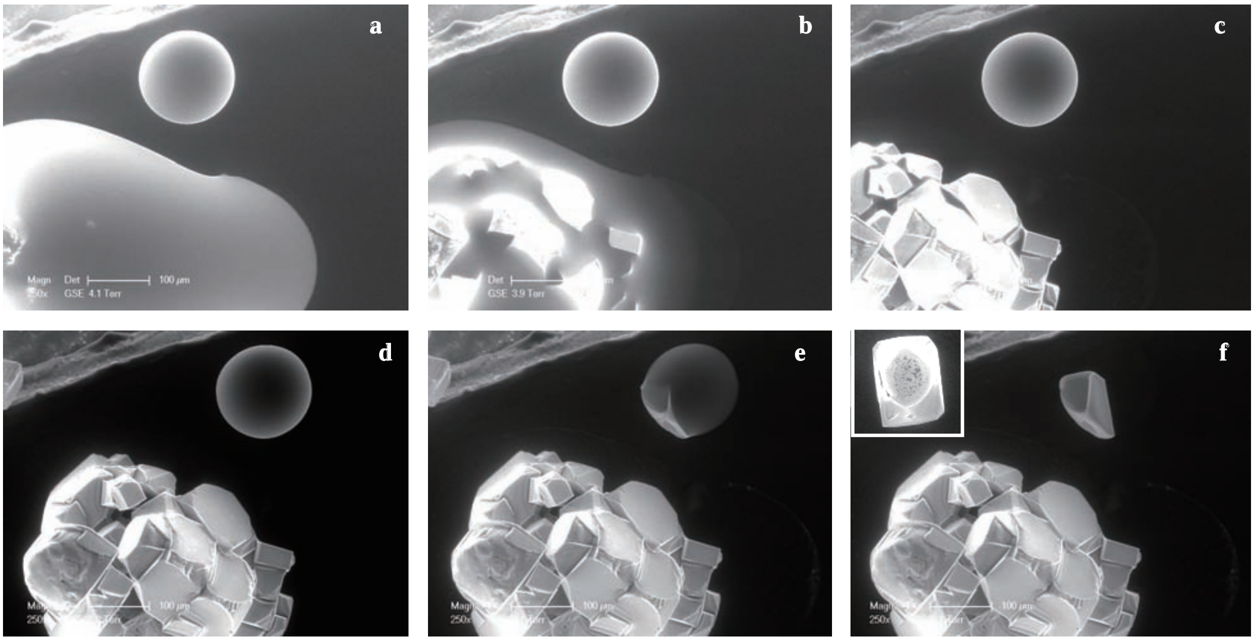

Fig. 8 Time sequence of ESEM images of the recrystallization of NaCl at $RH < DRH$ (a to f); size bar is 100 µm in all images.

rapidly evaporating from the agglomerate while the size of spherical solution droplet seems unchanged. The cluster looks completely dry on **Fig. 8d**, while the drop did not yet show the appearance of a solid. Only in **Fig. 8e** can one see the beginning of faceting on the periphery of the droplet. **Fig. 8f** shows the emergence of the solid phase while the agglomerate seems unchanged. The image in **Fig. 8f** reveals the final stage of drying: from the spherical solution droplet, one unique compact crystal has re-crystallized with a shape different from the initial crystal before dissolution (initial crystal can be seen in the insert on the top left-hand side of **Fig. 8f**).

The importance of modifications induced by partial dissolution followed by recrystallization is further illustrated in **Fig. 9** where the shape of NaCl aggregates before dissolution and after recrystallization is compared. It shows clearly that starting from two separate clusters (**Fig. 9a**), one bigger but more compact cluster is obtained after recrystallization (**Fig. 9b**). The ensemble of ESEM observations proves that due to the dissolution/recrystallization of crystals, caking is accompanied by significant changes with respect to initial size and shape of particles.

By means of ESEM observations of sample drying at microscopic scale, two distinct phenomena responsible for caking can be identified: the first one corresponds to the crystal growth from partially dissolved bigger aggregates, while the second one represents the formation of a crystal from homogeneous aqueous solution formed previously by complete dissolution of the small crystal. In order to verify this qualitative observation, one can perform quantitative analysis of dissolution and recrystallization kinetics. The drying experiments shown in **Fig. 10** were performed on the same sample but at different *RH*. Each

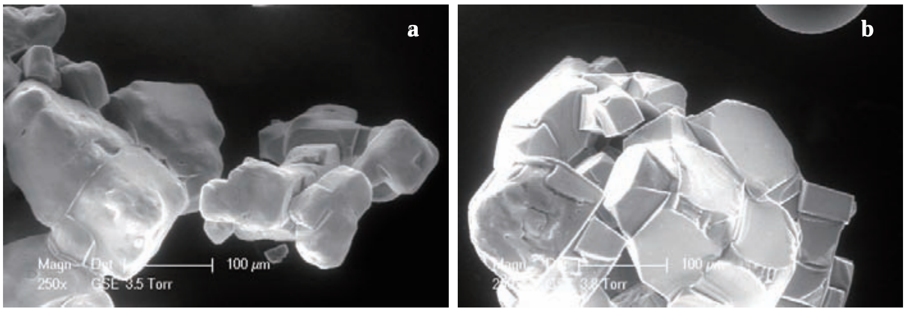

Fig. 9 Environmental scanning electron microscopy images of dry NaCl aggregates (a) before dissolution and (b) after recrystallization; size bar is 100µm in both images.

drying sequence was preceded by partial dissolution at 90% *RH*, meaning that one single NaCl sample was subjected to partial dissolution seven times.

The rate of water uptake or loss is deduced from quantitative measurements of sample mass as a function of time (such as data shown in **Fig. 6**). One should note again that negative signs for water loss rates come from the fact that water evaporation is measured. The first part of the curves represents seven experiments at imposed *RH=90%* (time scale between 0 and 14 400s) carried out on one single sample submitted to multiple cycles of partial dissolution followed by drying. The fact that the dissolution rate remains constant is in accordance with **Eq. (2)**, and its remarkable reproducibility suggests that the Knudsen coefficient remains constant.

By contrast, the kinetics of recrystallization at variable *RH* between 60% and 0% *RH* are all divided into two distinct periods: during the first one following the adjustment of *RH* to the imposed *RH* below *DRH* (*t >14400s*), the loss of water taking place at approximately constant rate is observed. Subsequently, the rate of evaporation seems to slow down slightly, goes through a minimum (in absolute values) followed by a sequence where the rate seems to accelerate. Coming back to the pictures obtained by ESEM (**Fig. 8**), one can suppose that the constant rate of evaporation corresponds to the evaporation of water from solution bathing partially dissolved aggregates. The process is governed by the imposed driving force for evaporation, i.e. *DRH-RH*. A subsequent decrease of the evaporation rate suggests that the solution in liquid drops becomes more concentrated, similarly to what was observed earlier for ammonium nitrate[9]. In such a case, the nucleation of a solid phase takes place when the solution reaches a critical concentration and is followed by the growth of crystals at a rate which depends on the degree of supersaturation of the solution contained in a drop. Indeed, ESEM observations (**Fig. 8c**) show that the spherical droplet remains liquid even though all water seems to be evacuated from the aggregate.

One can also observe that during drying, the time for total evaporation of the water is dependent on the imposed *RH*: it is short for *RH=0%* (◆) and much longer for *RH=60%* (●). Likewise, the evaporation rate during the first phase of crystallization and acceleration during the second phase both increase with decreasing imposed *RH* (i.e. by increasing the difference between *DRH* and imposed *RH*). Finally, the shoulder which appears more intensely at high *RH* (50 and 60% *RH*) at the end of evaporation can be interpreted as the loss of residual water in the crystal matrix, which is more difficult to evacuate at low driving force for crystallization (*DRH-RH*). Careful examination of the kinetics of evaporation will allow a better insight into the mechanism of recrystallization.

4. Conclusion

Aiming at a better understanding of the caking of hygroscopic solids, the role of ambient *RH* was examined in detail. Several processes participating in caking depend on the water vapor pressure in the ambient atmosphere: condensation of liquid water and subsequent formation of aqueous solution fol-

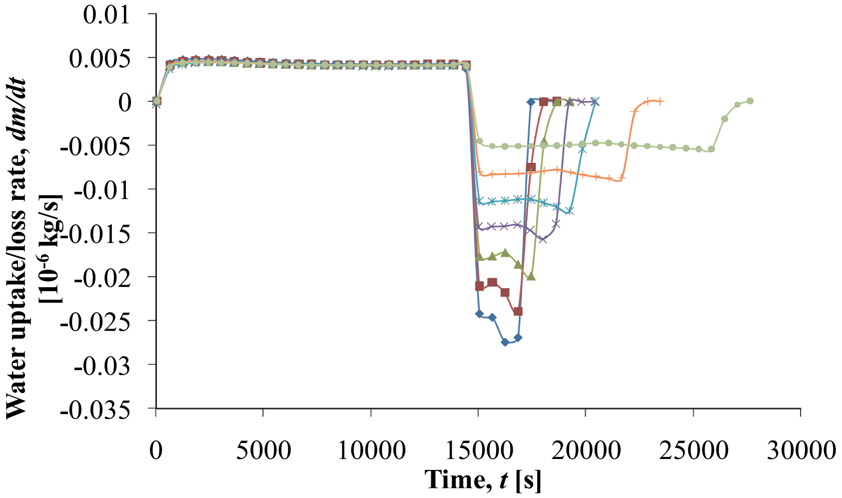

Fig. 10 Water uptake/loss rate of the sample of 12.92 mg of NaCl as a function of time at 25℃: dissolution at 90% *RH* followed by recrystallization at 0% *RH* (◆), 10% *RH* (■), 20% *RH* (▲), 30% *RH* (×), 40% *RH* (∗), 50% *RH* (+) and 60% *RH* (●)

lowed by recrystallization if *RH* decreases. The behavior of such solutions under industrially relevant conditions was studied on laboratory scale. By means of a model based on the Knudsen law, the amount of dissolved salt as a function of time can be calculated. The required time for dissolution or recrystallization can also be estimated for *RHs* corresponding to the storage/transport conditions of industrial powders. Moreover, by coupling the micro-gravimetric measurements with ESEM observations, some light could be shone on the way the recrystallization from aqueous solutions proceeds. Two distinct processes are evidenced: the first one is likely to correspond to the growth of partially dissolved crystals, while the second one should correspond to the formation of crystals in a supersaturated aqueous solution issued from the previous total dissolution of small NaCl crystals. Studies currently underway shall allow a better understanding of the behavior of mixtures of several crystalline powders.

Acknowledgements

Financial support for this project provided by the Department “Solid Products”, Nestle Research Centre, Lausanne, Switzerland, is gratefully acknowledged.

Nomenclature

a_w	Water activity [-]
a_w^*	Critical water activity [-]
DRH	Deliquescence relative humidity [%]
DVS	Dynamic Vapor Sorption
ESEM	Environmental Scanning Electron Microscopy
$K_{Knudsen}$	Knudsen coefficient [kg.Pa^{-1}.s^{-1}]
m	Water mass [g]
P	Imposed vapor pressure [Pa]
P_0	Saturated vapor pressure of pure water [Pa]
p_s	Water vapor pressure of solution at saturation [Pa]
RH	Relative humidity [%]
t	Time [s]
T	Temperature [K]
x_{NaCl}	Mass fraction of NaCl [-]
x_{water}	Mass fraction of water [-]

References

1) Martin, S.T.(2000): Phase Transitions of Aqueous Atmospheric Particles, Chem. Rev., 100, pp.403-3453.
2) Mauer, L.J. and Taylor, L.S. (2010): Water Solid Interactions: Deliquescence, Annu. Rev. Food Sci. Technol., 1, pp.41-63.
3) Tanaka, T. (1978): Evaluating the caking strength of powders, Ind. Eng. Chem. Prod. Res. Dev, 17, n° 3.
4) Peters, S.J. and Ewing, G.E. (1997): Water on salt: An infrared study of adsorbed H_2O on NaCl under ambient conditions, J. Phys. Chem. B, 101, pp.10880-10886.
5) Zasetsky, A.Y. (2008): Dissolution of solid NaCl nanoparticles embedded in supersaturated water vapor probed by molecular dynamic simulations, J. Phys. Chem., 112,pp.3114-3118.
6) Mullin, J.W. (1971): “Crystallisation”, The Butterworth Group, London.
7) Apelbat, A. and Korin, E. (1998): The vapor pressure of saturated aqueous solutions of sodium chloride, sodium bromide, sodium nitrate, sodium nitrite, potassium iodate and rubidium chloride at temperatures from 227K to 323K. J. Chem. Thermodynamics, 30, pp.59-71.
8) Komunjer, L. and Affolter, C. (2005): Absorption/evaporation kinetics of water vapor on highly hygroscopic powder: Case of ammonium nitrate, Powder Technology, 157, pp.67-71.
9) Komunjer, L. and Pezron, I. (2009): A new experimental method for determination of solubility and hypersolubility of hygroscopic solid, Powder Technology, 190, pp.75-78.
10) Tang, I.N. (1986): Water Activity Measurements with Single Suspended Droplets: The NaCl-H_20 and KCI-H20 Systems, Journal of Colloid and Interface Science, 114 (2), pp.409-415.

Author's short biography

Marina Langlet

Born in 1985 in Cambrai (North of France), Marina Langlet studied in the engineering school, Ecole Supérieure de Physique et Chimie Industrielles de Paris (ESPCI), where she specialized in physical chemistry and environment. She graduated in January 2011. After receiving a Master's degree in Environment at Mines of Paristech, she joined the team of the chemical engineering department of the Compiègne University of Technology (UTC) in October 2010 for a PhD thesis, where her current study is focused on powder caking. The objective is to characterize the conditions and the kinetics which lead to damage for product quality under industrial conditions. Her work is focused on hygroscopic substances from the more ordered materials (crystals of NaCl) to mixtures of deliquescent substances and more complex amorphous substances.

Metlas-Komunjer

Lea Metlas-Komunjer studied physical chemistry in former Yugoslavia. After obtaining her degree from the University of Zagreb, she joined the Laboratory for Precipitation Processes of the Rudjer Boskovic Institute in Zagreb to study crystallization phenomena under physiologically relevant conditions. After two years as a visiting fellow at the Laboratoire de Minéralogie et Cristallographie in Paris, she joined the Chemical Engineering Department of the Compiègen Univevsity of Technology (UTC) as a visiting professor. She currently holds a permanent position at the same university and her research interests include the stability of dispersed systems such as emulsions, dispersions and powders.

Mohammed Benali

Dr. Mohammed Benali is a lecturer-researcher at the Ecole Supérieure de Chimie Organique et Minérale (ESCOM). He received his Master's degree in chemical engineering and environment and his PhD in powder agglomeration from the Institut National Polytechnique of *Toulouse* (France) in 2006. After a post-doctoral degree with DSM Nutritional products in Basel (Switzerland), Dr Mohammed Benali spent one year at the Ecole Nationale Supérieure des Ingénieurs en Arts Chimiques Et Technologiques (ENSIACET) as a teacher-researcher in chemical engineering, he joined the ESCOM in 2008. His current research activities concern the size enlargement and treatment of powders, and liquid-solid reactions in a fluid bed reactor.

Khashayar Saleh

Khashayar Saleh received a B.S. degree in chemical engineering from the Sharif (Aryamehr) university of technology (Tehran, Iran) in 1992. He prepared a PhD thesis on the coating of fine powders in the Chemical Engineering Laboratory of Toulouse and obtained his doctor's degree in 1998 from the Institut National Polytechnique de Toulouse (France). Dr Saleh is currently associate professor in the chemical engineering department of the Compiègne University of Technology. His work is focused on powder technology including size enlargement technology and powder characterisation methods.

Author's short biography

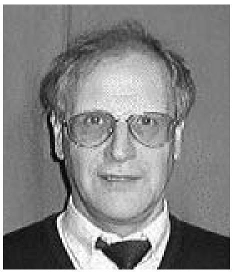

Pierre Guigon

Pierre Guigon is a chemical engineer from ENSIGC Toulouse (France 1971). He is a Master of Engineering Science, UWO London Ontario, (Canada 1974), a Docteur Ingénieur UTC Compiègne (France 1976), a Docteur es Science UTC Compiègne (France 1978), and also a fellow of the Institution of Chemical Engineers. He is head of the chemical engineering department of Compiègne University of Technology. His research is in the field of particle suspensions (fluidization, pneumatic transport) and particle technology (comminution and agglomeration).

Isabelle Pezron

Isabelle Pezron received an engineering degree from the Ecole Supérieure de Physique et Chimie Industrielles (ESPCI, Paris) in 1985 and a PhD in physical chemistry (Université Paris VI) in 1988. After a post-doctoral stay at the Institute of Surface Chemistry in Stockholm (Sweden), she joined the Université de Technologie de Compiègne (UTC) in 1990. She also spent 4 years in the Department of Pharmaceutical Sciences of the University of Missouri (Kansas City, USA) between 1997 and 2001 as a visiting associate professor. She is now professor in the Department of Chemical Engineering of UTC, and her current research activities concern the physical chemistry of interfaces and dispersed systems, and their role in chemical engineering processes.

Frederic Nadaud

Born in 1971, Frederic Nadaud graduated from the University of Créteil (France) in physical measures with specialty in instrumental techniques (IUT de Créteil) in 1992. Since 1994, he has been in charge of ESEM techniques in the Service d' Analyses Physico-Chimiques at the University of Compiègne.

Formulation Design and Experiment Interpretation Through Torque Measurements in High-Shear Wet Granulation [†]

Mauro Cavinato, Paolo Canu, Andrea C. Santomaso*
DIPIC, Department of Chemical Engineering, University of Padova[1]

Abstract

High-shear wet granulation is commonly used in many industries such as in the pharmaceutical industry to convert fine cohesive powders into dense and round granules. The purpose of this work was to determine the effects of some important powder properties (crystalline or amorphous nature, hygroscopicity, solubility and particle size) and process variables (liquid addition rate, impeller speed) on the early stages of the granulation process and on drug distribution in granules obtained by high-shear wet granulation. The glass transition concept coupled with on-line impeller torque monitoring and measurements of the time evolution of the particle size distribution were used to study mixtures of pharmaceutical excipients and some common active ingredients. In particular a formulation map for estimating the minimum amount of liquid binder required to induce appreciable granule growth is presented, thus outlining a new method to considerably increase the predictability of the behaviour of different formulations on the basis of the physical properties of each single component. The description of the effects of the wetting condition on drug uniformity content in some formulations with hydrophobic active ingredients is given as well.

Keywords: wet granulation, high shear mixer, glass transition, hydrophobic active ingredient

Introduction

High-shear wet granulation (HSWG) is often performed in many industries such as the pharmaceutical industry to convert fine cohesive powders into dense and round granules. Granules are produced by mixing and wetting a powdered mixture composed typically of a drug, some excipients and a solid binder1). The overall purpose of HSWG is to obtain a final product with improved characteristics such as better flowability, compressibility and reduced segregation potential of the components and in particular of the drug2). It is a batch operation carried out in a stainless steel bowl equipped with an impeller and a chopper. It is usually performed in three phases2): homogenization of dry powders, liquid binder addition and wet massing without further liquid addition. The correlation between process/formulation variables and granule property evolution is not fully understood, and deeper insight of the granule growth process is required to obtain a consistent product from batch to batch.

Motor power consumption and impeller torque have been used to study the granule growth process since they depend on the cohesive force of the wet mass or the tensile strength of the agglomerates3,4), which in turn are supposed to depend on the saturation degree of the powder mixture5-8). In particular they increase suddenly when the pendular state is reached, and become relatively constant by adding further liquid as soon as an equilibrium between granule growth and breakage is attained7).

Although attention has often been devoted to the end-point determination, much less effort has been put on the understanding of the onset of granulation. Accordingly, the initial granule formation phase and subsequent growth/breakage mechanisms are not completely clear, so that prediction of granule properties remains difficult9,10). In addition, granule growth behaviour in HSWG has often been described considering primary particles as inert materials held

---

[†] Accepted: September 10th, 2011

[1] via Marzolo 9, 35131 Padova, Italy

[*] Corresponding author:
E-mail: andrea.santomaso@unipd.it
TEL: (+39)49 8275491 FAX: (+39)49 8275 461

© 2011 Hosokawa Powder Technology Foundation

together by a simple Newtonian liquid added during the wetting phase. However, powders used in industry may interact differently with the wetting agent, modifying their properties. An amorphous powder within the initial mixture, for example, can have strong effects on the granule nucleation and subsequent growth behaviour[11,12]. Moreover, despite the essential importance of some specific powders in the formulation such as the active substance in pharmaceutical HSWG, relatively few works have presented a detailed analysis of the role of drug characteristics (such as drug type, particle size and shape, hygroscopicity) in granule nucleation and growth kinetics[13,14]. Differences in physical properties between drug and excipients or non-optimal process conditions may lead to selective agglomeration of certain components, causing content uniformity problems.

The role of various components differing in their amorphous or crystalline nature (specifically solid amorphous binders and crystalline drugs) are investigated here during the initial phase of the granulation process, i.e. during wetting. The glass transition concept for amorphous powders, coupled with online impeller torque measurements, has been used to identify the onset of granulation intended as the onset of significant granule growth. The onset of granulation has been identified as an abrupt increase in torque when the amount of added liquid binder exceeds a critical threshold. In particular, a formulation map has been developed which groups the elements of the formulation in three classes, namely diluent, dry binder and liquid binder. The critical amount of liquid can be correctly predicted by this map as a function of the formulation composition under some limitations. The effects of the active crystalline ingredients on the granulation process are also analysed by torque measurements. Particularly, the influence of some important particle characteristics such as size and hygroscopicity on the granule growth behaviour has been analysed. The effects of changes in process variables such as impeller speed or liquid flow rate have been considered as well.

2. Materials and methods

All the experiments were performed in a small scale, top-driven granulator (MiPro 1900 ml, ProCepT, Zelzate, Belgium) with a stainless steel vessel, a chopper and a three-bladed impeller. The granulator was able to measure and record impeller torque during granulation. Formulations were mixtures of both amorphous and crystalline pharmaceutical powders, and were granulated using deionized water at 20° C.

Two experimental sets without pharmaceutical active ingredients and one set with active ingredients are presented here. Firstly, granulation experiments were carried out to determine the influence of the impeller speed on impeller torque profiles and on the particle size distribution of the final granules. At this stage, the powder mixture composition was held constant and was (on a weight basis): lactose monohydrate 150M (73.5%), microcrystalline cellulose (20%), HPMC (5%) and croscarmellose sodium (1.5%). Variable conditions were: the impeller speed at 500, 850 and 1200 rpm, whereas the total amount of liquid and liquid addition flow rate were always fixed at 100 ml and 10 ml/min, respectively.

The second set of granulation experiments was performed with different formulation compositions under the same process conditions (i.e. impeller speed 850 rpm, chopper speed 3000 rpm, total amount of water added 100 ml and water addition rate 10 ml/min).

This experimentation was designed to determine the role of two different dry amorphous binders in the granule growth phase. The changes in the formulation composition involved the binder type (HPMC and PVP) and amount (in the range 2.5-10% w/w).

The third set of granulation experiments was carried out comparing the effect of three different crystalline active ingredients. The active ingredient was either acetylsalicylic acid, paracetamol or caffeine. The formulation was composed of: active ingredient (50%), lactose monohydrate 150M (23.5%), microcrystalline cellulose (20%), PVP (5%) and croscarmellose sodium (1.5%). Impeller speed during wetting was set at 500 or 1200 rpm, liquid flow rate at 8 or 12 ml/min according to the experiment. In order to emphasize the critical role of water addition (amount and distribution) in the early phases of the process and its implication on drug uniformity content, the three drugs all presented low hygroscopicity and solubility, but different average particle sizes (62, 113, 328 μm for paracetamol, caffeine and acetylsalicylic acid, respectively).

In order to investigate only the initial phases of granule formation and growth, all three sets of experiments were stopped at the end of the liquid addition phase, so wet massing was not performed. The volumetric fill level of the vessel was 40% for a weight of powder of about 400 g.

3. Results and discussion

3.1 On the onset of granule growth

Typical impeller torque profiles obtained from experiments are shown in the inset of **Fig. 1** as a function of the added liquid at three different impeller speeds (500, 850 and 1200 rpm). It can be observed that torque increases almost proportionally with increasing the stirring speed and that the profiles show a similar shape. Initially, torque values increase slightly with the amount of liquid, indicating a progressive densification of the mixture due to the action of capillary forces. The subsequent decrease of the slope is interpreted as lubrication of the mass, which reduces the stress on the impeller. When the added volume of water is larger than a certain value, an abrupt increase in torque is observed. The changes of slope can be studied by the first derivative of the torque profiles after numerical filtering in order to eliminate noise. A minimum in the curves can be visibly located just before the steep torque increase (marked by the circles in **Fig. 1**.)

To monitor the PSD evolution during agglomeration, digital images of the powders were taken to obtain a more accurate description of the nucleation phase. The operative conditions of the 850 rpm experiments were chosen as a reference and samples were progressively collected during granulation at different moisture contents (20, 40, 60, 80% of water addition). Some binary images of the samples are compared in **Fig. 2** with torque and torque first derivative profiles. Visual inspection of the images shows that a substantial increase in the size of the granules occurs after the addition of 40% out of 100ml of water (or 10% on batch weight), which corresponds roughly to the minimum in the derivative profile.

The corresponding liquid volume has therefore been identified as the critical liquid amount (or minimum liquid volume) required to yield substantial agglomeration of the mass for a given operating condition. This critical value will be used in the subsequent analyses as a distinctive, clearly identifiable and reproducible feature of the granulation process.

3.2 On the role of amorphous components

Having identified a critical amount of liquid as the marker of the onset of granulation, an explanation of what happens at the inflection point of the torque profile (or the minimum in the derivative profile) is required. Such an explanation can be found when considering the granulation process in the light of the glass transition theory.

When water is added to the dry powder mixture, the nuclei formation phase can start as described by the nucleation regime map proposed by Litster et al.[15]. Absorbed water is then split up among the formulation components on the basis of their hygroscopicity, and in particular the water absorbed by the dry amorphous binder acts as a strong plasticizer decreasing the amorphous binder glass transition temperature T_g. Decreasing the binder T_g down to the powder temperature (equal to ambient temperature) increases the molecular mobility of the binder and leads to migration of the amorphous material into the

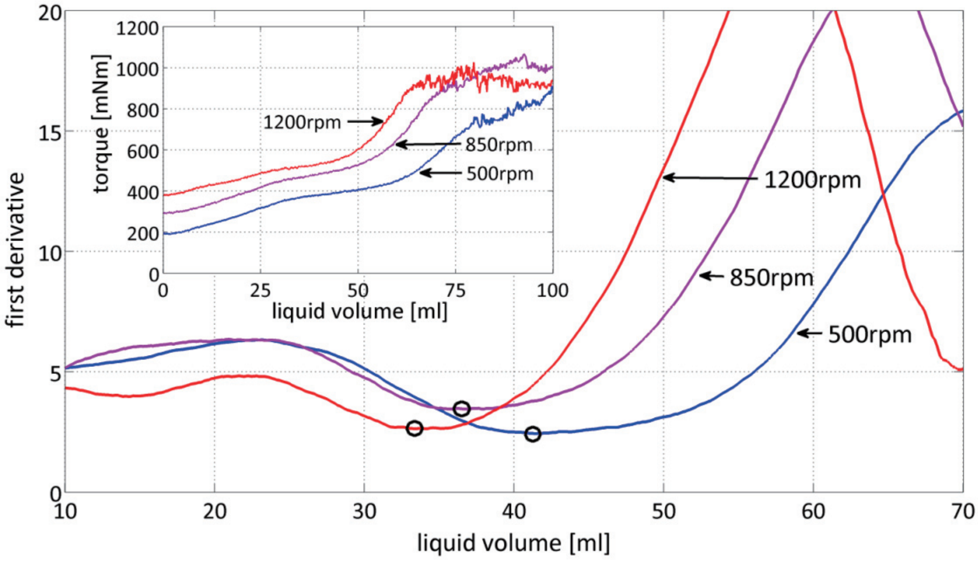

Fig. 1 Effect of impeller speed on impeller torque profiles (inset) and torque derivative profiles as a function of added liquid binder (water). The minimum on the derivative profile is marked with circles.

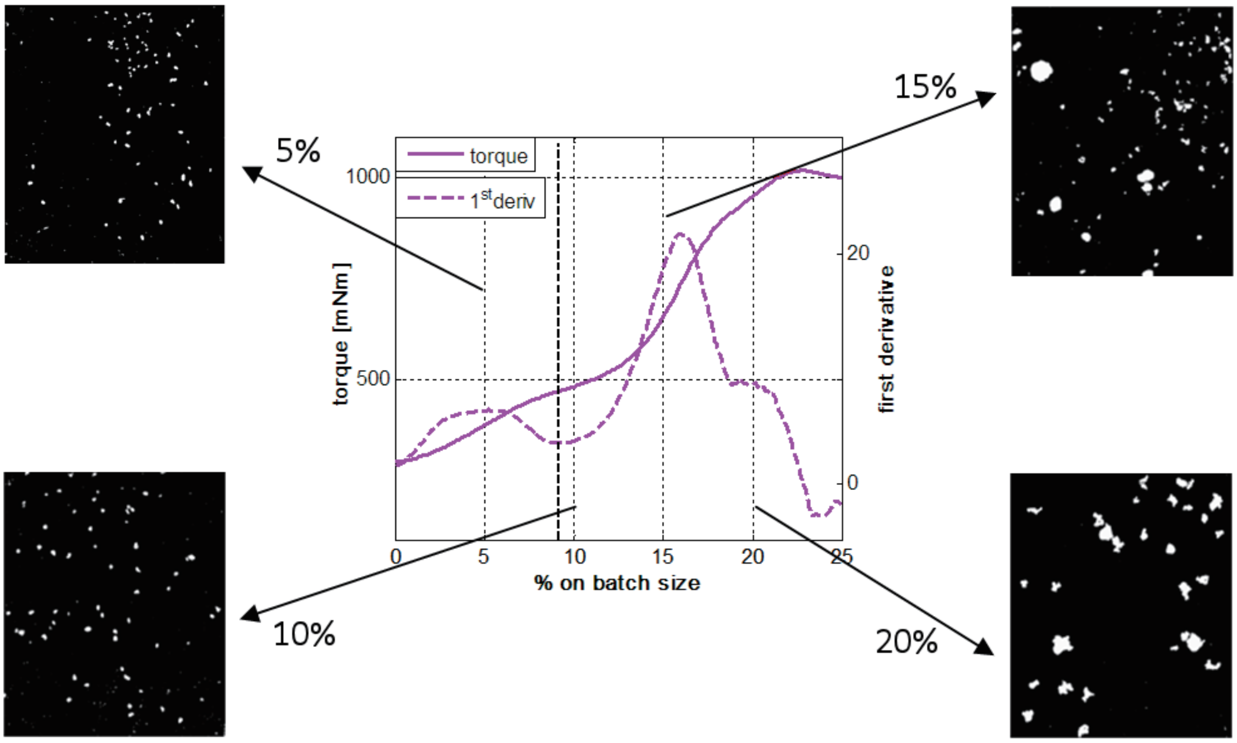

Fig. 2 Effect of the moisture content on the granule size evolution during the granulation process: pictures of the granules show a negligible growth until about 10% (40ml), whereas larger agglomerates can be counted after this point.

water on the particle surface. This creates a highly viscous layer on the binder particle surface, causing a significant increase in stickiness and promoting the agglomeration process[16,17]. As a consequence, the impeller torque value rapidly increases at the inflection point and the granule growth accelerates as qualitatively shown in **Fig. 2**. A formulation map is furthermore proposed in order to isolate the contribution of the amorphous binder to the water uptake. Each of the vertexes in the ternary diagram represents a main component (diluents, dry binder or liquid binder), whereas each edge represents a binary component combination.

The measured critical water amounts are represented in the ternary diagram by several markers where the dry binder (HPMC = circles; PVP = squares) ranges from 1 to 10%. As can be observed in **Fig. 3**, the markers are arranged in two straight lines which represent a specific diluent-dry binder-liquid system and which intersect the diluent-liquid and the binder-liquid axes. HPMC and PVP lines intersect the diluent-liquid axis very close to each other, outlining point (1). This point represents the water amount absorbed by the diluents and that is therefore not available for the dry binder. On the other hand, the intersection between the straight line and the binder-liquid axis appears to be strongly binder-specific. This difference clearly denotes a different dry binder-water interaction.

A dry formulation composition (0% liquid) can be identified as a point on the binder-diluent axis. With the addition of water, the point representing the actual composition of the granulating mixture moves from the binder-diluent axis along the dashed lines towards the 100% liquid vertex. Once the HPMC or PVP lines and the dashed line (corresponding to a given dry formulation composition) are defined, it is possible to use the diagram in a predictive way by determining the critical amount of liquid from their intersection.

In order to define the HPMC or the PVP lines, however, points (1), (2) and (3) are required. Points (2) and (3) can be estimated by a glass transition temperature measurement using the Gordon-Taylor equation[18]. The curves representing the glass transition temperature as a function of the equilibrium water content for HPMC and PVP are shown in **Fig. 4**.

The glass transition temperature of a wet binder sample has been estimated using the modified Gordon-Taylor[19] equation in order to best fit the experimental data:

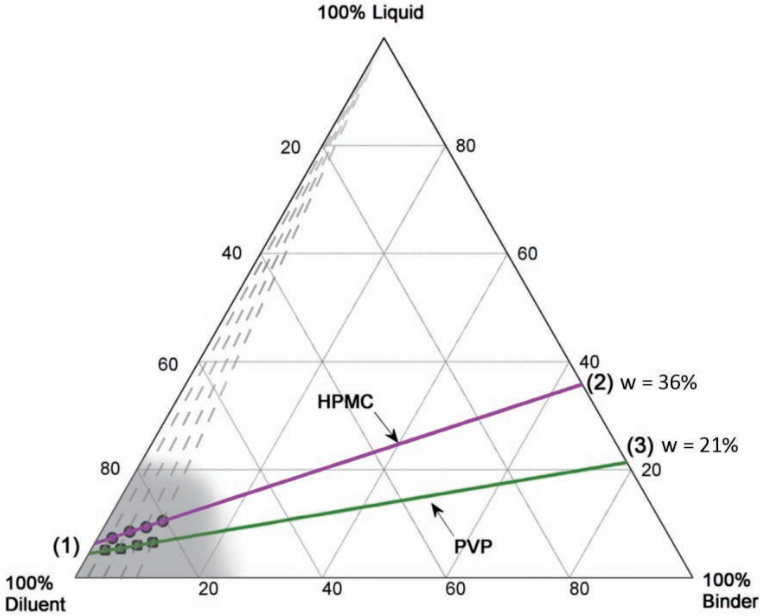

Fig. 3 Representation of the effect of the main formulation components on the critical water amount through a ternary diagram. Vertexes represent the key component: diluent (lactose monohydrate and microcrystalline cellulose), dry binder (HPMC or PVP) and liquid (water). The shaded zone corresponds to the granulation area which is of practical interest.

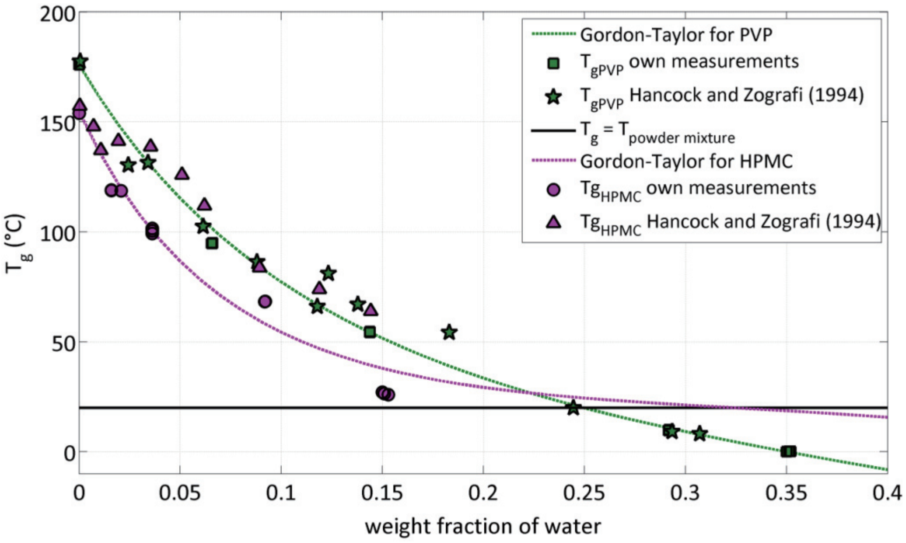

Fig. 4 Glass transition temperature as a function of water content in samples of (a) PVP and (b) HPMC: comparison between the experimental data, literature[19] and the dotted line representing experimental data and literature fitted to the modified Gordon-Taylor model[19].

$$T_g = \frac{w_1 T_{g1} + k w_2 T_{g2}}{w_1 + k w_2} + q w_1 w_2 \tag{1}$$

where k is an empirical constant, T_{g1} is the dry binder glass transition temperature, T_{g2} is the water glass transition temperature (-138℃), w_1 and w_2 are the binder and water weight fractions (with w_1 = 1-w_2), respectively, and q is an empirical constant reflecting the specific binder-water interaction.

Assuming the reference condition:

$$T_g = T_a \approx T_{powder}\,, \tag{2}$$

where T_a is the ambient temperature expected to be equal to the powder temperature T_{powder}, the corresponding water content w_2^* can be expressed as follows:

$$w_2^* = w_2(T_g \approx T_{powder}). \tag{3}$$

The experimental and literature data[19] in **Fig. 4** were fitted to the Equation (1). The intersection between the glass transition curves and the ambient temperature gives the water amount required to obtain the dry binder glass transition and the formation of a highly viscous mixture.

It can be noted in **Fig. 4** that the literature and the experimental data for PVP are in close agreement and are accurately fitted by the modified Gordon-Taylor model. The estimated moisture content required for the glass transition is 0.24. Agreement between experimental and literature data for HPMC is less satisfactory. Moreover, the maximum attainable moisture content for an HPMC sample in static conditions at 90% is about 0.20. As a consequence, not only the fitting of data is less accurate but also an extrapolation is required to estimate the moisture content for the HPMC glass transition. The value derived from extrapolation is 0.33 and should be treated with great caution. Nonetheless, the estimated values of moisture content for glass transition (0.24 and 0.33) and points (2) and (3) in **Fig. 3** (0.21 and 0.36 for PVP and HPMC, respectively) are in satisfactory agreement, suggesting that points (2) and (3) can be determined by static T_g measurements.

The water amount absorbed by the hygroscopic diluent components in point (1) can be roughly estimated by the water sorption isotherms in **Fig. 5**. The RH% at which the PVP glass transition occurs (corresponding to the water content w_2^*) can be considered as a reference condition for identification of the contribution of each hygroscopic diluent. Note that the dry binder (amorphous and water-soluble) has a higher hygroscopicity when compared to the diluents. For this reason, HPMC or PVP can be considered as the most important binding agent, while the other fillers (MCC and lactose, both crystalline) can be considered as sole diluents, which absorb water but have a weak binding strength.

The presence of a further component in the mixture, such as an active ingredient, can be taken into account by the map whenever its behaviour with respect to the liquid binder is known. This simply means to classify the drug as a diluent or as a binder according to its nature (amorphous or crystalline) and its hygroscopicity.

3.3 On the role of crystalline components

The water amount in crystalline powders generally increases slightly with the relative humidity and their mechanical properties do not change (below the solubilisation conditions). Moreover, the dissolution process of crystalline structures is much slower than that of amorphous ones due to the lower permeability of the crystalline matrix and the endothermic dissolution process[12]. These considerations further justify the choice of considering crystalline MCC and lactose as sole diluents in the previous analysis. Let's now consider in more detail the interaction of different crystalline powders with the liquid binder, in particular when they are the active ingredient. This

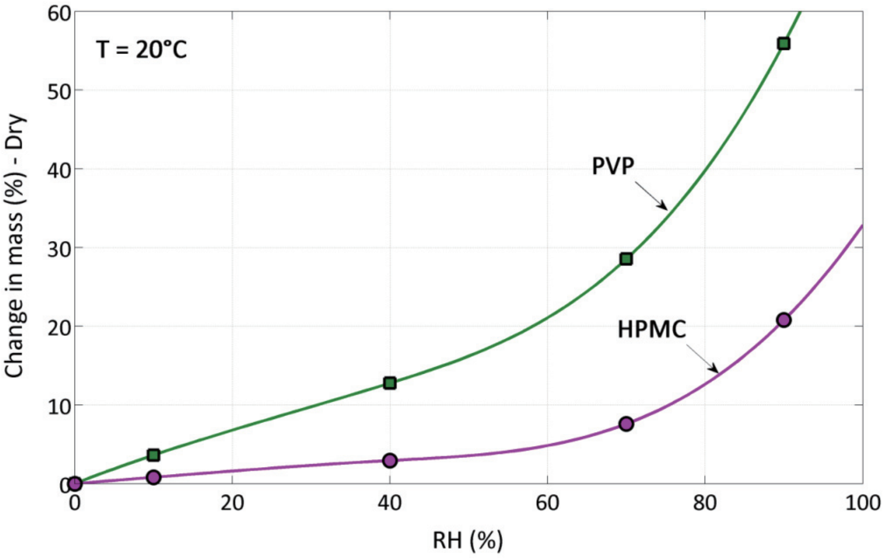

Fig. 5 Sorption isotherms (25℃) of the formulation components: PVP (squares), HPMC (circles), MCC (diamonds) and lactose monohydrate (circles).

is of major interest since liquid-active interaction can influence the final drug content uniformity.

Following again the approach based on the use of torque curves and their derivatives, we found that the powder mixture with the three different drugs considered for this study presented different liquid requirements in order to yield the sudden increase in torque profiles. Liquid amounts (%w/w on the initial batch size) corresponding to the inflection point in torque profiles (i.e. minimum in first derivative profiles) can be compared in **Fig. 6** at different operating conditions. As can be seen, the critical liquid amount clearly discriminates between the three different active ingredients. In particular it is possible to find a correlation with the drug particle size. In particular, the larger the particle size, the lower is the liquid amount corresponding to the inflection point in torque profiles and required to start most of the granule growth. For example, inflection points for paracetamol occurred on average after 10% water was added, whereas for acetylsalicylic acid about 5% water was required. Also, process conditions made a difference on the critical liquid amounts required to achieve torque profile inflection.

The finer the drug particle size, the larger the differences between the critical liquid amounts at low and high rotational speed (LS and HS, respectively, in **Fig. 6**). Especially for paracetamol, it can be noted that higher liquid amounts are necessary when the impeller speed is lower. Moreover, the highest liquid flow rate (HF) gives higher liquid amount percentages.

Summarizing, a finer particle size, lower impeller speed and higher liquid flow rate seem to cause a higher demand of liquid for the torque inflection point. According to the theory proposed by Leuenberger and co-workers[5-8], a higher liquid amount required for the torque inflection point also means that a higher liquid content is required to reach the pendular state and start the liquid bridge formation. So if the torque inflection point can be associated to the bridge formation, and a higher water amount is required for torque inflection when operating in poor wetting conditions (low impeller speed and high liquid flow rate), it can be argued that it is not the volume of the bridges but their number that is important. Poor wetting tends to give few large bridges (in contrast to optimal wetting which gives several small and homogeneously distributed bridges), and in order to increase their number, a higher liquid amount is required. This speculation is not in conflict with the glass transition theory since in the presence of amorphous particles, a larger concentrated volume of liquid would probably give a lower viscosity increase than small distributed bridges, since the resulting solution would be more diluted.

Wetting conditions are also of major importance for obtaining an optimal drug distribution, especially when the drug has a poor affinity with water. To investigate this problem, size fractions corresponding

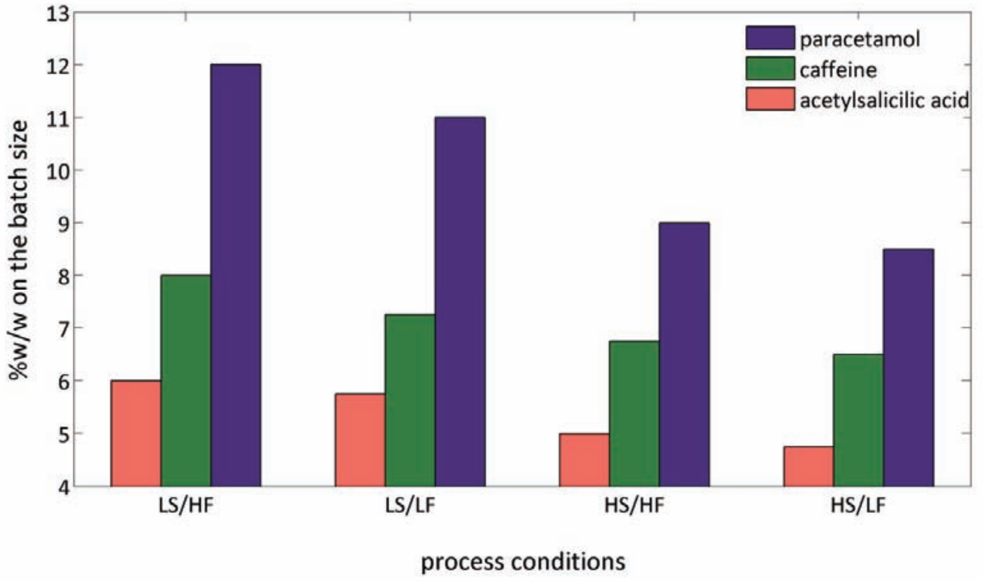

Fig. 6 Liquid amount (%w/w on the batch size) required to determine a sudden increase in the torque profiles during granulation experiments with different active ingredients and different process conditions: LS – lower impeller speed (500 rpm), HS – higher impeller speed (1200 rpm), LF – lower liquid flow rate (8 ml/min) and HF – higher liquid flow rate (12 ml/min).

to a 10th, 50th and 90th percentile for each granulation experiment were analysed. Results of content uniformity measurements and corresponding error bars are shown in **Fig. 7**.

The dashed line indicates the ideal condition of 50% w/w drug content in the final granule, according to the initial active ingredient load. Discrepancies between actual and ideal drug content might be due to selective agglomeration of certain components during the process. For example, in the presence of hydrophobic and hydrophilic primary particles, granule growth of hydrophilic materials tends to take place selectively, as described by Belohlav et al.[14]. As a matter of fact, each active ingredient used in the present research showed poor hygroscopicity and poor solubility compared to the two main excipients. These differences can therefore be considered as a potential cause of selective agglomeration. It can be noted in **Fig. 7** that most of content uniformity problems occurred with paracetamol, especially at lower impeller speed. Paracetamol-based granules obtained using the lowest impeller speed and highest liquid flow rate showed the highest discrepancies: a higher drug content in the larger granules and a very low drug content in the x_{50} size fraction. Caffeine-based granules obtained with the lowest impeller speed also showed content uniformity problems and a lower drug concentration in the x_{90} size fraction. On the other hand, granules with acetylsalicylic acid showed the highest gap at high impeller speed and liquid flow rate. In this case, the drug content was the highest in the fines and non-granulated product. The approach developed by Litster, Hapgood and co-workers[15,20] can be considered in order to explain the discrepancies between actual and ideal drug content. According to this approach, a finer particle size determines a higher liquid penetration time, thus worsening the liquid distribution within the wet mass.

Moreover, a lower impeller speed and higher liquid flow rate determine a higher dimensionless spray flux number and consequently a worse liquid distribution and poor wetting (see **Fig. 8**). It is therefore suggested that a poorer liquid distribution might lead to the presence of lumps and less wet areas, thus worsening drug distribution as well.

Whereas the cause of content uniformity issues for paracetamol and caffeine might be due to unsatisfactory liquid distribution conditions, the high concentration of acetylsalicylic acid in the fines can be explained by considering breakage phenomena that occur when the impeller speed is higher.

These phenomena might be the cause of the layering mechanism detected with SEM image analysis (**Fig. 9**). The use of a higher liquid flow rate probably led to less homogeneous wetting conditions, thus promoting the formation of less lubricated areas and more intensive breakage phenomena.

Conclusions

This work was aimed at developing more systematic and quantitative criteria for high-shear wet granulation design on the basis of the physical properties of the individual components. A formulation map has been presented which describes the onset of granulation as a function of three formulation variables: diluent, dry and liquid binder. Component classification in these three groups was performed according to their nature (amorphous or crystalline) and hygroscopicity. Results show that it is possible to carry out an early assessment of the critical liquid volume required to start most of the granule growth through an application of a Gordon-Taylor model and by performing some independent measurements of the initial formulation properties. The critical liquid amount was also unambiguously determined by online torque measurements in order to verify map predictions. Torque measurements were also used to study the effect of crystalline components in the formulation. In particular three hydrophobic drugs were considered since their uniform distribution into granulated products is of major interest. Results show the critical role of the wetting conditions. It was observed that the critical liquid amount increases with decreasing drug particle size. Different growth mechanisms were proposed in order to explain content uniformity discrepancies. For smaller particle sizes (paracetamol and caffeine), a selective agglomeration of the hydrophobic drug was observed because of poor wetting (high liquid flow rate and low mixing speed), while for larger particles (acetylsalicylic acid), problems of content uniformity were observed with ideally good wetting conditions (high mixing rate and low liquid flow rate) - probably because of the poor lubrication of the powder and the consequent particle breakage in the presence of intensive mixing.

References

1) Litster, J.D. and Ennis, B. (2004): "The science and engineering of granulation processes", Kluwer Academic Publisher.
2) Gokhale, R., Sun, Y., and Shukla, A.J. (2006): High-shear granulation. In: Parikh, D.M. (Ed.), "Handbook

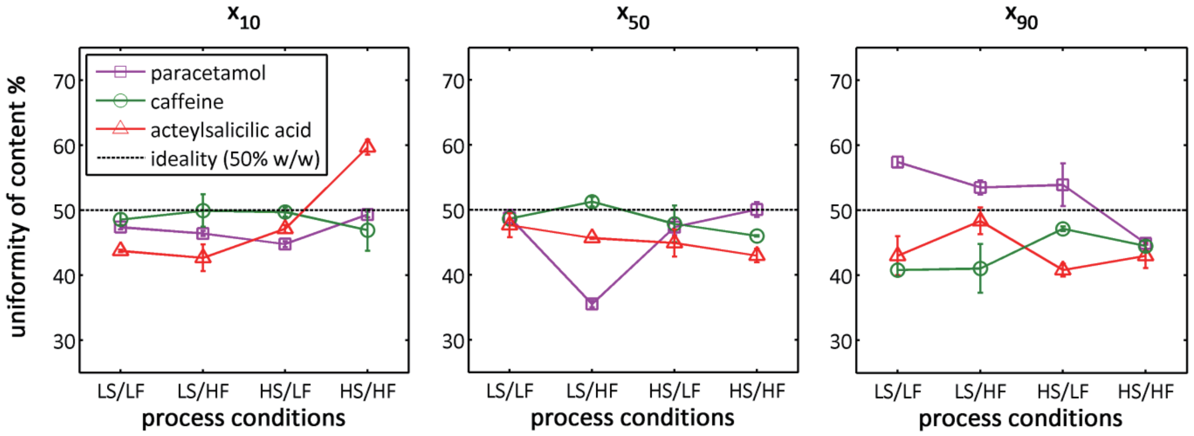

(a) (b) (c)

Fig. 7 Content uniformity analysis results: distribution of paracetamol, caffeine and acetylsalicylic acid in x_{10} (a), x_{50} (b) and x_{90} (c) size fraction. Process conditions: LS – lower impeller speed (500 rpm), HS – higher impeller speed (1200 rpm), LF – lower liquid flow rate (8 ml/min) and HF – higher liquid flow rate (12 ml/min).

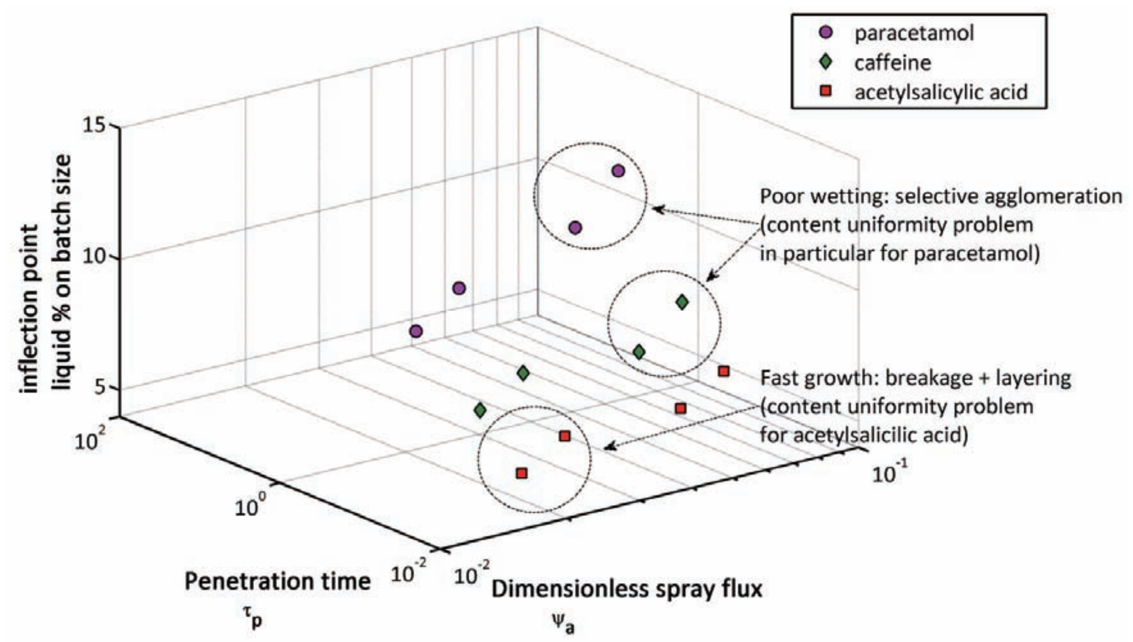

Poor wetting: selective agglomeration (content uniformity problem in particular for paracetamol)

Fast growth: breakage + layering (content uniformity problem for acetylsalicilic acid)

Fig. 8 Critical liquid amount and content uniformity problems as a function of penetration time and dimensionless spray flux number[15,20].

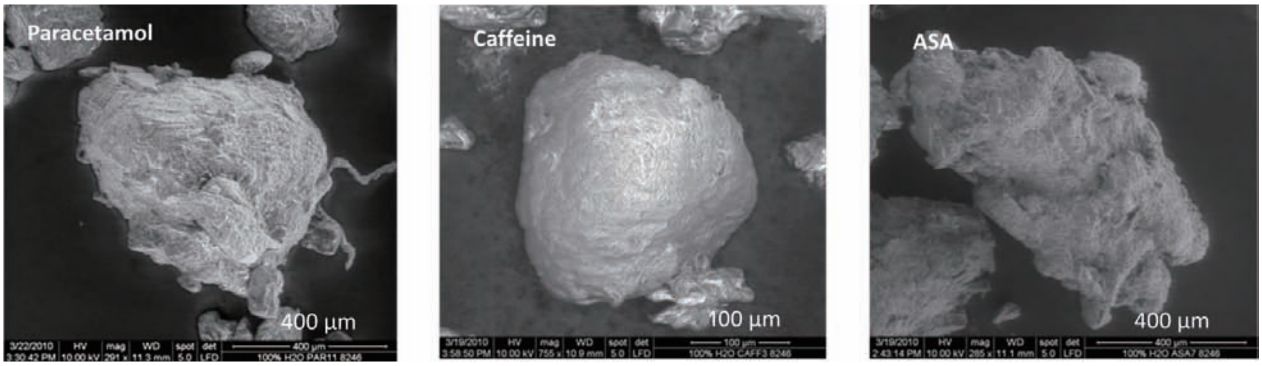

Fig. 9 SEM images of granules with different drugs. The layering mechanism is particular evident for acetylsalicylic acid-based granules, where large crystals are covered by fragments.

of Pharmaceutical Granulation Technology (2^{nd} ed.)", Taylor and Francis Group, New York.
3) Leuenberger, H. and Bier H.P. (1979): Bestimmung der optimalen Menge Granulierflüssigkeit durch Messung der elektrischen Leistungsaufnahme eines Planetenmischers, Acta Pharmaceutical Technology, Vol. ???, 1979, pp.41-44.
4) Bier, H.P., Leuenberger, H. and Sucker, H. (1979): Determination of the uncritical quantity of granulating liquid by power measurements on planetary mixers, Pharmaceutical Industry, 41, pp.375-380.
5) Imanidis, G. (1986): "Untersuchungen über die Agglomerierkinetik und die elektrische Leistungsaufnahme beim Granulierprozess im Schnellmischer", Doctoral thesis, University of Basel, Switzerland,.
6) Leuenberger, H., Bier, H.P. and Sucker, H. (1981): Determination of the liquid requirement for a conventional granulation process, German Chemical Engineering, 4, pp.13-18.
7) Leuenberger, H. (1982); Granulation, new techniques, Pharm. Acta Helvetica, 57 (3), pp. 72-82.
8) Leuenberger, H. and Imanidis, G. (1984): Steuerung der Granulatherstellung im Mischer durch Leistungsmessung, Chemical Industry, XXXVI, pp.281-284.
9) Faure, A., York, P. and Rowe, R.C. (2001): Process control and scale-up of pharmaceutical wet granulation processes: a review. Eur. J. Pharm. Biopharm., 52, pp.269-277.
10) Mort, P.R. (2005): Scale-up of binder agglomeration processes, Powder Technol., 150, pp. 86-103.
11) Cavinato, M., Bresciani, M., Machin, M., Bellazzi, G., Canu, P. and Santomaso, A.C. (2010): Formulation design for optimal high-shear wet granulation using on-line torque measurements, International Journal of Pharmaceutics, 387, pp.48-55.
12) Palzer, S. (2010): The relation between material properties and supra-molecular structure of water-soluble food solids, Trends in Food Science & Technology, 21, pp.12-25.
13) Nguyen, T.H., Shen, W. and Hapgood, K. (2010): Effect of formulation hydrophobicity on drug distribution in wet granulation, Chemical Engineering Journal, (in press).
14) Belohlav, Z., Brenkova, L., Hanika, J., Durdil, P., Rapek, P. and Tomasek, V. (2007): Effect of Drug Active Substance Particles on Wet Granulation Process, Chemical Engineering Research and Design 85, pp.974-980.
15) Litster, J.D., Hapgood, K.P., Michaels, J.N., Sims, A., Roberts, M., Kameneni, S.K. and Hsu, T. (2001): Liquid distribution in wet granulation: dimensionless spray flux, Powder Technology 114, pp.29-32.
16) Fitzpatrick, J.J. (2007): Particle properties and the design of solid food particle processing operations, Food and Bioproducts Processing, 85, pp.308-314.
17) Palzer, S. (2005): The effect of glass transition on the desired and undesired agglomeration of amorphous food powders, Chemical Engineering Science, 60, pp.3959-3968.
18) Gordon M. and Taylor, J.S. (1952): Ideal co-polymers and the second order transitions of synthetic rubbers. 1. Non-crystalline co-polymers, Journal of Applied Chemistry, 2, pp.493-500.
19) Hancock B.C. and Zografi G. (1994): The relationship between the glass transition temperature and the water content of amorphous pharmaceutical solids, Pharmaceutical Research, 11, pp.471-477.
20) Hapgood, K.P., Litster, J.D. and Smith R. (2003): Nucleation regime map for liquid bound granules, A.I.Ch.E. Journal 49, pp.350-361.

Author's short biography

Mauro Cavinato

Dr. Cavinato is a chemical engineer with a bachelor's degree, a master's degree and a PhD from the University of Padova, Italy. He recently joined Nestle, working in the Product Technology Centre in York, United Kingdom (main Nestle R&D centre for confectionery products). His research interests are in the area of food and pharmaceuticals processing: 1) design of new technologies and formulation for powder processing (mainly agglomeration and comminution), solid-liquid pastes and doughs, 2) aroma development and modification.

Paolo Canu

Professor Canu is a professor of applied physical-chemistry at the University of Padova, Italy. He graduated in chemical engineering from Politecnico di Milano and received his PhD in chemistry at the Scuola Normale Superiore di Pisa, working in Pisa, Milan, and the United States (UW-Madison). His research activity is focused on chemical reaction engineering and fluid mechanics, with special interest in the area of multiphase reactors (mostly fluid-solids), where the solid phase is relevant, both in dense or dispersed phases. To date, Professor Canu has published more than 100 papers, mostly abroad, including contributions to published books as well as two textbooks in his teaching field.

Santomaso Andrea Claudio

Dr. Santomaso is a researcher assistant of chemical engineering at the University of Padova, Italy. He received his PhD in chemical engineering from the University of Padova, discussing a thesis on the mixing of powders in rotating blenders. His main fields of interest are related to the understanding of mixing mechanisms and kinetics, to the agglomeration processes in agitated vessels (high and low shear), to powder mechanics and rheology (silo discharge), to the development of alternative sampling techniques and to powder flowability assessment with both empirical and modelistic approaches. His international publications and presentations in the above fields exceed 50 articles.

Gas-Phase Synthesis of Nanoscale Silicon as an Economical Route Towards Sustainable Energy Technology[†]

Tim Hülser[1*], Sophie Marie Schnurre[1], Hartmut Wiggers[2] and Christof Schulz[2]
Institut für Energie- und Umwelttechnik e.V. (IUTA)[1]
Institut für Verbrennung und Gasdynamik, Universität Duisburg–Essen and CeNIDE, Center for Nanointegration Duisburg-Essen[2]

Abstract

The silicon age that started in the 60s of the last century has changed the world profoundly, mainly related to the invention and development of microprocessor technology. Meanwhile, the demand for silicon is driven by the photovoltaics industry that consumes about 80% of the high-purity silicon produced worldwide. Independent of the final product, all high-purity silicon has passed through a couple of gas-phase reactions for purification. The most important gaseous species within this production chain are chlorosilanes and monosilane. We will discuss the direct formation of crystalline silicon by homogeneous gas-phase reactions as a direct and highly economical way to produce the required high-purity raw material for silicon solar cells. The direct formation of solid silicon particles from monosilane requires only a fraction of the energy compared to the established Siemens process based on the chemical vapor deposition of silanes. We have developed a method to synthesize nanocrystalline silicon powder using a hot-wall reactor, and the technology was scaled up to the pilot-plant scale. While an economical production strategy is decisive for solar cell production, the structure of the gas-phase product allows for additional, highly promising applications benefiting from the specific properties of the nanoscale particulate material. Both, thermoelectric generators as well as lithium-ion batteries benefit from the nanocrystalline structure of the gas-phase product due to high phonon scattering and short diffusion lengths, respectively. First successful examples with regard to these two topics will be discussed. In these fields, silicon finds potential new markets for sustainable energy technology because of its abundant availability and low-cost production.

Keywords: gas phase synthesis, silicon nanoparticles, pilot plant scale

Introduction

The demand for silicon for solar cell applications has increased by about 350% from 2003 to 2010[1] and has driven a couple of technologies to provide a sufficient amount of high-purity solar-grade silicon. Besides a couple of solid-state-based technologies such as the purification of metallurgical-grade silicon and the reaction of high-purity SiO_2 with high-purity carbon, the thermal decomposition of silicon-containing gaseous species is the established way to synthesize high-purity silicon from the gas phase[2]. Common methods used in industry are based on the Wacker process, the ASiMi process, the MEMC process or the Hemlock HSC process. Multiple reports can be found dealing with the pyrolysis of monosilane (SiH_4) as a precursor material[3-6]. The homogeneous as well as heterogeneous decomposition of silane in free space and fluidized bed reactors was investigated intensely by Flagan et al. in the 1980s[7, 8] and several groups continued investigating silicon nanoparticle synthesis in free space reactors[6, 9, 10]. One of these technologies was developed at the University of Duisburg-Essen[10] and was scaled up to production scale[11]. The description of silicon nanoparticle synthesis from monosilane in laboratory-sized reactors combined with the modeling of the process, i.e. reaction kinetics, nucleation and growth rates, thermodynamic driving force, particle size distributions and a comparison between experimentally obtained and

---

[†] Accepted: September 10th, 2011

[1] 47229 Duisburg, Germany
[2] 47057 Duisburg,
[*] Corresponding author:
E-mail: huelser@iuta.de
TEL: (+49)2065 418 302 FAX: (+49)2065 418 211

ⓒ 2011 Hosokawa Powder Technology Foundation

calculated particle size distributions was also investigated by several authors[9, 12-14]. The modeling of nucleation, particle growth and particle size distribution in different synthesis processes gained more and more attention in order to predict or verify experimental results[12, 15]. Furthermore, several reviews give an account about the synthesis of silicon nanoparticles (SiNPs) from the vapor phase via non-thermal synthesis routes, as well as from the thermal decomposition of silanes[16-19].

The finding of Canham et al. that silicon nanocrystals in the sub-10 nm regime exhibit visible luminescence[20] stimulated the development of new synthesis strategies to produce free-standing, luminescing silicon nanoparticles from the gas phase with tunable size and small particle size distribution utilizing laser or plasma pyrolysis of silane[17, 21, 22]. The luminescing properties of these materials are discussed with respect to labeling or photosensitizer applications in biological systems[23-25], and some investigations deal with electronic applications based on silicon nanoparticles such as memory devices, light emitters and transistors[26-30]. However, the production of narrow-sized SiNPs in the sub-10 nm regime requires highly diluted conditions of the silicon precursor leading to poor production rates. In the context of this article, we will focus on the economical formation of nanocrystalline silicon and promising applications utilizing its nanocrystalline properties. Since the economical and energy-efficient formation of silicon involves high precursor concentrations, applications requiring small and luminescing SiNPs will not be covered.

One of the main driving forces for the industrial utilization of silicon nanoparticle gas-phase synthesis[11] was the impressive energy balance with respect to alternative methods. The JSSI Company claims that the demand for electrical energy via this route can be reduced by about 90% compared to the conventional Siemens process based on chlorosilanes requiring more than 200 kWh/kg of silicon. The as-prepared silicon powder from silane pyrolysis is used to manufacture polycrystalline silicon solar cells by re-melting and directional solidification.

As shown by several groups, silicon powder synthesized by pyrolysis from monosilane exhibits a nanostructured crystallinity as a result of its formation process in the gas phase[6, 9, 10, 17], but the specific properties of the nanostructure are lost when the material is used for the production of polycrystalline solar cells. As a result, highly promising additional properties of the nanostructured silicon generated in this process are not yet being used in industrial applications despite the fact that a technology for the formation of such nanostructured materials is, in principle, available. Nanostructured silicon has been identified as an attractive material for a wide variety of energy-related applications such as photovoltaics[31], battery technology[32] or thermoelectrics[33, 34]. This opens highly rewarding application fields in a rapidly growing market.

In Li-ion batteries, the high storage capacity of nanostructured silicon for lithium (10-fold increase by weight compared to the state-of-the-art material graphite) enables the development of high-capacity anodes. However, a dramatic volume expansion and contraction during lithium storage and release causes bulk silicon to rapidly degrade. Nanosized silicon is believed to enable a sufficient long-time stability[32, 35].

Nanostructuring is also known to be one of the key technologies for a profound improvement of the figure of merit of thermoelectrics. The nanostructure promotes phonon scattering, leading to materials with highly reduced thermal conductivity while keeping the electric conductivity high. Nanostructured, silicon-based thermoelectrics are highly promising with respect to sustainability and price. Silicon-based materials can thus overcome one of the main hurdles of the widespread application of thermoelectric devices which is the limited availability of conventional raw materials such as tellurium.

The challenge concerning the utilization of nanosized silicon is an economical and reproducible approach toward tailor-made materials for specific applications. While wet-chemical synthesis usually yields surface-stabilized materials grown by thermodynamic control, gas-phase processes allow for kinetic control of the synthesis of high-purity nanoparticles. Therefore, this method is especially favorable for the formation of metastable materials such as highly-doped nanoparticles and nanocomposites. Continuous gas-phase processes have the additional advantage of scalability to industrial production scale. In this paper we discuss the path toward reasonable amounts of highly specific silicon nanopowders that can be utilized in thermoelectrics and lithium-ion batteries.

Pilot-plant facility

A multitude of highly specific nanomaterials have been synthesized in specific lab-scale reactors in the past. Typically, they are available in minute quantities only. Therefore, subsequent processing steps cannot be studied and many nanomaterials have not yet found their way into practical applications. To

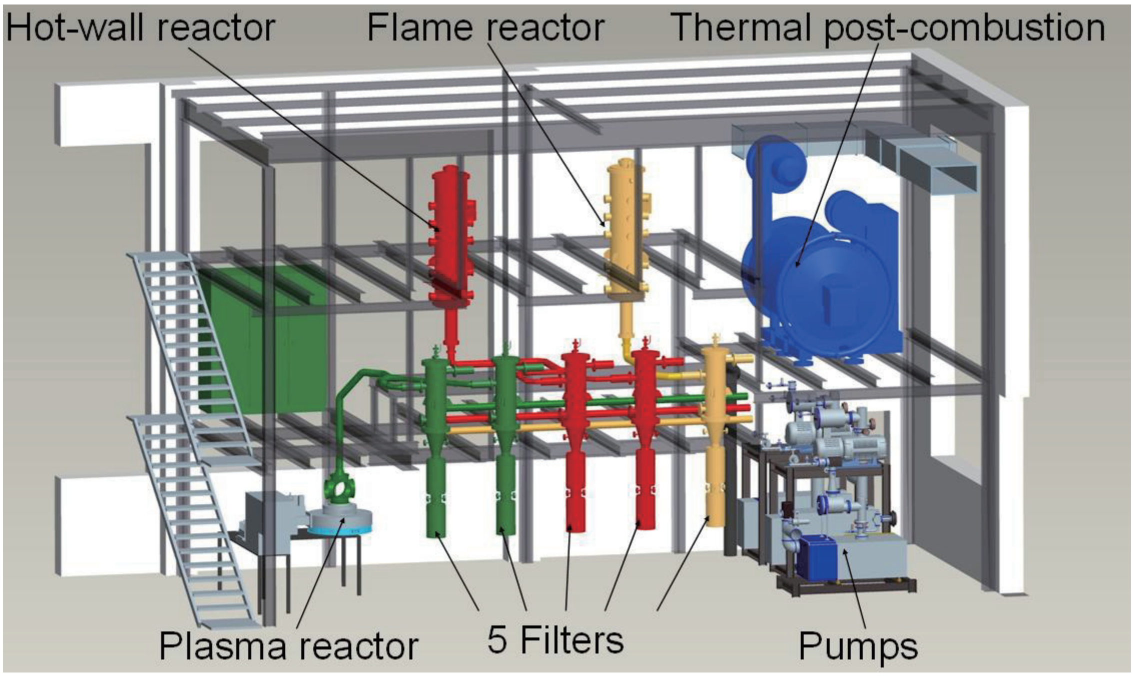

Fig. 1 Schematic of the pilot-plant facility consisting of plasma reactor (left, green), hot-wall reactor (middle, red), and flame reactor (right, yellow), the corresponding filters and the auxiliary devices (pumps and thermal post-combustion, blue).

make these materials available on the kg-scale, we designed a unique facility that combines three different synthesis routes via a hot-wall reactor (HWR), a flame reactor (FLR), and a plasma reactor (PLR) on the pilot-plant scale. In this work we will focus on silicon nanoparticles synthesized in the HWR which provides an efficient synthesis route with respect to the production rate and energy consumption of nanoscale silicon for a number of highly interesting application fields.

Detailed information about the kinetics of the gas-phase reactions of silane, particle formation and growth have been gathered from shock-tube and flow-reactor studies in the past[10, 36]. These results have been incorporated into numerical models that were used to develop a flexible reactor system for the synthesis of nanocrystalline and amorphous silicon. The facility consists of a hot-wall reactor, a vacuum system, filter devices, a thermal post-combustion chamber for off-gases, and several in-situ and ex-situ analytic systems for process diagnostics. **Fig. 1** shows a sketch of the three-level pilot-plant facility containing the HWR and the two additional reactors not used in the work reported here.

The hot-wall reactor is located on the third level of the pilot plant. Different process gases (sheath and carrier gases) and the precursor gases are injected at the top of the reactor via a multi-channel co-annular nozzle. After precursor decomposition and particle formation, the particle-laden hot gases are pneumatically delivered to the second level for filtration. The pumping unit which enables a pressure range between 10 and 120 kPa is located on the ground level, while the thermal post-combustion system for burning the off-gas of the pump is situated at an intermediate level above the pumps. The unit decomposes the gases (up to 200 l/min) at temperatures up to 1100° C.

Fig. 2 shows a photograph of the hot-wall reactor. The reactor is equipped with several ports that can be fitted with quartz windows to allow for optical in-situ diagnostics.

To enable operation of the HWR in continuous mode, a twin-filter system is installed. The particles are filtered alternately by one of the filter cartridges, while the other one can be freed from collected particles and prepared for further operation. Additionally, this double-filter system enables the separation of undefined particles that are generated in the first unsteady stages of production from those that are synthesized under the desired stable operating conditions. Such transient conditions occur after switching from inert gases to production gases due to changes in mass flow, heat capacity and temperature profile originating from the exothermic pyrolysis of silane. During the completely sealed bagging process, re-

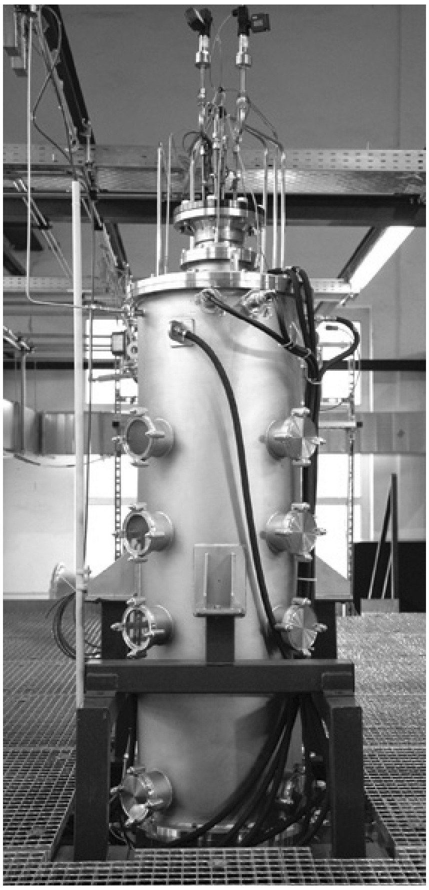

Fig. 2 Hot-wall reactor mounted in the pilot plant. Several ports allow for optical in-situ diagnostics in the hot reaction zone with nozzle on top of the reactor.

verse pulsing is applied to blow the particles off the filter so that they drop into a bag mounted at the first level below the filter devices.

Diagnostics

On-line diagnostics

In recent years, laser diagnostics have proved to be very powerful for the in-situ analysis of combustion processes[37] and have also transferred to the very promissing high-temperature gas-phase synthesis of nanoparticles. Recent applications of high-temperature gas-phase particle synthesis are very promising. Consequently, the pilot plant is equipped with in-situ laser diagnostics and gas-analysis systems consisting of particle mass spectrometry and laser-induced incandescence (LII) set-ups that are available for monitoring the particle and aggregate size during different stages of the formation processes. These techniques enable on-line monitoring of the final particle size, which allows the products to be adjusted with different properties depending on the process conditions[38, 39]. On-line gas-phase analysis of the reactor exhaust is realized by a continuously operating quadrupole mass spectrometer (QMS, MKS microvision IP 300 D), to ensure the intended conversion of the precursor materials.

Off-line diagnostics

Scanning electron microscopy (SEM, LEO 1530) and transmission electron microscopy (TEM, Phillips CM 12) are used to analyze the particle size and the state of agglomeration, while high-resolution transmission electron microscopy (HR-TEM, FEI Tecnai F20) is performed on selected materials to study details of the material structure. On-line and off-line results can be compared to specific surface area measurements, which were used to calculate mean particle sizes. The structure and crystallinity of the generated nanopowders are observed by X-ray diffraction (XRD, PANalytical X'Pert PRO). The crystallite size of multi-domain particle ensembles is then calculated using Scherrer's equation.

Silicon nanoparticle synthesis

Process conditions

Silicon particles are produced in the HWR under various operating conditions. To investigate the influence of the synthesis pressure, particles are synthesized in the pressure range between 15 and 100 kPa and a temperature range from 800° C to 1000° C. Particles are formed with a precursor concentration of 10 vol% silane in a H_2/N_2 atmosphere at an initial total gas flow of 100 slm, resulting in 110 slm after decomposition of SiH_4. The precursor concentration of 10% SiH_4 allows for a production rate of 0.75 kg/h. With respect to the reactor geometry and assuming a constant process gas temperature of 1000°C within the reactor, a gas velocity of 0.7 m/s at 100 kPa and 4.8 m/s at 15 kPa is reached. Due to a highly sophisticated nozzle geometry with several coaxial gas flows that allow independent injection of sheath and diluent gases into the reactor, silane is kept away from the inner hot reactor walls. As a result, the heating and pyrolysis of silane takes place in the center of the reactor tube while chemical vapor deposition of silicon onto the inside of the reactor tube is prevented and stable operation without clogging is ensured for days. Therefore, material loss at the reactor walls is negligible.

Fig. 3 shows the gas velocities and the corresponding residence times for 900 and 1000° C at

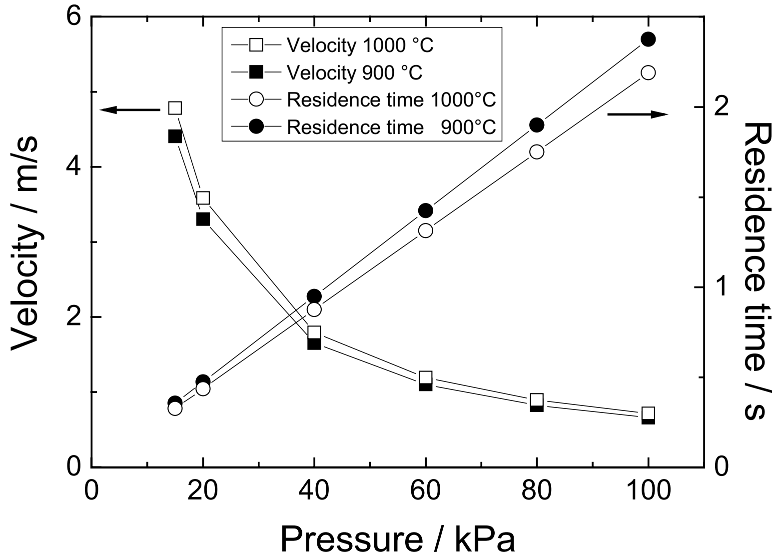

Fig. 3 Gas-flow velocities (squares) and residence times (circles) for Si-nanoparticle synthesis in the HWR for various pressures at 900 and 1000°C. The precursor concentration is kept constant at 10 vol%.

various pressures at 1000℃. The open symbols refer to reaction conditions that lead to a complete conversion of SiH_4 as monitored by the analysis of filter off-gas via QMS. At 1000℃, complete conversion of silane is observed for all investigated pressures, while SiH_4 traces are found at 900℃ at pressures lower than 80 kPa. Experiments at 800℃ with a precursor concentration of 10% show incomplete conversion in the entire pressure range and therefore reduced production rates.

Product analysis

To investigate the relation between particle size, morphology and synthesis conditions, several techniques were applied to characterize several material properties. A Beckman Coulter Delsa™ Nano C was used to measure the size of dispersed silicon nanoparticles with dynamic light scattering (DLS), and the average particle diameters were experimentally determined from the specific surface area by the Brunauer-Emmett-Teller (BET) adsorption isotherm method[40] assuming monodisperse, spherical particles with bulk density. For the DLS analysis, dispersions of silicon nanomaterial in acetone with 2.7 wt% were produced using an ultrasonic bath for one hour at 200 W. The overall volume of the dispersion was kept constant at 60 ml for the duration of sonication. **Fig. 4** shows a representative result of the DLS measurements. They reveal a decreasing mean particle diameter with decreasing process pressure, which is due to the reduced aggregation of particles at lower pressures originating from reduced collision rates in the hot zone of the reactor. For the BET analysis, silicon powders were taken from the sealed product bags and analyzed after 24 h of outgassing under vacuum at 250° C.

The BET results show an increasing specific surface area with decreasing process pressure due to the limited particle growth and decreasing residence time during synthesis, as is expected for gas-phase synthesis routes[41]. **Fig. 5** compares the mean particle diameter received from DLS measurements with those calculated from BET measurements assuming monodisperse, spherical particles.

The particle size increases with increasing process pressures as expected for the gas-phase synthesis route and as was also found for silicon particle formation[41-44]. The particle size determined from the BET measurements is significantly smaller than that measured by DLS. This is attributed to the fact that the sintered particles exhibit a fractal structure with a dimension smaller than 3, leading to the typical open structure as it is commonly observed for materials from gas-phase synthesis. The discrepancy between the BET and DLS diameters increases with pressure, indicating a decreasing fractal dimension. TEM measurements affirm this result.

Electron microscopy analysis

Electron microscopy investigations are performed using HR-TEM, TEM and SEM. For the HR-TEM and TEM investigations, silicon powders were dis-

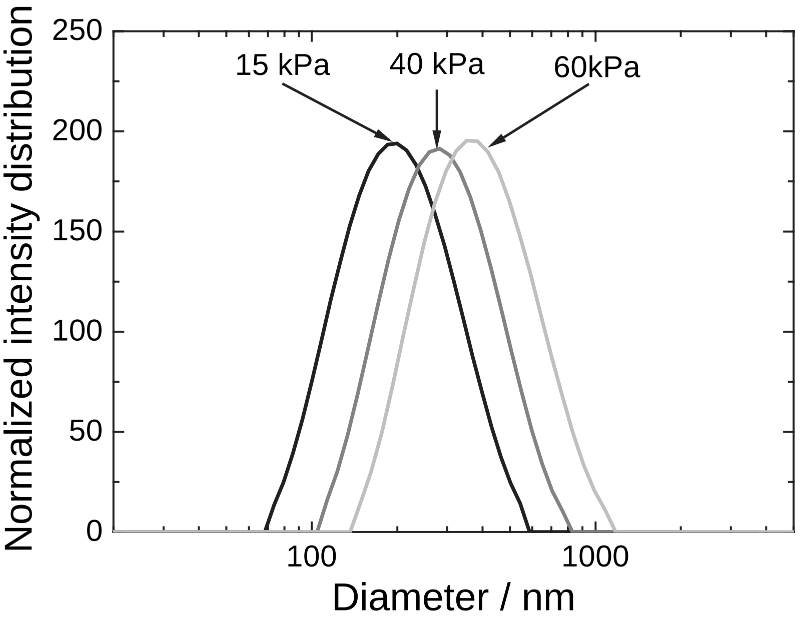

Fig. 4 DLS measurements of silicon nanopowders dispersed in acetone produced at different pressures. The maxima of the normalized graphs indicate the mean particle size.

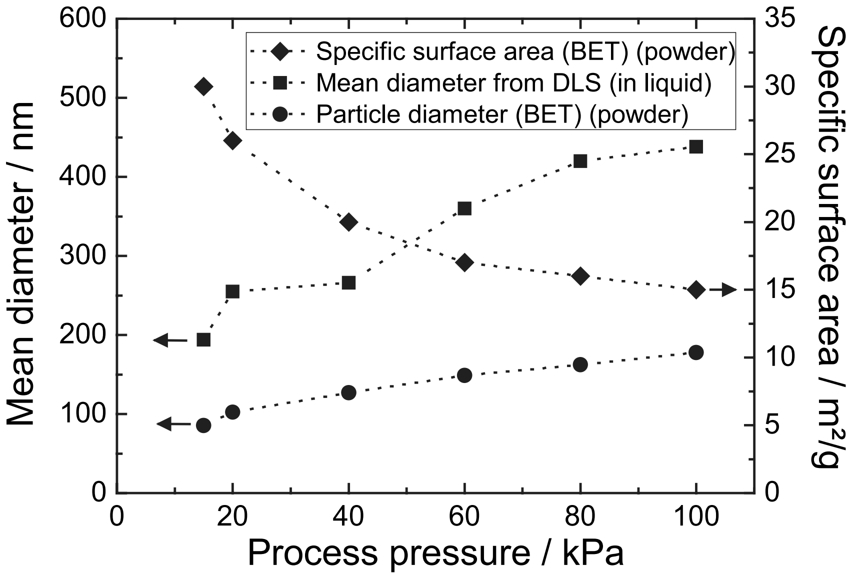

Fig. 5 DLS and BET measurements on silicon nanomaterials produced at different pressures at 1000°C. The DLS investigation is performed in the liquid-phase (acetone) and the BET measurements are performed with the as-synthesized powder.

persed into acetone and sonicated for one hour at 200 W. The dispersion was dispensed on TEM grids and prepared for electron microscopy analysis. **Fig. 6** shows a TEM micrograph of a typical sample of silicon nanoparticles from the hot-wall reactor. The particles show an aggregated structure of small units (primary particles) with diameters smaller than 100 nm. The overall aggregate size is in the same size regime as found in DLS measurements, while the smaller primary particles show faceting and distinct sintering necks to adjacent primary particles.

Primary particle size distributions were determined from aggregated primary particles with clearly visible sintering necks. From these analyses, size distributions with a geometric standard deviation σ = 1.2 to 1.3 are received, which is slightly lower than the expected value of 1.32 for a self-preserving particle size distribution in the continuum regime [45].

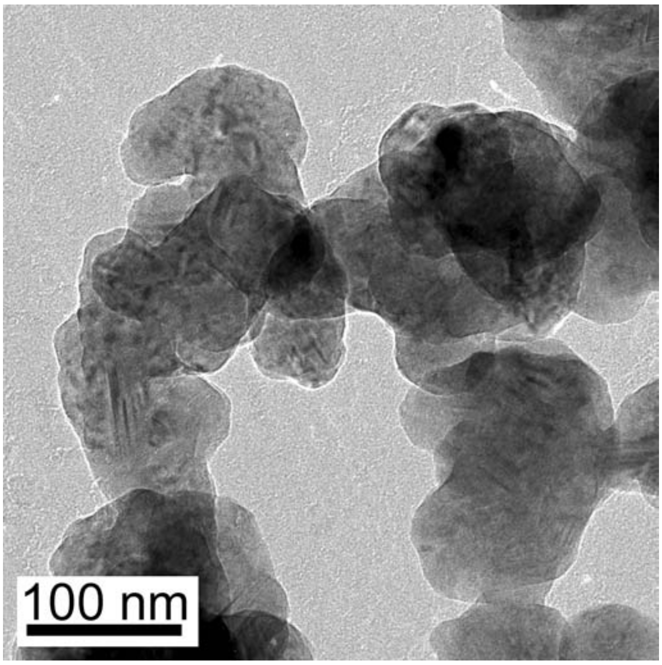

Fig. 6 TEM micrograph of aggregated Si nanoparticles from the HWR process at $T = 1000°C$ and $p = 300$ mbar.

Even the primary particles that form the large aggregates are polycrystalline, as can be seen from the contrasts in **Fig. 6** as well as from the HR-TEM bright field micrograph shown in **Fig. 7a**. The HR-TEM investigations reveal that the particles are polycrystalline with a high crystallinity throughout the particles, but also reveal a high defect density as stacking and twinning faults, which is obvious from the different shades of gray. The size of individual crystals is about 12 nm in diameter, which is significantly smaller than that of the primary particles. The images do not indicate the presence of an oxide shell on the particle surface, but due to handling in air, the highly reactive surface particles assumedly exhibit oxygen on the surface. Furthermore, a local enrichment of SiO_2 due to segregation areas in the particles is not observed[46, 47]. Therefore, the high defect density must be a result of lattice mismatches. **Fig. 7a** shows a HR-TEM micrograph of a Si particle and supports this assumption. It reveals the high crystallinity and also shows a couple of defects and stacking faults. **Fig. 7b** shows the border of the particle which proves the absence of an oxide layer on the particle surface, while **Fig. 7c** shows the Fourier transformation of the center image and underlines the polycrystallinity due to the appearance of closed rings in the illustration.

Fourier transform infrared (FT-IR) spectroscopy was applied to verify that the pristine particles are almost oxygen-free. Therefore, silicon nanopowder

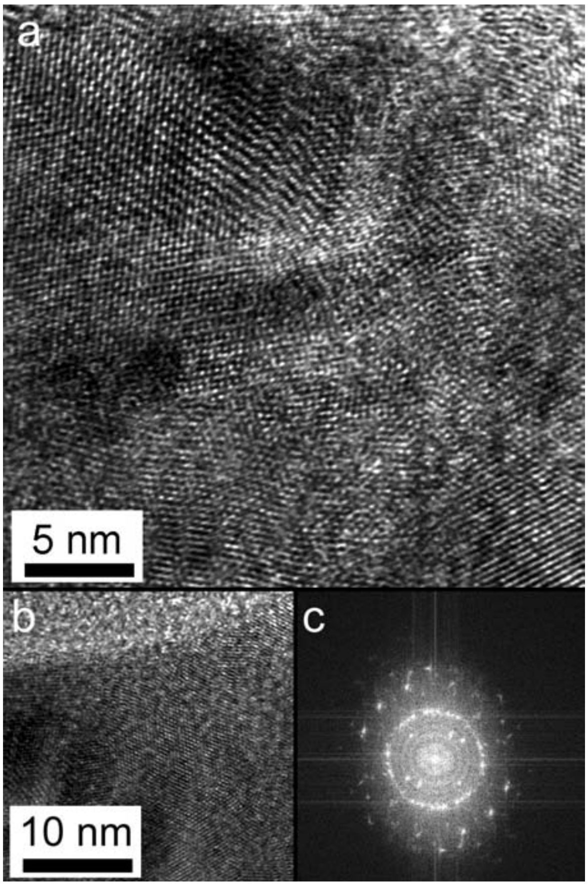

Fig. 7 HR-TEM images of a silicon nanoparticle. a) Core of the particle and lattice structure of the material. b) Border of the particle with the TEM grid, a distinctive oxide layer is not visible. c) Fourier transformation of the core area of the particle.

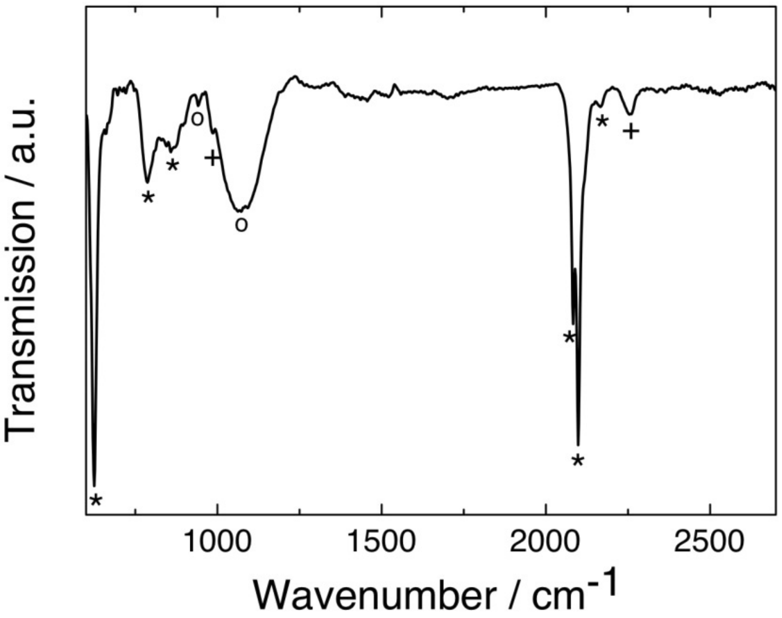

Fig. 8 FT-IR spectrum of silicon nanoparticle powder measured in diffuse reflection. The signals indicated by stars (*) are related to Si-H vibrations back-bonded to silicon, signals indicated by plus (+) are related to Si-H vibrations back-bonded to Si-O, and the signals indicated by circles (o) are related to Si-O-Si vibrations.

samples were taken from the sealed bags and measured in diffuse reflectance mode using a Bruker IFS66v/S spectrometer under ambient conditions. As can be seen from **Fig. 8**, the FT-IR spectrum is dominated by the two strong signals at 630 cm^{-1} and 2100 cm^{-1} which are related to Si-H vibration modes[48]. Additionally, the typical signal found for the Si-O-Si stretching mode is observed around 1070 cm^{-1}, and very small signals around 980 and 2250 cm^{-1} are found for vibrations of Si-H back-bonded to Si-O[49]. The signal at 1070 cm^{-1} is a highly sensitive proof for oxidation. From the fact that the intensities of the Si-H bands at 2100 cm^{-1} and 630 cm^{-1} are considerably large with respect to the Si-O-Si band at 1070 cm^{-1} (which exhibits a very high oscillatory strength), it can be deduced that the particle surfaces are only partially oxidized. This oxidation is most probably due to contact of the silicon nanopowder with air when removed from the sealed bag and during the FT-IR preparation procedure.

To analyze the influence of the synthesis temperature on the crystallite structure, XRD investigations were performed on selected samples. **Fig. 9** shows two typical normalized XRD patterns of nanoparticulate silicon synthesized at 800 and 1000° C. The vertical lines indicate the position of the Bragg maxima for bulk silicon. The broadening of the peaks is attributed to the nanocrystalline structure within the materials, and the crystallite size can be calculated from the patterns using the Scherrer equation:

$$\Delta 2\Theta = \frac{0.89 \cdot \lambda}{B \cdot \cos \Theta} \tag{1}$$

For silicon nanoparticles produced at 1000° C and 100 kPa, the crystallite size is in the regime of about 15 nm, while samples produced at 800° C and 20 kPa reveal crystallite sizes of around 10 nm. From Rietveld analysis on the sample produced at lower temperatures, a crystalline quantity of about 8 vol% within the nanoparticulate powder is calculated. However, the positions of the measured Bragg reflexes are in good agreement with the values found for bulk silicon and, therefore, prove the formation of crystalline silicon during the synthesis.

The experimental set-up also allows for the production of doped materials. A homogeneous mixture of silane (SiH_4, 10 vol%) and 0.02–3 vol% diborane/argon (2 vol% of diborane diluted in argon) was injected into the hot-wall reactor via the nozzle system. To visualize the effect of successful doping, two layers of doped and undoped silicon were prepared on one silicon wafer ready for SEM analysis utilizing the effect that brightness and contrast are different for similar materials with different conductivity, as described previously for different doped regions in silicon wafers[50]. **Fig. 10** shows the two materials located next to each other, separated by a channel free of particles with the layer of undoped silicon on the left-hand side

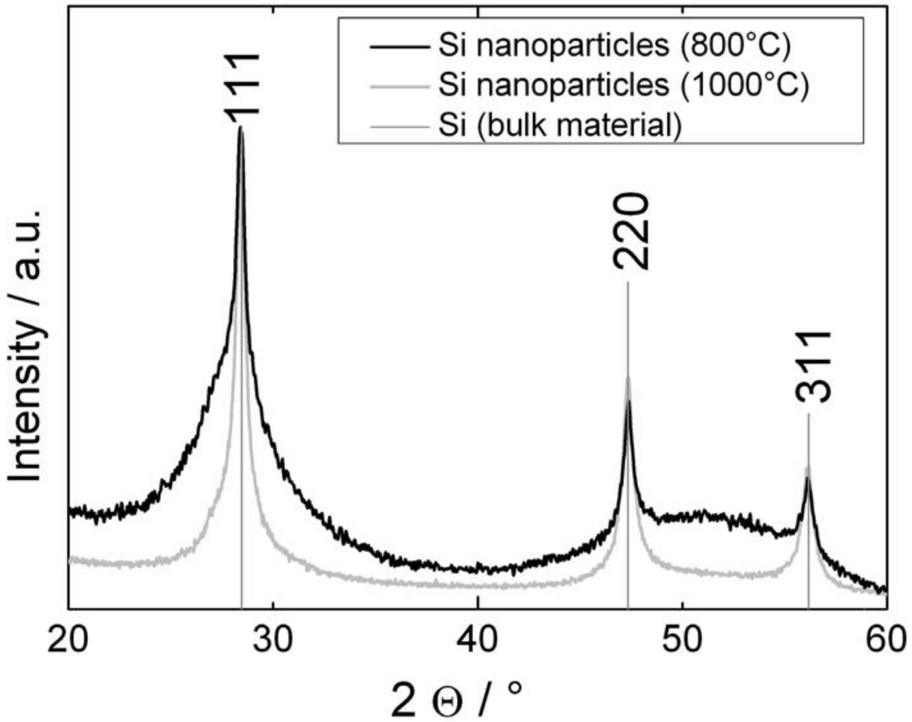

Fig. 9 XRD pattern of silicon nanoparticles produced at 800 and 1000°C. The vertical lines indicate the position of the Bragg maxima for bulk silicon.

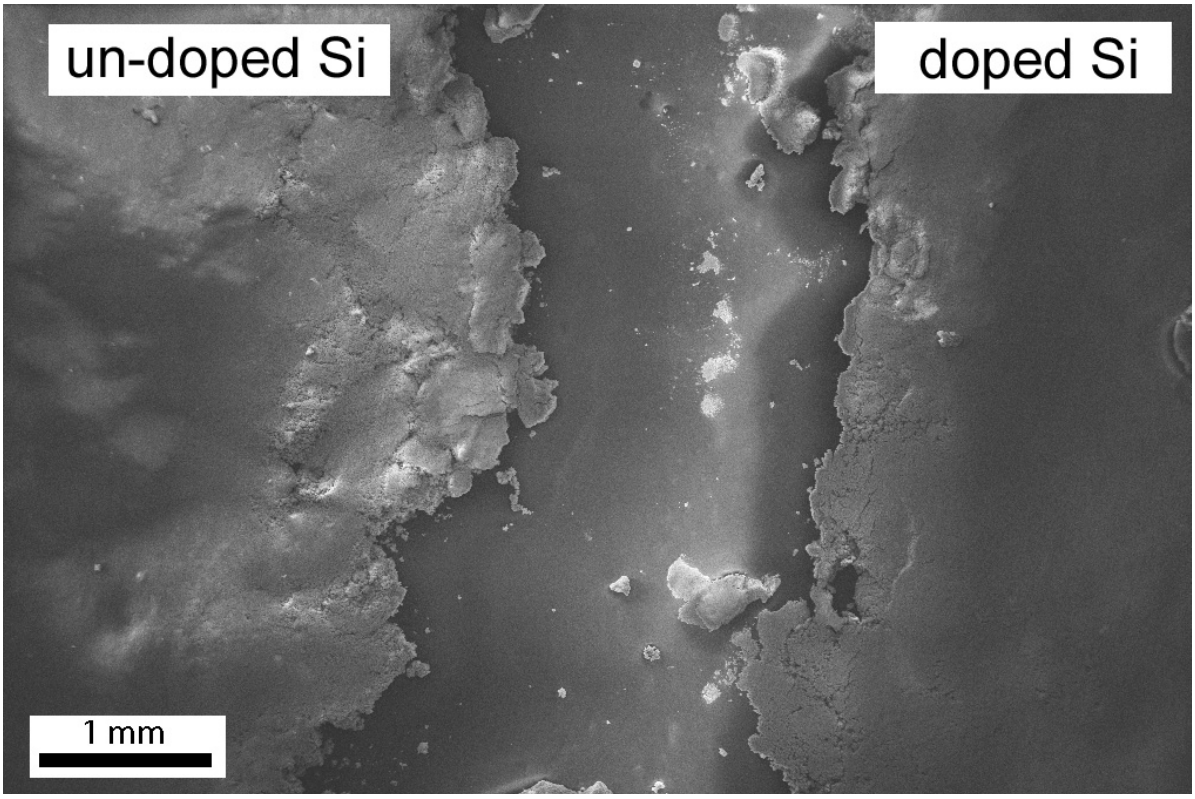

Fig. 10 SEM investigation of layers of undoped silicon (left) and boron-doped (p-type) silicon (right). Brighter contrast is observed for undoped materials.

and the layer of doped material on the right-hand side. The undoped material shows an inhomogeneous contrast and in some parts distortions within the sample area, indicating the build-up of surfaced charged areas. In contrast, the right layer shows a much more homogeneous surface. This behavior can be explained by the fact that a build-up of charges within the porous powder is less pronounced due to higher conductivity. As a result, the image indicates that even a porous particle layer of the as-prepared doped material shows higher conductivity than the undoped material.

Thermoelectric properties of silicon from gas-phase synthesis

Thermoelectric generators enable the direct transformation of thermal energy into electrical energy. Despite their low overall performance, thermoelectric generators are highly interesting for heat recovery[51], especially at high temperatures such as the waste heat from processing plants or from automobile exhaust systems, containing about 30% of the overall energy delivered from the fuel. Thermoelectric generators adapted to the exhaust systems of combustion engines can therefore improve the fuel economy by converting the waste heat to electric energy[52]. In modern cars, the demand for electric energy to drive the electrical components is still increasing and will be even higher for hybrid cars.

One important route toward thermoelectric generators with high efficiency is based on decoupling the heat and charge transport by keeping a high electrical conductivity and decreasing the thermal conductivity[53, 54]. The thermal conductivity – responsible for heat transport by phonons/lattice vibrations – is directly related to the mean free path of phonons. Grain boundaries as well as lattice mismatches are known for their efficient phonon scattering leading to a decreased thermal conductivity. As a result, scientists are investigating the possibility of further enhancing the efficiency of thermoelectric materials by the introduction of artificial nanostructures to yield materials with a significantly lowered thermal conductivity due to phonon scattering[55-57].

Highly doped silicon is a quite good conductor but it also shows high thermal conductivity. The mean free path for phonons in highly doped silicon is a few tens of nanometers, while that for electrons is below 10 nm[58]. Thus, nanostructuring of silicon is an appropriate tool for designing thermoelectric generators with enhanced properties[33], and alloying of the nanoparticles might give another degree of freedom[47, 59-61]. For this purpose, gas-phase synthesized silicon nanopowder doped with 1% of boron was spark-plasma-sintered for 180 s at a temperature of 1100° C into almost dense pellets. The sintered pellets were cut into blocks and the electrical conductivity σ, the thermal conductivity λ as well as the thermoelectric parameter, the Seebeck coefficient α, were measured to determine the figure of merit ZT using equation 2:

$$ZT = \frac{\alpha^2 \sigma}{\lambda} T \tag{2}$$

Fig. 11a shows the thermal conductivity λ versus temperature. The thermal conductivity decreases with increasing temperature and is significantly reduced compared to the thermal conductivity of bulk silicon which is in the range of 140 $\mathrm{Wm^{-1}K^{-1}}$. Nanocrystalline silicon materials synthesized from a microwave plasma process show that the thermal conductivity can be further reduced by minimizing the crystallite size of the used silicon nanoparticles[46]. The results of the measurement are fit using a polynomial function to receive a continuous set of data for further processing. The calculated power factor (see **Fig. 11b**) increases slightly with increasing temperatures, which results from a higher absolute slope of the increasing Seebeck coefficient compared to the absolute value of the smaller slope of the decreasing electrical conductivity. The data are also fit using a polynomial function, and the polynomial function of both the thermal conductivity and the power factor are used to calculate the figure of merit ZT. **Fig. 11c** shows the figure of merit for nanostructured p-doped silicon pellets. The samples exhibit a maximum of ~0.13 at 700°C, which is slightly higher compared to silicon bulk materials, and our most recent results of $ZT = 0.31$ at 700° C (not shown) demonstrate that there is plenty of room for further improvement.

The charge carrier concentration n was calculated from the measured Seebeck coefficient as assumed for degenerated semiconductors[62, 63]:

$$n = \frac{\pi}{3}\left(\frac{C \cdot m^* \cdot T}{\alpha}\right)^{3/2} \text{ with } C = \frac{8\pi^2 k_B^2}{3eh^2} \tag{3}$$

m^* is the band effective mass, k_B the Boltzmann and h the Prank's constant, and e the charge of the electron. The calculated charge carrier concentration of $n = 3.3 \times 10^{20}\,\mathrm{cm^{-3}}$ that is known to enable a maximum in ZT[62], and is very close to the normal doping concentration of $5 \times 10^{20}\ \mathrm{cm^{-3}}$. As a result, it can be stated that the gas phase approach is able to produce

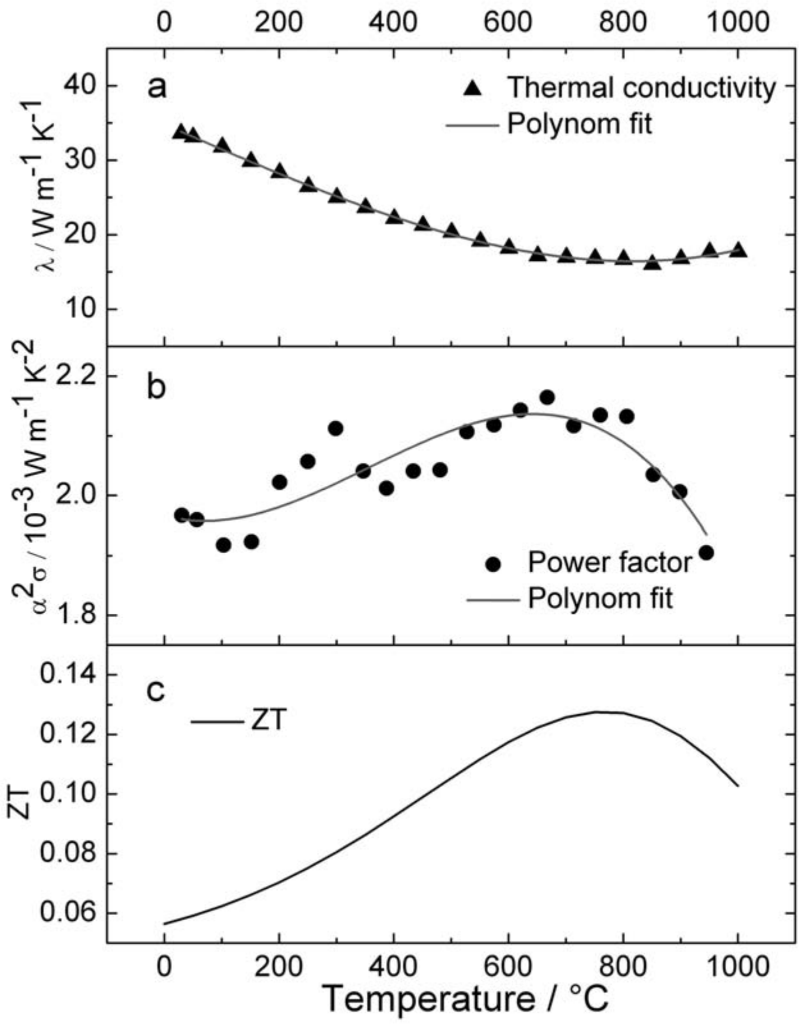

Fig. 11 (a) Thermal conductivity λ, (b) power factor $\alpha^2\sigma$, and (c) figure of merit ZT of nanocrystalline, boron-doped silicon from the hot-wall reactor.

raw materials for thermoelectrics with optimized morpohology and electrical properties.

Nanostructured silicon for lithium-ion batteries

Electricity is a mainstay of today's energy supply with increasing importance as it is easy to transfer for utilization in several different ways. Moreover, electrical energy storage is able to buffer fluctuating energy supply and use. It is obvious that energy storage is also of vital importance for mobile applications from laptops to electric vehicles, and an enormous demand for batteries with a high storage capacity and power density is predicted[64]. Especially the nanostructuring of materials and the synthesis of nanocomposites is a powerful way to meet the requirements of future electrical storage devices[65].

New silicon/carbon nanocomposites for a multifold increase of the anode capacity of lithium-ion batteries are under development due to the fact that silicon is able to increase the storage capacity of presently used graphite dramatically. While the theoretical capacity of graphite (forming LiC_6) is quite poor (372 mAh/g), the silicon-based lithium intermetallic phase $Li_{22}Si_5$ has a theoretical capacity of 4200 mAh/g[32]. Unfortunately, the high capacity is accompanied by extreme volume changes during lithium extraction and insertion of about 300%. Nanosized silicon particles are known to withstand the mechanical stress much better than bulk or micron-sized materials.

To investigate the ability of our nanosized silicon for battery applications, undoped silicon from the hot-wall reactor was used to prepare silicon/graphite composite electrodes. The electrodes were com-

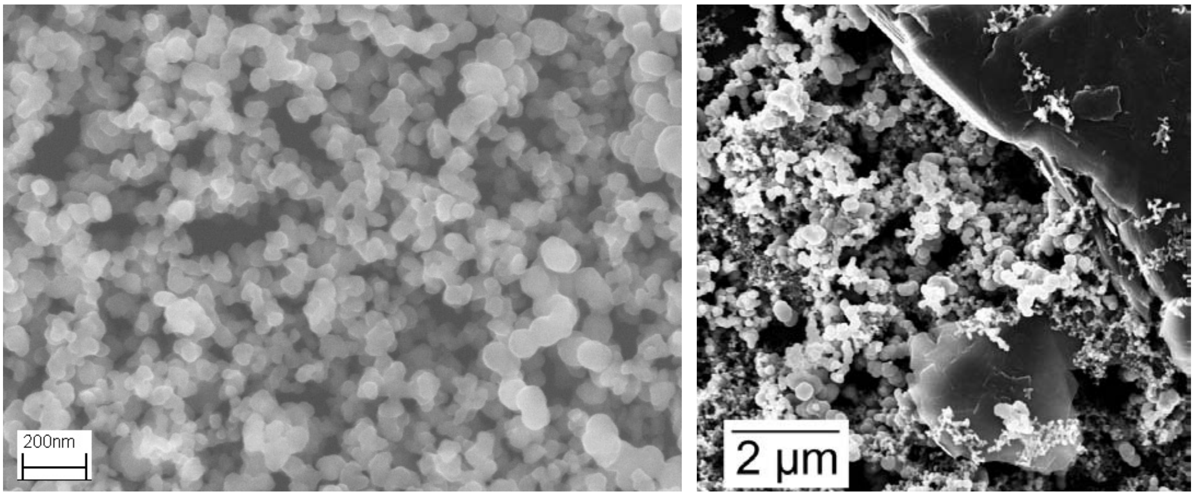

Fig. 12 SEM image of as-prepared silicon nanoparticles (left) and of the anode consisting of micron-sized graphite flakes, Super P®, binder, and silicon nanoparticles.

posed of 60 wt% graphite, 20 wt% silicon, 12 wt% of the commercial carbon black additive "Super P®" as the conducting agent and 8 wt% carboxymethylcellulose (CMC) as the binder (see **Fig. 12** right). The slurry was prepared by dispersing the mixture and it was then coated on a copper foil current collector.

The electrochemical behavior of the composite electrodes was tested by a cycling study shown in **Fig. 13**, and the capacity was limited to 80% of the theoretical capacity. The results show that the composite electrode can be processed for about 100 full cycles without significant degradation and an efficiency of about 95%. This result is very encouraging and among the best values ever reported in literature for silicon-containing electrodes.

Process energy consumption

The gas-phase synthesis of silicon nanoparticles from silane is a highly economical route for the generation of nanosized silicon. To determine the energy required to produce one kilogram of nanosilicon from monosilane (SiH_4), a standard test procedure was defined. The pressure was set to 100 kPa, which means that the process was carried out at atmospheric conditions. Therefore, the power consumption of the vacuum pumps can be neglected. The temperature in the reaction tube was set to 1000° C to ensure quantitative SiH_4 conversion and the sheath gas flow rate was kept constant at 120 slm, while the precursor flow rate was varied between 5 and 30 slm, which results in a corresponding precursor concentration of 4–20% by volume.

To allow for a uniform temperature throughout the entire hot-wall-reactor, the oven is separated into four heating zones. The current consumed by these heating zones was measured and used to calculate the demand for electrical energy to keep the hot-wall reactor at the given temperature for the different process conditions. The result of this calculation leads to a dimension for the total energy demand for the conversion of silane which is related only to the heating of the gases and heat losses, as the formation of silicon from silane is slightly exothermic:

$$SiH_4(g) \rightarrow Si(s) + 2H_2,\ \Delta H = -34\,\mathrm{kJ/mol} \tag{4}$$

Fig. 14 shows the relation between the production rate (in kg/h) and the electrical energy required (in kJ/kg). It can be clearly seen that low production rates result in a comparatively high energy demand, decreasing with increasing production rate. The squares indicate the total energy required to run the reactor while the circles show the energy required to heat sheath and diluent gases to 1000° C (calculated from their heat capacity and mass flow). The difference between both values is mostly related to heat losses. As a result, it can be estimated that a hot-wall reactor with optimized insulation and waste heat recovery is able to produce silicon from SiH_4 with an energy requirement for the process that is below 5000 kJ/kg silicon (about 1.4 kWh/kg).

Summary

Gas-phase synthesis is a highly suitable method to mass-produce nanostructured materials. The merit of its key benefits can be best capitalized by keeping

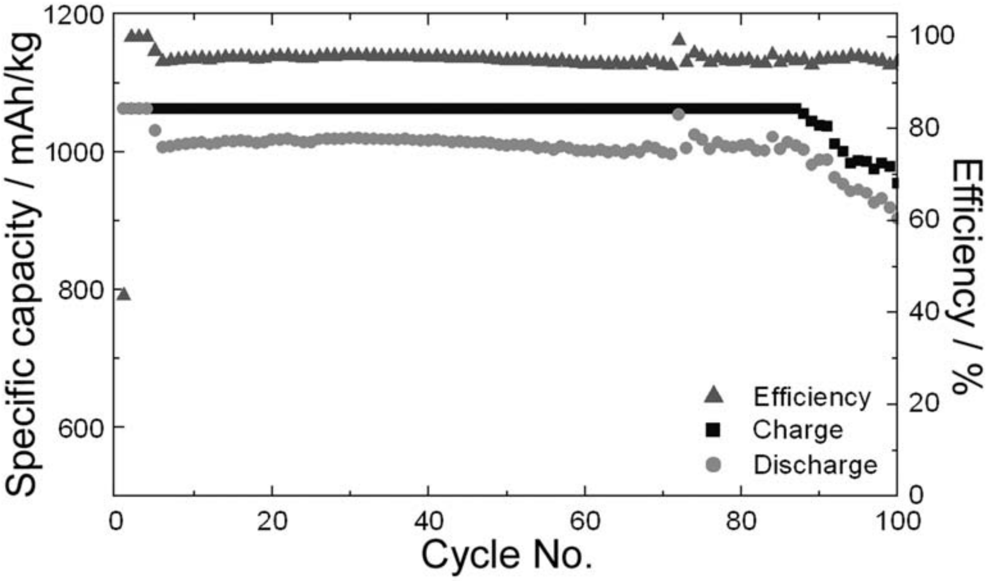

Fig. 13: Cycling study of the graphite/silicon composite electrode.

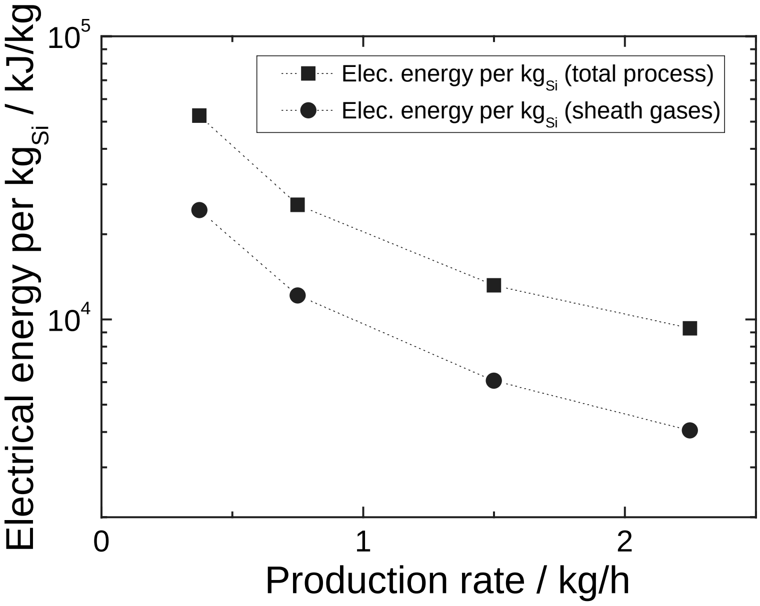

Fig. 14 Energy requirement for the production of a silicon nanomaterial from SiH_4 in the gas phase.

and utilizing the specific properties that are due to its nanostructure. Applications that require high surface areas for energy and mass transport or a specific structure size are the highly promising application fields for such materials.

In this work, silicon particles are produced in a hot-wall reactor under various temperature and pressure conditions using silane as the precursor material. Boron doping of the silicon nanoparticles is realized using diborane as the precursor material. Production rates of up to 0.75 kg/h are received without losing the specifications of the material. The energy required to synthesize silicon materials from silane via the gas-phase route is found to be impressively low compared to established technologies based on the chemical vapor deposition of chlorosilanes. Full conversion rates of silane are claimed and the influence of gas velocity and residence time within the reactor on particle properties is investigated.

The resulting materials are characterized using several analytic methods. Both DLS and BET analysis prove an influence of the process pressure on the generated materials. DLS measurements demonstrate a decreasing agglomerate size, while the BET analysis shows an increasing specific surface area with decreasing process pressure. Electron microscopy demonstrates that the particles in the size regime smaller than 100 nm are sintered with distinctive sintering necks, as can be expected for a gas-phase synthesis process with high particle mass loading. Furthermore, HR-TEM analysis proves that these polycrystalline particles exhibit a high crystalline disorder but do not show a visible oxide layer on the particle surface, which is supported by FT-IR spectroscopy. XRD measurements substantiate the results received from HR-TEM investigation. The analysis method reveals a high crystallinity of the materials synthesized at $T = 1000^\circ$ C and a high amorphous content in conjunction with small crystallites for lower temperatures ($T = 800^\circ$ C).

The application examples given in this paper such as silicon-based thermoelectrics and high-capacity Li-ion battery anodes make use of the particular advantage that nanosized materials can yield with respect to sustainable energy technology.

In the field of thermoelectrics, first measurements of the figure of merit ZT are presented which reveal promising ZT values higher than 0.1 at temperatures of 800°C, and the calculated charge concentration confirms the successful incorporation of the dopant.

First investigations of the applicability of the nanocrystalline silicon for lithium-ion batteries are shown. The material is tested in silicon/graphite composite electrodes and it is demonstrated that the composite electrode can be processed for at least 100 full cycles without significant degradation.

Many other applications could profit from the “nanoproperties”. Catalysis has been the traditional area of nanoparticles since decades, but the availability of advanced technologies for the synthesis and characterization of nanostructured materials will support an even increased use in numerous areas of application. Main fields of interest cover energy harvesting, energy conversion and energy storage. It is expected that nanomaterials will increasingly dominate batteries, super caps, fuel cells, or heterojunction solar cells and in most cases, gas-phase synthesis is the method of choice with respect to production rate, purity and costs.

Acknowledgements

The authors acknowledge the contributions of Hans-Gerhard Bremes, Helge Grimm, Vladimir Kalbfleisch, Victor Kessler, Gabi Schierning, Yee Hwa Sehlleier, Mathias Spree, Burkhard Stahlmecke and Ralf Theissmann for materials characterization. This work has been funded through the German Research Foundation within SFB445 and through the European Union and the Ministry of Innovation, Science and Research of the German State of North Rhine-Westphalia (Objective 2 Programme: European Regional Development Fund, ERDF).

References

1) Braga, A.F.B., et al. (2008): New processes for the production of solar-grade polycrystalline silicon: A review. Solar Energy Materials And Solar Cells, 92(4), pp.418-424.
2) Woditsch, P. and W. Koch (2002): Solar grade silicon feedstock supply for PV industry, Solar Energy Materials And Solar Cells, 72(1-4), pp.11-26.
3) Ogier, M.J. (1880): Combinaisons de l'hydrogène avec le phosphore, l'arsenic et le silicium, Annales de chimie et de physique, 5(T20), pp.5-66.
4) Hogness, T.R., T.L. Wilson, and W.C. Johnson (1936): The thermal decomposition of silane, Journal Of The American Chemical Society, 58, pp.108-112.
5) Purnell, J.H. and R. Walsh (1966): Pyrolysis Of Monosilane, Proceedings Of The Royal Society Of London Series A-Mathematical And Physical Sciences, 293(1435), pp.543-561.
6) Onischuk, A.A., et al. (1997): On the pathways of aerosol formation by thermal decomposition of silane, Journal Of Aerosol Science, 28(2), pp.207-222.
7) Wu, J.J., R.C. Flagan, and O.J. Gregory, Submicron Silicon Powder Production In An Aerosol Reactor, Applied Physics Letters, 1986. 49(2): p. 82-84.
8) Wu, J.J., H.V. Nguyen, and R.C. Flagan (1987): A Method For The Synthesis Of Submicron Particles, Langmuir, 3(2), pp.266-271.
9) Körmer, R., et al. (2010): Aerosol synthesis of silicon nanoparticles with narrow size distribution-Part 1: Experimental investigations, Journal Of Aerosol Science. 41(11), p. 998-1007.
10) Wiggers, H., R. Starke, and P. Roth (2001): Silicon particle formation by pyrolysis of silane in a hot wall gasphase reactor, Chemical Engineering & Technology, 24(3), pp.261-264.
11) News (2008): New solar silicon plant opened, in elements EVONIK SCIENCE NEWSLETTER, p.11.
12) Onischuk, A.A., et al. (2000): Aerosol formation under heterogeneous/homogeneous thermal decomposition of silane: Experiment and numerical modeling, Journal Of Aerosol Science, 31(8), pp. 879-906.
13) Giesen, B., et al. (2005): Formation of Si-nanoparticles in a microwave reactor: Comparison between experiments and modelling. Journal Of Nanoparticle Research, 7(1), pp.29-41.
14) Körmer, R., H.J. Schmid, and W. Peukert (2010): Aero-

sol synthesis of silicon nanoparticles with narrow size distribution-Part 2: Theoretical analysis of the formation mechanism, Journal Of Aerosol Science. 41(11): p. 1008-1019.

15) Talukdar, S.S. and M.T. Swihart (2004): Aerosol dynamics modeling of silicon nanoparticle formation during silane pyrolysis: a comparison of three solution methods, Journal Of Aerosol Science, 35(7), pp.889-908.

16) Kortshagen, U. (2009): Nonthermal plasma synthesis of semiconductor nanocrystals, Journal Of Physics D-Applied Physics, 42(11), p. 113001.

17) Swihart, M.T. (2003): Vapor-phase synthesis of nanoparticles. Current Opinion In Colloid & Interface Science, 8(1), pp.127-133.

18) Onischuk, A.A. and V.N. Panfilov (2001): Mechanism of thermal decomposition of silanes. Uspekhi Khimii, 70(4), pp.368-381.

19) Kruis, F.E., H. Fissan, and A. Peled (1998): Synthesis of nanoparticles in the gas phase for electronic, optical and magnetic applications - A review, Journal Of Aerosol Science, 29(5-6), pp.511-535.

20) Cullis, A.G. and L.T. Canham (1991): Visible-Light Emission Due To Quantum Size Effects In Highly Porous Crystalline Silicon. Nature, 353(6342), pp. 335-338.

21) Ledoux, G., et al. (2000): Photoluminescence properties of silicon nanocrystals as a function of their size, Physical Review B, 62(23), pp.15942-15951.

22) Mangolini, L., E. Thimsen, and U. Kortshagen (2005): High-yield plasma synthesis of luminescent silicon nanocrystals, Nano Letters, 5(4), pp.655-659.

23) O'Farrell, N., A. Houlton, and B.R. Horrocks (2006): Silicon nanoparticles: applications in cell biology and medicine, International Journal Of Nanomedicine, 1(4), pp.451-472.

24) Ruckenstein, E. and Z.F. Li (2005): Surface modification and functionalization through the self-assembled monolayer and graft polymerization. Advances In Colloid And Interface Science, 113(1), pp.43-63.

25) Kovalev, D. and M. Fujii (2005): Silicon nanocrystals: Photosensitizers for oxygen molecules. Advanced Materials, 17(21), pp.2531-2544.

26) Bapat, A., et al. (2004): Plasma synthesis of single-crystal silicon nanoparticles for novel electronic device applications, Plasma Physics And Controlled Fusion, 46, pp.B97-B109.

27) Ostraat, M.L., et al. (2001): Ultraclean two-stage aerosol reactor for production of oxide-passivated silicon nanoparticles for novel memory devices. Journal Of The Electrochemical Society, 148(5), pp.G265-G270.

28) Ding, Y.P., et al. (2006): Single nanoparticle semiconductor devices. Ieee Transactions On Electron Devices, 53(10), pp.2525-2531.

29) Cheong, H.J., et al. (2008): Visible Electroluminescence from Spherical-Shaped Silicon Nanocrystals, Japanese Journal Of Applied Physics, 47(10), pp.8137-8140.

30) Theis, J., et al. (2010): Electroluminescence from silicon nanoparticles fabricated from the gas phase. Nanotechnology, 21(45), p. 455201.

31) Stupca, M., et al. (2007): Enhancement of polycrystalline silicon solar cells using ultrathin films of silicon nanoparticle, Applied Physics Letters, 91(6). p. 063107.

32) Kasavajjula, U., C.S. Wang, and A.J. Appleby (2007): Nano- and bulk-silicon-based insertion anodes for lithium-ion secondary cells, Journal Of Power Sources, 163(2), pp.1003-1039.

33) Bux, S.K., et al. (2009): Nanostructured Bulk Silicon as an Effective Thermoelectric Material. Advanced Functional Materials, 19(15), pp.2445-2452.

34) Boukai, A.I., et al. (2008): Silicon nanowires as efficient thermoelectric materials, Nature, 451(7175), pp.168-171.

35) Chan, C.K., et al. (2008): High-performance lithium battery anodes using silicon nanowires, Nature Nanotechnology, 3(1), pp.31-35.

36) Mick, H.J., P. Roth, and V.N. Smirnov (1994): Determination Of Silane Dissociation-Energy By Measuring Decomposition And Recombination Rate Constants For SiH_4-Reversible-Arrow-Sih2+H-2, Kinetics And Catalysis, 35(6), pp.764-767.

37) Schulz, C. (2005): Advanced laser imaging diagnostics in combustion, Zeitschrift Fur Physikalische Chemie-International Journal Of Research In Physical Chemistry & Chemical Physics, 219(5), pp.509-554.

38) Roth, P. and A. Hospital (1994): Design And Test Of A Particle Mass-Spectrometer (Pms), Journal Of Aerosol Science, 25(1), pp.61-73.

39) Eremin, A.V., et al. (2006): TR-LII for sizing of carbon particles forming at room temperature, Applied Physics B-Lasers And Optics, 83(3), pp.449-454.

40) Brunauer, S., P.H. Emmett, and E. Teller (1938): Adsorption of gases in multimolecular layers, Journal Of The American Chemical Society, 60, pp.309-319.

41) Janzen, C. and P. Roth (2001): Formation and characteristics of Fe_2O_3 nano-particles in doped low pressure H-2/O-2/Ar flames, Combustion And Flame, 125(3), pp.1150-1161.

42) Knipping, J., et al. (2004): Synthesis of high purity silicon nanoparticles in a low pressure microwave reactor, Journal Of Nanoscience And Nanotechnology, 4(8), pp.1039-1044.

43) Friedlander, S.K. (2000): "Smoke, Dust, and Haze: Fundamentals of Aerosol Dynamics", New York, Oxford University Press.

44) Flagan, R.C. and M.M. Lunden (1995): Particle structure control in nanoparticle synthesis from the vapor phase, Materials Science And Engineering A-Structural Materials Properties Microstructure And Processing, 204(1-2), pp.113-124.

45) Pratsinis, S.E. (1988): Simultaneous Nucleation, Condensation, And Coagulation In Aerosol Reactors, Journal Of Colloid And Interface Science, 124(2), pp.416-427.

46) Petermann, N., et al. (2011): Plasma synthesis of nanostructures for improved thermoelectric properties, Journal Of Physics D-Applied Physics, 44(17), p. 174034.

47) Stein, N., et al. (2011): Artificially nanostructured n-type SiGe bulk thermoelectrics through plasma enhanced growth of alloy nanoparticles from the gas phase, J. Mater. Res., 26(15), pp. 1872 - 1878.

48) Lucovsky, G., R.J. Nemanich, and J.C. Knights (1979): Structural Interpretation Of The Vibrational-Spectra Of A-Si-H Alloys, Physical Review B, 19(4), pp.2064-2073.

49) Lucovsky, G., et al. (1983): Oxygen-Bonding Environments In Glow-Discharge Deposited Amorphous Silicon-Hydrogen Alloy-Films. Physical Review B, 28(6), pp.3225-3233.

50) Sealy, C.P., M.R. Castell, and P.R. Wilshaw (2000): Mechanism for secondary electron dopant contrast in the SEM, Journal Of Electron Microscopy, 49(2), pp.311-321.

51) Dresselhaus, M.S., et al. (2009): New composite thermoelectric materials for energy harvesting applications. JOM Journal of the Minerals, Metals and Materials Society, 61(4), pp.86-90.

52) Eder, A. and J. Liebl (2008): Thermoelectric waste heat recovery: A technology transfer from aerospace to the automotive industry? in Thermoelektrik - eine Chance für die Automobilindustrie, D. Jänsch, Editor., expertverlag, pp. 45-56.

53) Dresselhaus, M.S., et al. (2007): New Directions for Low-Dimensional Thermoelectric Materials, Advanced Materials, 19, pp.1043-1053.

54) Rowe, D.M., V.S. Shukla, and N. Savvides (1981): Phonon scattering at grain boundaries in heavily doped fine-grained silicon-germanium alloys. Nature, 290, pp.765-766.

55) Lan, Y., et al. (2010): Enhancement of thermoelectric figure-of-merit by a bulk nanostructuring approach, Advanced Functional Materials, 20(3), pp.357-376.

56) Minnich, A.J., et al. (2009): Bulk nanostructured thermoelectric materials: current research and future prospects, Energy & Environmental Science, 2(5), pp.466-479.

57) Poudel, B., et al. (2008): High-Thermoelectric Performance of Nanostructured Bismuth Antimony Telluride Bulk Alloys, Science, p.1156446.

58) Weber, L. and E. Gmelin (1991): Transport-Properties Of Silicon, Applied Physics A-Materials Science & Processing, 53(2), pp.136-140.

59) Joshi, G., et al. (2008): Enhanced Thermoelectric Figure-of-Merit in Nanostructured p-type Silicon Germanium Bulk Alloys, Nano Letters, 8(12), pp.4670-4674.

60) Wang, X.W., et al. (2008): Enhanced thermoelectric figure of merit in nanostructured n-type silicon germanium bulk alloy, Applied Physics Letters, 93(19), pp.193121-3.

61) Zhu, G.H., et al. (2009): Increased Phonon Scattering by Nanograins and Point Defects in Nanostructured Silicon with a Low Concentration of Germanium, Physical Review Letters, 102(19), pp.196803-4.

62) Snyder, G.J. and E.S. Toberer (2008): Complex thermoelectric materials. Nature Materials, 7(2), pp.105-114.

63) Sze, S.M. and K.K. Ng (2007): "Physics of semiconductor devices", 3rd Ed. ed., Hoboken, NJ, Wiley Interscience.

64) Broussely, M. and G. Archdale (2004): Li-ion batteries and portable power source prospects for the next 5-10 years. Journal Of Power Sources, 136(2), pp.386-394.

65) Arico, A.S., et al. (2005): Nanostructured materials for advanced energy conversion and storage devices, Nature Materials, 4(5), pp.366-377.Introduction

Author's short biography

Tim Hülser

Tim Hülser graduated from Duisburg University in physics and worked afterwards for four years at the Institute for Combustion and Gasdynamics, IVG, at the University of Duisburg-Essen in the field of nanoparticle characterization and gas sensing properties of nanoparticulate semi-conducting materials. Then he moved to the Association of German Engineers (VDI) and worked as consultant in the field of future technologies with emphasis on wireless data transport and automotive applications. Currently he directs the division "Nanomaterials Synthesis & Process Technology" at the Institute of Energy and Environmental Technology, IUTA, where highly-specific nanoparticles are synthesized from the gas-phase on the pilot-plant scale.

Dr. Sophie Marie Schnurre

Dr. Sophie Marie Schnurre graduated from Clausthal University of Technology in mathematics and received her PhD at the Institute of Metallurgy at Clausthal University of Technology. After working several years as quality manager for an automotive supplier she went back to research and started as scientific assistant in the division "Conversion & Storage of Energy" at the Institute for Energy and Environmental Technology (IUTA) in Duisburg. Here she became project manager for the build up of the pilot plant facility and the new division "Nanomaterials Synthesis & Process Technology".

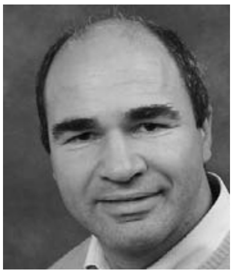

Dr. Hartmut Wiggers

Dr. Hartmut Wiggers graduated from Munster University in chemistry and received his PhD from Essen University. During his postgraduate research he was involved in the characterization of charge carrier transport processes in semiconducting and quantum-sized materials. He is heading the nanomaterials group at the Institute for Combustion and Gas Dynamics at University Duisburg-Essen. His current research interests are the formation, chemistry and physics of crystalline, nanosized inorganic materials.

Prof. Dr. Christof Schulz

Prof. Dr. Christof Schulz studied Chemistry at the University of Karlsruhe and received his PhD at the University of Heidelberg. From 1997-2004 he headed the group on "Laser diagnostics in combustion processes" in the Physical Chemistry Institute in Heidelberg where he also received his Habilitation in 2002. During this time he was for several subsequent research periods at Stanford University, from 2000-02 as Visiting Scholar and from 2002-04 as Consulting Associate Professor. In 2004 he assumed the Chair for Combustion and Gasdynamics at the University of Duisburg-Essen where he currently leads a group of 45 scientists. Since 2008 he is also a scientific director of the Institute for Energy and Environmental Technology (IUTA) in Duisburg. Since 2010 he is the director of the Center for Nanointegration Duisburg-Essen (CeNIDE) .

Tribo-Electrification and Associated Segregation of Pharmaceutical Bulk Powders[†]

E. Šupuk[1,2], A. Hassanpour[1], H. Ahmadian[1,3], M. Ghadiri[1*] and T. Matsuyama[4]
Institute of Particle Science and Engineering, University of Leeds[1]
KTP Associate at Bristol-Myers Squibb, Drug Product Science & Technology[2]
Procter and Gamble Technical Centres Limited[3]
Faculty of Engineering, Soka University[4]

Abstract

Powder handling operations can give rise to the tribo-electrification of particles, causing a number of problems such as risk of fire and explosion, particle adhesion to the walls of processing equipment and segregation. Current methods available for measuring the dynamic charging of bulk powders are unsuitable for testing/handling small quantities of powders, some of which are highly active. Furthermore, very little work has been reported on the effect of tribo-electrification on the segregation of components of mixtures.

A methodology has recently been developed for investigating the tribo-electrification of small quantities of bulk powders using a shaking device. Two common pharmaceutical excipients, namely α-lactose monohydrate (α-LM) and hydroxypropyl cellulose (HPC) were used as model materials. The electric charge transferred to the particles was quantified as a function of shaking time, frequency and container material. The temporal trend follows a first-order rate process.

Using numerical simulations based on the Distinct Element Method (DEM), the charge accumulation of an assemblage of alumina beads inside the shaking device was analysed based on the single particle contact charge obtained from the experiments. It was shown that the inclusion of electrostatic mechanisms into the DEM model leads to an improved prediction of the charge build-up, but the difference with experimental data is still notable.

Using the above method, segregation induced by tribo-electric charging was characterised for binary mixtures comprising α-LM and HPC. The bulk and wall-adhered particles were analysed for the mass fraction of each component using selective dissolution of one component and filtration of the non-dissolving component, followed by a gravimetric analysis. The findings reveal that a considerable level of segregation can take place on the wall-adhered particles.

The method described here has the potential to be used to characterise small quantities of pharmaceutical powders including active pharmaceutical ingredients (API), which are sparse in the early development stages.

Keywords: tribo-electrification, electrostatics, segregation, DEM modelling

1. Introduction

Tribo-electrification is a common phenomenon that occurs in many powder handling industries such as pharmaceuticals, foods and detergents, etc. Powder handling operations such as pneumatic conveying, sieving, mixing and milling cause particles to make frequent contact among themselves and with the walls of the processing equipment. During these interactions, charge transfer takes place through shearing[1)], impact[2)] or friction[3, 4)], a process which is commonly known as *tribo-electrification* or *tribo-electric charging*. When materials become charged, their behaviour can change and as a result they can adhere to each other easier or repel other charged materials[5)]. Excessive tribo-electrification of powders can be a nuisance as it causes problems such as dust

---

[†] Accepted: September 10th, 2011
[1] LS2 9JT, UK
[2] Moreton, CH46 1QW, UK
[3] Newcastle upon Tyne, NE12 9BZ, UK
[4] Tokyo 192-8577, Japan
[*] Corresponding author
E-mail: m.ghadiri@leeds.ac.uk
TEL: (+44) 113 34 32406

ⓒ 2011 Hosokawa Powder Technology Foundation

explosions[6], adhesion and coating or blockage of pipelines[7]. It can also lead to powder loss and difficulties in controlling the powder flow.

Pharmaceutical powders are usually semiconductors or insulators of small particle size and low bulk density, providing ideal conditions for electrostatic effects. In the pharmaceuticals industry, the problem extends further to the end-product quality, where the tribo-electrification of powders may cause segregation.

Segregation due to electrostatic effects is a relatively new area of research which has been identified as technologically important. A manifestation of this problem is susceptibility to a change in drug formulation in various processes such as tabletting. The pharmaceuticals industry is heavily regulated with a limited number of excipients and tight limits on content uniformity, hence an in-depth understanding is very important in order to control the electrostatic effects and to ensure that the end product is effective and safe to use.

At present, the industrial selection of appropriate excipients to form a stable blend is very often accomplished through trial and error. However, this approach is unattractive due to the significant resources required, including the use of large quantities of APIs which are sparse in the early development stages, in addition to the approach being very time-consuming. The ability to control the tribo-charging of pharmaceutical powders from an early stage of a process is therefore essential in improving the quality of the end product through minimising the deposition and powder loss in a process. From the currently available tribo-charging devices, the cyclone charger[8] is probably the most prominent device for characterisation of the tribo-electric properties of pharmaceutical powders. The cyclone is fitted with interchangeable contact surfaces of steel and polymers. The particles are fed from the side with the aid of a carrier gas and are charged by means of collisions with the inner surfaces of the cyclone charger. The charge-to-mass ratio is measured by a Faraday cup and an electrometer. However, this device has not yet found widespread use, as it suffers from being an 'open system' with risk of exposure to APIs. A simple test method has been developed by Šupuk *et al.*[9] for characterisation of the tribo-electric properties of powders in a shaking container by contacting the powder with imitations of common surfaces used in industry. In comparison, this is a closed system and has the added advantage that it is a rate process, from which the equilibrium condition can be quantified.

Šupuk *et al.*[9] used α-LM and HPC as model materials due to their non-toxic nature, allowing for extensive testing with minimal health risk implications. In the pharmaceuticals industry, α-LM and HPC are widely used as excipients for tabletting and encapsulation due to their bland taste and wide interacting capabilities with other active and excipient ingredients.

The tribo-electrification of particles against various surfaces during powder handling gives rise to bipolar charges within a formulation which can give rise to attractive or repulsive forces between the individual particles. The charging of particles with the opposite polarity has been utilised in the formation of stable ordered mixtures which have proven to minimise segregation[10]. However, in some cases, both components of a binary mixture may charge with the same polarity. This gives more chance for particles to adhere to the inner walls of the processing equipment rather than to each other. This may have a significant effect on the charging behaviour of powders and may cause segregation of particles during powder handling and processing. However, little work has been done on this topic. In addition to being highly dependent on particle size, shape and density, segregation may also be affected by electrostatic charges. It remains a challenge and an area which lags behind the rest of segregation studies, possibly due to the lack of simple tribo-electrification devices. Understanding the effects of particle adhesion and subsequent segregation of mixtures is therefore of particular interest.

To elucidate the temporal profile of tribo-electric charging, simulations by the Distinct Element Method (DEM) were carried out. This requires a model for single particle charging. Hence, experimental work was carried out on the tribo-electric charging of a single spherical alumina bead inside a shaking container. An empirical model is then fitted, relating the accumulated charge to the contact area of the bead with the capsule walls. This is then used in the DEM simulations with a number of beads to predict bulk charging and a comparison is made with experiments at different shaking frequencies. Furthermore, the effects of long-range forces, space charge and image charge at boundary conditions are investigated. At present, there are no methodologies available to predict the dynamic charging of bulk powders. A first attempt to analyse a simple system is herewith presented.

1.1 Tribo-electric charging devices

A common way of charging bulk particles triboelectrically is by using an inclined cylindrical tube or a plate[11-13]. In both cases, particles are poured from the top of the cylinder/plate, and as they roll and bounce on the way down, the particles are collected in a Faraday cup and the charges are measured. The inclined surface material can be changed to test the effect of the surface material on charge transfer.

Another way of tribo-electric charging is to use a vibrating device on which a box is placed[14]. Particles are put inside the box and are subjected to vibrations. The sample tested is then transferred into a Faraday cup connected to an electrometer, where the charge is measured. Mixing devices such as a high-shear mixer[15] or a low-shear tumble blender[16] have also been used, where the particles are charged as a result of collisions with the walls of the mixing devices and with each other. The charge measurement is done with a Faraday cup or the insertion of an induction probe inside the mixer.

Particle electrification is a common occurrence during pneumatic conveying due to numerous collisions between the particles and the pipe wall. One prominent method for measuring electrostatic charge transfer is to use a pipe in which the particles are pneumatically conveyed. A tribo-charging device based on this concept was developed by Matsusaka *et al.*[17] to analyse the electrostatic charge distribution of particles. The set-up consisted of various lengths of tribo-charging pipes and an Electrical Single-Particle Aerodynamic Relaxation Time (E-SPART) analyser. A table feeder was used to introduce the particles into the pipe and compressed air was used to transport the powder. The charge and particle size were measured after travelling through the pipe.

A cyclone[8] and more recently a dispersion device[18] have also been used to perform tribo-electric charging. The cyclone is fitted with interchangeable contact surfaces of steel or polymers. The pharmaceutical powders are charged by means of collisions with the inner surfaces of the cyclone charger. The charge-to-mass ratio is continuously monitored by Faraday cup and electrometer. In the dispersion device[18], a small quantity of powder, typically 36 mg, is sandwiched between two thin metal sheets, separated by a spacer. A pulse of pressurised air is applied to the cavity above the sheets, as a result of which the sheets burst open, dispersing the powder. The unit is mounted on a conventional Faraday cup connected to an electrometer to measure the net charge transfer due to dispersion.

Examples of other methods of tribo-electric charging include fluidised beds[19], rotary drums[20], vibratory feeders[21] and flexible hoses[22]. In this paper, the new test method based on shaking developed by Šupuk *et al.*[9] is described and analysed.

2. Shaking Test Method and Materials

A simple way to charge powders is to shake them in a container, where powder-wall contacts can induce tribo-electrification. The method provides good control of temperature and humidity, as it is enclosed, and the charging rate can be assessed by monitoring the charge as a function of time until the saturation level is achieved.

Šupuk *et al.*[9] used a Retsch MM200 shaking machine for this purpose. About one gram of powder is placed inside a 10-ml container and shaken to tribo-electrically charge the powder. The shaking container is subjected to reciprocal vibrations in a horizontal direction. Containers made of stainless steel, PTFE, PMMA (Perspex) or glass are used to test the effect of the contact surface material on tribo-electrification. The vibration frequency can be set between 3 and 30 Hz. The tribo-charging time can be digitally preset from 10 seconds up to 99 minutes. The amplitude of vibrations is fixed at 89 mm. After a specified time of shaking, the powder is emptied into a Faraday cage to measure its charge. A quantity of the powder sticks to the walls and would not come out. This is referred to as powder loss due to adhesion to the walls and correlates well with the charge level on the powder. The details of the device and its operation can be found in ref.[9].

To measure the electrostatic charge of the bulk powders, a Faraday cup is used which consists of two stainless steel cups isolated from each other by a PTFE spacer. The inner cup is connected to an electrometer (Keithley Model 6514) via a BNC cable, and the outer cup is earthed. The electrometer is connected to a computer and the data are recorded. The inner cup can be easily removed to measure the weight of the sample poured into the cup. A stainless steel lid, fitted to the outer cup, is used to reduce electric noise. The resolution of the charge measurement is in a nano-Coulombs (nC) order of magnitude.

In order to control the environmental conditions during the test, an isolator can be used wherein all of the test equipment, including the tribo-electric charging device, electrometer, Faraday cup, humidity and temperature meters and the test materials can be placed and sealed. Nitrogen can be supplied through an aperture on the side of the isolator to reduce humidity.

The test materials are placed inside the isolator via the side chamber. The humidity and temperature inside the isolator are monitored using a HydroPalm device. By adjusting the amount of dry gas coming into the isolator, the humidity can be reduced if required. With this arrangement, the active ingredients are easily contained, reducing the risk of exposure to dust and associated toxic hazards.

Tribo-electrification of the feed material in a shaking container is mainly achieved by impact and sliding against its inner wall. A high-speed video camera, (Redlake MotionXtra HG-100K) with a maximum acquisition speed of 100,000 frames per second (fps) is used to observe the particle movements. A glass container of the same geometry as the stainless steel and PTFE containers is used for this purpose.

2.1 Test materials

α-lactose monohydrate (α-LM) and hydroxypropyl cellulose (HPC) are widely used in the pharmaceutical industry as excipients for tabletting and encapsulation, and were selected for this work based on the current industrial and scientific interest regarding their charging tendencies. The reasons behind selecting these materials also lie in the fact that they are of a non-toxic nature so that extensive testing could be conducted with minimal risks to health.

The above two materials are fine and irregular in shape and are unsuitable for more basic studies of tribo-electrification, for which information about various contact parameters such as the contact area is required. For this reason, alumina beads were also used for comparison between the experimental work and numerical simulations by the Distinct Element Method (DEM). These particles are strong enough not to break or chip easily during the tribo-charging experiments inside a shaking container at high impact velocities. The splitting of particles would create additional surface area thus affecting charge transfer; therefore it was essential this was kept to a minimum via the choice of beads. Physical properties of the test materials are presented in **Table 1**.

3. Analysis of the New Test Method

Saturation Level The saturation charge level, i.e. the amount of charge generated as a result of particle impacts for which no further charge would occur, is a characteristic of the system, and for a given powder-container system it should be independent of the shaking frequency. Šupuk *et al.*[9] measured the charge-to-mass ratio as a function of shaking time for 1g of α-LM, HPC and a 50:50% by mass binary mixture in a PTFE container for 10, 20 and 30 Hz, and found this to be indeed the case. Their results are reproduced as **Table 2**, where for each system an equilibrium value is reached.

Šupuk *et al.*[9] also report that the charging temporal profile follows a first-order rate (equation 1).

$$q = q_{sat}(1 - e^{-\alpha t}) \tag{1}$$

where q_{sat} is the saturation charge. The rate constant α is obtained from the initial slope of the curves. The results show that increasing frequency increases the charging rate which follows the first-order process reasonably well for all the three frequencies.

The values of the rate constant and saturation

Table 1 Physical properties of test materials

Sample	Supply Source	Particle Density	Bulk Density	Tap Density	Particle Size Distribution (μm)			Aspect Ratio
		kg/m^3	kg/m^3	kg/m^3	d_{10}	d_{50}	d_{90}	
α-LM	Mallinckrodt Baker, USA	1520	725	825	196	334	527	1.71
HPC	Sigma-Aldrich, USA	1214	331	453	256	418	700	2.12
Alumina	IFP, France	1520	N/A	N/A	Diameter: 2 mm			1.05

Table 2 Saturated charge values for the test powders at 10, 20 and 30 Hz frequencies[9]

Frequency (Hz)	Saturated Charge (nC/g)		
	α-LM	HPC	Binary
10	24.6	2.3	12.1
20	24.7	2.7	11.8
30	22.7	3.0	11.9

Table 3 Values of the rate constant and saturation charge reported by Šupuk *et al.*[9] for α-LM.

Frequency (Hz)	α	q_{sat}
10	0.045	24.2
20	0.060	24.6
30	0.163	24.0

charge were reported by Šupuk *et al.*[9] and are reproduced in **Table 3**. An increase in the shaking frequency increases the rate constant. This is expected since the number of particle-wall collisions increases while the charge relaxation time between successive impacts is reduced. Furthermore, increasing the shaking frequency also leads to an increase in particle impact velocity, resulting in a larger contact area for charge transfer[3].

Wall Adhesion Tribo-electric charging gives rise to powder adhesion to the container walls, the extent of which was characterised for various samples and surface material by Šupuk *et al.*[9]. The adhered powder is highly charged and its mass increases with the charge level. The powder does not empty into the Faraday cup without gentle tapping on the outside of the container. However, the adhered powder cannot be scraped into the Faraday cup as this would additionally charge the powder. The highest mass loss at all frequencies tested is for α-LM. Approximately 10% of total loaded particles of α-LM adhere to the inner walls of the shaking container. HPC has the smallest mass loss at all the three frequencies, indicating a very low adhesion of particles to walls.

Effect of Initial Mass Powder mass affects the charging rate as well as the equilibrium charge, as it affects the dynamic of particle wall collisions and the surface area available for charging. Šupuk *et al.*[9] carried out tests with 0.33, 0.66 and 1 g of initial mass and report that the highest charge generation is with the smallest mass; i.e. 0.33g. This will be analysed later in Section 4.

Effect of Surface Material Šupuk et al.[9] evaluated the tribo-electric charging of the test powders against three solid surfaces, namely PTFE, stainless steel and glass. Their results for pure α-LM, HPC and a binary mixture (50:50% by mass) at 20 Hz show that the powders become positively charged against PTFE surfaces and negatively charged against glass and stainless steel containers. The magnitude of charge is highest with the PTFE and lowest in the stainless steel shaking container. The stainless steel container may allow the charge on the wall-adhered particles to dissipate through the charge relaxation process, explaining the reduced magnitude of charge obtained for this container.

The primary factor affecting the charging process is the work function of the contacting surfaces and the resulting contact potential difference. This together with contact mechanics of impacting particles influences the charging process. To account for these effects, a more detailed study of particle movement taking account of electrostatic charge is being undertaken by the distinct element method. Preliminary results are reported in Section 4.

High-Speed Video Analysis of Particle Motion Šupuk *et al.*[9] made observations of particle motion at three shaking frequencies by high-speed video recording, and report two patterns of particle dynamics: at 10 Hz the particles mainly slide at the bottom of the shaking container, with the number of particle-wall impacts considerably less than the other two frequencies. This suggests that particles are becoming charged primarily as a result of sliding friction which corresponds to the smallest amount of charge transferred at this frequency. At 20 Hz, a large proportion of the particles impact on the upper walls and rounded ends of the container and the rest slide at the bottom of the container. At 30 Hz, particle collisions are most prevalent. Particles are thus mainly charged as a result of particle-wall impacts and hence a rapid charging to the saturation level is expected for the 30 Hz frequency, as indicated by the rate constant for 30 Hz in **Table 3**. An analysis of the effect of particle motion is therefore helpful in understanding the charging process, and this is addressed further in Section 4 below.

4. Tribo-Electric Charging of Spherical Alumina Beads

In an attempt to elucidate the process of tribo-electric charging of particles by this method, spherical alumina beads were shaken in the same way as reported above and the charge level was characterised for two cases of a single bead and 230 beads.

4.1 Single bead experiments

A single alumina bead, 2 mm in diameter, was tribo-charged at 10, 20 and 30 Hz frequencies using the

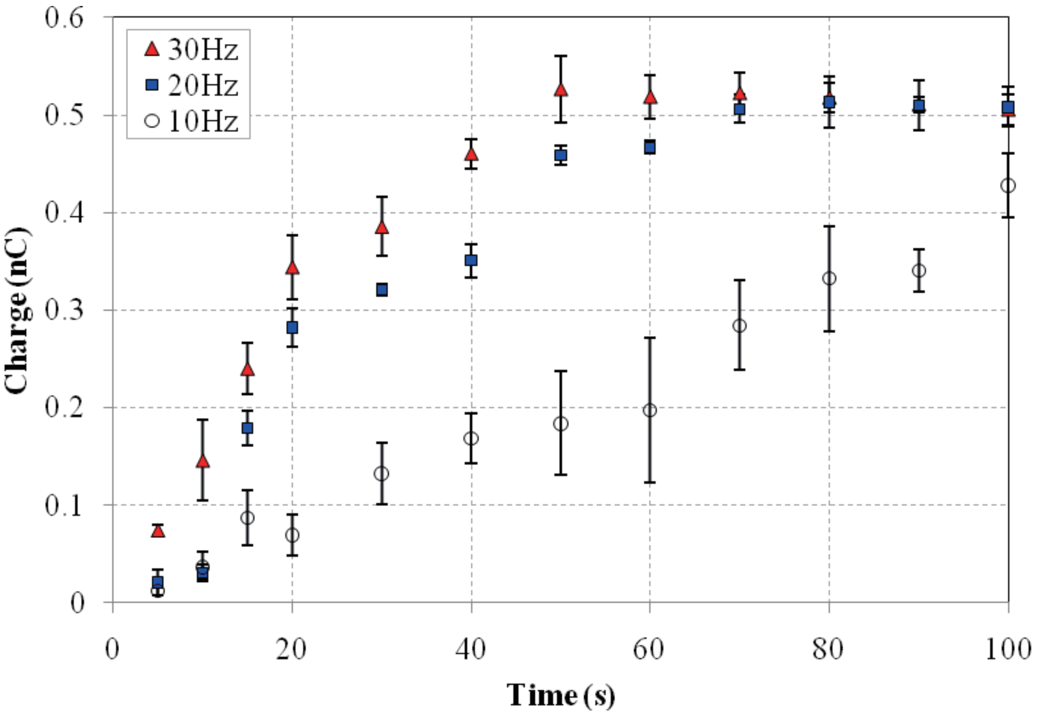

Fig. 1 Charge on single alumina beads as a function of shaking time following tribo-charging at 10, 20 and 30 Hz frequencies.

Table 4 α values for single and bulk tests of alumina beads

Frequency[Hz]	SINGLE		BULK	
	α [s^{-1}]	q_{sat} [nC]	α [s^{-1}]	q_{sat} [nC]
10	0.0109	–	0.0036	31.34
20	0.0371	0.52	0.0144	32.18
30	0.0539	0.51	0.0136	30.95

above method. The average mass of a single alumina bead is 4.4 ± 0.1 mg based on a random selection of 30 beads. Initially, each alumina bead was treated with ethanol and dried in an oven at 35°C for one hour prior to the tribo-electric charging tests. Following charge measurement, the alumina bead was discarded. The inner surfaces of the PTFE capsule was wiped with ethanol and dried. Each test was carried out with a fresh bead. This procedure was repeated a minimum of three times for each tribo-electric charging test and the average value was calculated. It should be noted that there was no breakage of alumina particles during the single particle tests at all three frequencies. The temperature and humidity range during single particle testing was 20.1-24.1°C and 34.1-42.3% RH, respectively.

The experimental results for a single alumina bead tribo-charged at three test frequencies are shown in **Fig. 1**. The charge values for 20 and 30 Hz shaking frequencies are close to each other, whilst those at 10 Hz are distinctly different. At 10 Hz, the time taken to reach the saturation charge is longer. This is most likely due to a smaller number of shaking cycles, as compared with those of the other two frequencies, and consequently to a lower number of particle-wall contacts as well as lower impact velocities. A first-order charging rate equation (Eq. 1) proposed by Hogue *et al.*[12] was fitted to the experimental data by linear regression. The fitted values are summarised in **Table 4**. The results show the charging rate constant is much higher at frequencies of 20 and 30 Hz as compared with that obtained at 10 Hz. For the last frequency, much longer times are required to reach saturation (not shown here).

4.2 Bulk shaking experiments

Two hundred and thirty alumina beads, corresponding to 1.012 ± 0.001 g, were used for bulk tribo-charging tests. These tests were carried out using the exact procedure described for the single bead

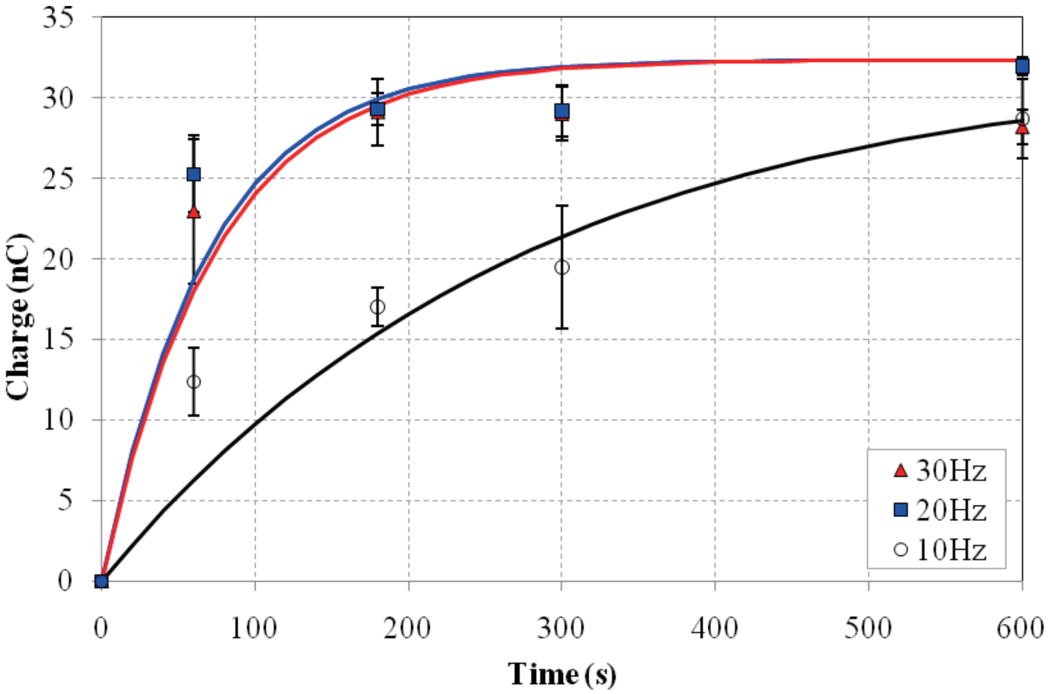

Fig. 2 Charge of 230 alumina beads following tribo-charging at 10, 20 and 30 Hz frequencies – lines show best fit using Eq. 1.

with a PTFE shaking capsule at time intervals of 1, 3, 5 and 10 minutes. A minimum of three runs were performed for each test. The charge on the beads was measured for each run and then averaged. The beads were then weighed to determine any mass loss due to breakage.

The temperature and humidity ranges during bulk particle testing were 20.7-23.3° C and 35.8-47.4% RH, respectively. The experimental results obtained at three test frequencies are presented in **Fig. 2**. Initially, the level of charge measured at 10 Hz was considerably lower than those at 20 and 30 Hz. However, as the length of shaking time is increased, the charge on the beads at the three test frequencies approaches asymptotically a saturated charge level. The saturated charge q_{sat} levels at each frequency are also shown in **Table 4**. As with the single bead results, a first-order charging rate equation (Eq. 1) was fitted to the bulk shaking data by linear regression. The values of the rate constant α for bulk charging are also summarised in **Table 4**. The results show the charging rate constant is lowest at 10 Hz. Interestingly, the value of the charging rate constant is highest at 20 Hz (not 30 Hz) for bulk shaking. This may suggest that at 20 Hz, the bead-wall contact frequency as well as the impact velocity is the highest. This is investigated further using DEM in the next section. Furthermore, it may be noted that the charge on the bulk beads is not 230 times higher than on a single bead. This may suggest that when the beads are shaken in bulk, the probability of individual beads making contact with the capsule walls decreases. There are also other hindering effects due to long-range forces, space charge and image charge at boundaries, as will be considered in the simulation section below.

4.3 Analysis of tribo-electrification inside the container using Distinct Element Method (DEM) - simulation results

Numerical simulations by the distinct element method is used to analyse the tribo-electric charging of an assemblage of particles based on information obtained from charging a single particle in the same device. The effects of long-range forces, space charge and image charge at boundary conditions are investigated.

4.3.1 Calibration procedure

The simulations were performed using the distinct element method, originally proposed by Cundall and Strack[23)] and implemented in PFC^{3D} software (ITASCA). In this method, the interactions between contiguous particles are modelled as a dynamic process and the time evolution of the particles is advanced using an explicit finite difference scheme. The interactions between the constituent particles are based

Table 5 Alumina beads and PTFE wall properties.

Property	Value
Particle diameter	2 mm
Particle friction	0.5
Particle normal stiffness	0.3 MN/m
Particle tangential stiffness	0.25 MN/m
Particle density	1100 kg/m^3
Contact damping factor	0.12
Wall normal stiffness	0.1 MN/m
Wall tangential stiffness	0.082 MN/m
Wall friction	0.5

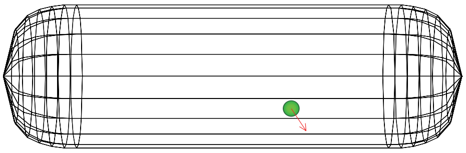

Fig. 3 A single bead inside the shaking capsule[25].

on theories of contact mechanics. In this work, a linear contact model is used to simulate particle-particle and particle-wall interactions. The mechanical properties of the alumina beads were measured[24] and are shown in **Table 5**. The ends of the capsule are designed by arranging five cone frustums around a cylinder positioned in the central region as shown in **Fig. 3**. The stiffness of the PTFE walls is lower than the alumina beads and was estimated using the elastic modulus.

Initially, a single sphere representing an alumina bead was simulated inside the capsule. The capsule was then vibrated at frequencies of 10, 20 and 30 Hz at an amplitude identical to the experimental device (simple harmonic motion). The maximum contact area for every particle-wall contact event was then calculated and recorded, as it is the main factor affecting the charge transfer[3, 4]. For a single contact event, the charge transfer was calculated by the linear relationship (Eq. 2) between the charge transfer Δq and the charge, q, held by the particle just before the contact:

$$\Delta q = \beta \Delta S \left(1 - \frac{q}{q_{sat}}\right) \tag{2}$$

where β is the proportionality constant and ΔS is the maximum contact area, calculated based on the maximum overlap and Hertz analysis. ΔS is the main process parameter affecting the charge transfer[3, 4]. Integration of Eq. 2 for multiple impacts from $q=0$ yields:

$$q = q_{sat}\left(1 - e^{-\beta \sum \Delta S / q_{sat}}\right) \tag{3}$$

For a long time scale, the accumulated maximum contact area can be treated as proportional to the operation time,

$$\sum \Delta S = \gamma t \tag{4}$$

therefore, Eq. 3 can be converted into Eq. 5:

$$q = q_{sat}(1 - e^{-\gamma\beta t / q_{sat}}) \tag{5}$$

This converts the time constant α in Eq. 1 to the accumulated contact area as a function of time, expressing a more practical term of physical event, and provides a basis to analyse the macroscopic charge development on single particles with the aid of DEM simulations. In the calculation, constants β and q_{sat} were fitted parameters obtained from the experimental data.

4.3.2 Bulk simulations

With the calibrated parameters, the simulation procedure was applied to bulk shaking with 230 particles. For a first attempt, the single particle procedure was simply applied without any extensions of electrostatic functions, which will be described in detail later. The results were simply given as 230 times of the single particle cases. However, the trends given by these values did not agree at all with the experimental results obtained (**Fig. 4**, dashed lines).

In the next stage, a number of electrostatic functions were incorporated into the DEM simulations for bulk shaking. These were long-range Coulombic forces, space charge effects, and boundary conditions.

For the boundary conditions, equipotential or conductive conditions on the capsule surfaces were considered. However, this differed from the actual experiments, where the capsule was made of PTFE, a non-conductive polymer, and hence this assumption could have affected the calculation results. This point should be addressed in future investigations. There are a range of options to calculate the electric field distribution inside the capsule. In this work, a charge simulation method was employed with discrete image charge array located outside the capsule.

The electrostatic field was calculated by the superimposition principle, whereby the contributions from every particle charge were added, including the vir-

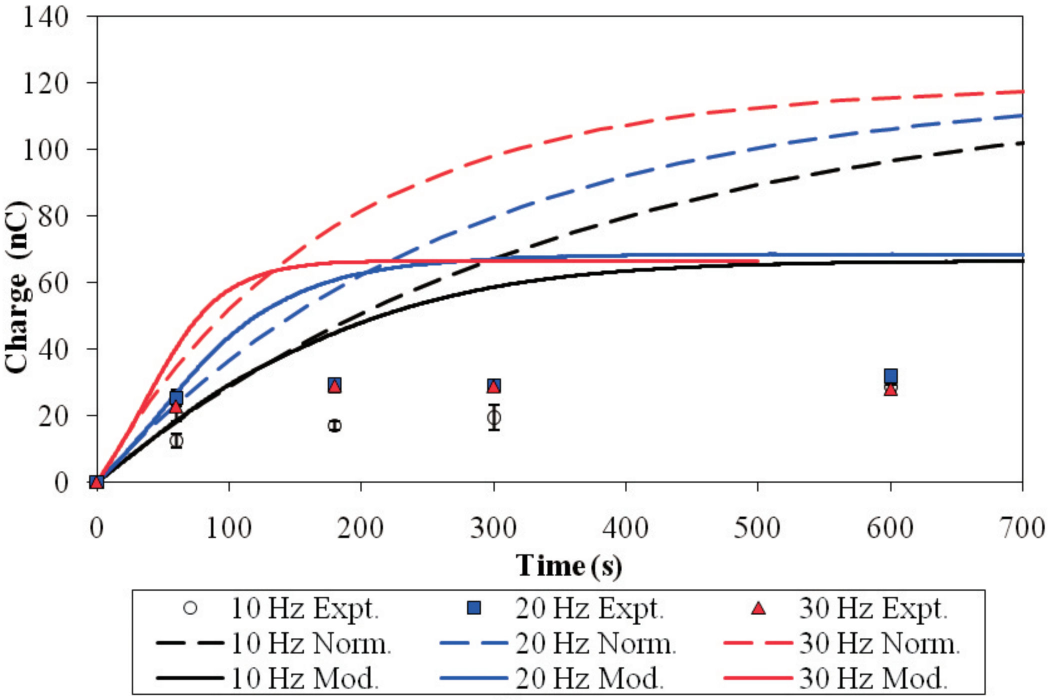

Fig. 4 Comparison of experimental charge accumulation on 230 alumina beads at three test frequencies with simulations predictions, with and without long-range force, space charge and image charge at the boundaries.

tual charges. The resulting electrostatic field affects an object not only by way of the external force (the long-range force) but also in the charge exchange (space charge effect). In the simulation procedure, the long-range force was calculated by Coulomb's law. For the space charge effect, an electric-field-equivalent method was used in which the charge q in Eq. 2 was modified with an additional charge, giving an equivalent field to the external field (space charge effect) at the particle surface.

The results following the incorporation of all the electrostatic functions are shown in **Fig. 4** (solid lines), where a drastic improvement is observed. The level of saturated charge was significantly reduced; however, it is still overestimated. There are several factors that might affect the level of saturated charge such as the boundary conditions. In the simulations, the walls are conductive and do not represent the actual experimental conditions. Additionally, the field-equivalent method used to calculate the space charge effect may be too simplistic. Such factors should be studied in detail in the future. It should also be noted that the long-range force resulted in expansion of the particle bed to some extent due to repulsion; however, the effect of the shaking frequency was more notable and the role of the bed expansion is not clear at this moment.

4.3.3 A comparison of experimental and simulation particle dynamics

Figs. 5.1 – 5.3 illustrate images of 230 alumina bead particles moving at shaking frequencies of 10, 20 and 30 Hz inside the container. The top images are obtained from high-speed video recordings of alumina beads inside a glass container. The bottom images are a product of the simulation work with the level of charge indicated by ball colour, given in the bar under simulated containers. In general, a qualitative comparison of the movement of particles, both from the experimental and simulation results can be achieved. The figures below show the particles moving from the left to right side of the container and back again at 80 seconds of tribo-charging time. The observations from the video recordings reveal two patterns of particle movements. At 10 Hz (**Fig. 5.1**), most of the particles slide along the bottom of the container with a minimal number of particle-wall impacts. However, at 20 Hz and 30 Hz (**Figs. 5.2** and **5.3**), the number of particles impacting on the top wall and becoming airborne increases, respectively. In the simulation results shown in the figures below, the colour variation of the balls and their charge distribution bar are a snapshot in a very narrow time window and represent the minimum charge to the maximum charge in that snapshot; i.e. they do not correspond to the absolute value of charge of the par-

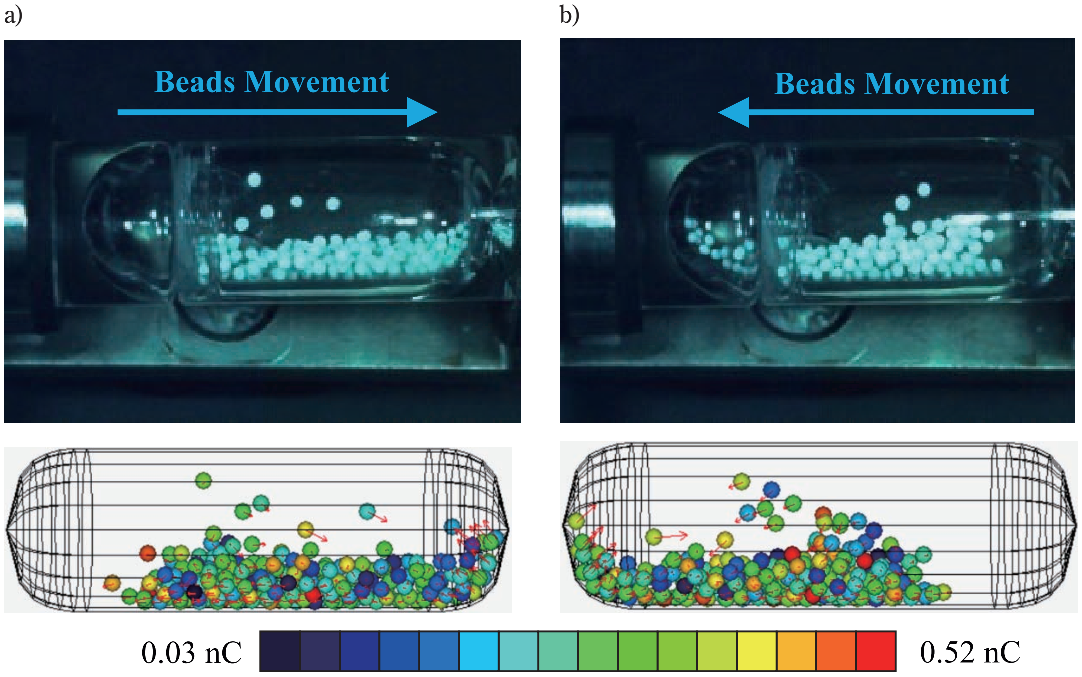

Fig. 5.1 Experimental (top) and simulation (bottom), a comparison of particle movement (time: 80 s, frequency: 10 Hz).

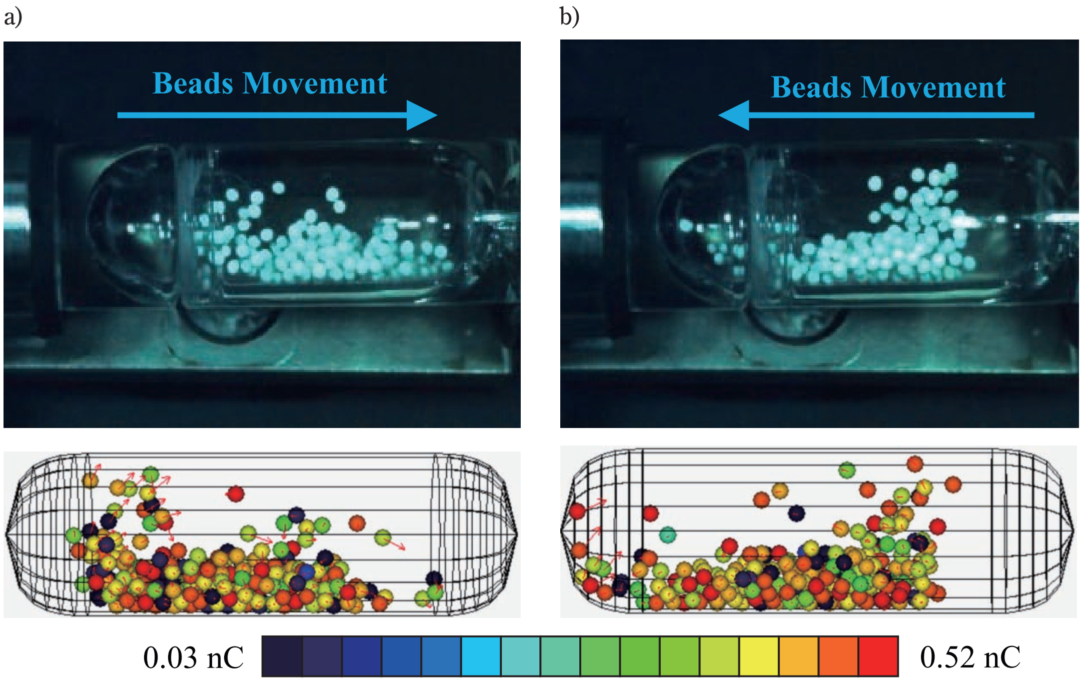

Fig. 5.2 Experimental (top) and simulation (bottom), a comparison of particle movement (time: 80 s, frequency: 20 Hz).

ticles.

As the shaking frequency is increased to 20 Hz (**Fig. 5.2**), a large proportion of the particles impact on the upper walls and rounded ends of the container and the remainder continues to slide along the bottom of the container.

A further increase in frequency to 30 Hz (**Fig. 5.3**) results in most particles impacting rather than sliding on the bottom.

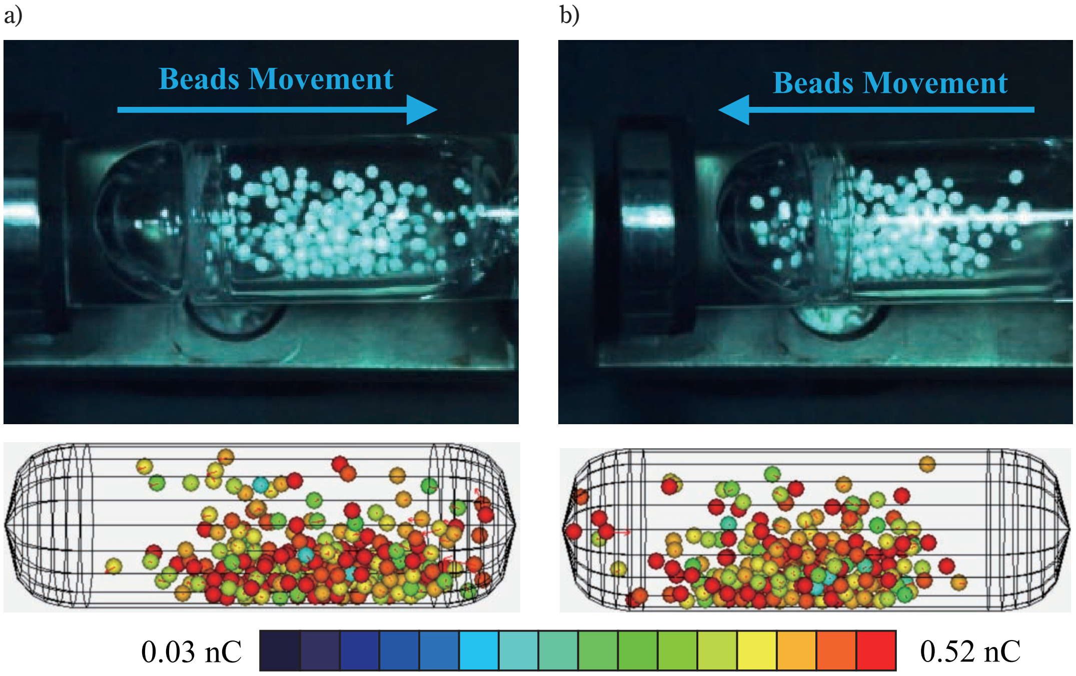

Fig. 5.3 Experimental (top) and simulation (bottom), a comparison of particle movement (time: 80 s, frequency: 30 Hz).

5. Analysis of Segregation Post Tribo-Electrification

A range of α-LM and HPC mass ratios (charging positively against a PTFE container as a result of tribo-electrification) was analysed for the level of material that had adhered to the walls. The particles were tribo-charged using the shaking device and container made from PTFE. The mixture composition post shaking was analysed by dissolution and filtration to determine the proportion of α-LM in comparison to the proportion of HPC. An attempt was made to link the tribo-electric charging tendencies of the selected excipients with the segregation tendencies by comparing the composition of particles adhered to the walls with that of the original formulations.

5.1 Segregation method

Binary mixtures were tribo-charged using the shaking device and the charge was measured by the Faraday cup and an electrometer. The powders were charged inside a PTFE container at 20 Hz. The shaking time was selected based on the time required to reach the saturated charge level for each binary system as shown in **Table 6**. The length of time that each binary mixture was tribo-charged prior to analysing the segregation study depended on the composition ratio of a mixture. A binary mixture was charged at time increments until no further increase in the net charge was measured, i.e. three consistent readings were obtained. At this point, it was anticipated that the charge had reached a saturation level.

The wall-adhered material was then recovered using an electrostatic gun together with a gentle tapping on the outer wall of the shaking container. Scraping the material from the sides was avoided to ensure that no particles were lost or broken. Following tribo-electric charging, the sample from the wall was collected, dispersed in the solvent and filtered. A known amount of wall-adhered mass of α-LM and HPC was dispersed in 50 ml of 2-propanol. The HPC particles dissolved, leaving only α-LM particles dispersed in the liquid. After filtering and drying in the oven at 35° C for one hour, the α-LM particles were weighed. **Table 6** below shows the binary mixture compositions by weight of α-LM and HPC particles. Systems 1 and 7 were used for calibration purposes and were not analysed. Approximately 1 g of pure α-LM was placed in 50 ml of 2-propanol. The dispersion was agitated and left for a period of 72 hours to allow enough time to test the extent of dissolution of the α-LM particles in 2-propanol. After this time, the sample was filtered and dried and the mass of α-LM was measured again. The procedure was repeated three times. The same procedure as above was carried out for the HPC sample including repeats. The HPC sample dissolved completely. The amount of α-LM recovered is slightly less than originally used.

Table 6 The average charge and adhesion of binary mixtures

System	α-LM:HPC	Shaking Time [min]	Q/m [nC/g]	M_i [g]	M_a [g]	$M_{\alpha\text{-LM}}$ [g]	M_{HPC} [g]
1	100:00	45	24.68	1.0018	0.0827	0.0827	-
2	80:20	30	16.67	1.0024	0.0802	0.0764	0.0039
3	60:40	30	14.21	1.0007	0.0757	0.0546	0.0210
4	50:50	20	11.89	1.0021	0.0695	0.0454	0.0241
5	40:60	20	10.49	1.0014	0.0673	0.0332	0.0342
6	20:80	15	5.01	1.0034	0.0552	0.0144	0.0408
7	00:100	10	3.03	1.0025	0.039	-	0.039

M_a: wall adhesion, $M_{\alpha\text{-LM}}$: amount of α-LM in M_a, MHPC: amount of HPC in M_a, Mi: initial mass.

This is less likely to have happened due to α-LM particles dissolving in 2-propanol, but rather due to some fine particles being lost as they adhered to walls following the drying stage.

5.2 Tribo-electrification of binary mixtures

Table 6 above shows the saturated charge-to-mass ratio (Q/m) for each binary mixture following tribo-electrification inside a PTFE container. Q/m decreases with the amount of α-LM present in a binary mixture decreasing. This is expected as the saturated charge measured on pure α-LM particles (24.7 nC/g) following tribo-electrification (inside a PTFE container at 20Hz) and the specific saturation charge are significantly higher in comparison with those measured of HPC (3.0 nC/g) in similar test conditions. The introduction of more α-LM particles into the system increases the chance of α-LM particles impacting on the walls of the shaking container.

In **Table 6**, the mass percentage of α-LM for an ideal mixture measured by the filtration method is shown for each binary mixture system. The amount of particles adhered to walls increases as the α-LM in the initial system is increased. The 80:20 system has the largest difference between the ideal and measured amounts of α-LM, and it is expected that this system will cause the largest extent of segregation in the main mixture.

5.3 Segregation of the main mixture

The level of segregation of the binary mixture in the bulk of the sample and in the powder mixture adhered to the walls of the container was analysed. The term "the main mixture" is used to refer to the mass recovered from the shaking container following tribo-electrification and it excludes the amount of powder adhered to the walls. In contrast, the term "wall-adhered mixture" is used to refer to wall-adhered material only. The change in α-LM concentration in the system can be used as an indicator of the extent of segregation of α-LM in the main mixture (SM). The segregation extent for the main mixture was determined by calculating the ratio between the amount of α-LM recovered at the end of tribo-electrification and the amount of α-LM initially used for each sample, as shown by:

$$S_M = 1 - \frac{\text{Conc.of } \alpha-\text{LM in the main mixture after}}{\text{Conc.of } \alpha-\text{LM in the main mixture before}} \quad (6)$$

An extent of segregation that is equal to one indicates a fully segregated system, whilst a value of zero indicates a system where no segregation has taken place. Therefore, an increase from zero indicates that more α-LM particles have adhered to the container walls and this indicates that the binary mixture has undergone segregation. In **Fig. 6**, the extent of segregation of α-LM in the main mixture is shown as a function of the charge-to-mass ratio. Despite the data scatter, a clear trend is observed. With higher charge-to-mass ratios, the extent of segregation is increased, which implies that the tendency of a binary mixture to segregate is adversely affected by tribo-electric charging of the mixture. However, the extent of segregation is relatively small (below 0.1).

5.4 Segregation of the wall-adhered mixture

In order to determine the extent of segregation of α-LM on the wall (SW), the following equation was used:

$$\left| SW \right| = 1 - \frac{(\text{Amount of } \alpha-\text{LM present on walls})}{\text{Ideal amount of } \alpha-\text{LM on wall}} \quad (7)$$

Fig. 7 shows the extent of segregation of the-wall adhered mixture as a function of the amount of α-LM in a binary mixture. The results show that the extent of segregation of α-LM decreases with an increase in the amount of α-LM present in a binary mixture. This is expected because an increase in the α-LM concen-

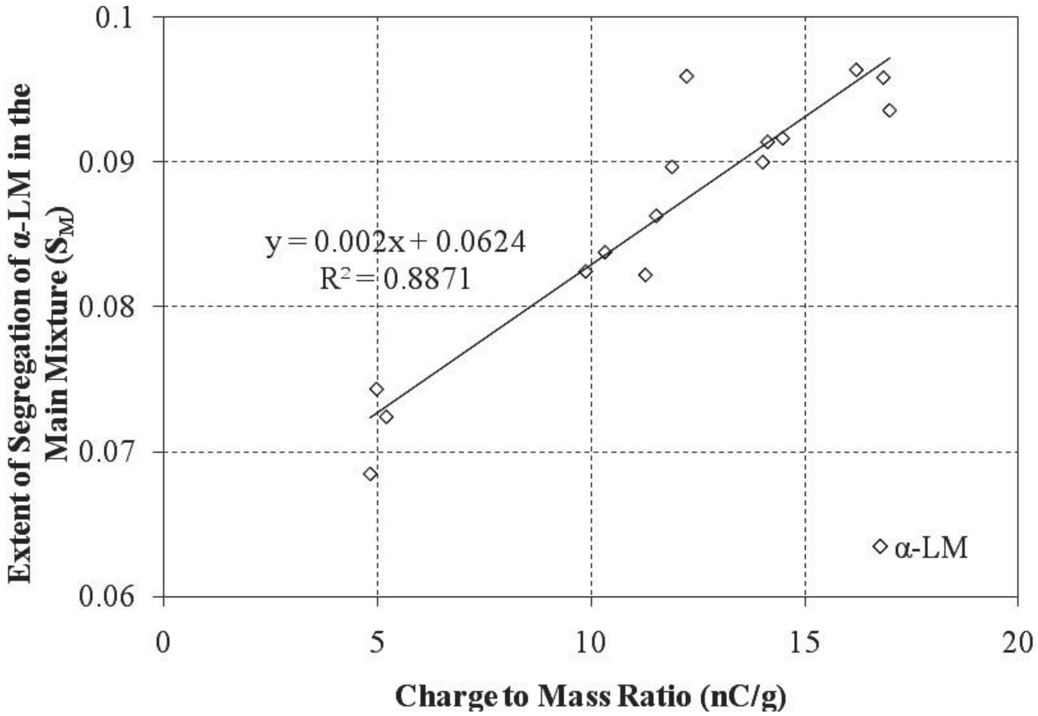

Fig. 6 The extent of segregation of α-LM in the main mixture as a function of the charge-to-mass ratio.

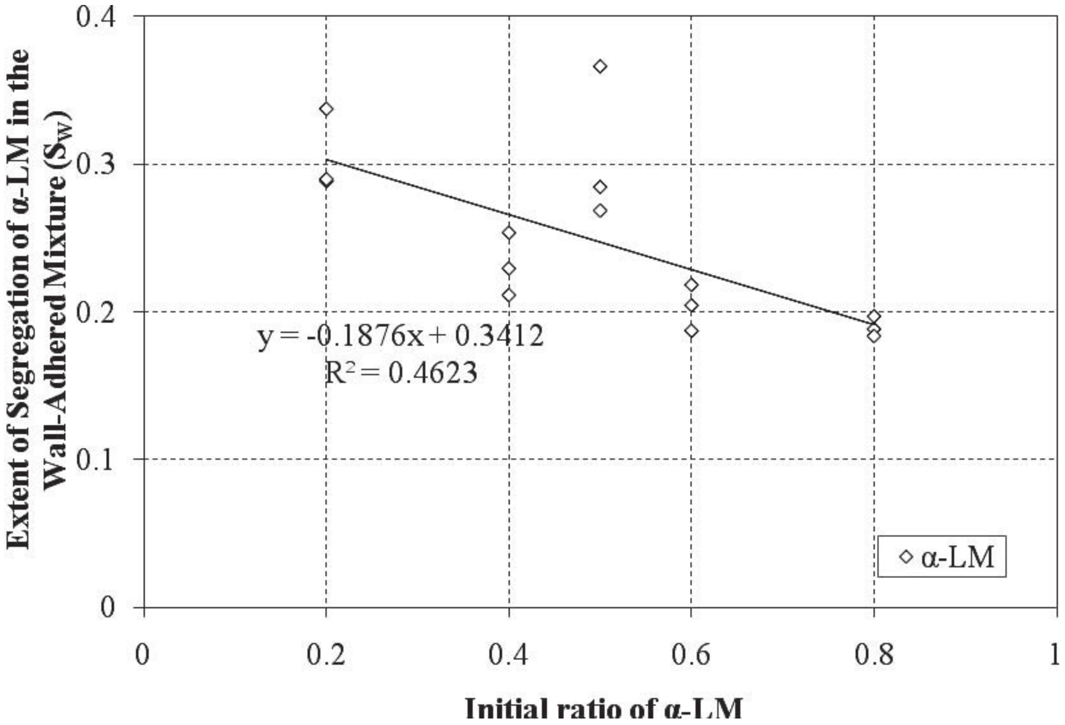

Fig. 7 Extent of segregation of α-LM in the wall-adhered mixture as a function of the initial ratio of α-LM.

tration in the mixture causes segregation to approach zero asymptotically. The extent of segregation in the wall-adhered powder mixture is remarkable and, in some instances, this value is over 0.3. However, even though the extent of segregation is high on the wall-adhered material, when considering the whole of the mixture, the extent of segregation is less than 0.1. Nevertheless, in an industrial context such as the pharmaceuticals industry, end products of high purity and good content uniformity are essential. The variations of components within a binary mixture adhered to walls play a significant role in the content uniformity. The mixture which is built up on the walls of the process equipment due to tribo-electric charging may fall off under its own weight due to gravity and upset the formulation. This phenomenon can take place further down the processing line, after the mixing and blending stages, leading to the formation of aggregates on the walls. These aggregates may be segregated and if falling into the main mixture at the packaging stage, they will cause a transient change in the mixture composition, thus having an immense and adverse impact on the content uniformity.

6. Conclusions

A new methodology has been developed for characterisation of the tribo-electric charging properties of powder materials. α-LM and HPC powders were used as model materials. The tribo-electric charging and segregation due to preferential wall adhesion were analysed. Furthermore, a simulation model based on the distinct element method was developed to predict the dynamic charging of bulk powders inside a shaking container. The key conclusions are summarised as follows:

- The tribo-electrification propensities of α-LM, HPC and a 50:50-by-weight binary mixture of the two powder materials were characterised by a mechanical shaking test method.

- All three powders charge positively against the PTFE container at all frequencies. The highest magnitude of charge observed at all three frequencies was with α-LM. The results show that the saturated charge is independent of the shaking frequency. Increasing the shaking frequency decreases saturation time, as intuitively expected. The charging trend follows a first-order rate process. All three test powders charge negatively against stainless steel and glass. The magnitude of charge is low compared to PTFE and is lowest against stainless steel.

- High-speed video recording was used to observe particle motion at different frequencies. The results show that particle motion can be classified into two types of flow regimes, i.e. sliding and impact. At the lowest frequency, the particle movement is mainly by the sliding of the powder bed. At intermediate frequency, particles are divided between sliding at the bottom of the bed and impacting on the ends and upper wall of the container. At the highest frequency, the particles seem to be more suspended.

- Tribo-electrification of spherical beads inside a horizontally shaken sealed capsule was analysed experimentally and simulated using a DEM model. An empirical first-order rate equation, based on experimental data obtained from a single particle charging rate, was incorporated in the DEM simulations. It was found that the model significantly overestimates the total charge build-up for bulk shaking, as compared with the experimental results. However, the inclusion of long-range forces, space charge effects and boundary conditions into the DEM model significantly improves the prediction of total charge build up.

- The results of the segregation analysis show that the extent of segregation in the main mixture increases linearly with an increase in the amount of α-LM and consequently with the net charge on binary mixtures. The extent of segregation is highest in the 80:20 and lowest in the 20:80 ratio binary mixtures. However, the extent of segregation does not exceed 0.1 when the main mixture is considered. The extent of segregation measured for the wall-adhered mixtures shows an opposite trend to that of the main mixture, i.e. decreasing linearly with the amount of α-LM increasing in the binary mixture. In this case, the extent of segregation is considerably higher than that of the main mixture with the highest value being 0.31 for the 20:80 ratio mixtures and the lowest of 0.19 for the 80:20 ratio mixtures.

It may be concluded that tribo-electric charging of powders can be carried out by the shaking container evaluated in this work. It can be used to quantify the electrostatic charge interactions between pharmaceutical powders and equipment surfaces. The interactions between particles and walls, which often result in particles adhering to walls, are relevant to many pharmaceutical operations. An understanding of the charge magnitude and polarity of pharmaceutical powders due to contact with containing surfaces is useful in the development of pharmaceutical formulations, where excipients and APIs are mixed together, as otherwise particles can be lost through particle-wall adhesion and could possibly cause segregation problems during mixing processes.

Acknowledgements

The authors would like to acknowledge Merck Sharpe & Dohme (MSD) and the Engineering and Physical Sciences Research Council (EPSRC) for their financial support. The authors would like to thank Dr Kendal Pitt, who coordinated the project when he was with MSD, and Dr Christian Seiler of MSD for his sound ideas, stimulating discussions and advice.

References

1) Šupuk, E., Antony, J., Seiler, C., and Ghadiri, M. (2007): "Charge Generation Due to Shear Deformation of Pharmaceutical Powders", *PARTEC 2007*, Nuremberg.
2) Watanabe, H., Ghadiri, M., Matsuyama, T., Ding, Y., Pitt, K.G., Maruyama, H., Matsusaka, S., and Masuda, H. (2007): "Triboelectrification of Pharmaceutical Powders by Particle Impact", International Journal of Pharmaceutics, 334, pp.149-155.
3) Matsusaka, S., Ghadiri, M., and Masuda, H. (2000): "Electrification of an Elastic Sphere by Repeated Impacts on a Metal Plate", Journal of Physics. D: Applied Physics, 33, pp.2311-2319.
4) Matsuyama, T. and Yamamoto, H. (1996): "Charge relaxation process dominates contact charging of a particle in atmospheric conditions II. General model", Journal of Physics D: Applied Physics, 30, pp. 2170–2175.
5) Matsusaka, S., Maruyama, H., Matsuyama, T., and Ghadiri, M. (2010): "Triboelectric Charging of Powders: A Review", Chemical Engineering Science, 65, pp.5781-5807.
6) Nomura, S. and Tanaka, T. (1992): "Theoretical Analysis of Dust Explosions", Powder Technology, 71, pp.189-196.
7) Matsusaka, S., and Masuda, H. (2003): "Electrostatics of Particles", Advanced Powder Technology, 14, pp.143-166.
8) Rowley, G. (2001): "Quantifying Electrostatic Interactions in Pharmaceutical Solid Systems", International Journal of Pharmaceutics, 227, pp.47-55.
9) Šupuk, E., Seiler, C and Ghadiri, M. (2009): "Analysis of a Simple Test Device for Tribo-Electric Charging of Bulk Powders", Particle and Particle Systems Characterization, 26, pp.7-16.
10) Staniforth, J.N., and Rees, J.E. (1981): "Powder Mixing by Triboelectrification", Powder Technology, 30, pp.255-266.
11) Greason, W.D. (2000): "Investigation of a Test Methodology for Triboelectrification", Journal of Electrostatics, 49, pp.245-256.
12) Hogue, M.D., Calle, C.I., Weitzman, P.S. and Curry D.R. (2008): "Calculating the Trajectories of Triboelectrically Charged Particles using Discrete Element Modeling (DEM)", Journal of Electrostatics, 66, pp.32-38.
13) Greason, W.D. (2000): "Investigation of a Test Methodology for Triboelectrification", Journal of Electrostatics, 49, pp.245-256.
14) Dascalescu, L., Urs, A., Bente, S., Huzau, M. and Samuila, A. (2005): "Charging of mm-size Insulating Particles in Vibratory Devices", Journal of Electrostatics, 63, pp.705-710.
15) Eliasen, H., Kristensen, H.G., Schaefer, T. and Greason W.D. (1999): "Electrostatic Charging during a Melt Agglomeration Process", International Journal of Pharmaceutics, 184, pp.85-96.
16) Engers, D.A., Fricke, M.N., Storey, R.P., Newman, A.W., Morris, K.R. (2006): "Triboelectrification of Pharmaceutically Relevant Powders during Low-shear Tumble Blending", Journal of Electrostatics, 64, pp.826-835.
17) Matsusaka, S., Umemoto, H., Nishitani, M., and Masuda, H. (2002): "Electrostatic Charge Distribution of Particles in Gas-Solids Pipe Flow", Journal of Electrostatics, 55, pp.81-96.
18) Zarrebini, A., Ghadiri, M., Dyson, M., Kippax, P., and McNeil-Watson, F.K. (2011): "Tribo-electrification of Powders due to Dispersion", Electrostatics 2011-13th International Conference on Electrostatics, IOP, Bangor.
19) Calin, L., Mihalcioiu, A., Iuga, A. and Dascalescu, L. (2007): "Fluidized Bed Device for Plastic Granules Triboelectrification", Particle Science Technology, 25, pp.205-211.
20) Inculet, I.I., Castle, G.S.P. and Brown, J.D. (1998): "Electrostatic Separation of Plastics for Recycling", Particle Science Technology, 16, pp.91-100.
21) Ban, H., Schaefer, J.L., Saito, K., and Stencel, J.M. (1994): "Particle Tribocharging Characteristics Relating to Electrostatic Dry Coal Cleaning", Fuel, 73, pp.1108-1113.
22) Nesterov, A., Loeffler, F., Konig, K., Trunk, U. Leibe, K., Felgenhauer, T., Stadler, V., Bischoff, R., Breitling, F., Lindenstruth, V. and Hausmann, M. (2007): "Non-contact Charge Measurement of Moving Microparticles Contacting Dielectric Surfaces", Review of Scientific Instruments, 78, pp.075111.
23) Cundall, P.A. and Strack, O.D.L. (1979): "A Discrete Numerical Model for Granular Assemblies", Geotechnique, 29, pp.47-65.
24) Couroyer, C., Ning Z. and Ghadiri, M. (2000): "Distinct Element Analysis of Bulk Crushing: Effect of Particle Properties and Loading Rate", Powder Technology, 109, pp.241-254.
25) Matsuyama, T., Šupuk, E., Ahmadian, H, Hassanpour, A. and Ghadiri, M (2009): "Analysis of Tribo-Electric Charging of Spherical Beads Using Distinct Element Method", Powders and Grains 2009, AIP, New York, pp.127-130.

Author's short biography

Enes Šupuk

Dr Enes Šupuk obtained his BEng in chemical engineering in 2005 and a PhD in 2009, both from the University of Leeds. Enes is currently working as a Knowledge Transfer Partnership (KTP) Associate in collaboration between the University of Leeds and Bristol-Myers Squibb (BMS) Pharmaceuticals Limited. He is working on investigating the scope for direct compression and variability of the dosage forms by developing an electrostatic portfolio for BMS in-house compounds.

Ali Hassanpour

Dr Ali Hassanpour graduated in chemical engineering from Sharif the University of Technology, Tehran, in 1997. He obtained his PhD from the University of Leeds in 2004 where he continued his research as a post-doctoral research fellow, working on a number of projects. In 2010 Ali was appointed a lecturer in petroleum engineering at the Institute of Particle Science and Engineering of the University of Leeds. Ali's research has mainly focused on modelling and experimental work in various areas of particle science and engineering.

Hossein Ahmadian

Dr Hossein Ahmadian completed BEng and PhD degrees in chemical engineering at the University of Leeds. After graduation from university, Hossein worked as a Knowledge Transfer Partnership (KTP) Associate in a collaborative partnership between the University of Leeds, Procter and Gamble, the Enzyme Dust Consortium and Hosokawa Micron, developing a novel granule strength test device. He is currently working for Procter and Gamble at Newcastle Technical Centre and his research interests are attrition and milling, granulation, powder flowability, triboelectrification of powders and Discrete Element Method (DEM) modelling.

Tatsushi Matsuyama

Professor Tatsushi Matsuyama is at the Department of Environmental Engineering for Symbiosis, Faculty of Engineering, Soka University. He graduated from the Department of Chemical Engineering at the University of Tokyo in 1987. He received a PhD degree in chemical engineering from the University of Tokyo in 1995, with his thesis on the mechanism of impact charging of single particles. Since then, he has been researching in the field of powder technology, and his major research interest is in the areas of powders and electrostatics. He spent two sabbaticals as a visiting researcher at Delft University of Technology, the Netherlands, with Prof. Brian Scarelett's group in 1998, and at the Institute of Particle Science and Engineering, the University of Leeds, UK, with Prof. Mojtaba Ghadiri's group in 2007.

Mojtaba Ghadiri

Professor Mojtaba Ghadiri is director of the Institute of Particle Science and Engineering, University of Leeds. His research area is in engineering science of processes involving particulate matter such as attrition, comminution, agglomeration, dispersion, compaction, nanopowder processing, electrical effects, mechanics of particle motion and super-critical fluid processing. The focal point of his work is the development of relationships between microscopic and macroscopic properties and phenomena; i.e. the way in which the microstructure of particulate solids and the micromechanics of their behaviour in process equipment influence the performance of the process and the characteristics of the product.

The Investigation of Breakage Probability of Irregularly Shaped Particles by Impact tests†

Sergej Aman*[1], Jürgen Tomas[1], Peter Müller[1], Haim Kalman[2], Yevgeny Rozenblat[2]
Mechanical Process Engineering, The Otto-von-Guericke University[1]
Laboratory for Conveying and Handling of Particulate Solids, Department of Mechanical Engineering, Ben-Gurion University of the Negev[2]

Abstract

The modelling of experimental distributions of breakage energy by compression and impact was carried out. In terms of our model, the part of the particle that is directly contacted with the stressing tool is admitted into the equation as a hemispherical asperity with known breakage energy distribution. The main contribution of stressing energy is accumulated by this hemispherical asperity that is responsible for crack generation and particle breakage. The breakage probability distribution of particles is calculated as a superposition of the breakage probabilities of asperities. Based on geometrical similarity, one can assume the same normalized log-normal size distribution of asperities for all tested particles of a given material. As a result, all experimental distributions of normalized breakage energy can be fitted with the same log-normal function for all particle sizes.

Keywords: particle breakage, compression, impact, breakage probability

1. Introduction

A complete description of physical phenomena that occur during particle breakage is not yet available. Especially difficult is prediction of the stressing and breakage parameters of irregularly shaped particles. For example, breakage is history-dependent, i.e. the number of micro-cracks and dislocations increases due to previous stressing events[1-5]. As a result, the mechanical properties and breakage parameters vary by testing the geometrically similar particles of the same size. The breakage probability that depends on the particle properties and stressing parameters was introduced to describe the breakage behaviour of particles. Two approaches are commonly applied to obtain the breakage probability as a percentage of the number of broken particles.

The first one is an energy approach that uses the particle fracture energy to calculate the breakage probability. The results obtained by compression, impact and shear tests can be compared using the mass-related breakage energy.

The second one is the stress or breakage force approach. This approach operates by applying stress to individual particles. The stress approach includes material properties such as stiffness, strength or hardness[6]. The breakage probability depends on the resulting force acting on the contact area, i.e. three-dimensional particle contact stress distribution. However, it is not necessary to consider the mechanical behaviour in detail before breakage.

The relationship between breakage energy distribution and force distribution by compression test was investigated by Aman et al.[7]. Every distribution was normalized by a mean arithmetic value of breakage energy or force, respectively. The dimensionless normalized distributions were fitted with log-normal functions. A correlation between the force distributions and energy distributions was observed. That means that the fit function of the normalized force distribution can be transformed into the fit function of the normalized energy distribution and vice versa. The equations that connect the parameters of both fit distribution functions are linear. The coefficients in these equations are constant. They do not depend on particle size and material properties. This invariant transformation of distribution can be based on the existence of two universal normalized distributions

---

† Accepted: September 12th, 2011
[1] Universitatsplatz 2, D-39 106 Magdeburg, Germany
[2] P.O. Box 653, Beer Sheva 84105, Israel
* Corresponding author:
E-mail:sergej.aman@ovgu.de
TEL: (+49)391-6712190 FAX: (+49)391-6712190

© 2011 Hosokawa Powder Technology Foundation

– force and energy. Both normalized distributions are independent of particle size and material. Consequently, the equations that connected the parameters of both fit functions remain the same.

Before the compression test one puts the particle on the plate. In all probability, an irregularly shaped particle takes an initially stable position on this plate that corresponds to the equilibrium state of the particle. In this case, the orientation of the particle to the stressing piston is not random. The top of the particle with its low cross-section will make contact with the piston first, see **Fig. 1**. The cross-section of the particle increases with distance from the contact area, i.e. the internal compressive stress or pressure is reduced with distance to the contact plane. That means that not all the volume of the particle is effectively involved in the initiation of fracture. The universal form of both distributions observed by compression test may be caused by this orientation of the particle. In this context, it is interesting to investigate the impact loading where the stressing occurs by random orientation of the irregular particle to the target, i.e. the stressing tool. Its basic assumptions of the developed model are valid not only for compression but also for impact loading, then the normalization by mean energy leads to a universal form of breakage energy distribution.

Generally speaking, when comparing the impact and compression loading, one has to take into account that the deformation and breakage performance can be dependent on the strain rate. However, the strain rate effects are often associated with the propagation of elastic waves within the particle during quick loading. However, Gildmeister and Schönert demonstrated that wave effects do not play any significant role in the brittle particle breakage behaviour at breakage rates up to 100 m/s[8)]. Tavares and King used the quasi-static approach to calculate the breakage probability by using double impact test equipment[4,5,9)].

On the other hand, Salman and Gorham investigated the variation forms of particle damage depending on particle diameter and impact velocity[10)]. At the lowest velocities, fractures occur mainly due to a brittle-elastic response, with typical Hertzian ring and cone crack systems. At the higher impact velocities, the deformations become more inelastic. This leads to characteristic patterns of fragmentation due to radial, lateral and median cracks.

The breakage behaviour of individual particles with given mechanical properties and shapes by impact and compression can be calculated using sophisticated numerical methods such as DEM (Discrete Element Method)[11,12)]. However, the practical application of any computer simulation to a large assembly of particles without any coupling with statistical methods is restricted due to a difference of particle properties and shapes. In this case, the complex statistical nature of particle fracture and the large difference in particle properties result in an enormous increase of calculation time.

According to this fact, it is interesting to investigate the breakage energy distribution by impact loading. A universal normalized distribution function will be found and applied to reduce the calculation time by the characterisation of breakage behaviour of particles in impact grinding machines.

2. Hemispherical Approach

In particle mechanics, one scaling problem deals with the effect of the particle size and form on its breakage probability[6)]. In terms of irregularly shaped particles, the theoretical investigation of scaling is restricted due to complex stress distribution in the contact area and within the particles. However, ac-

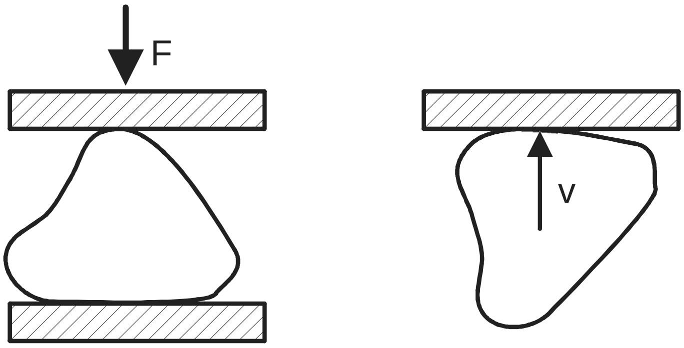

a) Compression a) Impact

Fig. 1 Particle orientation by compression (a) and impact (b).

cording to the dimensional analysis carried out by Rumpf[13)], a similar breakage pattern is expected at a constant ratio of elastic stored energy per unit particle volume W_V and initial particle diameter d:

$$d \cdot W_V = const \qquad (1)$$

or

$$a_R = \frac{W}{d^2} \qquad (2)$$

The similarity of breakage patterns at constant stressing intensity parameter a_R was successfully tested by the compression and impact of glass beads, quartz and limestone, and cement clinker[14)]. The particle size distribution $Q_3(d)$ after breakage, the so-called breakage function, was found to be a size-independent function of parameter W/d^2 that depends only on material properties. The detailed investigation of the relationship between fracturing energy and resulting fragment size distribution was carried out by Baumgardt et al.[15-17)].

Based on Rumpf's similarity principle, Weichert[18,19)] introduced the Weibull statistics[20)] to the field of comminution to describe the breakage probability of brittle spheres. The breakage probability P can be described as a function of mass-related energy W_m:

$$P = 1 - \exp(-cd^2 W_m^z) \qquad (3)$$

with constants c and Weibull exponent z. For the glass spheres with 4 mm diameter, z = 2.8 and c = $5.57 * 10^4$ $(\mathrm{kg/J})^{2.8}$ m^{-2}.

Antonyuk et al.[21,22)] performed single granule impacts to study the breakage behaviour of granules. The deformation behaviour was explained with the help of the particle caps contact model[23,24)]. The breakage probability was approximated by the use of Weichert's approach[19)]. The results conform to two-dimensional discrete element simulations of the particle deformation by impact.

Salman et al.[10,25,26)] conducted many research projects on the breakage rate of particles due to impact. He found a simple function of the impact velocity v that is based on a Weibull statistic[20)] and that provided a very close fit to most of his experimental

$$P = 1 - \exp\left(-\left(\frac{v}{v_0}\right)^m\right) \qquad (4)$$

with fit parameters v_0 and m. For aluminium oxide particles, v_0 = 19.5 m/s and m= 7.4.

The Eqs. (3-4) were originally introduced to calculate the breakage probability of spherical particles. For irregularly shaped particles, a distribution function of breakage probability is not precisely defined due to its sensitivity to particle shape. However, Tavares and King[5)] investigated the influence of particle shape on the fracture characteristics of quartz particles tested in the impact load cell. They demonstrated that the particle strength and stiffness decrease significantly as the particle shape becomes more irregular, whereas particle fracture energy is not significantly affected. In this context, it is interesting to test the fracture energy as a possible variable to calculate the breakage probability for irregularly shaped particles.

According to May, Baumgart, Buss and Schubert[27-30)], the breakage probability distribution of the irregularly shaped particles can be fitted with the log-normal distribution function:

$$P(X) = \frac{1}{\sigma_{\ln,x} \cdot \sqrt{2 \cdot \pi}} \cdot \int_0^x \exp\left[-\frac{1}{2} \cdot \left(\frac{\ln t - \mu_{\ln,x}}{\sigma_{\ln,x}}\right)^2\right] d(\ln t) \qquad (5)$$

In terms of breakage work $X=W_{m,break}$, where $W_{m,break}$ is the mass-related breakage work and $\mu_{\ln,X}$ and $\sigma_{\ln,X}$ are distribution parameters.

The breakage probability is a dimensionless function from physical variables. To calculate the breakage probability, it is necessary to represent the physical variables in a dimensionless form. For example in Eq. (3), the mass-related energy is divided by a combination of parameters with the unit of [J/kg]. A similar normalization procedure of impact velocity is presented in Eq. (4). It is necessary to represent the breakage probability as a function of the dimensionless breakage energy, i.e. in a form similar to Eqs. (3-4). Consequently, a relevant characteristic parameter with units of energy will be introduced. Let us consider the relationship between the characteristic breakage parameters in Eqs. (3-4) and the mean breakage energy. We will show that the arithmetic mean of breakage energy W_{mean} can be used as a relevant characteristic energy for those equations.

The mean value $W_{m,mean}$ of mass-related breakage energy can be calculated from probability distribution as follows[31)]:

$$W_{m,mean} = \int_0^\infty \left(\frac{dP}{dW_m}\right) W_m dW_m \qquad (6)$$

By using Weichert's approach, the breakage probability is calculated according to Eq. (3):

$$W_{m,mean} = \left(\frac{1}{cd^2}\right)^{\frac{1}{z}} \Gamma\left(\frac{1}{z}+1\right) \quad (7)$$

where Γ (1/z+1) is a gamma function from exponent *z*. By varying exponent z in a relevant interval between 1.5 and 2.5, see Weichert[18], the gamma function varies slightly from 0.885 to 0.905. In the future consideration, the gamma function will be assumed to be constant and equal to 0.9. Then the breakage probability distribution can be rewritten as:

$$P = 1 - \exp\left(-cd^2 W_m^z\right) = 1 - \exp\left(-\left(\frac{0.9 \cdot W_m}{W_{m,mean}}\right)^z\right) \quad (8)$$

For spherical particles with a narrow size distribution:

$$\frac{W_m}{W_{m,mean}} = \frac{W}{W_{mean}} \quad (9)$$

$$P = 1 - \exp\left(-\left(\frac{0.9 \cdot W}{W_{mean}}\right)^z\right) \quad (10)$$

As a result, the breakage probability is a function of the ratio between the breakage energy *W* and the arithmetic mean of the breakage energy W_{mean}. A similar transformation of the breakage probability function can be carried out for Eq. (4). As result, the direct dependence of *P* on particle size *d* disappears, see Eq. (10).

3. Simulation of Breakage Probability Distribution

The elastic-plastic contact behaviour of particles is modelled by means of hemispherical asperities or caps[23,24]. In terms of this model, the part (cap) of the irregularly shaped particle that is directly contacted with the stressing tool is admitted into the equation as a hemispherical asperity. This “directly contacted” particle cap is mainly stressed. Consequently, it is responsible for crack generation by stressing[7]. This fact can be used to calculate the breakage probability of particles based on equations formerly introduced for spherical particles. The breakage behaviour of *N* irregularly shaped particles of size *d* is seen statistically as common breakage behaviour of a combination of *N* hemispherical asperities of sizes $d_{r,i}<d$. The appearance frequency of asperities can be calculated from the asperity size distribution, i.e. the shape distribution of the particles. The breakage probability of particles of size *d* will be found as the sum of breakage probabilities of individual asperities divided by the number *N*. The irregularly shaped particles will show a similar contact and breakage behaviour for samples with a similar shape distribution. We will show that the breakage probability distribution is strongly affected by the size distribution of asperities.

It is difficult to find the relevant mass of stressed caps (asperities) to calculate the mass-related breakage energy. Based on this detail, we prefer to use the breakage energy (not mass-related) as an essential variable to describe the deformation and breakage behaviour of particles.

In terms of irregularly shaped particles, the breakage behaviour of *N* particles of a given size d will be simulated statistically as the breakage behaviour of a combination of *N* hemispherical asperities of sizes $d_{r,i}$. It was assumed that the sizes of asperities are distributed between d_{min} and *d*. The lower size limit of $d_{min}=(0.1)^{1/3}d$ was chosen due to the definition of breakage. According to the definition, the breakage occurs as soon as the mass loss of the particle is more than 10% of its initial mass[32]. The masses of small asperities of size $d_{r,i}<d_{min}$ are under this limit. They cannot satisfy the breakage condition. Consequently, the small asperities were not taken into account by simulation.

The size distribution of asperities corresponds to the size distribution of particle caps directly contacted by the stressing tool. It is expected that the particles are self-similar regarding the size scale. In other words, the caps of the particles are geometrically similar to the whole particles. Usually, the size distribution of irregular particles is the log-normal distribution[33]. Consequently, one can assume that the size distribution of caps, i.e. of asperities, is the log-normal distribution function.

The breakage probability of irregularly shaped particles of size *d* will be simulated by means of the following method. All we need to do is follow the five simple steps listed below:

1. The sizes of *N* asperities were generated as log-normal distributed numbers $d_{r,i}$ $d_{min}<d_{r,i}<d$ with $1 < i < N$ and $d_{min}=(0.1)^{1/3}d$.
2. The mean mass-related breakage energy $W_{m,mean}$ was calculated for spherical particles of diameter *d* , see Eq. (7).
3. The mean breakage energy was found from the mean mass-related breakage energy $W_{m,mean}$:

$$W_{mean} = W_{m,mean} \cdot \pi \cdot d^3 \cdot \rho/6 \quad (11)$$

For the future simulation, we have to establish the interval of stressing energy *W* that is applied to the particle. In our calculations, the stressing energy *W* varies in range from 0 to $3W_{mean}$ with step of $0.001W_{mean}$.

4. The breakage probabilities of the asperity of size $d_{r,i}$ were calculated according to Eq. (3) at every value of W (3000 values). To obtain the mass-related energy of asperity W_m, the stressing energy W was divided by the mass of a spherical particle (asperity) of size $d_{r,i}$. It is assumed that all the stressing energy applied to the particle of size d will be stored in the asperity.
5. To obtain the breakage probability distribution of irregular particles, the breakage probabilities of individual asperities were summarized at every value of kinetic energy and divided by the number of asperities.

$$P(W) = \frac{1}{N}\sum_{i=1}^{N}\left[1-\exp\left(-\left(0.9\cdot\frac{W\cdot d^3}{W_{mean}\cdot d_{r,i}^3}\right)^z\right)\right] \quad (12)$$

Fig. 2. shows the log-normal size distribution of asperities that corresponds to the distribution of asperities that describe the form of the irregularly shaped particles of size $d=6$ mm. Only the asperities in a size range from 2.78 mm to 6 mm were taken into account by the breakage simulation.

The breakage energy distribution normalized by W_{mean} was calculated for the spherical particles of size $d=6$ mm, see **Fig. 3**. According to Weichert[18], the Weibull exponent z varies between 1.5 and 2.7 for relevant materials. Based on this fact, the three values of z (lower - 1.5, middle - 2, and upper - 2.7) were used for the simulation. One can see that the distribution of breakage probability P is strongly affected by exponent z. The influence of exponent z is especially significant at the lower energy value. As mentioned above, see Eq.(10), the dependence on the particle size d disappears due to normalization of the breakage energy. In terms of normalized breakage energy, the calculated dependence on z reflects only the variance in particle material properties.

The resulting distribution after calculation of the breakage probability, see Eq. (12), is affected by the size distribution of the asperities. Especially at low energy, the influence of size distribution becomes significant. Indeed, at a given stressing energy, the fine asperities exhibit a higher breakage probability compared to large ones. One can assume that at a given energy W, the breakage probability $P \sim 1$ for all asperities of size:

$$d_{r,i} \le d\cdot(W/W_{meam})^{\frac{1}{3}} \quad (13)$$

Consequently, the breakage probability at low stressing energy will be proportional to the number of all particles of a size lower than $d_{r,i}$. That means that the probability distribution at low energy values is similar to the size distribution of asperities. However, the size distribution of asperities doesn't depend on exponent z. Indeed, the influence of exponent z on the probability distribution becomes less significant for irregular particles compared to single particles, see **Fig. 4**. The distribution obtained due to simulation is shifted to low energy values.

Another interesting result of simulation is that the distribution can be fitted by a log-normal distribution function. **Fig. 5**. shows the log-normal fit of distribution obtained for a combination of asperities at $z=2.7$. The coefficient of determination R^2 (R-square) is about 0.9996. This result is in agreement with the fact that many authors prefer the log-normal distribution to fit the breakage probability[4,27-30].

To test the relevance of the asperities model, the

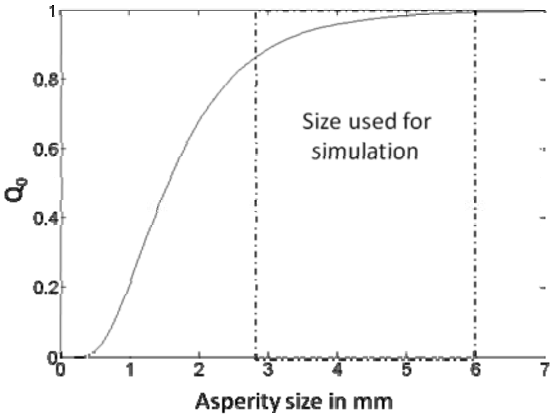

Fig. 2 Size distribution of asperities. Particle size $d=6$ mm. The asperities in a size range from dmin=2.78 mm to 6 mm were used for the breakage simulation.

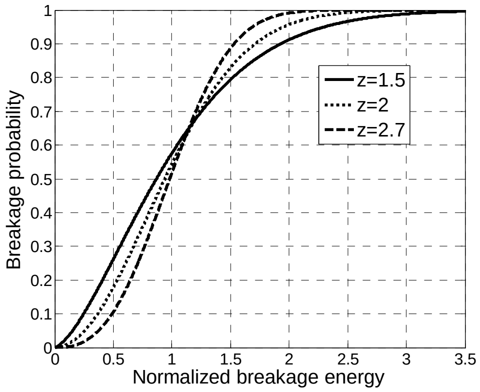

Fig. 3 Normalized breakage energy distribution calculated for spherical particles of size $d=6$ mm. The breakage probability distribution changes significantly under variation of exponent z.

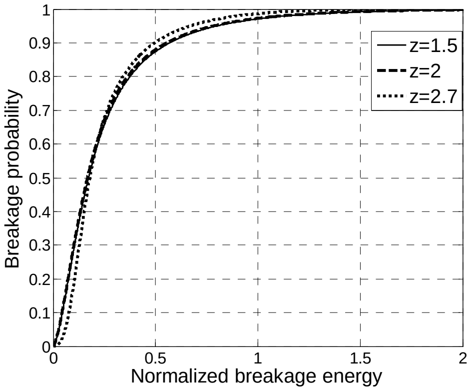

Fig. 4 Modelled breakage energy distribution calculated for the combination of asperities represented in **Fig. 2**. The difference between distributions with a different exponent *z* tends to disappear.

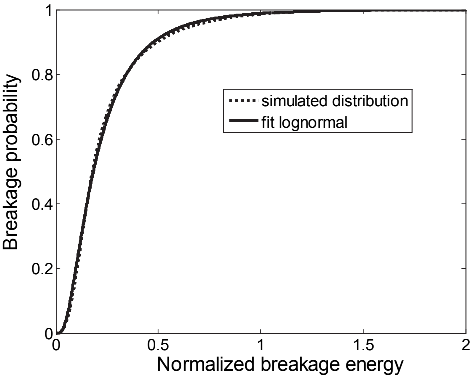

Fig. 5 Log-normal fit of modelled breakage energy distribution. The Weibull exponent *z* is equal to 2.7.

normalized breakage distributions of different particles will be compared. We will show that in terms of irregularly shaped particles, the normalized breakage probability distribution can be fitted with the log-normal distribution function. If the proposed contact model and simulation are correct, the parameters of the log-normal fit function remain the same for all tested particle sizes.

4. Impact Set-up and Tested Materials

A small-scale pneumatic cannon was designed to carry out the impact tests, see **Fig. 6**. The acceleration of the moving piston with particle occurs inside a 900-mm-long hard aluminium tube with a core diameter of 12 mm. For particles in the size range of 1.00 – 6.33 mm, velocities up to approximately 35 m/s were reproducibly obtained. The driving pressure of compressed air varies from 0.5 to 3 bar. The charge of the particle into the moving piston occurs at the end of the acceleration tube. The permanent magnet allows the piston with particle to be put in the start position.

The impact velocity was determined using the signals from two Hall sensors mounted along the tube and a vibration sensor mounted on the target. Two time intervals were used to measure the velocity. The first time interval corresponds to the movement of the piston with magnet and particle between two Hall sensors. The velocity of the piston was derived from this time interval. By stopping the piston at the end of the acceleration tube, the particle continues its movement up to collision with the target. The particle collision with the target was detected by the vibration sensor. Consequently, the particle velocity was measured by using the time interval between the passage of the second Hall sensor and the start of target vibrations caused by particle collision. The velocities of particle and piston were compared. The difference in velocities can be caused by attrition between the particle and the piston during deceleration of the piston. When the difference was greater than 5%, the test was not taken into account to exclude the possible particle fragmentation due to friction caused by the particle movement inside the piston during its deceleration.

In order to provide statistically significant data, about 300 particles were provided for every impact test. The mass of each particle was measured before and after impact. If a mass reduction of more than 10% occurs, then the particle was classified as “broken”.

The impact test was carried out with various size fractions of tested materials: NaCl from the Dead Sea, sugar, basalt and granules of Al_2O_3. All particles were irregularly shaped, see **Fig. 7**., **Fig. 7b**, **Fig. 7c**. The samples were sieved to obtain particles in the given size ranges, see **Table 1**. The size range of the tested particles was wide enough to permit selection of a representative probe.

5. Mean Energy Versus Particle Size

The cumulative experimental distribution of breakage probability *P* was obtained by variation of the impact energy *W* in the relevant range that corresponds to increasing the breakage probability from 0 up to about 0.9. The mean value of breakage energy W_{mean} was calculated by numerical integration of the experimental distribution according to Eq. (6).

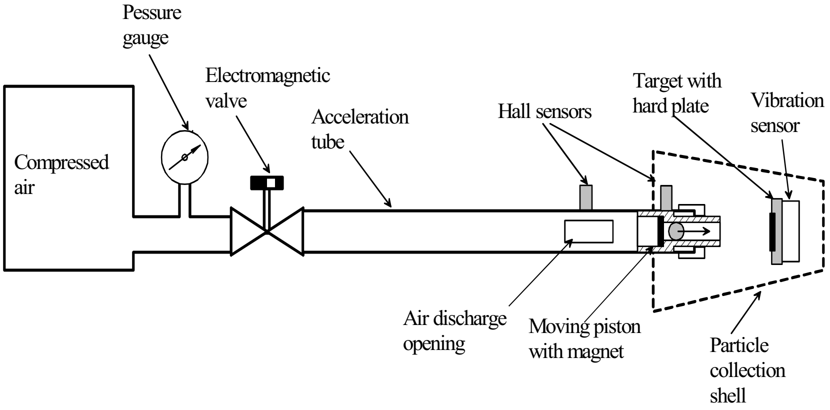

Fig. 6 Impact test equipment.

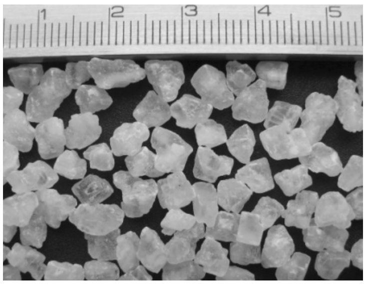	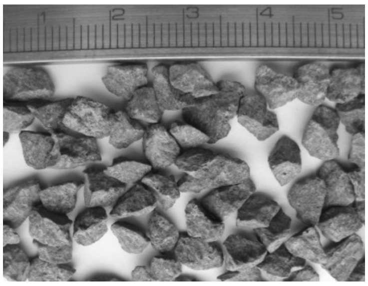	
Fig. 7a NaCl particles	**Fig. 7b** Basalt particles	**Fig. 7c** Sugar particles

Table 1. Particle size fractions used for the tests

No.	d_{min} (mm)	d_{max} (mm)
1	1.25	1.6
2	1.6	2.0
3	2.0	2.5
4	2.5	3.15
5	3.15	4.0
6	4.0	5.0
7	5.0	6.3

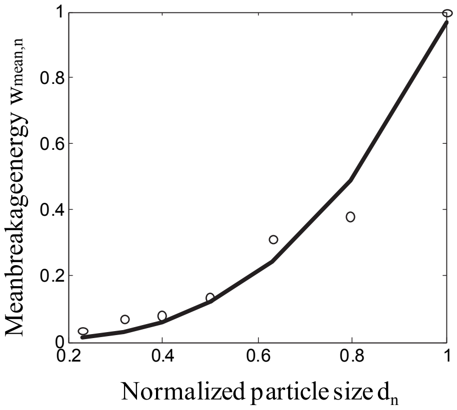

Fig. 7 Normalized mean of impact energy $w_{mean,n}$ of NaCl particles versus normalized particle size d_n.

Fig. 8. represents the dependence of the normalized mean impact energy $w_{mean,n}$ on the particle of NaCl of size d_n. The mean energy was normalized by its maximal value of 7.0 mJ, and the particle size was normalized by 5.65 mm. The increase in mean of impact energy W_{mean} with particle size d can be described as:

$$\left(\frac{W_{mean}}{7mJ}\right)=\left(\frac{d}{5.65mm}\right)^k \tag{14}$$

The data were fitted by a power function with exponent k=3.02. The coefficient of determination R^2 (R-square) is about 0.97.

A similar dependence was observed for sugar par-

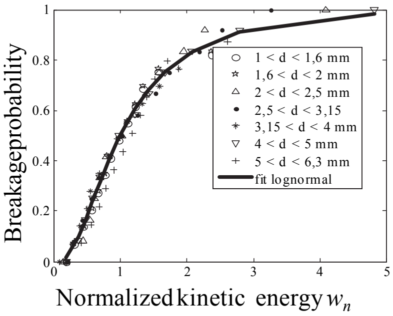

Fig. 8 Experimental breakage probability distributions of NaCl particles versus normalized kinetic energy $w_n=W/W_{mean}$. The particle size varies from 1 mm to 6.3 mm. The distribution was normalized by the mean impact energy W_{mean} that depends on the particle size d, see Eq. (14).

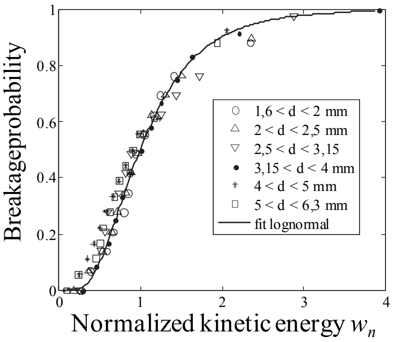

Fig. 9 Cumulative experimental distributions of breakage probability of sugar particles versus normalized kinetic energy $w_n=W/W_{mean}$. The distribution was normalized by the mean impact energy W_{mean} according to Eq. (15).

ticles:

$$\left(\frac{W_{mean}}{15.1mJ}\right)=\left(\frac{d}{5.65mm}\right)^k \qquad (15)$$

In the case of sugar particles, the exponent $k=3.42$ and R-square was about 0.96. Based on experimental data, one can conclude that the mean breakage energy is a power function of particle size.

6. Breakage Probability Versus the Normalized Impact Energy

The breakage behaviour of irregularly shaped NaCl particles was tested first. The cumulative experimental distributions of the normalized impact energy of NaCl particles are shown in **Fig. 9**. The particle size varies from 1 mm to 6.3 mm. Within the frame of experimental data accuracy, there is no difference in breakage probability behaviour for particles of different sizes. All data are fitted by the same log-normal function.

According to our simulation, the breakage probability can be fitted with a log-normal distribution function depending on the normalized energy. Within the frame of measurement accuracy, the parameters of the log-normal fit function will remain the same as for the tested particle sizes and materials.

The second sequence of experiments was carried out to investigate the breakage behaviour of sugar particles, see **Fig. 11**. The particle size varies in the same range as in the case of NaCl particles. Both materials – NaCl from the Dead See and the sugar – show a similar breakage behaviour. The log-normal function with the same parameters was applied to fit all experimental distributions.

The third tested material was basalt. Unlike the above two materials, it can be characterized as a brittle material[34] of high strength. However, like the NaCl and sugar particles, basalt exhibits a similar relationship between normalized kinetic energy and breakage probability, see **Fig. 11**. The parameters of the fit function remain the same as for the above materials.

Finally, it was interesting to apply the developed method to spherical granules of Al_2O_3. The granules of Al_2O_3 can show a different impact behaviour compared with the above-tested irregularly shaped solid particles[35]. Al_2O_3 granules in two size ranges – 2.5 mm < d < 3.15mm and 1.6mm < d < 2mm – were tested. The breakage probability of Al_2O_3 granules can be fitted with the log-normal function in a similar way to the NaCl, sugar and basalt particles, see **Fig. 12**.

The parameters of the fit function remain the same for all above tested materials. However, at the low normalized energy, the experimental data of granules show a small systematic deviation from the fit curve. It can be caused by the spherical form of the granules[21].

7. Conclusions

The impact breakage of irregularly shaped particles of Dead Sea salt, sugar, basalt and granules of γAl_2O_3 was tested. The breakage behaviour of the tested particles can be described in terms of a model of hemispherical asperities. According to this model, the cap of a particle directly in contact with the target is admitted into the equation as a hemispherical asperity. The main part of elastic energy that is stored

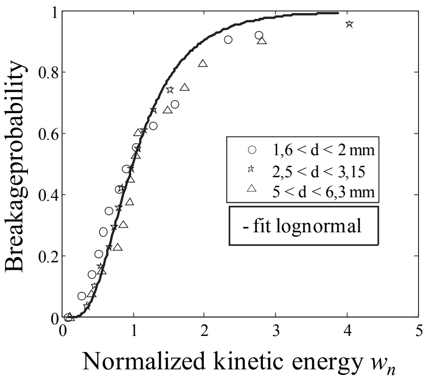

Fig. 10 Cumulative experimental distributions of breakage probability of basalt particles versus normalized kinetic energy $w_n=W/W_{mean}$. W_{mean} is equal to 2.56 mJ, 14.8 mJ and 78.3 mJ for particle size *d* at intervals 1.6<*d*<2 mm, 2.6<*d*<3.15 mm and 5<*d*<6.3 mm, respectively.

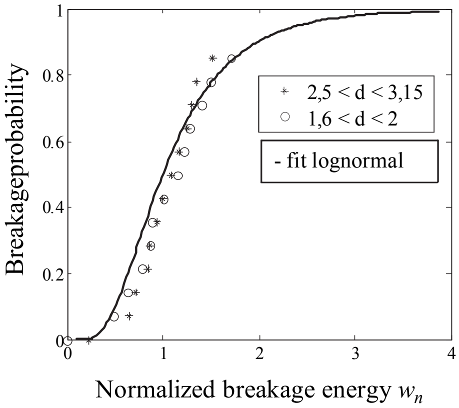

Fig. 11 Cumulative experimental distributions of the breakage probability of Al_2O_3 granules versus normalized kinetic energy $w_n=W/W_{mean}$. W_{mean} is equal and 0.91 and 2.6 mJ for particle size *d* at intervals 1.6<*d*<2 mm and 2.6<*d*<3.15 mm, respectively.

in the particle will be accumulated by this particle cap. This "directly contacted" particle cap is responsible for crack generation by stressing. Consequently, the breakage of particles is affected by the size distribution of those caps, i.e. asperities.

Usually, the size distribution of irregularly shaped particles is a log-normal function. The geometrical similarity of particle and caps was assumed. That means that not only particles but also caps, i.e. asperities, exhibit log-normal size distribution.

Simulation of the breakage probability distribution was carried out based on the contact model and the log-normal size distribution of asperities,. The breakage probability distribution of irregularly shaped particles was calculated as a superposition of the breakage probabilities of individual log-normal distributed asperities. The results of the simulation show the following specific features of the resulting breakage probability distribution:

a) the distribution can be fitted by a log-normal function,

b) due to the cumulative effect of log-normal distributed asperities, the specific material properties tend to disappear in simulated breakage probability distribution,

c) the distribution of breakage probability can be represented in simple universal form. In this representation, the breakage depends on the normalized breakage energy only. It does not depend on the particle size and material.

The results of experiments show a good agreement with the model for brittle irregularly shaped particles. In terms of elastic spherical granules of low stiffness, the model needs improvement.

Acknowledgments

This research project I-875-106.10/2005 was supported by a grant from the G.I.F., the German-Israeli Foundation for Scientific Research and Development.

Legend

a_R	stressing intensity parameter according to Rumpf, J/m^2
d_r	diameter of hemispherical asperity, mm
c	constant, (kg/J)^z mm^{-2}
Γ	gamma function
d	particle size, mm
d_n	normalized particle size
d_{min}	minimal size of asperities particle, mm
W	kinetic energy by particle impact, J
P	parameter
v	particle velocity, ms^{-1}
v_0	constant, ms^{-1}
v_{50}	velocity that corresponds to breakage of 50% of particles, ms^{-1}
W_m	mass-related kinetic energy of spherical particles, Jkg^{-1}
$W_{m,min}$	threshold energy, Jkg^{-1}
w_n	normalized kinetic energy
W_{mean}	arithmetic mean of kinetic energy, J
$W_{m,mean}$	arithmetic mean of mass-related kinetic energy, Jkg^{-1}
$w_{mean,n}$	normalized arithmetic mean of kinetic en-

	ergy, []
f_{mat}	material constant, $Jm^{-1}kg^{-1}$
P	breakage probability
z	Weibull exponent

References

1) Han, T. and Kalman, H. (2003): Theoretical and experimental study of multicompression particle breakage. Advanced Powder Technol., Vol. 14, No. 5, pp. 605-620.
2) Han, T., Petukhov, Y., Levy, A. and Kalman, H. (2006): Theoretical and Experimental Study of Multi-Impact Breakage of Particles," Advanced Powder Technology, Vol. 17, pp. 135-157.
3) Kalman, H., Hubert, M., Grant, E., Petukhov, Y. and Haim, M. (2004): Fatigue Behavior of Impact Comminution and Attrition Units, Powder Technology, Vol. 146, No. 1-2, pp.1-9.
4) Tavares, L.M. and King, R.P. (1998): Single-particle fracture under impact loading, Int. J. Miner. Process, 54, pp.1-28.
5) Tavares, L.M. and King, R.P. (2002): Modelling of particle fracture by repeated impacts using continuum damage mechanics. Powder Technology, Vol. 123, pp.138-146.
6) Bažant, Z. P. and Luigi, C. (1991): "Stability of Structures: Elastic, Inelastic, Fracture and Damage Theories", New York: Oxford University Press.
7) Aman, S.,Tomas, J. and Kalman, H. (2010): Breakage probability of irregularly shaped particles, Chem. Eng. Sci., 65, pp.1503-1512.
8) Gildmeister, H. and Schönert, K. (1972): Berechnung zur Wellenausbreitung in Kugeln und Bruchphänomene in Kreisscheiben bei Prallbeanspruchung. Dechema Bd.69 , Nr.17, pp.1-35.
9) Tavares, L. M. (2007): Breakage of Single Particles: Quasi-Static, Handbook of Powder Technology, Vol. 12, Particle Breakage, ed. by: Salman A. D., Ghadiri M. and Hounslow M.J., pp.3-68.
10) Salman, D., Fu, J., Gorham, D. A. and Hounslow, M. J. (2003): Impact breakage of fertiliser granules, Powder Technology, Volume 130, Issues 1-3, pp.359-366
11) Schubert, W., Khanal, M. and Tomas, J. (2005): Impact crushing of particle-particle compounds - Experiment and simulation. Int. J. Miner. Process, 75, pp.41-52.
12) Ghadiri, M., Moreno-Atanasio, R. and Matsusaka, S. (2002): Impact damage analysis of agglomerates by Distinct Element Method, Journal of the Society of Powder Technology, Japan, 39, pp.885-892.
13) Rumpf, H. (1973): Physical aspects of comminution and new formation of law of communition, Powder Technology, Vol. 7, pp.145-159.
14) Stiesβ, M. (1976): „Die Druckbeanspruchung von elastischen und inelastischen Kugeln bis zum Bruch“, Dissertation TU Karlsruhe.
15) Baumgardt, S. (1976): Beitrag zur Einzelkornschlagzerkleinerung sproder Stöffe, Freiberger Forsch.-H., A560, pp.29-106.
16) Baumgardt, S., Buss, B., May, P. and Schubert, H. (1976): On the comparison of results in single grain crushing under different kinds of load, Proceedings of the 11th International Mineral Processing Congress, Cagliari, p. 3.
17) Baumgardt, S., Buss, B., May, P. and Schubert, H. (1978): Zum Vergleich von Zerkleinerungs-ergebnissen der Einzelkornzerkleinerung bei verschiedenen Beanspruchungsarten, Powder Technology, 8, pp.107-115.
18) Weichert, R. (1991): Theoretical Prediction of Energy Consumption and Particle Size Distribution in Grinding and Drilling of Brittle Materials, Part. Part. Syst. Charact., 8, pp.55-62.
19) Weichert, R. (1992): Anwendung von Fehlstellenstatistik und Bruchmechanik zur Beschreibung von Zerkleinerungsvorgängen, Zement-Kalk-Gips, 45(1), pp.1-8.
20) Weibull, W. (1939): A statistical theory of the strength of materials. Ingeniörsvetens-kakademiens Handlingar 151, Generalstabens Litografiska Anstalts Förlag, Stockholm
21) Antonyuk, S., Tomas, J., Heinrich, S. and Mörl, L. (2005): Breakage behavior of spherical granulates by compression, Chem. Eng. Sci., Vol. 60, pp.4031-4044.
22) Antonyuk, S., Khanal, M.,Tomas, J., Heinrich, S. and Mörl, L. (2006): Impact breakage of spherical granules: experimental study and DEM simulation, Chem. Eng. Sci., Vol. 45, pp.838-856.
23) Tomas, J. (2007): Adhesion of ultra fine particles—a micromechanical approach. Chem. Eng. Sci., 62, pp.1997-2010.
24) Tomas, J. (2007): Adhesion of ultra fine particles—energy absorption at contact. Chem. Eng. Sci., 62, pp.5925-5939.
25) Salman, D., Fu, J., Gorham, D. A. and Hounslow, M. J. (2003): Impact breakage of fertiliser granules, Powder Technology, Volume 130, Issues 1-3, pp. 359-366.
26) Salman, D., Reynolds, G. K., Fu, J. S., Cheong, Y. S., Biggs, C. A., Adams, M.J. ,Gorham, D. A., Lukenics, J. and Hounslow, M. J. (2004): Descriptive classification of the impact failure modes of spherical particles, Powder Technology, Volumes 143-144, 25 June, pp. 19-30.
27) May, P. (1976): Einzelkorndruckzerkleinerung von spröden Stoffen. Freiberger Forsch.-H. A550, pp. 85-179.
28) Baumgardt, S., Buss, B., May, P. and Schubert, H. (1978): Zum Vergleich von Zerkleinerungs-ergebnissen der Einzelkornzerkleinerung bei verschiedenen Beanspruchungsarten, Powder Technology 8, pp. 107-115.
29) Baumgardt, S. (1976): Beitrag zur Einzelkornschlagzerkleinerung spröder Stoffe, Freiberger Forsch.-H., A560, pp. 29-106.
30) Buss, B. and Schubert, H. (1978): Ergebnisse von Un-

tersuchungen zerkleinerungstechnischer Mikroprozesse, Neue Bergbautechnik, 8, 12, pp. 706-710.
31) Strom, R. (1986): Wahrscheinlichkeitsrechnung, mathematische Statistik und statistische Qualltätskontrolle, Leipzig, Fachbuchverl., pp. 42-43.
32) Schubert, H. (2003): „Handbuch der Mechanischen Verfahrenstechnik. Bd. 1“, Weinheim: Wiley-VCH Verlag.
33) Kolmogorov, A.N. (1941): On the logarithmic normal size distribution of particles by grinding, Dokl. Akad. Nauk., SSSR 31, pp. 99-101.
34) Violay, M., Gibert, B., Mainprice, D., Evans, B., Pezard, P.A. and Flovenz, O. (2009): Brittle ductile transition in experimentally deformed basalt under oceanic crust conditions. Geophys. Res. Abstr. 11, (EGU2009-5507-7, EGU General Assembly 2009).
35) Agniel, Y. (1992): „Bedeutung der Einzelgranalieneigenschaften zur Defektvermeidung in trockengepressten keramischen Modellpulvern“, Dissertation, Universität Karlsruhe (TH).

Author’s short biography

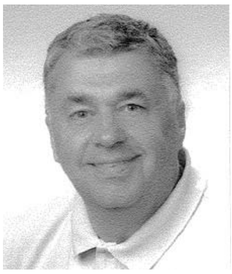

Sergej Aman

Education: Novosibirsk University, Physics, 1989. Dr. Aman (born 1950) at the present works at the Department of Mechanical Process Engineering, Otto-von Guericke University Magdeburg, Germany. He becomes Candidate in Physics 1991 in the Institute of Thermophysics of Novosibirsk Scientific Center. His area of interests includes physics of breakage and fracto-emission. He has more than 12 referred journal publication and over 22 international conference presentations.

Jürgen Tomas

Short version:
1975 Diploma in Chemical Engineering (Systems Engineering) at TH Merseburg, 1982 pro-motion (PhD-theses) and 1991 habilitation (Sc.D.-theses) at Bergakademie Freiberg, since 1994 Professor of Mechanical Process Engineering at Otto-von-Guericke-Universität Magde-burg, since 2005 Chairmen of the ProcessNet working group „Agglomeration and Bulk Solids Handling Technology“, since 2006 full member of Saxon Academy of Science of Leipzig, since 2007 faculty dean of “Process and Systems Engineering”, since 2009 vice speaker of DFG graduate school 1554 „Micro-Macro-Interactions in Structured Media and Particle Sys-tems“ and coordinator of German Research Foundation (DFG) priority program 1486 „Particles in Contact - Micromechanics, Microprocess Dynamics and Particle Collectives“.

Author's short biography

Peter Mueller

Peter Mueller is a Research Scientist at the Institute of Process Engineering, Mechanical Process Engineering at the Otto-von-Guericke University of Magdeburg. He joined the research group in 2006 and finished his PhD thesis in March 2011. The work was supported by the Graduiertenkolleg 828 "Micro-macro Interactions in Structured Media and Particle Systems". His research interests include the experimental and numerical investigation of the compression, impact and breakage dynamics of granules.

Haim Kalman

Haim Kalman earned his Ph.D. in Mechanical Engineering from Ben-Gurion University at 1989 and is a faculty member since then. Since 2008 he is a full professor. He is interested in various aspects of powder technology and mainly in size reduction of particles and particle-gas flows. He published more than 70 papers in peer-reviewed journals and more than 150 papers in conference proceedings. He was involved in organizing of many national and international conferences. He is the founder of the International CHoPS (Conveying and Handling of Particulate Solids) Conferences and the former president of the International Freight Pipeline Society. Since 2008, he is the Head of department of Mechanical Engineering.

Yevegny Rozenblat

Yevegny Rozenblat graduated from the Ben-Gurion University of the Negev, Israel with a B.Sc. (2004) and M.Sc. (2007) degrees in Chemical Engineering. He is currently finishing a Ph.D. thesis at Mechanical Engineering of the same University. The subject of his study is the investigating size reduction functions for DEM applications.

Synthesis and on-line size Control of Silicon Quantum Dots[†]

Olivier Sublemontier*, Harold Kintz, Frédéric Lacour, Xavier Paquez, Vincent Maurice, Yann Leconte, Dominique Porterat, Nathalie Herlin-Boime and Cécile Reynaud
CEA, IRAMIS, SPAM, Laboratoire Francis Perrin CNRS URA 2453, 91191 Gif sur Yvette, France.

Abstract

The synthesis of silicon quantum dots is performed in the [3-5 nm] range using CO_2 *laser pyrolysis of* SiH_4*. This size range is particularly relevant for potential applications in photovoltaic devices and biomedical imaging. The laser pyrolysis technique offers convenient control of the synthesis parameters in the case of nanoparticle production. However, controlling the size of small silicon objects remains difficult. The original approach consists here in a time-control of the energy injected into the reaction by gating the laser. The laser gate-on duration is adjusted in the range of 10 to 80 μs while keeping the average power constant. In parallel, supersonic expansion and on-line time-of-flight mass spectrometry are performed for on-line size characterization. A monotonic increase of the size as a function of the gate-on duration is observed for several* SiH_4 *volume concentrations. The results are discussed qualitatively.*

Keywords: Gas-phase nanoparticle synthesis, silicon quantum dots, on-line size control, laser pyrolysis, aerosol characterization by TOF-MS

1. Introduction

Controlling the size of quantum dots is a key issue for applications requiring materials with precisely adjustable properties brought about by nanostructuration[1]. A typical example is the case of Silicon Quantum Dots (Si-QDs), which exhibit strong size-dependent properties. Various applications are expected in different domains including optical and electronic devices[2], photovoltaic solar cells[3] and markers for *in vivo* biological structures imaging[4]. The band gap can be adjusted as a function of the size below 8 nm according to the quantum confinement model prediction[5], which correctly fits the experimental observations for sizes down to about 3 nm. In addition, in the case of silicon, the spatial confinement of the exciton induced by an incident UV photon leads to an efficient photoluminescence (PL) of surface-passivated Si-QDs at room temperature[6]. Most of the applications require sufficient quantities (more than a few hundred mg) of small and high-quality Si-QDs in terms of purity, average size control and size distribution. CO_2 laser-driven pyrolysis is an efficient method to synthesize various high-purity nanopowders, oxides and non-oxides, in a gas-phase bottom-up approach[7]. It has been proven to be an efficient way to synthesize and deposit photoluminescent Si-QDs using a nanosecond-pulsed CO_2 laser[8]. It was recently found that this method could be optimized for relatively large production rates of small Si-QDs using a microsecond-gated CO_2 laser[9]. However, as their properties change rapidly as a function of their size, a precise control at the synthesis stage and on-line diagnostics are needed for specific applications. The aim of the present paper is to investigate the ability of a gated CO_2 laser, in combination with Time-of-Flight Mass Spectrometry (TOF-MS), to control the size of Si-QDs on-line. The idea is to gain better control over the growth of nanoparticles by varying the amount of energy available for the reaction in time.

[†] Accepted : September 12th, 2011

[1] 91191 Gif sur Yvette, France.
[*] Corresponding author
E-mail: olivier.sublemontier@cea.fr
TEL: (+33) 1 69 08 77 91, FAX: (+33) 1 69 08 12 13

© 2011 Hosokawa Powder Technology Foundation

2. The laser pyrolysis method

Laser pyrolysis, also called Laser Chemical Vapor Pyrolysis (LaCVP), is a gas-phase process first introduced in 1982[10]. It is currently used for the synthesis of various kinds of nanoparticles[7]. It is based on the resonance between the emission of a laser, usually a CO_2 laser at 10.6 μm, and the absorption by a gaseous (or liquid) precursor molecule. In this thermal process, the CO_2 laser is used as a spatially well-defined and easily adjustable heat source allowing collision-induced decomposition of precursor molecules. The pyrolysis mechanism at the microscopic level was detailed earlier[11, 12]. Experimental descriptions are given elsewhere[7, 10]. A significant improvement and upscaling of the technique was recently proposed[13]. Briefly, the precursor's flow, guided by a coaxial inert gas flow, intersects the laser beam orthogonally in a reaction chamber kept under controlled pressure. The temperature increases rapidly in the laser-crossing region. If the particle formation temperature is reached, nucleation occurs from dissociated species and particles grow rapidly. The reaction zone shows a luminescent flame originated by the thermal emission of the particles and possible emission contributions from excited radicals. The confinement by the inert gas flow avoids any reaction with the chamber walls and thus prevents particles from contamination.

Studies on the dynamics of particle formation by gas-phase processes were carried out[14, 15]. The thermal decomposition of SiH_4 was studied experimentally and numerically[16, 17]. In the pyrolysis process, nucleation occurs when the dissociation temperature threshold of precursor molecules is reached. Particles then grow either by coagulation of nuclei and atom addition to their surface induced by vapor condensation in a supersaturated environment[18], or by chemical heterogeneous reactions on their surface[19]. A second step of coagulation between grown particles may occur after the first primary particle growth step. In that case, a second growth mechanism occurs by melted particle-particle collision or by solid-state diffusion between two hot solid particles. This leads to relatively large and non-agglomerated particles. If the reaction temperature is relatively low, or if it drops quite rapidly after the first growth process, then primary particles may only agglomerate or aggregate in larger fractal-like objects[20, 21]. The growth process, the primary particle size and phase, plus the structure and size of agglomerates, are the consequence of the reaction temperature history. In the laser pyrolysis process, controlling the synthesis parameters, such as precursor molecules flow, pressure in the reaction chamber and laser power and focusing, provide the opportunity, to a large extent, of controlling the temperature history. Instantaneous temperature at a point of the reaction zone is the result of a balance between the heat generated by absorption of the laser radiation and the cooling brought about by radiation from hot particles and gas diffusion. In some cases, energy release or absorption by chemical reactions may also play a significant role.

In addition to these usual parameters, it is possible to dilute the reactant precursor flow. Simple dilution in an inert gas flow induces different changes in the reaction zone. First, if the amount of reacting precursor molecules is kept constant, the total gas flow is increased, leading to a decrease of the residence time in the laser zone and thus to a decrease of the reaction duration and temperature. Second, if the total flow rate is kept constant, the dilution gas acts as a thermal bath. The collision frequency between dissociated species is lowered, as the partial pressure of reactant molecules is smaller. The energy in the reaction is also decreased because of less absorption of the laser radiation. The balance tilts in favor of the cooling process. Furthermore, the cooling rate of the reaction can be increased by making a careful choice of the thermophysical properties of the diluting gas. The diffusion coefficient of He in gases is more than 3 times higher than that of Ar[22]. It is 0.617 cm^2/s for He at room temperature. In addition, the thermal conductivity of He is about a factor of 10 higher than that of Ar[22]. It is 156 mW/m.K for He at room temperature. It is then a good candidate for accelerating the growth quench of Si-QDs.

3. Experimental set-up optimization

The basic pyrolysis reactor was upgraded by instrumentation and equipments that provide on-line characterization of the particles size (see **Fig. 1**), aiming at an optimization for small Si-QDs synthesis. It is composed of three vacuum chambers. The first one is a source chamber that includes the pyrolysis reactor. The second one is an on-line film deposition chamber and the third one is a TOF-MS chamber. Previous work[23] inspired the general configuration of this set-up.

3.1 Source chamber design

The synthesis itself takes place in the flow reactor placed in the source chamber as shown in **Fig. 1**. The precursor molecule is SiH_4, which is a very ef-

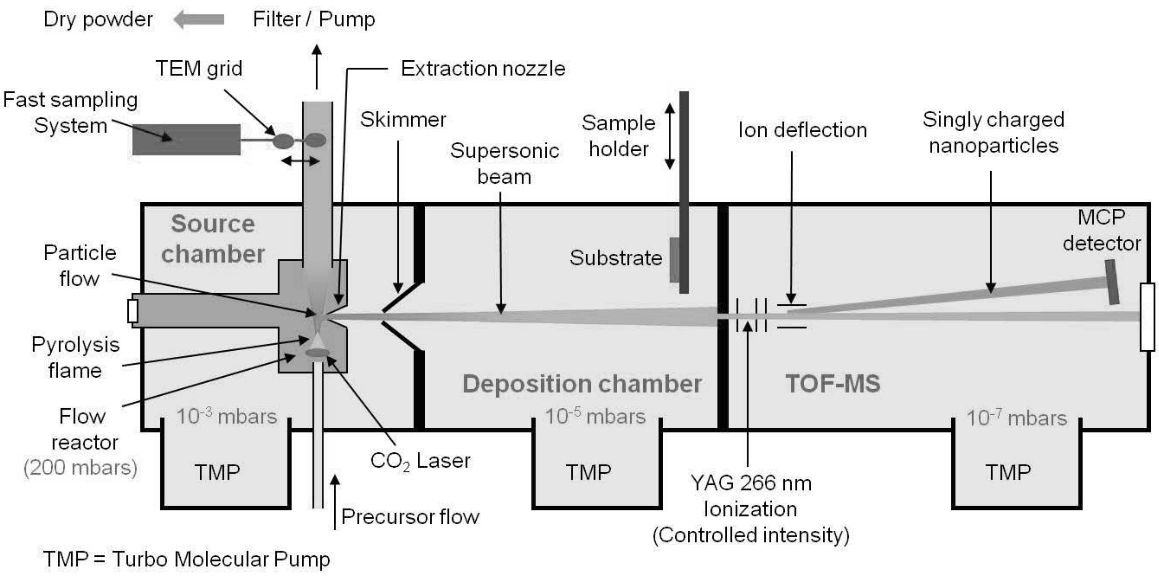

Fig. 1 Experimental set-up.

ficient absorber of the 10.6 µm wavelength radiation used here. SiH_4 is diluted in He. The volume concentration of SiH_4 is set at several fixed values from 3.2% to 9.6%. It is introduced into the flow reactor from the bottom. The laser is focused and crosses the precursor flow at 90 degrees above the injection nozzle. The pressure in the flow reactor is set at 200 mbar in order to minimize the growth rate. It is maintained constant with the help of an electronically controlled valve and a closed-loop system. The pressure in the source chamber is set at 10^{-3} mbar with a turbo-molecular pump (TMP). A fraction of the Si-QDs flow is collected on a filter placed downstream in the pumping line on the top of the flow reactor. The remaining fraction is extracted horizontally through a skimmer-shaped extraction nozzle by the pressure difference between the flow reactor and the source chamber. The extraction nozzle axis is placed orthogonally with respect to the gas flow. Its aperture is positioned at 5 to 10 millimeters above the top of the pyrolysis flame (see **Fig. 1**). A supersonic beam of gas carrying the Si-QDs is then formed with a second differential pumping system through a skimmer between the source chamber and the deposition chamber.

3.2 Deposition process

The pressure in the deposition chamber is 10^{-5} mbar so that nanostructured films can be prepared by deposition of particles carried by the supersonic gas jet. It is simply achieved by introducing a substrate on the sample holder in front of the jet. With a 10-mm deposition spot diameter, a routine deposition rate around 12 nm/min is observed during more than 4 hours. **Fig. 2** shows Scanning Electron Microscopy (SEM) micrographs of a nanostructured film realized by the deposition of 4 nm Si-QDs on a quartz substrate. The experimental settings correspond to those given in section 3.5. The laser is used in the gated mode (T_{on} = 20 µs, duty cycle = 0.2) detailed in section 3.5. The average power is 400 W. The total flow rate is 0.64 l/min. The SiH_4 volume concentration in He is 7.2%. The film thickness is about 180 nm for 15 min. continuous wave operation. **Fig. 2(a)** is an edge view of the nanostructured film and **Fig. 2(b)** is a normal to surface view. It illustrates the porous feature of the layer. The deposition rate is measured with a calibrated quartz crystal microbalance Maxtek model TM-200 that can be introduced into the particle beam during the deposition process. This instrument measures a mass deposited on a known area by measuring the change in frequency of a quartz crystal resonator. The calibration is realized by measuring the thickness of a film deposited during a determined time by SEM. With a deposition rate of 12 nm/min., a film porosity of 70% was estimated by the quartz crystal microbalance calibrated with bulk silicon data. This value is comparable to measured values reported elsewhere24).

If only dry powder is needed, the extraction nozzle can be removed, so that the total particle production is collected on the filter. In both cases, Transmission Electron Microscopy (TEM) analyses are carried out with the help of a fast sampling system (see **Fig. 1**). This system allows deposition on TEM grids exposed

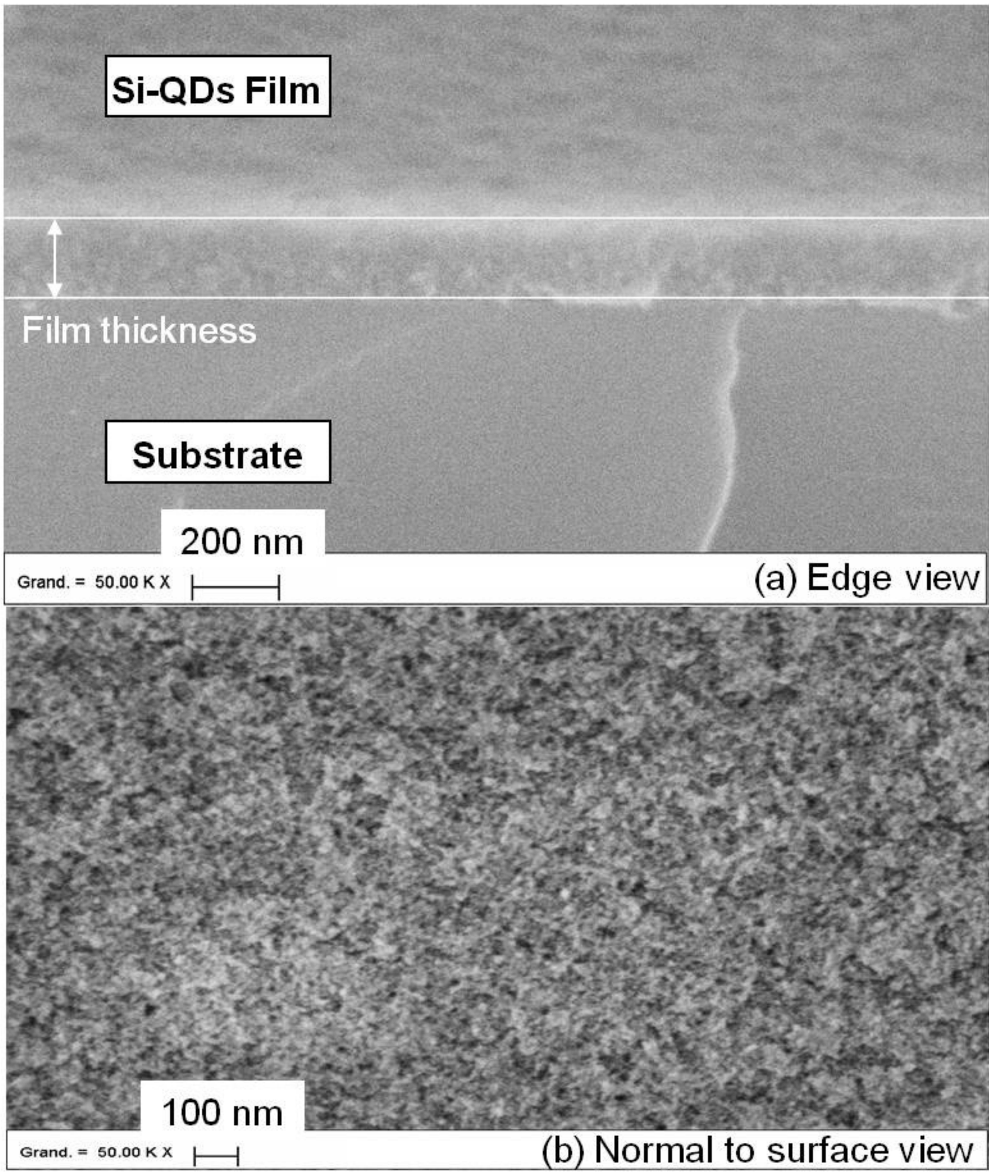

Fig. 2 Scanning electron micrographs of a Si-QDs-based film on a quartz substrate. The edge view (a) shows the film thickness. The normal to surface view (b) illustrates its nanostructured porous feature.

to the aerosol flow during very short times (down to 30 ms) by fast translation of a pneumatic cylinder. It allows direct analysis of the shape and morphology of agglomerates from the gas phase.

3.3 Laser beam spatial management

The laser focusing spot is 0.5 mm high and 3 mm wide. The height is as short as possible in order to limit the reaction time while the width is chosen large enough to maintain a good overlap with the reactant gas flow. Reactant molecules flow out from the 2-mm circular injection nozzle. The spatial shaping of the laser spot is realized with the help of a tandem cylindrical lens system illustrated in **Fig. 3**. Both lenses have a focal length of 500 mm. The first lens focuses in the vertical direction, and is placed at 500 mm from the reaction zone. The second lens focuses in the horizontal direction, and is placed at an adjustable distance from the reaction zone. An elliptical and width-adjustable spot is obtained in the reaction region. This allows short growth times and high production rates of small particles. With the extraction nozzle removed, a typical production rate of 300 mg/h is achieved for 4-nm Si-QDs. The production rate can be dramatically increased when larger sizes are needed. Larger sizes are obtained by increasing the vapor pressure of dissociated species. It is achieved, for example, by increasing the laser average power,

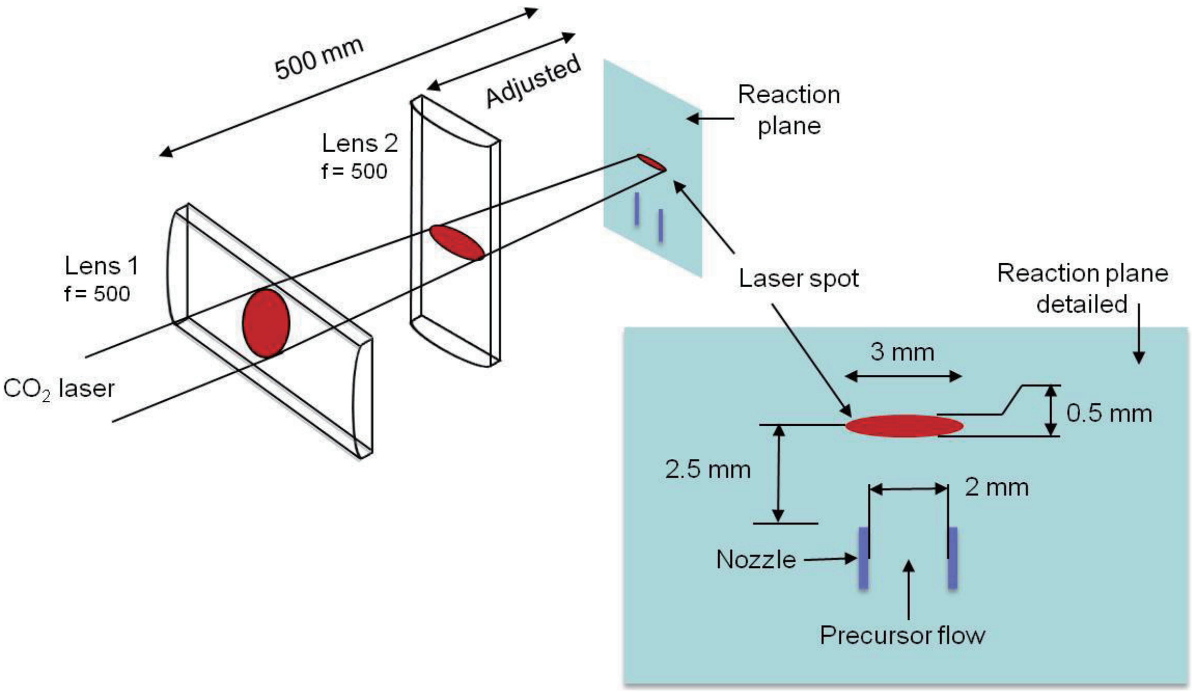

Fig. 3 Laser spot spatial profiling and geometrical data of the reaction region.

by decreasing the absolute precursor flow rate or by increasing the SiH_4 volume concentration. For example, a production rate for 9.5-nm Si-QDs about ten times larger than that for 4.2 nm Si-QDs was observed earlier[9]. The distance between the nozzle end and the laser spot horizontal axis is chosen at 2.5 mm with the help of computational fluid dynamics investigations (see below).

3.4 Aerodynamic flow modelling

We performed simple 3-dimensional (3D) aerodynamic flow modeling illustrated in **Fig. 4**. The calculations were carried out with commercial software FLOW-EFD V5 and took into account the true 3D geometry of the flow reactor, as well as the actual initial conditions (pressure, respective volume flows) and gas characteristics. **Fig. 4(a)** is a 2-dimensional (2D) velocity map in the vertical plane along the injection axis. The scale is limited to the 0 – 2 m/s range for a better visualization in the laser reaction zone. The injection gas tube provides diluted reactant molecules to the flow reactor. A second 10-mm diameter tube for argon coaxial flow surrounds it. The total flow (He + SiH_4) in the 2-mm inner diameter injection nozzle is 0.64 l/min. The coaxial argon flow is 1.74 l/min. The SiH_4 volume concentration in He is 7% in these calculations. Reactant and coaxial flows are numerically optimized in order to obtain a laminar, well-confined and smooth flow rate in the laser interaction region. These calculations are in good agreement with experimental observations. **Fig. 4(c)** shows the velocity profile along the injection axis. The maximum velocity in the reactant injection tube is more than 6 m/s, although the average velocity is around 3.4 m/s in this region. This is due to friction on the inner wall and to the small dimensions of the injection tube. It causes an important radial velocity gradient in the tube. The consequence is an important and fast drop of the longitudinal velocity at the entrance of the flow reactor that even begins before the nozzle end. The distance between the laser position and the nozzle end is chosen at 2.5 mm in order to have the interaction region in a smoother longitudinal velocity zone while the SiH_4 volume fraction is still high. This distance should be kept constant from one experiment to another. It is checked by a digital camera (*Basler A102*) equipped with high magnification collection optics that images the interaction region.

The calculated gas velocity profile in the laser horizontal plane is given in **Fig. 4(b)**. The minimum velocity is less than 0.6 m/s on the sides, the maximum is close to 1 m/s on the axis and the average velocity is 0.78 m/s. Considering this calculated result and the 0.5-mm-high laser beam, the average residence time of reactant molecules in the laser region is about 640 µs.

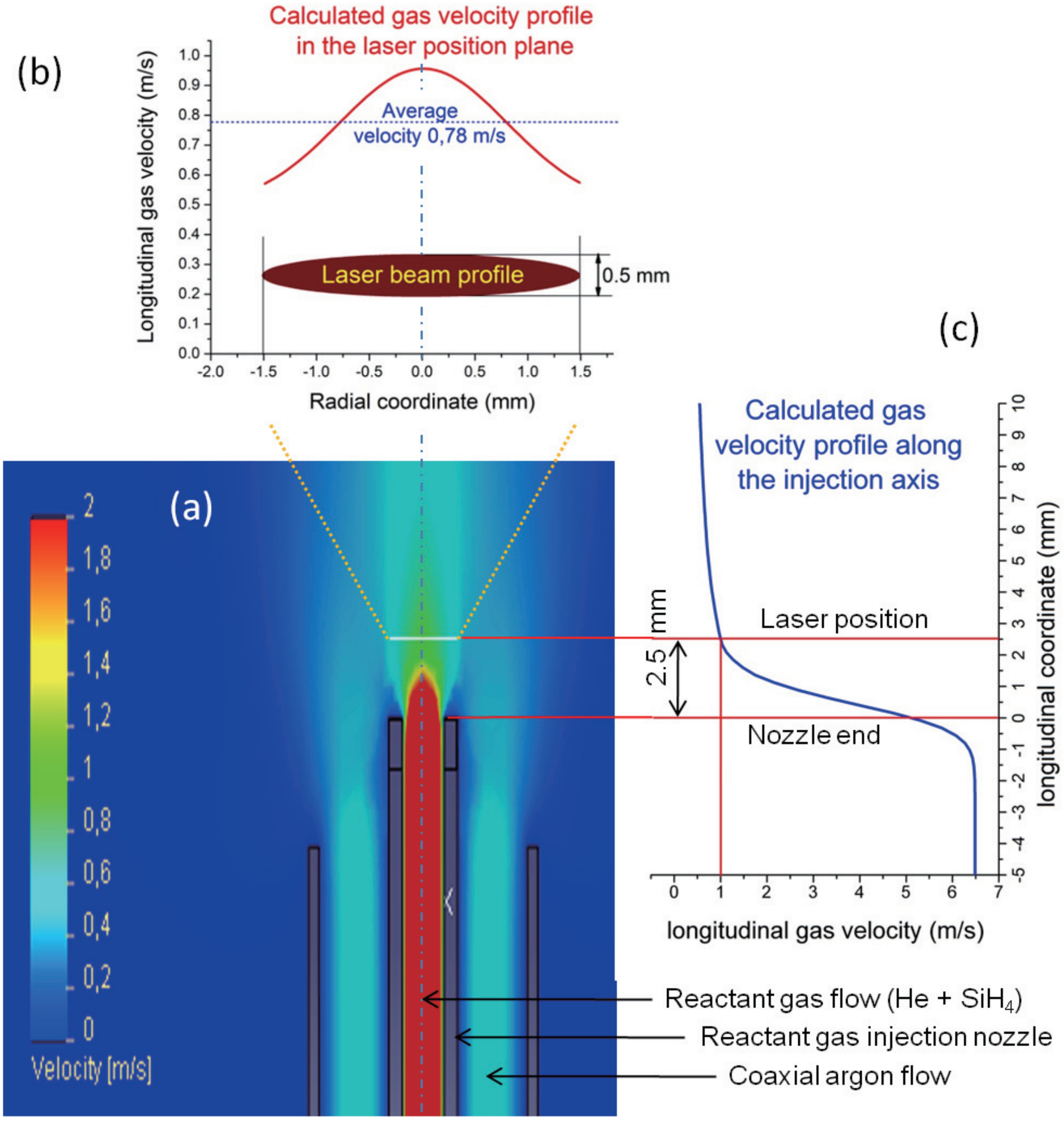

Fig. 4 Aerodynamic modelling of the gas injection region in the laser pyrolysis flow reactor. 2D velocity map in the vertical plane (a), longitudinal velocity profile in the laser position horizontal plane (b), and longitudinal velocity profile along the gas injection axis (c).

3.5 Laser beam temporal management

The CO_2 laser used for this work is a Trumpf TLF 2400. It provides up to 2400 W output power and delivers either a Continuous Wave (CW) radiation or a time-gated one. The gate-on duration control T_{on} is adjustable from 10 µs to continuous. The gate-off duration control T_{off} is adjustable from 40 µs. However, the true temporal power profile is significantly different from the gate control. Different temporal profiles of the laser output power are given from the supplier and reported in **Fig. 5** for T_{on} = 10, 20 and 50 µs. The duty cycle control $T_{on}/(T_{on}+T_{off})$ is kept constant and equal to 0.2, so that T_{off} is adjusted proportionally. The maximum power and the power rise time increase as a function of T_{on}. For example, for T_{on} = 20 µs, the maximum power (arbitrary units) and power rise time are 0.54 and 18.5 µs, respectively. For T_{on} = 50 µs, the corresponding values are 0.70 and 47 µs, respectively. The fall time appears to be also slightly dependent on T_{on}. It can be as long as 160 µs for very large T_{on} (not shown in **Fig. 5**). Longer T_{on} inevitably induces greater maximum power. In spite of this, the average output power delivered by the laser at the reaction point, measured with the help of a classic water-cooled calorimeter Coherent model LM-2500, is approximately constant (400 W in this case) if the duty cycle control is constant.

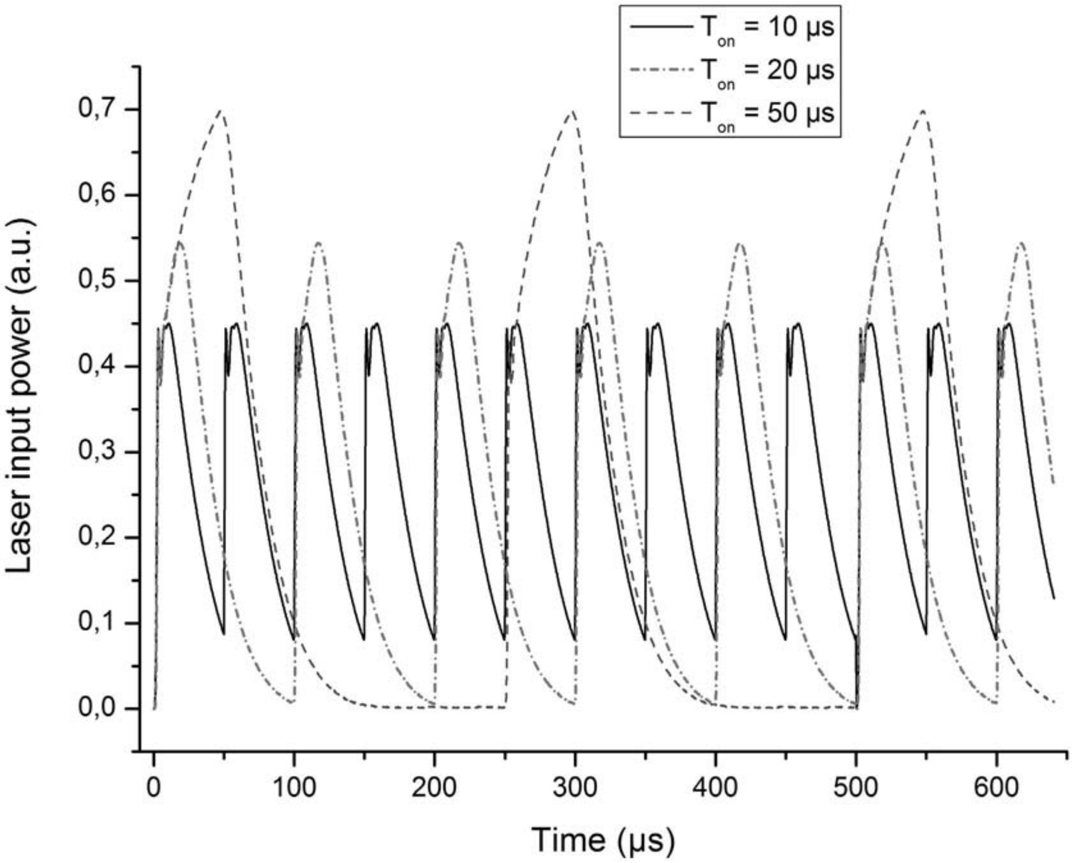

Fig. 5 Measured temporal profile of the laser power for different values of T_{on} and with a constant duty cycle control of 0.2.

3.6 On-line size measurement by TOF-MS

TOF-MS is used for on-line size characterization of the synthesized particles. The ionization is performed by an Nd:YAG laser at 266 nm wavelength. The ionized part of the particle beam is slightly deflected after acceleration with the help of polarized deflection plates in order to avoid deposition of the neutral component on the micro-channel plate (MCP) detector (see **Fig. 1**). The TOF spectra show two separated components. The first component is related to Si_n peaks (n = 1 - 12), which are ascribed to fragments formed from small nanoparticles during the ionization step, as reported elsewhere[25]. The second is related to Si-QDs. The ionization laser intensity is kept sufficiently low to make sure that multi-photon induced multi-ionization processes can not occur so that the higher mass distribution is only related to singly charged nanoparticles.

The initial kinetic energy of neutral nanoparticles in the supersonic beam is not negligible when compared to the energy given by TOF-MS acceleration potentials. Measurement of this initial kinetic energy is then necessary to establish a correct correspondence between time of flight and mass. It is achieved by deliberately changing the acceleration potentials of the spectrometer, so that the acceleration energy given to the ions is changed proportionally in the case of singly charged particles. We measure two most probable time-of-flights (time at maximum signal) t_1 and t_2, t_1 with the normal acceleration energy U_1, and t_2 with the modified acceleration energy U_2. It is then easy to retrieve the initial kinetic energy using the classic TOF-MS equations[26]. Considering that the acceleration time is small compared to the total time of flight for very high masses, the simple following expression of the most probable initial kinetic energy K_{E0} is deduced:

$$K_{E0} = (t_1^2U_1 - t_2^2U_2) \ / \ (t_2^2 - t_1^2) \qquad (1)$$

Fig. 6 shows an example with two mass spectra for different acceleration energy conditions. In the first one (solid line), U_1 = 1.9 keV. In the second one (dotted line), U_2 = 0.95 keV. The deduced average initial kinetic energy from equation (1) is 1.4 keV. This high value is due to the dense and high-speed supersonic

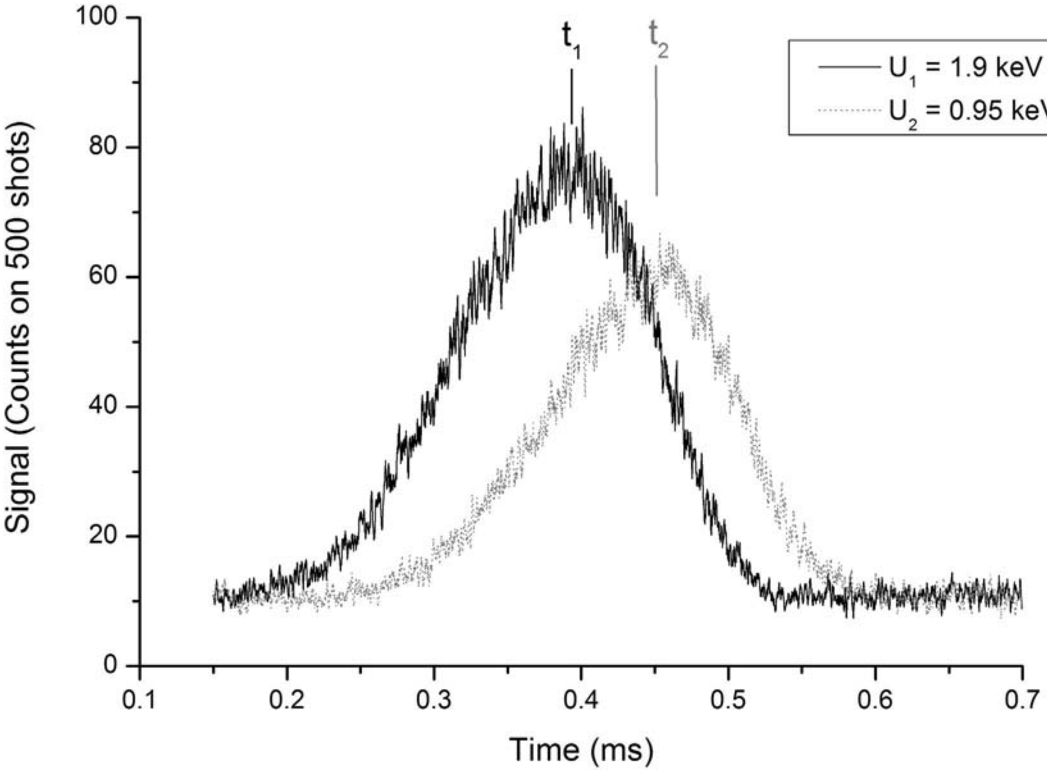

Fig. 6 Si-QDs TOF spectra with two different acceleration energies U_1 and U_2 in the TOF-MS.

gas beam that carries the particles. K_{E0} is then introduced into TOF-MS equations[26] to obtain the most probable size corresponding to t_1. In this example, the most probable size of the Si-QDs is 4 nm. Size measurements by TOF-MS, taking into account the initial kinetic energy, are in good agreement at 4 nm with high-resolution TEM observations of a TEM grid exposed to the supersonic jet during a few seconds.

The signal intensity is less in the lower acceleration energy case in **Fig. 6**. We assume it is due to the lower detection efficiency of MCP when the incoming ion speed decreases.

4. Characteristics of the synthesized Si nanocrystals

4.1 Comparison between CW and gated laser modes

In order to evaluate the interest of the gated-mode of the laser in terms of quality of products, a comparison between nanoparticles obtained in the CW beam mode and some obtained in the gated beam mode is proposed. In both cases, other synthesis parameters are similar, and the laser average power is about 660 W. SiH_4 is highly diluted in He (SiH_4 volume concentration about 7%), and the reactant total flow is 0.64 l/min. The laser beam focusing conditions are the ones presented in the experimental optimization part. **Fig. 7** shows TEM micrographs in each mode (CW mode on the left; gated mode on the right) and the corresponding primary particle size distributions obtained by software analysis of 50 particles for each representative TEM micrograph. The software is Image J (open source). The particle size can be visualized by the outer lines drawn around two particles on each micrograph. The primary particle size and morphology of agglomerates can be compared with the same scale in both modes.

In the CW mode, the minimum average primary particle size we are able to reach is about 8 nm, even in this optimized parameter regime for the production of small particles. The average size of the primary particles is 8.3 nm and the sample standard deviation is 1.3 nm. Particles are partially sintered in a strongly agglomerated form. Agglomerates are quite compact. The laser CW mode is well-suited to the synthesis of high quantities of Si nanocrystals, but the size range available is still too high to observe significant quantum confinement. In addition, control of the average size of small primary particles in this mode is not precise.

Typical particles produced in the gated laser mode are shown on the right TEM micrograph of **Fig. 7**.

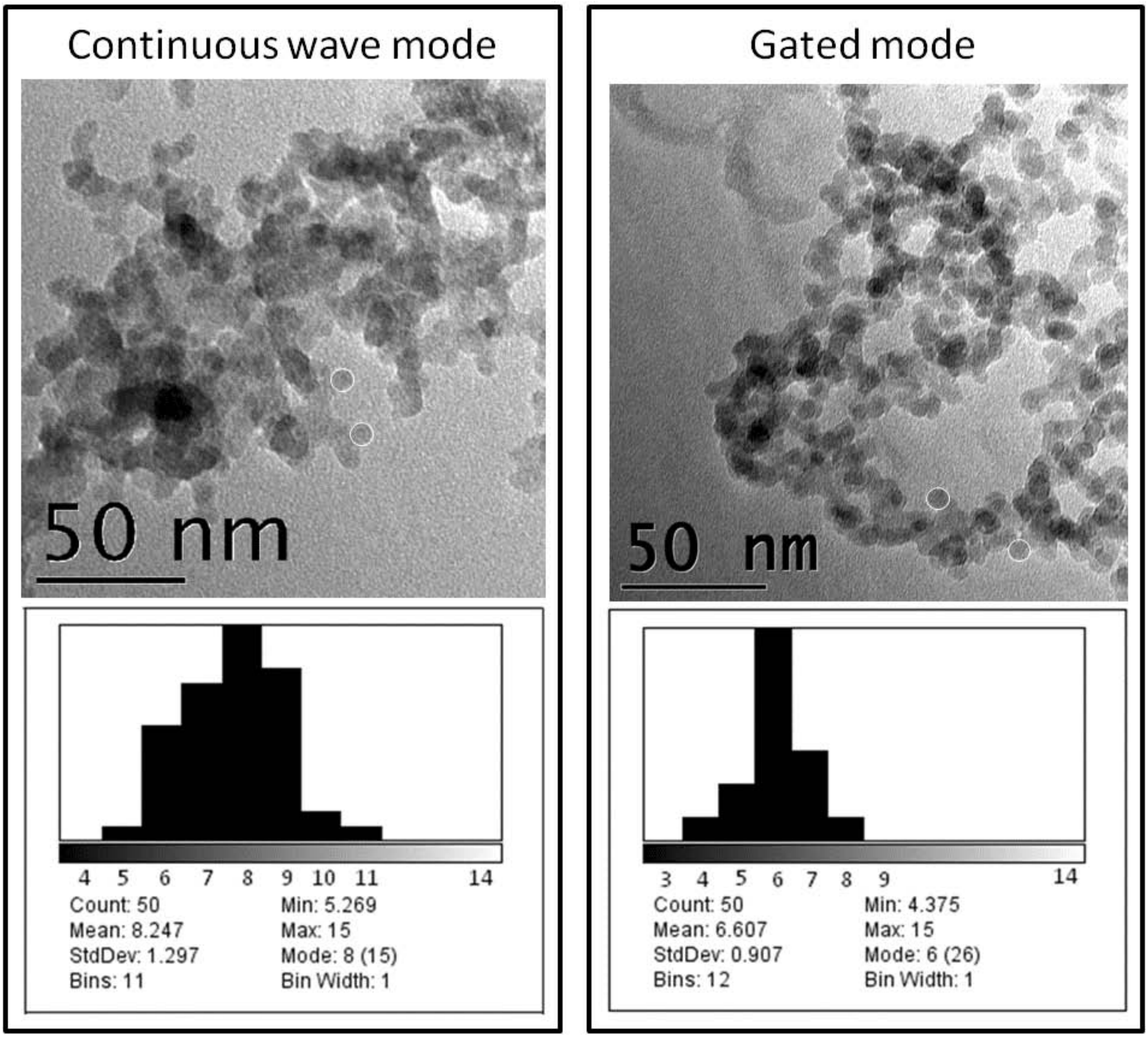

Fig. 7 TEM micrographs of Si-QDs synthesized with the laser CW mode (left) and with the gated laser mode (right). The gate-on duration is 50 µs and the duty cycle is 0.33 in the gated mode.

The corresponding primary particle size distribution is given. In this experiment, the gate-on duration was 50 µs and the duty cycle was 0.33. These conditions appeared to be suitable for a relatively high production rate (400 mg/h) of highly crystalline Si-QDs. The average size is 6.6 nm and the sample standard deviation is 0.9 nm. Particles are still highly agglomerated. **Fig. 7** (right TEM micrograph) clearly shows that they are more individualized. Moreover, the size distribution is narrower. These particles were found to be adequate as a starting material for biomedical imaging applications, for which a photoluminescence maximum is needed in the near infrared. The final material is obtained by chemical post-treatment and functionalization9).

4.2 Controlling the size of Si-QDs

The influence of the CO_2 laser gate-on duration control T_{on} on the Si-QDs size is studied for T_{on} values in the 10 to 80 µs range, with a constant duty cycle of 0.2 and with different SiH_4 volume concentrations C_{SiH4}. The Si-QDs most probable sizes are deduced from the TOF spectra taking into account the initial kinetic energy for each measurement point. Si-QDs agglomerates may be present in the supersonic beam as well as individualized primary particles. We assume that the detected particles are initially individualized primary particles or primary particles from agglomerates that are separated at the ionization stage in the TOF mass spectrometer. As the mass of agglomerates is too high to be detected, it is not possible to measure their size by TOF-MS.

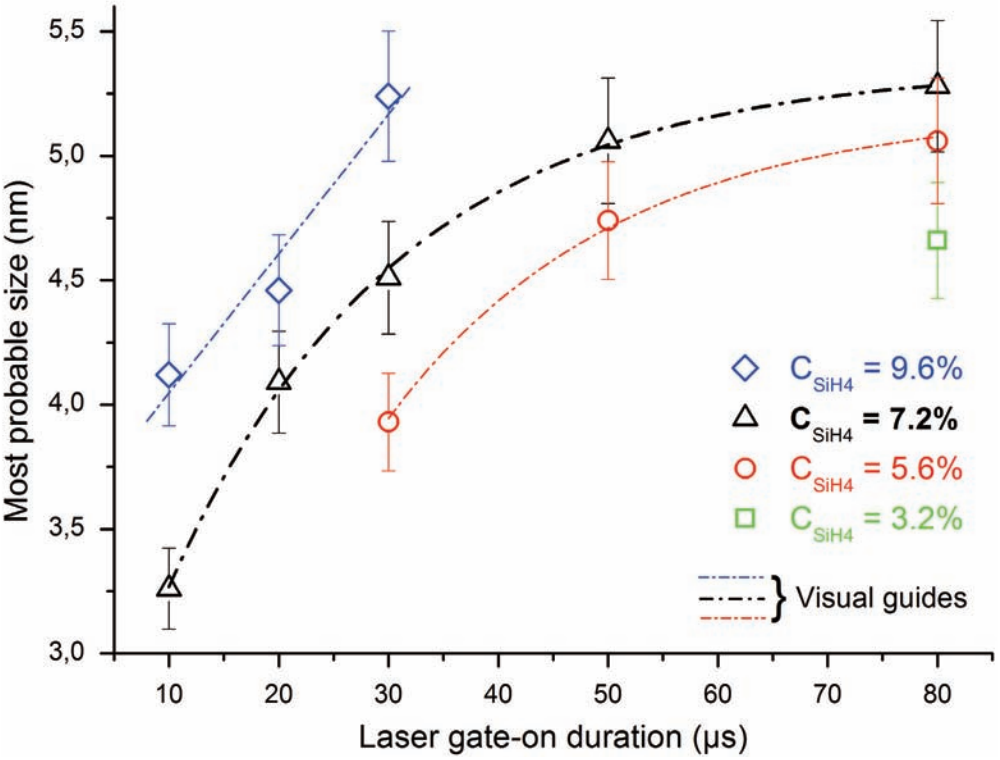

Fig. 8 Si-QDs most probable size as a function of the laser gate-on duration control T_{on} for different values of SiH_4 volume concentration C_{SiH4} and for a constant duty cycle $T_{on}/(T_{on}+T_{off}) = 0.2$. Size increases monotonically with the laser gate-on duration at a constant laser average power for a given C_{SiH4}.

Si-QDs most probable size as a function of T_{on} is plotted in **Fig. 8** for four different C_{SiH4} values: 3.2%, 5.6%, 7.2% and 9.6% with a constant total flow rate. As expected, we observe a significant increase of the production rate when C_{SiH4} increases. For $C_{SiH4} = 3.2\%$, only one point is recorded at $T_{on} = 80$ µs because no signal was detectable for lower values. We have an equivalent observation for $C_{SiH4} = 5.6\%$ for T_{on} values lower than 30 µs. For $C_{SiH4} = 9.6\%$, it was not possible to record data for T_{on} values above 30 µs because of the extraction nozzle clogging in these high production rate regimes. In addition, for the measurement points reported in **Fig. 8**, important signal amplitude fluctuations are experimentally observed in TOF-MS spectra with this high volume concentration. We assume it is due to intermittent and partial obstruction of the extraction nozzle. The size measurement may then present significant errors caused by erratic fluctuations in the particles' kinetic energy in the supersonic beam. The absolute values obtained with $C_{SiH4} = 9.6\%$ in **Fig. 8** should be treated with caution.

The size distribution width is not strictly deducible from the TOF-MS spectra because the initial kinetic energy is slightly dependent on the size (see experimental part). Nevertheless, the size distribution width is included in ± 15% (FWHM) of the most probable size. This value is usually observed in laser-pyrolysis-produced nanopowders[7] and is in good statistic agreement with HRTEM observations of 4-nm-sized Si-QDs. The error bars are related to the uncertainty on the most probable size determination by the TOF-MS and the analyzing process. It is estimated at ± 5% of the most probable size, based on the uncertainty on the determination of the most probable time of flight and the initial kinetic energy measurement. This uncertainty should not be confused with the size distribution.

5. Discussion

5.1 Laser gate-on duration effect

For a given SiH_4 volume concentration and with a constant duty cycle, a monotonic increase of Si-QDs size as a function of T_{on} is observed (**Fig. 8**). The first steps of nucleation involve numerous physical and chemical processes detailed elsewhere[17]. If the nucleation threshold temperature is reached in given conditions of pressure and dilution, nucleation starts and growth occurs rapidly. The thermal decomposition of silane was studied in the range of 100 ppm to 10% volume fraction in different carrier gases[27]. Diluted in He or in Ar, the particle formation threshold temperature was found to be between 770 K and 800 K for a volume concentration of SiH_4 in the 1 to 10% range. This threshold temperature is much lower than the melting point temperature of the bulk phase at 1687 K. If the temperature goes back below the threshold, the nucleation process stops by closing key physical and chemical pathways. Thus, growth can only occur by coagulation of particles, which leads to full coalescence in cases of liquid-liquid or liquid-solid particles collisions. It was shown that temperatures approaching the melting point of the bulk phase (1687 K) or higher are necessary to achieve full coalescence of previously grown solid crystallites of a few nm in size[21]. At temperatures higher than 1687 K, particles are non-agglomerated single crystals with a quite large (a few tens of nm) diameter depending on the vapor pressure of the dissociated species. At temperatures lower than 1687 K, particles are either small (a few nm) agglomerated monocrystals, or non-agglomerated polycrystalline spherical particles resulting from the sintering of several primary particles. In our experimental conditions, particles are small (a few nm) and agglomerated, as shown in **Fig. 7**. Previous works showed that they were monocrystalline in similar synthesis conditions[9]. Therefore, we assume that the maximum reaction temperature during gate-on slots in our case is between 770 K and 1687 K, and depends on T_{on}. In these conditions, the size is essentially governed by two parameters, i.e. the reaction temperature and the reaction time. The reaction temperature is directly related to the SiH_4 dissociation efficiency, and thus to the vapor pressure of dissociated species. Higher temperature leads to higher vapor pressure, more nuclei and faster growth rate. For a given reaction time, a higher reaction temperature, corresponding to a higher laser power, leads to a larger Si-QDs diameter in the considered temperature range[21]. The reaction time controls the nucleation duration while SiH_4 is not completely decomposed. In our experiment, the decomposed fraction of SiH_4 is 3% at most. The reaction time then controls both nucleation and growth durations. At a given temperature, a larger reaction time leads to a larger Si-QDs diameter. Considering the temporal profiles of the laser power given in **Fig. 5**, the maximum amplitude increases as a function of the gate-on duration T_{on}. The direct expected consequence is a higher maximum reaction temperature with longer T_{on}. Moreover, the total reaction time is the same for all values of T_{on}. As the duty cycle is constant, the integrated time spent above the nucleation temperature threshold is about the same or slightly higher as a function of T_{on} during the total reaction time. It is then reasonable to think that the increase of Si-QDs size as a function of T_{on} is due primarily, to an increase of the average vapor pressure of dissociated species as a consequence of an increase in the maximum reaction temperature.

5.2 SiH_4 volume concentration effect

The dependence of the size of Si-QDs as a function of C_{SiH4} has already been reported by other authors[28]. For a given gate-on duration, sizes are smaller as the C_{SiH4} decreases. For example, for T_{on} = 80 μs, sizes are 5.3, 5.0 and 4.6 nm for C_{SiH4} = 7.2%, 5.6% and 3.2%, respectively. This is explained by lower laser absorption and a lower average collision rate between dissociated species when increasing SiH_4 dilution. Furthermore, for C_{SiH4} = 3.2%, no signal is detected below T_{on} = 80 μs, and for C_{SiH4} = 5.6%, below T_{on} = 30 μs. Increasing the dilution is equivalent to lowering the heating rate of the reaction which results in lowering the growth time. In addition, it has been shown that the threshold temperature for nucleation was dependent on the SiH_4 volume concentration[27]. More highly diluted SiH_4 needs higher temperatures for particles formation. This explains why it is difficult to reach very small sizes with small C_{SiH4}. In this case, the minimum temperature for nucleation onset is too high to be reached with small values of T_{on}. It results in a limitation for lower C_{SiH4} to reach very small sizes. This introduces the idea of an optimum in SiH_4 volume concentration. In our experiment, this optimum is around 7%, where a minimum probable size of 3.3 nm is obtained. However, the use of a higher volume concentration is limited by our experimental set-up due to the high production rate that induces clogging of the extraction nozzle. For C_{SiH4} = 7.2%, a simple visual guide suggests in **Fig. 8** that the size can be controlled precisely between 3.3 and 5.3 nm by adjusting T_{on} with a constant duty cycle. This observation could be of importance for applications depending on the changing properties of Si-QDs in this size range.

6. Conclusion

Applications in various fields need large quantities of size-controlled Si-QDs. The CO_2 gated laser-driven pyrolysis of SiH_4 can provide a precise size control in the relevant range by adjusting the laser gate-on duration with a constant average power and on-line TOF-MS. The size evolution as a function of T_{on} and SiH_4 volume concentration in He is qualitatively discussed. We assume that the maximum reaction temperature reached during the laser gate-on slots mostly controls the Si-QDs size. This means controlling the average vapour pressure of the dissociated species in the reaction zone. In a more general consideration, controlling the time and amplitude of the input energy in the reaction zone should be convenient when small particles with a precise size control are difficult to obtain by other means.

Acknowledgements

The French National Research Agency (ANR) supported this work within the framework of the NANOPLEIADES and DUOSIL projects. It was also part of the BONSAI project funded by the European Union. The authors would like to thank Jérôme Yon from CORIA - UMR 6614 (Rouen, France) and François-Xavier Ouf from IRSN - LPMA (Saclay, France) for their technical support on the fast sampling system that allowed on-line aerosol deposition on TEM grids. Thanks also go to Patrick Bonnaillie from CEA (Saclay, France) for SEM micrographs.

References

1) Alivisatos, A.P. (1996): Semiconductor Clusters, Nanocrystals, and Quantum Dots, Science 271, 5251, pp.933-937.
2) Feng, T., Yu, H., Dicken, M., Heath, J.R. and Atwater, H.A. (2005): Probing the Size and Density of Silicon Nanocrystals in Nanocrystal Memory Device Applications, Applied Physics Letters 86, 033103.
3) Conibeer , G., Green, M., Corkish, R., Cho, Y., Cho, E.-C., Jiang, C.-W., Fangsuwannarak, T., Pink, E., Huang, Y., Puzzer, T., Trupke, T., Richards, B., Shalav, A. and Lin, K.-L. (2006): Silicon Nanostructures for Third Generation Photovoltaic Solar Cells, Thin solid films, 511-512, pp.654-662.
4) Sato, K., Yanagisawa, S., Funakubo, A., Fukui, Y., Hirakuri, K. and Higami, T. (2007): Biological Properties of Nanocrystalline Silicon Particles for Biomedical Applications, Materials Research Society Proceedings, 958, 0958-L10-19.
5) Delerue, C., Allan, G. and Lannoo, M. (1993): Theoretical Aspects of the Luminescence of Porous Silicon, Physical Review, B 48, pp.11024-11036.
6) Ledoux, G., Gong, J., Huisken, F., Guillois, O. and Reynaud, C. (2001): Effect of Passivation and Aging on the Photoluminescence of Silicon Nanocrystals, Applied physics letters, 79, 4028.
7) Herlin-Boime, N., Mayne-LHermite, M. and Reynaud, C. (2004):” Encyclopedia of Nanoscience and Nanotechnology”, Naiwa Ed. Vol. 10, pp.1-26.
8) Ledoux, G., Amans, D., Gong, J., Huisken, F., Cichos, F. and Martin, J. (2002): Photoluminescence of Size-separated Silicon Nanocrystals: Confirmation of Quantum Confinement, Applied Physics Letters, 80, 4834.
9) Lacour, F., Guillois, O., Portier, X., Perez, H., Herlin, N. and Reynaud, C. (2007): Laser Pyrolysis Synthesis and Characterization of Luminescent Silicon Nanocrystals, Physica, E 38, pp.11-15.
10) Cannon, W.R., Danforth, S.C., Flint, J.H., Haggerty, J.S. and Marra, R.A. (1982): Sinterable Ceramic Powders from Laser-Driven Reactions: I, Process Description and Modeling, Journal of American Ceramic Society, 65, 7, pp.324-330.
11) El Diasty, F. (2004): Simulation of CO_2 Laser Pyrolysis During Preparation of SiC Nanopowders, Opt. Commun., 241, pp.121-135.
12) Borsella, E., Botti, S., Caneve, L., De Dominicis, L. and Fantoni, R. (2008): IR Multiple-photon Excitation of Polyatomic Molecules: A Route Towards Nanostructures, Physica Scripta, 78, 058112.
13) Van Erven, J., Munao, D., Fu, Z., Trzeciak, T., Janssen, R., Kelder, E. and Marijnissen, J.C.M. (2009): The Improvement and Upscaling of a Laser Chemical Vapor Pyrolysis Reactor, KONA Powder and Particle Journal, 27, pp.157-173.
14) Wegner, W., Pisery, P., Vahedi Tafreshi, H. and Milani, P. (2006): Cluster Beam Deposition: A Tool for Nanoscale Science and Technology, Journal of Physics D: Applied Physics, 39, pp.439-459.
15) Beaucage, G., Kammler, H.K., Mueller, R., Strobel, R., Agashe, N., Pratsinis, S.E. and Narayanan, T. (2004): Probing the Dynamics of Nanoparticle Growth in a Flame Using Synchrotron Radiation, Nature Materials 3, pp.370-374.
16) Swihart, M.T. and Girshick, S.L. (1999): Thermochemistry and Kinetics of Silicon Hydride Cluster Formation during Thermal Decomposition of Silane, Journal of Physical Chemistry, B 103, pp.64-76.
17) Onischuk, A.A., Levykin, A.I., Strunin, V.P., Ushakova, M.A., Samoilova, R.I., Sabelfeld, K.K. and Panfilov, V.N. (2000): Aerosol Formation Under Heterogeneous/Homogeneous Thermal Decomposition of Silane: Experiment and Numerical Modeling, Journal of Aerosol Science, 31, 8, pp.879-906.
18) Wegner, K., Walker, B., Tsantilis, S. and Pratsinis, S.E. (2002): Design of Metal Nanoparticle Synthesis by Vapor Flow Condensation, Chemical Engineering Science, 57, pp.1753-1762.
19) Nijhawan, S., McMurry, P.H., Swihart, M.T., Suh, S.-M., Girshick, S.L., Campbell, S.A. and Brockmann, J.E. (2003): An Experimental and Numerical Study of Particle Nucleation and Growth During Low-pressure Thermal Decomposition of Silane, Journal of Aerosol Science, 34, pp.691-711.
20) Flagan, R.C. and Lunden, M.M. (1995): Particle Structure Control in Nanoparticle Synthesis from the Vapor Phase, Materials Science and Engineering, A 204,

pp.113-124.

21) Di Nunzio, P.E. and Martelli, S. (2006): Coagulation and Aggregation Model of Silicon Nanoparticles from Laser Pyrolysis, Aerosol Science and Technology, 40, pp.724-734.

22) "CRC Handbook of Chemistry and Physics" (2011), 91st Edition, W. M. Haynes Editor.

23) Ehbrecht, M., Ferkel, H., Smirnov, V.V and Stelmakh, O.M. (1995): Laser - driven Flow Reactor as a Cluster Beam Source, Review of Scientific Instruments, 66, 3833.

24) Amans, D., Callard, S., Gagnaire, A., Joseph, J., Ledoux, G. and Huisken, F. (2003): Ellipsometric Study of Silicon Nanocrystal Optical Constants, Journal of Applied Physics, 93, 4173.

25) Ehbrecht, M. and Huisken, F. (1999): Gas-phase Characterization of Silicon Nanoclusters Produced by Laser Pyrolysis of Silane, Physical Review, B 59, 2975.

26) Wiley, W.C. and McLaren, I.H. (1955): Time-of-Flight Mass Spectrometer with Improved Resolution, Review of Scientific Instruments 26, 12, pp. 1150-1157.

27) Slootman, F. and Parent, J.-C. (1994): Homogeneous Gas-phase Nucleation in Silane Pyrolysis, Journal of Aerosol Science, 25, pp.15-21.

28) Botti, S., Coppola, R., Gourbilleau, F. and Rizk, R. (2000): Photoluminescence from Silicon Nano-particles Synthesized by Laser-induced Decomposition of Silane, Journal of Applied Physics, 88, pp.3396-3401.

Author's short biography

Olivier Sublemontier

Olivier Sublemontier is research engineer of the French Atomic and Alternative Energy Commission (CEA) in Saclay, France. He holds a Master Engineering degree from the Conservatoire National des Arts et M e tiers (CNAM, Paris). He has twenty years of experience in the field of Chemical Physics, including Laser-Induced Processes and Nanomaterials Processing. He has special expertise in the synthesis of nanoparticles by laser processes and applications. He is involved in fundamental research programs aiming to study interactions of isolated nanoparticles with synchrotron radiation. He is also involved in application programs of silicon quantum dots for bio-imaging and photovoltaic solar cells. He has (co-) authored about 61 peer-referred papers, 1 book chapter and 6 patents.

Harold Kintz

Harold Kintz received his M. Sc in Materials Science From Pierre et Marie Curie University, Paris. In 2010, he joined the PhD program in the Francis Perrin laboratory at CEA Saclay in France. He is currently conducting research on Si-based nanomaterials for third generation solar cells. He can be reached at harold.kintz@cea.fr

Frederic Lacour

Frederic Lacour was graduated in 2004 from the National Institute of Applied Science in Toulouse (INSA). He obtained his PhD in 2007 at the Francis Perrin laboratory (CEA Saclay, DSM/IRAMIS). His work was devoted to the synthesis of small silicon nanoparticles and the study of their properties and applications. Frederic Lacour is currently holding a research engineer position at Saint-Gobain, France.

Xavier Paquez

Xavier Paquez, born in 1982, finished his master degree in materials science at the Paris-Sud University in 2007. Following this, he began a PhD in the Francis Perrin laboratory (CEA Saclay, DSM/IRAMIS). The topic was the development of deposition processes in order to build nanocomposites thin films based on doped silicon nanoparticles with a diameter small enough to exhibit quantum confinement. This work also focused on the electrical doping of silicon nanoparticles. The aim of this work was to incorporate nanostructured films in a silicon-based photovoltaic cell to improve the global efficiency of the cell.

Vincent Maurice

Vincent Maurice was born in 1984 and graduated in 2007 from the National School of Chemistry in Paris (ENSCP). He obtained his PhD in 2010 at the Francis Perrin laboratory (Cea Saclay, DSM/IRAMIS). His work was centered on the functionalization of silicon nanoparticles in order to produce silicon based fluorescent tracers for bioimaging. Vincent Maurice is currently holding a post-doc position. His research focuses on the synthesis of ceramic nanoparticles by soft methods.

Author's short biography

Yann Leconte

Yann Leconte is a Research Scientist in the Nanometric Structures Group of CEA-DSM/IRAMIS/SPAM. He received his MSc degree in Physics in 1999 in Lower Normandy University (Caen, France).

He later earned his PhD from the same institution in Semiconductors Science in 2003, working on Si thin films deposition by PVD for microelectronic applications. His research interests in CEA concern the study of the modification in materials properties owing to nanostructuration. He is involved in the synthesis and applications of various nanoparticles by Laser Pyrolysis. His main addressed topics are nanostructured ceramics for nuclear and aerospace applications, Ti or Mo based catalysts for pollutants destruction, and Si quantum dots for photovoltaic applications.

Pilot Plants for Industrial Nanoparticle Production by Flame Spray Pyrolysis †

Karsten Wegner[1,2]*, Björn Schimmoeller[1], Bénédicte Thiebaut[3], Claudio Fernandez[4] and Tata N. Rao[5]
Particle Technology Laboratory, ETH Zurich[1]
Wegner Consulting[2]
Johnson Matthey Technology Center[3]
Tecnan SL[4]
Centre for Nanomaterials, ARCI[5] [5]

Abstract

With the rapid advancement of nanotechnology and with nanoparticles beginning to enter into products, the demand for production-level quantities of advanced nanopowders such as multi-component or coated oxides is rising. Such advanced nanoparticles can be effectively made by flame spray pyrolysis (FSP), and research with laboratory reactors yielded a spectrum of new nanomaterials for catalysis, pigments, ceramics, optics, energy and biomaterials, among others. Here, the transfer of FSP nanopowder synthesis from gram-level lab-scale to pilot reactors with up to 10 metric tons annual production rate is investigated by the example of FSP pilot plants that were realized in industrial-oriented settings. Design considerations for such pilot-scale systems are addressed and guides to production cost estimates are given. Special attention is brought to safe and contained nanoparticle manufacture in order to address the growing awareness of the potential health and environmental effects of nanoparticles.

Keywords: nanoparticles, flame spray pyrolysis, aerosol synthesis, pilot-plant, scale-up

1. Introduction

The past decade has seen intense research on nanoparticle development with special attention paid to gas-phase processes, as these typically produce dry and thermally stable crystalline nanoparticles in one step without the need to handle large liquid volumes, surfactants or precipitation agents (Mädler, 2004). Last but not least, the development of flame synthesis processes for the industrial production of carbon black, fumed silica and pigmentary titania in the first half of the last century showed that the production rate of gas-phase processes can be scaled to several tons per hour per reactor, catering, e.g. to a world market of approximately 300,000 tons of fumed silica in 2010 (China Chemical Reporter, 21.11.2010).

The operation principle of classic flame synthesis of silica and titania, the so-called chloride process, relies on the evaporation of metal chlorides prior to their introduction into the flame reactor. This limits the process to synthesis of materials with precursors exhibiting sufficient vapor pressure and thermal stability at moderate temperatures. The development of flame spray pyrolysis (FSP, Bickmore et al., 1996; Mädler et al., 2002) overcame this limitation by directly feeding a liquid precursor-solvent mixture into the flame reactor, atomizing and igniting it. The organic solvent and the precursor thereby provide the combustion enthalpy that drives droplet evaporation, precursor oxidation, cluster formation and growth to product nanoparticles by coagulation and coalescence and/or surface growth in the high-temperature environment (typically > 2000℃) of the spray flame (Mädler, 2004). With FSP technology, almost all periodic table elements can now be transformed into oxide, salt and sometimes even metal nanoparticles, as is apparent from the recent review of Teoh et al. (2010).

---

† Accepted: September 12th, 2011
[1] 8092 Zurich, Switzerland
[2] 8008 Zurich, Switzerland
[3] Sonning Common, Reading RG4 9NH, United Kingdom
[4] 31210 Los Arcos, Spain
[5] Hyderabad 500 005, India
* Corresponding author:
E-mail: wegner@ptl.mavt.ethz.ch
TEL: (+41)44-6322489 FAX: (+41)44-6321595

ⓒ 2011 Hosokawa Powder Technology Foundation

Most material development studies using FSP were realized with laboratory-scale reactors that are now even available commercially (Tethis, 2011) and produce gram quantities of nanoparticles in batch operation. In addition to custom-made solutions addressed in his article, a continuous system to produce nanoparticles by FSP is also available on the market: Hosokawa provides a nanoparticle generator that uses the Flash Creation Method (FCM), a kind of plasma-assisted FSP which is capable of producing ZrO_2 nanoparticles at a capacity of 0.97 kg/h (Watanabe et al. 2007) or even several kg per hour depending on the material (Watanabe et al., 2006). Like FSP, the Flash Creation Method can generate not only nanoparticles of single-component oxides but also differently structured nanocomposite particles. Today's challenge is the translation of these achievements into an industrial production environment through continuously operated pilot plants.

Rather little information is available on FSP process scale-up, design criteria and operational experience for the continuous production of nanoparticles at pilot-plant level. Bickmore et al. (1996) realized the first FSP plant on a pilot scale with a production rate of already up to 100 g/h spinel nanopowder. They reported continuous operation for about twelve hours at a rate of 85 g/h. With an optimized system, it was possible to increase the production rate to 400 g/h of ceria-zirconia nanoparticles (Laine et al., 2000). Mueller et al. (2003) produced silica nanoparticles with a pilot-scale reactor at rates up to 1.1 kg/h. They systematically investigated the effect of the precursor concentration and delivery rate as well as the dispersion gas flow on the product's primary particle diameter. A similar parameter study was carried out for zirconia at rates up to 600 g/h (Mueller et al., 2004a), whereas temperature and particle diagnostics were employed to understand the growth of zirconia nanoparticles at production rates of 100 and 300 g/h and to develop and validate a simple particle growth model (Mueller et al., 2004b). Heine and Pratsinis (2005) further characterized the spray of this FSP reactor and developed a model accounting for multi-component droplet combustion and zirconia particle growth. Heel et al. (2010) produced cathode materials for solid-oxide fuel cells with an FSP pilot plant at 35 to 400 g/h production rate. They investigated the use of water-based precursor solutions and provided additional enthalpy by a concentric acetylene-oxygen flame. Kilian and Morse (2001) employed an ultrasonic nozzle for atomization of the precursor solution rather than the gas-assisted nozzle used by the other research groups, and manufactured zirconium and aluminum oxide nanoparticles at rates up to 180 g/h.

Here, the scale-up of nanoparticle synthesis by flame spray pyrolysis is reviewed and the design and operation of FSP pilot systems is discussed using the example of pilot plants with >100 g/h production rate. Guidelines for safe and contained nanoparticle manufacture are proposed and production cost structures estimated.

2. Process Flow Diagram

Fig. 1 is an example of an FSP process flow sheet. One or more solid or liquid precursors along with organic solvents are introduced into a stirred tank reactor where dissolution and/or chemical conversion and mixing of the raw materials takes place. A pump meters the precursor solution to the spray nozzle where it is atomized with oxygen dispersion gas. Gases including the oxygen and gaseous fuel for spray ignition and stabilization are typically delivered from cylinders to the FSP reactor using mass flow controllers. Filtered ambient air is used to dilute and quench the hot flame aerosol prior to its introduction into the collection device.

For product nanopowder collection in FSP pilot plants, baghouse filters (Mueller et al., 2003; Akurati et al., 2008) or electrostatic precipitators (Bickmore et al., 1996) have been employed. The accumulated product nanopowders in the bottom cone of the baghouse filter are periodically discharged through a butterfly valve or shutter to the product silo below the filter. From here, they can be pneumatically conveyed to a packaging station or directly filled into containers. The process off-gas consisting mainly of air, water and CO_2 flows through a second particle collector to remove nanoparticles that might have escaped the primary one. In the process with baghouse filter (**Fig. 2**), this is typically a high-efficiency particulate air filter (HEPA), while Bickmore et al. (1996) installed a wet scrubber downstream of their electrostatic precipitator. The air flow through the entire system is usually established and controlled by a centrifugal fan which creates a slightly negative pressure in the unit. Unless further off-gas treatment such as DeNOx in the case of nitrate precursor combustion is required, the exhaust fumes are vented to the environment.

2.1 Precursor selection and preparation

The selection and preparation of precursor solutions is among the most challenging tasks in the

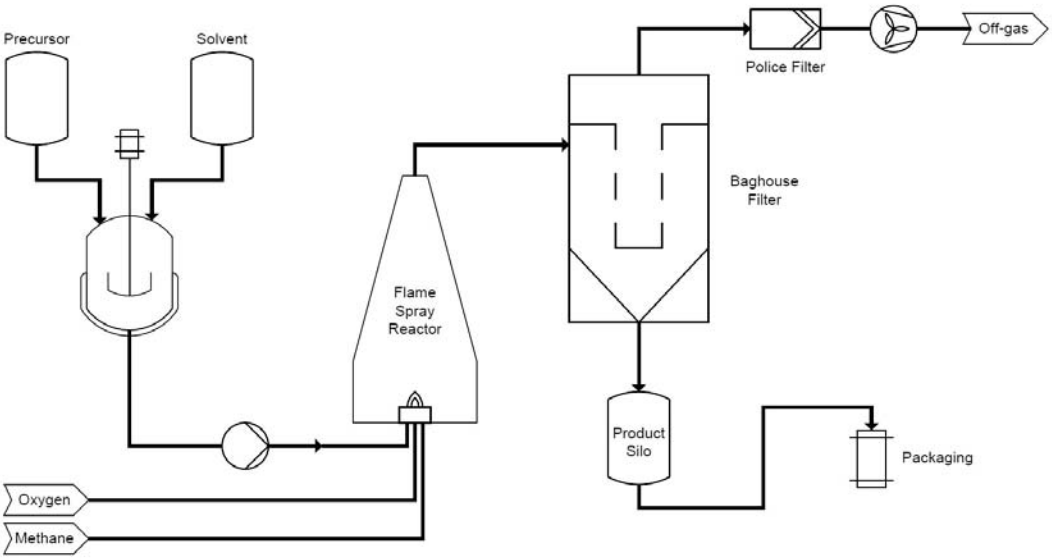

Fig. 1 Flow chart of a plant for nanoparticle synthesis by flame spray pyrolysis with stirred tank for precursor preparation, FSP reactor, baghouse filter for nanoparticle collection and police filter for off-gas cleaning.

flame spray synthesis of nanoparticles, especially if multi-component materials are produced, since the following criteria must be considered: homogeneity of product nanopowders, production costs, CO_2 formation and carbon balance, as well as precursor handling.

A homogeneous product powder consisting of fine nanoparticles requires particle formation via gas-to-particle conversion in which the precursor species evaporate from the spray droplet, react and subsequently nucleate to cluster embryos of the product material. In the case of insufficient precursor volatility, undesired precipitation inside the spray droplet can occur resulting in several-hundred-nanometer large hollow or dense particle impurities in the nanopowder by droplet-to-particle conversion (Kodas and Hampden-Smith, 1999).

Process economics suggest the use of low-cost raw materials such as nitrates, chlorides, or carbonates dissolved in simple organic solvents such as ethanol or acetic acid as feed to the FSP reactor. Such solutions, however, are prone to form inhomogeneous product powders, as has been observed both with lab- (Jossen et al., 2005b; Strobel and Pratsinis, 2011) and pilot-scale FSP systems (Hinklin et al., 2004; Jossen et al., 2005a). Reaction of simple metal salt precursors with carboxylic acids prior to their introduction into the flame was shown to significantly increase the nanopowder homogeneity for nitrates (Chiarello et al., 2007; Strobel and Pratsinis, 2011) and carbonates (Jossen et al., 2005a; Kim et al., 2008, 2009), and might be a good trade-off between product powder quality, raw materials costs and complexity of precursor preparation.

Due to their volatility, organometallic compounds are typically well suited for flame spray synthesis, but high market prices and difficulties in handling the often moisture-sensitive species do not make them appear an attractive FSP feedstock. However, like in the synthesis of metal carboxylates, integrating the formation of organometallic precursors into the FSP plant might reduce production costs. For instance, Bickmore et al. (1996, 1998) used aluminum, magnesium or titanium oxides and hydroxides along with ethanolamines as starting materials that were converted into organometallic compounds. Pokhrel et al. (2010) formed tungsten alkoxides by reacting tungsten chlorides with benzyl alcohol under Cl release and used the precursor for the synthesis of WO_3 nanoparticles by FSP.

Jossen et al (2005b) reported that the tendency toward the formation of inhomogeneous nanopowders from simple metal salt precursors can be reduced by increasing the combustion enthalpy density and by selecting solvents with boiling points higher than the melting or decomposition point of the precursor. This was also observed by Heel et al. (2010) using mainly water-based nitrate precursor solutions and an acetylene-oxygen supporting flame surrounding the spray. When producing multicomponent materials, precursor selection can affect the product quality, as was reported by Stark et al. (2003) producing ceria-zirconia catalyst supports: the two elements were evenly distributed in the product particles when carboxylic (lauric and acetic) acid-derived precursors were used while segregation of a zirconia-like phase was observed using acetic acid, 2-butanol and iso-octane as solvents for cerium-acetatehydrate and zirconium-acetylacetonate.

In view of production costs and CO_2 formation, it is desirable to operate with precursor solutions of high molarity with respect to the total metal concentration. Here, precursors with a low carbon content such as a zirconium-carbonate-derived Zr-propionate with an elemental ratio of Zr:C = 1:6 (Kim et al., 2009) might be more advantageous then zirconium-n-propoxide (Zr:C = 1:12; Mueller et al., 2004a) or zirconium-2-ethylhexanoate (Zr:C = 1:32; Stark et al., 2005).

Further aspects to consider in the design of a precursor-solvent mixture are its soot formation tendency, viscosity and surface tension. Increasing the metal content of the precursor is limited by the increasing viscosity of the solution (Laine et al., 2000) which impedes pumping and spray atomization. In air-assist atomizers, larger liquid viscosity and surface tension result in coarser sprays (Lefebvre, 1989), which in turn affects the temperature and velocity profiles of the flame.

2.2 Reactant feeding

The precursor should be delivered at a low pulsation rate to the FSP reactor since spray flames are sensitive to oscillations in the liquid fuel supply which can affect nanoparticle growth conditions. Lab-scale systems typically use syringe pumps for the low-pulsation delivery of 50 – 100 ml quantities of precursor (Mädler et al., 2002), and some pilot studies have adopted the approach by using large 1l precision syringe pumps (Mueller et al., 2003). A dual pump system (Heel et al., 2010) allows quasi-continuous production by re-filling one syringe while the other is feeding the reactor. Bickmore et al. (1996) delivered the precursor from the precursor tank to the FSP reactor by applying a nitrogen head pressure to the vessel.

Gear pumps have been used for continuous precursor delivery (Killian and Morse, 2001) and provide accurate control over the precursor flow rate by adjusting the drive speed, but they suffer from pulsations. These can be reduced by the design of the gears as in the micro-annular gear pump used by Grass and Stark (2005) for precursor dispensing. A drawback of gear pumps is their susceptibility to particles and the need to thoroughly clean the pump after use. In the FSP pilot plant at ETH Zurich, a centrifugal pump (KSB microchem) designed for the pulsation-free delivery of small liquid volumes was used to feed the flame spray reactor. Unlike gear pumps it is not sensitive to particles in the pumped fluid and is easy to clean. Drawbacks are the need of a mass flow control, sensitivity to downstream pressure changes and no self-priming behavior.

The supply of gases is typically from cylinders with flow rates being controlled by mass flow controllers. Gas consumption is dominated by the dispersion gas, usually oxygen. As a rule of thumb, the production of 1 kg of nanopowder by FSP requires approximately 10l of precursor solution and 5 m^3 of oxygen dispersion gas. Dispersion with air appears to be more economic but lowers the oxygen partial pressure in the flame which might result in incomplete combustion, as observed by Mueller et al. (2003) for silica production rates > 100 g/h. Air-operated FSP nozzles exhibit lower flame temperatures than those run with oxygen as the additional nitrogen not taking part in the combustion needs to be heated up, resulting in smaller product particles (Mädler et al., 2002; Mueller et al., 2003).

2.3 Reactor

The flame spray pyrolysis reactor consists of an atomizing nozzle for dispersion of the precursor-solvent mixture that typically is surrounded by co-flowing streams of gaseous fuel and oxidant feeding the pilot flame. While most work was done with two-phase atomizers, Kilian and Morse (2001) used an ultrasonic nozzle for dispersion of the precursor stream. Ultrasonic atomizing nozzles have the advantage of a relatively narrow distribution of small droplets which might lead to fast and more homogeneous evaporation. Furthermore, the large dispersion gas flow rates required for breaking up the liquid in two-phase atomizers are not needed. As a result, the spray flames are typically laminar and exhibit longer particle residence times than the turbulent flames of a two-phase nozzle spray.

Two-phase nozzles are frequently used in flame spray synthesis since they produce fine sprays, are able to effectively atomize high-viscosity liquids and vigorously mix the oxidizing dispersion gas with the liquid precursor (Lefebvre, 1989). Spray velocities are often > 100 m/s (Heine et al., 2005) and can even reach sonic speed resulting in highly turbulent spray flames with a flame temperature above 2500K (Mueller et al., 2004b). High gas velocities cause significant entrainment of ambient air into the spray flame, diluting and quenching it (Heine and Pratsinis, 2006).

Fig. 2 shows the effect of precursor and dispersion gas feed on the primary particle diameter of zirconia nanoparticles made with the FSP pilot plant at ETH Zurich. The precursor solution was prepared by reacting zirconium carbonate with the stoichiometric amount of 2-ethylhexanoic acid for obtaining zirconium 2-ethylhexanoate, and using acetic acid as a solvent to achieve a Zr concentration of 0.5 mol/l. The reaction was carried out in a heated stirred tank at 100℃ under reflux. Results for 60 l/min dispersion gas flow (circles) are compared to Mueller et al. (2004a), who used zirconium n-propoxide in ethanol/n-propanol at concentrations of 0.5 mol/l as feedstock with dispersion gas flow rates of 25 (squares) and 50 l/min (triangles). **Fig. 2** shows the BET-equivalent particle diameter, derived from a measurement of the specific surface area and assuming monodisperse spherical particles, for production rates of 50 to 300 g/h.

Increasing the precursor flow increases the primary particle diameter in all experiments, attributed to increased time for nanoparticle growth in longer and hotter flames. On the other hand, the primary particle diameter is decreased by increasing the dispersion gas flow rate due to faster mixing of reactants and oxidizer as well as higher entrainment of ambient air that cools and dilutes the flame. Both effects lead to shorter and colder flames yielding smaller particles. Please note that the ZrO_2 particles produced in this study with the carbonate precursor and a slightly higher dispersion gas flow rate of 60 l/min are much smaller than those made from the zirconium n-propoxide solution at the same production rate and concentration of 0.5M. A possible explanation is the lower enthalpy content of the precursor mixture employed here that was -5.4 kJ/(g gas) while the precursor of Mueller et al. (2004a) had a specific enthalpy of -8.3 kJ/g at 130 g/h. A lower enthalpy content will lead to lower flame temperatures and therefore smaller nanoparticles.

When keeping the mass flow rates of liquid precursor and dispersion gas constant but increasing the dispersion gas pressure drop of the atomizer from 2 to 7 bar, the specific surface area of $FePO_4$ nanoparticles increased from 91 to 108 nm, as shown in **Fig. 3**. The delivery rate of the precursor solution containing stoichiometric ratios of iron nitrate and tributylphosphate dissolved in a 1:1 by volume mixture of 2-ethylhexanoic acid was 20 ml/min, while 40 l/min (STP) of oxygen dispersion gas was used. The increase in pressure at constant mass flow rate was realized by decreasing the area of the dispersion gas gap leading to higher gas velocities which improves atomization. This is in agreement with Lefebvre (1989) who reported smaller droplet Sauter mean diameters for higher pressure drops in air-assist atomizers. Smaller droplets lead to faster evaporation and shorter flames which results in shorter high-temperature residence times for particle growth and smaller product particles.

2.4 Particle collection

For the collection of silica nanoparticles produced at rates up to 1.1 kg/h, Mueller et al. (2003) employed a baghouse filter with four PTFE-coated

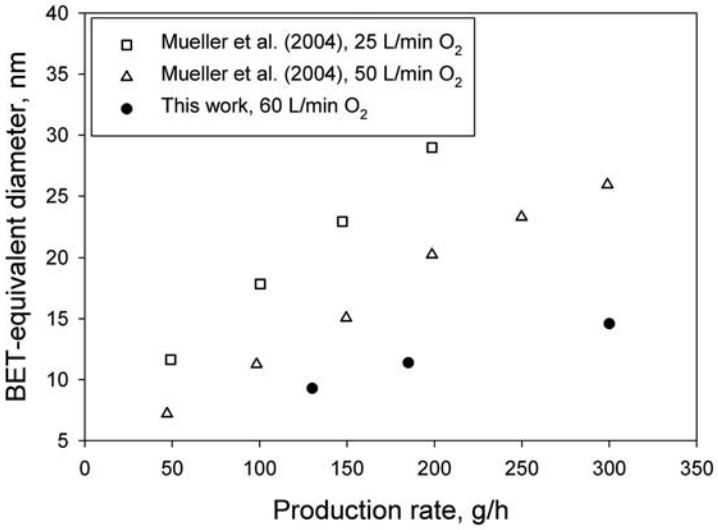

Fig. 2 BET-equivalent diameter of FSP-made ZrO_2 nanoparticles as a function of the powder production rate for dispersion gas flows of 25 and 50 l/min (Mueller et al., 2004b)) and 60 l/min (this work). Increasing the production rate by higher flows of the precursor solution at a constant 0.5 mol/l Zr concentration increases the primary product particle diameter.

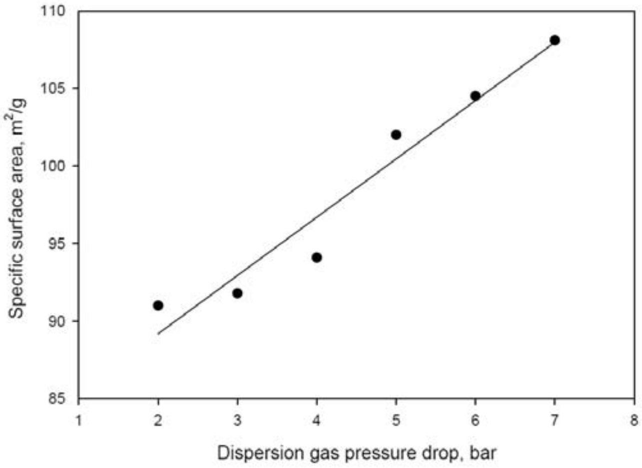

Fig. 3 Specific surface area of $FePO_4$ nanoparticles as a function of the dispersion gas pressure drop at constant liquid and dispersion gas mass flow rates. Increasing the dispersion gas pressure increases the particle specific surface area and decreases their size.

Nomex bags and 1.7 m^2 total filtration area. Particles were removed from the filter medium by periodically (every 30 s) introducing a short reverse pulse of pressurized air into individual filter bags while filtration continued with the remaining three bags. The maximum capacity of the centrifugal fan used by Mueller et al. (Stäfa-Wirz AG, Switzerland, type MKV 012) can be estimated at 1000 m^3/h, leading to a filter load of approx. 10 $m^3/(m^2 \times min)$. This is extremely high compared to the filtration of commercial fumed silica nanoparticles employing a filter load of approx. 0.8 $m^3/(m^2 \times min)$ (Gore, 2011), and might not be suitable for continuous production. Using the same filter, Jossen et al. (2005a) report the installation of a check-valve in the aerosol line from the flame reactor to the filter to avoid disturbance of the flame by back-flowing aerosol during back-pulse cleaning while producing up to 350 g/h yttrium-stabilized zirconia. This further indicates an insufficient filter size especially for continuous production.

Our latest pilot plant at ETH Zurich is equipped with a baghouse filter of 15 m^2 filtration area (Mikropul GmbH, Germany) by 21 filter bags (GORE® membrane on aramid needle felt, W.L. Gore & Associates GmbH, Germany). **Fig. 4** shows the pressure drop across the filter bags during production of iron phosphate nanoparticles with 20 nm primary particle size. The production rate was 270 g/h at total gas volume flows of 1125 m^3/h (circles) and 1500 m^3/h (triangles), corresponding to filter loads of 1.25 and 1.67 $m^3/(m^2 \times min)$, respectively. About half an hour after production start-up, the pressure drop across the filter reached stable values of 1450 - 1550 Pa at 1125 m^3/h flow. Reverse-pulse cleaning was initiated when 1400 Pa were reached. At 1500 m^3/h or 1.67 $m^3/(m^2 \times min)$ filter load, a stable operation point could not be established, and after half an hour of operation, the suction limit of the centrifugal fan downstream of the filter was reached. As the pressure drop continued to increase, the capacity of the centrifugal blower decreased leading to overheating of the filter since insufficient cooling air was introduced into the unit.

The particle concentration and size in the off-gas duct downstream of the baghouse filter installed at ETH Zurich was determined with a scanning mobility particle sizer (SMPS, TSI DMA model 3081 with CPC model 3775). The measurements were performed during production of the $FePO_4$ nanoparticles at intervals of 5 min. Scans in the size range of 10 to 365 nm were carried out with 60 s scan time and assuming unit particle density. **Fig. 5** shows a representative particle size distribution recorded 40 minutes after production start-up. A total concentration of 72,900 particles per cm^3 was measured and lies within the range of 69,800 and 83,600 / cm^3 observed for 4 scans during 20 min. of operation. The particle concentration in the workspace was 1100 ± 200 per cm^3 independent of the FSP pilot plant operation. Thus, an approximately 70 times higher particle concentration was observed in the off-gas of the filter during stable operation with reverse-pulse cleaning switched on.

The particle size distribution (**Fig. 5**) shows that most particles have diameters of > 50 nm with the calculated count mean diameter being 129 nm. This indicates agglomerates of the $FePO_4$ primary particles with 20 nm BET-equivalent particle diameter which must have penetrated through the filter bags

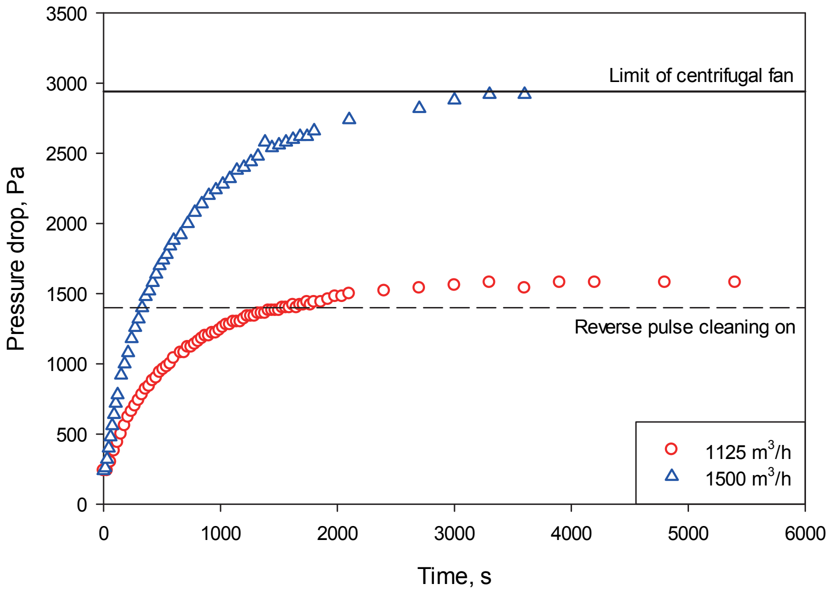

Fig. 4 Development of the pressure drop across the filter following start-up of $FePO_4$ nanoparticle production at 1125 (circles) and 1500 m^3/h (triangles) volume flow. A stable operation line is obtained for the smaller flow rate, while the pressure drop for 1500 m^3/h reaches the suction limit of the centrifugal fan even though reverse-pulse cleaning starts at 1400 Pa.

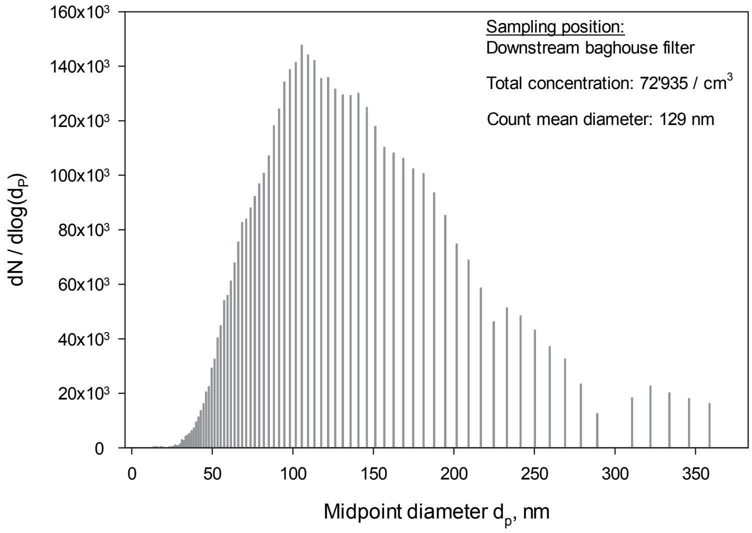

Fig. 5 Particle size distribution measured by a scanning mobility particle sizer in the off-gas downstream of the baghouse filter during production of $FePO_4$ nanoparticles with 20 nm primary particle diameter. The total concentration was approx. 73,000 / cm^3.

or the bag seal at the filter head plate which separates the product compartment from the clean gas compartment. Even at full capacity of the centrifugal fan (1,500 m^3/h), the mass of particles penetrating through the filter bags is in the range of mg/h at 290 g/h production rate leading to a very high filter efficiency of > 99.9%.

The disadvantage of baghouse filters in FSP pilot plants is their large size required by handling the diluted aerosol at temperatures of maximum 220℃ and the need to replace all filter bags for a product change in order to avoid cross-contamination. **Fig. 6** shows how the baghouse filter dominates the FSP pilot plant installed at ARCI, Hyderabad, India. It is designed for a nanoparticle production rate of 1-2 kg/h and is equipped with a filter holding 70 bags with a total area of ~50 m^2. Such a system is oriented toward small-scale production while pilot plants with lower capacities and less filter bags are recommended for research-oriented units.

Wire-in-cylinder electrostatic precipitators were used by Bickmore et al. (1996) for collection of FSP-made spinel nanoparticles from a magnesium-aluminum double alkoxide. At 100 g/h production rate, a collection efficiency of 65 – 75% is reported. The remaining particles were removed from the off-gas with a counter-current packed bed water scrubber or a baghouse filter (Sutorik and Baliat, 2002). Since the low bulk density product powders caused filling of electrostatic precipitator tubes and restriction to the gas flow, two precipitator tubes were operated in parallel: one was used for nanoparticle collection while the powder was manually recovered from the other (Sutorik et al., 1998). Due to its simple geometry, the wire-in-cylinder electrostatic precipitator has the advantage of easy cleaning and maintenance between runs with different products. The use of metal and ceramic components enables collector operation at higher a temperature, e.g. 400℃ (Bickmore et al., 1998), which in turn reduces the quenching gas requirement.

2.5 Off-gas and effluents

The typical off-gas of an FSP plant not employing chloride precursors contains the combustion products CO_2 and water highly diluted with the process cooling air. As shown in **Fig. 5**, the particle concentration in the gas stream behind a baghouse filter was up to 10^5 / cm^3. In order to eliminate this particle contamination, the off-gas is passed through a high-efficiency particulate air filter (HEPA) before it is vented to the environment. This filter also acts as a police filter in the case of failure of the primary particle collector. Particle size and concentration measurements downstream of the class H13 HEPA filter (Camfill-FARR, Switzerland) installed in the ETH pilot plant gave a particle concentration of only 35 / cm^3, about 30 times less than in the workspace. Particles of size 14 to 280 nm were detected which might have penetrated through the seals or imperfections in the filter media of the HEPA filter. In the event that other combustion by-products are formed, such as NOx from nitrate precursors, appropriate off-gas treatment units (e.g. DeNOx) must be installed in the off-gas duct in agreement with local regulations.

Nanoparticle-contaminated effluents are not generated during the dry nanoparticle production process. However, water is used to clean the aerosol piping and nanopowder collector for a product change or maintenance. Resulting nanoparticle suspensions cannot be discharged to the communal waste-water system since waste-water treatment plants might not be able to fully remove the nanoparticles. Limbach et al. (2008) showed that 6wt% of cerium nanoparticles escaped through a model waste-water treatment plant. The strategy employed in our pilot plants is the collection and thickening of the nanoparticle suspensions in designated settling tanks with the help of

Fig. 6 Front view of the FSP pilot plant during installation at ARCI (Hyderabad, India) for production of several kg/h of nanoparticles with the baghouse filter for nanoparticle collection (~50 m^2 filtration area) at the back in the center, the stirred tank for precursor preparation on the right and the control cabinet for process automation on the left side of the platform.

surfactants and evaporation. The resulting slurry is recovered and disposed of as hazardous waste or is treated at high temperature to destroy the ceramic nanoparticles by sintering.

3. Safety Considerations

Three hazards can be associated with the flame spray synthesis of nanoparticles that might not be as pronounced in other chemical production processes: hazards due to the handling of relatively large quantities of organic solvents and metal-organic compounds as feedstock, flame combustion at high temperature and hazards associated with the nanoparticles produced. As the first two hazards are typically well known and addressed by national or international regulations, the main challenge is to avoid the release of nanoparticles into the environment and the workspace. Therefore, the entire processing unit should be fully enclosed with well-defined and secured access and interface points. The placement of the centrifugal fan at the end of the process chain ensures a slightly negative pressure inside the entire unit that minimizes the escape of nanoparticles. The cooling air inlet duct should be equipped with appropriate filters that not only purify the inflowing air but also prevent the release of nanoparticles in the case of a pressure build-up in the unit and generation of an aerosol backflow, as was reported by Jossen et al. (2005a) during reverse-pulse cleaning of the baghouse filter. The FSP reactor itself should be fully enclosed (see **Fig. 7**) and well sealed since individual nanoparticles are present in and above the flame. Nanoparticles are immobilized again during particle collection, in the form of a filter cake or wall deposit. **Fig. 7** shows by example of the FSP pilot plant at Tecan, Spain, how the distance between the flame reactor and the filter was kept as short as possible to minimize the volume in which individual nanoparticles and small agglomerates are present as well as the amount of particle losses to the walls.

As pilot plants see frequent product changes, cleaning of the unit and change of the filter bags must be realizable in a safe and comfortable manner for the personnel with minimum nanoparticle release to the workspace. It is therefore recommended that the filter bags are changed from the clean gas side on the top of the baghouse filter without the need to access the product compartment as this will result in the release of nanoparticles. Wet-cleaning of the filter and the aerosol ducts before a filter change or maintenance with fixed installations of clean-in-place (CIP) nozzles is highly recommended since this removes the majority of the nanopowder from the system and agglomerates or binds remaining nanoparticles, minimizing dust formation.

Fig. 7 Fully enclosed FSP pilot plant at Tecnan (Los Arcos, Spain): The cooling air inlet is equipped with a filter to purify the air and to prevent the release of nanoparticles in the case of an aerosol backflow. The nanoparticle-producing spray flame is located inside the reactor chamber that is directly connected to the baghouse filter, minimizing the aerosol volume.

A process control system (PLC) monitors all relevant process streams during automated production including nanoparticle concentrations in the off-gas. The process should safely shut down in an automated routine in the case that process parameters are off-limits or a high nanoparticle concentration indicates a leakage in the filter. The process control system should be complemented by continuous workplace exposure measurements using submicron particle counters, as performed by Wang et al. (2011) during pilot-scale production of silicon nanoparticles and Demou et al. (2009) during lab-scale nanoparticle synthesis.

Ideally, the nanoparticle production unit should be placed in a designated and fully enclosed room that is only accessible to personnel with appropriate personal protection equipment via an air lock, as is shown in **Fig. 8** by the example of the FSP pilot system at Johnson Matthey Technology Center (UK). The control of the process is performed from outside the nanoparticle production space, and all workplaces requiring nanoparticle handling inside the room are

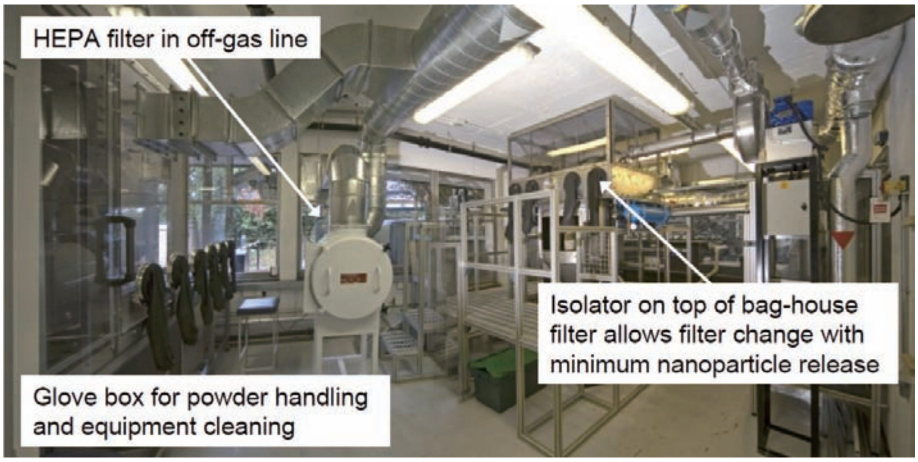

Fig. 8 FSP pilot plant at Johnson Matthey Technology Center located in a fully enclosed production space accessed only through an air lock. Workplaces for nanopowder handling inside the room are equipped with glovebox isolators.

additionally equipped with glove-box isolators.

4. Economic Considerations

Production cost estimates for the FSP-manufacture of nanopowders at the pilot or even industrial plant level are difficult due to the lack of available raw material prices, their market-dependent variability and the geographically varying labor costs. Here, we make an attempt to analyze the cost structure for the continuous production of bismuth oxide from bismuth-nitrate and zirconium oxide from zirconium-2-ethylhexanoate nanoparticles based on a pilot plant with 1.25 kg/h production rate located in Switzerland. Prices for precursors and solvents are current market prices for ~200 kg barrels. Gases (methane, oxygen, air) are assumed to be delivered from a pipeline network in an industrial chemical production setting. Continuous operation with 4 shifts (1 person per shift plus partial supervising and assistance) over 330 days per year and 24 h/day is assumed, resulting in ~8000h of production and 10t annual production rate. A capital investment of 750,000 EUR is considered for the pilot plant, linearly depreciated over ten years. Costs for maintenance, utilities, supplies, laboratory charges and packaging (combined “Others”) are estimated as fractions of the capital investment or labor costs according to Peters, Timmerhaus and West (2003). For comparison, the cost structure for a small production plant with a ten-times-higher production rate is shown in **Fig. 9** as well.

Even though both materials are based on different precursors, relatively low-cost bismuth nitrate and the more expensive zirconium-2-ethylhexanoate, the combined precursor and solvent costs have approximately the same share, namely ~45% for the 10t/yr plant and ~80% for the 100 t/yr production. This is due to the requirement of additional solvents such as 2-ethylhexanoic acid for the conversion of the nitrate precursor while these are already present in the zirconium raw material. At 10 t/year production rate, expenditures for labor constitute about 40% of the total production costs but only 10% for 100 t/year. This is due to the fact that the fully automated pilot plants require approximately the same number of operators independent of their production rate. Expenses for gases are almost negligible in all cases but will be much higher if cylinders or liquid oxygen are used. Depreciation of the capital investment costs accounts for 3 – 7% while maintenance, consumables such as filter bags, packaging, utility and laboratory charges (“others”) are 6 to 7% of the total costs.

Uncertainties in raw material price estimates thus have a huge influence on the total production costs and purchasing in larger quantities will significantly reduce costs. Furthermore, the aim should be the use of low-cost solvents such as ethanol or acetic acid and operation at a metal concentration in the precursor solution that is as high as possible. It should be possible by optimization of the precursor solution and processing conditions to produce oxide nanomaterials at costs of some tens of euros per kg at pilot plant level. Economy of scale will help to reduce these costs in industrial manufacturing units, but it will be hard to beat the production costs of the current chloride process for fumed silica or titania, since FSP precursors and organic solvents will remain more expensive than the metal chlorides, hydrogen and oxygen.

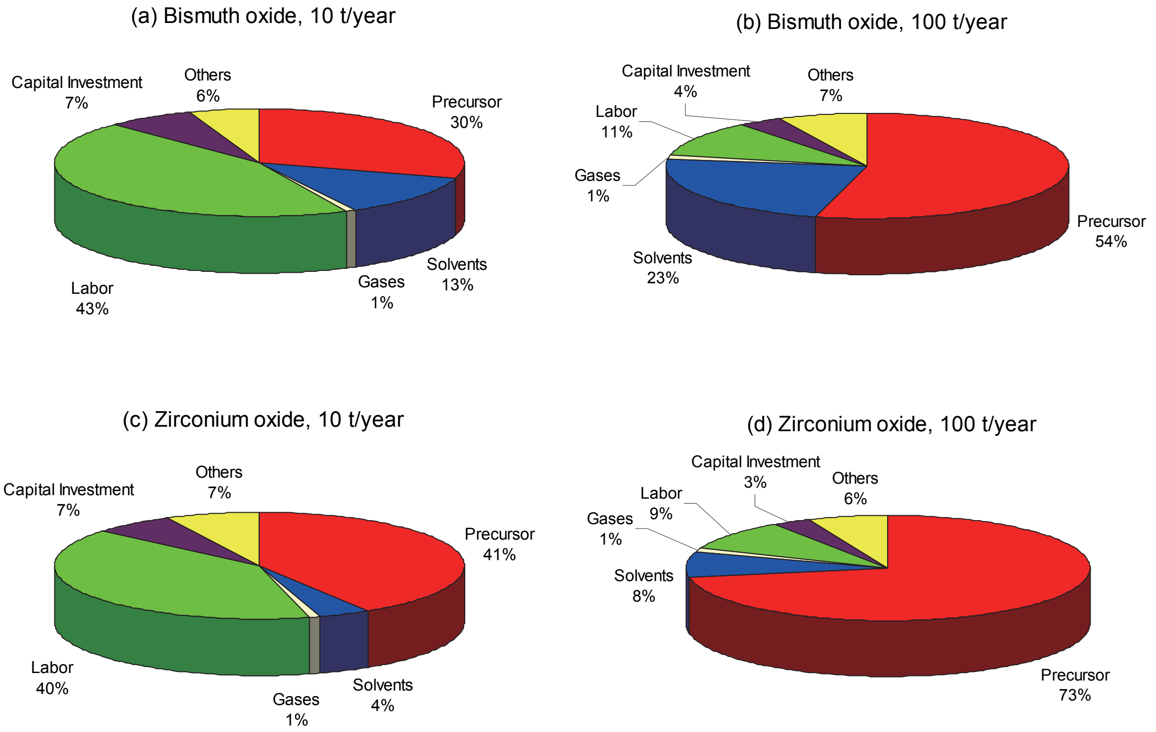

Fig. 9 Estimated production cost breakdown for (a, b) bismuth and (c, d) zirconium oxide nanoparticles produced with FSP pilot plants operating at 1.25 kg/h (10t/year) and 12.5 kg/h (100 t/year). At the higher production rate, the raw materials (precursor and solvents) account for approximately 80% of the production costs.

5. Conclusions

Nanoparticle synthesis by flame spray pyrolysis has been successfully transferred from the laboratory to the pilot plant level with production rates of a few kilograms per hour, as several examples have shown. The process can be operated continuously in a safe manner with the help of process automation. Pilot plant production costs for simple oxides can be estimated at below 100 EUR/kg with raw materials being the largest cost factor.

Prime research needs are the design of low-cost precursor solutions with higher metal-to-carbon ratios, a better utilization of the heat generated during combustion and strategies for more efficient flame quenching. This would reduce the amount of organic solvents supplied to the system and lead to a reduction of raw material costs and CO_2 emissions. Furthermore, this would reduce the volume flow of cooling gas, allowing more flexible operation with smaller nanoparticle collectors, e.g. baghouse filters. These challenges should be tackled by a combined experimental and modeling approach. The latter must include process fluid dynamics, combustion as well as droplet and particle dynamics, and should guide the design of new FSP reactors and the next scale-up step.

Furthermore, strategies for contained product nanoparticle packaging and handling must be developed in view of industrial nanoparticle manufacture. The identification of hazards associated with FSP synthesis of nanoparticles must be identified more systematically. The existing pilot units will be used to carry out hazard and operability studies aiming at the development of design and operational guides for larger FSP systems.

Acknowledgements

The research leading to these results has received funding from the European Community's Seventh Framework Programme (FP7 / 2007-2013) under grant agreement n° 228885.

References

Akurati, K.K., Vital, A., Dellemann, J.-P., Michalow, K., Graule, T., Ferri, D. and Baiker, A. (2008): Flame-made WO_3/TiO_2 nanoparticles: Relation between Surface Acidity, Structure and Photocatalytic Activity, Appl. Cat., B, 79, pp.53-62.

Bickmore, C.R., Waldner, K.F., Treadwell, D.R. and Laine, R.M. (1996): Ultrafine Spinel Powders by Flame Spray Pyrolysis of a Magnesium Aluminum Double Alkoxide, J. Am. Ceram. Soc., 79, pp.1419-1423.

Bickmore, C.R., Waldner, K.F., Baranwal, R., Hinklin, T., Treadwell, D.R. and Laine, R.M. (1998): Ultrafine Titania by Flame Spray Pyrolysis of a Titanatrane Complex, J. Eur. Ceram. Soc., 18, pp.287-297.

Chiarello, G.L., Rosetti, I. and Forni, L. (2005): Flame-spray Pyrolysis Preparation of Perovskites for Methane Catalytic Combustion, J. Catal., 236, pp.251-261.

Demou, E., Stark, W.J. and Hellweg, S. (2009): Particle Emission and Exposure during Nanoparticle Synthesis in Research Laboratories, Ann. Occup. Hyg., 53, pp.829-838.

Gore (2011): Filtration Products, Case History No. 7 “Fumed Silica”, W.L. Gore and Associates GmbH, Putzbrunn, Germany. http://www.gore.com/en_xx/products/filtration/baghouse/filtration_ch_34.html, accessed on 22.05.2011.

Grass, R.N. and Stark, W.J. (2005): Flame Synthesis of Calcium-, Strontium-, Barium Fluoride Nanoparticles and Sodium Chloride, Chem. Commun., No. 13, pp.1767-1769.

Heel, A., Holtappels, P., Hug, P. and Graule, T. (2010): Flame Spray Synthesis of Nanoscale $La_{0.6}Sr_{0.4}Co_{0.2}Fe_{0.8}O_{3-\delta}$ and $Ba_{0.5}Sr_{0.5}Co_{0.8}Fe_{0.2}O_{3-\delta}$ as Cathode Materials for Intermediate Temperature Solid Oxide Fuel Cells, Fuel Cells, 10, pp.419-432.

Heine, M. and Pratsinis, S.E. (2005): Droplet and Particle Dynamics during Flame Spray Synthesis of Nanoparticles, Ind. Eng. Chem. Res., 44, pp.6222-6232.

Heine, M., Jossen, R., Madler, L. and Pratsinis, S.E. (2006): Direct Measurement of Entrainment during Nanoparticle Synthesis in Spray Flames, Combust. Flame, 144, pp.809-820.

Hinklin, T., Toury, B., Gervais, C., Babonneau, F., Gislason, J.J., Morton, R.W. and Laine, R.M. (2004): Liquid-feed Flame Spray Pyrolysis of Metalloorganic and Inorganic Alumina Sources in the Production of Nanoalumina Powders, Chem. Mater., 16, pp.21-30.

Jossen, R., Mueller, R., Pratsinis, S.E., Watson, M. and Akhtar, M.K. (2005a): Morphology and Composition of Spray-Flame-made Yttria-stabilized Zirconia Nanoparticles, Nanotechnology, 16, pp.S609-S617.

Jossen, R., Pratsinis, S.E., Stark, W.J. and Madler, L. (2005b): Criteria for Flame-Spray Synthesis of Hollow, Shell-Like, or Inhomogeneous Oxides, J. Am. Ceram. Soc., 88, pp.1388-1393.

Kilian, A. and Morse, T.F. (2001): A Novel Aerosol Combustion Process for the High-Rate Formation of Nanoscale Oxide Particles, Aerosol Sci. Technol., 34, pp.227-235.

Kim, M., Hinklin, T.R. and Laine, R.M. (2008): Core-shell Nanostructured Nanopowders along $(CeO_x)_x(Al_2O_3)_{1-x}$ Tie-Line by Liquid-Feed Flame Spray Pyrolysis (LF-FSP), Chem. Mater. 20, pp.5154-5162.

Kim, M. and Laine, R.M. (2009): One-Step Synthesis of Core-Shell $(Ce_{0.7}Zr_{0.3}O_2)_x(Al_2O_3)_{1-x}$ [$(Ce_{0.7}Zr_{0.3}O_2)$@Al_2O_3] Nanopowders via Liquid-Feed Flame Spray Pyrolysis (LF-FSP), J. Am. Ceram. Soc., 131, pp.9220-9229.

Kodas, T.T. and Hampden-Smith, M. (1999): “Aerosol Processing of Materials”, Wiley-VCH, New York, USA.

Laine, R.M., Hinklin, T., Williams, G. and Rand, S.C. (2000): Low-Cost Nanopowders for Phosphor and Laser Applications by Flame Spray Pyrolysis, Mater. Sci. Forum, 343-346, pp.500-510.

Lefebvre, A. (1989): “Atomization and Sprays”, Hemisphere Publishing Corporation, New York, USA.

Limbach, L.K., Breiter, R., Muller, E., Krebs, R., Galli, R., and Stark, W.J. (2008): Removal of Oxide Nanoparticles in a Model Wastewater Treatment Plant: Influence of Agglomeration and Surfactants on Clearing Efficiency, Environ. Sci. Technol., 42, pp.5828-5833.

Madler, L., Kammler, H.K., Mueller, R. and Pratsinis, S.E. (2002): Controlled Synthesis of Nanostructured Particles by Flame Spray Pyrolysis, J. Aerosol Sci., 33, pp.369-389.

Mädler, L. (2004): Liquid-fed Aerosol Reactors for One Step Synthesis of Nano-Structured Particles, KONA Powder and Particle, 22, pp.107-120.

Mueller, R., Maedler, L. and Pratsinis, S.E. (2003): Nanoparticle Synthesis at High Production Rates by Flame Spray Pyrolysis, Chem. Eng. Sci., 58, pp.1969-1976.

Mueller, R., Jossen, R., Pratsinis, S.E., Watson, M. and Akhtar, M.K. (2004a): Zirconia Nanoparticles made in Spray Flames at High Production Rates, J. Am. Ceram. Soc., 87, pp. 197-202.

Mueller, R., Jossen, R., Kammler, H.K., Pratsinis, S.E. and Akhtar, M.K. (2004b): Growth of Zirconia Particles Made by Flame Spray Pyrolysis, AIChE J., 50, pp.3085-3094.

Peters, M.S., Timmerhaus, K.D. and West, R.E. (2003): “Plant Design and Economics for Chemical Engineers”, 5th ed., Mc Graw Hill, New York, USA.

Pokhrel, S., Birkenstock, J., Schowalter, M., Rosenauer, A. and Madler, L. (2010): Growth of Ultrafine Single Crystalline WO_3 Nanoparticles Using Flame Spray Pyrolysis, Crystal Growth Design, 10, pp.632-639.

Stark, W.J., Madler, L., Maciejewski, M., Pratsinis, S.E., and Baiker, A. (2003): Flame Synthesis of Nanocrystalline Ceria – Zirconia: Effect of Carrier Liquid, Chem. Commun., pp.588-589.

Stark, W.J., Grunwaldt, J.-D., Maciejewski, M., Pratsinis, S.E. and Baiker, A. (2005): Flame-Made Pt/Ceria/Zirconia for Low-Temperature Oxygen Exchange, Chem. Mater., 17, pp.3352-3358.

Strobel, R. and Prastinis, S.E. (2011): Effect of Solvent Composition on Oxide Morphology during Flame Spray Pyrolysis of Metal Nitrates, Phys. Chem. Chem. Phys. 13, pp.9246-9252.

Sutorik, A.C., Neo, S.S., Treadwell, D.R. and Laine, R.M. (1998): Synthesis of Ultrafine β" - Alumina Powders via Flame Spray Pyrolysis of Polymeric Precursors, J. Am. Ceram. Soc., 81, pp.1477-1486.

Sutorik, A.C. and Baliat, M.S. (2002): Solid Solution Behavior of $Ce_xZr_{1-x}O2$ Nanopowders Prepared by Flame Spray Pyrolysis of Solvent-Borne Precursors, Mater. Sci. Forum, 386-388, pp.371-376.

Teoh, W.Y., Amal, R. and Madler, L. (2010): Flame Spray Pyrolysis: An Enabling Technology for Nanoparticles Design and Fabrication, Nanoscale, 2, pp.1324-1347.

Tethis (2011): Tethis Sr.l., Milan, Italy, http://www.tethis-lab.com, accessed 21 May 2011.

Wang, J., Asbach, C., Fissan, H., Hulser, T, Kuhlbusch, T.A.J., Thompson, D. and Pui, D.Y.H. (2011): How Can Nanobiotechnology Oversight Advance Science and Industry: Examples from Environmental, Health and Safety Studies of Nanoparticles (nano-EHS), J. Nanoparticle Res., 13, 1373-1387.

Watanabe, A., Fukui, T., Nogi, K., Kizaki, Y., Noguchi, Y. and Miyayama, M. (2006): High-Quality Lead-free Ferroelectric Ceramics Prepared from the Flash-Creation-Method-Derived Nanopowder, J. Ceram. Soc. Japan, 114, 97-101.

Watanabe, A., Fujii, M., Kawahara, M., Fukui, T. and Nogi, K. (2007): Fabrication and Particle Size Control of Oxide Nanoparticles by Gas Phase Reaction Assisted with DC Plasma, J. Soc. Powder Technol. Japan, 44, 447-452.

Author’s short biography

Karsten Wegner

Karsten Wegner studied process engineering at the University of Karlsruhe (Germany), graduated in 1998 and then obtained his Ph.D on gas-phase synthesis of nanoparticles from ETH Zurich in 2002. He was co-founder and CEO of the start-up company FlamePowders that focused on industrial flame synthesis of nanopowders. Since 2005 he works as a consultant for aerosol manufacturing of nanomaterials and counts major industries, research centers and the start-up Tethis (Milan, Italy) to his customers. Together with his partners, he has designed and built customized FSP pilot plants around the globe. Karsten Wegner also holds a position as lecturer and senior researcher at ETH.

Björn Schimmöller

Björn Schimmöller received his diploma in process engineering from the University of Karlsruhe (Germany) in 2005. He then joined the Particle Technology Laboratory at ETH Zurich for his Ph.D thesis with focus on the “Structure of Flame-Made Mixed-Metal Oxide Catalysts” . After receiving his degree in 2010 he stayed at ETH as a postdoctoral fellow and has recently joined Cabot Corporation in Boston, USA. His research interests lie in flame synthesis of mixed-metal-oxide and metal nanoparticles focusing on control of material properties and their performance as well as process scale-up.

Bénédicte Thiebaut

After obtaining her PhD from Heriot-Watt University, Edinburgh (UK), Bénédicte Thiébaut joined Johnson Matthey 13 years ago. Since then, she worked on numerous projects specializing in the nanotechnology area including flame spray synthesis of nanoparticles. The technique proved of interest to various Johnson Matthey businesses and her work was then dedicated to the investigation of catalyst preparation and novel products by this method. Bénédicte led the successful creation of a development scale Flame Spray Pyrolysis unit and now is in charge of the new facility as well as the various projects associated with the technology.

Claudio Fernandez

Claudio Fernandez is managing director of the Technological Centre Lurederra in Los Arcos, Spain as well as president of TECNAN Nanoproducts. He developed a rich background in materials technology, management, and entrepreneurship e.g. through positions at the Royal Institute of Technology in Stockholm (Sweden), Gaiker and LEIA Technology Centers (Spain), and Commercial Laminate Iberia SA (Akzo Nobel Group). His latest venture, TECNAN, provides custom-manufacture of nanopowders by FSP, nanodispersions as well as other final nanoproducts and caters to customers worldwide. With Lurederra, Claudio Fernandez has managed and coordinated numerous European Research Projects, the latest of which is “Advance-FSP” focussing on the scale-up of flame spray synthesis of nanoparticles.

Author's short biography

Tata Narasinga Rao

Tata Narasinga Rao is leader of the Center for Nanomaterials at the International Advanced Research Center for Powder Metallurgy and New Materials (ARCI) in Hyderabad, India. He holds a MSc degree in physical chemistry and obtained his Ph.D. in electrochemistry from Banaras Hindu University (BHU), Varanasi, in 1994. After working at IIT Chennai, he moved to the University of Tokyo as a JSPS postdoctoral fellow and was appointed assistant professor in 2001. His center at ARCI is equipped with several techniques for nanoparticle synthesis, among them a FSP pilot plant capable of continuous nanoparticle production at semi-industrial level allowing to pursue application-oriented nanomaterials development in an industrial context.

A Multiscale Approach for the Characterization and Crystallization of Eflucimibe Polymorphs: from Molecules to Particles[†]

S. Teychené and B. Biscans
Laboratoire de Génie Chimique UMR CNRS 5503, Université de Toulouse[1]

Abstract

We present in this paper a generic multiscale methodology for the characterization and crystallization of eflucimibe polymorphs. The various characterization techniques used have shown that eflucimibe polymorphism is due to a conformational change of the molecule in the crystal lattice. In addition, the two polymorphs are monotropically related in the temperature range tested and have similar structures and properties (ie. interfacial tension and solubility). Consequently, it was found that for a wide range of operating conditions, the polymorphs may crystallize concomitantly. Induction time measurements and metstable zone width determination allow to infer the origin of the concomitant appearance of the polymorphs. A predominance diagram has been established which allows to perfectly control the crystallization of the desired polymorph. However, even if the stable form can be produced in a reliable way, the crystal suspension went toward a very structured gel-like network which limits the extrapolation process. Based on microscopic observation of the crystallization events performed in a microfluidic crystallizer, we propose a range of operating conditions suitable for the production of the stable form with the desired handling properties.

Keywords: Crystallization, Rheology, microfluidic, Polymorphism, Nucleation

Introduction

Crystallization from solution is a core technology in pharmaceutical industries. Usually, this process is a part of a wide processing system, including solid–liquid separation, particle design, and formulation. Chemical engineers must develop a robust crystallization process that delivers the active pharmaceutical ingredient (API) with both high yield and appropriate attributes that are conducive to drug product development (e.g., purity, polymorph and particle size distribution). Crystal polymorphism, which has been extensively studied in the past ten years, is the ability of a molecule to crystallize as more than one distinct crystal phases that have different arrangement and/or conformation of the molecule in the crystal lattice. Polymorphism of drug substances is very common and concerns about 90% of small organic molecules (Lipinsky 2001, Griesser 2003). It influences every aspect of the solid-state properties of a drug. It also leads to dramatic effects in biological activity between two forms of the same drug. The most important consequences of polymorphism in pharmaceuticals are the possibility of conversion among polymorphic forms and the variation in bioavailability of the drug substances. In addition to these constraints the crystallization process have to be designed to produce crystals with good handling properties which can be very tricky when dealing with complex and flexible molecules that crystallize only as needles or fibers (i.e. particles with aspect ratio greater than 10). The aim of this paper is to present characterization measurements, at multiscales and process design of a complex molecule, eflucimibe (S)-2',3',5'-trimethyl-4'-hydroxy-α-docecyl acetanilide, a new acyl-coenzyme A-cholesterol O-acyltransferase (ACAT) inhibitor developed by Pierre Fabre Research Centre. The first part of the paper is dedicated to the solid-state characterization of the different polymorphs of eflucimibe using a combination of different analytical techniques (XRPD, Raman spectroscopy, MNR spectroscopy and

---

[†] Accepted : September 16th, 2011

[1] 4 allée Emile Monso 31432 Toulouse Cedex 4, FRANCE
* Corresponding author
E-mail:sebastien.teychene@ensiacet.fr.
TEL: (+33)534323637 FAX: (+33)34323697

ⓒ 2011 Hosokawa Powder Technology Foundation

thermal analysis). This approach allows us to determine the thermodynamic relationships between polymorphs and the solid(s) – liquid equilibrium. Then, for designing a robust crystallization process to produce the stable form, the control and the knowledge of the nucleation step from solution is the key parameter. The second part of the paper deals with the determination of nucleation kinetics of eflucimibe, using classical crystallization experiment (i.e. induction time) and by non-classical experiment using a microfluidic crystallizer recently developed. In the final part of the paper, the crystallization process itself is explored. Based on the rheological experiments performed on eflucimibe suspension, we propose a solution for operating the crystallization process to produce in a reliable way the desired polymorph with good handling properties. This paper has been written in order to present a generic methodology from the molecular scale to the crystallization process scale.

1. Solid State Characterization

1.1 X-Ray diffraction patterns

As eflucimibe crystals are weakly diffracting, classical XRPD does not allow the discrimination of the two polymorphs, XRPD patterns were obtained from synchrotron radiation (ESRF Grenoble, France).

The samples were mounted in 1.0mm borosilicate capillaries the diffraction investigations. Wavelength of 0.515529Å was selected using a double Si(111) monochromater. Data were collected at room temperature using a Ge(111) analyzer crystal/NaI scintilliator/PMT detector arrangement, which allows very high angular resolution (<0.003° 2θ). Data were collected between 0.75 and 20° 2θ. Diffraction data upon heating were taken using a 2D detector system (Fiber optic coupled CCD camera) having an angular resolution of 0.02° 2θ in this configuration. This arrangement allows rapid acquisition of diffraction patterns with good counting statistics. Upon heating the angular range covered was 0.7° <° 2θ<15°. Samples were heated in air with 0.3℃ steps from 25℃ to 135° C. After each step, the samples were allowed to equilibrate for 20-30 s, followed by a 5s acquisition time. The temperature stability of the furnace was around 0.1℃

Representative high-resolution diffraction patterns obtained for the two pure phase samples are given in **Fig. 1**.

Both samples are weakly diffracting, display significant peak broadening, and do not scatter at very high angle. Due to the poor crystallinity of the samples, it was not possible to derive even the unit cells from any of the diffraction patterns. The first three diffraction peaks appear to be multiples of a long axis (35Å at room temperature). In addition, these peaks and further multiples (identified as 00L in **Fig. 1**) are sharper than the other peaks, indicating that all belong to the same zone axis ; the narrow width of these peaks indicating a better crystalline order in this direction. The broadening observed in non-00L peaks indicates a greater degree of disorder along the long axis, consistent with the prolate form

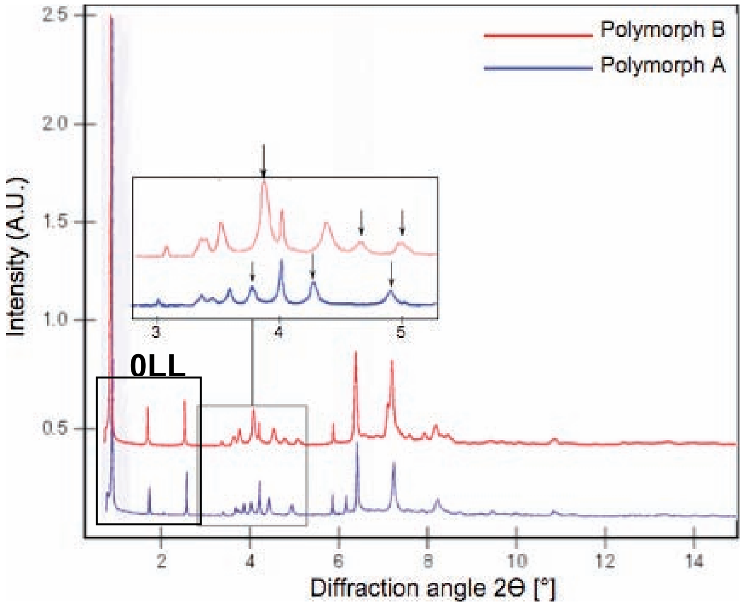

Fig. 1 Synchrotron Powder X-Ray diffraction pattern of Eflucimibe polymorphs.

of the molecule. As the first non-00L peaks appear at smaller d-spacing (<8.2 Å) the other axes appear more shorter. Thus, structures for both phases may be hypothesized in which the molecules are aligned along the long cell axes (d~ 35 Å). This is consistent with the presence of the two aliphatic chains in the cell axes. Different phases would be due to different orientation settings of the molecules about this axis, a typical situation for such organic molecules. An hypothetic structure is given in **Fig. 2**.

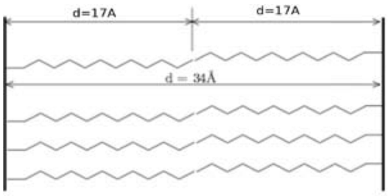

Fig. 2 Molecular arrangement of eflucimibe molecules in the crystal lattice.

Identification of the different polymorphs is performed using the most representative peaks of the two phases. As shown in **Fig. 1**, reasonably well separated peaks belonging only to one of the two polymorphs can be identified in the range 3 to 6° 2θ. Portions of the diffraction patterns collected on heating samples of phases A and B are given in **Fig. 3a** and **3b** respectively. For the A form, a clear 1st order phase transition is obvious, beginning near 110℃. A complex thermal event that extends from 75℃ to 105℃ is more subtle and can be attributed to an alteration of the lamellar structure. Melting occurs at 130℃.

For form B, two first order transitions are observed, occurring near 75℃ and 110℃. Melting occurs, also, near 130℃. In addition, by comparing the behaviour of both polymorphs under heating, no common diffraction peaks (or phases) were found, i.e. no transition between A and B are observed in the temperature range tested.

Even if single crystal diffraction patterns, and thus the crystal structure, are not available, this study allows us to determine an identification method for discriminating the two eflucimibe polymorphs.

1.2 Thermal analysis

1.2.1 Thermogravimetric analysis (DTA)

Thermogravimetric analysis were performed in a TA 2000 (TA instrument). 15 to 20 mg of eflucimibe crystals were weighted and placed in a platinium furnace under a nitrogen purge (Q=20ml.min^{-1}) and heated from 20 to 450℃ with a heating rate of 5℃.min^{-1}. For all the samples tested, no mass loss was detected in the temperature range from 25 to 150℃. For both polymorphs, decomposition occurs at 180℃. These results show that there is no solvates and Differential Scanning Calorimetry can be used to study the polymorphism of eflucimibe crystals.

1.2.2 Differential Scanning Calorimetry (DSC)

Thermograms were obtained in a DSC 2920 from TA instrument. 2 to 4mg of the samples were weighted and placed in a sealed aluminium furnace. The sample was then heated from -40 to 140℃ at a constant rate of 5℃.min^{-1} under a nitrogen purge (Q=20ml.min^{-1}). The reversibility of the thermal events observed was checked by performing heating and cooling cycles before melting. Representative thermograms of the A and B forms are given in **Fig. 4**.

All the thermal event observed are consistent with the results obtained from XRPD diffraction patterns. In addition, the phase transition observed at 35℃ is reversible and very fast. As a consequence, only the A1 form (stable form at 35℃) of polymorph A will be considered in this study.

As the results obtained by DSC and XRPD are in good agreement, DSC could be used as a semi-

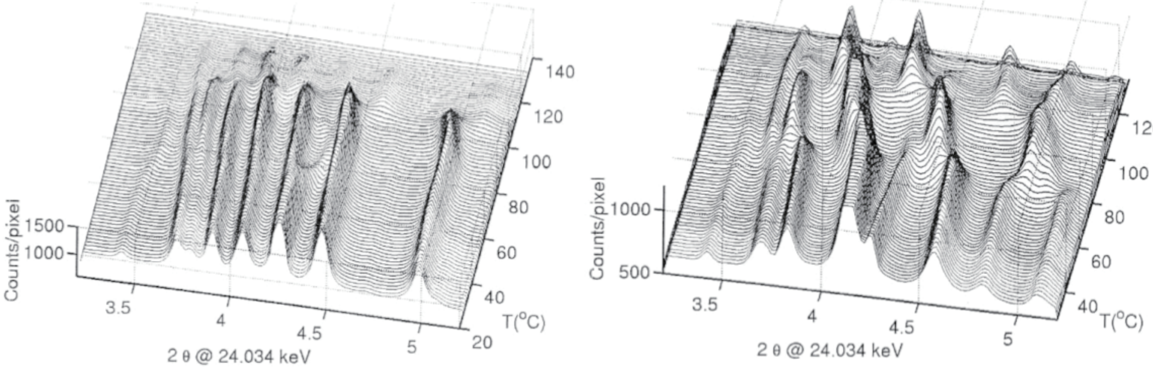

Fig. 3 XRPD diffraction pattern as function of temperature (a) Polymorph A (b) Polymorph B.

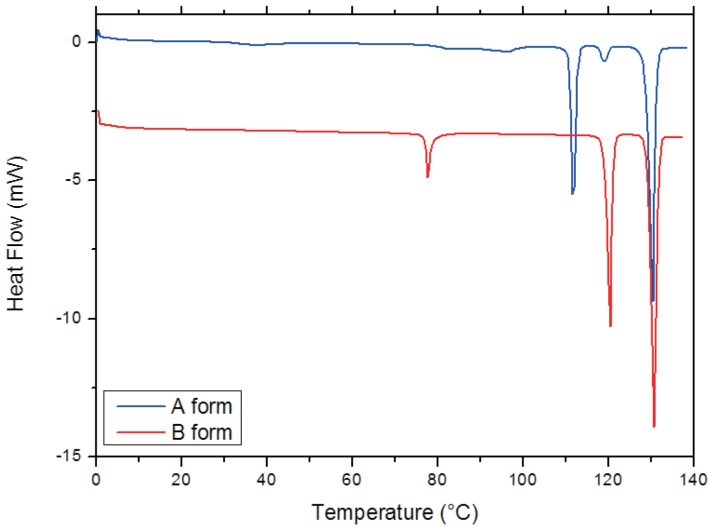

Fig. 4 DSC thermogramms of eflucimibe polymorphs (red: B form, blue: A form).

quantitative method for determining the amount of polymorph in a mixture. The polymorphic composition of the powder is then obtained by the following equation:

$$w_A = \frac{1}{2}\frac{A_{fus}^{ref}}{A_{fus}}\left(\frac{A_{110}}{A_{110}^{ref}} + \frac{A_{35}}{A_{35}^{ref}}\right) \qquad (1)$$

Where the superscript *ref* refers to the pure A form, and A_{fus}, A_{110}, A_{35} are the area of the characteristics peaks of the A form at 130℃, 110℃ and 35℃ respectively.

This method has been used to characterize physical mixtures of eflucimibe polymorphs. The results obtained are given in **Table 1**.

The results obtained in **Table 1**, expressed in terms of standard deviation and reproducibility, suggest that this method is at most semi quantitative, and can be used to know precisely if pure A or B polymorph is obtained.

1.3 Spectroscopic analysis

1.3.1 Solid State CPMAS-MNR Spectroscopy

Eflucimibe ^{1}H and ^{13}CRMN/CP-MAS spectra were obtained with a Bruker DMX-500 spectrometer operating at 125.7 MHz. 50 mg of powder samples were packed into 7mm zirconium rotors and spun at 8 kHz at the magic angle of 54° 44''. Spectra were acquired using a cross polarization contact time of 500µs, decoupling of 1H is performed during the acquisition of ^{13}C signal.

As shown in **Fig. 5**, the spectra obtained for the two polymorphic forms are similar, which suggests similar arrangement of the molecules in the crystal lattice for the two polymorphs. Attribution of the spectral band of the solid-state ^{13}C MNR spectra are based on the comparison with high resolution MNR spectra of DMSO. Resonance from the three carbons at 168ppm (C-1), 146ppm (C-4') and 22ppm (C-11'') are split in doublets, which indicates that two or four eflucimibe molecules are in the crystal asymmetric unit. The chemical shift of the methyl group between 15 and 5ppm is different from a polymorph to another. This difference could be attributed to a conformational difference of the corresponding benzyl group. These results suggest that the two polymorphs are due to a difference in the conformation of the molecule in the crystal lattice (conformational polymorphism) (Yu et al. 2000). This conclusion is in agreement with FTIR spectroscopy performed in previous study (Teychene et al 2004, Ribet et al. 2001), in which it was found that the main differences between the two polymorphs spectra are due to different intramolecular hydrogen bond involving the -OH group of the molecule.

1.3.2 Raman Spectroscopy

Raman spectra were collected using a Raman microscope (Kaiser Optical Systems, Leica DM1) equipped with a thermoelectrically cooled CCD detector. The source was a 400mW diode laser operating at 785nm, with an average power output of 100 - 200mW through a 20x, 11 mm working distance objective. The spot size of the laser beam through the objective was approximately 20µm. The microscope was coupled to the spectrometer with multi-mode

Table 1 Characterization by DSC of physical mixture of A and B polymorphs

Sample	Mass fraction of A	Calculated mass fraction of A	Standard deviation (mf)	Number of tested samples
1	0.81	0.83	0.2	3
2	0.5	0.54	0.18	4
3	0.33	0.25	0.13	5
4	0.25	0.18	0.1	5

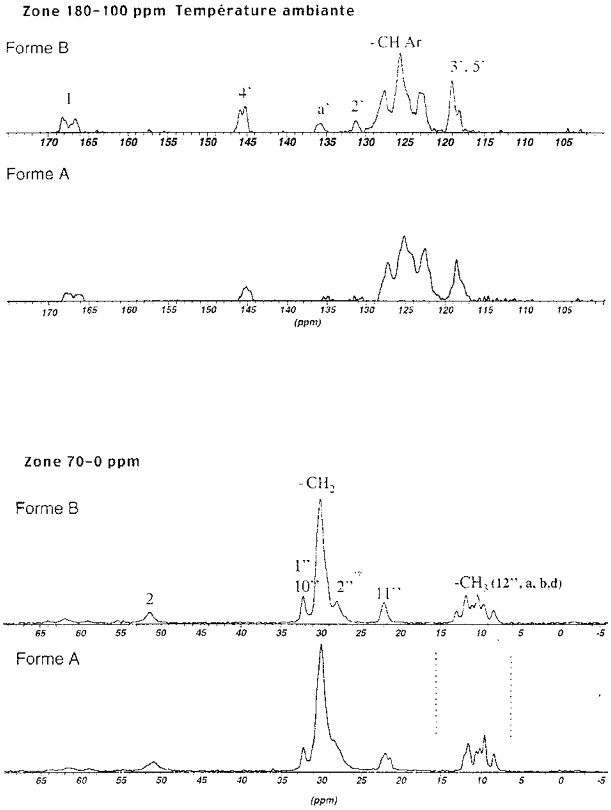

Fig. 5 MNR Spectroscopy of eflucimibe polymorphs (upper trace: B).

fibre optic cables; 50μm diameter was employed for excitation, and 62.5μm diameter for collection. The collection range was 100–3100 cm^{-1}. Raman spectra were collected using approximately 1mg of compound. Samples were placed on a microscope slide, and first focused visually, using a white light source and subsequently re-focused to maximize the Raman signal. An integration time of 1min was used for most samples as this gave good signal-to-noise ratios without damaging the sample.

The Raman spectra obtained for form A and B of eflucimibe are given in **Fig. 6**. The two polymorphs have very similar spectra except for a number of small differences.

In the range of wave number lower than 250 cm^{-1}, no differences in the Raman spectra can be identified, this result suggests that the crystal lattice of the two polymorphs is nearly the same. However, as shown in **Fig. 5**, in the range 1180 – 1210 cm^{-1} form B has a characteristic peak. This peak can be attributed to a change of the vibration mode of the –OH groups involved for example in different hydrogen bond arrangement between the crystalline states. Form B has also characteristic peaks in the range of 600 cm^{-1} and 940-950 cm^{-1}. This peaks are more subtle to interpret but it may be postulated that they may be due to different vibrational mode of the –CH group linked to the aromatic ring.

In that case Raman spectroscopy can be used as a reliable analysis tool for identifing the polymorph nature of the powder. However, it was not possible to achieve a good chemiometric procedure in order to perform quantitative analysis, because mixing of calibration samples and inhomogeneities (due to the

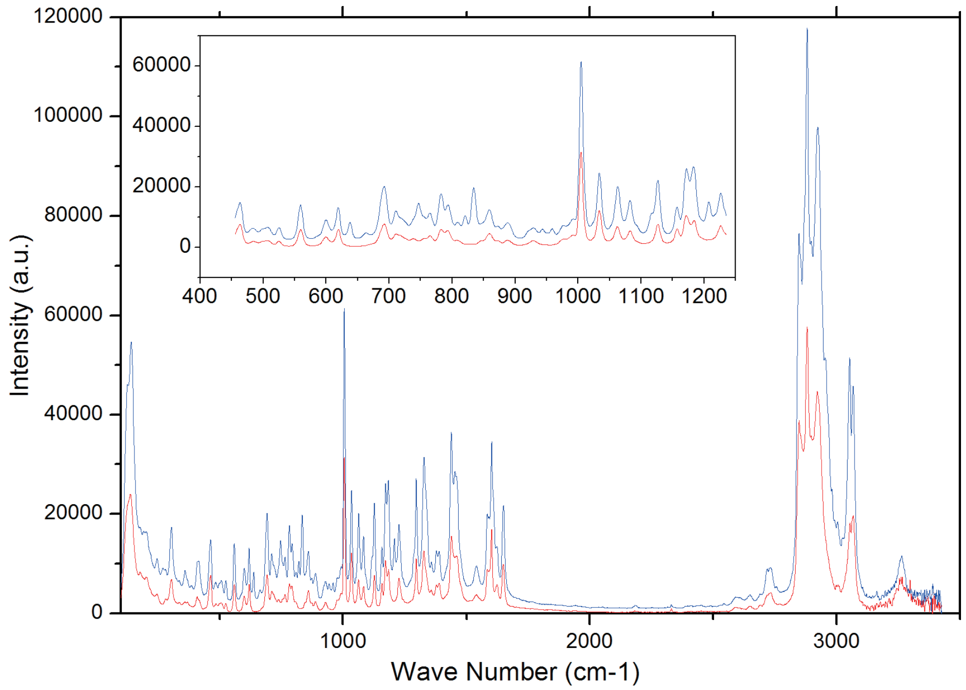

Fig. 6 Raman spectra of A and B polymorphs.

low special resolution of the system (~20μm)) are sources of large experimental errors. In addition, due to the low solubility of eflucimibe in solvents, liquid state analysis is below the detection threshold of the system.

2. Solid Liquid equilibria

2.1 Solubility

In previous study (Teychené et al. 2006), solubility of eflucimibe polymorphs was determined in different solvents and solvents mixtures. The solubility of the two forms is very close in all solvents and temperature tested. From solubility data determined in pure ethanol, it can be stated that in the temperature range of the crystallization process (from 20 to 55℃), the A form has the lowest solubility, and is the thermodynamic most stable polymorph (**Fig. 7a**). In the range of temperature tested, the two polymorphs are monotropically related.

As shown in **Fig. 7b**, in mixtures of ethanol and n-heptane, the solubility profiles of the two polymorphs reach a single maximum. From solvent solubility parameters analysis, it can be stated that, if no solid–solid transition occurs during solubility measurements, the solubility enhancement obtained in solvent mixture is explained in terms of enthalpy–entropy relationships. The entropic gain from loss of ethanol structure (due to the non-polar part of the molecule) is responsible, at first, for the solubility increase. Above a certain concentration of co-solvent, the solubility increase is favored by the enthalpy decrease, due to the solvent–solute hydrogen bond formation mainly due to the evolution of solvent–solute polar interactions. (Domanska 1989, Bustamante et al. 2002).

Several thermodynamic models were tested for the prediction of solubility in ethanol/n-heptane mixtures. The prediction of solubility by using the UNIQUAC equation, with interaction parameters for binary solvent mixture taken from vapour liquid equilibrium, gives satisfactory results. This model describes well ($P^2 > 0.97$) the solubility curves and the solubility maximum found for each polymorphs experimentally at a solvent ratio Ra = 0.7.

As the UNIQUAC model considers the energetic contribution of the crystal form in the solubility calculations, it is highly useful for predicting the polymorphs solubility in solvents mixtures even though the polymorphs properties are very close.

2.2 Phase transition experiments

To ensure that the A form is the stable one, ripening experiments were performed. In these experiments weighted quantity of both pure polymorphs were placed in an ethanol-heptane mixture (Ra=0.7) in an hermetically sealed vessel under slow mixing rate at ambient temperature for four days. Samples

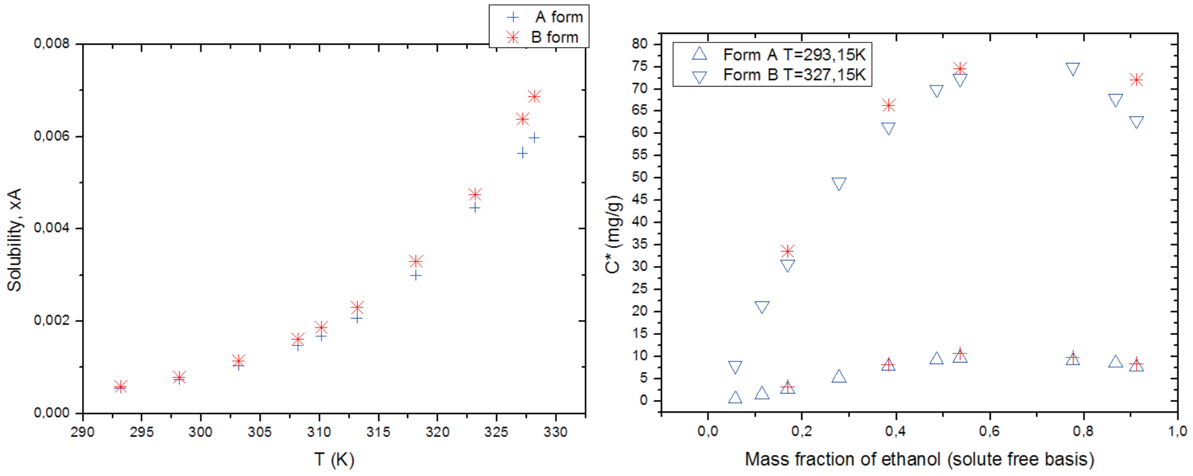

(a) **(b)**

Fig. 7 Solubility of eflucimibe polymorphs in (a) pure ethanol (b) ethanol / n-heptane mixtures.

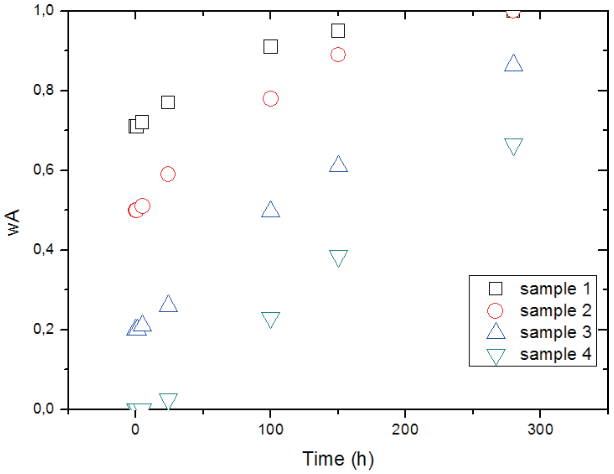

Fig. 8 Evolution in solution of polymorph composition at 300K.

were withdrawn at fixed time intervals. The polymorph composition of the powder was assessed by DSC. The operating conditions and the results obtained in terms of polymorph composition are given in **Fig. 8**.

This figure clearly show that in solution, even if the experimental results are tainted with an experimental error of about 20% due to the analytical technique used (DSC), form B slowly evolves to form A. This result is in agreement with the fact that the A form is the stable one. In addition, from a process point of view, due to the low A to B kinetic transition, it seems unreasonable to perform a maturation step after the crystallization process to obtain pure A form.

3. Nucleation and metastable zone width.

The main objective of eflucimibe crystallization process is to produce the stable form A. As a general rule, the stable polymorph of a drug is produced to ensure constant solid-state properties of the molecule during the whole life of the drug. Producing the stable form avoids unwanted solid-to-solid transitions during handling, storage and formulation. In addition, due to the similar structure of the two polymorphs and their low solubility differences, the metastable form does not increase bioavailability compared to the stable one. Considering that the transition from the metastable to the stable form of eflucimibe is very slow, the production of the stable form of the drug has to be controlled by the crystallization process. As the initial step of crystallization, nucleation is the key factor for controlling the appearance of the desired polymorph (Ulrich et al. 2002). Nucleation of eflucimibe polymorphs has been extensively studied in previously published papers (Teychené et al. 2004). In these previous papers, the metastable zone widths of eflucimibe were determined in a stirred reactor in ethanol and n-heptane mixtures. The operating conditions tested were the initial concentration, the temperature, the mixing rate, the cooling rate, and the amount of seed introduced during the process. It was found that when crystallization is performed without seeding, for most of the operating conditions tested, both polymorphs appear concomitantly. However, at low initial concentration, the A form seems to crystallize preferentially. At higher initial concentration, the reverse is observed.

When seeds of polymorph A are introduced in the crystallizer, at high initial concentration, nucleation of polymorph B cannot be avoided. When the crystallizer is seeded with polymorph B, the B form is always obtained. The unsuccessful seeding procedure may be explained either by the presence of undetected amount of polymorph B in the seeds or by the narrow window of seeding due to the very low solubility difference between the two forms (lower than 2℃ at higher concentration).

The results obtained are summarized in a “polymorph occurrence diagram” given in **Fig. 9**.

To get more detailed information about nucleation, induction time measurements were performed in a stirred tank. In this work, eflucimibe dissolved in ethanol/n-heptane (Ra=0.75) mixture were quenched from different initial temperatures (ranging from 55 ℃ to 37℃) toward 35℃. The induction time was determined by detecting the pour point of the solution.

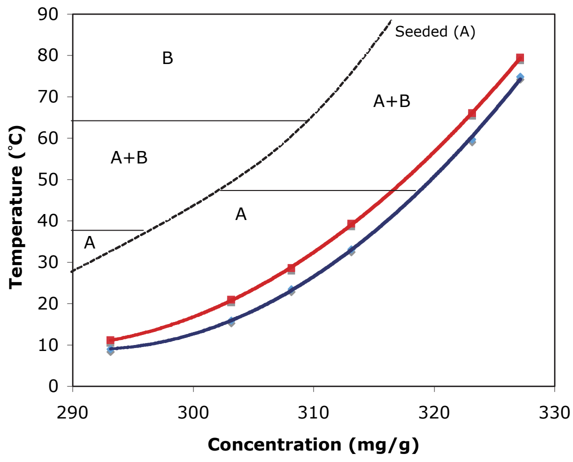

Fig. 9 Occurrence diagram of eflucimibe polymorphs for seeded and unseeded crystallization.

The results presented in Teychene et al. 2008, show that the nature of the nucleating polymorph greatly depends on the supersaturation level of the solution. At high supersaturation, this polymorphic system follows the Ostwald rule of stage. In addition, it was also found that the proportion of nucleating polymorph, in the solid recovered soon after nucleation, is directly linked to the relative nucleation rate of the polymorphs.

From a thermodynamic point of view, by taking the classical nucleation theory, the Gibbs free energy of a nucleating crystal is written as follows (Kashief 1995, Zetttlemoyer 1969):

$$\Delta G_{nucl} = \Delta G_{nucl}^{surf} + \Delta G_{nucl}^{vol} = 4\pi r^2 \gamma_{SL} - \frac{4}{3}\frac{\pi r^3}{v} RT \ln(S) \qquad (2)$$

Where r is the diameter of the critical cluster (m), v is the molar volume of the molecule ($m^3.mol^{-1}$) and γ_{SL} ($mJ.m^{-2}$) is the interfacial energy between the nucleus and the saturated solution. The value of γ_{SL} are respectively 5.23 $mJ.m^{-2}$ and 4.17 $mJ.m^{-2}$ for the A and B polymorph, respectively (Teychene et al. 2008). The evolution of the Gibbs free energy during nucleation is given in **Fig. 9a** for a supersaturation ratio of 1.6 and in **Fig. 9b** for S=3.

Fig. 9a and **9b** clearly show that at lower supersaturation, the Gibbs free energy of nucleation is lower for polymorph A than for polymorph B. At higher supersaturation the contrary is observed. This means that, for instance at low supersaturation, the energy barrier for nucleation and the corresponding critical radius are lower for the A form. **Fig. 9c** and **9d** show the evolution of the nucleation barrier (ΔG_{crit}) and of the critical radius as a function of supersaturation. These figures indicate that the trend is reversed for a supersaturation ratio about 1.8. At intermediate supersaturation ratio (from 1.7 to 2), corresponding to the supersaturation range characteristic of the crystallization process, the critical Gibbs free energy and the corresponding critical cluster are nearly the same for both polymorphs, leading to a concomitant appearance of the two polymorphs.

Given the low differences in physico-chemical properties of the two polymorphs, the production of pure polymorph A during a crystallization process can be performed only at low supersaturation level and low temperature. To induce nucleation, and to speed up the crystallization process, A form seeds may be introduced nearly at the equilibrium temperature.

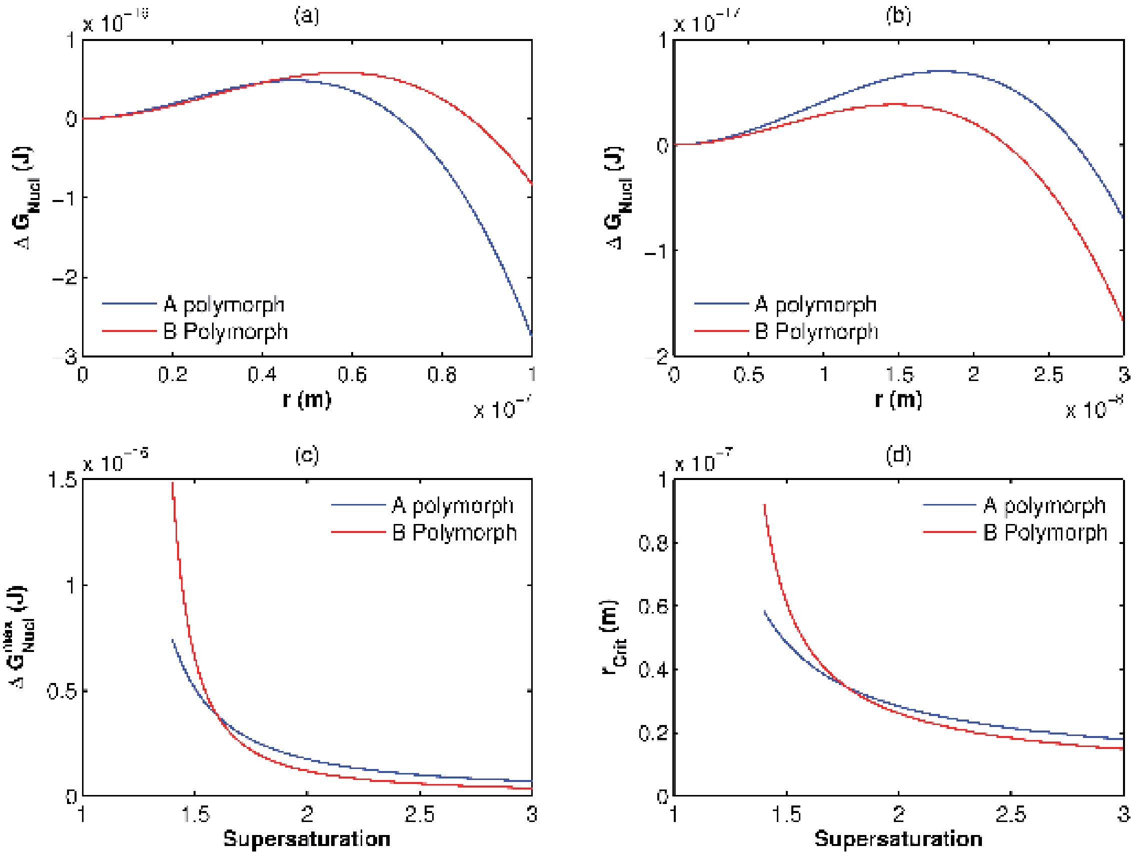

Fig. 10 Evolution of the Gibbs free energy during nucleation (a) and (b) Evolution of the gibbs free energy of nucleation of both polymorphs at S=1.6 and S=3, respectively. (c) Evolution of ΔG^{Max}_{Nucl} vs. Supersaturation. (d) Evolution of the critical radius diameter vs supersaturation.

4. Conventional crystallization process

4.1 Crystallization experiments

Cooling crystallization experiments were carried out in a 1L glass double-jacketed reactor mounted in a Labmax automated system (Mettler Toledo). Mixing is ensured by an A310 propeller from Lightnin (d=6cm). The stirring rate and the corresponding torque were measured during the process. Suspension turbidity was followed during the experiment by a backscattering light probe (FSC 402, Mettler Toledo). Eflucimibe solutions of several concentrations ranging from 82 mg.g^{-1} to 31 mg.g^{-1} in a mixture of ethanol and n-heptane (Ra=0.7) were heated up to 5℃ above the solubility temperature and then cooled down to 20℃ at a constant cooling rate (from 5 to 20℃.h^{-1}). Activated seeds of polymorph A were introduced when saturation temperature of form A was reached. The obtained suspension were either sampled and characterized by rheology or filtered and slowly dried and analyzed by DSC, XRPD, and SEM.

Whatever the operating conditions are, the results obtained in terms of polymorph composition at the end of the process are in good agreement with the results previously obtained in nucleation and metastable zone width experiments. The occurrence diagrams are neither influenced by the stirring rate nor cooling rate, nor scale-up. For instance, the evolution of the polymorph composition of the crystals during the process are given in **Table 2** for a cooling rate of 10℃.h^{-1} and a stirring rate of 200 rpm and for different initial concentrations.

Even if the polymorph purity of eflucimibe crystals can be handled during the crystallization process, handling properties of the suspension obtained at the end of the process is still difficult. Indeed, soon after the nucleation step the system evolves trough a very structured gel-like network that induces a jamming of the suspension. The evolution of the suspension in the reactor is shown in **Fig. 11**.

The evolution of turbidity during the crystallization process for four initial concentrations is given in **Fig. 12**. These results clearly show that for initial concentration above 31mg.g^{-1}, after the introduction of the seeds in the crystallizer, turbidity increases quickly

Table 2 Evolution of polymorph composition and crystallization yield during the seeded crystallization process of eflucimibe

C° (mg.g-1)	T (℃)	Yield (%)	WA (DSC)
81.79	326.5	2%	0.75
	325.3	10%	0.65
	324.7	17%	0.53
	320.5	37%	0.33
	318.9	42%	0.18
	317.2	49%	0.15
	315.5	56%	0.13
	307.7	74%	0.11
	298.2	87%	0.11
59.69	319.9	4%	0.70
	318.3	18%	0.64
	317.1	36%	0.56
	315.9	36%	0.47
	314.8	40%	0.41
	307.3	62%	0.31
	304.4	69%	0.30
	295.3	82%	0.27
43.53	316.3	2%	0.95
	315.0	7%	0.96
	313.6	16%	0.97
	302.8	63%	0.98
	298.3	72%	0.98
31.74	312.1	0%	1.00
	310.9	4%	1.00
	309.6	14%	1.00
	295.2	68%	1.00
	286.1	68%	1.00

and reaches a plateau around NTU =65 -70% before the end of the crystallization process. The turbidity plateau is due to the jamming of the reactor, dense agglomerates are formed around the turbidity probe, the optical thickness of the suspension is increased inducing saturation of the turbidity signal. From this point, the turbidity sensor gives only information about the surrounding agglomerates and not on the overall suspension in the crystallizer.

The volume fraction of solid, obtained by sampling the suspension during the crystallization process, corresponding to the gelation threshold is around 2% at 23℃ and 5% at 40℃. In **Fig. 12** photographs of dried powder are shown. For the whole operating conditions tested, needle like crystal are obtained with width around 200nm and length ranging from 10 to 30μm.

4.2 Characterization by rheology

As all the classical characterization techniques (BET surface area, Laser diffraction, Back scattering light...) failed to describe the structural evolution of the suspension during the crystallization process, suspensions where characterized by rheology. During these experiments, evolutions of the elastic modulus and the yield stress were recorded as a function of the shear rate or strain for different solid volume fractions. By taking the assumption that the elementary particles, that are responsible for the suspension gel-like structure have a spherical shape, The yield stress and the macroscopic elastic modulus of the network are function of the state of aggregating particles, characterized by the fractal dimension and of the mechanical properties of the particles making up the network. This approach relies on the assumption that the primary particles, responsible


(a) (b) (c) (d)

Fig. 11 Evolution of the crystal suspension during the crystallization process (a-b) nucleation and crystal growth: formation of the suspension (c) Suspension thickening (d) Crystallizer jamming.

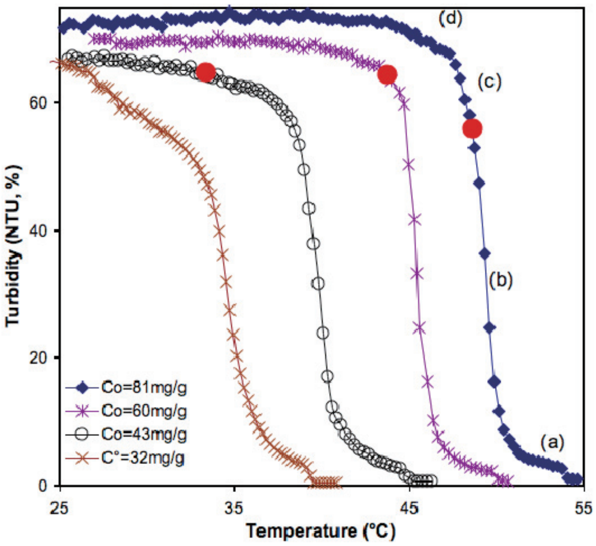

Fig. 12 Evolution of solution tubidity during the crystallization process. The letters (from a to b) correspond to the photographs shown in **Fig. 11**.

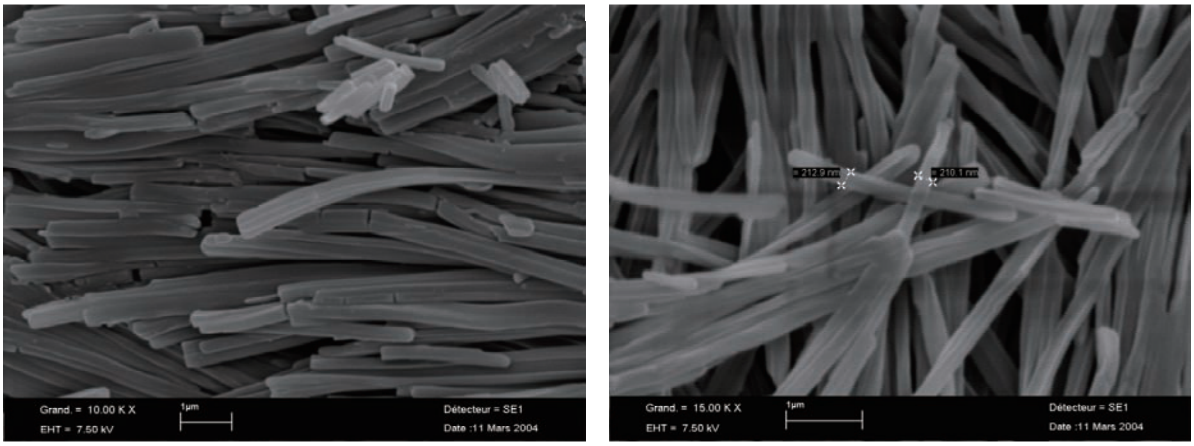

Fig. 13 MEB photomicrographs of eflucimibe crystals obtained at the end of the process.

of the suspension gel-like behavior, have a spherical shape. Knowledge of the fractal dimension as well as the dependence of the rheological properties of the particles with the particle volume fraction are used to infer the mechanism by which the network was formed. (Brown et al. 1985, Buscall 1988) .

Suspension rheology experiments were performed in simple shear and oscillatory mode at 298K in a Bohlin rheometer equipped with parallel-grooved plates (gap=1.2mm, d=2.5mm) to avoid any sliding effect on the surface of the plate. A solvent trap was used to limit solvent evaporation. Before measurements, the suspensions were pre-sheared at 20℃ at γ=60 s^{-1} for 1min followed by a recovery period of 10s. This pre-shear was indented to eliminate irreversible structures that can be formed during storage and suspension handling. This procedure allows to define a reference state of the suspension and to ensure a good reproducibility of rheological measurements.

Specific evolution of the rheological properties of the suspension are given in **Fig. 13**.

In the case of eflucimibe suspensions, the evolution of the shear rate is reasonably well described by the Herschel-Buckley model :

$$\begin{aligned}&\frac{d\gamma}{dt}=0 \quad for \quad \tau<\tau_c\\&\frac{d\gamma}{dt}>0 \quad and \quad \tau=\tau_c+K\left(\frac{d\gamma}{dt}\right)^n \quad for \quad \tau>\tau_c\end{aligned} \qquad (3)$$

where τ_c is the yield stress, K and n are the model factors.

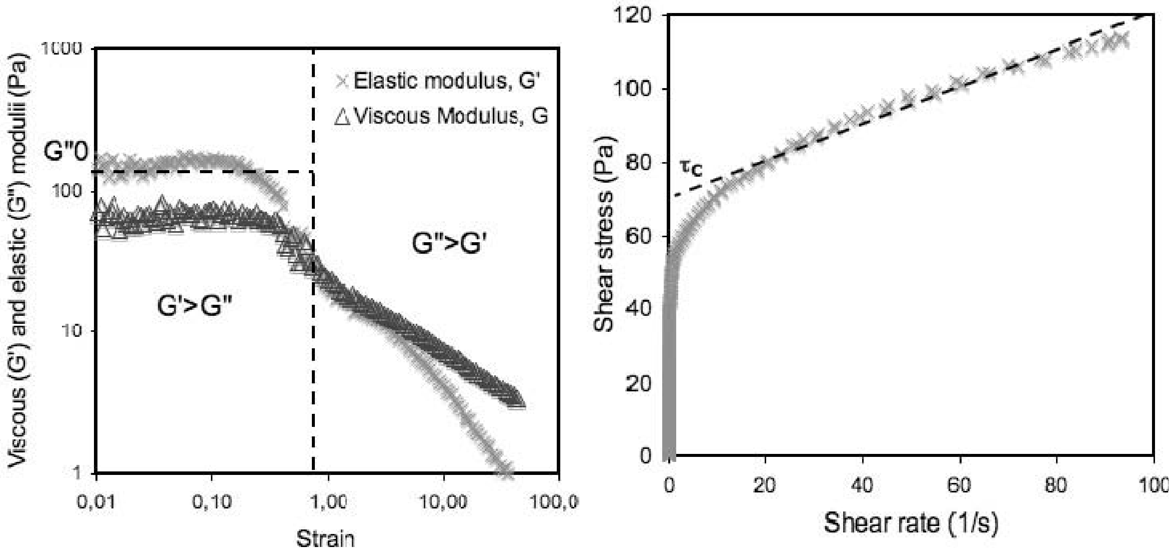

(a) (b)

Fig. 14 Eflucimibe suspension rheology for a volume fraction of solids $\phi = 4\%$ (a) Oscillatory strain rheology (b) Simple shear rheology.

It was found that the rheological properties of the suspension are strongly dependent on solid volume fraction. **Table 3** summarizes the elastic modulii and yield stresses obtained for different concentrations.

This table shows that the yield stress and the elastic modulii increase when the solid volume fraction is raised. The low values of the elastic modulii and the yield stress suggest that the particle network is very weak. In addition, as observed during crystallization experiments, the yield stress, and thus the crystal network, disappear for a solid volume fraction lower than 2%. In addition, the visco-elastic properties of the suspension (i.e. τ_c and G'_0) are directly linked to the interparticle forces that build up the network. Theoretical development and experimental rheological studies (Brown 1988) suggest a power law dependence of the elastic modulus and the yield stress to the solid volume fraction. The exponent of the power law for the elastic modulus and the yield stress is linked to the aggregation mechanism and to the fractal dimension D_f by the following equations (Buscal et al. 1988):

$$G_0' \propto \phi^n \rightarrow n = \frac{4.2}{3 - D_f} \qquad (4)$$

$$\tau_c \propto \phi^m \rightarrow m = \frac{3}{3 - D_f} \qquad (5)$$

The macroscopic elastic modulus (Eq. 4) is a function of both the spatial distribution of the aggregating particles, characterized by the fractal dimension D_f, and of the mechanical properties of the particles making of the network. The evolution of G'_0 versus ϕ is used to infer the mechanism by which the network was built. The m value was predicted to be 4.5 and 3.5 for a RLCA (reaction limited) and DLCA (diffusion limited) mechanisms, respectively.

Fitting of the power law on the experimental data are given in **Table 4**.

The results obtained for the elastic modulus scaling exponent m=3.4 is in good agreement with the theoretical values of a DLCA process. Moreover, the fractal dimension obtained by the two approaches are very close, Df = 1.7, suggesting a loose structure of the network.

Due to the weakness of the particles, it was impossible to sample the suspension and to analyze the particles by microscopy. As the shape and size of the primary particles are unknown, all the attempts made to model the particle organization in the network were unsuccessful. However, if a spherical shape can be supposed for the primary agglomerates, with a typical close packing of around 74%, it is found that, in order to reach a gelation threshold at 2%, the primary spherical particles have to be very porous with a void fraction around 70 to 80%. This observation is consistent with the fact that the particulate network is built with spherultic crystals (urchin-like crystals).

Table 3 Evolution of elastic modulii and yield stresses with the solid volume fraction of eflucimibe suspensions

Solid Volume Fraction, ϕ_s	**Elastic Modulus, G_0' (Pa)**	**Yield Stress, τ_c (Pa)**
0.019	-	-
0.022	164.2	7.0
0.028	420.5	9.1
0.035	744.4	17.2
0.041	1384.4	28.2
0.049	2366.1	37.5

Table 4 Results of the power law fitting of G'_0 and τ_c vs. ϕ

	Exponent	R^2	Df
G'_0	3.4 ± 0.2	0.996	1.7 ± 0.1
τ_c	2.2 ± 0.3	0.987	1.8 ± 0.1

5. Unconventional crystallization process : microfluidic tools

To get a better understanding of the process, crystallization experiments were performed in a microfluidic crystallizer. The “micro-crystallizer” consists in a 3m long crystallization channel with 220x100 μm cross sectional dimension. The microfluidic chip was designed in this study and built by Micronit company. In this system, droplets containing the organic solvent and solute are generated in water, each droplet acts as an independent crystallization container. The size of the droplet, and thus the crystallization volume can be finely tuned by altering the volume flow rate of each phase. Two phase flow microfluidic experiments, performed with five organic solvent in water, have enable to establish a correlation for predicting the droplet size from the physicochemical properties of the fluids and the volumetric flow rate of each phase. The obtained correlation (eq. 1) allows us to predict the droplet size with a precision around 10%.

$$\frac{L_{drop}}{d_{Channel}} = 1.5\left(\frac{Q_{disp}}{Q_{cont}}\right)^{0.2} Ca^{-0.2}\left(\frac{\mu_{disp}}{\mu_{cont}}\right)^{-0.2}\left(\frac{\rho_{disp}}{\rho_{cont}}\right)^{1/3} \quad (6)$$

In this study, as the dispersed and continuous phases are immiscible, a temperature gradient is applied to the chip to induce crystallization. Consequently, two temperatures regions, controlled by Peltier elements, have been defined: a heated zone (at the droplet generation) to avoid channels clogging, and a cooled region to induce nucleation.

The system is observed under microscope (Axio observer – Zeiss) and images are acquired using a sensitive CCD color camera (Sensicam PCO). The experimental setup is presented in **Fig. 15**.

To study the crystallization of eflucimibe in octanol, up to 2000 droplets were generated at 45℃ with a flow rate of 200μ l.h − 1 and 500μ l.h − 1 for octanol and water respectively. In this experiment, eflucimibe concentration was C°=13.78mg.g^{-1} and corresponds to its solubility in octanol at 40℃. Once the droplets are stored, the system is cooled down to either 20 or 5℃. The solubility of eflucimibe in octanol at 20 and 5℃ is 7.84 and 4,88 mg.g^{-1} respectively.

The first crystals were obtained in the droplet for an induction time of 75min at 20℃ and 45min at 5℃. Photographs of the crystals obtained at 20 and 5℃ are given in **Fig. 16**.

At 20℃ (**Fig. 16a**), the spherulitic crystal tends to occupy all the space available in the droplet. If the droplet flows in the channel, the crystal blocks the flow inside the droplet. These observations, at the micrometric scale, can be linked to the rheological behavior of the suspension obtained in a stirred crystallizer. At 5℃, as shown in **Fig. 16b**, the crystals obtained are still spherulites but with a denser structure which might be easier to handle than in a crystallizer.

In that case, if the droplet flows inside the channel, the crystal moves freely inside the droplet.

In addition, nucleation kinetics and crystal growth kinetics have been determined in this system. Nucleation kinetics of eflucimibe in octanol has been deter-

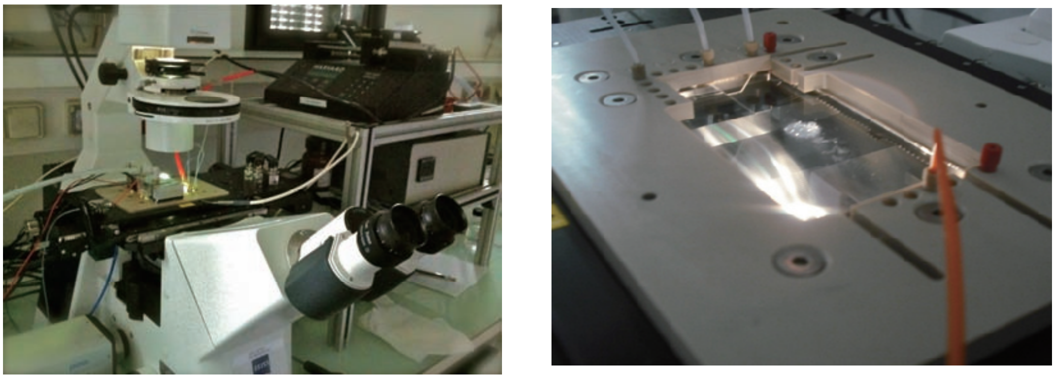

Fig. 15 (a) Experimental setup (b) microfluidic chip and housing.

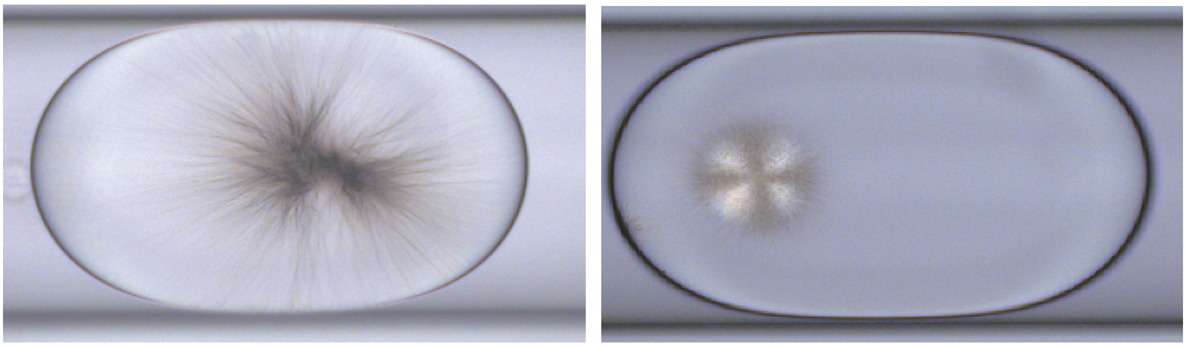

Fig. 16 Photographs of Eflucimibe crystals in octanol droplet under flow at (a) T=20℃ (b-c) T=5℃.

mined by counting the number of appearing crystals as a function of time in 2000 droplets generated at 45 ℃ and quenched to 20℃. The evolution of the number of uncrystallized droplets as a function of time is given in **Fig. 17a**. As shown in this figure, nucleation rate is not of first order and cannot be described by a classical Poisson distribution.

To describe the heterogeneous origin of the nucleation process, the model of Pound and Lamer (Pond and Lamer 1952) has been applied to the eflucimibe/octanol system. This approach provides a good fit of the experimental data and allows us to determine, in a single experiment, both heterogeneous and homogeneous nucleation rates. At low time scale, eflucimibe in droplets containing impurities will crystallize first and thus yields a rapid initial rate (i.e. heterogeneous nucleation rate). As these droplets are depleted, leaving only the droplets that are free of impurities, the rate will fall off, which allows to determine the homogeneous nucleation rate. The different nucleation rate thus obtained are given in **Table 5**.

Once a crystal is formed in a droplet, it is also possible to isolate droplets for measuring the crystal growth rate as a function of time. As an example, evolution of the crystal size in a droplet is plotted as a function of time in **Fig. 17b**. The radius scales with time as $t^{1/2}$, characteristic of diffusion-controlled growth.

In addition, using the crystal density determined by helium pycnometry (ρ_c=11200 kg/m^3), and assuming that the spherulites have a spherical shape, the void fraction of the crystals obtained at the end of the process (i.e the solution is at the thermodynamic equilibrium) can be calculated using the following expression:

$$\varepsilon = 1 - \frac{\rho_{spherulite}}{\rho_c} = 1 - \frac{(m_s^i - m_s^f)V_{spherulite}}{\rho_c} \qquad (7)$$

Where m_s^i and m_s^f are respectively, the mass of eflucimibe in the solution before and after crystallization (ms = C^*V_{drop}), $V_{spherulite}$ is the spherulite volume ($V_{spherulite}=\pi d_3/6$). The void fraction obtained is 73%, which is in agreement with the void fraction previously supposed for the particles responsible of the crystallizer jamming.

This example clearly shows that microfluidic tools coupled with analytical techniques can be very useful to study, qualitatively and quantitatively, the crystallization process of complex structures under flow at a microscopic scale.

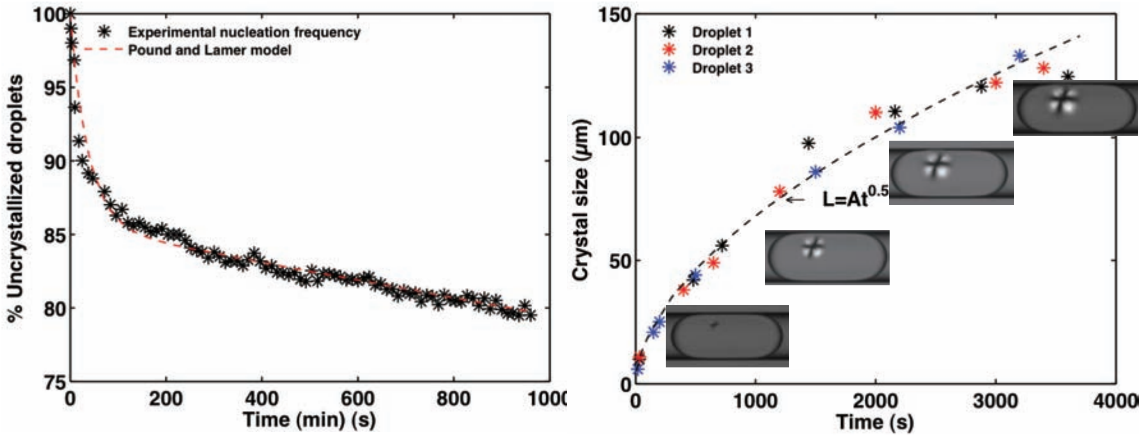

Fig. 17 Nucleation and growth of eflucimibe crystals in octanol droplet s(a) Nucleation rate : ratio of uncrystallized droplet vs. time and (b) growth kinetics of eflucimibe crystals (crystal size vs. time).

Table 5 Nucleation rate constant of the Pound and Lamer model

m*	J homogeneous (s^{-1})	J heterogeneous (s^{-1})
0.16	1.23 10^{-6}	4.24 10^{-4}

* m : mean number of impurities per droplet

Concluding remarks

In this study, we have shown that a multidisciplinary approach: from the molecules (solid state analysis, thermodynamics...) to the particles (rheology, microfluidic...) allows us to define the optimum operating conditions of a crystallization process to produce an API with a good yield, chemical purity and polymorphic purity. However, at this point, the suspensions obtained have poor handling properties such as flowability, filterability, bulk density... But, the results obtained at the micrometric scale show that eflucimibe crystallizes as spherulites under gentle hydrodynamic conditions (static or laminar flow in the microfluidic apparatus).

By taking into consideration all these observations, seeded crystallizations have been performed with low mixing intensity (N<50rpm). As shown in **Fig. 18**, the particles thus obtained are nearly spherical particles of polymorph A and present good flowability and filterability.

To conclude, we present in this paper a generic methodology for the crystallization of complex API: from molecular level studies to the crystallization process itself. In addition, we have shown how microfluidic tools, coupled with classical analysis or characterization techniques, can provide useful additional information about nucleation, growth and agglomeration of crystals.

Nomenclature

C^*	Saturation concentration	[mg/g]
C^o	Initial concentration	[mg/g]
Ca	Capillary number	[-]
Df	Fractal dimension	[-]
ΔG	Gibbs free energy difference	[J/mol]
G'	Elastic modulus	[Pa]
G''	Viscous modulus	[Pa]
J	Nucleation rate	[number/m^3/s]
Q	Volumetric flow rate	[m^3/s]
r	Nucleus radius	[m]
Ra	Molar fraction of ethanol in the solvent mixture on a solute free asis	
S	Supersaturation	[-]
T	Temperature	[℃]
V	Volume	[m^3]
w	Mass Fraction	[-]

Greek letters

μ	Viscosity	[Pa.s]
γ_{sl}	Solid-liquid interfacial tension	[mJ/m]
υ	Molcular volume	[m^3]
τ_c	Yield stress	[Pa]
ρ	Density	[Kg/m^3]
φ	Volume fraciton	[-]
ε	Void fraction	[-]

Subscripts

cont	Continus phase

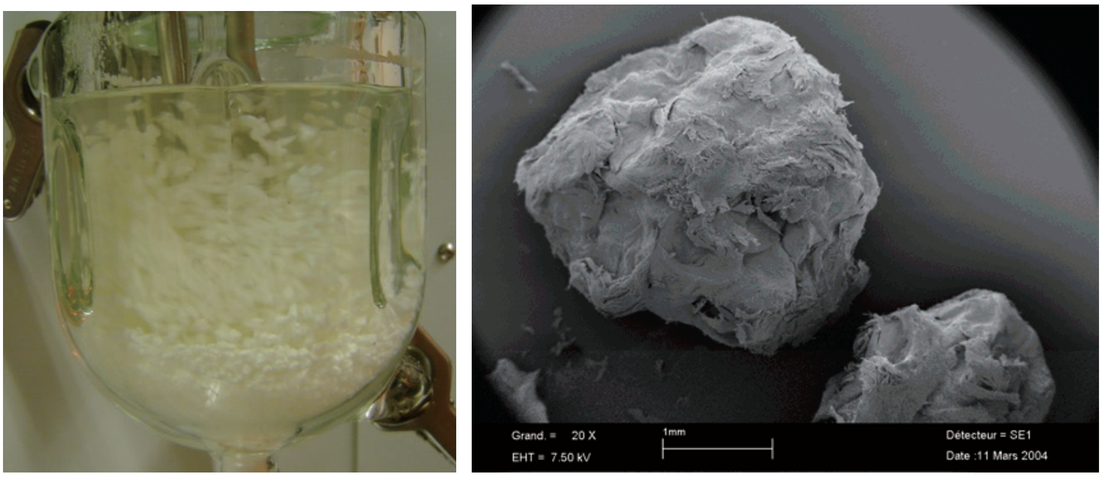

Fig. 18 Photograh of efflucimibe agglomerates (a) In the crystallizer (b) TEM images of agglomerates.

disp	Dispersed phase
crit	Critical
nucl	Nucleation
i	Component i

Acknowledgments

The author would like to thank Pierre Fabre Company for supporting this study and Richard Pena for his help in the solid state analysis.

References

Brown, W.D. and Ball, R.C. (1985): Computer simulation of chemically limited aggregation, J.Phys. A18, L517-L521

Buscall R., P. Mills, J.W. Goodwin, D.W. and Lawson, J. (1988): Scalling behavior of the rheology of aggregate networks formed from colloidal particles, J.Chem. Soc. Faraday Trans., 1, 84, pp.4249-4260.

Bustamante P, Navarro S, Romero S, Escalera B. (2002): Thermodynamic origin of the solubility profile of drugs showing one or two maxima against the polarity of aqueaous and non aqueous mixtures: Niflumic acid and caffeine, J PharmSci., 91, pp.874 883.

Domananska U. (1989): Solubility of acety-substitued naphtols in binary solvent mixtures, Fluid Phase Equilib., 55, pp.125-145.

Kashchiev, D. (2000): Nucleation, Basic Theory with Applications, Butterworth - Heinemann, Oxford.

Pound G. and La Mer V.K. (1952): Kinetics of Crystalline Nucleus Formation in Supercooled Liquid Tin, J. Am Chem. Soc., 74, pp.2323-2332.

Ribet, J. P., Pena, R., Chauvet, A., Patoiseau, J. F., Autin, J. M., Segonds, R., Basquin, M. and Autret, J. M. (2002): Polymorphisme cristallin de l'éflucimibe. Ann. Pharm. Fr., 60, pp.177-186.

Ulrich, J. and Strege, C. (2002): Some aspects of the importance of metastable zone width and nucleation in industrial crystallizers, J. Cryst. Growth, 237-239, pp.2130-2135.

Teychené, S., Autret, J. M., and Biscans, B. (2004): Crystalligation of Efluccimibe Drug in a Solvent Mixture, Effects of Process Conditions on Polymorphism Crystal Growth & Design 4 (5), pp.971 977.

Teychene, S., Autret, J. M., and Biscans, B. (2006): Determination of solubility profiles of eflucimibe polymorphs: Experimental and modeling, J. Pharm. Sci., 95 (4), pp.871-882.

Teychene, S. and Biscans, B. (2008): Nucleation kinetics of polymorphs: Induction period and interfacial energy measurements Crystal Growth & Des., 8 (4), pp.1133-1139.

Teychene, S., Autret, J. M. and; Biscans, B. (2006): Influence of crystallization conditions on rheology and microstructure of dense suspensions of crystals of eflucimibe, Chem. Eng. & Technol., 29 (2), pp.251-256.

Yu, L., Reutzel-Edens, S. M. and Mitchell, C. A. (2000): Crystallization and Polymorphism of Conformationally Flexible Molecules: Problems, Patterns, and Strategies, Org. Proc. Res. Dev., 4, pp.396 – 402.

Zettlemoyer, A. C. (1969): "Nucleation", Marcel-Dekker, New York,.

Author's short biography

S. Teychené

S. Teychené is an assistant professor in chemical engineering at the Laboratoire de Génie Chimique de Toulouse, Université de Toulouse (France). He received his engineer degree in chemical and environmental engineering in Institut National de Sciences Appliquées (INSA, Toulouse) in 2000, and his master degree in chemical engineering in 2001. He holds a Ph. D degree in chemical engineering from Toulouse university.

He joined the Laboratoire de Génie Chimique de Toulouse in 2006 in the team of Beatrice Biscans. His research interests are directed towards the thermodynamic and kinetics aspects of nucleation and phase transitions in the crystallization processes of organic coupounds.

Béatrice Biscans

Béatrice Biscans, Toulouse, France. Dr Béatrice Biscans obtained her degree in Chemical Engineering from the National Polytechnical Institute of Toulouse in 1982 and was awarded for her PhD in chemical and process engineering in 1985. After a post-doctoral position, she is working for the National Centre for Scientific Research (CNRS) since 1987 in the Chemical Engineering Laboratory of Toulouse (LGC). Her research is focused on Solid and Particles Processes. She is leading a group working on crystallization and formulation processes and nanoparticles production. She is today the Director of the Chemical Engineering Laboratory of Toulouse, as well as the President of the Working Party on Crystallization of the European Federation of Chemical Engineering and of the Working Party on Powders and Particles of the French Society of Chemical Engineering. She has an official position in CNRS as the French representative expert in Chemical Engineering.

Information Articles

The 45th Symposium on Powder Technology

Hosokawa Powder Technology Foundation held the 45th Symposium on Powder Technology on August 30th, 2011 at Senri Hankyu Hotel with the support of Hosokawa Micron Corporation. The symposium attracted a large attendance of 174 including 22 academic people. The theme of the symposium was "Construction of Nanoparticle Technology and Evolution to Practical Realization". Fruitful discussion took place as usual.

• Opening Address	Prof. Hiroaki Masuda (Kyoto Univ.)
Session 1 Chairperson: Prof. Jusuke Hidaka (Doshisha Univ.)	
• Control of Shape and Porous Structure of Nanoparticles for Material Application	Kikuo Okuyama (Hiroshima Univ.)
• Dispersion behavior control of nanoparticles and its applications	Hidehiro Kamiya (Tokyo University of Agriculture and Technology)
Session 2 Chairperson: Prof. Ko Higashitani (Kyoto Univ.)	
• Coating, drying, and microstructuring of suspensions	Masato Yamamura (Kyushu Institute of Technology)
• Development and Application of High Performance Graphite Material	Tetsuro Tojo (Toyo Tanso Co. Ltd.)
Session 3 Chairperson: Prof. Makio Naito (Osaka Univ.)	
• High Thermal Conductive Epoxy Composite with Controlled Nanostructures	Yoshitaka Takezawa (Hitachi Chemical Co., Ltd.)
• New powder processing for the development and improvement of manufacturing technologies of battery materials – Particle design technology for the advanced functioning of lithium ion rechargeable battery –	Toyokazu Yokoyama (Hosokawa Micron Corp.)
• Closing Address	Yoshio Hosokawa (Hosokawa Micron Corporation)

GENERAL INFORMATION

HISTORY OF THE JOURNAL

In the history of KONA Powder and Particle Journal, two organizations have been playing an important role. The one is the Council of Powder Technology, Japan (CPT) and the other is the Hosokawa Powder Technology Foundation (Hosokawa Foundation). The CPT was established in 1969 by Hosokawa Micron Corporation as a nonprofit organization to enhance the activities of research and development on powder science and technology. The Hosokawa Foundation was established in 1991 as a public-service corporation approved by the Ministry of Education, Culture, Sport, Science and Technology of Japan. The issues from No.1 (1983) to No.12 (1994) of KONA were published by CPT and the issues from No.13 (1995) by the Hosokawa Foundation.

The aim of KONA in the early days was to introduce excellent Japanese papers to the world and thus KONA consisted of papers recommended by some Japanese academic societies and translated from Japanese to English. From the issue of No.8, the CPT changed its editorial policy to internationalize the KONA and to incorporate papers by authors throughout the world in addition to translated papers. In response to this change, three editorial blocks have been organized in the world; Asian-Oceania, American and European. The policy and system have not changed even after the Hosokawa Foundation has taken over from the CPT. From the issue of No.27(2009), publication of translated papers has been terminated and only original papers have been published. The CPT is active still today and collaborates with the Hosokawa Foundation.

AIMS AND SCOPE

KONA publishes papers in a broad field of powder science and technology, ranging from fundamental principles to practical applications. The papers descriping technological experiences and critical reviews of existing knowledge in special areas are also welcome.

The submitted papers are published only when they are judged by the Editor to contribute to the progress of powder science and technology, and approved by any of the three Editorial Committees. The paper submitted to the Editorial Secretariat should not have been previously published except .

CATEGORY OF PAPERS

- Invited papers
  Original research and review papers invited by the KONA Editorial Committees.
- Contributed papers
  Original research and review papers submitted to the KONA Editorial Committees, and refereed by the Editors.

SUBMISSON OF PAPERS

Papers should be sent to each KONA Editorial Secretariat.

- Asia/Oceania E'ditorial Secretariat
  Mr. T. Kawamura
  Hosokawa Powder Technology Foundation
  Shodai-Tajika,1-9, Hirakata, 573-1132 Japan
- Europe/Africa E'ditorial Secretariat
  Dr. J. Stein or Mrs. P. Krubeck
  Hosokawa Micron
  Division of Hosokawa Alpine AG.
  Welserstr. 9-11, 51149 Koeln, GERMANY
- Americas Editorial Secretariat
  Dr. C.C. Huang
  Hosokawa Micron Powder Systems
  10 Chatham Road, Summit NJ 07901 USA

Publication in KONA Powder and Particle Journal is free of charge.

PUBLICATION SCHEDULE

KONA is published annually. The publication date is December 25th.

SUBSCRIPTION

KONA Powder and Particle Journal is distributed free of charge to senior researchers at universities and laboratories as well as to institutions and libraries in the field throughout the world. The publisher is always glad to consider the addition of names of those who want to obtain this journal regularly to the mailing list. Distribution of KONA is made by each Secretariat.

Free electronic publication of KONA Powder and Particle Journal is available in
http://www.kona.or.jp

INSTRUCTIONS TO AUTHORS

(1) Manuscript format

- Electric files should be submitted to the Editorial Secretariat by online. Authors' short biography and photograph should be attached to the final version.
- The structure of manuscripts should follow the following order; title, authors, affiliations, abstract, keywords, main text, (acknowledgement), (appendix), (nomenclature), references. The items with parentheses are not mandatory. The text should be in single-column format. Figures and tables can be imported into the main text. If figures and table are collated in a separate section at the end of the article, indicate their approximate locations directly in the text. If symbols are defined in a nomenclature section, symbols and units should be listed in alphabetical order with their definition and dimensions in SI units If symbols are not defined in a nomenclature section, they should be defined in the text.
- Full postal addresses must be given for all the authors. Indicate the corresponding author by the mark“*” after the name. Telephone and fax numbers and e-mail address should be provided for the corresponding author.
- Abstract should not exceed 200 words.
- The appropriate number of keywords is 5 or 6.
- Symbols and units should be listed in alphabetical order with their definition and dimensions in SI units.
- Concerning references, either the numbering system or the alphabetical system should be adopted. In the numbering system, references should be numbered in sequence starting at the beginning of the paper. References should be given in the following form:
  1)Carslaw, H. C. and Jaeger, J. C.(1960): “Conduction of Heat in Solids” , 2nd ed., Clarendon Press, Oxford, England.
  2)Howell, P. A. (1963):US Patent, 3, 334,603
  3)Jia, R. (1990): “Surface Properties of Coal and Their Role in Fine Coal Processing,” Ph.D. Dissertation, University of California at Berkeley.
  4)Zhang, N. and Rosato, A. D. (2006): Experiments and Simulations on Vibration Induced Densification of Bulk Solids, KONA Powder and Particle Journal, No.24, pp.93-103.
  In the alphabetical system, all publications cited in the text should be presented in alphabetical order of the authors. In the text make references by name and year, e.g. Zhang and Rosato (2006). Reference to papers with more than 3 authors should show the name of the first author followed by “et al.”

(2) Reprint

- The authors shall receive 50 free reprints. Additional reprints will be furnished when ordered with return of galley proof.

(3) Copyright and permission

- Original papers submitted for publication become immediately the property of the Hosokawa Powder Technology Foundation and remain so unless withdrawn by the author prior to acceptance for publication or unless released by the Editor. The original papers in KONA should not be reproduced nor published in any form without the written permission of the Hosokawa Foundation. Authors are responsible for obtaining permission from the copyright holder to reproduce any figures and photos for which copyright exists.

HOSOKAWA MICRON

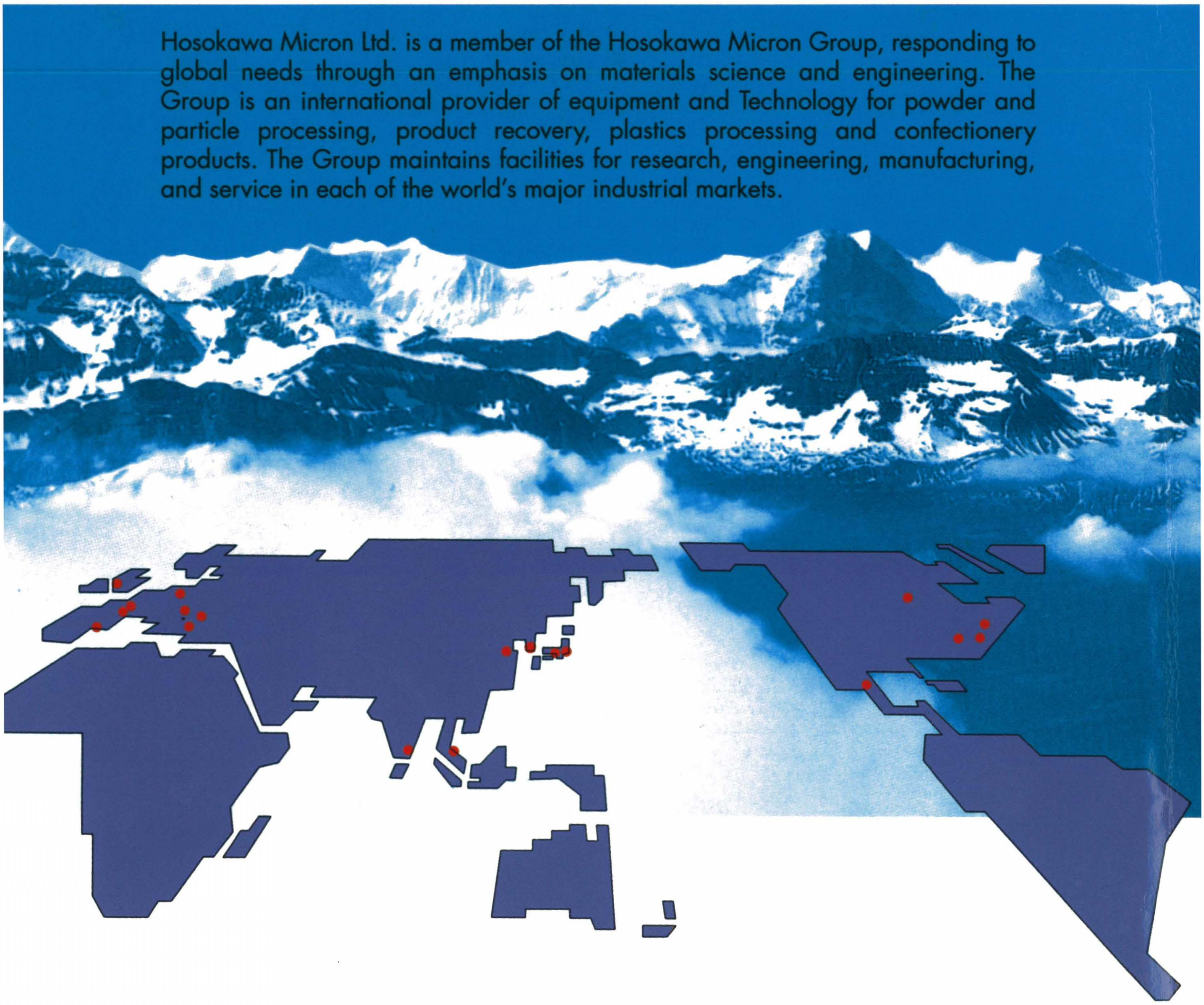

Hosokawa Micron Ltd. is a member of the Hosokawa Micron Group, responding to global needs through an emphasis on materials science and engineering. The Group is an international provider of equipment and Technology for powder and particle processing, product recovery, plastics processing and confectionery products. The Group maintains facilities for research, engineering, manufacturing, and service in each of the world's major industrial markets.

Process Technologies for Tomorrow

HOSOKAWA MICRON

Headquarter Locations;
HOSOKAWA MICRON CORPORATION
http://www.hosokawamicron.co.jp